Experimental and theoretical Investigation of a radiative flat heat pipe based heat exchanger for waste heat recovery in the steel industry

A thesis submitted for the degree of Doctor of Philosophy (PhD)

By:

Sulaiman Almahmoud

Department: of Mechanical, Aerospace and Civil Engineering

College of Engineering, Design and Physical Sciences

Brunel University London

October 2019

Abstract

Waste heat recovery in an energy-intensive industry such as steel industry contributes in enhancing energy efficiency, saving fuel bills, and reducing carbon dioxide emissions. Waste Heat recovery by radiation from hot sources is one of the most challenging applications for the state-of-the-art waste heat recovery technologies.

The main objective of this study is to examine and characterise a radiative heat pipe as a viable solution for waste heat recovery in the steel industry. The research consisted of examining experimentally and theoretically two heat pipe heat exchanger systems.

The first heat pipe was a lab-scale single radiative heat pipe made of stainless steel of 1 m long. The heat pipe was cooled by a water flow through a double pipe heat exchanger at the condenser section. The thermal performance of the radiative single heat pipe was investigated by testing it in a laboratory scale kiln. The kiln consisted of ceramic heaters installed at the bottom and insulted walls. The single heat pipe was studied at different heater temperatures and inclination angles. The effect of the emissivity of the heat pipe on heat recovery and thermal performance was also investigated. The influence of each factor was analysed separately showing a significant impact on the heat recovery.

The other system was a flat heat pipe heat exchanger (FHP). The FHP consisted of parallel stainless-steel tubes connected by a bottom collector and a shell and tube top header. The structure of the heat pipe heat exchanger was attached to a flat stainless-steel sheet at the back forming a flat-shape heat pipe heat exchanger. The FHP was cooled by a water flow through the condenser. The FHP was mounted on a special designed stand to facilitate its testing at different heights and inclination angles. The FHP was tested in laboratory conditions to recover the heat from electrical heaters simulating hot steel to assess its heat recovery potential. In addition, the FHP was tested at a steel factory in real conditions at different steel temperatures between 450 °C and 600 °C.

A theoretical modelling tool was built to predict the thermal performance of the single heat pipe and the FHP, each. The theoretical modelling was based on electrical analogy approach, and by applying the most appropriate correlations of two-phase heat transfer based on experimental evaluation. The theoretical heat recovery results were compared with the experimental results, and showed a good agreement within an error of less than 10% for the single heat pipe and 30% for the FHP

The research outcomes demonstrated that the FHP is a novel technology to enhance the energy efficiency in the steel industry by reducing the energy consumption used to power cooling fans and energy used for heating purposes. The validated theoretical modelling tool can be used to predict the performance of the FHP for waste heat recovery by radiation in other industries.

Declaration

No part of this thesis has been submitted in support of an application for any degree or qualification of Brunel University London or any other University or Institute of Learning.

Acknowledgment

First, I would like to express my sincere gratitude and appreciation to my supervisor Prof. Hussam Jouhara who has offered me the opportunity of studying a PhD degree in the field of heat pipe based heat exchangers. I appreciate his tremendous support and invaluable comments and guidance. I appreciate his encouragement, motivating, and being available to assist me anytime. I learned from him a lot in the field of heat pipes, and enabled me to overcome challenges.

I would like also to thank Prof. Brian Axcell with a lot of appreciation for his valuable suggestions and advice.

I would like to thank all the members in Prof. Jouhara's research group and special thanks to my friend Amisha Chauhan for her support during my PhD study.

I would like to thank Bertrand Delpech for his help on conducting CAD designs and setting-up the experiments.

I would like to thank Darem Ahmad for his support in the laboratory, and Lujean Ahmad for her warm support.

Finally, I would like to thank my family with appreciation for their support and encouragement during my PhD study.

Publications

Published Journal papers

[1]. Almahmoud S, Jouhara H. Experimental and theoretical investigation on a radiative flat heat pipe heat exchanger. **Energy 2019;**174:972–84. doi:10.1016/j.energy.2019.03.027.

[2]. Jouhara H, Almahmoud S, Chauhan A, Delpech B, Bianchi G, Tassou SA, et al. Experimental and theoretical investigation of a flat heat pipe heat exchanger for waste heat recovery in the steel industry. **Energy 2017;**141:1928–39. doi:10.1016/j.energy.2017.10.142.

[3]. Jouhara H, Almahmoud S, Chauhan A, Delpech B, Nannou T, Tassou SA, et al. Experimental investigation on a flat heat pipe heat exchanger for waste heat recovery in steel industry. **Energy Procedia**, vol. 123, **2017**. doi:10.1016/j.egypro.2017.07.262.

[4]. Jouhara H, Chauhan A, Nannou T, Almahmoud S, Delpech B, Wrobel LC. Heat pipe based systems - Advances and applications. **Energy 2017;**128. doi:10.1016/j.energy.2017.04.028.

[5]. Jouhara H, Khordehgah N, Almahmoud S, Delpech B, Chauhan A, Tassou SA. Waste heat recovery technologies and applications. **Therm Sci Eng Prog 2018**;6. doi:10.1016/j.tsep.**2018**.04.017.

[6]. Jouhara H, Khordehgah N, Serey N, Almahmoud S, Lester SP, Machen D, et al. Applications and thermal management of rechargeable batteries for industrial applications. **Energy 2019.** doi:10.1016/j.energy.2018.12.218.

[7]. Delpech B, Milani M, Montorsi L, Boscardin D, Chauhan A, Almahmoud S, et al. Energy efficiency enhancement and waste heat recovery in industrial processes by means of the heat pipe technology: Case of the ceramic industry. **Energy 2018**;158. doi:10.1016/j.energy.2018.06.041.

[8]. Guichet V, Almahmoud S, Jouhara H. Nucleate pool boiling heat transfer in wickless heat pipes (two-phase closed thermosyphons): a critical review of correlations. **Therm Sci Eng Prog 2019**;13:100384. doi:10.1016/j.tsep.2019.100384.

International conference papers

[1]. International Conference on Sustainable Energy Use in Food Chains-ICSEF2017 - Symposium on 'Heat Recovery and Efficient Conversion and Utilization of Waste Heat',2017, UK, "Experimental investigation on a flat heat pipe heat exchanger for waste heat recovery in steel industry"

[2]. International Conference on Advances in Energy Systems and Environmental Engineering 2017- ASEE17, 2017, Poland, “Experimental and theoretical investigation on a flat heat pipe heat exchanger for waste heat recovery in steel industry”

[3]. SEEP 2018 11th International Conference On Sustainable Energy & Environmental Protection, 2018, UK, “Experimental investigation on a radiative heat pipe heat exchanger”

[4]. 35th Heat Exchanger Action Group (HEXAG) meeting, 2018, UK, “Experimental investigation on a radiative heat pipe heat exchanger”

[5]. 36th Heat Exchanger Action Group (HEXAG) meeting, 2019, London, UK, “Experimental investigation on a single radiative laboratory-scale heat pipe heat exchanger”

[6]. International Conference on Advances in Energy Systems and Environmental Engineering 2019- ASEE19, 2019, Poland, “Theoretical investigation on a single radiative laboratory-scale heat pipe heat exchanger”.

The paper won the best paper award by ChemEngineering journal, July 2019.

[7]. International Conference on Advances in Energy Systems and Environmental Engineering 2017- ASEE17, 2017, Poland, “Experimental and theoretical investigation on heat pipe shell and tube heat exchanger”

[8]. International Conference on Advances in Energy Systems and Environmental Engineering 2019- ASEE19, 2019, Poland, “Experimental and analytical investigation of a multi-pass air to water heat pipe heat exchanger performance based on the ε-NTU method”

[9]. International Conference on Advances in Energy Systems and Environmental Engineering 2019 ASEE19, 2019, Poland, “Theoretical investigation on a single radiative laboratory-scale heat pipe heat exchanger”

Table Of Contents

List of Figure

List of Tables

Nomenclature

Symbol	
A	Surface area (m²)
C_p	Specific heat (J/kg.K)
C_{sf}	constant, determined from experimental data
D	Diameter (m)
E	Emitted heat per surface area (W/m²)
F	View factor
F_{12}	View factor between the heaters plate and external surface of the FHP
F_{13}	View factor between the heaters plate and surrounding
F_{21}	View factor between external surface of the FHP and the heaters plate
F_{23}	View factor between external surface of the FHP and surrounding
G	Irradiation (W/m²)
g	Gravitational acceleration (m/s²)
Gr	Grashof number
h	Heat transfer Coefficient (W/m^2. K)
h_{fg}	Latent heat of vaporisation (J/kg)
I	Radiation intensity (W/m²)
J	Radiosity (W/m^2)
Ja	Jakob number
k	Thermal conductivity (W/m. K)
L, l	Length (m)
$\dot{m}$	mass flow rate (kg/s)
N	number of pipes
Nu	Nusselt number
P	Pressure (N/m²)
Pr	Prandtl number
Q	Heat transfer rate (W)
q	Heat flux (W/m²)
R	Thermal resistance (K/W)
r	Radios
Ra	Rayleigh number, $Ra = Gr.Pr$
Re	Reynolds number

T	Temperature (K)

Greek Symbols

α	Absorptivity
ε	Radiation emissivity
θ	Angle from vertical
η	Efficiency
λ	Wavelength (μm)
μ	Dynamic viscosity (kg/m.s)
ρ	Density (kg/m^3)
σ	Surface tension (N/m)
σ_0	Stefan–Boltzmann constant which is equal to 5.67×10^{-8} $\mathrm{W/(m^2.K^4)}$
τ	Transmissivity
φ	Angle from horizontal

Subscripts

c	Condenser section
ci	Corresponds to inner wall of condenser
co	Corresponds to outer wall of condenser
cold	Cooling fluid
cold, in	Cooling fluid inlet
cold, out	Cooling fluid outlet
Cond, e	Evaporator wall conduction
Cond, c	Condenser wall conduction
e	Evaporator
ei	Corresponds to inner wall of evaporator
eo	Corresponds to outer wall of evaporator
f	Film
FHP	Corresponds to Flat Heat Pipe
H	Heat source, heaters
l	Liquid
rad	radiation
surr	surroundings
v	Vapour

Superscripts

n	experimental constant that depends on fluid
λ	spectral

Chapter 1: Introduction

1.1 Motivation

Heat pipe heat exchangers for waste heat recovery applications are a topic of research interest nowadays. The motivation for this research was to characterise and model a novel heat pipe heat exchanger to recover heat by radiation. The initial application for this system was in the steel industry, which is one of the largest energy-consuming industries. The system developed can contribute in reducing the energy demand for heating purposes and, in so doing, reduce the carbon footprint of the plant and increase the overall efficiency of the industrial process. CO_2 emissions varies between 1000 and 2100 kgCO2/t of crude steel depending on the furnace technology [1]. Global steel production emissions are accounting for 2.6 Gt CO_2e which represents 7% of the CO_2 global emission [2,3]. In addition, developing a theoretical modelling tool for the novel heat pipe design offers the opportunity of predicting the performance of the system and facilitating a preliminary evaluation for implementing the system in various applications where a heat source at a temperature higher than 400 °C is available.

1.2 General background on waste heat recovery

Huge amounts of energy are often rejected to the environment by the end of industrial processes, increasing the footprint of greenhouse effects. Moreover, the increase in energy demand has been a global concern. The industrial sector of the UK is responsible for 20% of the country's total energy consumption and 32% of total CO_2 emissions [4]. In addition, 73% of the industrial energy demand is used for heating purposes [4]. The most thermal energy demanding sectors are industries which produce cement, ceramics, iron, steel, glass, chemicals, paper, pulp, food and drink products, and refineries; usually the cost of their thermal processes corresponds to 40% of their total production costs [4]. Furthermore, steel industries are responsible for about 5% of the world's energy consumption. The production of 1 tonne of steel emits 1.9 tonnes of CO_2 [5], with energy costs representing about 30 % of total production costs. Therefore, the recovery of waste heat can reduce the total energy consumption in industries, and minimise the dependency on fossil fuels for heating applications. Furthermore, it can diminish toxic gas emissions leading to decreases in total production costs and improvements in the overall energy efficiency of the plant.

The steel industry comprises complex sequential processes and items of plant. Steel manufacturing processes implement different ovens and furnaces such as coke ovens, blast, oxygen, and electrical arc furnaces, and waste heat recovery sources in the steel industry can be solid product streams such as slag or hot exhaust gases.

Hot flue gases, cooling water and heat losses from equipment and products represent approximately 25-55% of the energy used in electric arc furnaces (EAF) in steelmaking processes [6] but less than 10% of the high-grade waste heat. Exhaust gases are mainly rejected from ovens and furnaces with a temperature up to 1550 °C. Furthermore, molten slag is exhausted with high temperatures of 1450-1550 °C, a potential resource of energy and raw materials [5]. The majority of research currently focuses on technologies for heat recovery from the molten slag and exhaust gases because of their high temperatures. Some steel manufacturing plants recover heat from all of the by-product gases.

However, heat recovery from steel manufacturing processes is a huge challenge due to many difficulties such as the space available for installing heat exchangers and matching the waste heat stream to the heat sink demand. Recovering excess heat from the processes could reduce greenhouse gas emissions and significantly reduce production costs. However, conventional technologies have reached their maximum potential in the area of industrial waste heat recovery. The main challenge they face is the implementation of waste heat recovery units to existing equipment and processes economically with minimal extra costs. Heat pipe-based heat exchangers (HPHEs) are one of the most promising technologies facilitating waste heat recovery. HPHEs have been investigated widely for heat recovery from exhaust gases. Each heat pipe of the heat pipe heat exchanger performs as an individual heat exchanger.

A heat pipe is normally a cylindrical evacuated tube filled with a small amount of working fluid, which transfers heat from one end to the other with a very small temperature difference. When heat is applied to the evaporator section, the working fluid, which is in the liquid phase, evaporates and the vapour then travels passively through the adiabatic section to the condenser. Then the vapour transfers the heat to the condenser surroundings, which causes the condensation of the working fluid. The working fluid then flows back to the evaporator by gravity or by using a wick structure to provide capillary forces. Exhaust gases from by-products in the steel industry are very challenging because they might be corrosive and contaminated with a high content of particles. This harsh environment reduces the life span of heat exchangers and degrades their effectiveness.

Other waste heat sources are the products themselves, which represent more than 50% of the high-temperature heat sources. Although they represent a significant potential waste heat source, they are often neglected as heat sources and the technologies implemented for this purpose are very limited. There are many limitations for utilising technologies for waste heat recovery from the products such as the space availability, the temperature of the industrial environment, the technology and installation costs which might require modifying the production facility uneconomically, and the

intermittence of the production process. These limitations and challenges have minimised the interest in utilising products as a waste heat source.

1.3 The research gap

It can be noted that waste heat sources of temperature higher than 400 °C in industry represent a high potential for direct heat recovery by radiation. Based on the published literature, this field of research has not been investigated sufficiently. The technologies implemented for waste heat recovery by radiation are very exceptional. Furthermore, the implementation of heat pipe technology to recover heat by radiation in real industrial conditions has not been reported in the literature. In addition, there is a gap in the experimental and theoretical modelling of radiation heat transfer for complex geometries. Theoretical modelling for a radiative heat pipe for heat recovery by radiation has not been presented before. Developing a thermal technology, which is capable of heat recovery by radiation from hot sources, and considering the limitations in harsh environments such as the steel industry, contributes significantly in this field of research.

As a result, the main objective of this research is to investigate and characterise a heat pipe based heat exchanger as an efficient solution for waste recovery by thermal radiation.

The aims of this research will be achieved from the following approach:

- A single radiative heat pipe will be tested in a laboratory scale kiln. The experimental work will investigate the key parameters of heat transfer by radiation which are the source temperature, the emissivity of the heat pipe surface, and the view factor for the radiation heat transfer. The findings on the single heat pipe will give deep understanding on the performance of the heat pipe heat exchanger under radiation.
- A full scale radiative flat heat pipe will be tested in the laboratory and factory conditions. The novel flat heat consists of parallel pipe connected by a bottom collector and a top header. The aim of the experiments is to characterise the thermal performance of the flat heat pipe at different sets of conditions.
- To develop a theoretical modelling tool which can predict the thermal performance of the single heat pipe.
- To develop another theoretical modelling tool which can predict the thermal performance of the flat heat pipe.
- The modelling tools include developing a programmed code, which will implement the appropriate correlations available in the literature.
- A semi-empirical and analytical approach will be followed to determine the heat transfer by radiation which will be validated experimentally

- Compare the experimental results of the single and the flat heat pipe with the theoretical predictions to validate the theoretical models.
- The validation the theoretical modelling tool will extend its use in predicting the thermal performance of the system for any new conditions or applications

The research approach is presented in Figure 1-1.

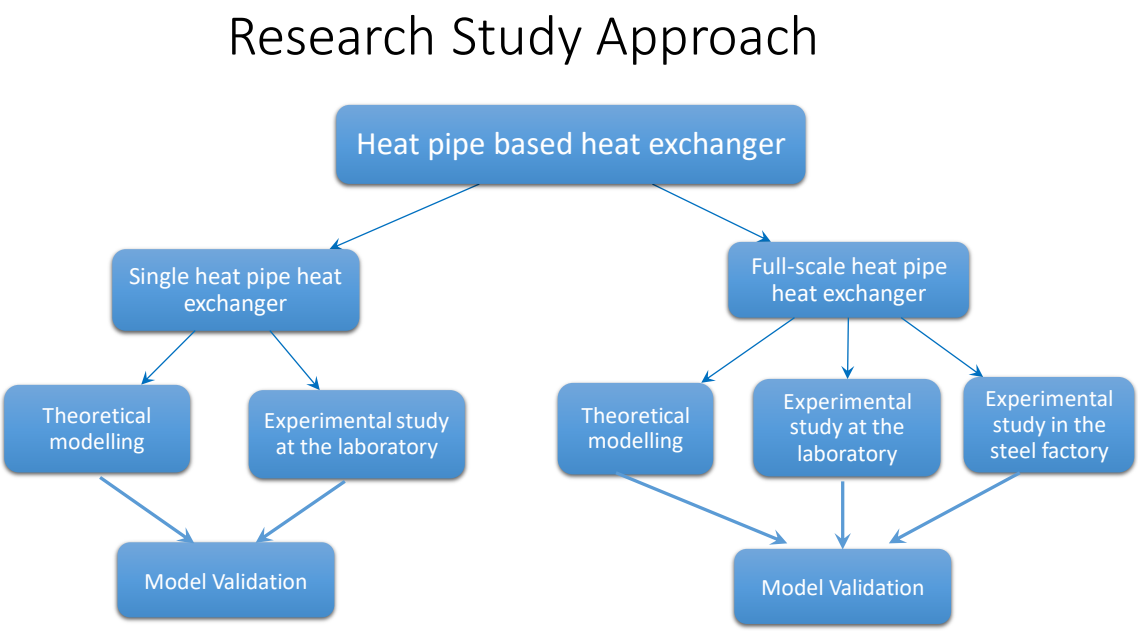

Figure 1-1 Research study approach

This thesis describes the study in the following chapters:

Chapter 1 provides a background on the subject and the main objectives, aims, methodology and overview of the chapters.

Chapter 2 presents the state of the art on waste heat recovery technologies in the steel industry and on the flat heat pipe technology in the literature.

Chapter 3 describes the single radiative heat pipe and the flat heat pipe mechanical design and the experimental apparatus which was constructed to validate the flat heat pipe technology. In addition, it describes the application and the set-up of the flat heat pipe in the factory. It also presents the experimental conditions and instruments used for collecting the results.

Chapter 4 presents the theoretical model and the theoretical approach followed to model the flat heat pipe including correlations used and assumptions. The chapter describes the complexity of the

radiation heat transfer parameters in addition to the two-phase heat transfer in the flat heat pipe and the single-phase heat transfer through the condenser section to the coolant flow.

Chapter 5: presents the experimental and theoretical research outcomes and discusses the results of the study. The chapter also compares and discusses the experimental and theoretical results.

Chapter 6 presents the conclusions of this research and recommendations for the optimisation of the flat heat pipe technology and for future work in this field of research.

Chapter 2: State of the art on waste heat recovery in steel industry and flat heat pipe technology

2.1 Introduction

This chapter presents a general description of the steel manufacturing process, the previous work in waste heat recovery technologies in the steel industry and industrial heat exchangers for waste heat recovery by radiation.

The next section is a general background on heat pipes and their operating principles. This section also presents the common working fluids and casing materials of heat pipes.

The last section is a review and discussion on the previous investigations on heat pipes in various applications.

2.2 Steel industry manufacturing process

Steel manufacturing comprises complex processes. Steel is mainly produced by two routes, the blast furnace and the electric arc furnace. The blast furnace route includes many processes such as coking, sintering, iron making, and rolling processes.

In the coking process, a blend of selected grades of clean coal is fed into the coke oven where it is converted to coke. Then the coke is cooled and graded before it is fed into the blast furnace. The exhaust gas produced during the coking process is used as a fuel in the manufacturing process.

The sintering process agglomerates iron ore fines with coke and limestone and this is heated to form an iron-rich clinker called ‘sinter’. The sintering process saves energy and coke and enhances the furnace efficiency.

In the blast furnace, the main input materials are the sintered iron ore, coke, limestone and other substances. The input materials are charged into the blast furnace from the top, while hot air is blasted into the furnace from the bottom. This process removes chemically the oxygen from molten iron which is fed into the basic oxygen furnace later. The additional products from the blast furnace are hot flue gases and molten slag. The molten slag results from the combination of the limestone with impurities and molten rock from the iron ore and sinter. In the next step which is the basic oxygen furnace, pure oxygen is forced in the basic oxygen furnace to remove the carbon from the iron producing crude steel. The hot gases rejected from the blast furnace and basic oxygen furnace are used in other processes or for power generation.

The other route, which is the electric arc furnace, is used to process scrap steel and galvanised steel without the use of primary raw materials such as iron.

Then the molten steel from the furnaces passes through continuous casters and is cast into a cooled mould. The steel then starts to solidify and it is withdrawn using supporting rolls. After the steel is fully solidified, it is then cut into the desired length and it is sent for further processing as slabs, billets, or blooms. The steel is formed into the desired shape through the hot rolling process which removes any defects in the desired shape of the steel and its quality.

After that the steel product is passed into secondary processes to create the final shape. The secondary processes include cold rolling, machining, thermal treating, coating, joining and pressing.

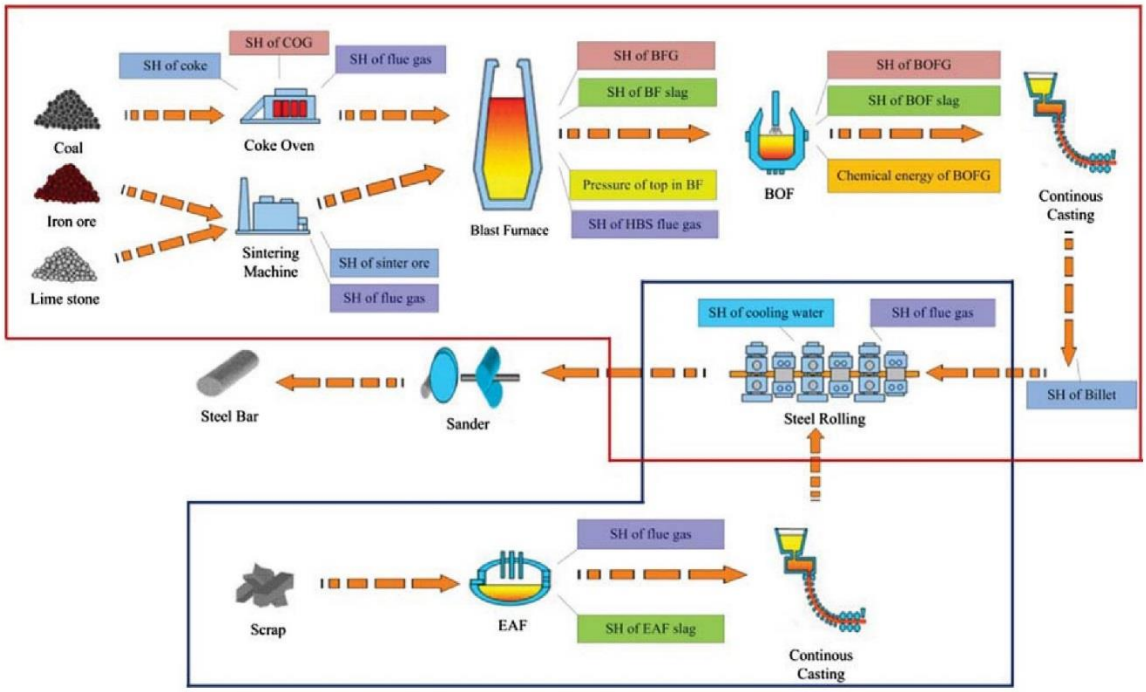

Figure 2-1 Simplified Steel manufacturing routes, processes, and main waste heat energy sources [7]

2.3 State of the art of Steel industry recovery technologies

The majority of research on waste heat recovery in the steel industry is focused on waste heat recovery from molten slag utilising fluidized bed heat exchangers [5]. Four waste heat recovery systems have been investigated: Air blast, Single Drum, Twins Drums, and the Spinning Cup methods; typically these systems have an average efficiency of approximately 50%.

Liu et al. [8] have studied a gravity bed waste heat boiler to recover the heat from slag particles. The research investigated the effect of the slag particles' diameter on the heat recovery efficiency. *Trashorras* et al. [9] studied the performance of a heat recuperator for waste heat recovery from steel

slag. The CFD modelling conducted in the study showed that the heat recuperator can recover up to 23.2 MW of heat. The power generation performance was analysed using a numerical method.

Kaşka [10] proposed an Organic Rankine Cycle for power generation using the excess heat of a walking beam slab reheat furnace. The system proposed was tested with different working fluids for two working conditions. The first case was with a gross power production of 260 kW. The second case was with a gross power production of 200 kW. The ORC designed had energy and exergy efficiencies of 10.2%, 48.5% and 8.8%, 42.2%, respectively, for the two cases.

Ghosh et al. [11] carried out a theoretical study on radiant heat recovery from hot steel slabs by thermoelectric generators as shown in Figure 2-2. The radiation heat transfer parameters such as surface emissivity and view factor were considered in addition to heat loss by natural convection. The module surface dimensions were 50 x 50 mm² and it was cooled by water at the heat sink. It was assumed that the distance between the slab and the module was between 0.1 and 4 m. The effect of the heat transfer coefficient at the heat sink was investigated. It was recommended that the value of the heat transfer coefficient should be higher than 3000 W/m²K. The effect of the slab distance on the power output and the efficiency of the system were also studied. It was noted the electrical power density can reach up to 1.5 kW/m² from a hot steel temperature of 1200K with an efficiency of 5% at distance of 2 m. The study was based on calculated heat flux input range between 6 kW/m² and 30 kW/m². The heat recovery through the heat sink was not reported. However, TEG devices are not designed to have high thermal conductivity between the hot side and the cold one. TEG modules are utilised to harness the thermal energy from hot sources and convert it directly to an electrical energy with an efficiency around 10%. However, if electrical energy is not needed at the site, then recovering the heat to use it for other purposes will be more efficient. On large scale heat recovery technologies, the recovered heat can be linked with Organic Rankine Cycle (ORC) to generate electric with higher efficiency than TEG modules.

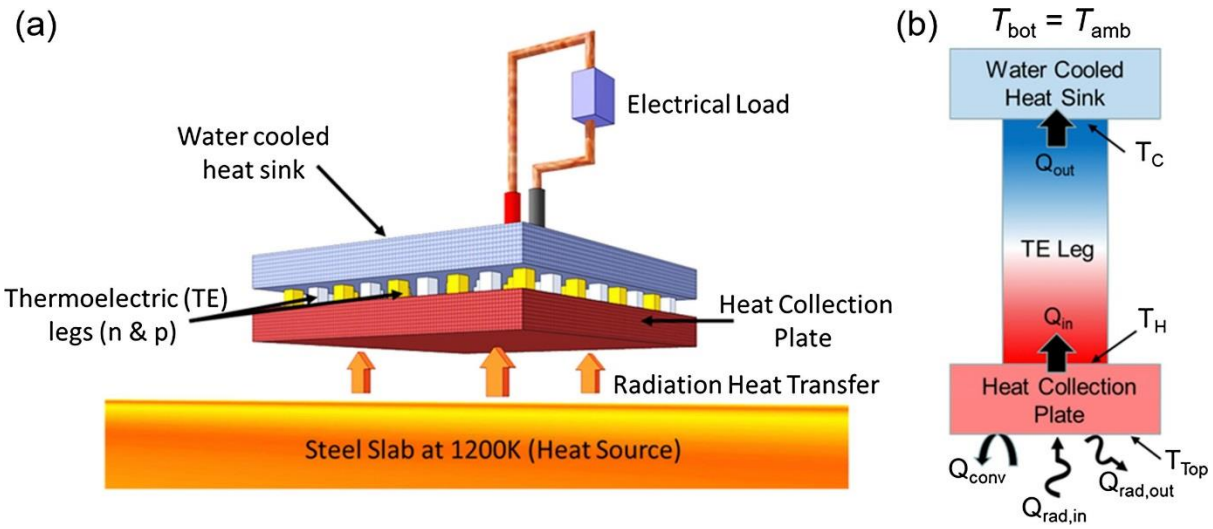

Figure 2-2 Schematic of the thermoelectric module over radiating steel slab. (b) heat transfer and boundary temperatures in the proposed study by Ghosh et al. [11]

2.4 Conventional heat recovery by radiation with other technologies

Yin et al. [12] conducted a study to determine the design requirements of nine heat exchangers for waste recovery by radiation from a rotary kiln for cement. The design parameters were experimentally and theoretically obtained based on optimising the heat loss along the rotary kiln from the shell. The heat loss from the kiln and the required shell temperature were based on the chemical reaction requirements inside the kiln. The mass flow rate and the heat transfer area of each heat exchanger were determined.

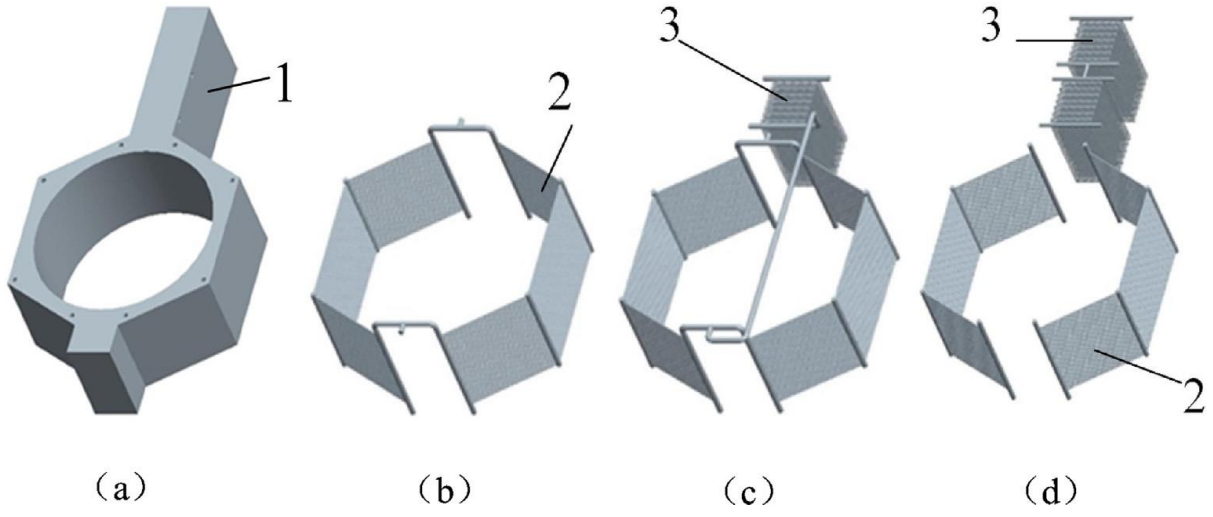

Figure 2-3 a schematic of the heat recovery exchangers presented by Du et al. [13] (a): External shell of the heat exchanger, (b) radiant type heat exchanger, (c) and (d) radiant and force convection type heat exchanger [12]

In a later study, *Du* et al. [13] presented experimental results from the system. The nine heat exchangers were categorized into three different types: radiant only heat exchanger Figure 2-3 (b)

where a water stream passes through the pipe and the pipes recover the heat by radiation. A radiant type with one layer of coiled pipes is shown in Figure 2-3 (c) and a radiant type with two layers of coiled types is shown in Figure 2-3 (d). Coiled pipes absorb the heat from an air stream and transfer the heat to a water stream inside the pipes. The investigation studied the effect of the temperature, pressure, and mass flow rate on the heat recovery of the heat exchangers. The results indicated that the heat recovery system had an important role in controlling the temperature of the shell of the kiln. The system presented the ability to make the shell temperature uniform, eliminating any thermal stress and minimising maintenance costs. The uniformity of the shell temperature was achieved by using some of the radiant heat exchangers to warm the shell in some section, while they were used to absorb the heat from the shell in other sections of it.

As it can be observed that the heat exchanger was used to control the temperature of the shell. The heat exchanger was cooled by a water stream flowing through the pipes which can results in high pressure drop. In contrast, the FHP presented in this research was designed to recover the heat by radiation without interfering with the temperature profile of the steel being cooled over the conveyor. Another advantage of the FHP over conventional technologies is that the water passes in tubes separated from the parallel tubes which are exposed to the direct radiation from the hot steel. The heat was transfer from the parallel tubes to the water tubes by the working fluid in the heat pipe which was hermetically sealed. The FHP was provided with a rupture disk that releases the working fluid into the air without any contact with the steel. This safety factor was considered during the selection of the working fluid which is explained in a separate section in this thesis.

2.5 Heat pipe technology

A heat pipe comprises an evacuated sealed tube structure charged with a small amount of working fluid. It is capable of transporting the heat from one end to the other passively with no moving parts, using only the phase change (liquid-vapour) process inside. A heat pipe mainly consists of an evaporator and condenser section with or without an adiabatic section in between. Heat pipes operate when the evaporator is exposed to a heat source where the liquid working fluid inside the heat pipe boils and evaporates. Then the vapour flows toward the condenser due to a minimal pressure difference between the evaporator and condenser. The vapour condenses at the condenser by rejecting the latent heat and the condensate flows back to the evaporator. The condensate can flow back to the evaporator by capillary forces provided by a wick structure (a wicked heat pipe) or by gravity forces (a gravity assisted heat pipe). Hence a wicked heat pipe can operate in any direction, while a gravity assisted heat pipe can only operate when the evaporator is at a level lower than that of the condenser. Figure 2-4 illustrates the structures of a wicked heat pipe and a gravity assisted heat pipe (or thermosyphon).

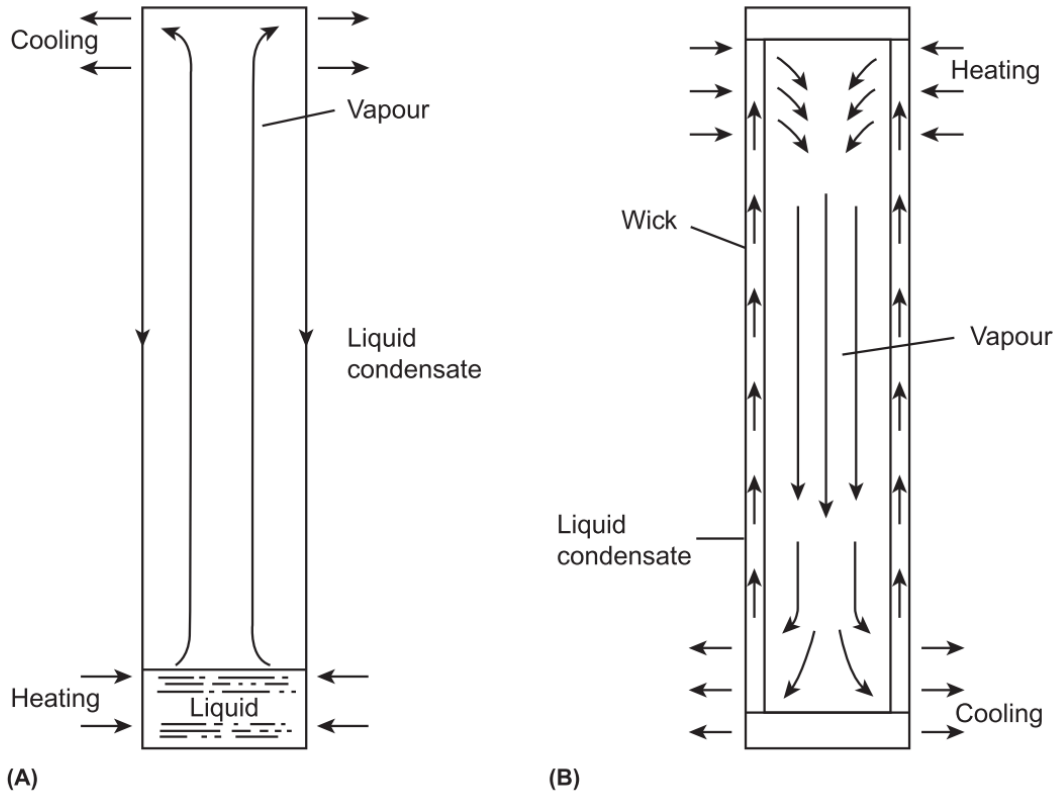

Figure 2-4 Structure of heat pipes: (A) thermosyphon, (B) wicked heat pipe [14]

The operating process of heat pipes offers many advantages such as the following:

- An isothermal surface feature which means a uniform temperature across its surface
- The capability of transporting heat for long distances at very small temperature differences between the evaporator and the condenser.
- A heat pipe is considered as a passive heat transfer device since it does not have any moving parts.
- Heat pipes have long life expectancy, more than 20 years without any need for maintenance.

Each individual heat pipe can be considered as a heat exchanger. However, heat pipes can be integrated into a heat exchanger system, forming a heat pipe heat exchanger (HPHE) system. The integration of heat pipes in heat exchangers benefits from the advantages of heat pipe technology and enhances the thermal performance over conventional heat exchangers. Some of the advantages of HPHEs can be summarised in the following:

I. Heat pipe heat exchangers have smaller surface areas, which means a smaller mass than for conventional exchangers. Since the thermal resistance of heat pipes is between 0.01–0.03 K/W [15], heat pipe structures are capable of transferring larger amounts of heat compared to conventional small cross-sectional area units [16].

II. No cold spots are detected on the heat transfer surfaces, due to the isothermal operation of the evaporator and condenser of the heat pipe. This prevents the possibility of condensation of the moisture in the hot source stream and protects the heat sink stream from being exposed to any high temperatures.
III. The heat transfer area of the cold stream can be different from the hot one so the implementation of fins is not essential [17].
IV. Ease of assembly and installation, versatility, scalability, reliability, and adaptability of design [17].
V. A HPHE isolates the hot stream from the cold stream physically which is very important in some heat recovery applications such as medical or industrial applications.
VI. The failure of a few heat pipes does not affect significantly the thermal performance of the HPHE. In addition, the failed heat pipes can be replaced easily during the maintenance cycle.

Heat pipes can only operate when the working fluid is selected properly according to the temperature range of the application. In addition, the shell case material has to be compatible with the working fluid and the operating temperature of the heat pipe.

The most common working fluids of heat pipes with their specific properties are listed in Table 2-1.

It should be noted that an incompatible selection of shell case material with the working fluid leads to the generation of non-condensable gases and failure of the heat pipe.

The shell case material is selected based on the compatibility with working fluid, mechanical strength, corrosion resistance if required, weight, and cost. The most common materials of heat pipes are copper and aluminium. These materials are the most preferred because of their high thermal conductivity, light weight, and low cost. However, the operating temperature limit of these materials is around 120 °C where mechanical strength starts to decrease significantly. Increasing the wall thickness or selecting a shell case material with low thermal conductivity will increase the thermal resistance by conduction of the heat pipe wall and the overall heat pipe thermal resistance. Stainless steel has a low thermal resistance but it is very suitable when the heat pipe is employed in a corrosive medium. The compatibility of metals with working fluids is reported in Table 2-2.

Table 2-1 Thermodynamic properties of common working fluids used in heat pipes [18–25]

Fluid	Symbol/ Formula	Melting Point,	Normal Boiling Temp	Critical Temp	Critical Pressure	Useful Range
		(°C)	(°C)	(°C)	(atm)	(°C)
Helium	He	−272.2	−268.9	−267.95	2.24	-271 to -269.1
Hydrogen	H	-259.14	-252.87	−239.95	12.8	-259 to -242
Neon	Ne	-248.6	-246.08	−228.75	27.2	-246 to -236
Nitrogen	N_2	-210	-195.8	-146.9	33.5	-203 to -170
Oxygen	O_2	-218.3	-182.9	−118.6	49.8	-200 to -154
Methane	CH_4	-182.4	-161.7	-82.5	510.8	-182 to -113
Ethane	C_2H_6	-183.2	-88.5	32.4	48.2	-123 to -33
Freon R22	$CHClF_2$	-175.42	-159.15	96.1	49.1	-80 to 50
Freon R410a		-155	-48.5	72.8	48.85	-100 to 35
Propane	C_3H_8	-187.69	-42	96.8	41.9	-85 to 57
Ammonia	NH_3	-77.73	-33.34	132.4	111.3	-65 to 100
Freon R134a	CH_2FCF_3	-103.3	-27	101	40.06	-75 to 50
Freon R408a		N/A	-44.4	83.3	43.65	-82 to 48
Acetone	C_3H_6O	-94.3	56.1	235	47.37	0 to 120
Methanol	CH_3OH	-97.6	64.7	240	78.5	10 to 130
Ethanol	C_2H_6O	-114.35	78.35	241	62.17	0 to 130
Water	H_2O	0	100	373.95	217.7	10 to 287
Toluene	C_7H_8	−95	111	318.64	40.5	50 to 200
Dowtherm A		12	257.1	497	30.9	150 to 395
Caesium	Cs	28.44	671	1664.85	92.77	450 to 900
Potassium	K	63.38	759	1949.85	157.9	500 to 1000
Sodium	Na	97.72	883	2299.85	345.4	600 to 1200
Silver	Ag	961.78	2212	N/A	N/A	1800 to 2300

Table 2-2 Compatibility between heat pipe working fluids and shell materials [26]

Working fluid	Compatible material	Incompatible material
Acetone (Pure)	Aluminium, Stainless Steel	
Methanol (Pure)	Stainless Steel, Copper	Aluminium, Titanium
Water	Copper, Monel, Nickel, Titanium, Stainless Steel, Carbon steel	Aluminium, Inconel
Dowtherm A	Aluminium, Stainless Steel, Titanium, Carbon steel	Copper, copper nickel

It should be noted that water can be used as a working fluid in stainless steel or carbon steel heat pipes after doing a special passivation process for the internal surface of the pipes. This passivation process prevents the chemical reaction between the pipe material and the water which would lead to the heat pipe failing to function.

The performance of a heat pipe is basically affected by the thermo-physical properties of the working fluid inside. A heat pipe can have more than one candidate of a suitable working fluid within a given operating temperature range. The physical properties of a wicked heat pipe can be evaluated using the figure of merit which is defined in Equation (2-1) as reported in ESDU [27]:

$$\boldsymbol{\Phi_1 = \frac{h_{fg}\rho_l\sigma}{\mu_l}\ (\mathrm{W/m^2})} \qquad \textbf{(2-1)}$$

The figure of merit in wicked heat pipes represents the effect of the thermo-physical properties of the working fluid on the maximum heat transfer rate of the wicked heat pipe; i.e., the heat transfer rate of a heat pipe is limited by the flow rate of the working fluid in the wick. A higher merit number for a heat pipe means a better thermal performance and, as can be seen from the equation, a fluid with a high latent heat of vaporisation or density, or low viscosity will have a high merit number.

The figure of merit of the most common working fluids used in wicked heat pipes is presented in Figure 2-5.

Thermosyphons (gravity assisted heat pipes) can be evaluated by a figure of merit, which is presented in Equation (2-2) obtained from [27]:

$$\boldsymbol{\Phi = \left(\frac{h_{fg}k_l^3\rho_l^2}{\mu_l}\right)^{1/4}\ (\mathrm{kg/K^{3/4}\,s^{5/2}})} \qquad \textbf{(2-2)}$$

where h_{fg} is the latent heat of vaporisation of the working fluid (J/kg), k_l is the thermal conductivity of the working fluid (W/m.°C), ρ_l is the working fluid density (kg/m³), μ_l is the liquid viscosity (Pa.s), and σ is the surface tension (N/m).

The figure of merit of the most common working fluids used in thermosyphons is presented in Figure 2-6 within the temperature range of -150 to 400 °C.

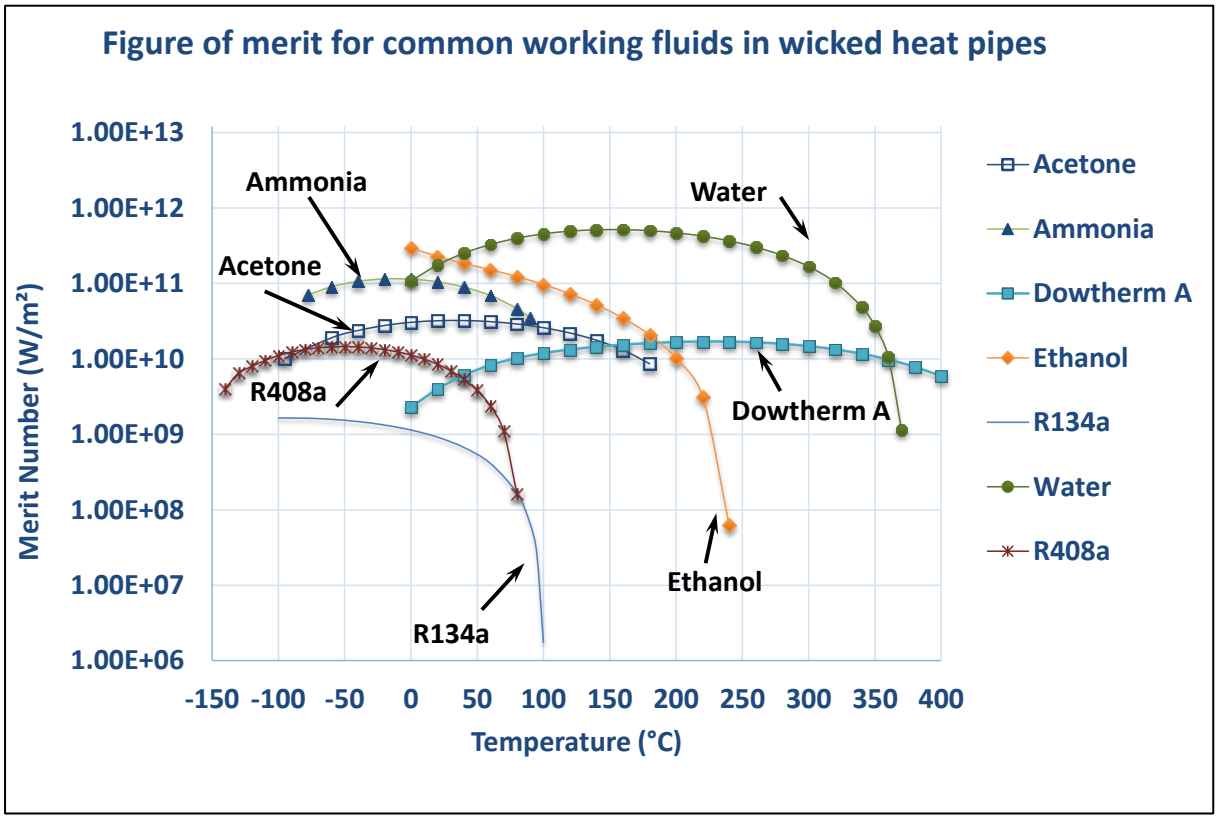

Figure 2-5 Figure of merit of the most common working fluids used in wicked heat pipes

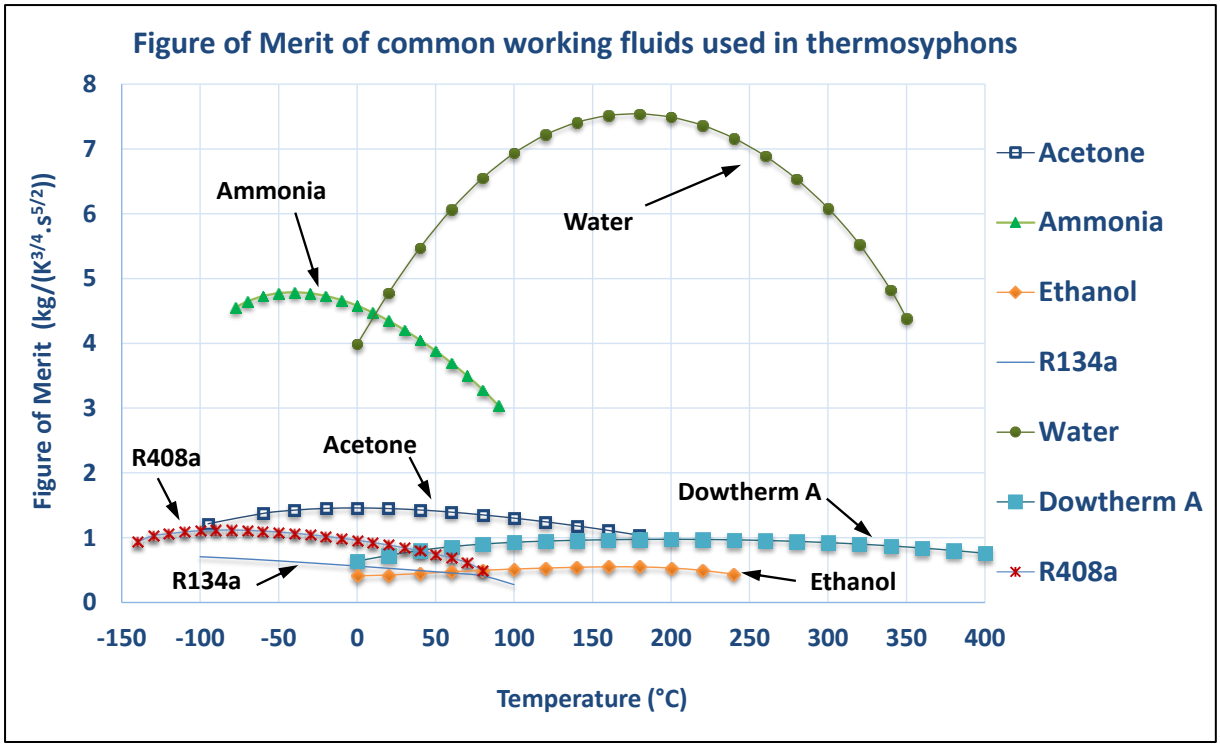

Figure 2-6 Figure of merit of the most common working fluids used in thermosyphons

A high figure of merit in thermosyphons means the heat pipe will have a low temperature difference between its two ends. Therefore, a heat pipe with a high figure of merit can achieve good performance due to its low thermal resistance and high heat transfer capability.

Water is widely used as a working fluid in heat pipes because it has many advantages over the other working fluid such as high latent heat, availability, cheapness and environmental-friendliness. Utilising water as a working fluid in heat exchangers results in a reduced working pressure inside the pipe which reduces the stress on the pipe wall. In addition, a heat pipe heat exchanger charged with water can transport higher amounts of heat in comparison to heat pipe heat exchangers with the same dimensions charged with another fluid. This results in reducing the overall size, weight, and cost of the heat pipe heat exchanger.

2.6 Flat heat pipe technology

Heat pipes generally are cylindrical, however the evaporator or condenser or both can be flat. In this case it is called a flat heat pipe (FHP). The advantages of flat heat pipe technology are the isothermal characteristics and flat evaporator surface which maximises the radiation absorbing area [28]. Heat pipes cannot only be in cylindrical shell case design, but they can also be in a flat shape or a flat evaporator with a cylindrical condenser. A flat heat pipe (FHP) utilises the features of heat pipes and additionally it maximises the heat transfer area and transforms a flat surface into an isothermal

surface. Flat heat pipes expand the range of applications of heat pipes especially in thermal management applications.

2.7 State of the art on heat pipe applications

2.7.1 Heat pipe technology in waste heat recovery

Conventional heat recovery technologies are often not able to recover waste heat economically. This caused by the challenging waste streams such corrosion, fouling, cost of maintenance and limitations on the weight and the size of the conventional heat exchanger. However, utilising heat pipe-based heat exchangers for waste heat recovery is a promising solution that can address this issue.

Heat pipe technology has been investigated for many different applications such as waste heat recovery and solar applications. *Mat et al*. [29] studied experimentally a heat pipe heat exchanger for waste heat recovery in the steel industry. The HPHE was designed to recover the heat from waste water used to cool slag and to transfer it to a clean water stream. The HPHE consisted of multiple heat pipes gathered using a separation plate. The authors studied the effect of the waste water flow rate on the heat transfer rate. It also investigated the effectiveness and exergy efficiency of the heat pipe. The optimum waste water flow rate corresponding to the highest effectiveness and exergy was determined. The impact of an on-line cleaning system from fouling on the heat transfer rate was also investigated. The descaling effect of the cleaning system increased the effectiveness and the exergy efficiency of the system by about 10% and 8% respectively.

Tian et al. [30] studied a new type of heat pipe-based heat exchanger for waste heat recovery from flue gases. The heat pipe consisted of horizontal smooth tubes where the exhaust passed inside the tubes, and the external surface of the tubes was the evaporator surface comprising a boiling chamber as shown in Figure 2-7. The boiling of the working fluid was on the external surface of the horizontal smooth tubes.

Figure 2-7 A heat pipe heat exchanger presented by Tian et al. [30]

The condenser section was vertical finned tubes where clean air passed over the external surface of the pipes, whereas the working fluid condensed on the inner surface of the tubes. The heat pipe system was tested for three months on continuous operation heat recovery. However, the thermal performance of the HPHE was not reported in this study which focused only on the impact of the HPHE on the reduction on natural gas consumption. The study reported that the clean air was used to pre-heat the burner air supply, leading to a reduction of 15% in natural gas consumption and therefore a reduction in greenhouse gas emissions. Since the system comprises a boiling chamber with flat external walls, the thickness of the walls would be expected to be high leading to increase the weight and the cost of the heat pipe heat exchanger.

Delpech et al. [31] investigated the application of a HPHE in enhancing the energy efficiency in the ceramic industry. The effect of the HPHE on the kiln operating conditions was conducted by numerical modelling where the heat transfer rate of the HPHE was determined theoretically. The numerical modelling simulated the compressed gas flow through the kiln module considering the thermo-dynamic properties of the gases. The HPHE was designed to recover the heat from flow gases and pre-heat the air fed into the burners of the kiln. It was concluded that utilising the HPHE in waste heat recovery in the kiln will result in significant savings in energy costs. The study estimated the energy savings that can be achieved by installing the HPHE. The potential of energy saving was estimated to be 865 MWh per year and reducing emissions of 164 tonnes per year for carbon dioxide.

Waste heat recovery from high temperature exhausts are challenging for HPHEs. The construction materials of the heat pipe and the heat exchanger have to withstand with the high temperature and the corrosive composition and fouling in the exhaust stream. *Meisel et al.* [32] studied a sodium heat pipe for high temperatures and abrasive streams. The heat pipe was constructed from Inconel 600 enveloped with a ceramic shell and filled with sodium as working fluid. A numerical prediction model for the axial heat transfer was presented and validated experimentally at different evaporator temperatures between 700 °C and 950 °C. The developed model predicted the axial heat transfer rate within 17% of the experimental data.

Jung and Boo [33] conducted numerical modelling on a counter-flow HPHE for high temperature applications. The finned heat pipes of the HPHE were constructed from stainless steel and charged with sodium. The developed numerical model was validated using the experimental data provided in an earlier study by *Yoo et al.* [34]. The thermal performance modelling was performed considering the effect of the ratio between hot and cold surface areas and Reynolds number on various parameters including the inlet and outlet temperatures of the hot and cold air, heat recovery, radiation heat transfer, HPHE effectiveness, and heat losses by radiation to the surroundings.

2.7.2 Electronics and similar applications

Flat heat pipes are commonly used in heat dissipation of electrical and electronic devices as they are able to transport high heat fluxes and make thermal management of such devices feasible. A substantial amount of research has been conducted on flat heat pipes and vapour chambers. The main focus of the investigation was on the effect of the heat transfer rate on the thermal resistance of the heat pipe and the isothermal characteristics of the heat pipe. Utilising Heat pipe technology in electronics can enhance the cooling of the heat source which is generally a CPU without compromising the thickness of the device. The size of heat pipe in such applications is in centimetres and the heat pipe is provided with a wick to enhance the boiling heat transfer in the evaporator and to return the condensate from the condenser to the evaporator.

Wang et al. [35] fabricated and examined experimentally the effect of the evaporator and condenser length of a flat plate heat pipe (FPHP). The length of FPHP was 255 mm and the width 25 mm and it was filled with water. The FPHP has a higher heat transfer contact area when compared with a conventional heat pipe. It was observed that the thermal resistance of the FPHP decreased and the heat transfer limit increased by increasing the evaporation section length. In contrast, the FHPH had a lower heat transfer limit for a longer condenser where the dry-out limit was reached for a lower

heat input. It was observed that the FPHP achieved the best performance when the evaporator and condenser had the same length.

Wang and Vafai [36] carried out an experimental investigation of the thermal performance of a flat plate heat pipe. The length of the copper wicked heat pipe was 190.5 mm and the width 139.7 mm with a thickness of 3.175 mm. The heat pipe was heated from the top face and cooled from the bottom face. The results indicated that the heat pipe wall surfaces were isothermal at different heat inputs. It was noted that the main thermal resistance was caused by the porous wick in the evaporator section affecting the performance of the heat pipe. Correlations for the maximum temperature difference as a function of the heat input in addition to the time response were obtained from the experimental data.

Tsai et al [37] conducted an experimental study on the thermal resistance of a vapour chamber which is shown in Figure 2-8. The dimensions of chamber were 90 mm x 90 mm x 3.5 mm. the vapour chamber transferred the heat from a heater block to a water-cooled plate. The experiments were conducted at a power input from 5 W to 50 W corresponding to heat flux range between 617 W/m².°C and 6170 W/m².°C. The thermal resistance of the heat pipe and the experimental setup were examined at various heat inputs. The influence of the inclination on the vapour chamber performance and temperature distribution were also investigated. The inclination did not show an effect on the temperature uniformity but the thermal resistance was strongly affected.

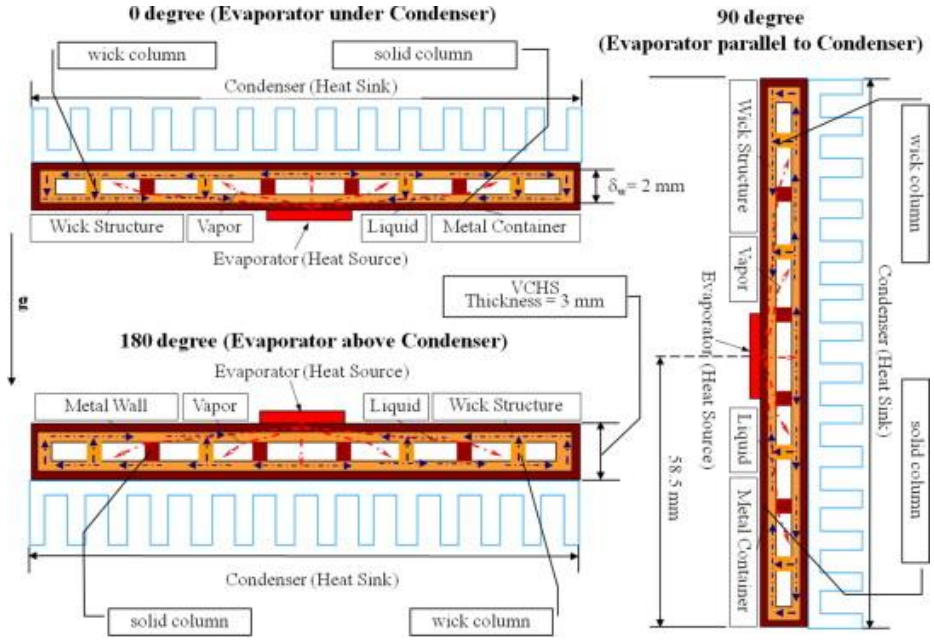

Figure 2-8 A schematic of a vapour chamber presented by Tsai et al [37]

Ji et al. [38] presented a vapour chamber with an extended condenser surface for high heat fluxes and a large heater area. A layer of sintered porous wick was fitted on the evaporator surface while the

condenser surface was wicked by grooves. The thermal resistance of the heat pipe developed was investigated at different inclinations and heat inputs. The results were compared with results from the literature. The thermal resistance decreased with increasing heat input. A minimum thermal resistance of 0.03 K/W was reached for the bottom heating. The heat flux reached up to 450 W/cm^2 without reaching the dry-out limit. The effect of the filling ratio was also investigated and the optimal filling ratio was determined to be 0.3. The filling ratio is defined as the ration of the working fluid volume to the evaporator volume.

Tang et al. [39] fabricated and examined a multi-artery vapour chamber. The investigation was carried out experimentally on the thermal performance of the vapour chamber. The vapour chamber comprised top and bottom plates, two sintered copper powder layers, copper columns and sintered copper powder rings. The thermal performance of the vapour chamber was evaluated by determining the thermal resistance and compared with other results in the literature. The vapour chamber was tested at different heat loads, heating areas and heating modes. It was noted that the lowest thermal resistance was less 0.04 K/W. The maximum heat flux reached 300 W/cm² without reaching the capillary or boiling limits.

Peng [40] conducted an investigation on a flat plate heat pipe vapour chamber (FPHP) for electronic cooling. The vapour chamber comprised two aluminium flat plates of 2.5 mm thickness. The overall dimensions of the vapour chamber were 80 mm x 75 mm x 15 mm. The influence of the filling ratio and air cooling velocity on steady-state heat transfer characteristics of the FPHP were also studied. It was noted from the experimental results that the filling ratio and degree of vacuum had a great impact on the thermal performance of FPHP. Two different working fluids were used, namely acetone and water. The FPHP charged with acetone demonstrated better heat transfer compared with water for the same filling ratio. The FPHP dissipated heat of 100W for a heating source temperature less than 60° which meets the requirements of many electronic cooling applications.

Filling ratio and leakage influences on the thermal performance of flat plate heat pipe (FPHP) were examined experimentally by *Chen and Chou* [41]. The FPHP was made from aluminium with internal channels and capillary groves and charged with acetone. The dimensions of the FPHP were 150 mm x 50 mm x 2.5 mm which are shown in Figure 2-9. The investigation on the FPHP was conducted with different filling ratios and heat inputs to measure the temperature uniformity along it and to determine the thermal resistance of the heat pipe and the effective thermal conductivity. The experimental results indicated that the optimal filling ratio which corresponds to the best performance was obtained to be 25% of the channel's volume. The corresponding maximum heat transfer capability, minimum thermal resistance, and maximum effective thermal conductivity were

about 47 W, 0.254 K/W, and 3150 W/m K, respectively. Moreover, thermal performance of the FPHP with inappropriate vacuum and incorrect sealing was investigated and compared with aluminium and copper blocks. It was shown that these conditions significantly decreased the effective thermal conductivity.

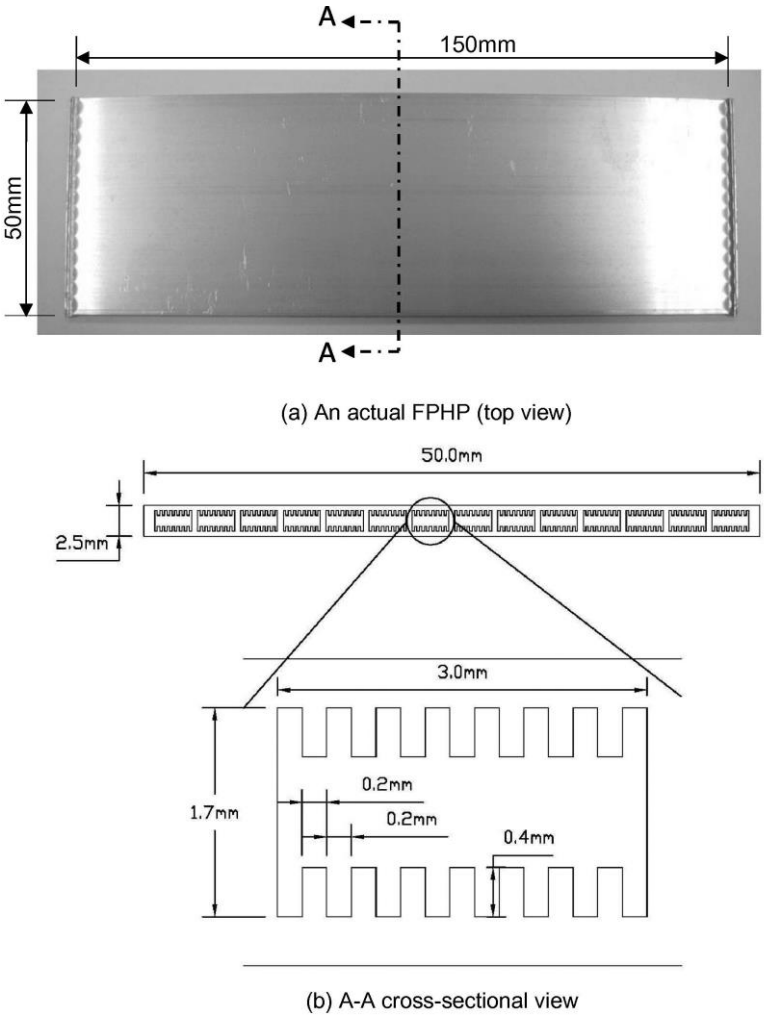

Figure 2-9 A flat plate heat pipe studied by Chen and Chou [41]

Aghvami et al. [42] analysed the performance of flat heat pipes for different heating and cooling conditions shown in Figure 2-10. The authors developed an analytical thermal-fluid model in order to predict the thermal and hydrodynamic performance of flat heat pipes with different heating and cooling configurations. The effect of the heat input on the surface temperature, pressure drop, and fluid velocity was analysed. The results for the flat heat pipes demonstrated that thermal performance is influenced by the heat source area and position.

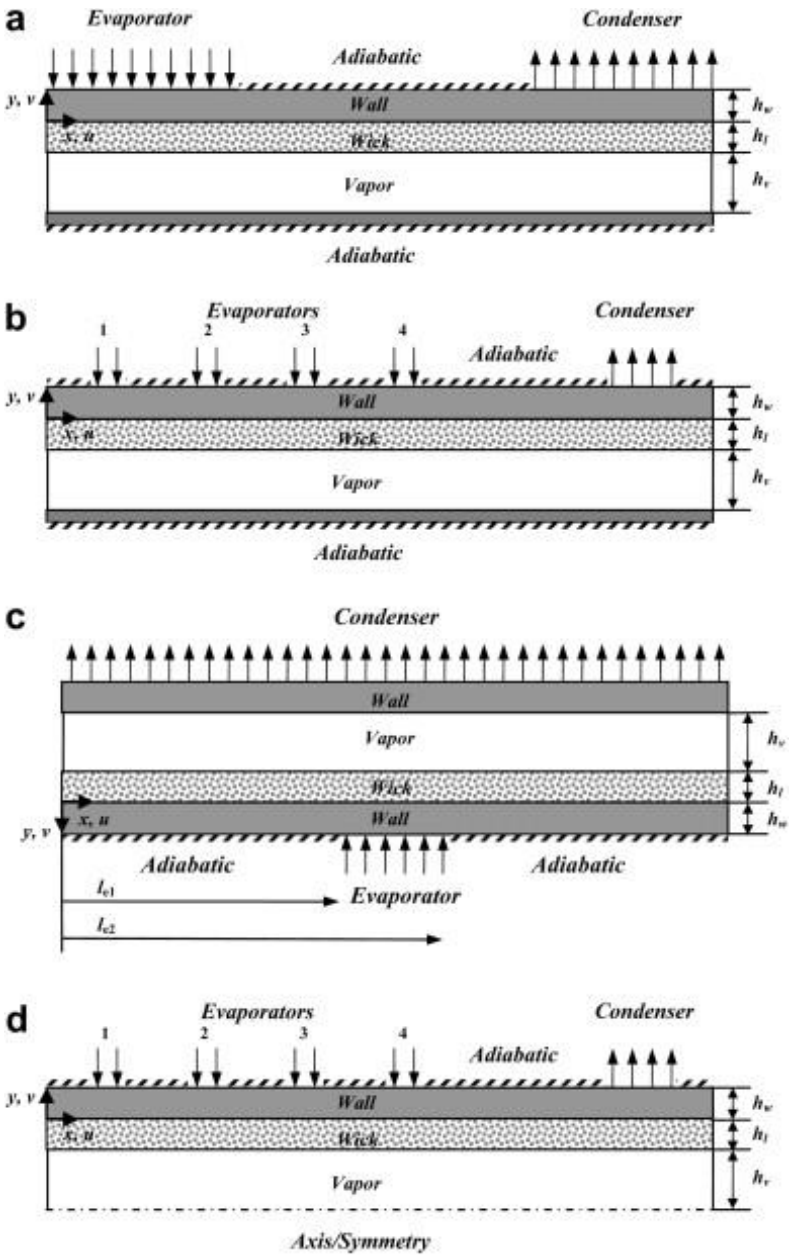

Figure 2-10 Flat heat pipes with different heating/cooling configurations: a) configuration I, single heat source and sink at top; b) configuration II, multiple heat sources and sink at top; c) configuration III, heat source at the bottom and heat sink on the top; and d) configuration IV, multiple heat sources and sink at both top and bottom, investigated by Aghvami et al. [42]

Liu et al. [43] conducted a study on the effect of different working fluids on the operational characteristics of a flat plate loop heat pipe (LHP) which is presented in Figure 2-11. The flat plate LHP system consisted of a flat evaporator, an air-cooled fin-and-tube type condenser, a vapour line and a liquid line. The heat pipe was made of copper and provided with a stainless steel mesh wick. The study compared the performance of the LHP with two different working fluids, acetone and methanol. The parameters of the performance included analysing the thermal resistance, the start-up characteristics of the LHP with different filling ratios and tilt angles, and temperature oscillations. The research

outcomes demonstrated that the LHP with acetone has a better start-up with a lower temperature of evaporator wall and lower thermal resistance compared with a methanol-filled LHP. Furthermore, the acetone LHP performed better than the methanol one in relation to temperature oscillations.

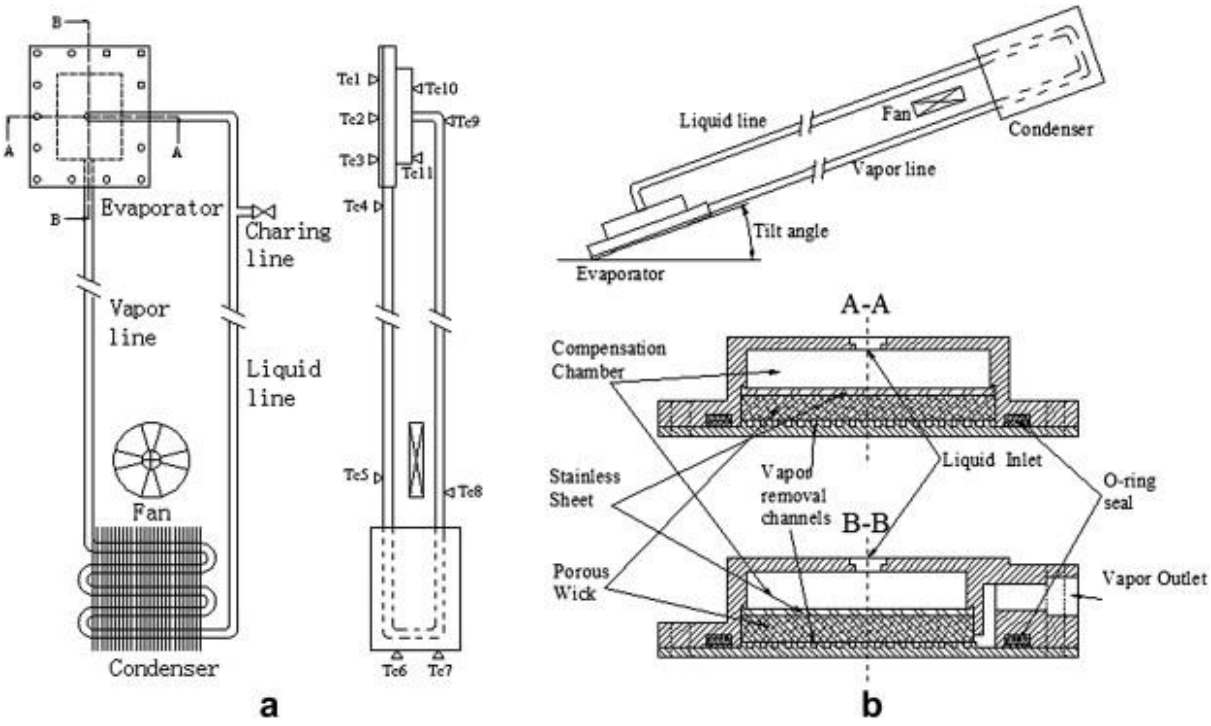

Figure 2-11 Loop heat pipe investigated by Liu et al. [43]

Oro et al. [44] presented a flat heat pipe for fuel cell cooling. The FHP was examined experimentally and theoretically at different power inputs. The flat heat pipes were similar to cylindrical pipes but having one side flattened. The FHPs were assembled within the fuel cell stack to absorb the heat generated by the cell. The flat heat pipes were made of stainless steel tube of 3mm outer diameter and 100mm length. A theoretical analysis was performed to determine the capillary limit at different temperatures. The performance of the FHP was validated experimentally to measure the FHP resistance by measuring the heat input and the temperature difference between the evaporator and the condenser. The FHP was able to cool the fuel cell within its operating limits.

Ye et al. [45] conducted an experimental study on a micro flat heat pipe array (MHPA) used to cool lithium-ion battery packs. A schematic of the heat pipe setup is presented in Figure 2-12. The flat heat pipe was made by extrusion, comprising several micro heat pipes inside. The internal surface of these pipe was micro-finned providing capillary forces and increasing the heat transfer surface area. The MHPA was attached to a battery pack and provided with a finned heat sink at the condenser section. The battery temperature during charging and discharging cycles was measured with and without utilising the heat pipe system. The heat pipe system was cooled by natural convection and by forced convection using a fan. The results indicated that the temperature difference between the battery

cells was uniform with less than a 6.5 °C difference by cooling them using the MHPA. The study reported the impact of the MHPA on the battery temperature limit and cell temperature uniformity without any details about the thermal resistance of the heat pipe during the tests.

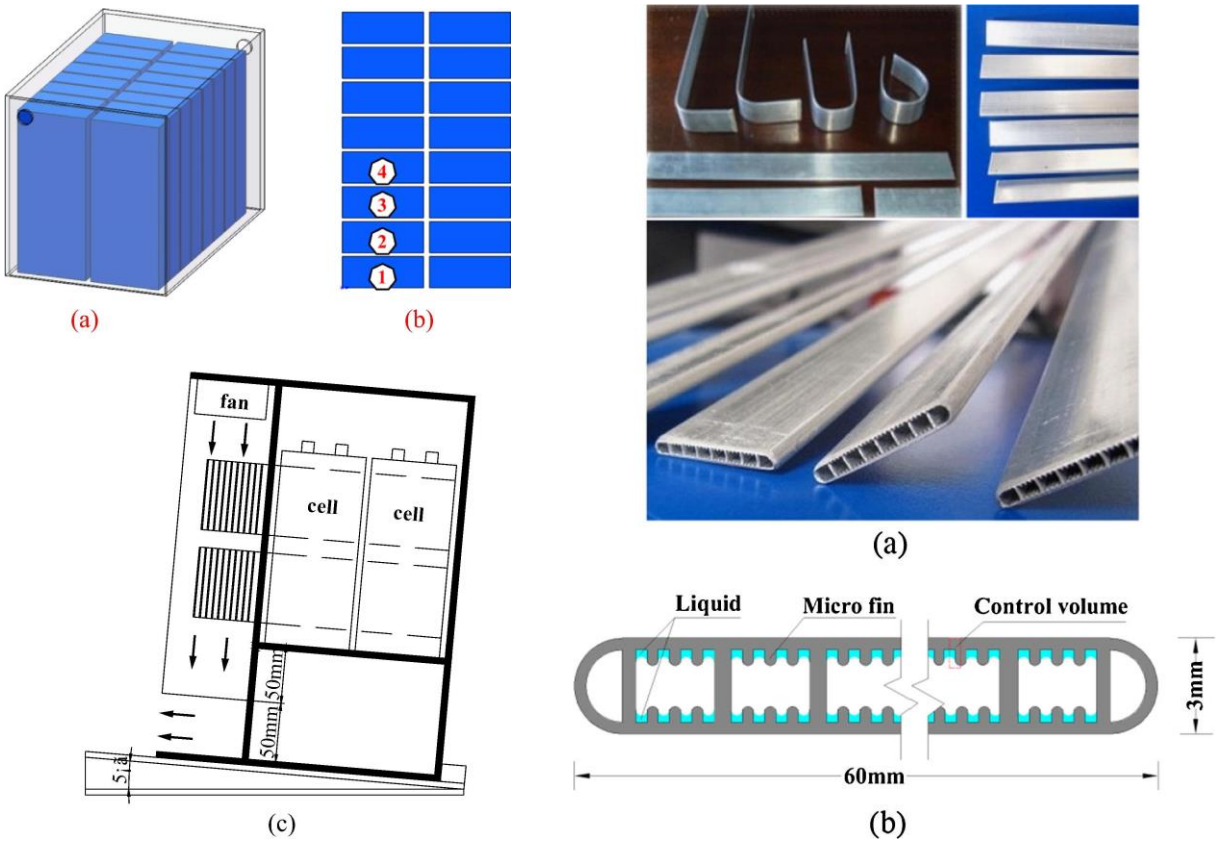

Figure 2-12 Flat heat pipe for battery cooling presented by Ye et al. [45]

Heat pipes for electronic thermal management applications are different from the heat pipe heat exchangers at larger scale. This application requires a wick structure in the heat pipe which makes the fabrication process very complicated and expensive on larger scales. Moreover, the presented heat pipe designs in this application cannot handle high pressure due to the structure and the mechanical design of the vapour chamber. Therefore, vapour chambers were not reported to be used in a large scale at temperature higher than 100 °C. In addition, based on the heat source temperature in electronic application, the working fluid is normally acetone or ammonia while the water is a common working fluid in heat pipes for waste heat recovery in industrial applications.

2.7.3 Solar applications

Heat pipe technology has been implemented in different applications for solar energy harnessing. Solar radiation is the energy emitted from the sun where the highest energy density is within the visible spectral range. The solar irradiance on the earth surface can reach up to 1360 W/m² which highlights its potential to be exploited as a free energy source. However, heat recovery from solar

energy is limited by the intermittency of the source availability represented by the sun. The need for an efficient, quick response, low cost technology can be addressed by the heat pipe technology which meets these requirements.

Azad [46] examined the heat pipe solar collector illustrated in Figure 2-13. The design comprised a horizontal copper tube connecting six vertical copper tubes of 12.7mm diameter. The condenser of the heat pipe is a copper shell of 50 mm diameter and four copper tubes of 12.7 mm diameter. The heat pipe was charged with ethanol as a working fluid and two layers of stainless steel mesh were used as the wick in the evaporator section. The outlet temperature and the efficiency of the system were compared experimentally with the theoretical predictions, in addition to reporting the temperature of the heat pipe and cooling fluid and the collector efficiency. A good agreement was observed between the theoretical and experimental results. Wick structure increases the wettability of the evaporator, however it increases the cost of the heat pipe and makes the manufacturing process more complex.

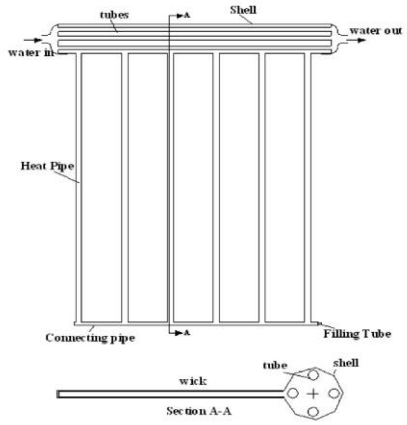

Figure (a) Interconnected heat pipes solar collector.

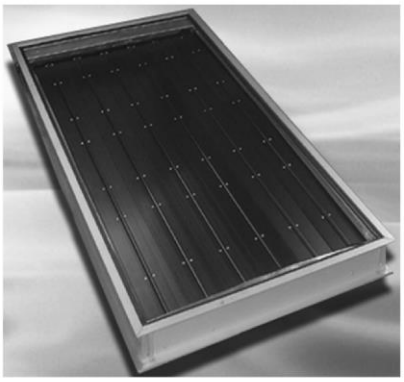

Figure (b) Solar collector.

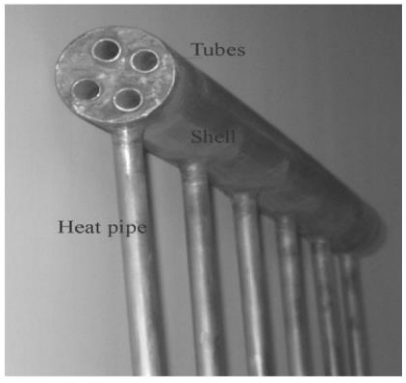

Figure (c) Interconnected heat pipes with heat exchanger.

Figure 2-13 Heat pipe solar collector presented by Azad [46]

In later study *Azad* [47] presented a design of a flat heat pipe solar collector and examined its performance theoretically and experimentally. Figure 2-14 illustrates the heat pipe design. The flat heat pipe evaporator consists of six tubes connected to a bottom header and fitted with one layer of stainless steel mesh. The evaporator was connected from the top end to a condenser which was a copper shell and tube of three passes. The evaporator was finned with aluminium fins and filled with distilled water. The investigation studied the heat pipe temperature, water outlet temperature, and the collector efficiency. The calculated results were in a good agreement with the experimental data.

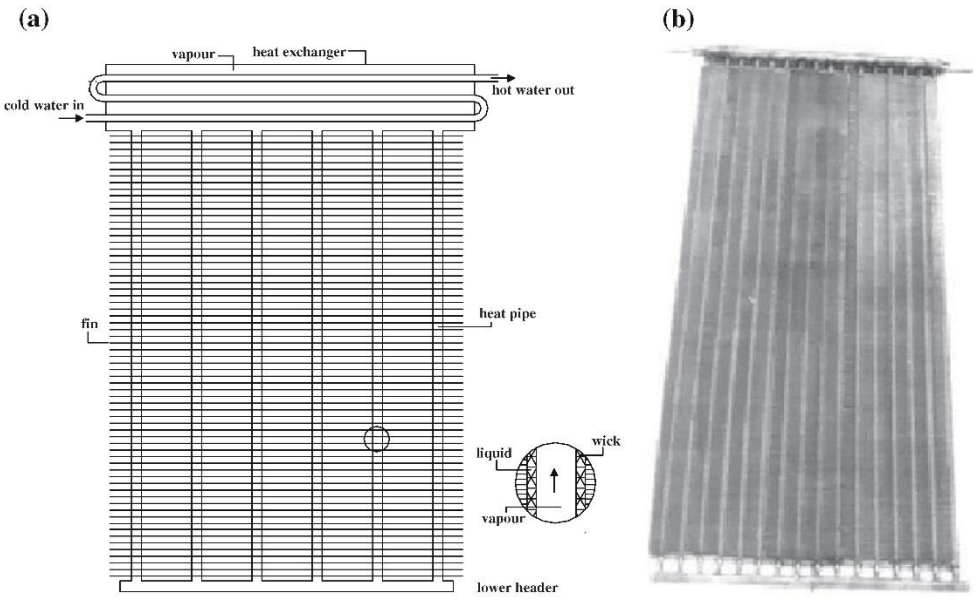

Figure 2-14 Wicked heat pipe solar collector presented by Azad [47]

Zhu et al [48] studied a compound parabolic concentrator (CPC) solar air collector (SAC) with flat micro-heat pipe arrays (FMHPA) shown in Figure 2-15. The thermal performance of the system was tested experimentally and analysed theoretically. The heat pipe was made from aluminium and charged with acetone with a filling ratio of 20%. The study investigated the thermal efficiency, the temperature of the FMHPA at different points, and the solar irradiance variations versus the time. Furthermore, the study conducted the thermal efficiency and pressure drop at different cooling fluid

flow rates. It was noted that the FMHPA had a quick thermal response and the thermal efficiency of the system increased with increasing average solar irradiance.

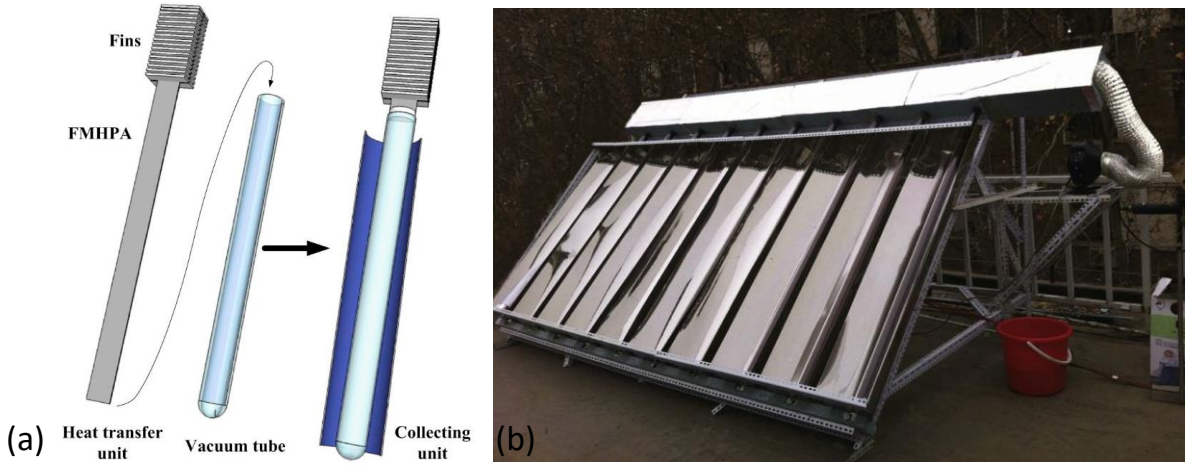

Figure 2-15 Micro array heat pipe for solar collector presented by *Zhu et al* [48]

A photovoltaic thermal (PV/T) panel is a system which produces electricity and thermal energy simultaneously from solar energy. The investigation on PV/T performance has been reported in the literature since 1970s as presented by [49]. A conventional PV/T panel consists of a PV panel and an assembled cooling system on the back. The PV panel absorbs the solar energy and converts a part of it to electrical energy while the remainder is converted into heat. The cooling system can be cylindrical pipes where water passes through and absorbs the heat, or it can be a finned heat sink cooled by air. The electrical energy conversion efficiency of the PV panel is very sensitive to the temperature and it decreases significantly when the PV panel temperature increases. In addition, a high operating temperature of a PV panel and the presence of hotspots result in thermal stresses which reduce its life expectancy. Conventional cooling systems in the PV/T panels have disadvantages such as a non-uniform distribution of temperature along the panel and the difficulty in using water as a coolant in cold regions because of freezing. The complications of the design can be overcome by implementing heat pipe technology as the thermal cooling system in the PV/T panels. The utilisation of heat pipes in PV/T panels provides benefits from the advantages of generating both electrical and thermal energy, in addition to the advantages of heat pipes.
The advantages of heat pipe PV/T systems can be summarised as follows:

- Overcoming space availability limitations
- Contributions to the architectural uniformity of buildings
- Enhancing electrical and thermal performance of the PV/T panel
- The thermal performance enhancement leads to a reduction in the space occupied by the system

- Producing an isothermal PV surface and providing an efficient thermal management system
- Reducing the pressure drop in the cooling circuit, leading to a smaller pump size and power, where the coolant path is shorter and has simpler design.

The main performance parameters of PV/T panels are the energy recovery, operating temperature, energy efficiency, and exergy efficiency. The performance of the heat pipe is commonly evaluated in the literature by determining the thermal efficiency, which is the ratio of heat recovery to the solar irradiance, considering the surface area of the system.

The focus in the literature was to cool down the PV panels through the heat pipe and use the recovered energy to heat water for different applications. It should be noted that if the heat pipe doesn't provide sufficient cooling, the operating temperature of the PV panels, which depends on the temperature of the heat pipe evaporator, will increase to reach the energy equilibrium state where the thermal energy released by the PV to the heat pipe is equal to the heat transferred to cooling fluid in addition to the thermal energy losses to ambient. Various heat pipe PV/T designs have been proposed in the literature. They can be summarised in two main categories as follows: Cylindrical heat pipe heat exchangers and flat heat pipe heat exchangers.

The performance of a PV/T panel can be evaluated based on its energy efficiency by the first law of thermodynamics. The total efficiency of the system is the sum of thermal and electrical efficiencies, which are given by the following correlations based on the first law of thermodynamics [50,51]:

$$\eta_{PV/T} = \frac{\int_{t1}^{t2}(A_c \dot{E}_{th} + A_{PV}\dot{E}_e)}{A_c \int_{t1}^{t2} G dt} = \eta_{th} + \xi\, \eta_e$$

$$\eta_{th} = \frac{Q}{A_c G} \times 100$$

$$\eta_e = \frac{P_{max}}{A_{PV} G} \times 100$$

$$\xi = \frac{A_{PV}}{A_c}$$

$$Q = \dot{m}.C_p.(T_{w,o} - T_{w,i})$$

where $\dot{E}_{th}$ is the thermal output power per unit collector area, $\dot{E}_e$ is the electrical output power per unit cell area, η_{th} is the thermal efficiency of the collector, η_e is the electrical efficiency of PV cells, A_c is the collector area, A_{PV} is the PV cell area, G is the solar irradiation per area, P_{max} is the electrical energy output of PV cells, Q is the thermal energy output of the PV/T panel, $\dot{m}$ is the mass flow rate of the cooling water, C_p is the specific heat capacity of water, $T_{w,o}, T_{w,i}$ are outlet and inlet water

temperature, respectively, and ξ is PV cell packing factor, which is the ratio of PV panel area to the collector area.

Moradgholi et al. [51] conducted an experimental investigation on a heat pipe photovoltaic/thermal (PV/T) system. A thermosyphon heat pipe was utilised to cool the solar PV panel by absorbing the heat and transporting it to a cooling fluid which was water, as shown in Figure 2-16. The PV/T system was examined in two different seasons using methanol and acetone as working fluids of the heat pipe. The investigation studied the temperature of the PV/T panel, the electrical output, and the electrical and total efficiency of the PV/T. The results of testing the PV/T were compared with a PV panel without cooling. The electrical output of PV/T was higher than of the PV by 5.67% to 7.7%, while the total efficiency was increased between 15.3% and 44.38% in comparison to the conventional PV system.

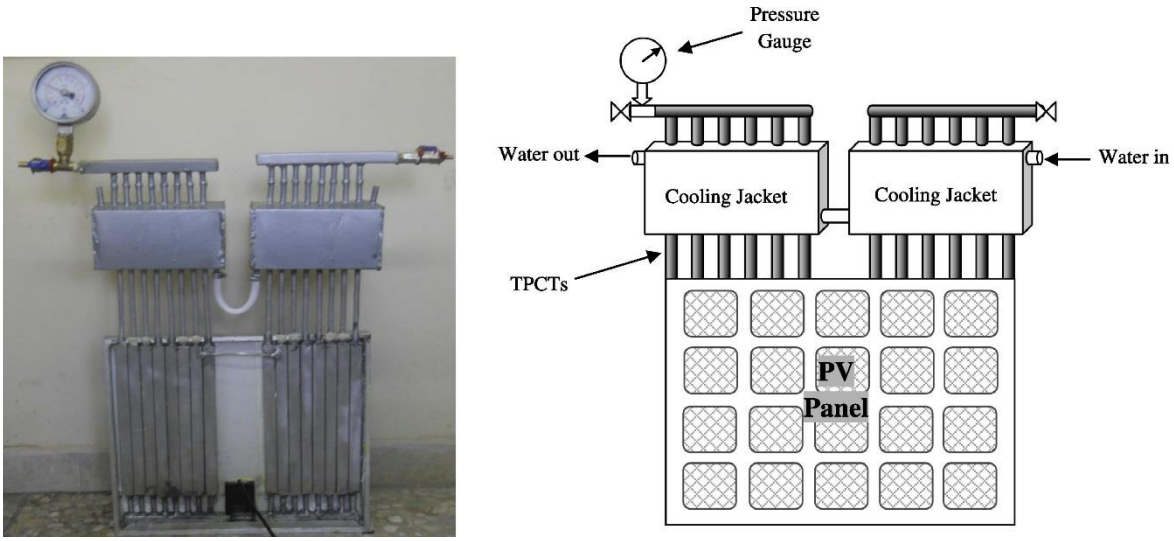

Figure 2-16 Photovoltaic/thermal system without insulation [51]

Hu et al. [52] investigated the impact of inclination angle on the two different heat pipe PV/T systems presented in Figure 2-17.

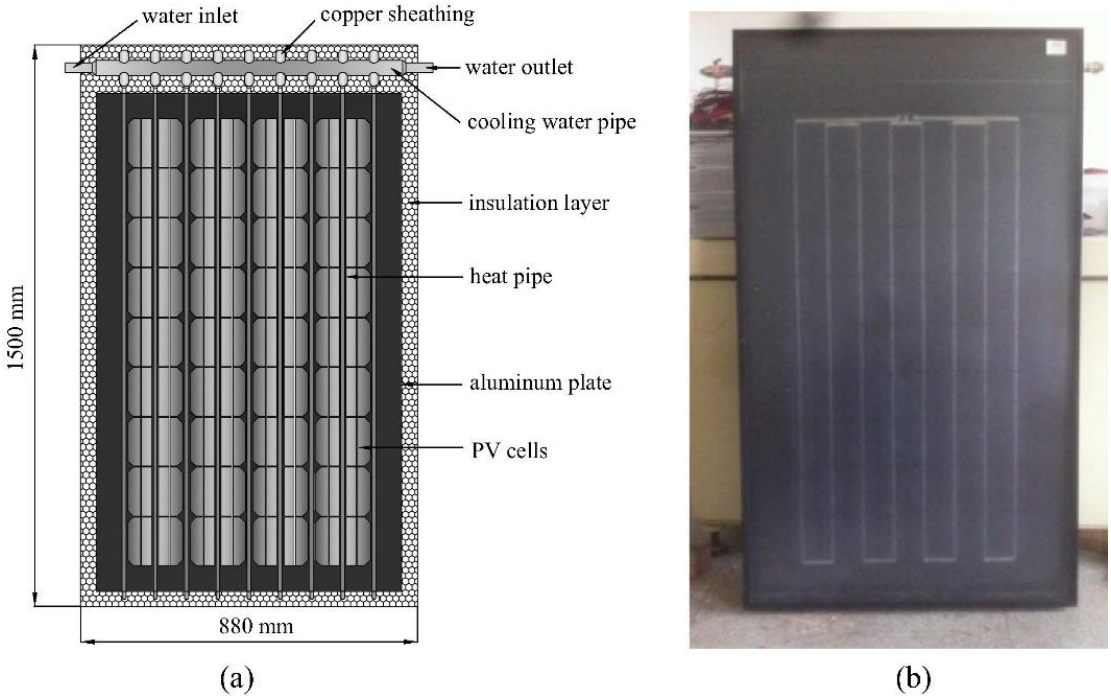

Figure 2-17 A heat pipe PV/T solar collector studied by Hu et al. [52]

One of the heat pipes was a wickless one while the other was provided with a wire-mesh wick. The investigation was conducted using solar simulator parallel to the heat pipe PV/T. Therefore, the inclination angle had an effect only on the heat pipe due the change of the gravity force which significantly affects the two phase heat transfer in the heat pipe. However, in real application where the heat pipe absorbs the heat from the solar irradiation,, the inclination angle also affects the total solar irradiance incident on the heat pipe. It was noted that the thermal performance of wickless heat pipes was strongly influenced by the inclination angle, unlike the wire-mesh heat pipes. Furthermore, the wickless heat pipe exhibited better performance when utilised with an inclination of more than 20° from vertical, while the results indicated the wicked heat pipe had a better performance used in inclinations of less than 20°. The highest thermal efficiency of both types of heat pipes was obtained at an inclination angle of 40°.Wu et al. [53] investigated the heat pipe photovoltaic-thermal (PV/T) system illustrated in Figure 2-18. The investigation was conducted experimentally, and a theoretical model was developed to analyse the heat transfer performance by mean of the thermal and electrical efficiency and exergy. The effect of various parameters on the performance and the PV cells' temperature were investigated. The wicked heat pipe system was made of copper pipes of 0.12 m diameter and a length of 0.92 m. The length of evaporator section was 0.75 m and the length of condenser section was 0.1 m. It was observed that the thermal and electrical efficiency decreased significantly by increasing water inlet temperature. Both parameters were increased by increasing the water flow rate. The effect of the packing factor and the heat loss coefficient were also studied. It was concluded that thermal efficiency decreases at higher packing factor while it has the opposite effect

on the electrical efficiency. It was also noted that heat loss coefficient can considerably reduce the thermal efficiency. The system presented achieved thermal and electrical efficiencies of 63.55% and 10.26%, respectively.

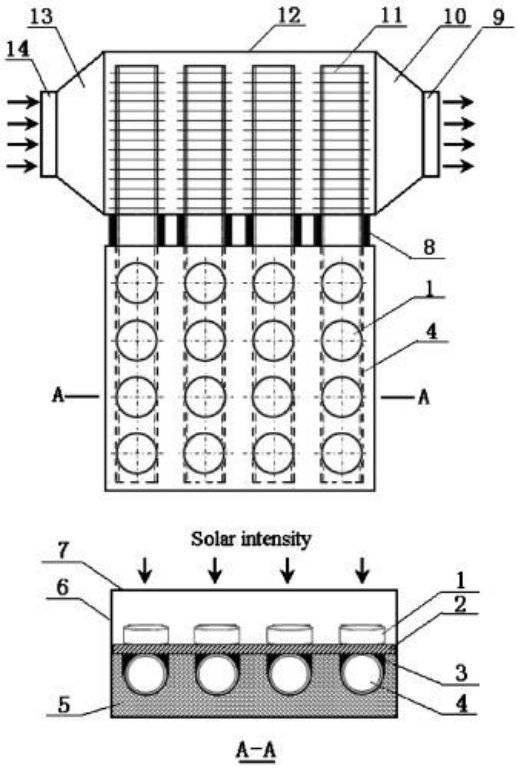

Figure 2-18 A heat pipe PV/T system presented by Wu et al. [53]

It was proven from the results reported in the literature that PV/T systems can greatly enhance the electrical efficiency of the PV panel. However, utilising cylindrical heat pipes with PV panels has some limitations [54]:

- The contact area between the PV panel and the surface of the heat pipe is minimal, leading to temperature gradients on the PV surface in the distance between two heat pipes which decreases the electrical efficiency of the system
- A cylindrical heat pipe increases the thickness of the system and limits the integration of the PV/T system into the structure of buildings.

Flat heat pipes can also be utilised in solar applications when combined with PV panels. Joining heat pipes with PV panels makes the system produce electricity and heat simultaneously. This combination of flat heat pipes with PV panels increases the efficiency of the PV panels by decreasing their working temperatures.

A Micro heat pipe array (MHPA) comprises of separated channels where each channel represents an individual heat pipe, as developed and patented by *Yanhua et al.* [55]. The internal surface of the channel is provided with micro grooved fins which increases the heat transfer area and the wetting

area of the liquid in the evaporator and the condenser. The benefits of integrating MHPA with PV/T panels are summarised as follows:

- Flat heat pipes have a higher contact area between the panel and the evaporator of the heat pipe therefore giving a higher heat transfer area between the heat pipe and the panel.
- A reduced hydraulic resistance as the condenser can be cooled using a manifold consisting of straight tubes
- A high reliability as each heat pipe consists of many micro heat pipe channels separated from each other and operating individually.
- Flat heat pipes have a relatively low manufacturing cost, as they are manufactured by an extrusion process using aluminium which is also a low-cost material.

Hou et al. [56] studied a flat heat pipe for photovoltaic/thermal collector cooling as shown in Figure 2-19. The performance was investigated experimentally and also theoretically by a developed mathematical tool. The experimental set up consisted of two photovoltaic/thermal collector systems where a photovoltaic panel was covered by a glass layer on one side and attached to a micro flat heat pipe array (MHPA) system on the back side. In addition there was a water pump and a water tank. Each of the two PV panels had dimensions of 1580 mm × 808 mm. The developed mathematical model was based on a thermal node analogy considering the experimental set-up where the thermal performance parameters of the MHPA were obtained from experimental data. The theoretical results were validated experimentally from a test running for a day. It was noted that the PV temperature was 60 °C at the end of the day at an ambient temperature of 40 °C due to the cooling water reaching about 63 °C. The total efficiency of the system was about 53%. The simulation results using the mathematical model were consistent with experimental results to within an error of less than 10%. Moreover, experimental results on the system performance for a year indicated that the thermal efficiency of the MHPA was about 20% during the winter and it increased significantly to 40% in the summer.

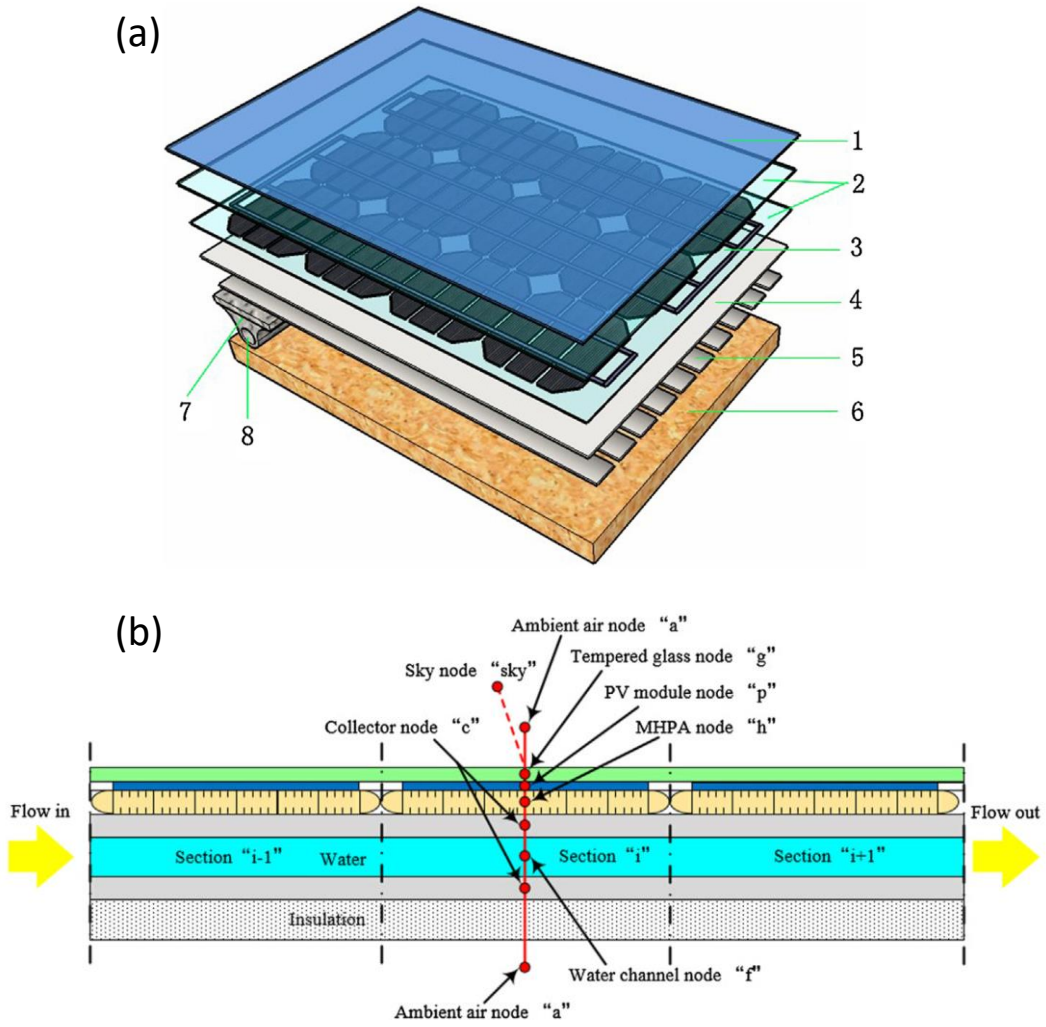

Figure 2-19 A heat pipe PV/T system presented by Hou et al. [56]: (a) structural diagram of the heat pipe PV/T system , (b) node diagram of the model. 1: toughened glass, 2: EVA, 3: monochrystaline silicon, 4: TPT, 5: MHPA, 6: Insulation, 7: collector, 8: water inlet

Jouhara et al. [57] proposed a novel flat heat pipe based photovoltaic thermal (PV/T) system which was called a heat mat. The heat mat was developed to perform as a building envelope which is shown in Figure 2-20. *Jouhara et al*. [58] investigated the effects of cooling cycles on the electrical output and the temperature of the heat pipe PV/T panels on three heat mats at different configurations. It was noted that the electrical efficiency was increased by 15% with the use of an active cooling cycle in the panels. Furthermore, the temperature of the panels decreased from the range of 40°C - 58°C to the range of 28°C - 33°C. The thermal efficiency of the heat mat without the PV layer was around 64%, while the efficiency of the heat mat with the PV layer was around 50%. Combining the PV panel with the heat mat adds a conduction thermal resistance and increases the losses by reflection from the PV surface in radiation heat transfer. The capability of the heat mat to absorb heat from the ambient air under a no radiation condition was also investigated in the laboratory environment. The convection

gain depends on the temperature difference between the ambient air and the coolant in addition to the wind speed.

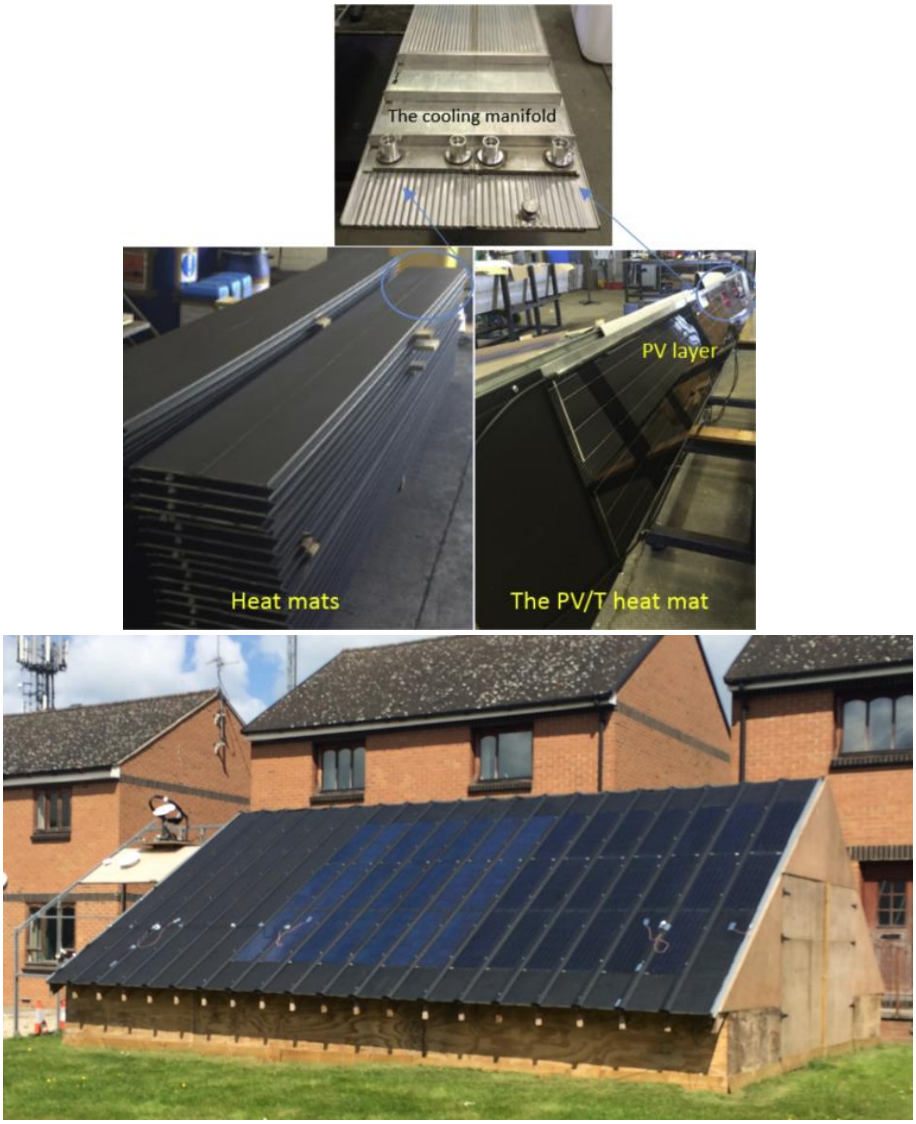

Figure 2-20 The PV/T heat mat system by Jouhara et al. [58,59]

In later study *Jouhara et al*. [59] examined the performance of a flat heat pipe combined with PV/T panels. The flat heat pipe PV/T panels were tested with six different configurations for different levels of solar irradiance. The configurations consisted of four flat heat pipe PV/Ts in which two were cooled while the other two were uncooled, in addition to a cooled flat heat pipe with a thermal panel (no PV attached to it) and an uncooled PV panel. The investigation studied the following parameters: the temperature of the panels, the thermal heat recovery, and solar to thermal conversion efficiency. The experimental data was used to perform a numerical simulation for the implementation of five solar panels with a cooling water tank, hot water tank and water-water heat pump. The results of the study indicated that the heat pipe system was capable of providing sufficient cooling for the solar panels

where the temperatures of the cooled PV/T panels were 23.5 °C lower than for the uncooled ones. It was noted from the simulation that the flat heat pipe PV/T system could cover 41% to 100% of the energy demand for domestic hot water (DHW) applications depending on the available solar irradiance.

Table 2-3 summarises the thermal and electrical efficiencies from the studies on heat pipe PV/T systems discussed. The performance of PV/T is influenced by the site, the water temperature, the climate conditions, the PV quality, and the heat pipe cooling system. However, it can be concluded that the thermal efficiency of such a system exceeds 60% and the electrical efficiency of the PV panel can be increased experimentally by more than 45%. The heat pipes summarised in Table 2-3 had different designs where the design presented *Moradgholi et al*. [51] presented in Figure 2-16 comprised of parallel tubes connected by a bottom collector and a top header and cooled externally by a water cooling jacket. It can be noticed the large size of the cooling jacket of the heat pipe. The system achieved a total efficiency of 55% and thermal efficiency of 45.14% in the summer where the solar irradiance reached 1080 W/m². However, it can be seen that the heat pipe PV/T system presented by Wu et al. [53] achieved higher thermal efficiency reaching 63.35%. This can be attributed to better insulation and less thermal resistance between the PV panel and the pipe. In addition, the heat pipe system was made of copper. The novel design presented by Hou et al. [56] achieved thermal efficiency up to 40% in the summer which is lower than the former technologies. However, the design presented by Jouhara et al. [58,59] achieved thermal efficiency of 64% without insulation or PV panels which minimises the overall heat transfer thermal resistance of the system but increases the losses to the ambient. The thermal efficiency of the system assembled with a PV panel reached about 52%. In general, it can be noted that thermal efficiency of a heat pipe PV/T system efficiency can exceed 50%. The efficiency of the system can be enhanced further by employing better thermal interface material between the PV panel and the heat pipe. Another aspect is the PV panel material thermal conductivity and thickness which represents a thermal resistance between the heat pipe and the solar irradiation.

Table 2-3 Summary of the results from different heat pipe PV/T systems

Author	**Heat pipe system**	**Working fluid**	**Highlights**
Moradgholi et al. [51]	Aluminium thermosyphon heat pipe. Evaporator dimensions are: 350mm × d=8mm Condenser Dimensions are: 100× d=8mm	Methanol (spring test)	During the spring $\frac{\eta_{\text{electrical,PV/T}}-\eta_{\text{electrical,PV}}}{\eta_{\text{electrical,PV}}} = 15.3\%$ $\eta_{total,PV/T} = 30\%$

		Acetone (Summer test)	During the summer $\eta_{total,PV/T} = 55\%$
Wu et al. [53]	The heat pipe material is copper with the following dimensions: outer diameter is D=0.122 m and total length is 0.92 m, the length of the evaporator is Le=0.75 and the condenser is 0.1m and pitch distance between two pipes is W=0.135 m.	Not mentioned	$\eta_{th} = 63.65\%$ $\eta_{electrical} = 8.45\%$ $\varepsilon_{PV/T} = 10.26\%$
Hou et al. [56]	Heat pipe is micro heat pipe array Dimensions:800 × 60 × 3mm Case material: aluminium	Acetone	$\eta_{\mathrm{th,PV/T}} = 19.9 - 40\%$ $\eta_{\mathrm{electrical,PV/T}} = 11.7 - 15\%$ $\eta_{\mathrm{total,PV/T}} = 30 - 50\%$
Jouhara et al. [58]	The heat pipe is a multi-channel flat heat pipe (it is referred to as the PV/T heat mat). Total dimensions are: 4m in length and 0.4m in width. Three heat mats were tested. One is without PV panel on it, the others are with PV panels one with cooling and one without cooling	Ammonia	$\eta_{th} = 64\%$ $\eta_{PV} = 6.1\%$ $\eta_{\mathrm{th,PV/T}} = 49.4\%$ $\eta_{\mathrm{electrical,PV/T}} = 7.0\%$ $\eta_{\mathrm{total,PV/T}} = 56.5\%$ $\frac{\eta_{\mathrm{electrical,PV/T}} - \eta_{\mathrm{electrical,PV}}}{\eta_{\mathrm{electrical,PV}}} = 15\%$
Jouhara et al. [59]	Heat pipe is a flat heat pipe where the shell is: aluminium. The length is 4 m and the width is 0.4 m. Six Flat heat pipes were tested, four of them equipped with PV panels.	Ammonia	$\eta_{th} = 45.4 - 64.2\%$ $\eta_{\mathrm{th,PV/T}} = 34.8 - 52\%$ $\eta_{cooling} = 18.1 - 47.8\%$

The key-elements of the heat pipe solar collectors an heat pipe PV/T systems is that the solar irradiation is below 1.5 kW/m², they are normally cooled by water as they are used for domisted heating applications, and the solar irradiation is incident from the top in angle range between 20° and 40°. Wick structure is needed within the evaporator of the heat pipe since the heated surface is the

upper side while the condensate return is on the down side. The wick structure adds more limitations on the heat pipe thermal performance, cost, and complication in the manufacturing process.

Solar irradiance is not steady during the day and it is unavailable during the night, which highlights the need to find a solution to meet steady demands and expand the working duration. Therefore, heat recovery in solar applications is normally combined with thermal energy storage to overcome these drawbacks. Phase change materials (PCMs) can be used for thermal energy storage proposals, however the low conductivity and solidification and melting process requires an isothermal surface with a high thermal conductivity between the solar absorber and the PCM. Heat pipes meet the requirements for such an application due to their quick response and the capability of transferring high heat fluxes.

Mahdavi et al. [60] investigated numerically the hydrodynamic and thermal performance of a high temperature heat pipe for concentrated solar energy storage systems, as illustrated in Figure 2-21. The working fluid of the heat pipe was sodium due to its low vapour pressure at high temperatures. Heat transfer limits of the heat pipe were determined, which were caused by heat pipe geometry, working fluid, wick structure, and operational temperature. The impact of heat input on the vapour flow and pressure was investigated. The effect of the adiabatic section radius on the temperature distribution along the heat pipe was also studied. The thermal resistance of the heat pipe was also determined at different input powers. It was concluded that the thermal resistance of the heat pipe decreases with increasing the heat input.

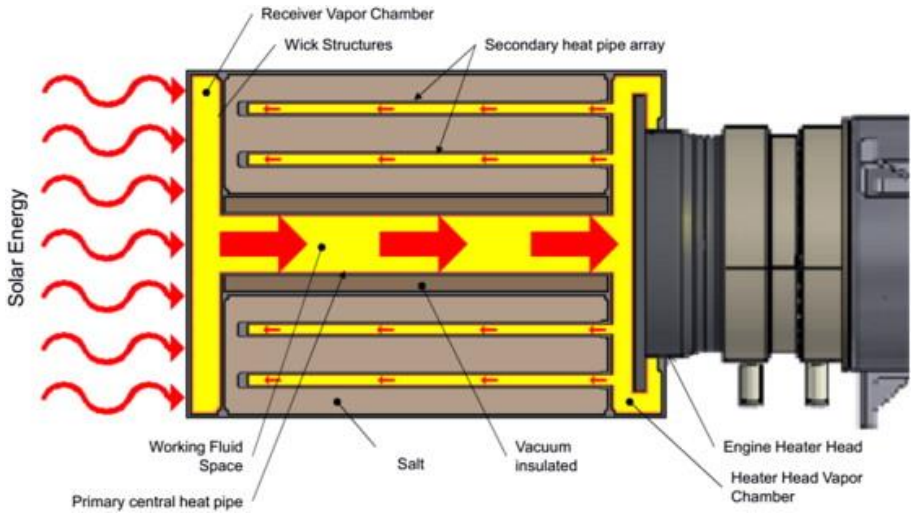

Figure 2-21 Heat pipe and thermal energy storage module by Mahdavi et al. [60]

Liao and *Faghri* [61] presented a novel heat pipe solar central receiver for a molten salt solar power system. This consisted of a reflector, heat pipe, and a receiver tube as shown in Figure 2-22. A numerical simulation was performed to investigate the thermal performance of the heat pipe. The

research investigated the impact of the number of flow passes of the cooling fluid in the receiver tube on the receiver efficiency and the evaporator temperature at various concentrated heat flux densities. It was observed that the receiver efficiency increased with concentrated heat flux density and decreased linearly with the number of flow passes. The results obtained showed that the proposed heat pipe system could increase the daily operating duration of the receiver.

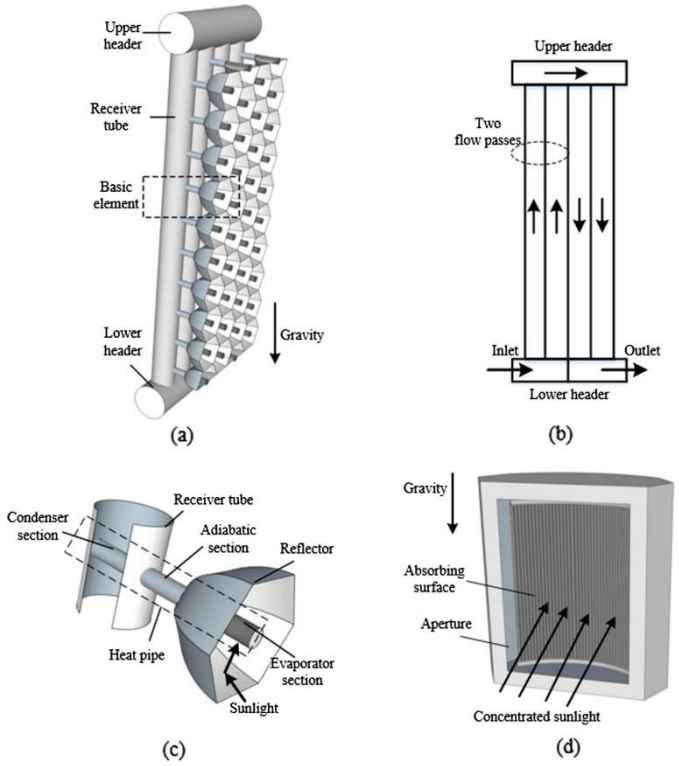

Figure 2-22 Schematic of a heat pipe solar central receiver: (a) receiver panel; (b) two dimensional receiver panel; (c) basic element; (d) receiver structure proposed by Liao and Faghri [61]

Yang et al. [62] conducted an experimental study on a high temperature flat heat pipe receiver used in a solar power plant. The heat pipe illustrated in Figure 2-23 was made of stainless steel 310 and it was charged with sodium as a working fluid. The heat pipe was cooled by a water jacket and serrated fins. The study investigated the thermal performance and start-up time characteristics were investigated at constant heat input. The impact of inclination angle and the heat flux on the start-up time was also studied. It was noted that the thermal performance and start-up time are considerably influenced by inclination angle and heat input. The results indicated the best performance at an angle of 45°. It was noted that the thermal resistance decreased with increasing the heat input. Moreover, the flat heat pipe exhibited a uniform temperature distribution, excellent thermal conductivity and fast response.

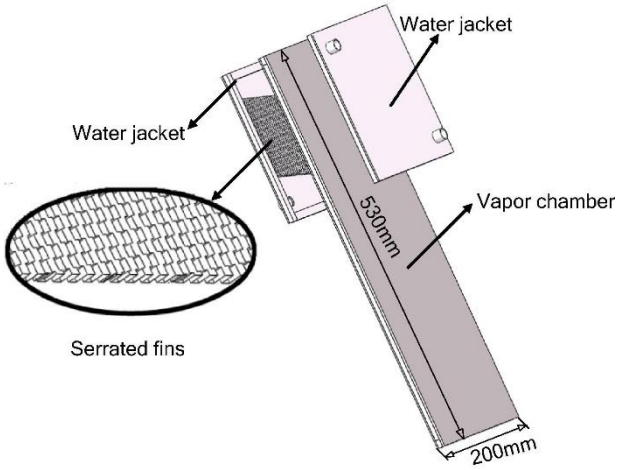

Figure 2-23 Heat pipe presented by Yang et al. [62]

Boo et al. [63] conducted an experimental study on loop heat pipes to transport thermal energy from a concentrated solar receiver. The fabricated heat pipe which is shown in Figure 2-24 was designed to transfer the heat from a solar receiver to an alkali metal thermal to electricity converter (AMTEC). The heat pipe was designed to transfer 1.2 kW at 1000 °C. The heat pipe was charged with sodium and tested at different filling ratios in laboratory conditions using an electric heater. It was noted that the fill ratio has an impact on thermal resistance, effective thermal conductivity, isothermal characteristics, and the start-up time. The optimal filling ration based on the evaporator inner volume corresponding to the best performance was found to be 32%.

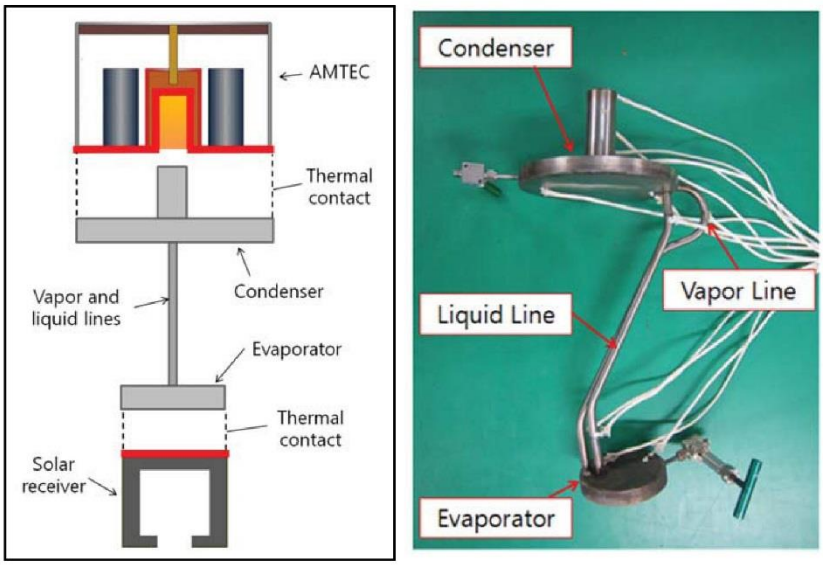

Figure 2-24 loop heat pipes to transport thermal energy from a concentrated solar receiver Boo et al. [63]

A solar thermochemical reactor is considered as a special case of solar receiver. It utilises the concentrated solar energy to carry out a chemical reaction that produces hydrogen as a solar fuel from

splitting the water [64]; heat pipes with flat evaporators are also used in such devices. A high temperature heat pipe design which combines a flat evaporator and a cylindrical condenser (HTSSHP) was investigated by *Wang et al.* [65]. The heat pipe was designed to be utilised in a thermochemical solar reactor. The investigation studied the start-up characteristics, isothermal performance and thermal resistance. The temperature distribution along the heat pipe for different cooling conditions was also investigated. The flat heat pipe exhibited the capability of preventing the formation of hot spots on the absorber surface. The cylindrical heat pipe which represented the condenser section showed the potential to enhance the temperature distribution in the reaction chamber.

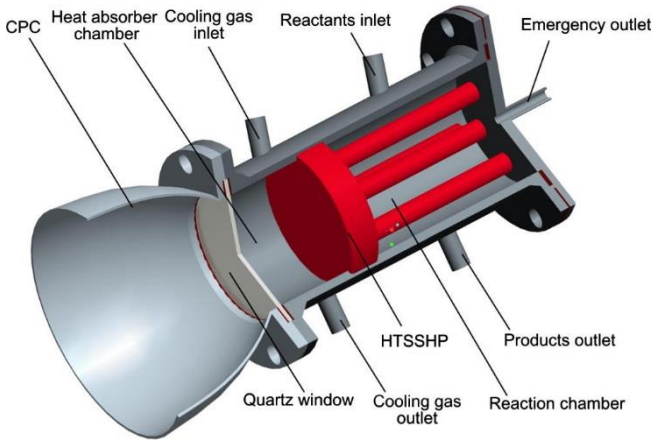

Figure 2-25 Schematic of A high temperature heat pipe design proposed by Wang et al. [65]

A later investigation conducted by *Ma et al.* [66] was carried out on a modified HTSSHP where the wall thickness was reduced to enhance the start-up performance. Start-up characteristics were examined under different inclination angles and heat fluxes. The HTSSHP exhibited successful performance at inclination angles between 0°and 45° and it was observed that start-up time is reduced with an increase of heat flux.

Liquid heat pipes for high temperature in nuclear applications can be very attractive for heat recovery in others application such as waste heat recovery by radiation. However, the cost of manufacturing a liquid heat pipe is considerably higher than a wickless heat pipe heat exchanger due to the cost of the wick and the liquid metal working fluid. Moreover, a wicked liquid metal heat pipe encounters more limitations than a wickless heat pipe such as the sonic limit and viscosity limit. A wickless heat pipe normally have quicker response time than a liquid metal heat pipe with the absence of frozen start-up condition presented in the liquid metal heat pipes. Therefore, liquid metals are commonly utilised only for high temperature applications where the working fluid temperature exceeds 400 °C.

2.7.4 Nuclear applications

Heat pipes are common as a heat rejection system for space nuclear applications because of their high reliability. Space power reactors feature as an energy source with the absence of solar energy to meet

the high power demand in space explorations [67]. The feature of the independency of heat pipe operation from the other heat pipes is vital where a failure of a heat pipe does not result in a failure of the whole heat rejection system. The performance of heat pipes for heat rejection by radiation can be enhanced by attaching fins to the pipes which increases the heat transfer area. Radiation heat transfer between the fins and the heat source or surroundings complicates the theoretical derivation of the fin efficiency. *Zhang* et al [68] conducted a thermal analysis of the liquid metal heat pipe radiator (HPR) presented in Figure 2-26 for a space power reactor. The proposed system comprised heat pipes provided with integral fins covering the pipes. Potassium was used as a working fluid in the heat pipe, which was wicked by stainless steel wire-mesh and Inconel was used as shell material of the heat pipe. The performance of the heat pipe system was studied numerically. The temperature distribution along the heat pipe radiator fins was compared with pumped loop radiator fins. The results revealed that the heat pipe fins have an isothermal characteristic in the direction of the heat pipe length. The performance of the heat pipe was also compared at different coolant temperatures. In addition, the heat pipe operating limits and heat rejection were studied. The proposed heat pipe had a lower mass and higher operational limits in comparison to the conventional radiator for the same heat rejection, in addition to an isothermal surface feature.

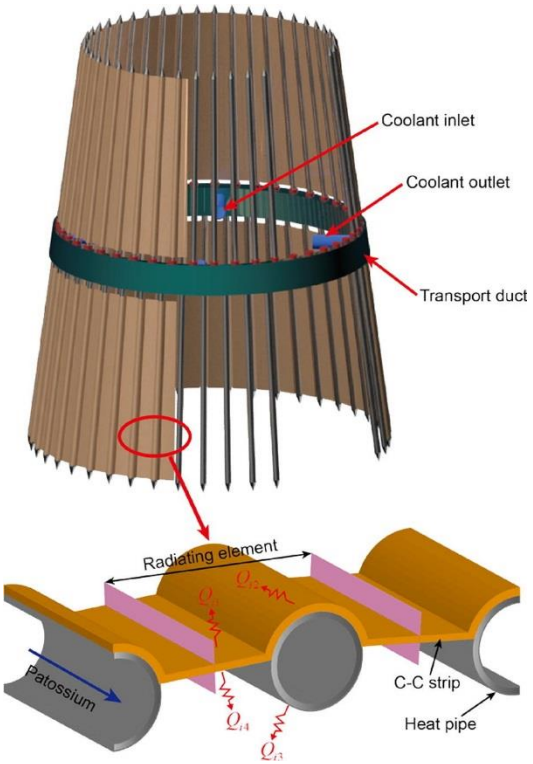

Figure 2-26 Heat pipe radiator presented by Zhang et al. [68]

Wang et al. [69] analysed the performance of a potassium heat pipe radiator for a nuclear space power reactor. One of the characteristics of liquid metal heat pipes is the start-up characteristic which

determines the response time of the heat pipe until it reaches the steady state operation. In addition, it highlights the ability of the heat pipe to adapt to any changes in the operating conditions. A theoretical model of the heat pipe studied was validated by comparing the predictions to a previous experimental study [70]. The temperature and pressure along the heat pipe were investigated in addition to the operating limits. The investigation revealed that the sonic limit of the heat pipe could be encountered during the start-up stage until the condenser temperature increased and dissipated heat by radiation.

In the presented studies on heat pipes in nuclear application, the heat pipe was used to dissipate heat from a coolant such as NaK by radiation. Due to the high temperature of the coolant (>500 K) which reaches 800 K while the heat pipe is being cooled by emitting the heat to the space, the suitable working fluid should be a liquid metal such as potassium. Comparing the liquid metal heat pipe presented by *Zhang* et al [68] to the design of the flat heat pipe in this research, the design proposed by by *Zhang* et al [68] rejects the heat to the space which is considered as a black body. The heat pipe radiator system was consisted of individual heat pipes assembled to together by fins to increase the heat emitting area. The heat pipe was transferring the heat from the coolant to the heat pipes by forced convection through a jacket. In such applications where the heat pipe acts as a cooling radiator, the view factor is not very important as the heat pipe system rejects the heat in all direction to the space and thus the view factor is equal to one. In addition, the emissivity of the space is considered to be 1 as the space is considered a black body. Hence, the overall radiation thermal resistance between the heat pipe radiator system in space applications is much lower than the flat heat pipe heat exchanger presented in this research. The overall radiation resistance of the flat heat pipe is subjected to the emissivity of the hot steel, emissivity of the flat heat pipe surface, and the view factor between the flat heat pipe and the hot steel.

2.7.5 Radiation heat recovery applications

Delpech et al. [71] investigated experimentally a radiative heat pipe in a lab-scale kiln for waste heat recovery by radiation in the ceramic industry. The proposed system is presented in Figure 2-27. The heat pipe consisted of 10 parallel tubes which had 28 mm outer diameter. The parallel tubes were connected at the bottom by a collector and by a shell and tube condenser at the top. The tubes had a length of 430 mm and the heat pipe was charged with water and cooled by water as a heat sink. The heat pipe system was designed to absorb the heat by radiation and natural convection from the ceramic heaters and transfer the heat to the water coolant. The research was conducted at different heater temperatures used to simulate the hot ceramic. The effect of the water flow rate was also investigated, which did not significantly influence the heat transfer rate. The study analysed the thermal performance and compared the heat recovery by radiation and natural convection

theoretically. It was observed that the radiant heat recovery was dominant over natural convection heat recovery at heater temperatures above 300 °C.

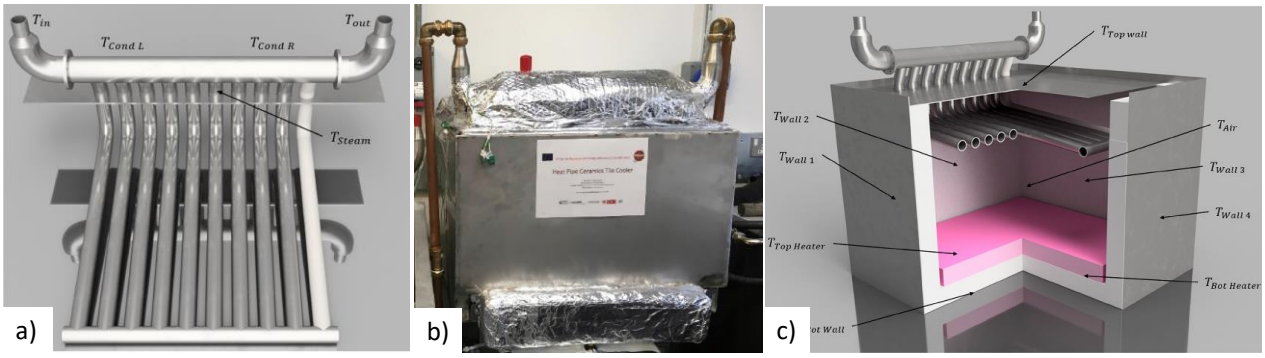

Figure 2-27 Radiative heat pipe system by Delpech et al [71]

The heat pipe heat exchanger presented by *Delpech* et al. [71] was designed to function where the evaporator is inclined at 5° angle from horizontal. The curved evaporator tube connected to the condenser does not allow the heat pipe heat exchanger to function at vertical orientation of the evaporator as it prevents the condensate from returning back to the evaporator. Since the scale of the heat pipe heat exchanger is different from the flat heat pipe heat exchanger of this research, the ratio of the evaporator area to the condenser area is different. The heat pipe heat exchanger had ten parallel tubes connected together with a bottom header of 0.46 m long, while the FHP presented in this research consisted of 14 parallel tubes connected by 1 m long bottom collector. The kiln which was used to test the heat pipe heat exchanger is the same one used in this study. The performance and heat flux of the *Delpech* et al. [71] will be compared with the radiative heat pipe heat exchangers presented in this research.

It can be concluded from the literature that heat recovery technologies by radiation are very limited. The main focus of the research in heat recovery in industry is on the heat recovery from slag, exhaust streams, and kilns. The most challenging heat source is the hot temperature solid waste which led to focus the research on heat recovery from slag. This can be explained as slag carries high quality thermal energy which is rejected as waste heat which can be transferred to pre heat gases used in other processes. Exhaust streams are commonly very attractive waste heat recovery sources due to the flexibility in installing heat exchangers to recover the heat in addition to its high temperature. One of the most important considerations for evaluating a waste heat recovery technology is the capital cost and the modification of the infrastructure to adapt the technology developed. Hence, the final product in the steel industry, as an example, is not exploited as a heat recovery source although the final process in steel manufacturing is a controlled cooling stage. The space availability, the

intermittence of production, the access required and the machines for maintenance represent challenging limitations for utilising conventional technologies. Heat pipe technology which is adaptable, scalable and highly efficient thermally can overcome these challenges economically.

Heat pipe technology has widely been reported in various applications varying from low temperature to high temperature applications such as electronic cooling, waste heat recovery from exhaust gases and solar heat recovery applications, although solar energy can be considered as special case of heat recovery by radiation. However, a solar heat pipe collector or a heat PV/T system absorbs the heat from the upper face and is limited with inclination angles between 20° to 45° for optimal operating conditions. The performance of heat pipes in solar applications is studied under measured heat fluxes or solar irradiance and evaluated from the thermal efficiency of the system. Apart from this, heat pipes for heat recovery by radiation from hot sources are hardly reported in the literature.

It is preferred to implement heat pipes made of copper or aluminium in solar applications to increase the thermal efficiency of the system. Acetone, ethanol, and ammonia are very suitable working fluid candidates that are compatible with the presented shell materials. However, for applications such as hot steel where the sourced temperature exceeds 500 °C, the shell material needs to be stainless steel or carbon steel to withstand higher temperature of the application and the pressure inside the heat pipe.

In this study, a novel heat pipe technology for heat recovery by radiation from hot sources of temperature higher than 400 °C has been presented. The heat pipe consists of multiple parallel vertical pipes connected with a bottom header and a top header, resulting in a flat heat pipe shape. The flat heat pipe thermal performance is characterised at different configurations and experimental conditions to obtain the optimal performance. The optimal performance is defined by the highest heat recovery achieved. The configuration includes the impact of the hot source temperature, and the heat pipe surface emissivity. The flat heat pipe has been also tested in real conditions in a factory for validation. A theoretical modelling tool has been constructed in order to predict and analyse the thermal performance of the flat heat pipe. The theoretical results obtained from the model were validated experimentally. The theoretical model can be used for predicting heat recovery by radiation from different heat sources. The outcome of this research provides further knowledge about heat pipe performance under radiation heat recovery and the flat heat pipe system developed contributes to energy waste reduction and efficiency enhancement.

Chapter 3: Apparatus and experimental procedure

3.1 Introduction

The experimental investigation was conducted using two different heat pipe heat exchangers. The first heat pipe heat exchanger was a single radiative heat pipe heat exchanger tested in a laboratory scale kiln. The other heat pipe heat exchanger was a full-scale heat pipe heat exchanger which is called a Flat Heat Pipe (FHP).

The full-scale heat pipe heat exchanger was tested both in laboratory conditions using electrical heaters fixed on a plate to simulate a heat source and in real industrial conditions in a steel factory.

In the first part of this chapter, the apparatus used to test the single heat pipe and the experimental procedure which was followed will be explained in detail. The aim of testing a single radiative heat pipe under controlled conditions was to understand the radiation and two phase heat transfer regimes at different inclination angles and different heater temperatures.

The second part of this chapter describes the flat heat pipe: the design of the flat heat pipe, instrumentation, the laboratory rig, and operational procedure. The aim of the laboratory tests was to investigate the thermal performance of the FHP under controlled conditions including the FHP temperature and the heat recovery before testing it in industrial conditions.

The third part of the chapter provides detailed information about testing the flat heat pipe in the steel factory. The hot steel cooling facility, the test conditions, and the operational procedure are described in detail. The aim of testing the FHP in factory conditions was to study the thermal performance of the FHP and the heat recovery under industrial conditions.

3.2 Single heat pipe investigation apparatus

The apparatus of the single heat pipe consisted of a heat pipe which was tested in a laboratory-scale kiln at different inclination angles. The mechanical design of the single heat pipe, the test rig, and the instrumentation are presented in the following sections.

3.2.1 Mechanical design

The heat pipe was made from a stainless steel 304 cylindrical tube of length 1m. The condenser was a double pipe heat exchanger of length 200 mm. The annular channel of the water path was provided with helical fins which have a thickness of 1 mm and pitch of 3mm. The fin material was also stainless steel 304. The heat pipe was installed inside a kiln to absorb heat by radiation and it was cooled by a water stream flowing through the condenser.

The heat pipe was tested without paint (plain stainless steel surface) and with a painted surface using black coal paint which will be described later. The heat pipe was charged with water as a working fluid with a 50 % filling ratio of the evaporator volume.

The dimensions of the heat pipe are illustrated in Figure 3-1.

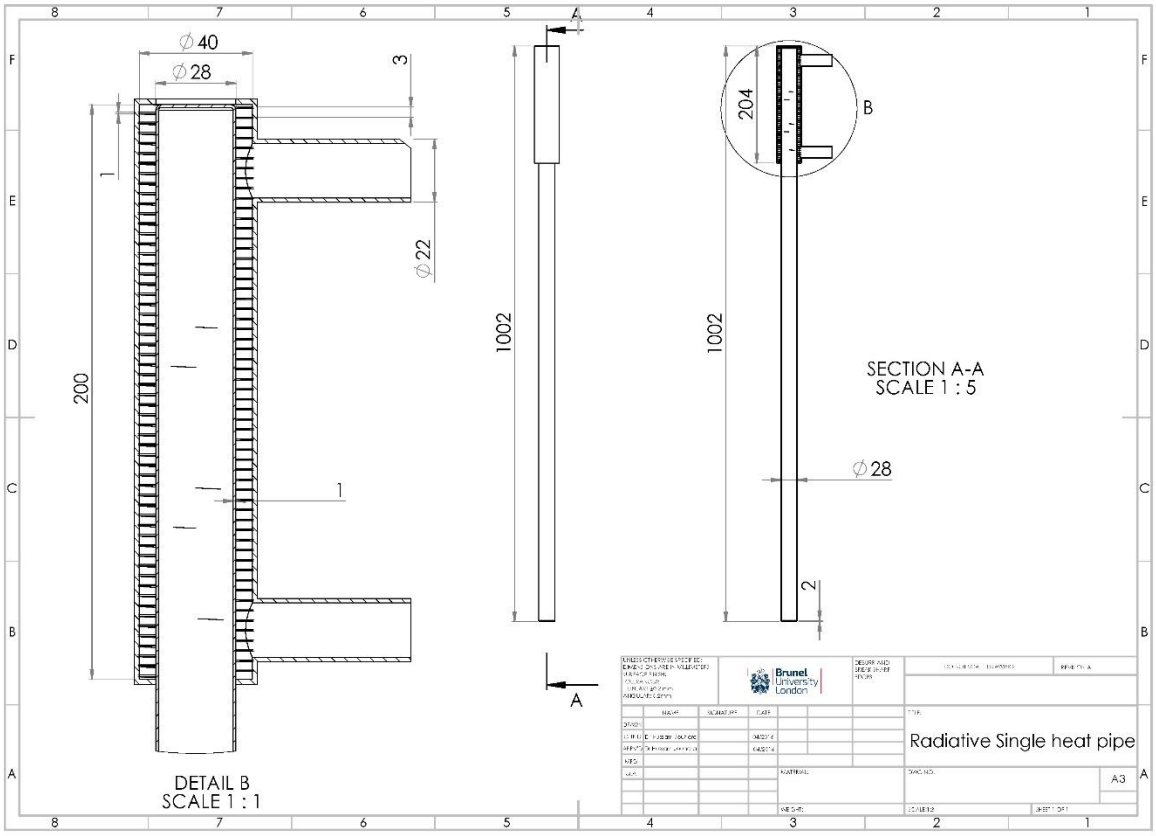

Figure 3-1 Mechanical design and dimensions of the single heat pipe

3.2.2 Test rig

The test rig consisted of a laboratory-scale kin, the single heat pipe and the water circuit.

The kiln comprised electrical ceramic heaters installed on the bottom surface which was made from bricks and the four side walls were also made from bricks. The top surface of the kiln was a stainless-steel cover sheet insulated on the outside.

The brick walls were insulated on the outside with super-wool thermal insulation and clad with stainless steel sheets. The inner surfaces of the four side walls were also insulated and cased with stainless steel wire mesh. A schematic drawing showing the kiln parts is illustrated in Figure 3-2.

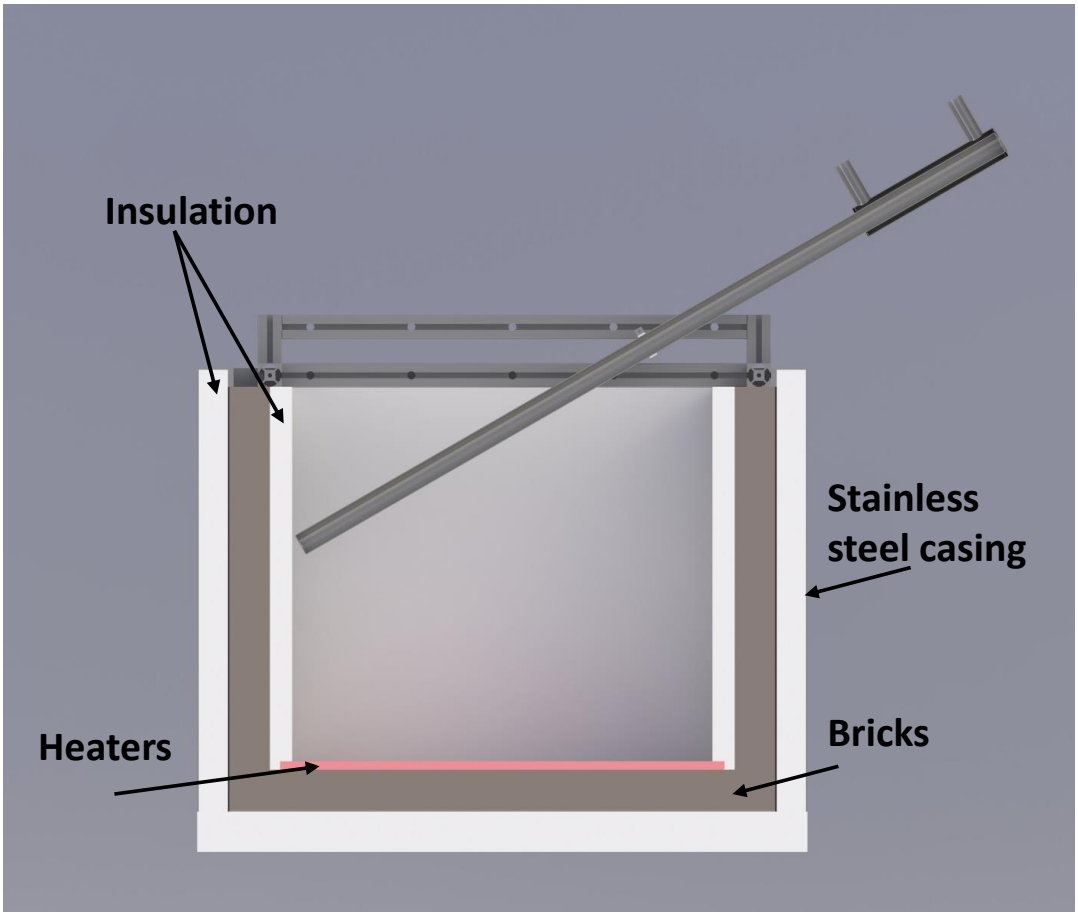

Figure 3-2 Schematic of the kiln

The thickness of the insulation for the brick walls was 27.5 mm on the inside and 36 mm on the outside. The brick wall thickness was 50 mm for both the side walls and the base of the kiln. The inner surface dimensions of the kiln were 520 x 520 x 464.5 mm^3. The dimensions of the kiln and the components are illustrated in Figure 3-3. A photo of the inside of the kiln and a three-dimensional section of it are presented in Figure 3-4. A picture of the test rig with the control system and the instrumentation is shown in Figure 3-5. The heat pipe adiabatic section and condenser section were insulated using super-wool thermal insulation. The superwool insulation is a calcium-magnesium silicate which has a density of 128 kg/m^3 and thermal conductivity of 0.04 W/m.K at temperatures less than 2000 °C.

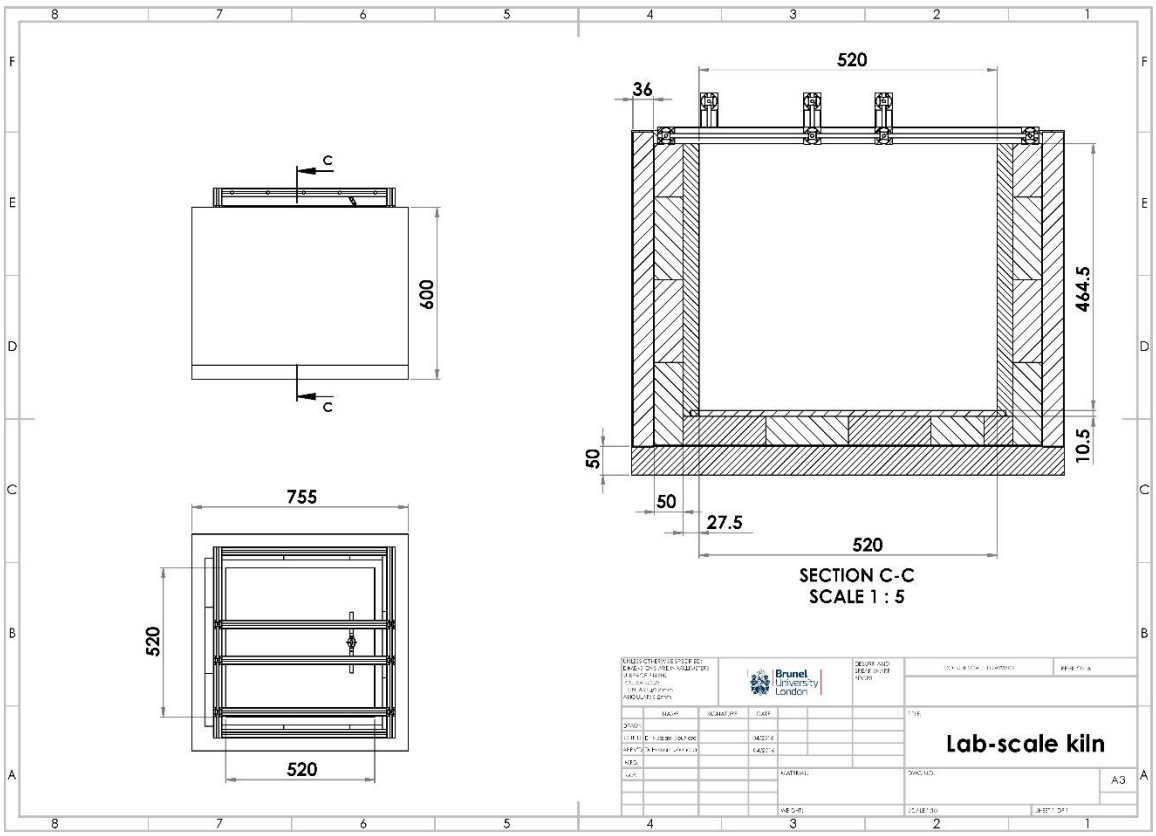

Figure 3-3 Dimensions of the test rig

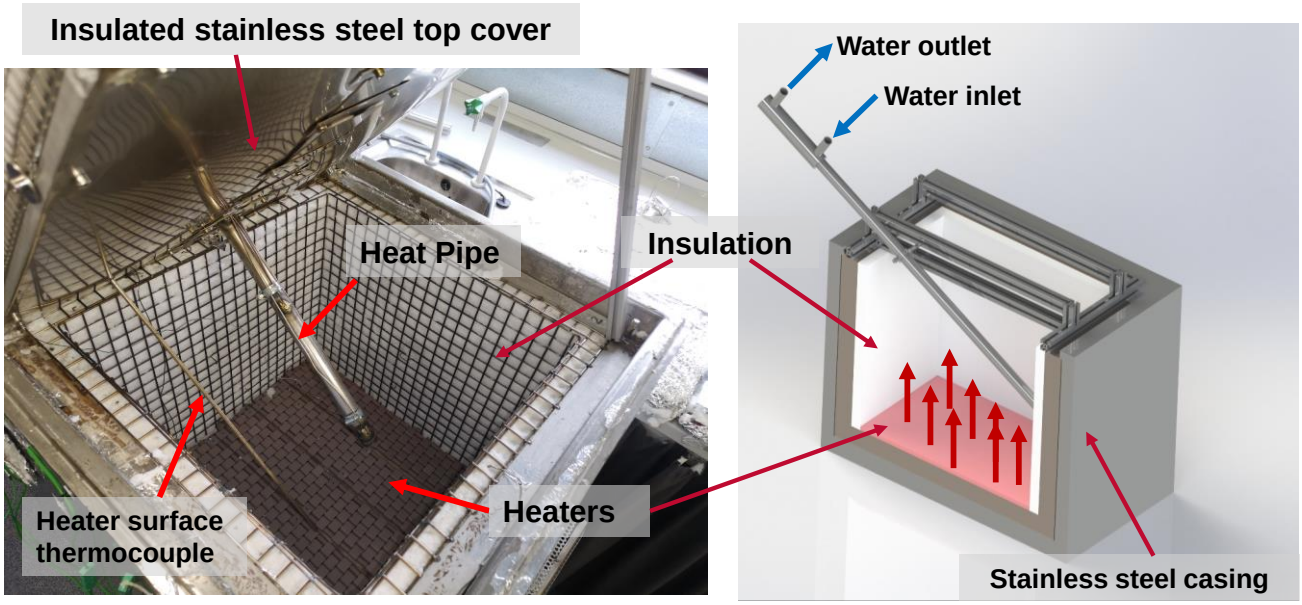

Figure 3-4 A picture and three-dimensional drawing of the test rig

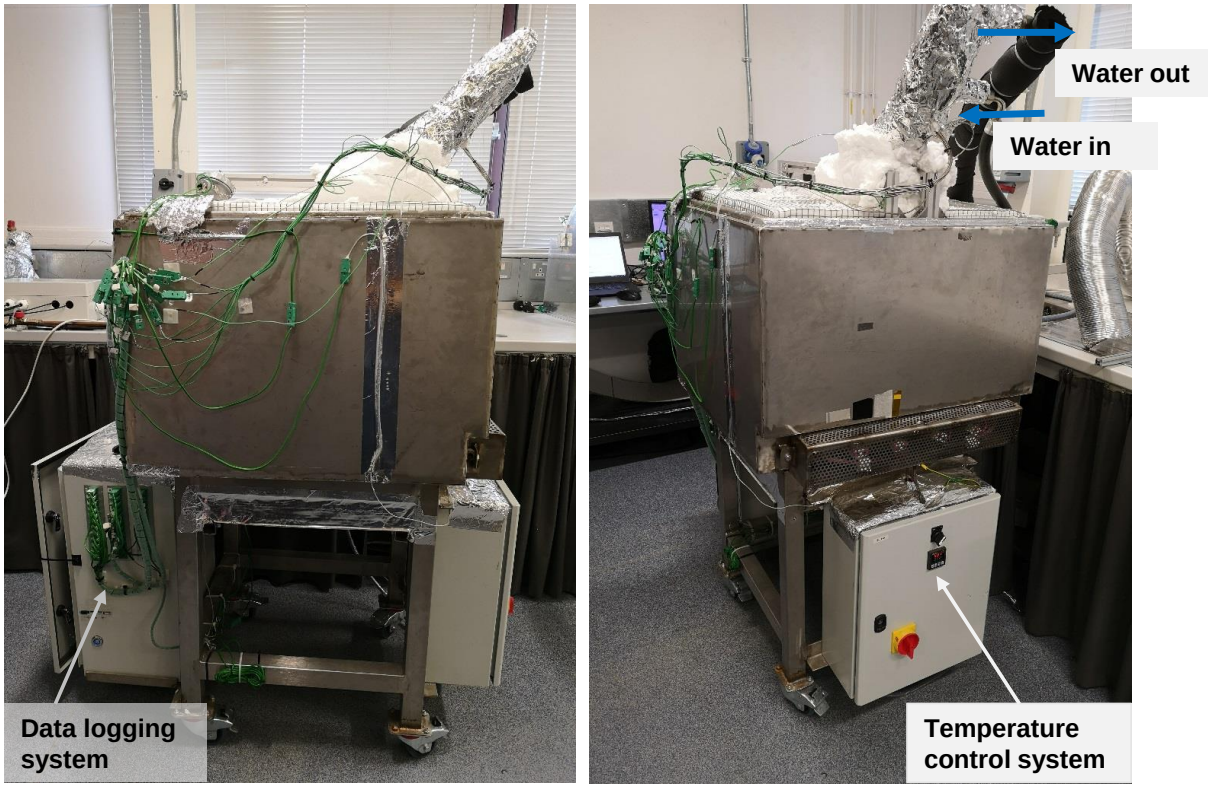

Figure 3-5 Laboratory-scale kiln test rig

3.2.3 Water circuit

The heat pipe was cooled using an open loop water circuit. A schematic diagram of the water circuit is shown in Figure 3-6. The water circuit was used to cool down the heat pipe and maintain its temperature constant during the test. The water was supplied from a mains tap at a temperature varying between 15 and 22 °C and the flow rate was controlled manually using a butterfly valve. The flow rate was measured using a flow meter connected to an individual screen.

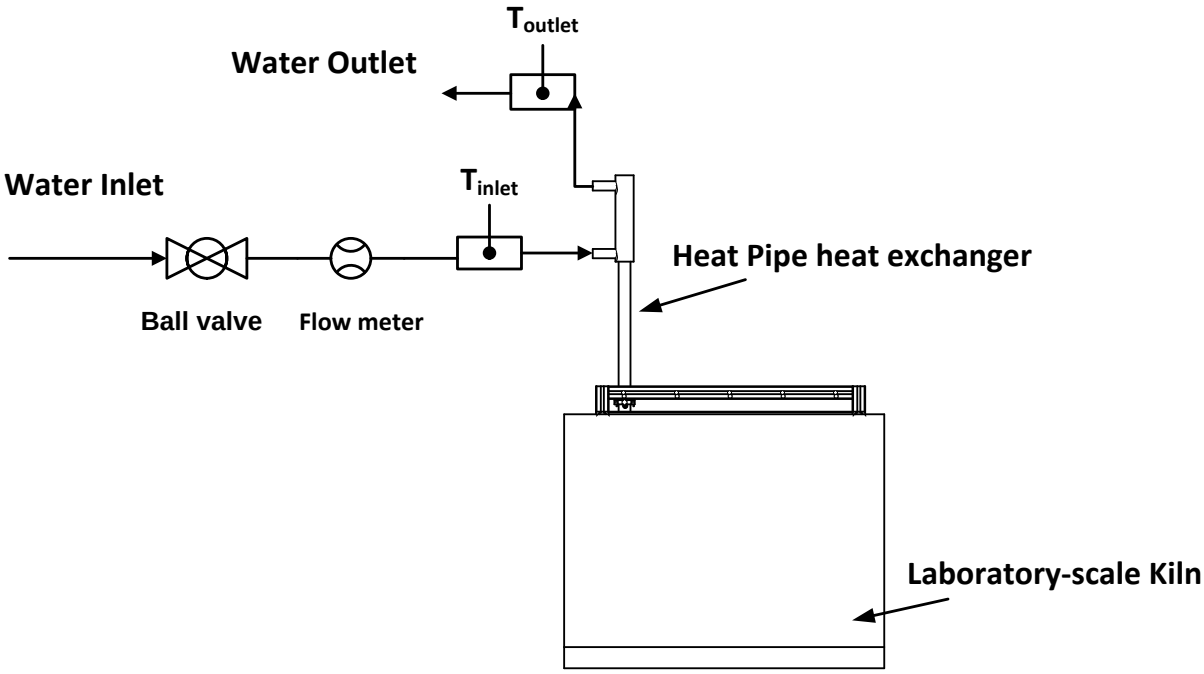

Figure 3-6 Schematic of the water circuit

3.2.4 The heaters

The heaters used in the test rig were flexible ceramic pad heaters from Artech services LTD. Each heater is composed of ceramic beads made of aluminium oxide and a nickel chromium (NiCr 80/20) low resistance wire going through the beads. The use of such heaters ensures a good reliability for the test rig and the possibility of running the experiment at high temperature (maximum temperature of 1050°C). Each heater was rated at 60V, 45 amps current and 2.7kW electrical power consumption. Five identical heaters were connected in series and supplied by a 250 Volt electrical source with a rated current of 32A. It can be concluded that the voltage applied for each heater was 48V since they were identical. The temperature of the heaters was controlled through a thermocouple attached to the top surface of the heaters and connected to a temperature control system. The electrical heaters used in the test rig are shown in Figure 3-7.

Figure 3-7 Picture of the electrical heaters used in the kiln

The specifications of the ceramic heaters are presented in Table 3-1.

Table 3-1 Specifications of the ceramic heaters

Specific heat at 20°C J/kg.°C	419
Melting range	1380-1400°C
Electrical resistivity at 20°C μΩ/cm	108
Mean co-efficient of resistance per °C	20 - 100°C = 0.00008 20 - 500°C = 0.00014
Ceramic beads	
Colour	Pink/white
Density g/cm^3	3.6
Porosity	0°

A picture of the ceramic beads which the ceramic heaters are made of is presented in Figure 3-8.

Figure 3-8 Ceramic beads of the electrical heaters

3.2.5 Control system

The temperature of the heaters was controlled using a PID temperature control system. In order to control the surface temperature of the tiles, a thermocouple for high temperatures was placed on the top surface of the ceramic pad heaters. The signal from the thermocouple was used as an input for the PID system. The PID system monitors the ceramic pad heaters' temperature, compares it with the set temperature, and then controls it by switching on and off the electrical supply to the heaters. The desired temperature is set up in the PID. When the actual heater temperature is less then than set temperature, the PID connects the electrical power to the heaters. If the ceramic heaters' temperature is higher than the set temperature, then the PID switches off the electrical supply to the heaters until their temperature is less than the set temperature. The electrical connections of the PID system are illustrated in Figure 3-9. The PID controller is shown in Figure 3-10.

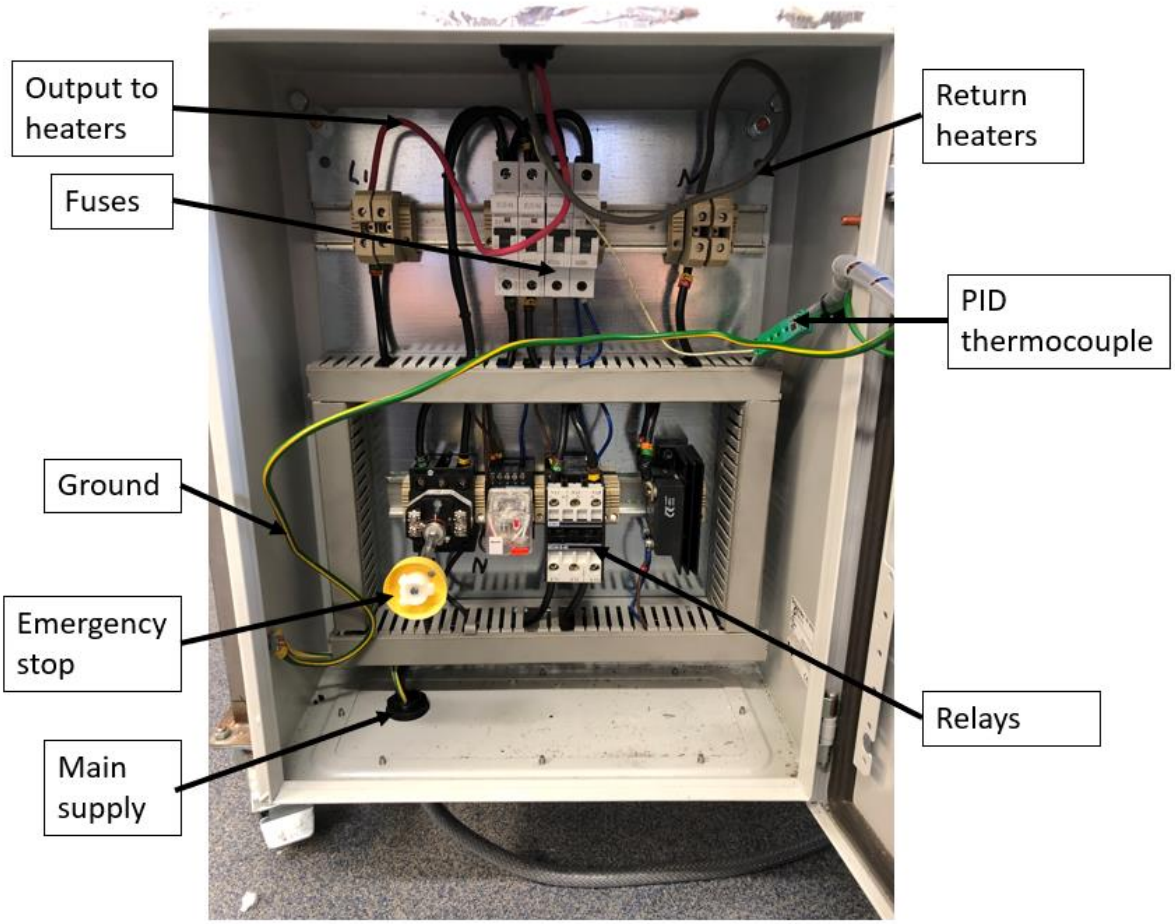

Figure 3-9 PID temperature control system electrical connections

Figure 3-10 PID temperature control system components

3.2.6 Instrumentation

The instrumentation used in the experimental investigation on the single heat pipe consisted of thermocouples, a flow meter, a data logging device and data logging software. A schematic diagram of the test rig with the instrumentation is presented in Figure 3-11.

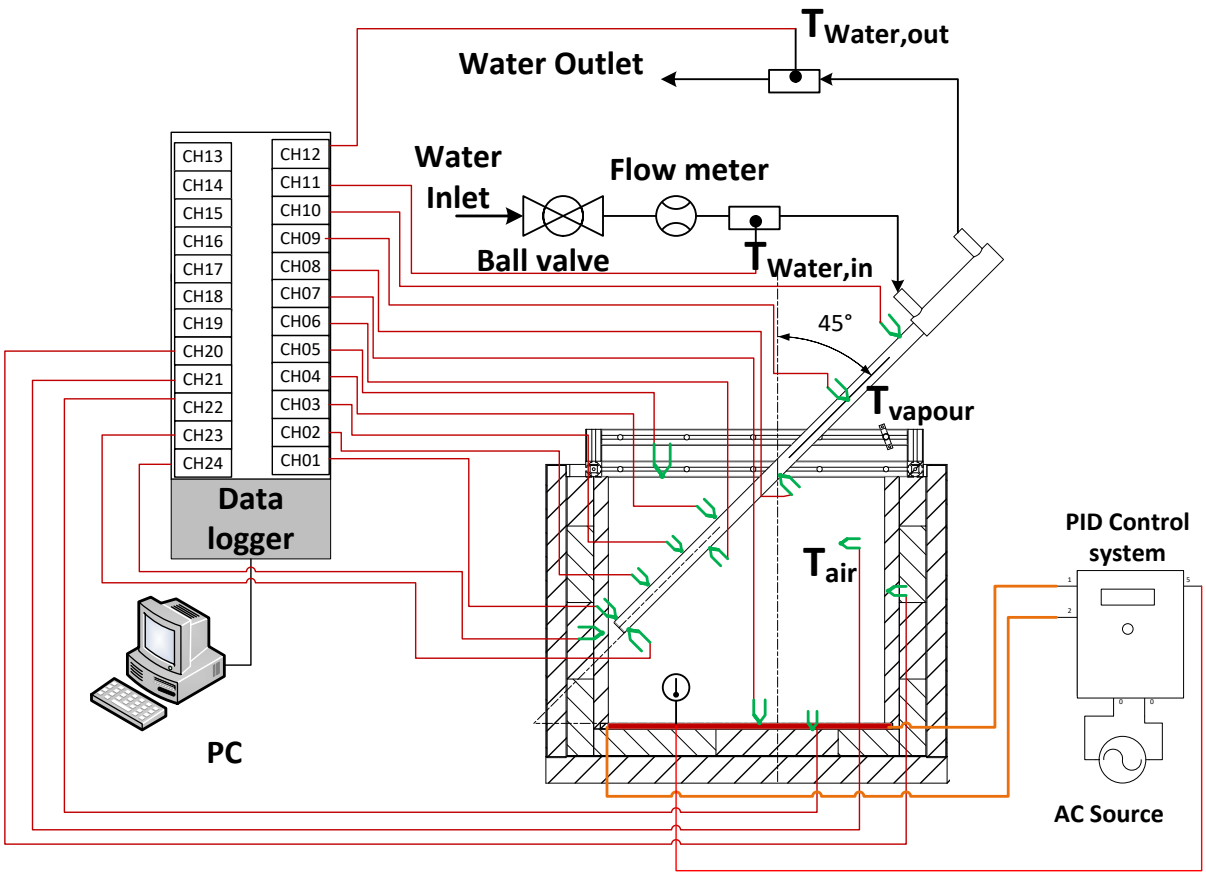

Figure 3-11 Schematic diagram of the instrumentation of the single heat pipe heat exchanger

3.2.6.1 Thermocouples

To characterise the test rig and the heat pipe thermally, multiple thermocouples were used. The heat pipe temperatures were monitored using K-type thermocouples of thickness 3mm welded onto the external surface of the heat pipe. Seven thermocouples were welded on the evaporator surface of the heat pipe which was placed in the kiln. A thermocouple was welded on the adiabatic section of the heat pipe before the condenser jacket. To measure the vapour temperature in the adiabatic section accurately, a hole was drilled in the heat pipe and a thermocouple was inserted into the heat pipe and welded to keep the heat pipe as a sealed structure. The thermocouples placed on the heat pipe can be seen in Figure 3-12.

The water inlet and outlet temperatures were also monitored using K-type thermocouple probes which have diameter of 1.5 mm.

The ceramic heaters' temperature was monitored using a high temperature thermocouple placed on the top surface and connected to the data logging device. A K-type thermocouple was also placed between the ceramic heaters and the inner side of the bottom brick wall. A K-type thermocouple of diameter 1.5 mm was used to monitor the air temperature inside the kiln.

The wall temperature was monitored using K-type thermocouples of diameter 3mm placed in the insulation. A three- dimensional drawing of the thermocouple positioning is shown in Figure 3-13 and Figure 3-14.

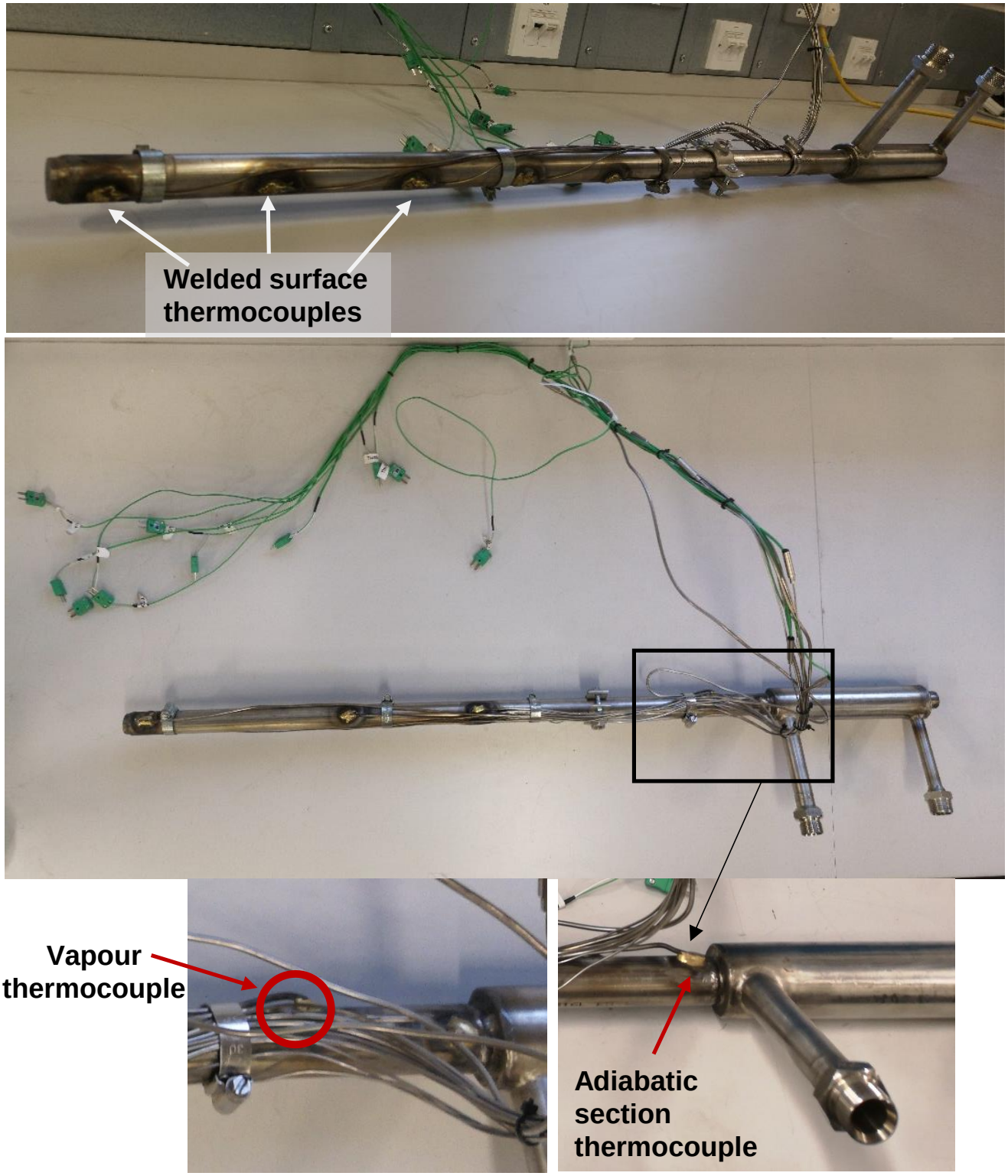

Figure 3-12 Thermocouples placed on the single heat pipe

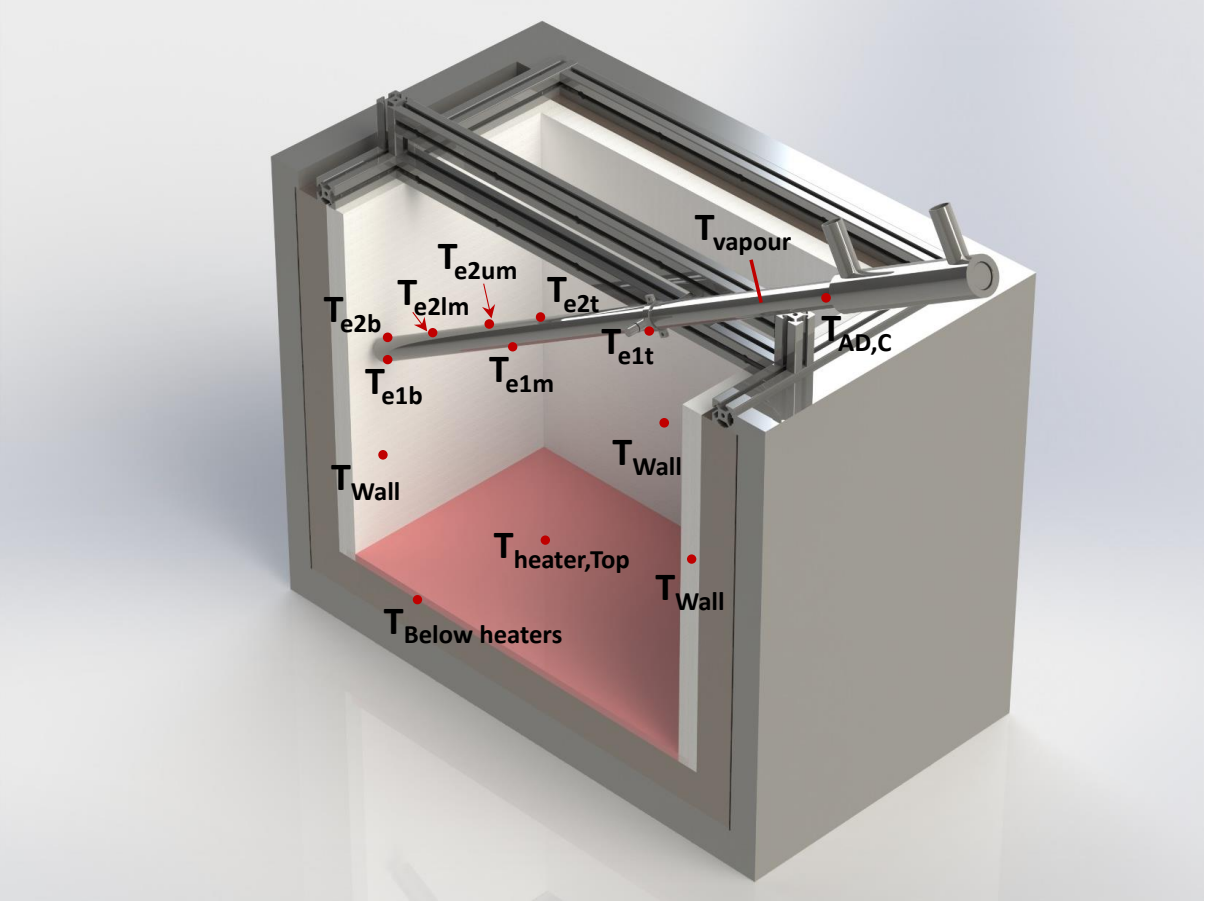

Figure 3-13 Thermocouple positioning in the laboratory kiln experiments

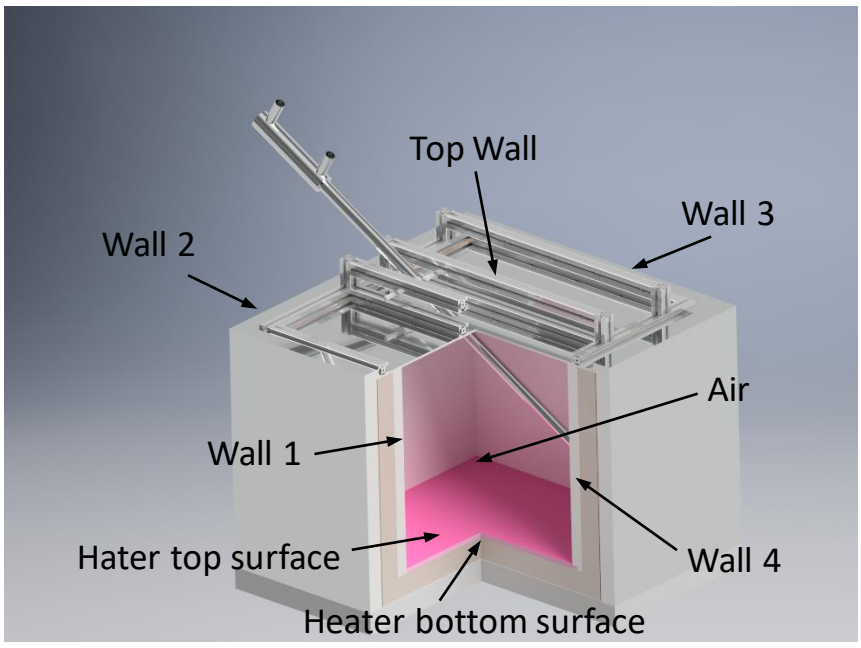

Figure 3-14 Thermocouple positioning on the walls in the laboratory kiln experiment

3.2.6.2 Data logging system

The data logging system was composed of a PC PXIe-1071 and a data acquisition system NI PXIe-4353 from National Instruments®. The data acquisition system has 32 thermocouple channels with high speed (90 Sample/s per channel) and high accuracy (1 Sample/s per channel) modes. The typical accuracy of this system is 0.30 °C.

Table 3-2 includes the error of the module and the terminal block.

Table 3-2 thermocouple type K measurement accuracy

		-100 °C	0 °C	100 °C	300 °C	500 °C	700 °C	900 °C	1100 °C	1400 °C
High Resolution	Typical 23 °C ±5 °C	0.44	0.31	0.28	0.38	0.37	0.46	0.58	0.66	0.88
	Max 23 °C ±5 °C	0.74	0.53	0.49	0.62	0.62	0.74	0.89	1.00	1.30
	Max 0 °C to 55 °C	1.15	0.80	0.71	0.93	1.02	1.24	1.51	1.76	2.29
High Speed	Typical 23 °C ±5 °C	0.67	0.47	0.44	0.57	0.57	0.69	0.83	0.95	1.24
	Max 23 °C ±5 °C	1.02	0.73	0.70	0.86	0.86	1.00	1.18	1.33	1.70
	Max 0 °C to 55 °C	1.43	1.00	0.91	1.14	1.25	1.49	1.80	2.09	2.68

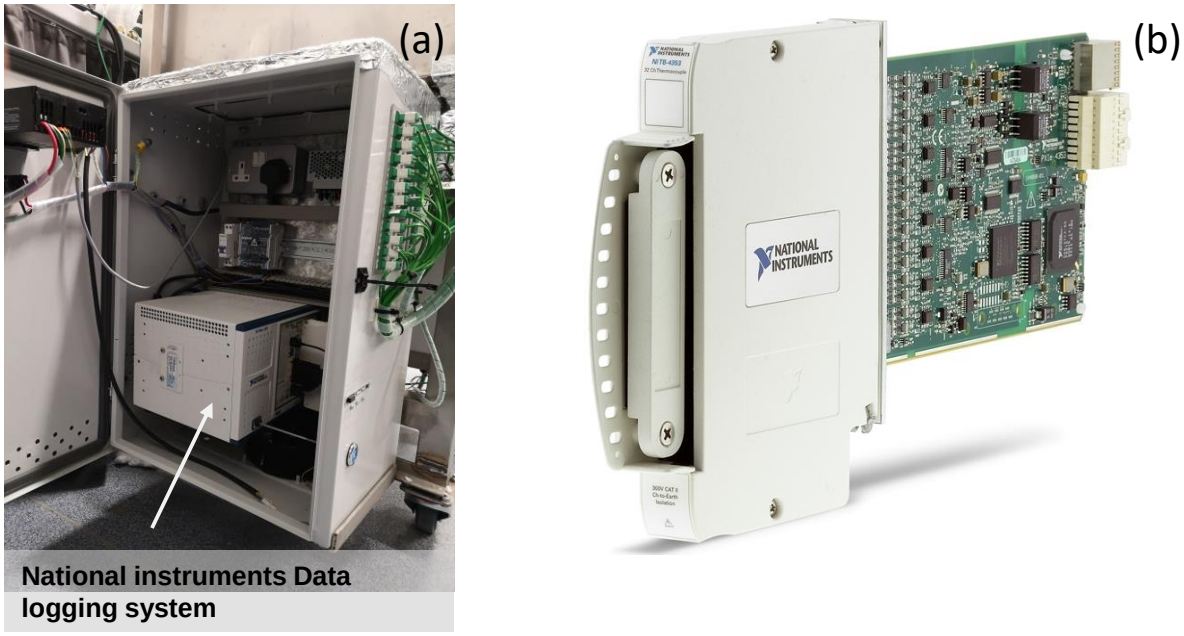

Figure 3-15 Data logging system: (a) the data logging PC PXIe-1071, (b) data acquisition card NI PXIe-4353

The data logging system has a built-in pc where the data can be collected using NI SignalExpress software. A photo of the software during the data collected is shown in Figure 3-16. NI SignalExpress software enables monitoring and recording the data at the same time where it can be exported at the end of the recording process to an Excel sheet to be analysed. The software has the feature of illustrating the data in histograms as well.

Figure 3-16 A picture of SignalExpress software interface

3.2.6.3 Flow meter

The flow rate was measured using Omega® turbine flow sensor FTB371-G. The flow meter was installed in line with the water circuit and connected to a digital display. The turbine flow meter comprises an axial turbine flow meter which is rotated by the fluid flowing through the sensor, which generates a signal readable by a digital display. The accuracy of the FTB371-G was acceptable for these tests. The flow rate of water during the tests was maintained at 1 l/min, which is less than the measurement range of the flow meter. Therefore the flow meter was calibrated by measuring the flow rate manually. The calibration was performed by measuring 900 ml of water in a laboratory beaker and measuring the required time to fill it. The experimental value of the flow rate was compared to the value read on the screen and a correction factor was obtained. It was found that when the value on the screen was 0.677 l/min, the actual flow rate was 1 l/min. The calibration procedure was repeated for every test to ensure the water flow rate was the same for all tests.

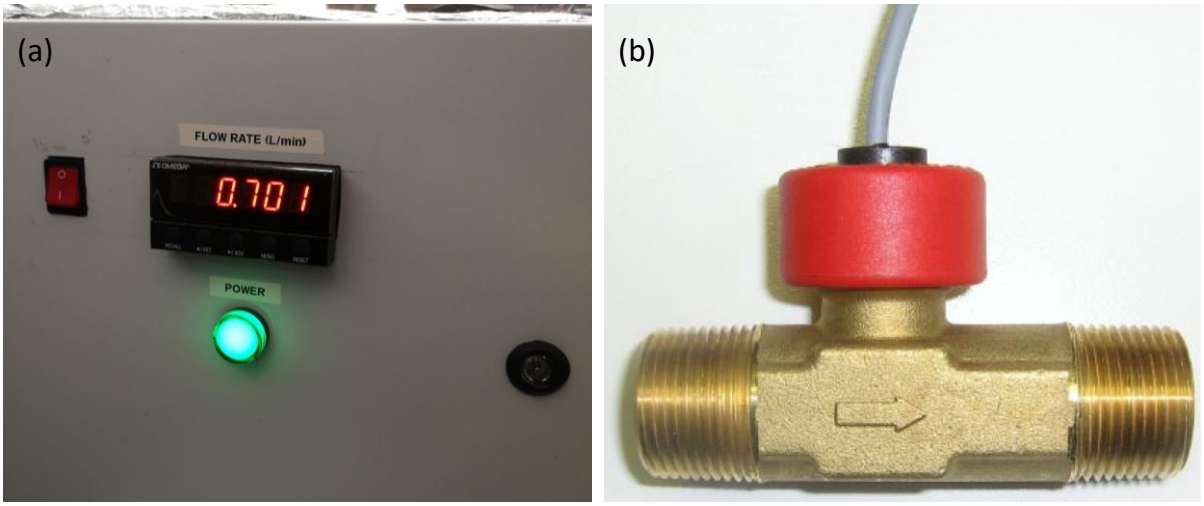

Figure 3-17 Flow rate screen

The specifications of the flow meter are presented in Table 3-3.

Table 3-3 Flow meter specifications

Type	FTB 371
Characteristics measurement device *1)	
Measuring range	2 to 40 l/min with continuous operation max. 20 l/min
Accuracy	±1 % of range
Repeatability	±0.2 %
Signal output from	< 0.3 l/min
Sensor	Hall-sensor
Characteristics output signal	
Pulse rate / K-factor	855 pulses/l
Resolution	1.2 ml/pulse
Signal shape	Square wave
Signal current, max.	10 mA
Pull-up-resistor	5 kΩ (recommendation)
Electrical characteristics	
Supply voltage	4.5...24 V_{DC}
Current consumption	< 10 mA
Electrical connection: - Cable, screened T_{max} =	1.5 m PVC 70 °C
Degree of protection (EN 60529)	IP 54
Process variables	
Medium temperature, max.	85 °C
Medium temperature, min.	0 °C, not freezing
Ambient temperature	0…75 °C

Nominal diameter	**DN 15**
Nominal pressure	**PN 10**
Particle size in the medium	**< 0.5 mm**
Process connection	**¾" BSP male with union nuts and flat seals**
1) The stated values refer to operation with water at 20 °C. Monitoring of fluids with higher viscosities is possible with the effect of deviations from mentioned values.	

3.2.7 Experimental conditions

Figure 3-18 presents the inclination angles of the heat pipe. The performance of the heat pipe was investigated for four positions of the heat pipe as follows: vertical position next to the wall and inclinations of 12.5°, 45°, and 60° angles to the vertical. The evaporator length was maintained constant and the same for the four tests. For each inclination angle, the heat pipe was tested at four different heater temperatures as follows: 200 °C, 300 °C, 400 °C, and 500 °C. These conditions were selected based on the maximum and minimum limit of the inclination angle, and heaters working temperature. The orientation angle varied between vertical position and the maximum inclination of the heat pipe where it was still possible to install it in the kiln with the same length of the evaporator. The minimum heater temperature was selected to be 200 °C as the radiation heat transfer will not be significant below that temperature. The maximum heat temperature was selected based on the

After the experiments were conducted for an unpainted evaporator surface, the heat pipe evaporator surface was painted with black coal paint to increase the emissivity of the evaporator surface and the heat pipe was tested at the same inclination angles and heater temperatures.

The tests are summarised in Table 3-4:

Table 3-4 experimental conditions of single heat pipe tests

Test #	Angle from vertical	Heater temperature °C	Water flow rate l/min	Evaporator surface (unpainted/ black painted)
Test 1	0° (vertical)	200, 300, 400, 500	1.01	Unpainted
Test 2	12.5°	200, 300, 400, 500	1.01	Unpainted
Test 3	45°	200, 300, 400, 500	1.01	Unpainted
Test 4	60°	200, 300, 400, 500	1.01	Unpainted
Test 5	0° (vertical)	200, 300, 400, 500	1.01	Black painted
Test 6	12.5°	200, 300, 400, 500	1.01	Black painted

Test 7	45°	200, 300, 400, 500	1.01	Black painted
Test 8	60°	200, 300, 400, 500	1.01	Black painted

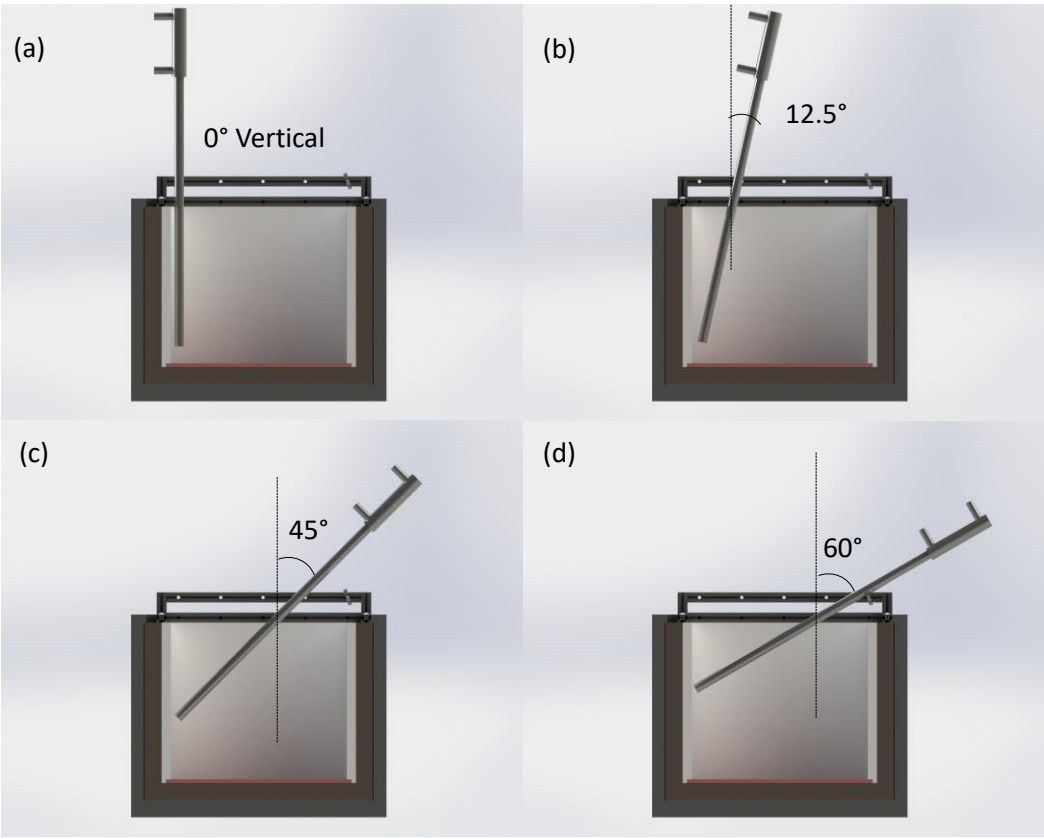

Figure 3-18 Single heat pipe inclination tests: (a) testing the heat pipe in vertical position, (b) inclination angle of 12.5°, (c) inclination angle of 45°, inclination angle of 60°

Figure 3-19 shows a picture of the black paint that was used (Regin REGZ65 black coal paint), a product suitable for high temperature applications such as ovens up to 1100 °C. There was no data about the emissivity or other properties of the paint.

Figure 3-19 Picture of the black paint used: Regin regz65

Figure 3-20 to Figure 3-23 show the dimensions of the heat pipe during the tests at inclination angles from 0° to 60° from the vertical. The dimensions illustrated were used to calculate the view factor for the radiation heat transfer.

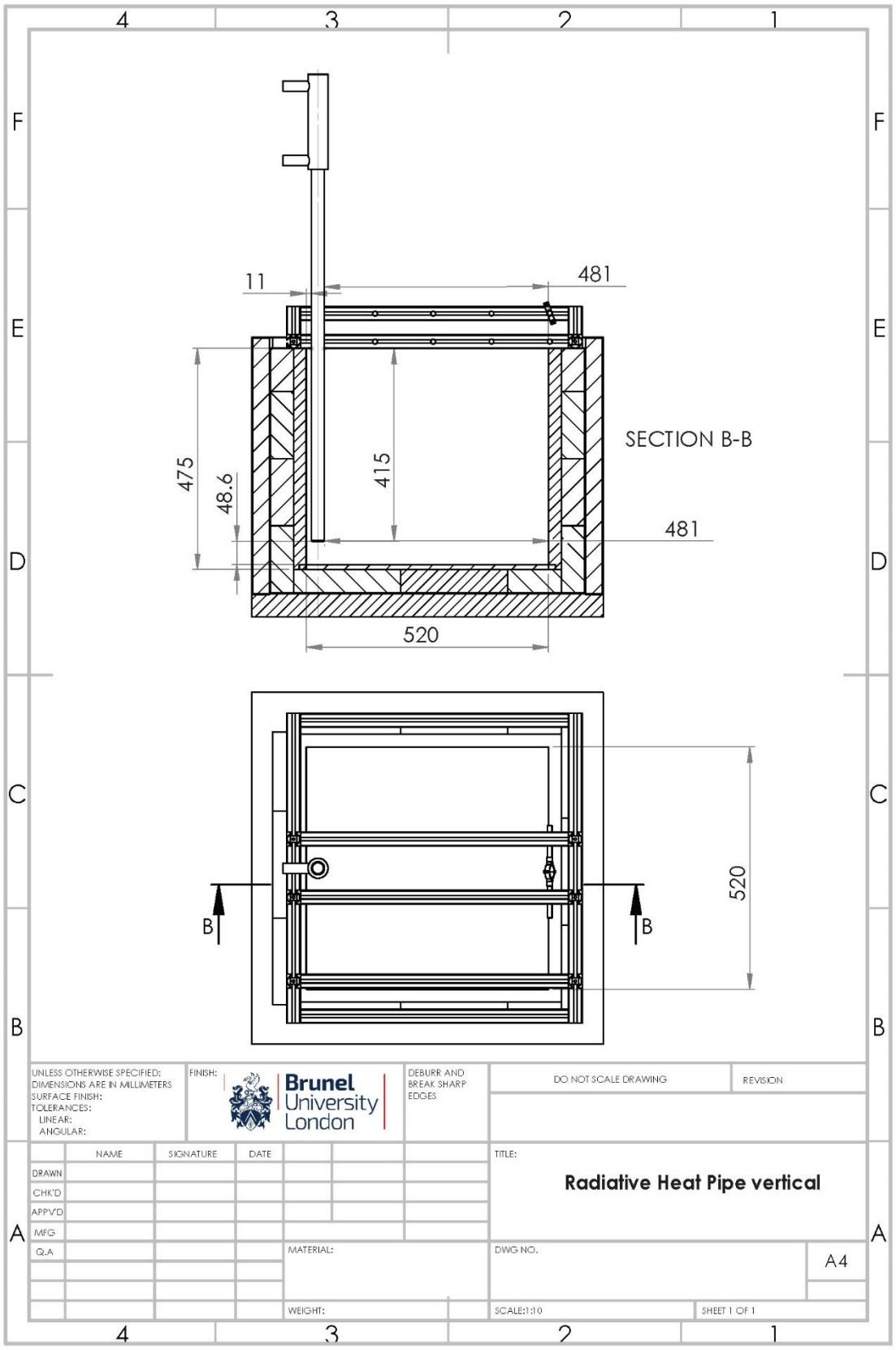

Figure 3-20 Two-dimensional drawings of the single heat pipe at vertical test

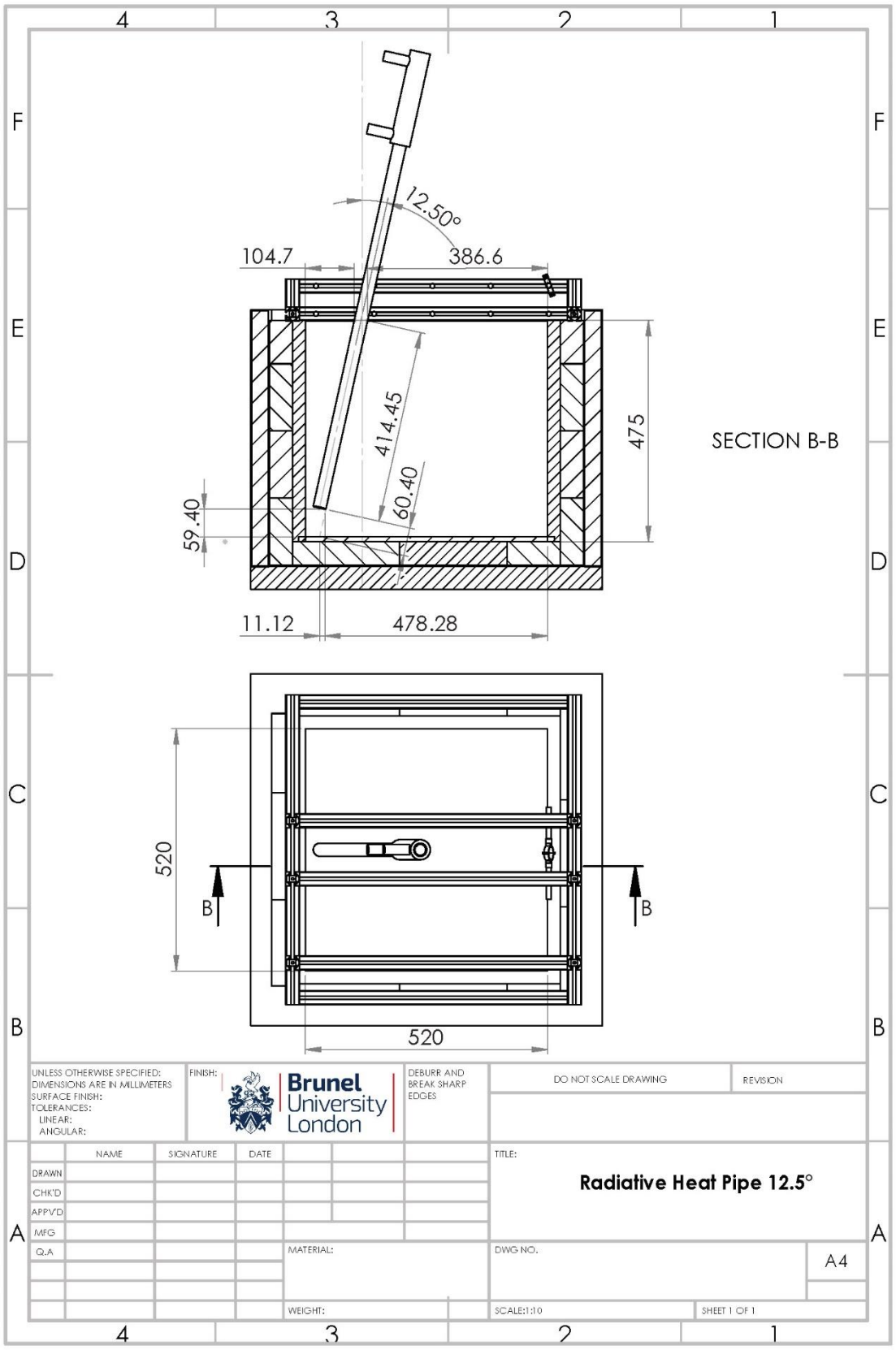

Figure 3-21 Two-dimensional drawings of the single heat pipe at 12.5° inclination test

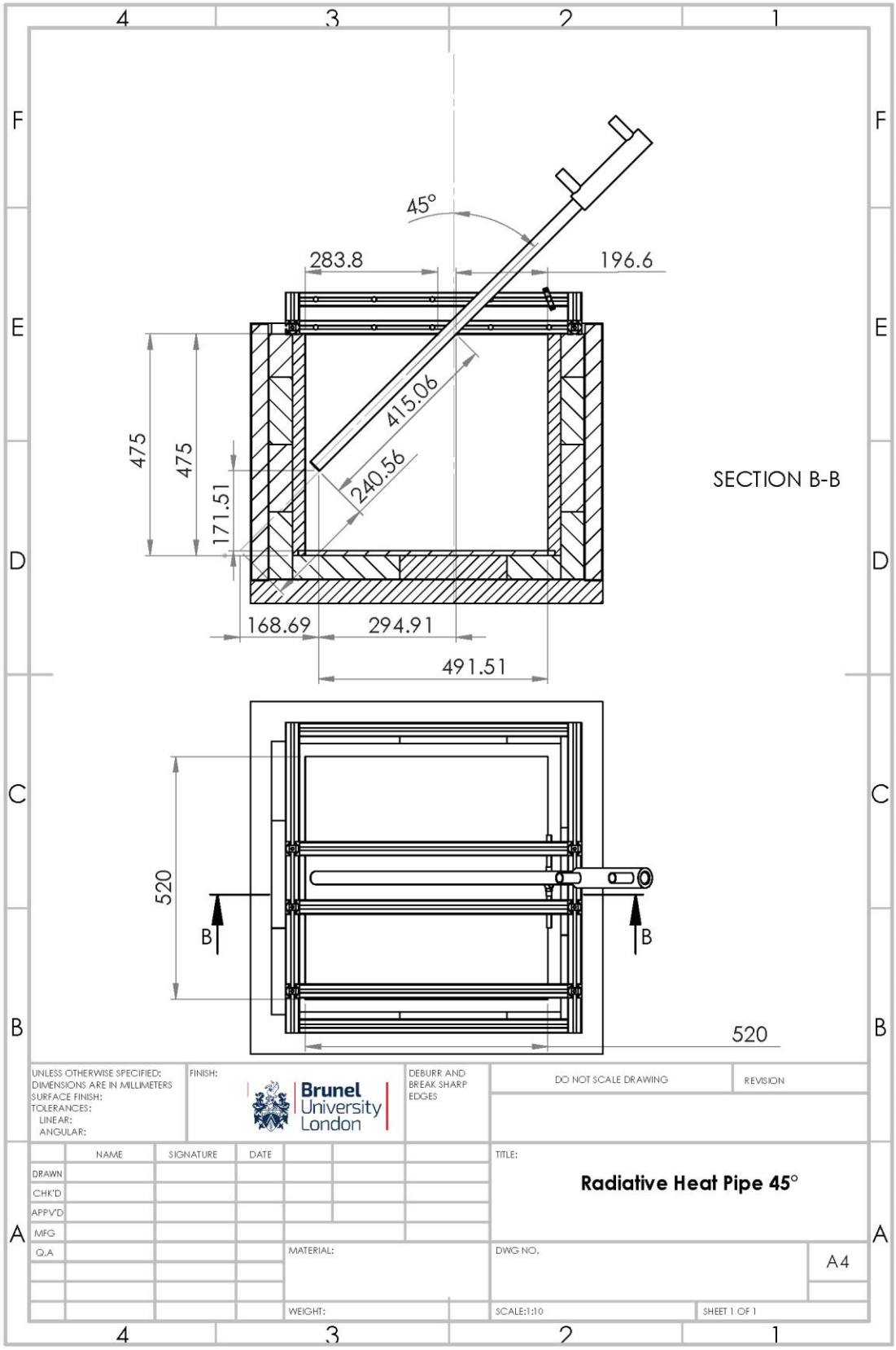

Figure 3-22 Two-dimensional drawings of the single heat pipe at 45° inclination test

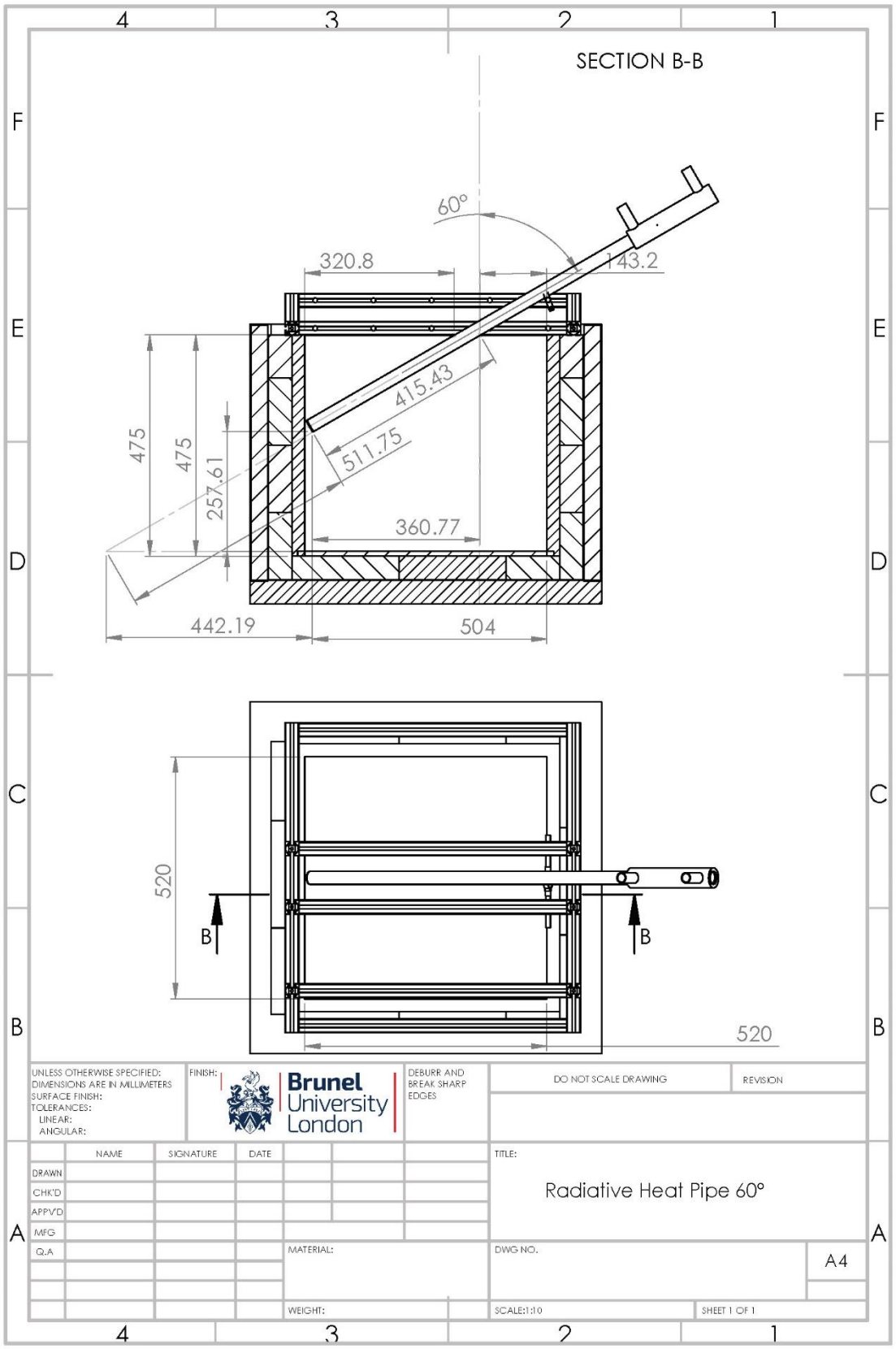

Figure 3-23 Two-dimensional drawings of the single heat pipe at 45° inclination test

3.2.8 Operational procedure

The tests started by switching on the computer and the data logger to record and monitor the temperatures. Then the thermocouple which measures the ceramic heater top surface temperature was put in place. After that, the PID control system was switched on and the set temperature was input to be 200 °C. The ceramic heaters were heating up and heating the air and the walls in the kiln. The temperature of the heat pipe was monitored not to exceed 70 °C. Once the heat pipe temperature was between 50 °C and 70 °C, the water valve was opened and controlled to maintain a water flow rate of 1 to 1.018 l/min. The aim of opening the valve after warming up the heat pipe was to reduce the time required to get the heat pipe in the steady operating state.

The PID system was controlling the ceramic heater temperature within the set value ±4 °C. The data was monitored until a 30 minutes period of a steady state was achieved. The steady state was determined by monitoring the heat pipe temperatures and the ceramic heater temperatures. The required time to get the steady state condition was about 20 minutes. Then, the set temperature of the heaters was increased to the following value. The process was repeated until the testing of the heat pipe at all the defined heater temperatures was complete.

The water flow rate was monitored during the test by monitoring the digital screen and the flow though the valve was modified if the flow rate deviated from the required value. The water inlet temperature depended on the weather and the main supply water temperature and was not controlled.

When the test was finished and all the data were collected, the PID system was switched off and the top cover was opened to cool down the kiln, while the water was flowing through the heat pipe to cool it down and maintain its temperature below 200 °C to protect it from the high vapour pressure inside.

The procedure was repeated for each inclination angle. The length of the evaporator was measured, to ensure that it was equal for all the tests, in addition to the inclination angle using a digital level.

3.3 Flat Heat pipe

This section describes the Flat Heat Pipe (FHP) design and the experimental apparatus corresponding to the tests conducted on the flat heat pipe in the laboratory and the factory.

3.3.1 Mechanical design

The full-scale heat pipe is illustrated in Figure 3-24. It consisted of 14 stainless steel pipes with a length of 1 m and external diameter of 28 mm. The 14 vertical pipes were connected by a bottom header and a shell and tube heat exchanger at the top. The bottom collector had an external diameter of 38

mm while the top header had an external diameter of 50 mm. The shell and tube heat exchanger consisted of 8 stainless steel smooth tubes of 10 mm external diameter within a stainless steel shell as can be seen in Figure 3-26. The FHP was made of stainless steel 304 and charged with water as a working fluid with 50% filling ratio of the evaporator length. A stainless steel sheet of 1 m × 1 m × 1 mm thickness was fixed at the back of the evaporator section to increase the efficiency of the heat pipe system. The back panel was assembled with the FHP using a fixation plate as illustrated in Figure 3-27. The overall dimensions of the flat heat pipe were 1.1 m height by 1 m width. It can be seen that the depth of the flat heat pipe system at the evaporator was about 29 mm including the back stainless steel sheet. The high magnitude of the height and the width in comparison with the depth presented the heat pipe system with a flat shape, from which it obtained its name. The FHP was provided with a rupture disk for safety purposes during operation. The rupture disk will release the water vapour when the operating pressure in the FHP exceeds 85 bar.

A stand has been designed and manufactured from stainless steel 304 to hold the system in place as shown in Figure 3-28. The stand was designed to allow the FHP system to be tested at different inclination angles and heights as seen in Figure 3-29. It was provided with a water tank that provides a balance weight to move the FHP safely.

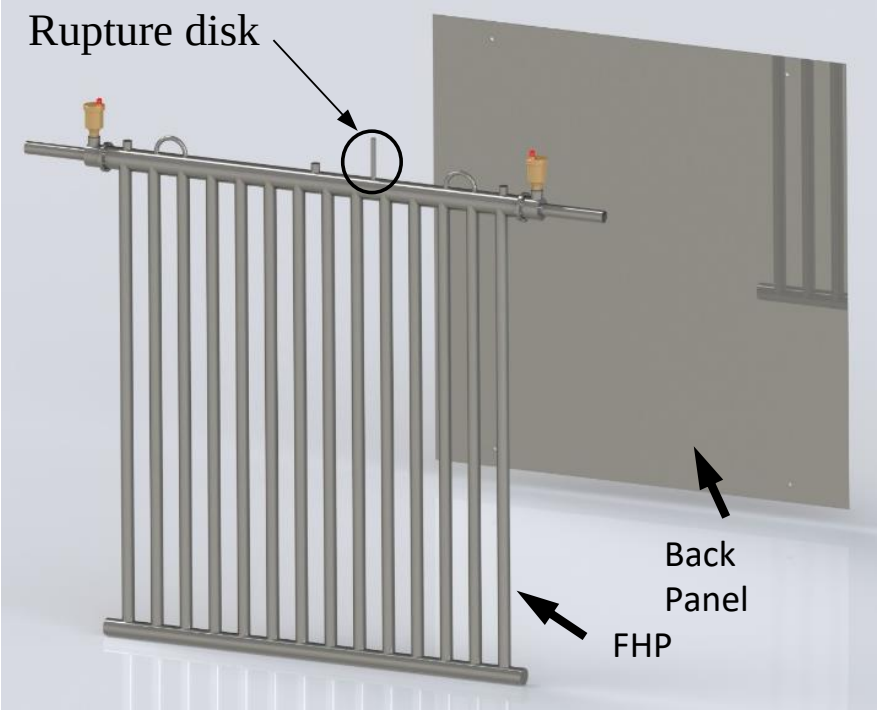

Figure 3-24 Three dimensional drawing of the flat heat pipe system

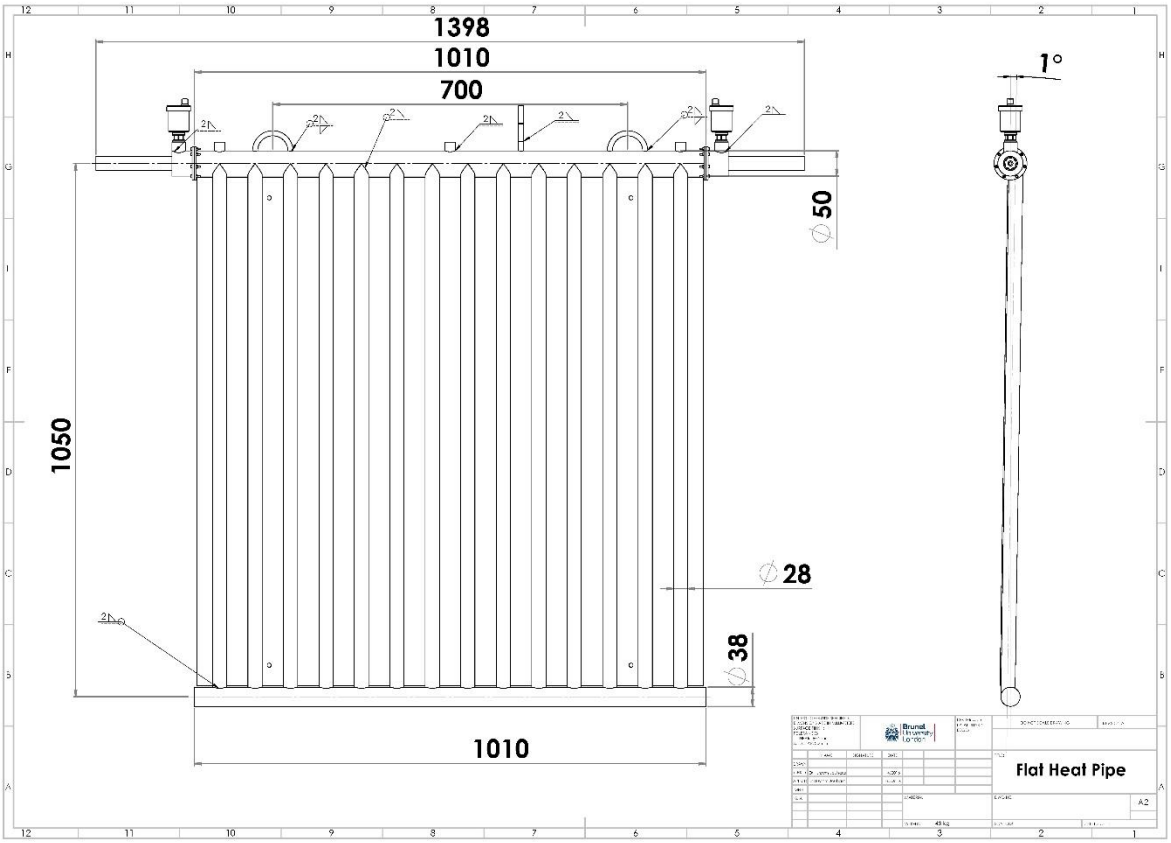

Figure 3-25 Mechanical drawing of the flat heat pipe system

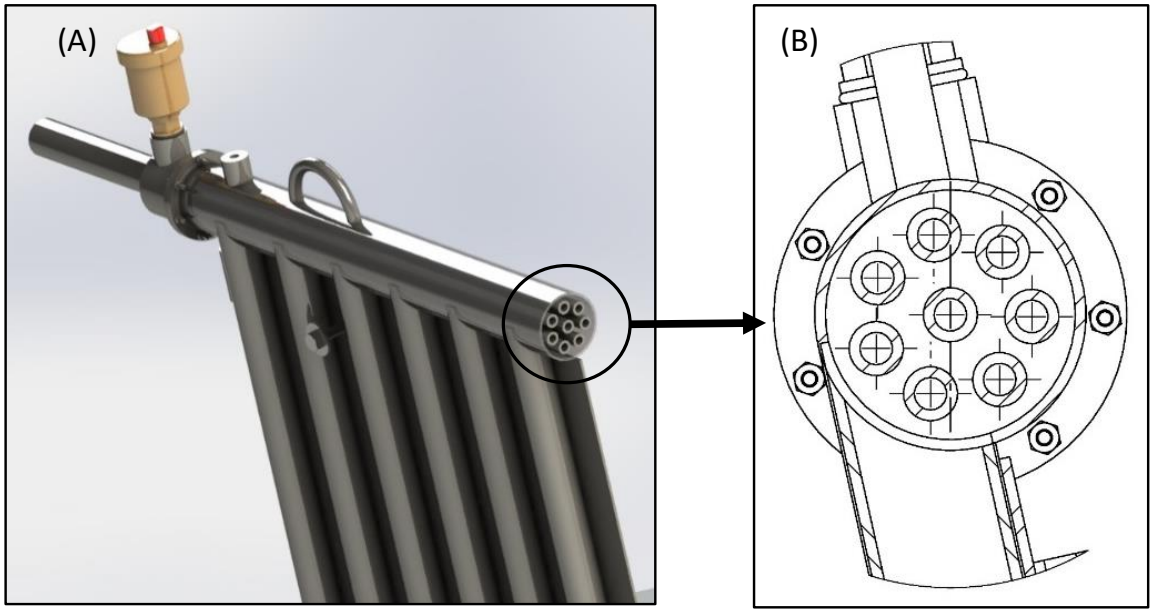

Figure 3-26 Section view of the condenser of the FHP

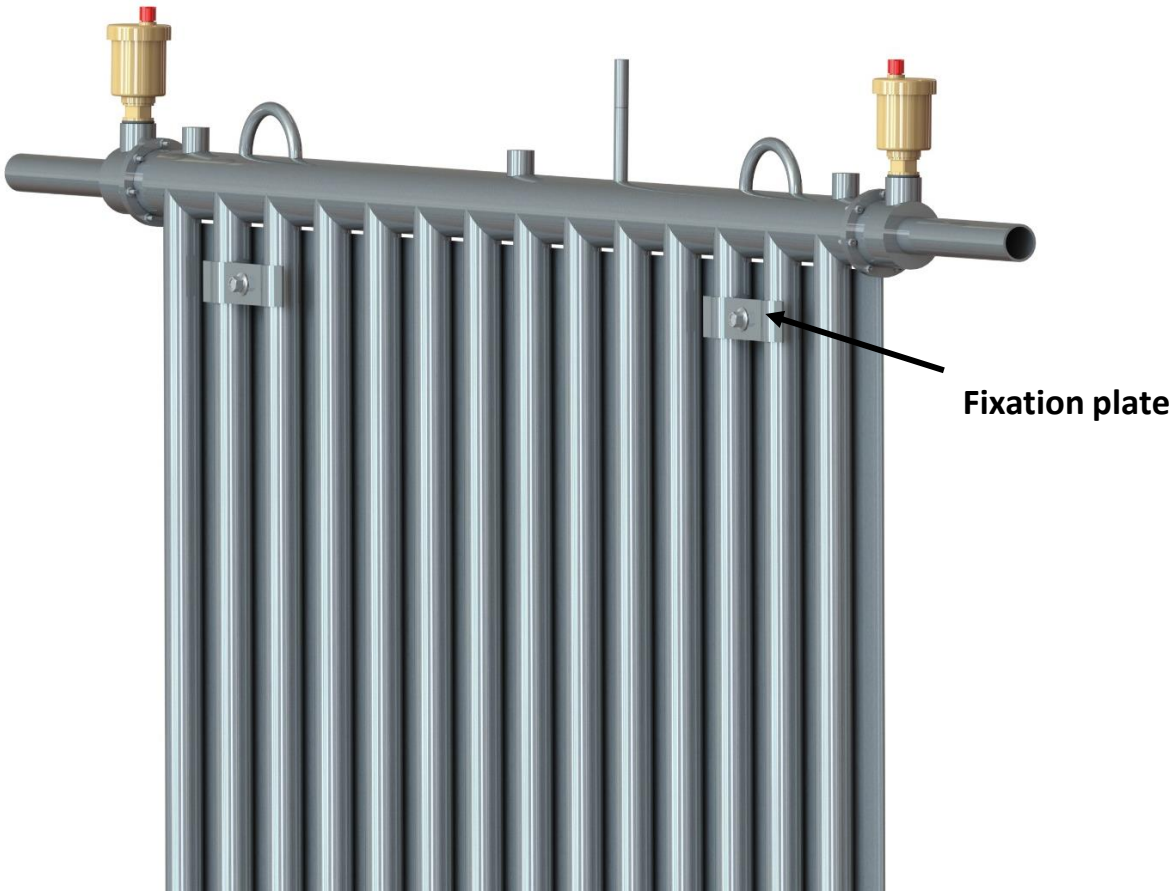

Figure 3-27 three-dimensional design of the FHP with the fixation plate

Figure 3-28 Three dimensional design of the Flat Heat Pipe mounted on the stand

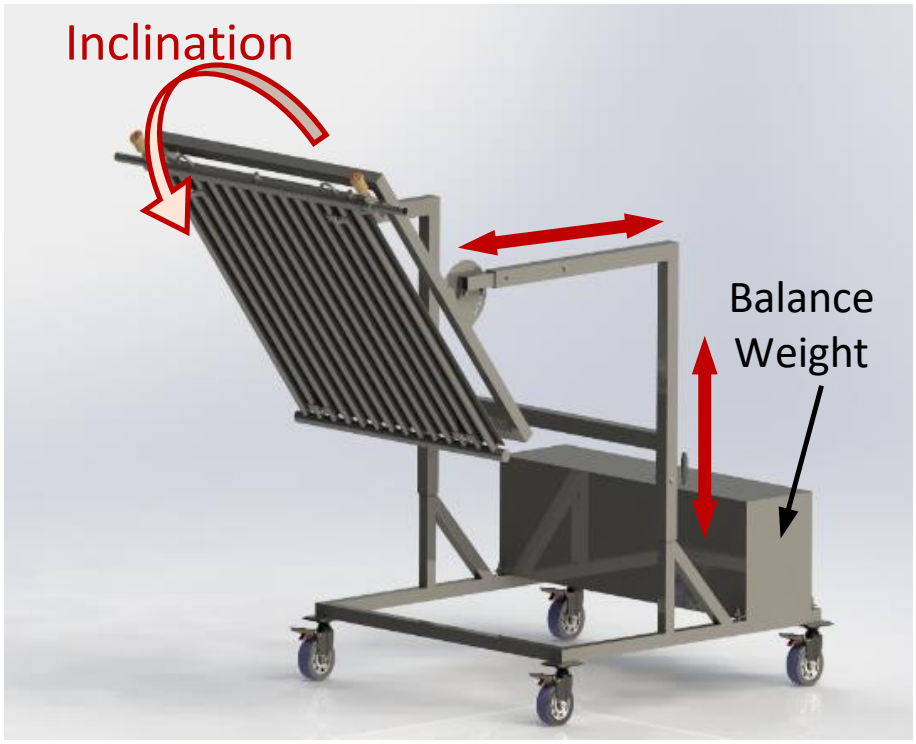

Figure 3-29 FHP stand demonstration

3.3.2 Test rig in the laboratory

The test rig is shown in Figure 3-30. The FHP was mounted in front of electrical heaters assembled on an inclined plate to capture the radiative heat from the hot source. The FHP was installed at an initial inclination angle of 12.5° when receiving the heat from the bottom of the plate. The top plate heaters were not used during this tests. A mechanical drawing of the heater plate is presented in Figure 3-31. The heater plate was mounted with inclination of 36° from horizontal. It comprised 36 infrared heaters which will be described in a separate section. The heater plate was 1200 mm height × 1200 mm width.

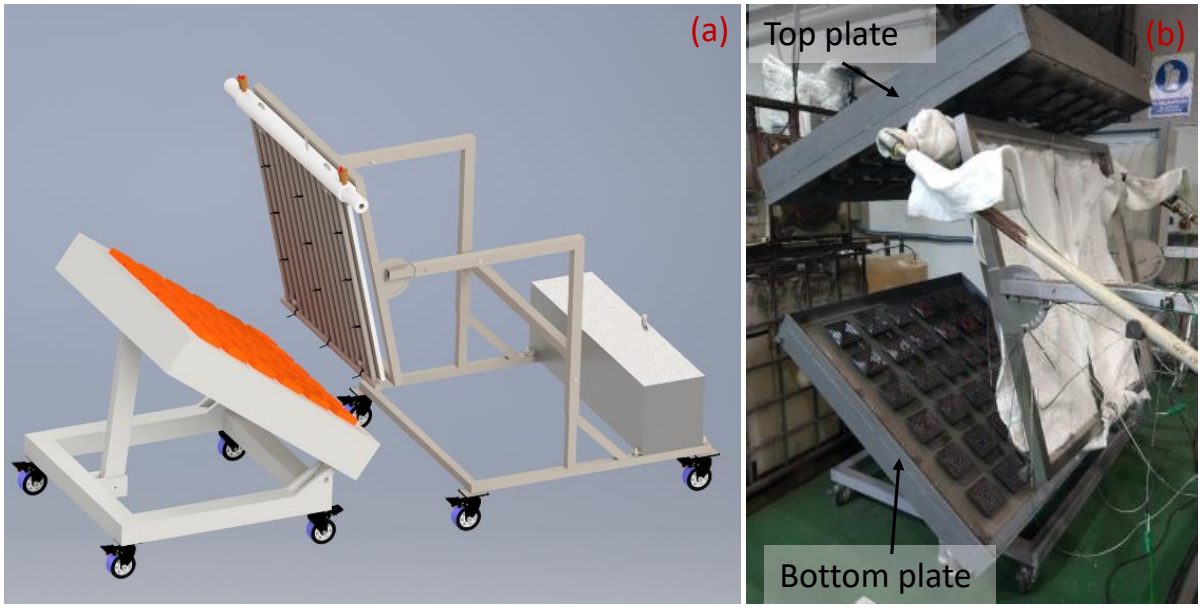

Figure 3-30 (a) Three dimensional design of the test rig, (b) Picture of the test rig

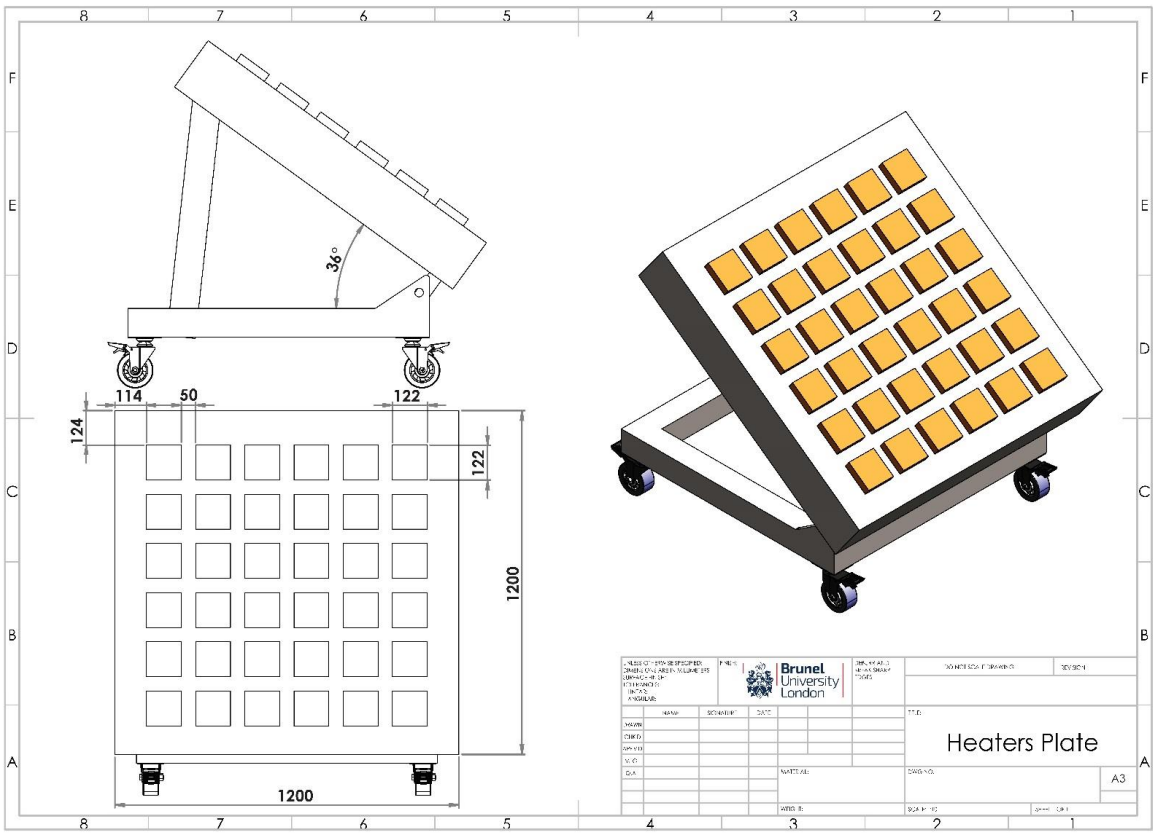

Figure 3-31 Mechanical drawing of the heater plate

3.3.3 The heaters

The heaters used in the laboratory tests shown in Figure 3-32 had dimensions of 120 mm × 120 mm. The heaters were made of ceramics using NiCr wires cast directly into the ceramics. The wavelength curve in Figure 3-33 shows that the percentage of the radiation from the front face is around 96%. It also shows that the radiation is emitted in the wave length range between 2 -12 µm and the maximum radiation is emitted at a wavelength of 4 µm. They had maximum electrical power input of 800 W where the heaters reached a temperature of around 680 °C as provided in the information from the manufacturer in the heating curve in Figure 3-33. It can also be seen from the heating curve that the heating time required is about 12 minutes to reach a steady state of the heater temperature. The ceramic heaters have uniform temperature distribution. The specifications of the heaters are listed in Table 3-5.

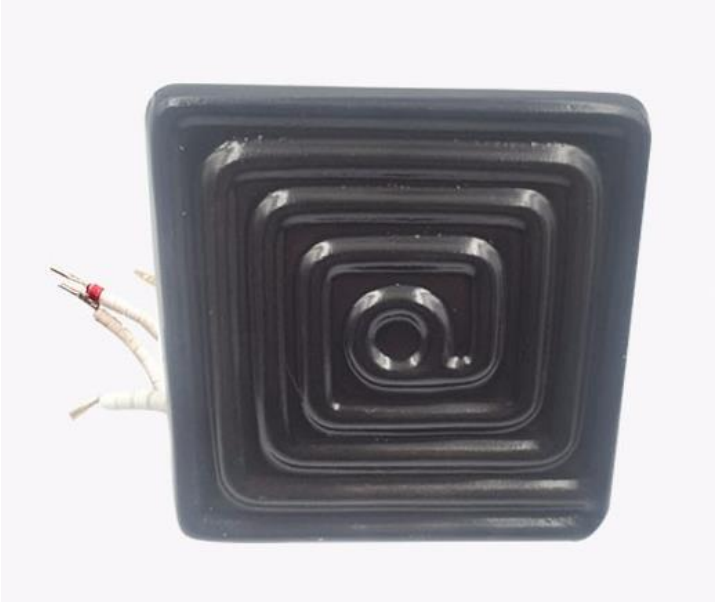

Figure 3-32 A picture of the ceramic heaters used to simulate the hot steel

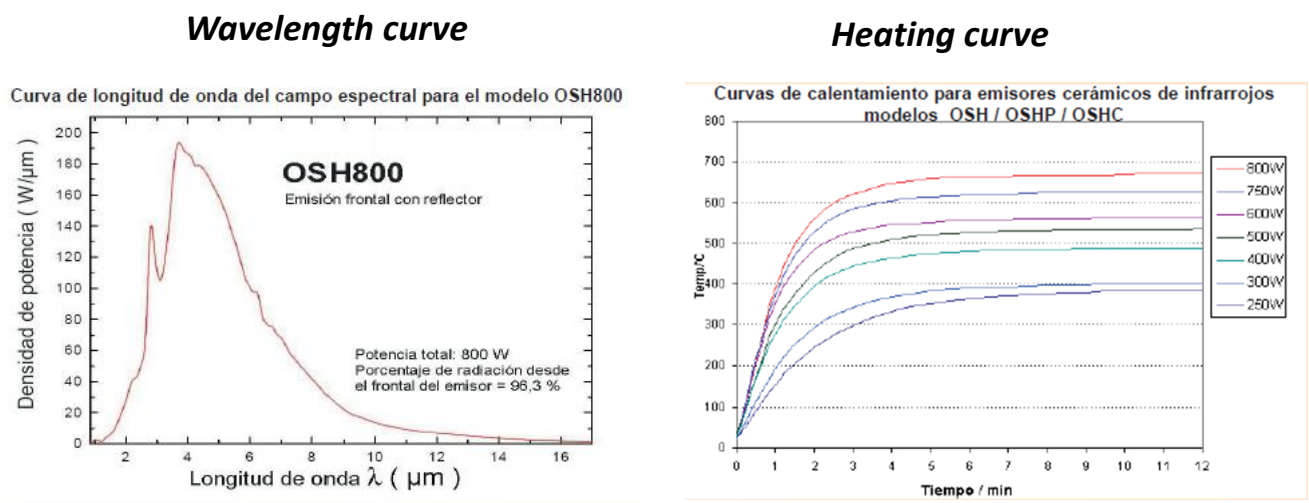

Figure 3-33 Heater characterisation graphs

Table 3-5 Laboratory heaters specifications

Radiating temperature inhomogeneity	**15%**
Power error: The rated working voltage	5%

3.3.4 Water circuit

The water circuit of the FHP was an open loop water circuit where the water is supplied from a main water supply tap and water flows through the condenser of the FHP and then to the drain. A flow

meter was fitted in the loop to measure the flow rate and this is described in a separate section. A schematic of the water circuit is shown in Figure 3-34.

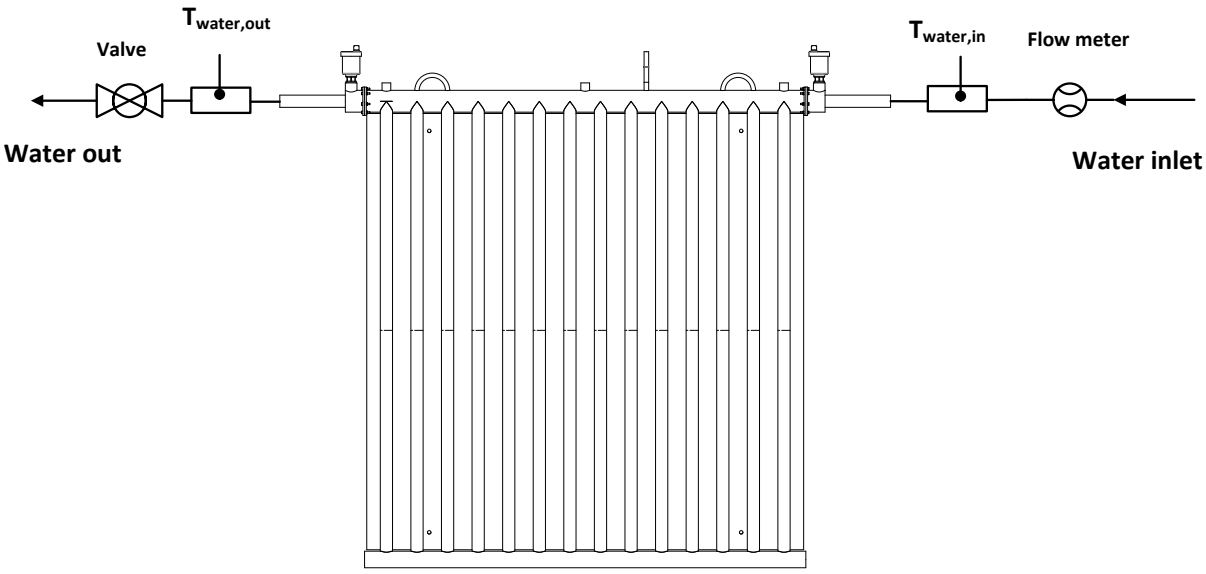

Figure 3-34 Schematic diagram of the water circuit of the FHP

3.3.5 Instrumentation

This section describes the instrumentation used in the experiments conducted on the FHP in the laboratory. The instrumentation consisted of thermocouples, a flow meter, a data logging system, and data logger software. A schematic diagram of the instrumentation is presented in Figure 3-35.

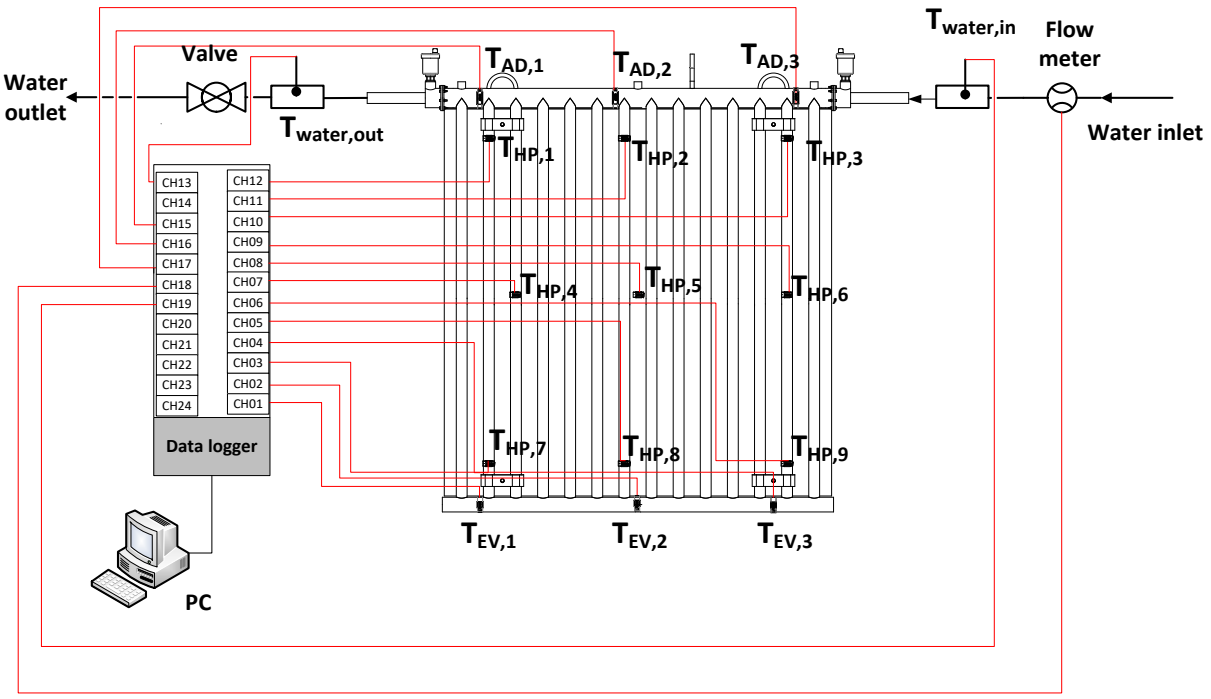

Figure 3-35 Schematic diagram of the instrumentation

3.3.5.1 Thermocouples

The temperatures of the FHP were measured using K type thermocouples. The thermocouples are fitted in adjustable rings as shown in Figure 3-36. In the earlier experiments at the laboratory, three thermocouples were installed on the bottom header (EV 1-3) as can be seen in Figure 3-37. An additional five thermocouples were installed on the vertical pipes to measure the surface temperature (HP 1-5) as shown in Figure 3-37. Three thermocouples were fitted on the top header which represents an adiabatic section to measure the saturation temperature of the working fluid (AD 1-3). Later on, additional thermocouples were installed on the vertical heat pipes to measure the surface temperature where the total number became nine thermocouples (HP 1-9) and two thermocouples were installed on the bottom collector and two thermocouples on the top header as shown in Figure 3-38. A thermocouple was installed on the back face of the back panel of the FHP (BP) as shown in Figure 3-39. Two thermocouples (stainless steel probe, 3mm) were used to measure the water inlet and outlet temperatures using special tube fittings for thermocouples as presented in Figure 3-40.

Figure 3-36 Thermocouple K-type used in FHP experiments

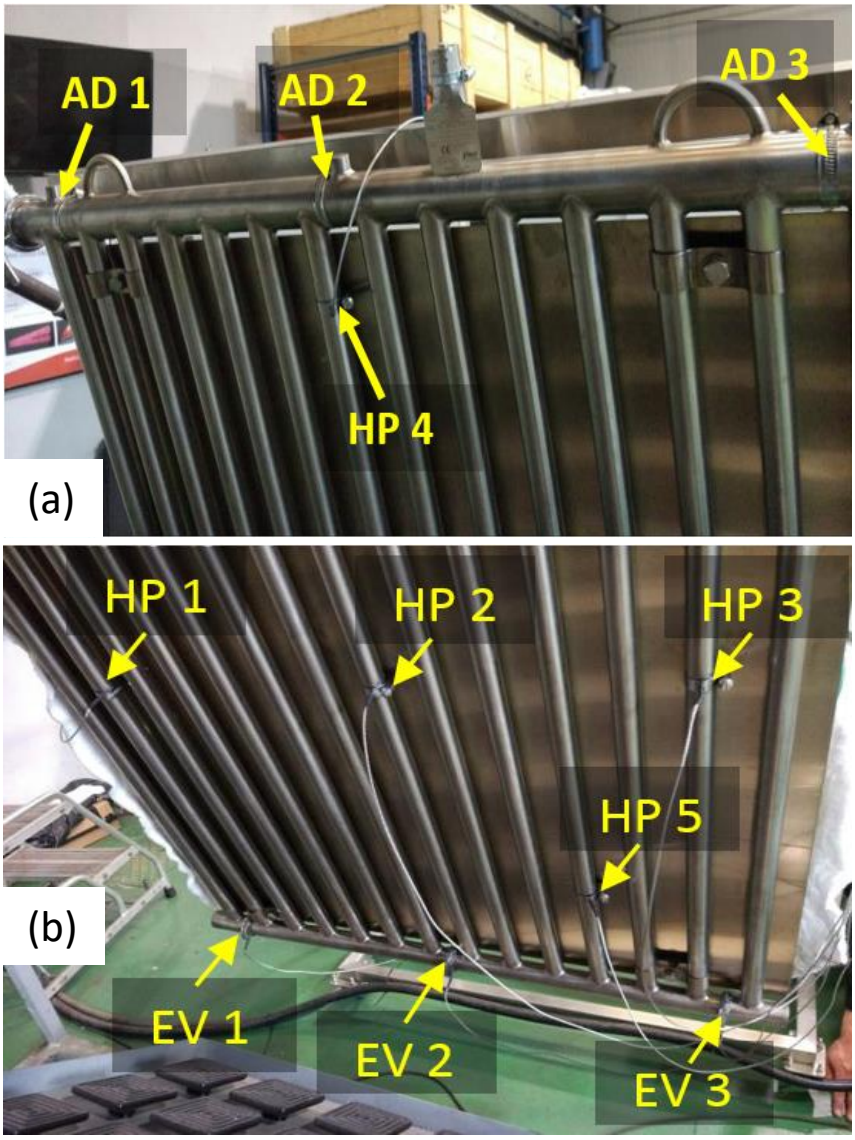

Figure 3-37 Thermocouple positioning on the FHP in the laboratory experiments

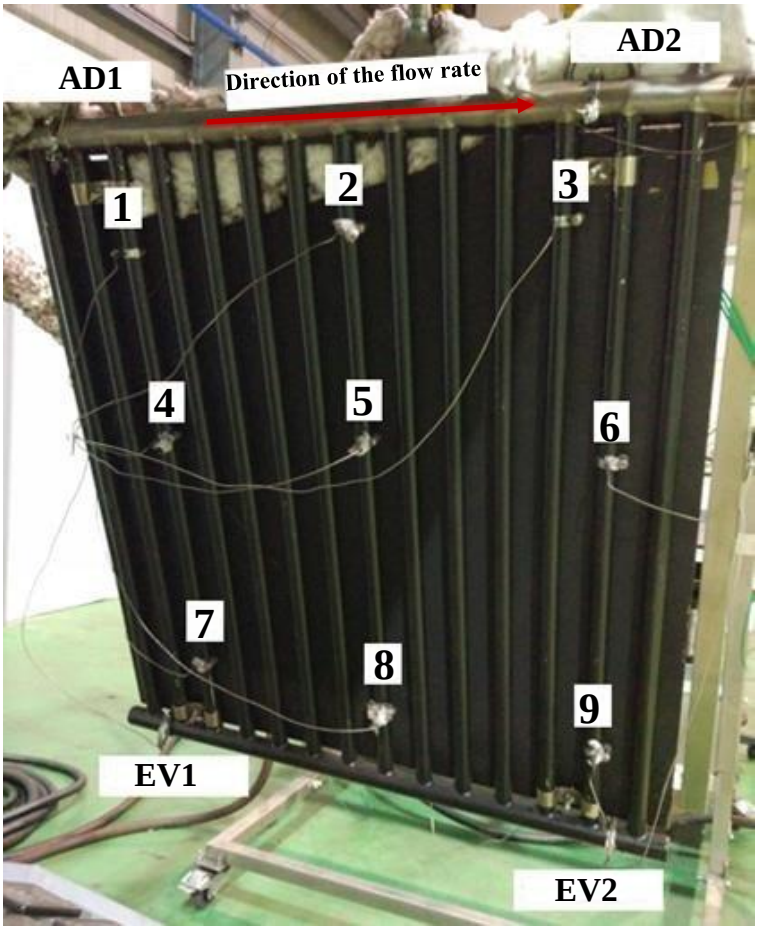

Figure 3-38 Thermocouple positioning on the FHP in the laboratory experiments

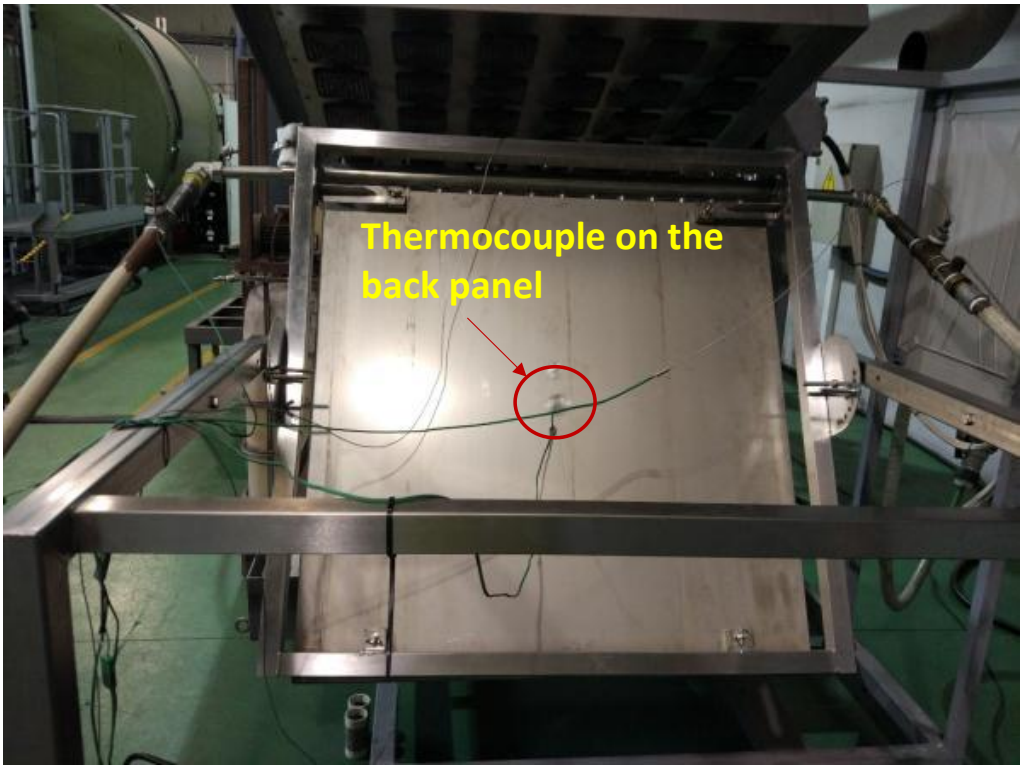

Figure 3-39 Thermocouple positioning on the back panel of the FHP

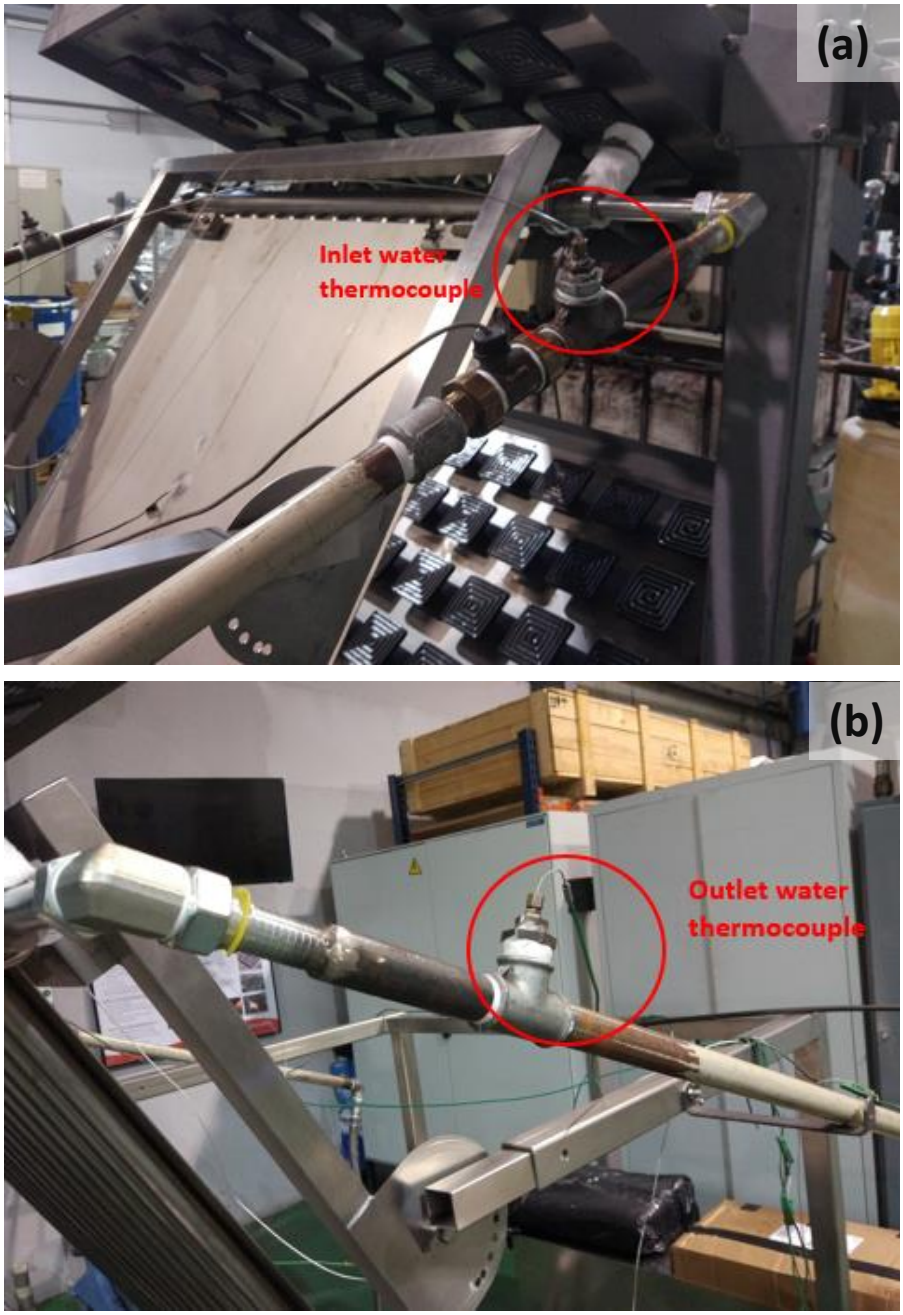

Figure 3-40 Water temperature measurement: (a) Water inlet thermocouple, (b) Water outlet thermocouple

3.3.5.2 Data logging system

The thermocouples and the flow meter were connected to a National Instruments data logger which uses the module NI-TB4353 presented in Figure 3-41. This data logger was the same model as the one used for collecting the data from tests on the single heat pipe. This data logger device is very reliable with the feature readings noise filtering and offers high resolution of readings.

Figure 3-41 Data loggers used for the FHP experiments

3.3.5.3 Flow meter

The flow rate was measured using a flow meter Omega FTB 371 turbine flow sensor. The flow meter was the same model as used in the single heat pipe tests. However, the flow meter was connected to the data logger to record the flow rate over time in the FHP experiments. Figure 3-42 shows the flow meter fitted in the water circuit of the FHP.

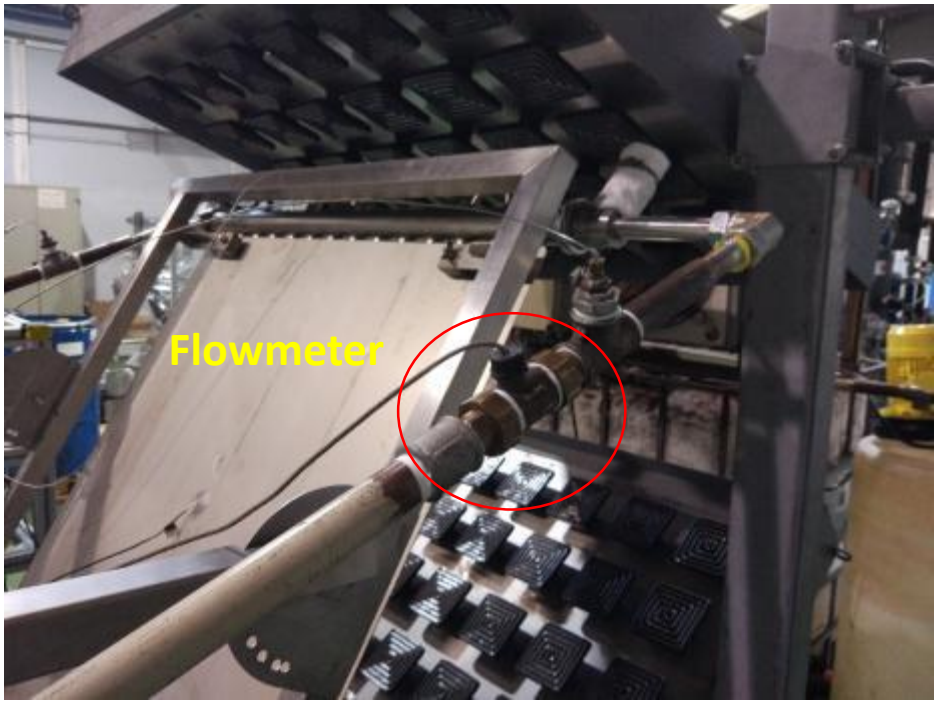

Figure 3-42 Picture of the flowmeter installed in the water circuit for the FHP tests

3.3.5.4 Infrared thermometer

The temperature of the heaters was controlled by controlling the power input to the heaters. The temperature of the heaters was measured using an infrared thermometer which was Testo 845 as shown in Figure 3-43. The measuring range of the thermometer is -30 to +950 °C with an accuracy of ± 0.75% of the measured value for the range +100 to +950 °C. The thermometer is shown in Figure 3-43 (e). Figure 3-43 (a, b, c, and d) show the thermometer measurements during the experiments conducted in the laboratory.

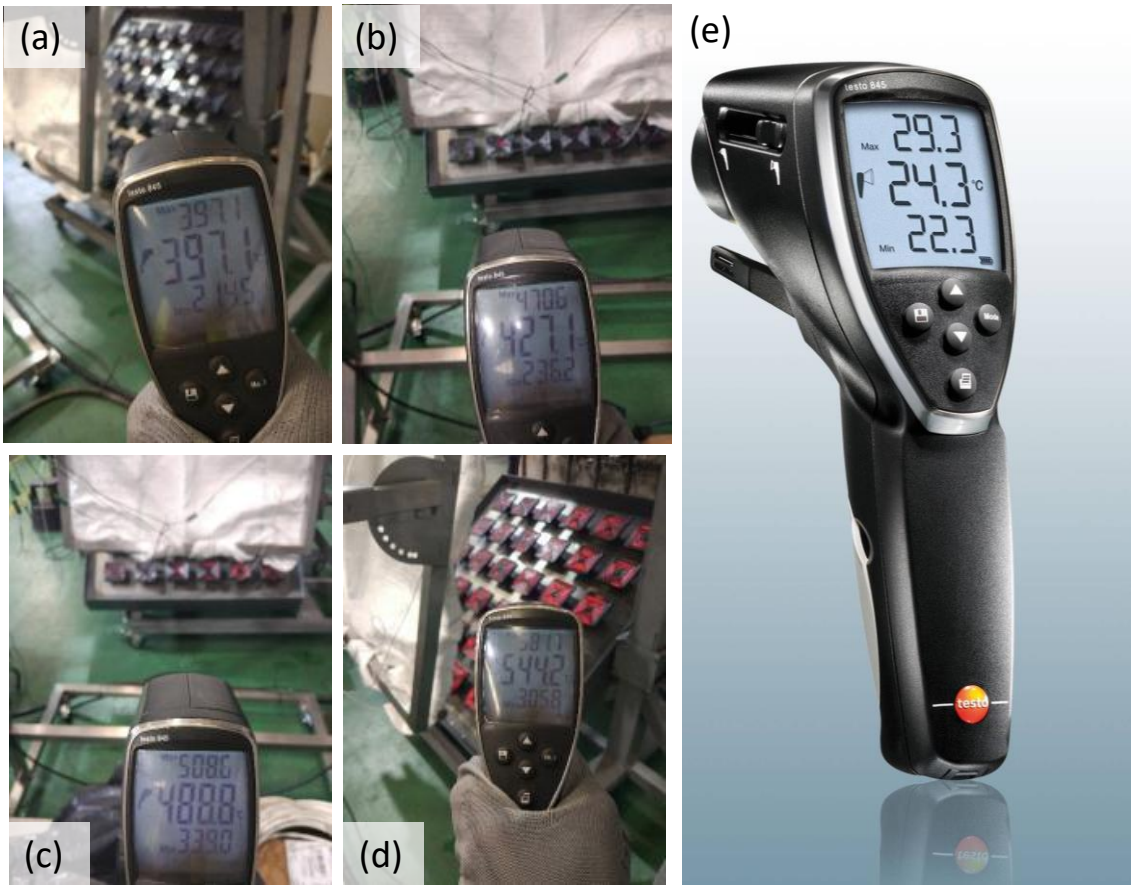

Figure 3-43 Thermometer Test 845 used to measure the heater temperature: (a) Heaters set point 400 °C, (b) Heaters set point 470 °C, (c) Heaters set point 470 °C, and (d) Heaters set point 580 °C

3.3.6 FHP laboratory experiments description

The FHP was tested without a back panel as presented in Figure 3-44. The top header and the water inlet and outlet pipes were insulated using superwool insulation of the same material used in the single heat pipe experiments. The high temperature thermal insulation (superwool) was also used to insulate the back panel to minimize heat losses to the surroundings. The FHP was inclined at 12.5° from the vertical and was tested at different heater temperatures (400, 470, 500, and 580 °C). The

FHP was also tested with the back panel attached to the FHP and insulated from the back face to minimise the heat loss by radiation and natural convection as presented in Figure 3-45. The thermocouples were removed and the FHP was painted with a black matt paint for high temperature applications. The black painted FHP was tested without a back panel as shown in Figure 3-46. Then the back panel, which was also painted in black, was attached to the FHP and tested as illustrated in Figure 3-47. However, to compare the impact of the back panel, it was not insulated from the back. The water inlet of these tests was from the main supply and the water inlet temperature was depending on the weather and the climate. The FHP was also tested at a water inlet temperature of 70° to test the capability of the FHP as a waste heat recovery technology where the water can be a part of an industrial process. The back panel of the FHP in this test was insulated from the back as presented in Figure 3-48.

Figure 3-44 FHP laboratory testing without back panel and no paint

Figure 3-45 FHP laboratory testing with a back panel and no paint

Figure 3-46 FHP laboratory testing without back panel and painted black

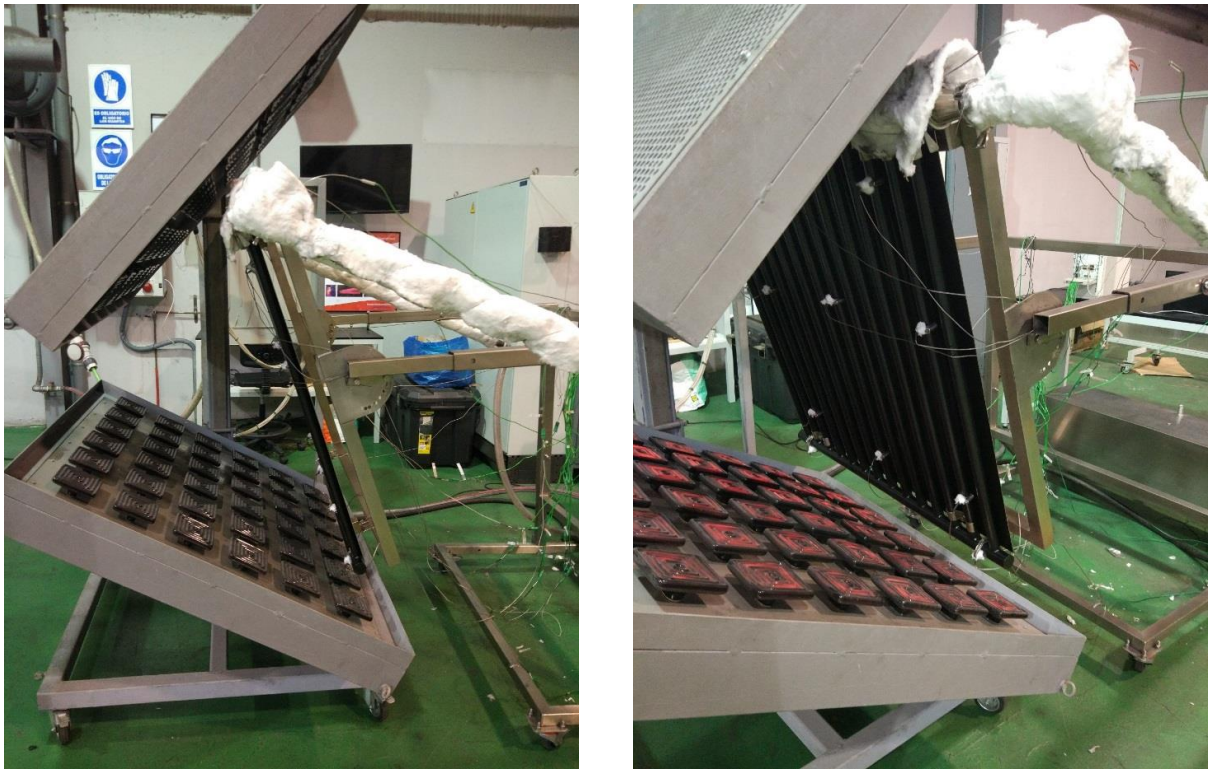

Figure 3-47 FHP laboratory testing with a back panel and black paint

Figure 3-48 FHP laboratory testing with a back panel and black paint, water inlet temperature 70 °C

3.3.7 Operational procedure

The experiments were conducted after preparing the setup of the FHP and installing the insulation. The FHP was positioned in front of the heater plate where the bottom collector is aligned to the edge of the heater plate while the heaters were off. The experiment commenced by starting the data-logging system and monitoring the temperatures of the FHP. After that, the water valve was opened to allow the maximum flow rate through the condenser of the heat pipe. Then the heaters were switched on and the temperature was increased gradually and slowly while the temperatures of the FHP were being monitored until the heater temperature reached 400 °C. Then the collection of data for the first test was started. The experiments conducted were to study the steady state performance of the FHP. After collecting the data for the first value of heater temperature of 400 °C, the heater temperature was increased to 470 °C while the FHP performance was being monitored. The test was carried out for 20 minutes of steady state then the heater temperature was increased to 500 °C and the data were collected. The last value of the heater temperature was 580 °C where the data were collected then the heaters were switched off while the water flow was still running through the condenser. When the heater temperature was below 200 °C, the water valve was turned off and the FHP was moved away from the heater plate to be prepared for the next experiment. This approach was applied for each experiment for safety reasons to avoid any sudden temperature increase in the FHP at start up.

3.4 Industrial application in a steel factory

The flat heat pipe was tested in real conditions in a steel factory where hot wire rods were being cooled.

3.4.1 General description of the testing facility at the factory

The factory produces steel wire rods through the wire rod mill process. The last two stages of this process is delivering the rods from a laying head on a conveyor to cool them in the cooling zone. The cooling process can be performed at ambient temperature by natural convection or by forced convection using 29 fans blowing the air from below the conveyor. The cooling program and the speed of the fans are selected depending on the material produced and the quality required. The conveyor length is about 70 m and the fans are located in the first 47m starting from the laying head. A schematic of the cooling line is shown in Figure 3-49. The FHP tests were conducted between section 1 and section 6. Figure 3-50 and Figure 3-51 illustrate the laying head and the hot steel wire rods in the cooling line, respectively.

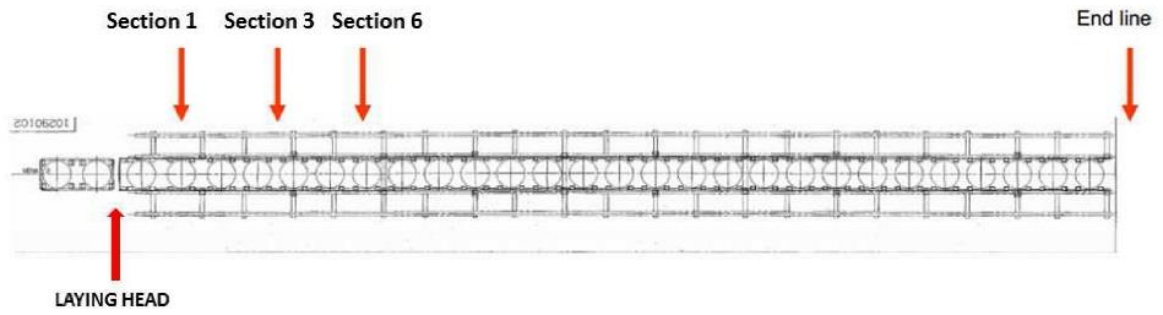

Figure 3-49 Schematic of the cooling line [72]

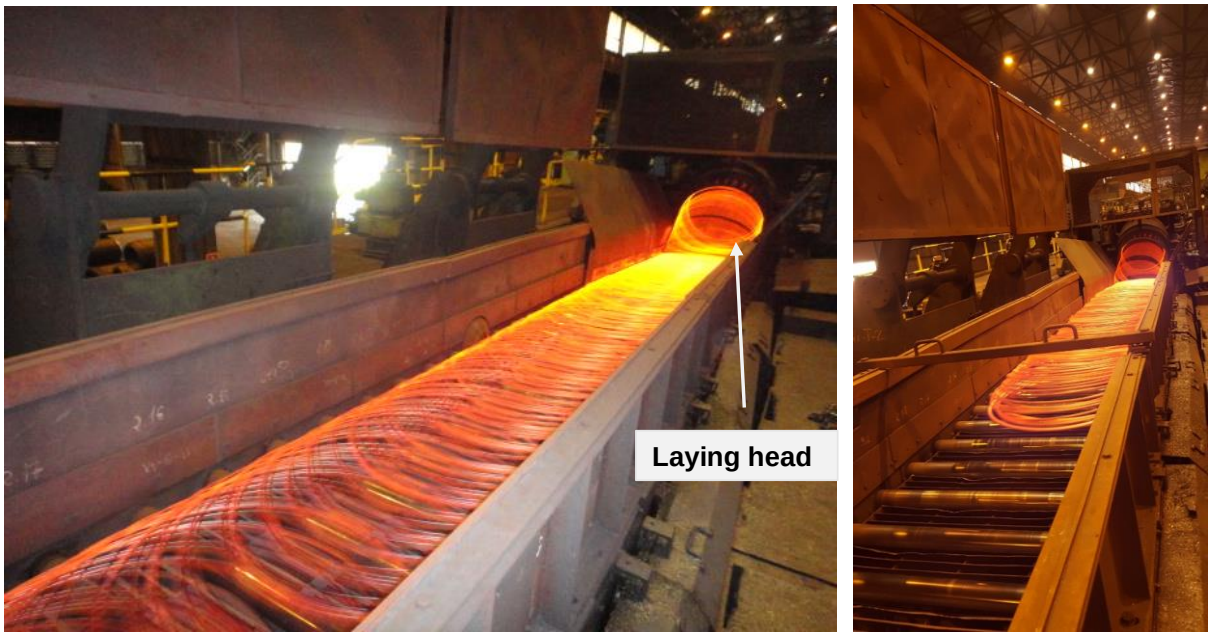

Figure 3-50 The laying head and the conveyor cooling line

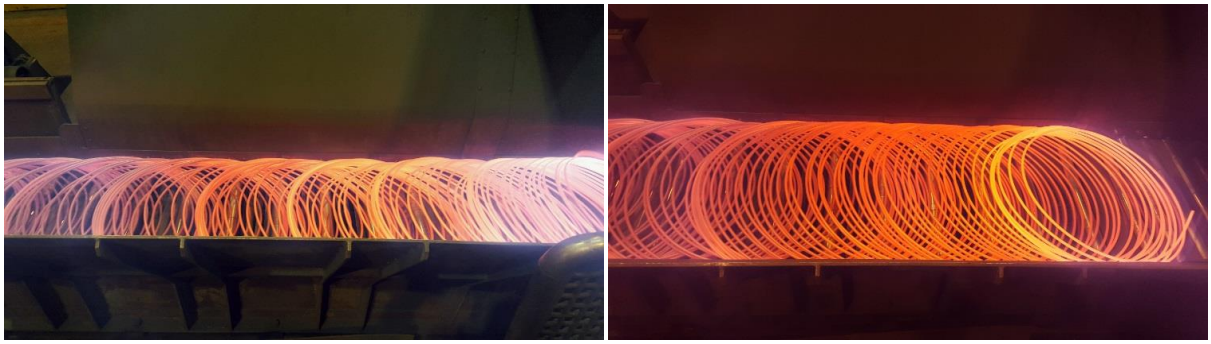

Figure 3-51 Hot steel wire rods in the cooling line

Thermal characterization of the cooling zone has been carried out to measure the temperature of the wires. The fans cool down the steel wire rods from a temperature of 920°C to 250 °C. Figure 3-52 shows a thermal image of the hot wires in the cooling zone where it can be seen that highest

temperature of the steel is at the edge, while the centre of the steel wire rings has a lower temperature.

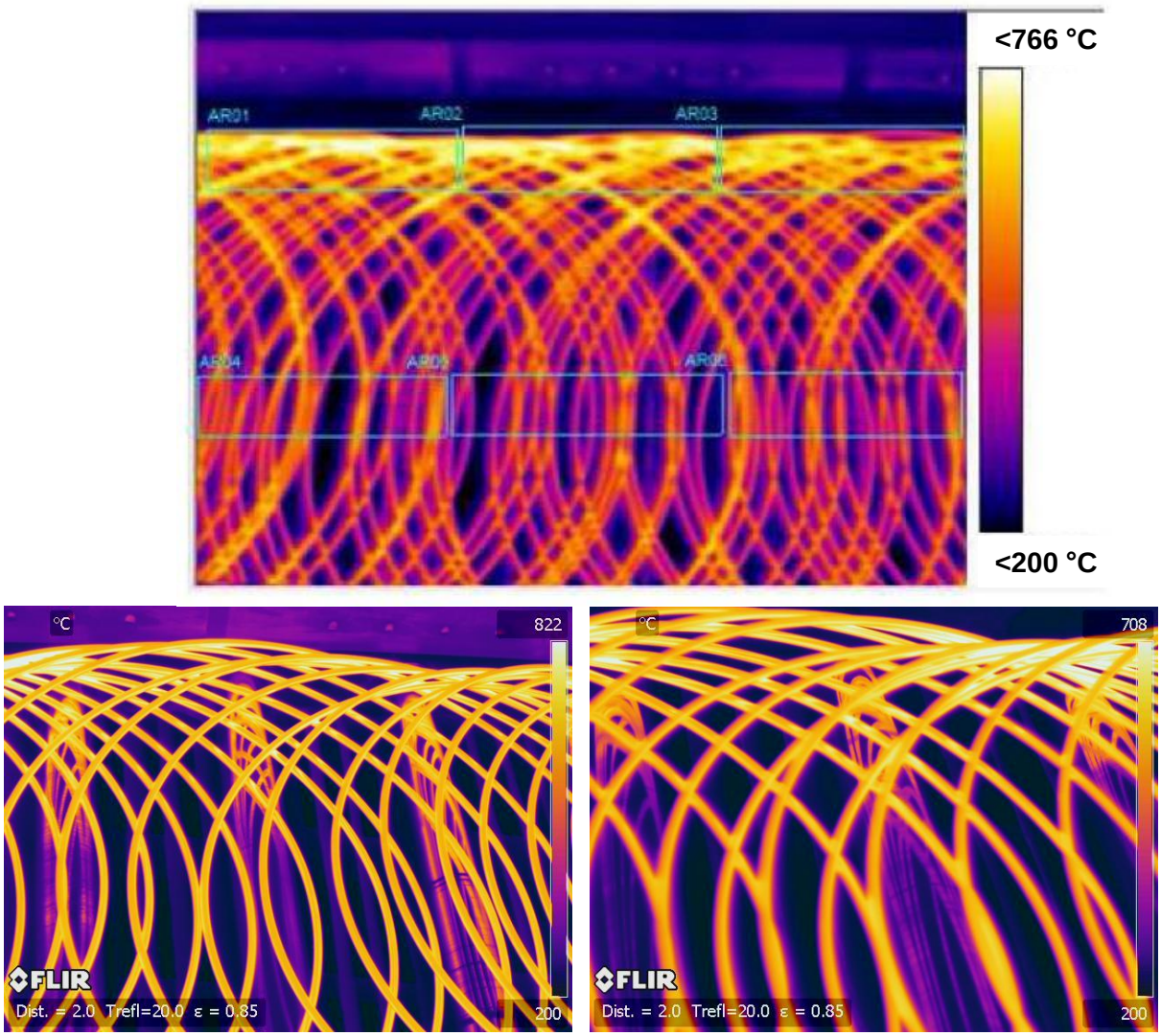

Figure 3-52 Thermal imaging of the hot wire rods in the cooling zone

Figure 3-53 shows a thermal image analysis of the steel wire rods' temperature profile. It can be seen that 26% of the steel is in the temperature range between 580 and 518 °C. The thermal images will be analysed in detail in the theoretical study chapter.

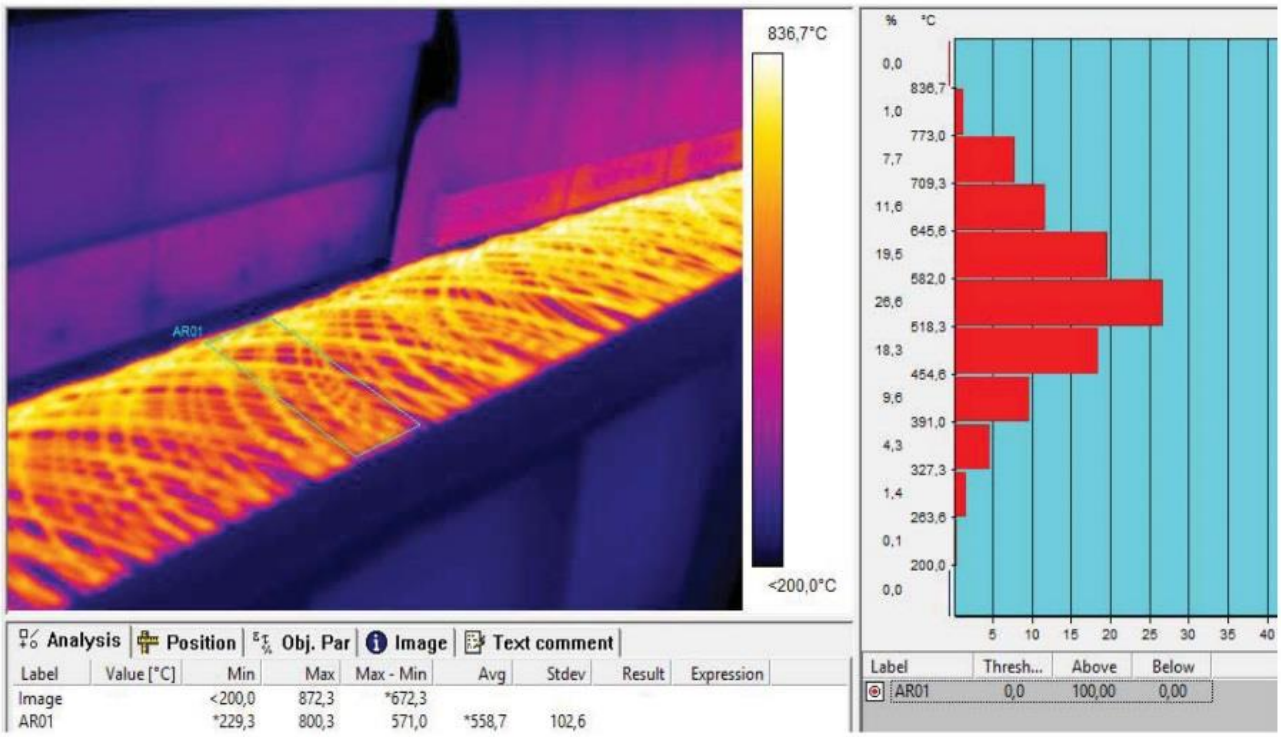

Figure 3-53 A thermal image of the steel wire rods' temperature profile [72]

Figure 3-54 shows the variation of the steel wire temperature versus the distance from the laying head where the cooling zone starts. These measurements were taken when the fan speed is at its lowest value, and it should be noted that the temperature of the steel wires can be different at the same distance from the laying head depending on the class of materials and the quality standards. Figure 3-54 shows two main categories of measurements where the edge represents the temperature of the wires at the edge close to the wall where the highest temperature was noted. The centre represents the temperature of the steel in middle of the conveyor between the two walls. It can be seen that the temperature of the steel decreases with distance from the laying head and the edge of the steel had always higher temperatures than the centre.

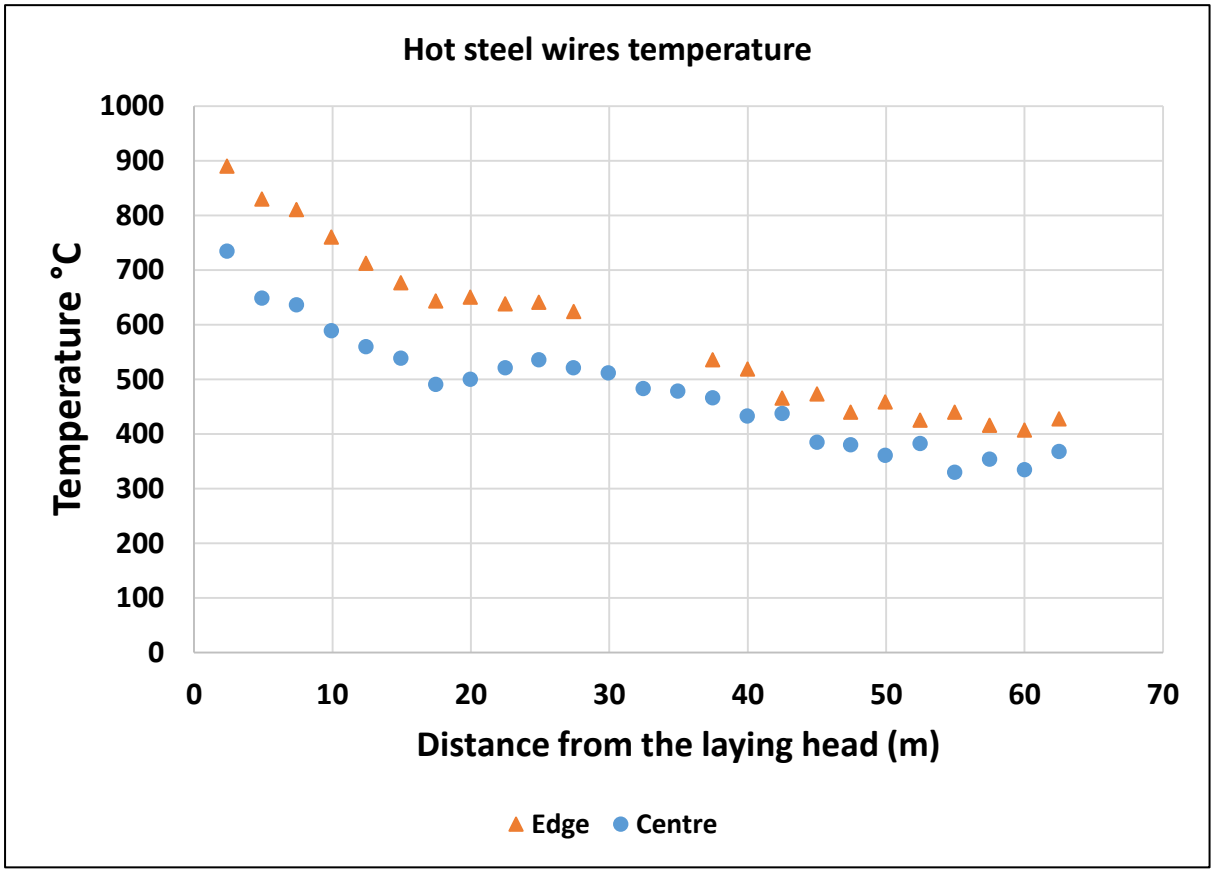

Figure 3-54 Thermal characterisation of the hot wire temperature per distance from the laying head [73]

The steel wire temperature at the beginning of the cooling line is measured using a thermal imaging camera (Land branded) as shown in Figure 3-55 (a). The average temperature of the wire rods can be read from the screen shown in Figure 3-55 (b).

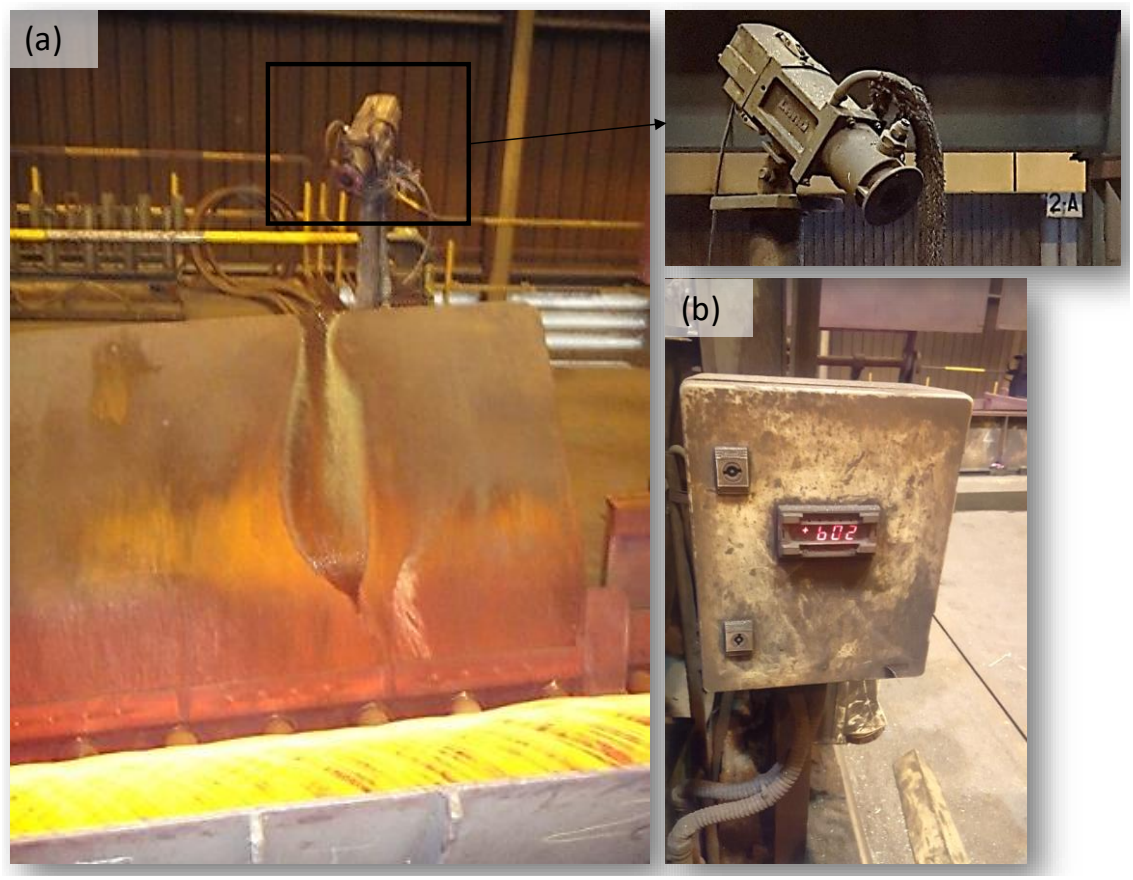

Figure 3-55 Temperature monitoring (a) Land thermal camera for temperature monitoring, (b) Temperature measurement screen

The air temperature and velocity over the conveyor were also investigated using a pitot tube. The air temperature in section 1 of Figure 3-49 could not be measured due to the high temperature. The air temperature was measured in sections 3 and 6. It can be seen that the air velocity was typically between 3.5 and 5 m/s. The air temperature was between 55 °C and 58 °C.

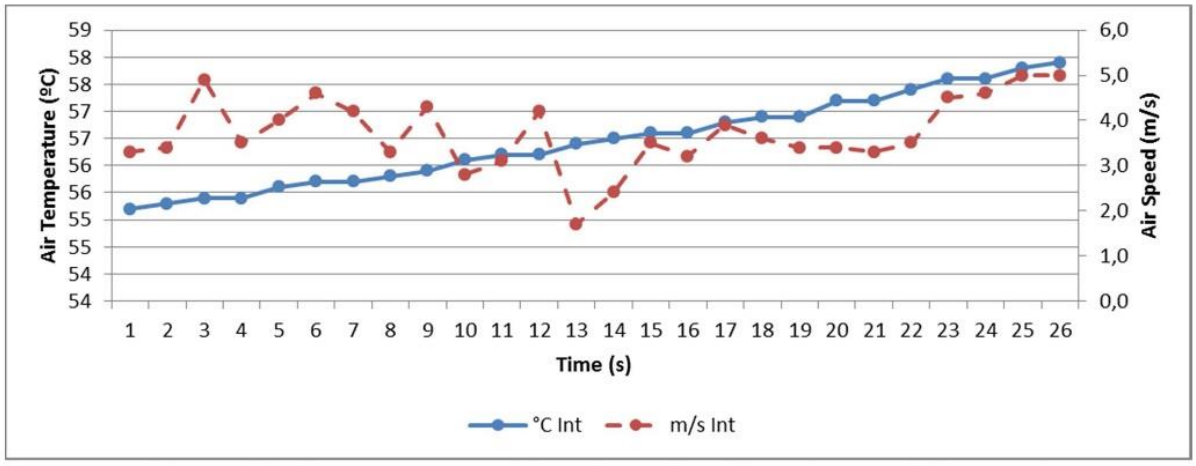

Figure 3-56 Air velocity and temperature in section 3 [73]

The wall temperature was also investigated as presented in Figure 3-57. The wall temperature was in the range of 125 °C to 235 °C. The wall temperature also varies with the section and the distance from the laying head depending on the steel temperature.

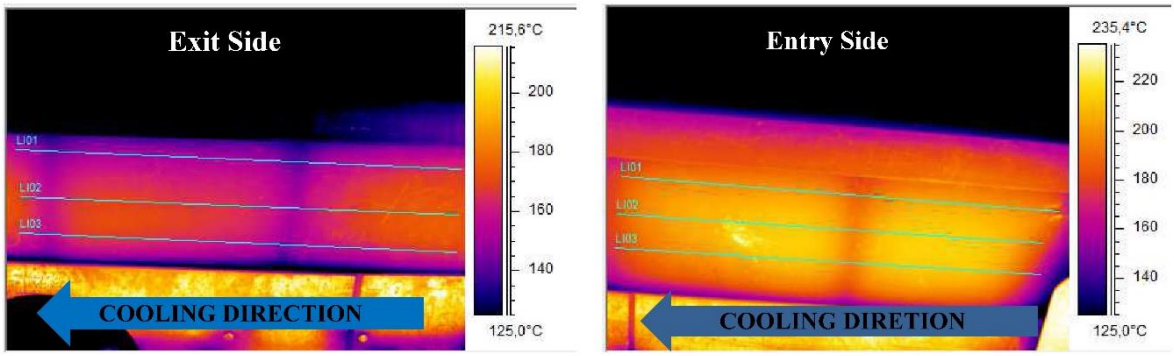

Figure 3-57 Thermal imaging of the walls in the cooling line [73]

Conducting the experiments at the production line had a lot of challenges such as the high temperature and the harsh environment. An additional challenge during the tests was moving covers which were folded down to cover the conveyor to control the steel temperature as shown in Figure 3-58.

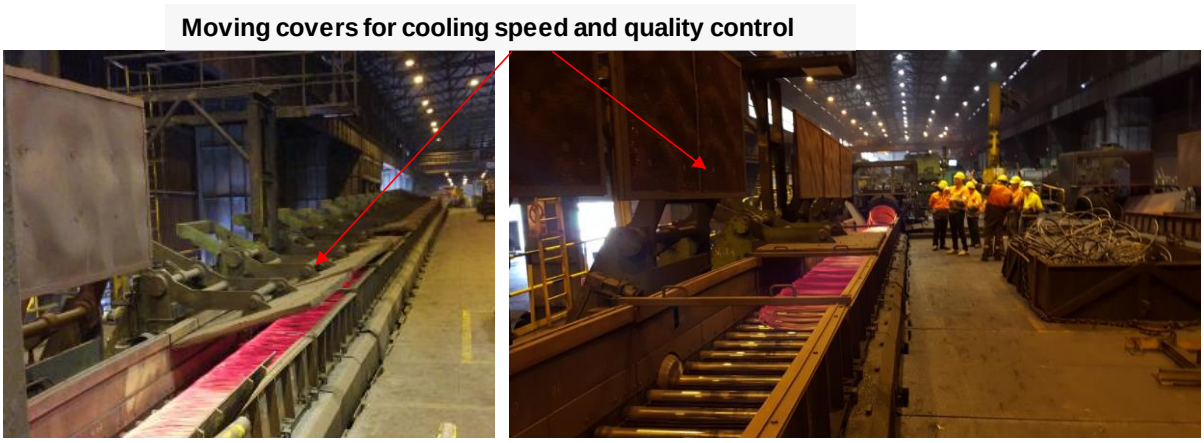

Figure 3-58 Moving covers for steel quality control

The floor level in the plant was not the same causing a higher edge of the conveyor than the stand maximum height preventing the FHP from being tested at a distance of more than 12m from the laying head.

Figure 3-59 Floor level challenge during testing the FHP

3.4.2 Instrumentation

The instrumentation used in the factory tests was the same as in the laboratory tests including the thermocouples, flow meter, and a data-logging system.

3.4.2.1 Thermocouples in factory tests

The experimental setup of the FHP for conducting the tests at the factory is shown in Figure 3-60. Figure 3-61 (a) shows the installation of the thermocouples on the FHP. Figure 3-61 (b) shows the insulation on the back panel and the water pipes. The thermal insulation used was superwool silica insulation which was the same as during the laboratory experiments. The thermocouple positioning is presented in Figure 3-62. The thermocouple positions were similar to the laboratory setup where three K-type thermocouples were installed on the bottom collector (EV1-EV3), and nine

thermocouples were placed on the vertical pipes (HP1-HP9). In addition, three thermocouples were placed on the top header(AD1-AD3). The thermocouples placed on the bottom header and the vertical pipes were to measure the temperature of the heat pipe at the evaporator and determine the temperature difference across the heat pipe. The water inlet and outlet temperatures were monitored using the same water pipeline connection as in the laboratory tests with the same K-type thermocouples.

Figure 3-60 Flat Heat Pipe set-up at factory tests

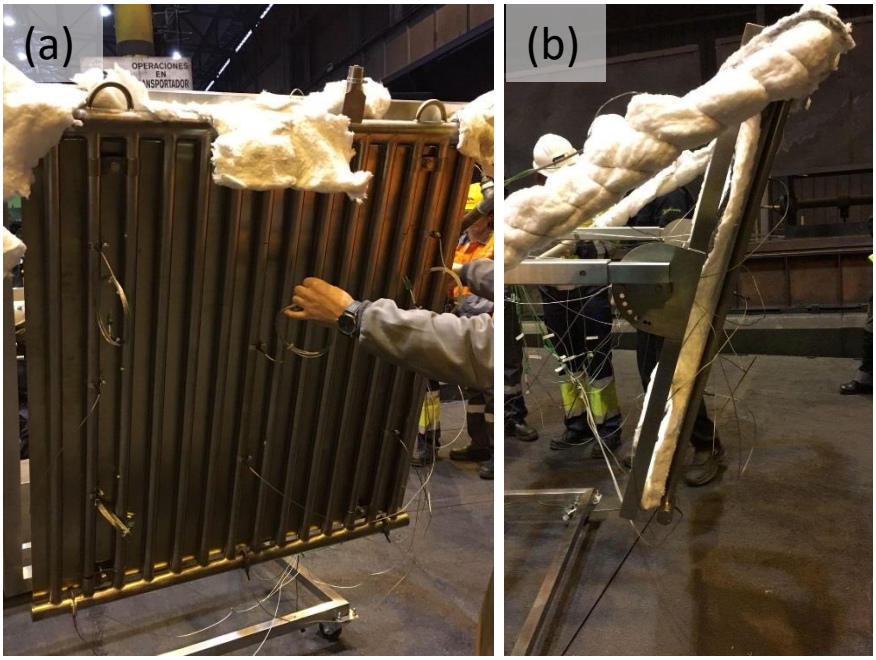

Figure 3-61 FHP experimental set-up at the factory: (a) thermocouple installation, (b) insulation of the back panel and the water pipeline

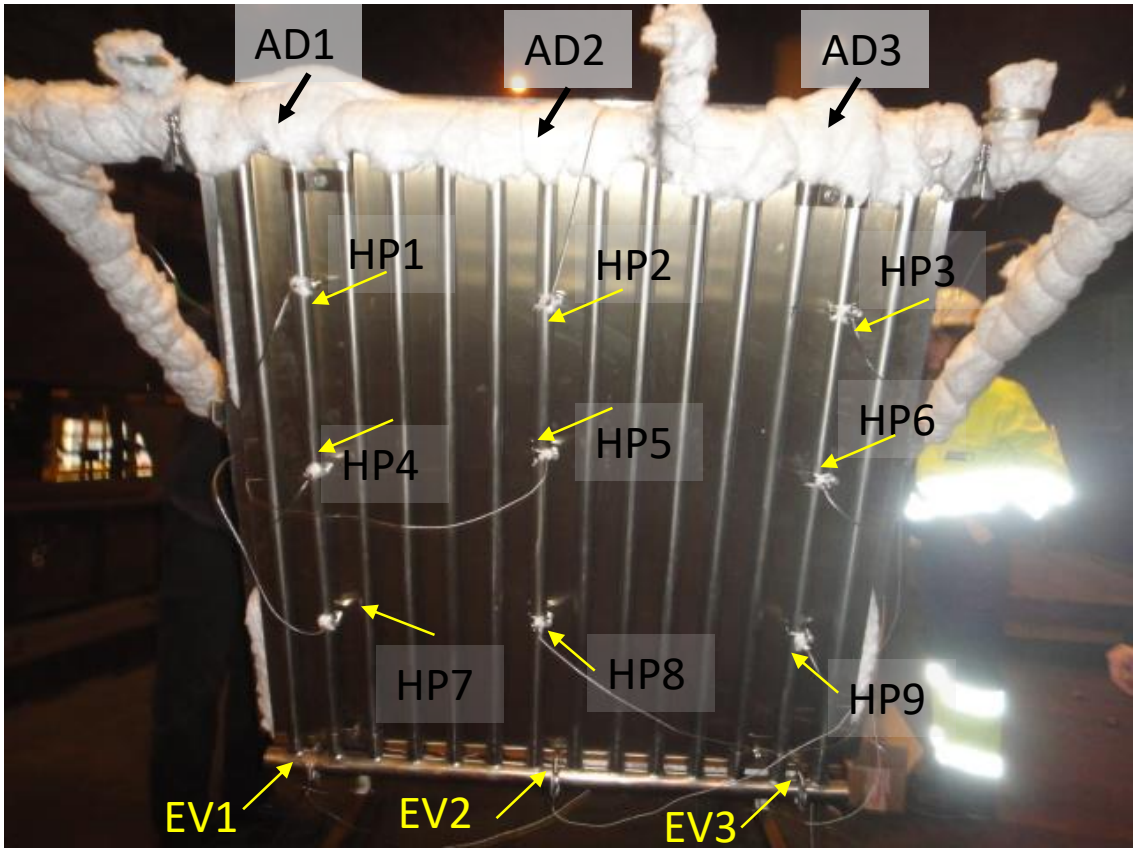

Figure 3-62 Thermocouple positioning

3.4.3 Experimental conditions

The FHP was tested at inclination angles of 12.5° and 25° at various conditions. The FHP was also tested at 40°, but the FHP was unable to function properly due to the low heat flux. Therefore, the results are not going to be reported. The conditions were cooling fan speed, steel wire diameter, average temperature of the steel and density of the wire rolls, which depended on the rolling mill speed. These conditions were uncontrollable as they were determined by the production program to control the quality of the steel produced. Other conditions were the distance from the laying head, the distance of the bottom collector from the edge of the conveyor as illustrated in Figure 3-63. The FHP was tested for the same configurations as in the laboratory where it was tested unpainted with a back panel, without a back panel, black painted with a back panel, black painted without a back panel. Figure 3-64 presents pictures of the FHP during the tests conducted at the factory. Figure 3-64 (a), (b), (c), and (d) are for testing the FHP at an inclination angle of 40°. Figure 3-65 (a) shows the FHP test at 25°. Figure 3-65 (b), (d) shows FHP testing at an inclination angle of 12.5°. Figure 3-65 (c) shows the FHP test where the FHP was above the production line.

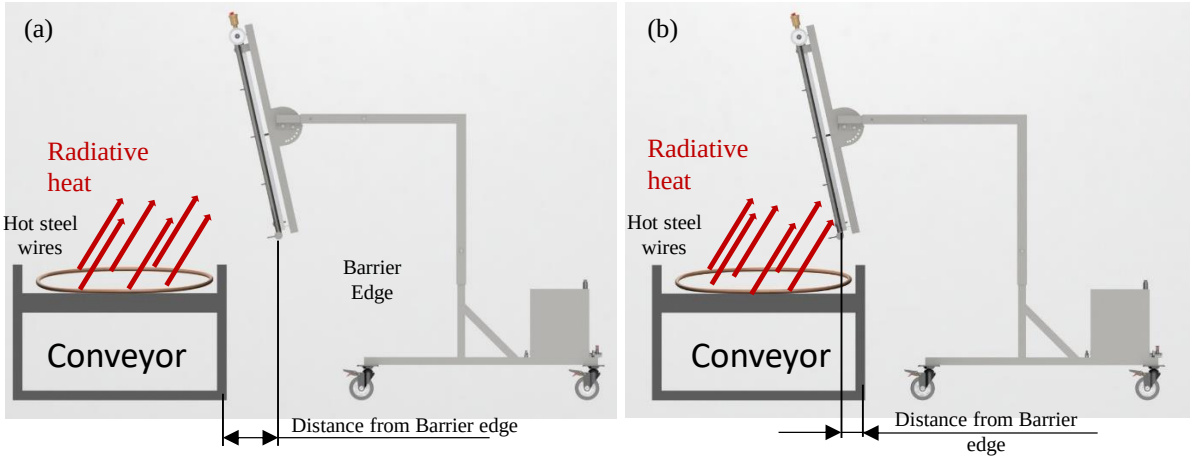

Figure 3-63 Illustration of testing the FHP and the position of the bottom collector of the FHP: (a) the FHP is far from the edge of the conveyor, (b) the FHP is FHP is above the conveyor

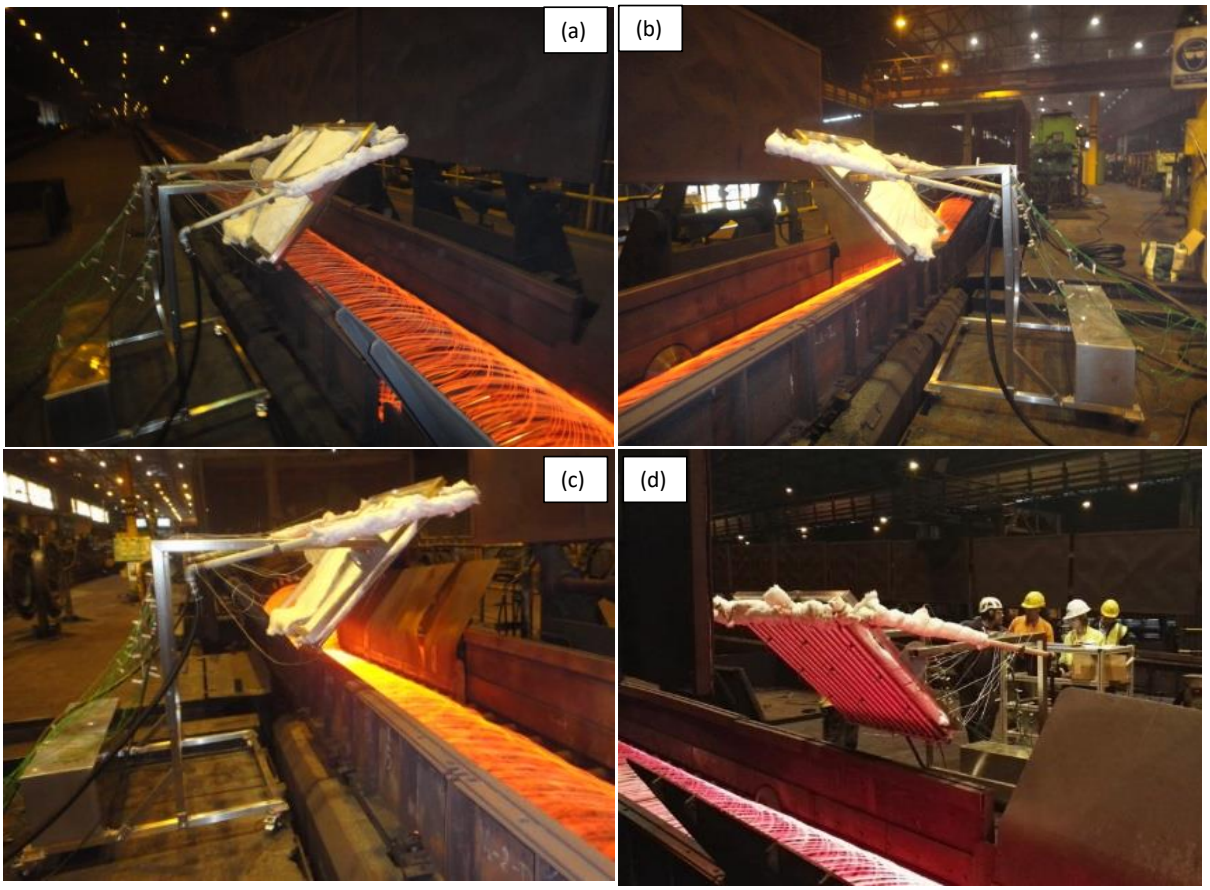

Figure 3-64 FHP testing conditions at the factory at inclination angle of 40°

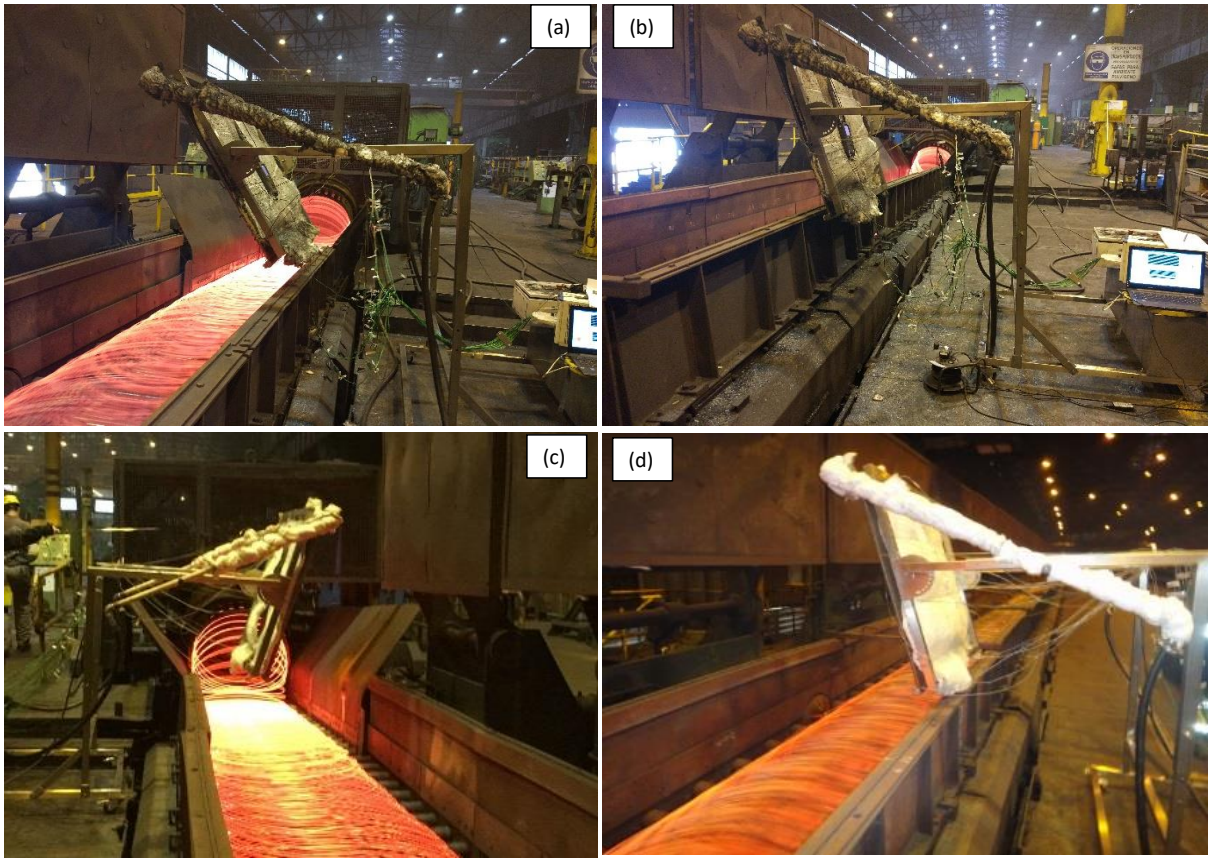

Figure 3-65 FHP testing at the factory at different positions (a): inclination angle of 25°, (b), (c), (d) FHP testing at inclination angle of 12.5°

The FHP was tested when painted black without a back panel after assessing the effect of the black paint in the laboratory, as seen in Figure 3-66. The FHP was not tested without a back panel when it was unpainted due to the unsatisfactory performance of the FHP in the laboratory for that condition.

Figure 3-66 FHP testing at the factory black painted without a back panel

The FHP was also tested black painted and with the back panel as shown in Figure 3-67.

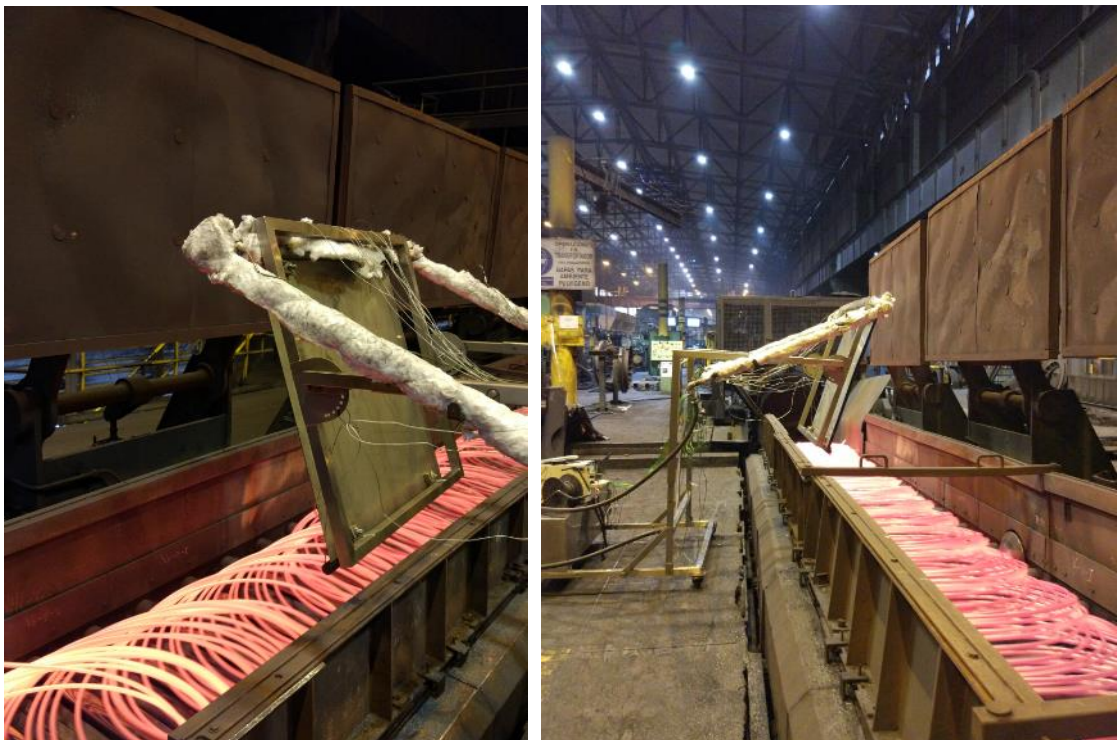

Figure 3-67 FHP testing black painted with a back panel

3.4.4 Operational procedure

The experiments at the factory were conducted with a similar procedure to the experiments conducted in the laboratory. The experiment started by running the data-logging software to record and monitor the temperatures of the FHP. The water valve was opened to allow the maximum water flow rate through the condenser of the FHP. The FHP was positioned away from the production line, then it was moved towards the edge of the conveyor carefully while monitoring the FHP temperatures and specifically the temperature of the thermocouples placed on the top header. The key element of the tests was the inclination angle of the FHP and the distance of bottom collector from the edge of the conveyor. The test position distance from the laying head also had a significant role where the steel temperature decreased as the distance from the laying head increased. The FHP was tested at inclination angles of 12.5° and 25° at different positions of the bottom collector from the conveyor edge. The FHP was tested also during the manufacture of different diameters of steel between 5.5 and 23 mm at different distances from the laying head. The experiments conducted were to study the performance of the FHP with real conditions during a steel manufacturing process. The duration of the test was limited by the duration of the steel manufacturing. After collecting the data for the test, the FHP was moved back from the production line and the data recording was stopped. This procedure was followed for each experiment for safety reasons to avoid any sudden temperature increase in the FHP at start up.

Chapter 4: Heat transfer theoretical modelling

4.1 Introduction

This chapter presents heat transfer fundamentals and discusses the modelling of the heat pipes. The modelling of the heat pipes is divided into three sections. One section discusses the modelling of the single heat pipe in the laboratory kiln and a second section discusses the modelling of the flat heat pipe in the laboratory and the factory tests. The last section describes the modelling tool which was developed to predict and analyse the thermal performance of the single heat pipe and the FHP at the experimental conditions.

4.2 Heat transfer Background

4.2.1 Radiation

Radiation is the fastest mode of heat transfer (at the speed of light) and it occurs in solids, liquids and gases and without any attenuation in a vacuum.

Radiant energy can be considered as transported by photons or by electromagnetic waves.

In 1864, James Clerk Maxwell proposed that the electromagnetic waves represent the emitted energy by an object due to the changes in the electronic configurations of the atoms or molecules. The electromagnetic waves were proved experimentally by Heinrich Hertz later.

Electromagnetic waves travel at the speed of light in a vacuum, which is $c_0 = 2.9979\,3 \times 10^8$ m/s. This speed is equal to the product of the frequency and the wavelength of the radiation [74]:

$$c = \lambda v \tag{4-1}$$

where λ is the wavelength (m) and v is the frequency (s^{-1}).

Thermal radiation is the relevant electromagnetic radiation emitted by a body as a result of energy transitions of its molecules, atoms, and electrons as a function of the temperature, where the temperature determines the strength of the activity at microscopic level. Thermal radiation is continuously emitted by any body with a temperature higher than absolute zero and it increases with temperature. Thermal radiation is emitted by solids and liquids and it is transmitted through a vacuum. The complete spectral range of electromagnetic radiation is presented in Figure 4-1. Thermal radiation is the electromagnetic radiation in the wavelength range of $0.1\ \mu m\ to\ 100\ \mu m$. The visible light spectrum is the radiation in the wavelength range of 0.4 to 0.7 μm.

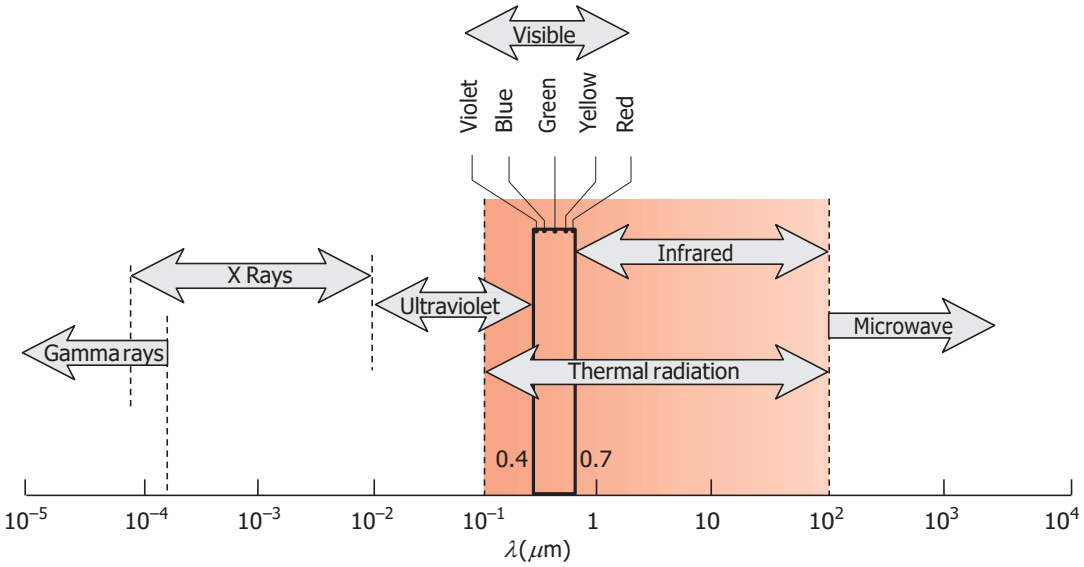

Figure 4-1 Spectrum range of electromagnetic radiation [75]

Thermal radiation in heat transfer practice is considered as a surface phenomenon.

4.2.2 Black body radiation

A body at a thermodynamic (or absolute) temperature above zero emits radiation in all directions over a wide range of wavelengths. The amount of radiation energy emitted from a surface at a given wavelength depends on the material of the body and the condition of its surface as well as the surface temperature.

A **black body** is defined as a perfect emitter and absorber of radiation. At a specified temperature and wavelength, no surface can emit more energy than a black body. A black body absorbs all incident radiation, regardless of wavelength and direction. Also, a black body emits radiation energy uniformly in all directions per unit area normal to direction of emission. Hence, a black body is a diffuse emitter. The term diffuse means "independent of direction." The radiation energy emitted by a black body per unit time and per unit surface area was determined experimentally by Joseph Stefan in 1879 and by Ludwig Boltzmann theoretically in 1884 and it is expressed as [74]:

$$E_b(T) = \sigma T^4 \tag{4-2}$$

The relation for the spectral black body emissive power $E_{b\lambda}$ was developed by Max Planck in 1901 in conjunction with his famous quantum theory. This relation is known as Planck's law and is expressed as:

$$E_{b\lambda} = \frac{C_1}{\lambda^5 \left[\exp\left(\frac{C_2}{\lambda T}\right) - 1\right]} \tag{4-3}$$

where $C_1 = 3.74177 \times 10^8$ W. $\mu m^4/m^2$, $C_2 = 1.43878 \times 10^4$ $\mu m. K$

Also, *T* is the absolute temperature of the surface, λ is the wavelength of the radiation emitted. This relation is valid for a surface in a vacuum or a gas. For other mediums, it needs to be modified by replacing C_1 by $C_1 1/n^2$, where *n* is the index of refraction of the medium. The term spectral indicates dependence on wavelength.

The variation of the spectral black body emissive power with wavelength is plotted in Figure 4-2 for selected temperatures.

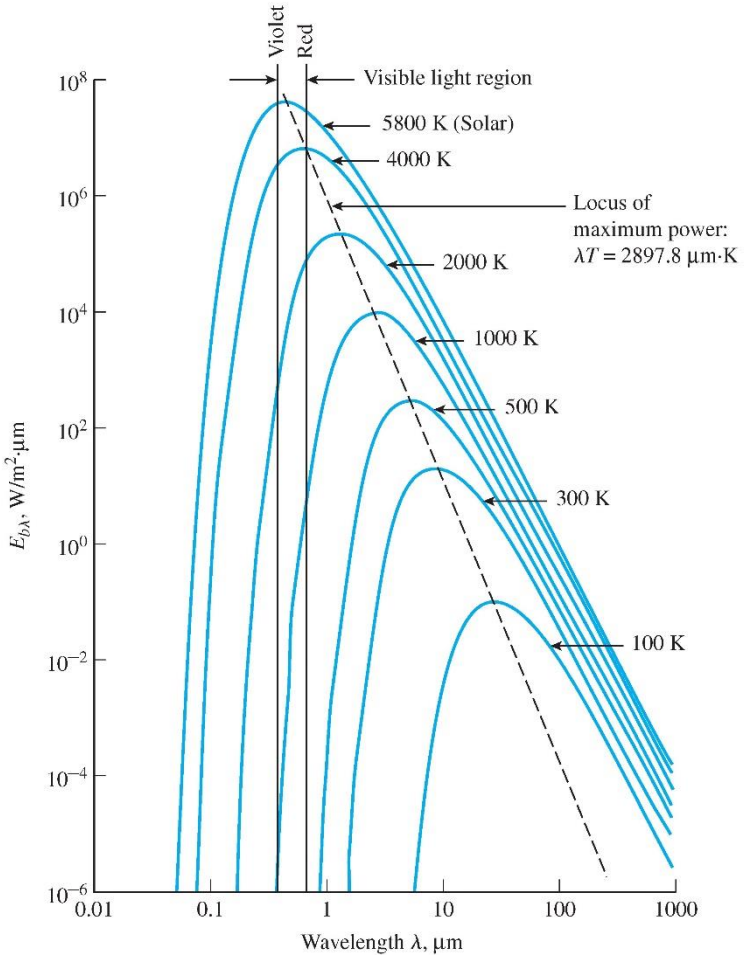

Figure 4-2 Black body emissive power variation with wavelength and temperature [76]

The following can be observed from the figure:

1. The thermal radiation is a continuous function of wavelength. At any specified temperature, it increases with wavelength, reaches a peak, and then decreases with increasing wavelength.
2. At any wavelength, the amount of emitted radiation increases with increasing temperature.
3. As temperature increases, the curves shift to the left to the shorter wavelength region. Consequently, a larger fraction of the radiation is emitted at shorter wavelengths at higher temperatures.
4. The radiation emitted by the sun, which is considered to be a black body at 5780 K, reaches its peak in the visible region of the spectrum. Therefore, the sun is in tune with our eyes. On the other hand, surfaces at T < 800 K emit almost entirely in the infrared region and therefore they are not visible to the eye unless they reflect light coming from other sources.

The wavelength of the peak at a specified temperature can be determined by Wien's displacement law as follows:

$$(\lambda T)_{\max power} = 2897.8\ \mu\text{m.K} \tag{4-4}$$

The integration of Planck's law of the spectral emissive power of a black body over the entire wavelength spectrum gives the total black body emissive power E_b as follows:

$$E_b(T) = \int_0^\infty E_{b\lambda}(\lambda, T)d\lambda = \sigma T^4\ (\text{W/m}^2) \tag{4-5}$$

σ is Stephan-Boltzmann constant where $\sigma = 5.67 \times 10^{-8}\ \text{W/m}^2\text{K}^4$

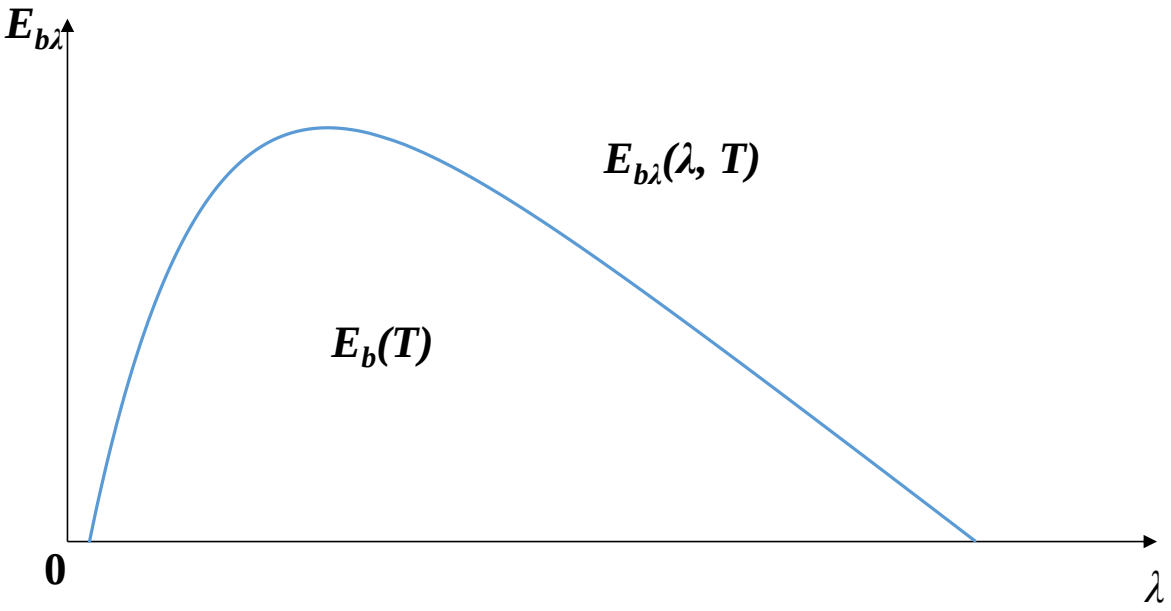

Figure 4-3 Total and spectral emissive power of a black body

4.2.3 Intensity of radiation

The amount of radiation propagating in a given direction is determined through the intensity of radiation I. The radiation is emitted by a surface in all directions into the hemisphere above the surface. The directional distribution of the emitted radiation is uniform. Therefore, the direction of the radiation passing through a point is described in spherical coordinates where the zenith angle is θ and the azimuth angle is ϕ as presented in Figure 4-4. The radiation emitted from a surface dA varies with the zenith and azimuth angles which is represented though the intensity of radiation.

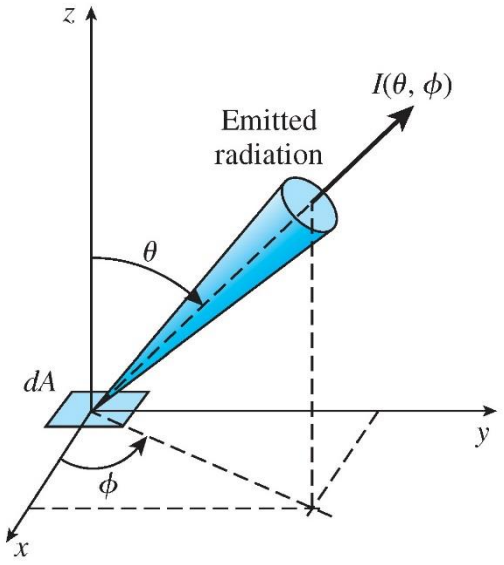

Figure 4-4 Schematic of the radiation intensity [76]

It can be seen from Figure 4-5 that the area of a surface on a sphere of unit radius is equivalent in magnitude to the solid angle it subtends.

The solid angle of a hemisphere can be obtained from the following approach by considering a differential surface area on a sphere $dS = r^2 \sin\theta \ d\theta \ d\phi$

$$S = \int_{sphere} dS = \int_{\phi=0}^{2\pi} \int_{\theta=0}^{\pi} r^2 \sin\theta \, d\theta \, d\phi = 4\pi r^2 \tag{4-6}$$

For a hemisphere of diameter $r = 1$ the solid angle is $\omega = 2\pi$ sr.

The differential solid angle subtended by a differential area dS on a sphere of radius r can be expressed as:

$$d\omega = \frac{ds}{r^2} = \sin\theta \, d\theta \, d\phi \tag{4-7}$$

The radiation intensity for emitted radiation $I_e(\theta, \phi)$ is defined as the rate at which the radiation energy dQ_e is emitted in the (θ, ϕ) direction per unit area normal to this direction and per unit solid angle about this direction.

$$I_e(\theta, \phi) = \frac{d\dot{Q}_e}{dA \cos\theta \, d\omega} = \frac{d\dot{Q}_e}{dA \cos\theta \sin\theta \, d\theta \, d\phi} \left(\frac{\mathrm{W}}{\mathrm{m^2 sr}}\right) \tag{4-8}$$

where the effective area of emission projecting onto a plane normal to θ is $dA_n = dA\ \cos\theta$ as seen in Figure 4-6

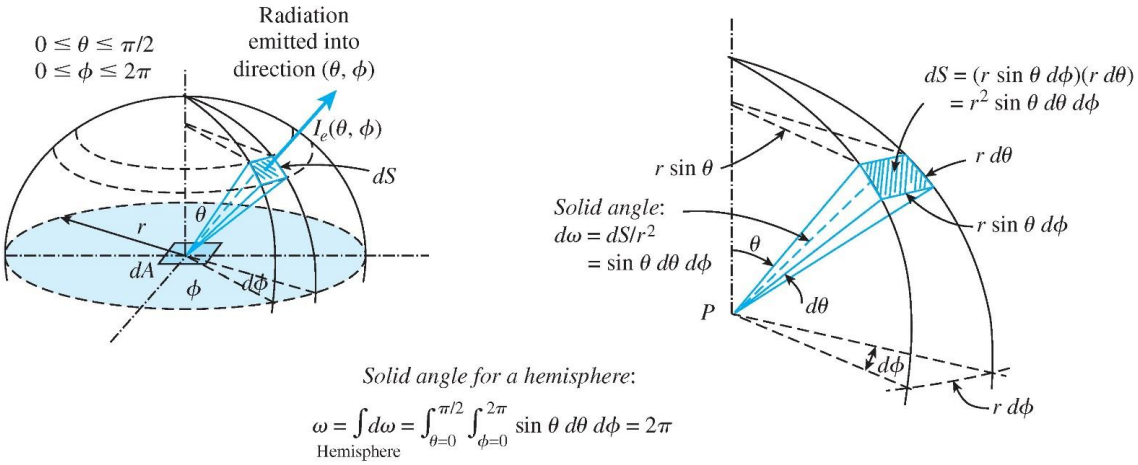

Figure 4-5 schematic of emitted radiation from a differential surface element into the surroundings [77]

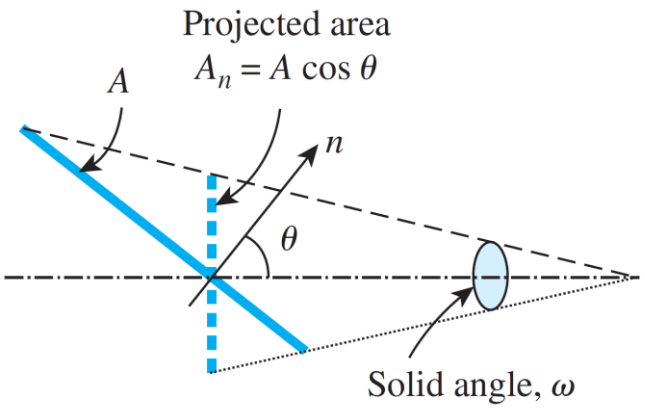

Figure 4-6 Schematic of the effective area projected onto a plane normal to the direction of radiation emission

Therefore the radiation flux for emitted radiation which is the emissive power or the radiation energy emitted per unit of emitting surface can be expressed as follows:

$$dE = \frac{d\dot{Q}_e}{dA} = I_e(\theta, \phi)\cos\theta\ \sin\theta\ d\theta\ d\phi\ (\mathrm{W/m^2}) \tag{4-10}$$

$$E = \int_{\phi=0}^{2\pi} \int_{\theta=0}^{\pi/2} I_e(\theta, \phi)\cos\theta\ \sin\theta\ d\theta\ d\phi\ (\mathrm{W/m^2}) \tag{4-9}$$

For diffuse surfaces where the radiation intensity is independent of direction i.e. radiation intensity is equal in all directions, then the radiation flux equation can be simplified into the following:

$$E = \pi I_e \ (\mathrm{W/m^2}) \tag{4-11}$$

where the emissive power is based on the actual surface area

Surfaces not only emit radiation but also receive radiation emitted or reflected by other surfaces.

The radiation flux incident on a surface from all directions is defined as irradiation *G*, and expressed as follows:

$$G = \int_{hemisphere} dG = \int_{\phi=0}^{2\pi} \int_{\theta=0}^{\pi/2} I_i(\theta, \phi) \cos\theta \sin\theta \, d\theta \, d\phi \ \ (\mathrm{W/m^2}) \tag{4-12}$$

As shown in Eq. (4-12) the incident radiation represents the rate of radiation energy incident on a surface per unit area of the surface.

For a diffuse surface then the irradiation becomes as follows:

$$G = \pi I_i \ (\mathrm{W/m^2}) \tag{4-13}$$

It should be mentioned that the irradiation is related to the actual surface area similarly to the emissive power.

4.2.4 Radiation properties

4.2.4.1 Emissivity

The emissivity of a surface is defined as the ratio of the radiation energy emitted by a surface at a given temperature to the radiation of a black body at the same temperature. The emissivity is symbolised with ε and varies within the range of $0 \leq \varepsilon \leq 1$ where the case of $\varepsilon = 1$ is for a black body surface.

It should be noted the emissivity of a black body is equal to 1 at any wavelength, direction, or temperature. However, this is not the case of a real body. Therefore, a spectral directional emissivity is presented as the ratio of the intensity of radiation emitted by a surface at a specified wavelength in a specified direction to the intensity of radiation emitted by a blackbody at the same temperature and wavelength.

$$\varepsilon_{\lambda,\theta}(\lambda, \theta, \phi, T) = \frac{I_{\lambda,e}(\lambda, \theta, \phi, T)}{I_{b\lambda}(\lambda, T)} \tag{4-14}$$

The subscripts λ, θ are to specify spectral and directional quantities.

The emissivity can be averaged over all directions where it is defined as spectral hemispherical emissivity or the monochromatic emissivity which is defined as follows:

$$\varepsilon_{\lambda}(\lambda, T) = \frac{E_{\lambda}(\lambda, T)}{E_{b\lambda}(\lambda, T)} \tag{4-15}$$

It can be seen from Eq. (4-15) that the emissivity is a function of the wavelength and the temperature of the surface emitting the radiation and varies between one wavelength and another. The emissivity of a surface regarding the entire wavelength range is called the total hemispherical emissivity or the average emissivity which depends on the surface temperature only as follows:

$$\varepsilon(T) = \frac{E(T)}{E_b(T)} \tag{4-16}$$

It can be concluded from the definitions presented above that radiation heat transfer is a complex phenomenon of heat transfer and depends on different factors such as the surface temperature, direction, wavelength, and surface emissivity which also complicate the phenomenon more.

In heat transfer practice, an approximation can be made where the studied body is considered as a grey body. A grey body is defined as a surface with a monochromatic emissivity $\varepsilon_{\lambda,T}$ independent of wavelength. Hence, the emissivity of a greybody is equal to its total hemispherical emissivity because it is independent of direction and wavelength as illustrated in Figure 4-7 (a).

The illustration in Figure 4-7 (a) compares the emissivity of a black body, a grey body, and a real body. The emissivity of a black body is constant at 1 and independent of the wavelength. The emissivity of a grey body is also independent of the wavelength at a value between 0 and 1. It is also shown that emissivity of a real body varies with the wavelength. The effect of the emissivity on the emissive power is shown in Figure 4-7 (b). The maximum value of emissive power at any wavelength is as for the black body. The emissive power of the grey body is less than that of the black body and Planck's law applies for both bodies. However, the emissive power curve of a real body does not follow Planck's distribution and may have peaks and troughs. Since the grey body has to emit the same radiation energy of a real body at the same temperature, then the area below the curve of the grey body and the real body has to be equal in order to consider the real body as a grey body.

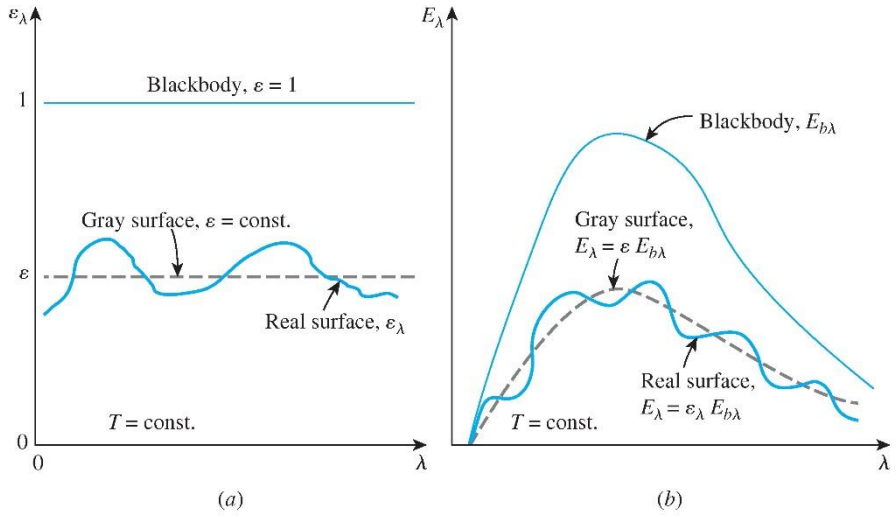

Figure 4-7 Comparison of the (a): emissivity, (b) emissive power between black body, grey body, and real body [77]

4.2.4.2 Absorptivity, transmissivity and reflectivity

When radiation is incident on a real semi-transparent material at irradiation G, it reflects part of the radiation, absorbs part of it, and transmits the last part as illustrated in Figure 4-8. Hence, absorptivity, reflectivity, and transmissivity of a material describe how the total irradiation is distributed.

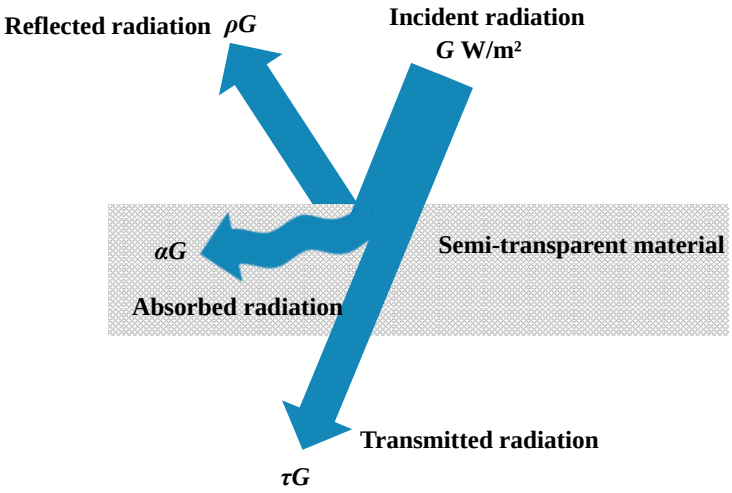

Figure 4-8 Reflection, absorption, and transmission of incident radiation by a semi-transparent material

The absorptivity of a surface α is defined as the fraction of the irradiation absorbed by the body. The reflectivity of a surface ρ is defined as the fraction of the irradiation reflected from the surface. The transmissivity of a body τ is the fraction of the incident radiation that is transmitted. Applying the energy balance on a surface yields:

$$\alpha G + \rho G + \tau G = G \tag{4-17}$$

Dividing the equation by G yields:

$$\alpha + \rho + \tau = 1 \tag{4-18}$$

An ideal black body is a perfect absorber where $\rho = 0, \tau = 0, and\ \alpha = 1$

For opaque surfaces we obtain:

$$\alpha + \rho = 1 \tag{4-19}$$

It should be highlighted that these properties are independent of wavelength or direction since they are defined for irradiation G which is the radiation flux incident on a surface from all directions of a surrounding hemisphere over all the wavelengths. The definition of these properties can be expanded so they become specified by the wavelength and direction similar to the emissivity definition. The spectral hemispherical absorptivity can be presented as follows:

$$\alpha_\lambda = \frac{G_{\lambda,abs}(T)}{G_{\lambda,i}(T)} \tag{4-20}$$

where the subscript λ means that the absorptivity is obtained at a specified wavelength.

Similarly, for the reflectivity

$$\rho_\lambda(T) = \frac{G_{\lambda,ref}(T)}{G_{\lambda,i}(\lambda,T)} \tag{4-21}$$

Figure 4-9 presents an illustration of the reflection of the irradiation from two different surfaces: (A) reflection from a diffuse surface, (B) reflection from a real surface. The reflectivity in a real surface depends on the direction of the incident radiation and the direction of the reflected radiation. In heat transfer practice, the reflectivity is simplified by assuming the surface is diffuse where the radiation is equally reflected in all directions. In radiation analysis, a surface can be considered as diffuse unless the surface roughness is much smaller than the wavelength of the incident radiation. The absorptivity is independent of the surface temperature but it strongly depends on the incident radiation source temperature [77].

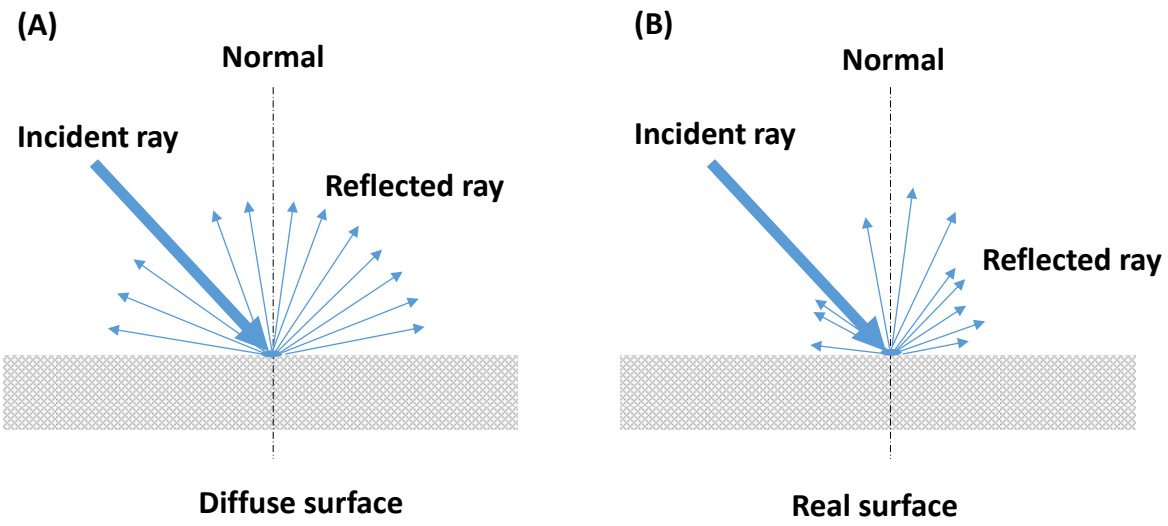

Figure 4-9 Schematic of reflection from a surface: (A) diffuse surface, (B) real surface

4.2.4.3 Radiosity and emittance of a surface

The radiation leaving a surface is the total of the radiation emitted by a surface and the reflected radiation. The total radiation energy leaving a surface per unit area in all directions can be defined as the radiosity J $(\mathrm{W/m^2})$ as shown in Figure 4-10.

The radiosity can be expressed as follows:

$$J = \int_{\phi=0}^{2\pi} \int_{\theta=0}^{\pi/2} I_{e+ref}(\theta, \phi) \cos\theta \sin\theta \, d\theta \, d\phi \ \ (\mathrm{W/m^2}) \tag{4-22}$$

where I_{e+ref} is the total radiation intensity consisting of the emitted and reflected radiation intensity.

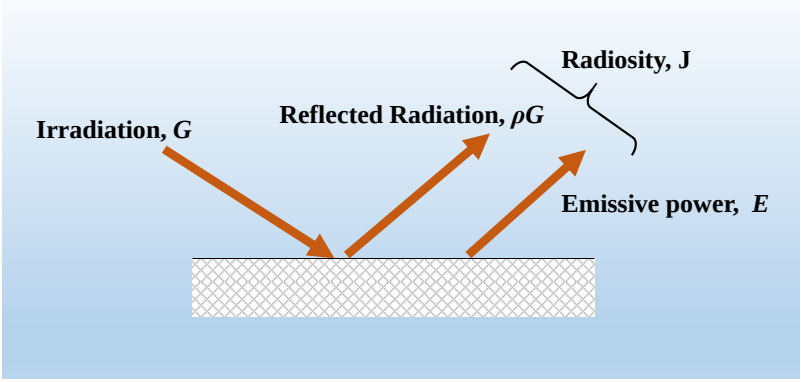

Figure 4-10 Schematic of three kinds of Radiant flux: Irradiation, Radiosity, Emissive power

A diffuse emitter and reflector yields:

$$J = \pi I_{e+ref} (\mathrm{W/m^2}) \tag{4-23}$$

For a blackbody, the radiosity will be equal to the emissive power of the blackbody surface E_b since the blackbody does not reflect any radiation.

4.2.4.4 Kirchhoff's law

Kirchhoff's law, which was first developed by Gustav Kirchhoff in 1860, supposes a body placed in an isothermal black enclosure at a temperature T. By considering that the two bodies are at thermal equilibrium from the second law of thermodynamics, since the body in the enclosure is too small to interfere with the black body nature, the incident radiation on the small body is equal to the emitted radiation by the black body at the same temperature T:

$$G = E_b = \sigma T^4 \tag{4-24}$$

The absorbed incident radiation by the body is equal to the emitted radiation:

$$G_{abs} = \alpha G = \alpha \sigma T^4 \tag{4-25}$$

By applying the energy balance between the two bodies, all the absorbed incident radiation on the small body will be equal to the energy it emits:

$$\alpha \sigma T^4 = \varepsilon \sigma T^4 \tag{4-26}$$

Hence:

$$\varepsilon(T) = \alpha(T) \tag{4-27}$$

The total hemispherical emissivity of a surface at temperature T is equal to its total hemispherical absorptivity at the same temperature.

The derivation of the relation between the emissivity and the absorptivity of a surface can be repeated to obtain the spectral form of Kirchhoff's law:

$$\varepsilon_\lambda(T) = \alpha_\lambda(T) \tag{4-28}$$

4.2.4.5 Summary of blackbody characteristics

The black body characteristics can be summarised as follows:

The black body absorbs all incident radiation regardless of wavelength and direction. No surface can emit energy more than a black body at a specified temperature and wavelength.

A black body is a perfectly diffuse emitter where the emitted radiation is function of the temperature and wavelength, but it is independent of direction.

Hence, the black body is an ideal emitter and absorber at any direction, any temperature, and any wavelength. The blackbody is considered as a standard to which the real surface priorities can be compared.

4.2.4.6 Grey bodies

As defined before, the emissivity of a grey body is dependent on the wavelength where a grey surface emits radiation at a constant fraction of the monochromatic emissive power of a black body at the same temperature. Therefore, the total emissivity and the total absorptivity can be obtained from the spectral emissivity at a specified wavelength. Furthermore, the total values of absorptivity and emissivity can be considered equal even if the body is not in thermal equilibrium with its surroundings [76]. In heat transfer practice, an average value of the absorptivity is selected based on the condition of the heat source, while the average emissivity is selected based on the temperature of the surface of the body that receives and emits radiation. If the emissivity of the grey body is not equal to the absorptivity, then it is called a called a selectively grey body.

4.2.4.7 Real bodies

Radiation from real surfaces is different from black body or grey body radiation in different aspects. The radiation of a real surface is always less than a black body at any temperature. A real surface emits a fraction of ε_λ of the black body radiation. However, this fraction is not constant and depends on the wavelength and the real surface temperature. Moreover, the spectral emission of the real body differs from the spectral emission of a black or grey surface. The average of the grey surface emission curve should be equal to the average of the real surface spectral curve in order to assume the real surface as a grey body.

4.2.5 View factor

4.2.5.1 The view factor definition

Radiation heat transfer depends on the surface temperature, properties, geometry, and orientation. Therefore, to study the radiation exchange between surfaces, an expression called the view factor F_{12} is defined as the fraction of the radiation energy leaving a surface 1 and intercepted by surface 2. The view factor is also called configuration factor, angle factor, and shape factor.

A general expression of the view factor can be developed as follows. We consider two differential surfaces dA_1 and dA_2 on two arbitrarily oriented surfaces A_1 and A_2, respectively. The distance between dA_1 and dA_2 is r, and the angles between the normals of the surfaces and the line which connects dA_1 and dA_2 are θ_1 and θ_2, respectively as shown in Figure 4-11. The solid angle subtended by dA_2 when viewed by dA_1 is $d\omega_{12}$, where the solid angle can be determined by dividing the projected area of the receiving surface in the direction of the incident radiation by the square of the distance between dA_1 and dA_2 as follows:

$$d\omega_{12} = \cos\theta_2 \frac{dA_2}{r^2} \tag{4-29}$$

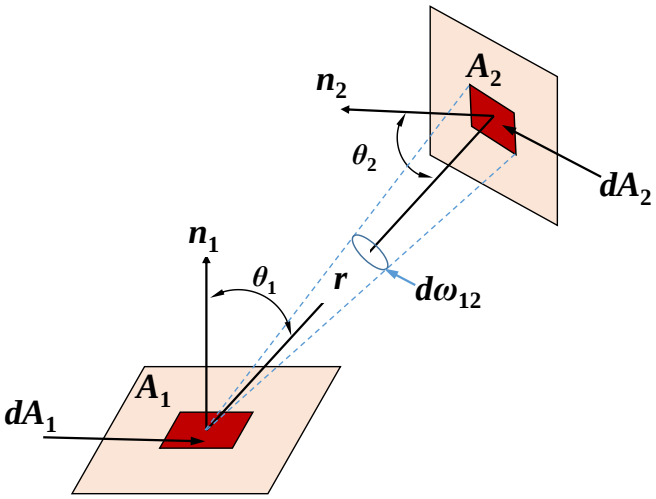

Figure 4-11 Illustration of geometric view factor derivation

The portion of radiation that strikes surface dA_2 is found as follows.

The total radiation rate leaving the surface dA_1 and received by dA_2 is given by:

$$dQ_{12} = I_1 \cos\theta_1 \, dA_1 d\omega_{12} \tag{4-30}$$

where I_1 is the intensity of total radiation (reflection and emission) leaving surface dA_1, $dA_1 \cos\theta_1$ is the projected area of dA_1 as seen from dA_2, and $d\omega_{12}$ is the solid angle subtended by receiving area dA_2 with respect to centre point dA_2.

The radiosity of the surface dA_1 is

$$J_1 = \pi I_1 \tag{4-31}$$

and the entire radiation leaving surface A_1 is

$$Q_1 = J_1 A_1 = \pi I_1 A_1 \tag{4-32}$$

Substituting Eq.(4-29) and Eq.(4-31) into Eq.(4-30) yields:

$$dQ_{12} = J_1 \left(\frac{\cos\theta_1 \cos\theta_2}{\pi r^2} \right) dA_1 dA_2 \tag{4-33}$$

and the radiation leaving surface A_2 and striking surface A_1 is:

$$Q_{12} = J_1 \int_{A_1} \int_{A_2} \left(\frac{\cos\theta_2 \cos\theta_1 \, dA_1 dA_2}{\pi r^2} \right) \tag{4-34}$$

By analogy, the total radiation leaving surface dA_2 and striking surface dA_1 is:

$$dQ_{21} = J_2 \left(\frac{\cos\theta_2 \cos\theta_1}{\pi r^2} \right) dA_1 dA_2 \tag{4-35}$$

The net rate of radiation between the surfaces dA_1 and dA_2 is

$$dQ_{1\rightleftarrows 2} = (J_1 - J_2)\left(\frac{\cos\theta_2 \cos\theta_1 \, dA_1 dA_2}{\pi r^2}\right) \tag{4-36}$$

The net radiation between the entire surfaces A_1 and A_2 can be obtained from the integration of the previous equation over both surfaces:

$$Q_{1\rightleftarrows 2} = (J_1 - J_2)\int_{A_1}\int_{A_2}\left(\frac{\cos\theta_2 \cos\theta_1 \, dA_1 dA_2}{\pi r^2}\right) \tag{4-37}$$

where it is assumed that the radiosity is uniform over the two surfaces.

From the view factor definition by dividing the radiation leaving the surface A_1 and striking surface A_2 in Eq.(4-34) by the total radiation leaving surface A_1 in Eq.(4-32):

$$F_{12} = \frac{1}{A_1}\int_{A_2}\int_{A_1}\left(\frac{\cos\theta_1 \cos\theta_2}{\pi r^2}\right) dA_1 dA_2 \tag{4-38}$$

It can be seen that the view factor is independent of the radiosity of the surface.

In similar approach, the view factor of the radiation leaving the surface A_2 and strikes surface A_1

$$F_{21} = \frac{1}{A_2}\int_{A_2}\int_{A_1}\left(\frac{\cos\theta_1 \cos\theta_2}{\pi r^2}\right) dA_1 dA_2 \tag{4-39}$$

Hence Eq.(4-34) can be written:

$$Q_{12} = J_1 A_1 F_{12} \tag{4-40}$$

And for the radiation from surface A_2 to surface A_1 is:

$$Q_{21} = J_2 A_2 F_{21} \tag{4-41}$$

It should be noted that for a black body, the radiosity is equal to the total emissive power E_b.

Eq.(4-40) and Eq. (4-41) yield:

$$A_1 F_{12} = A_2 F_{21} \tag{4-42}$$

Eq.(4-42) is called the reciprocity relation

4.2.5.2 The analytical approach and relations in calculating the view factor

In addition to the reciprocity relation, there are other relations used in view factor algebra which are the following:

4.2.5.2.1 Summation rule

From energy conservation the view factors from surface i of an enclosure to all surfaces of the enclosure, including to itself, must equal unity. This is rule is known as the summation rule for an enclosure and is expressed as

$$\sum_{j=1}^{N} F_{ij} = 1 \tag{4-43}$$

where i is the emitting surface and j is the receiving surface.

4.2.5.2.2 Superposition rule

The superposition rule can be expressed as the view factor from a surface i to a surface j is equal to the sum of the view factor from surface i to the parts of the surface j.

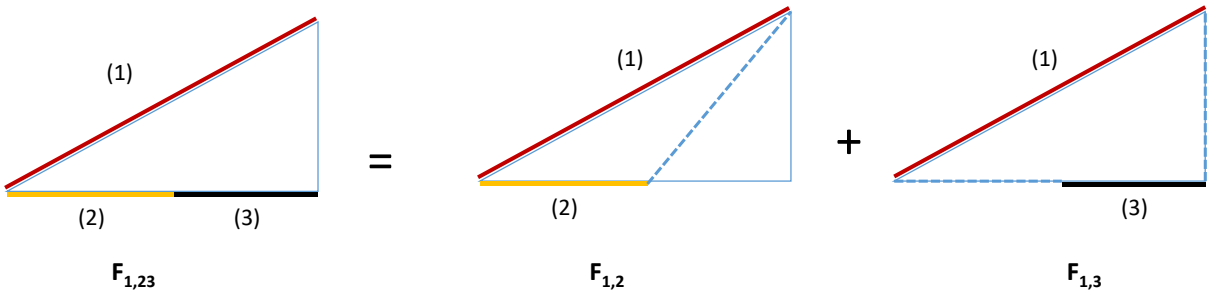

Figure 4-12 Illustration of the superposition rule of the view factor

As illustrated in Figure 4-12 the view factor from surface 1 to the combined surfaces 2 and 3 is:

$$F_{1\to(2,3)} = F_{12} + F_{13} \tag{4-44}$$

The view factor $F_{(2,3)\to1}$ can be obtained from rearranging Eq.(4-44) as the following:

$$A_1 F_{1\to(2,3)} = A_1 F_{12} + A_1 F_{13} \tag{4-45}$$

The reciprocity rule yields:

$$A_1 F_{1\to(2+3)} = (A_1 + A_3) F_{(2,3)\to1} \tag{4-46}$$

Applying the reciprocity between surface 1 and 2 yields:

$$A_1 F_{12} = A_2 F_{21} \tag{4-47}$$

By applying the reciprocity between surfaces 1 and 3 yields:

$$A_1 F_{13} = A_3 F_{31} \tag{4-48}$$

Hence:

$$(A_1 + A_3) F_{(2,3)\to1} = A_2 F_{21} + A_3 F_{31} \tag{4-49}$$

4.2.5.2.3 The symmetry rule

The symmetry rule can simplify the view factor algebra for symmetrical geometry as shown in Figure 4-13. The rule can be expressed as follows: the two or more surfaces with symmetry about a third surface will have identical view factors from that surface.

$$F_{12} = F_{13} \tag{4-50}$$

Using the reciprocity rule yields:

$$F_{21} = F_{23} \tag{4-51}$$

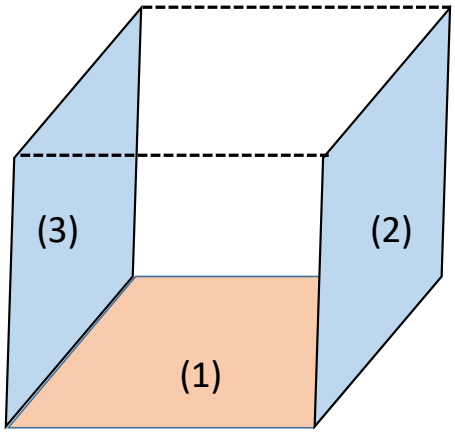

Figure 4-13 Illustration of the summation rule

4.2.5.2.4 Literature review on view factor equations

View factors for common geometries and cases have been studied and reported in the literature. A catalogue of the view factors for common geometries and shapes is reported by Howell [78]. The view factors can be calculated using analytical, mathematical, and numerical methods.

The view factor of radiation between two rectangles with one common edge and an angle $\emptyset$ as seen in Figure 4-14 has been reported by [79]. The view factor is reported in Eq. (4-52):

$$\begin{aligned} F_{1-2} = &-\frac{\sin 2\emptyset}{4\pi B}\left[AB\sin\emptyset + \left(\frac{\pi}{2} - \emptyset\right)(A^2 + B^2) + B^2\tan^{-1}\left(\frac{A - B\cos\emptyset}{B\sin\emptyset}\right)\right. \\ &\left. + A^2\tan^{-1}\left(\frac{B - A\cos\emptyset}{A\sin\emptyset}\right)\right] \\ &+\frac{\sin^2\emptyset}{4\pi B}\left\{\left(\frac{2}{\sin^2\emptyset} - 1\right)\ln\left[\frac{(1+A^2)(1+B^2)}{1+C}\right] + B^2\ln\left[\frac{B^2(1+C)}{(1+B^2)C}\right] + A^2\ln\left[\frac{A^2(1+A)^{\cos 2\emptyset}}{C(1+C^2)^{\cos 2\emptyset}}\right]\right\} \\ &+\frac{1}{\pi}\tan^{-1}\left(\frac{1}{B}\right) + \frac{A}{\pi B}\tan^{-1}\left(\frac{1}{A}\right) - \frac{\sqrt{C}}{\pi B}\tan^{-1}\left(\frac{1}{\sqrt{C}}\right) \\ &+\frac{\sin\emptyset\sin 2\emptyset}{2\pi B}AD\left[\tan^{-1}\left(\frac{A\cos\emptyset}{D}\right) + \tan^{-1}\left(\frac{B - A\cos\emptyset}{D}\right)\right] \end{aligned} \tag{4-52}$$

$$+\frac{\cos\emptyset}{\pi B}\int_0^a \sqrt{1+\xi^2\sin\emptyset}\left[\tan^{-1}\left(\frac{\xi\cos\emptyset}{\sqrt{1+\xi^2\sin^2\emptyset}}\right)+\tan^{-1}\left(\frac{A-\xi\cos\emptyset}{\sqrt{1+\xi^2\sin^2\emptyset}}\right)\right]d\xi$$

where: $A=\frac{a}{c}, B=\frac{b}{c}, C=A^2+B^2-2AB\cos\emptyset, D=(1+A^2\sin^2\emptyset)^{1/2}$.

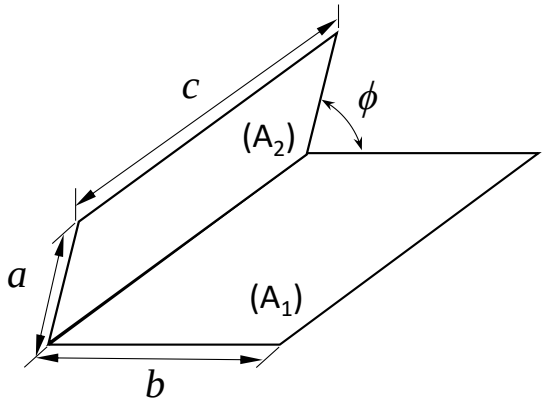

Figure 4-14 Schematic of two rectangles with one common edge and included angle of ϕ

The equation is applicable for the range of $0° < \emptyset < 180°$.

For two finite rectangles of the same length having one common edge and at an angle of 90° to each other as shown in Figure 4-15, the view factor is reported by [79,80] in the Eq. (4-53).

$$F_{1-2}=\frac{1}{W\pi}\left(W\,tan^{-1}\frac{1}{W}+H\,tan^{-1}\frac{1}{H}-\sqrt{H^2+W^2}\,tan^{-1}\sqrt{\frac{1}{H^2+W^2}}\right.$$
$$\left.+\frac{1}{4}\ln\left\{\frac{(1+W^2)(1+H^2)}{1+W^2+H^2}\left[\frac{W^2(1+W^2+H^2)}{(1+W^2)(W^2+H^2)}\right]^{W^2}\left[\frac{H^2(1+H^2+W^2)}{(1+H^2)(H^2+W^2)}\right]^{H^2}\right\}\right) \quad (4\text{-}53)$$

where $H=h/l, W=w/l$.

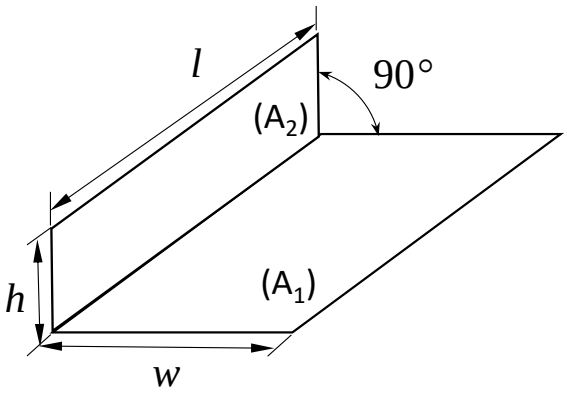

Figure 4-15 A schematic of two rectangles having the same length of one common edge at angle of 90° to each other

A general equation to determine the view factor of radiation between two rectangles in a perpendicular plane as shown in Figure 4-16 is reported by [81] in Eq.(4-54) and was also studied by Gross *et al.* [82], Boeke and Wall [83], and Chkhovskii [84] .

$$F_{1-2} = \frac{1}{(x_2 - x_1)(y_2 - y_1)} \sum_{l=1}^{2} \sum_{k=1}^{2} \sum_{j=1}^{2} \sum_{i=1}^{2} \left[(-1)^{(i+j+k+l)} G(x_i, y_j, \eta_k, \xi_l) \right] \tag{4-54}$$

$$G = \frac{1}{2\pi} \left\{ \begin{array}{c} (y-\eta)(x^2+\xi^2)^{\frac{1}{2}} \tan^{-1}(K) \\ -\frac{1}{4}\left[(x^2+\xi^2)\ln(1+K^2) - (y-\eta)^2 \ln\left(1+\frac{1}{K^2}\right) \right] \end{array} \right\} \tag{4-55}$$

where:

$$K \equiv (y-\eta)/(x^2+\xi^2)^{1/2} \tag{4-56}$$

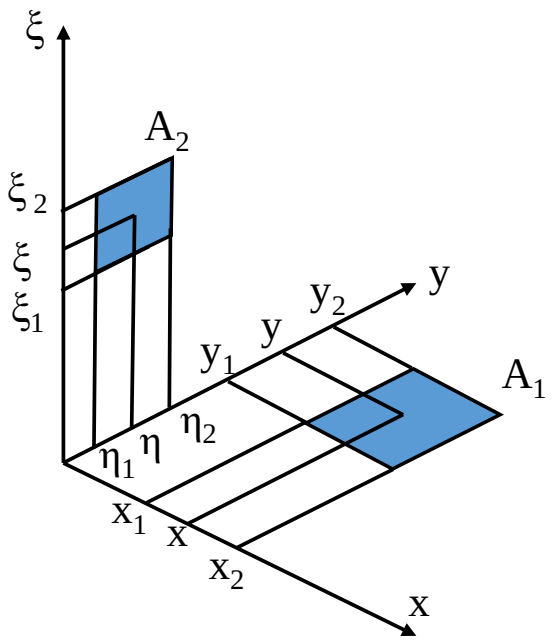

Figure 4-16 A schematic of the geometry of two rectangles in a perpendicular plane

The view factor of radiation between two rectangles in parallel planes illustrated in Figure 4-17 was reported by Ehlert and Smith [81] and was also studied by Gross *et al.* [82], Byrd [85], Boeke and Wall [83], and Chkhovskii [84] in a general equation based on the view factor algebra and integration of analytical expressions as shown in Eq.(4-57):

$$F_{1-2} = \frac{1}{(x_2 - x_1)(y_2 - y_1)} \sum_{l=1}^{2} \sum_{k=1}^{2} \sum_{j=1}^{2} \sum_{i=1}^{2} (-1)^{(i+j+k+l)}\, G(x_i, y_j, \eta_k, \xi_l) \tag{4-57}$$

$$G = \frac{1}{2\pi} \begin{pmatrix} (y-\eta)[(x-\xi)^2 + z^2]^{1/2} \tan^{-1}\left\{\dfrac{y-\eta}{[(x-\xi)^2 + z^2]^{1/2}}\right\} \\ +(x-\xi)[(y-\eta)^2 + z^2]^{1/2} \tan^{-1}\left\{\dfrac{x-\xi}{[(y-\eta)^2 + z^2]^{1/2}}\right\} \\ -\dfrac{z^2}{2} \ln[(x-\xi)^2 + (y-\eta)^2 + z^2] \end{pmatrix} \tag{4-58}$$

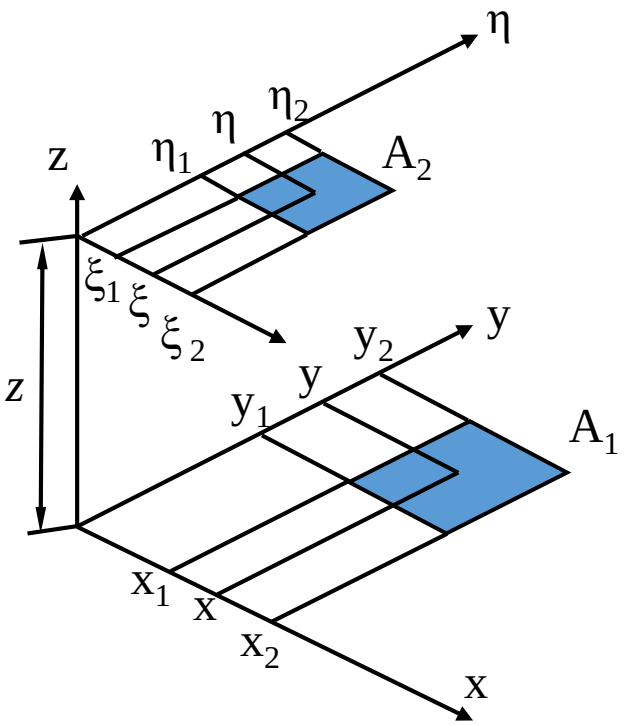

Figure 4-17 A schematic of the geometry of two rectangles in a parallel plane

The view factor of radiation from a rectangle to another rectangle on a plane intersecting the plane containing the first rectangle presented in Figure 4-18 was reported by [82] in Eq. (4-59) and was studied also by Krishnaprakas [86] and Yuen [87]. And it should be mentioned that this equation is not valid for rectangles having a common edge [78].

$$F_{1-2} = \frac{1}{A_1}\sum_{i=1}^{2}\sum_{j=1}^{2}\sum_{k=1}^{2}\sum_{l=1}^{2}\left[(-1)^{(i+j+k+l)}\, G\left(x_i, y_j, \eta_k, \xi_l\right)\right] \qquad (4\text{-}59)$$

where:

$$G = -\frac{(\eta - y)\sin^2\alpha}{2\pi}\int_{\xi}\left(\frac{(x-\xi\cos\alpha)\cos\alpha - \xi\sin^2\alpha}{(x^2 - 2x\xi\cos\alpha + \xi^2)^{1/2}\sin^2\alpha}\tan^{-1}\left[\frac{\eta - y}{(x^2 - 2x\xi\cos\alpha + \xi^2)^{1/2}}\right]\right.$$
$$+\frac{\cos\alpha}{(\eta - y)\sin^2\alpha}\left\{[\xi^2\sin^2\alpha + (\eta - y)^2]^{\frac{1}{2}}\tan^{-1}\frac{x - \xi\cos\alpha}{[\xi^2\sin^2\alpha + (\eta - y)^2]^{\frac{1}{2}}}\right. \quad (4\text{-}60)$$
$$\left.\left. - \xi\sin\alpha\tan^{-1}\left(\frac{x - \xi\cos\alpha}{\sin\alpha}\right)\right\}\right.$$
$$\left.+\frac{\xi}{2(\eta - y)}\ln\left[\frac{x^2 - 2x\xi\cos\alpha + \xi^2 + (\eta - y)^2}{x^2 - 2x\xi\cos\alpha + \xi^2}\right]\right)d\xi$$

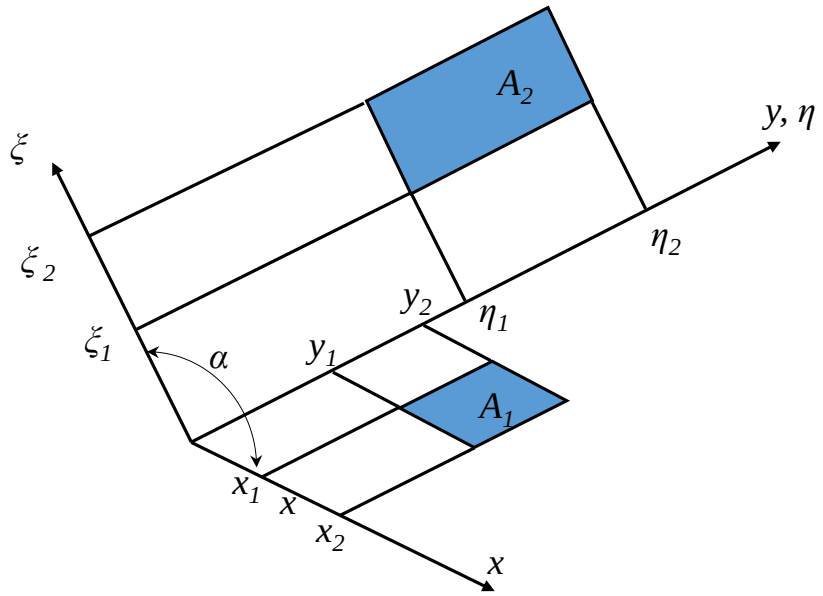

Figure 4-18 A schematic of the geometry of two rectangles in intersecting planes

The view factor between two cylinders of the same diameter seen in Figure 4-19 can be calculated from the following [88,89]:

$$F_{12} = F_{21} = \frac{1}{\pi}\left(\sqrt{X^2 - 1} + \sin^{-1}\frac{1}{X} - X\right) \quad (4\text{-}61)$$

where $X = 1 + s/2r$

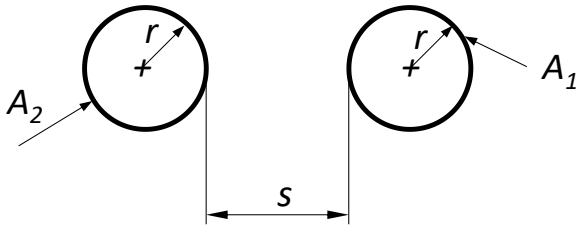

Figure 4-19 A schematic of geometry of the view factor between two infinitely long cylinders

The view factor between a cylinder and a strip as shown in Figure 4-20 can be calculated from [79,90]:

$$F_{12} = \frac{1}{2\pi}(\tan^{-1} B_1 - \tan^{-1} B_2) \tag{4-62}$$

$$B_1 = \frac{b_1}{a}, B_2 = \frac{b_2}{a}$$

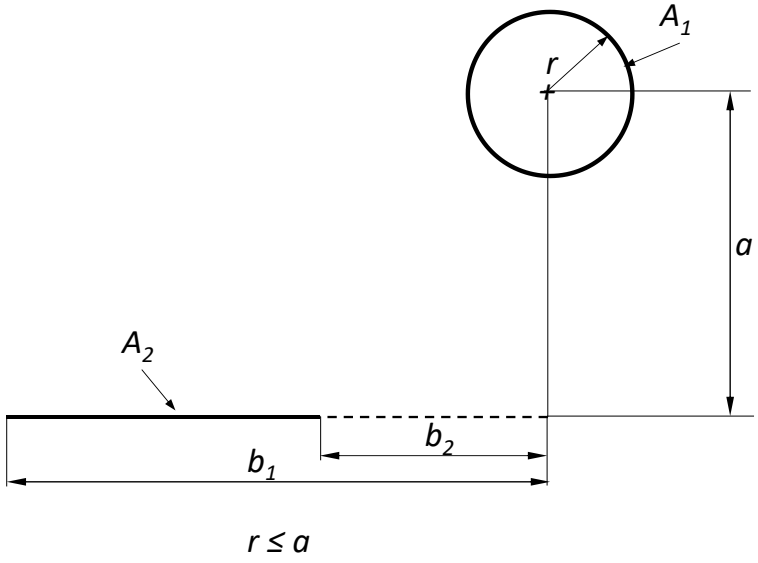

Figure 4-20 Schematic of the geometry of the view factor between infinitely long cylinder and a strip

4.2.6 Net heat radiation in three-surface enclosures

Radiative surfaces in heat transfer applications are normally not black bodies where they reflect the radiation in addition to the emitted heat. The radiosity of a surface which was defined previously as the total radiation leaving a surface can be expressed for a grey, opaque body as follows:

$$J_i = (Radiation\ emitted\ surface\ i) + (Radiation\ reflected\ \ surface\ i) \tag{4-63}$$

$$J_i = \varepsilon_i E_{bi} + \rho_i G_i \tag{4-64}$$

Since the surface i is considered as a grey body i.e.: $\varepsilon_i = \alpha_i$ and for an opaque surface $\rho_i + \alpha_i = 1$

Hence:

$$J_i = \varepsilon_i E_{bi} + (1 - \varepsilon_i) G_i \tag{4-65}$$

In radiation heat transfer, the opaque body surface receives radiation from other surfaces and absorbs part of it and reflects the rest of the radiation. In addition it loses heat by emitting radiation. The body either gains or loses energy depending on the energy balance between the incident radiation and the total radiation leaving the surface, hence:

$$Q_i = \begin{pmatrix} Radiation\ leaving \\ entire\ surface\ i \end{pmatrix} - \begin{pmatrix} Radiation\ incident \\ on\ entire\ surface\ i \end{pmatrix} \tag{4-66}$$

$$Q_i = A_i (J_i - G_i) \tag{4-67}$$

Solving for G_i from Eq.(4-65) and substituting into Eq.(4-67) yields:

$$Q_i = A_i \left(J_i - \frac{J_i - \varepsilon_i E_{bi}}{1 - \varepsilon_i} \right) = \frac{A_i \varepsilon_i}{1 - \varepsilon_i} (E_{bi} - J_i) \ \text{(W)} \tag{4-68}$$

By applying the electrical analogy on Eq.(4-68), it can be found that

$$Q_i = \frac{E_{bi} - J_i}{R_i} \ \text{(W)} \tag{4-69}$$

$$R_i = \frac{1 - \varepsilon_i}{A_i \varepsilon_i} \tag{4-70}$$

where R_i is the surface resistance to radiation, the quantity $E_{bi} - J_i$ represents the potential difference, and the net radiation Q_i corresponds to the current in Ohm's law analogy as presented in Figure 4-21.

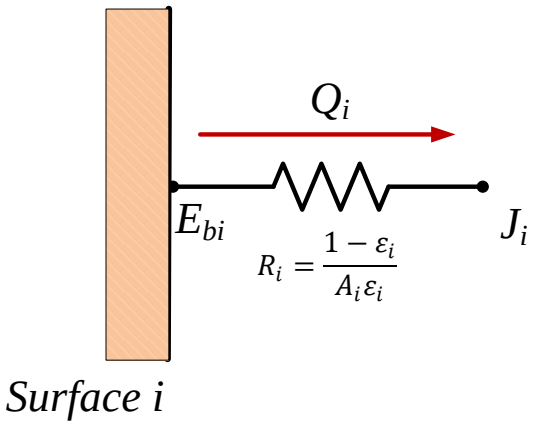

Figure 4-21 Electrical analogy of surface resistance to radiation

It can be seen from Eq.(4-69) that the surface gains energy when $E_i < j_i$ while the heat transfer is from the surface when $E_i > J_i$.

If surface i is insulated and at a steady state and the effect of the natural convection is neglected, then the radiation leaving the surface will be equal to the incident radiation on the surface:

$$Q_i = 0 \Rightarrow E_i = J_i = \sigma T^4 \ \ (\mathrm{W/m^2}) \tag{4-71}$$

The net heat transfer by radiation between two diffuse grey opaque bodies which have uniform surface temperature can be analysed as follows:

$$Q_{ij} = \begin{pmatrix} Radiation\ leaving \\ the\ entire\ surface\ i \\ and\ striking\ surface\ j \end{pmatrix} - \begin{pmatrix} Radiation\ leaving \\ the\ entire\ surface\ j \\ and\ striking\ surface\ i \end{pmatrix} \tag{4-72}$$

$$Q_{ij} = A_i F_{ij} J_i - A_j F_{ji} J_j \tag{4-73}$$

Applying the reciprocity rule yields:

$$Q_{ij} = A_i F_{ij}(J_i - J_j) = \frac{J_i - J_j}{R_{ij}} \ (\mathrm{W}) \tag{4-74}$$

where R_{ij} corresponds to the space resistance between the two surfaces where:

$$R_{ij} = \frac{1}{A_i F_{ij}} \tag{4-75}$$

The quantity $J_i - J_j$ corresponds to the potential difference between the two surfaces and Q_{ij} is the current in the electrical analogy.

The net radiation transfer in an N surface enclosure can be obtained from the energy conservation principle where the net heat transfer from surface i is equal to the net radiation between surface i and each surface in the N surface enclosure. Figure 4-22 presents the electrical analogy of the radiation heat transfer between surface i and the N surface enclosure.

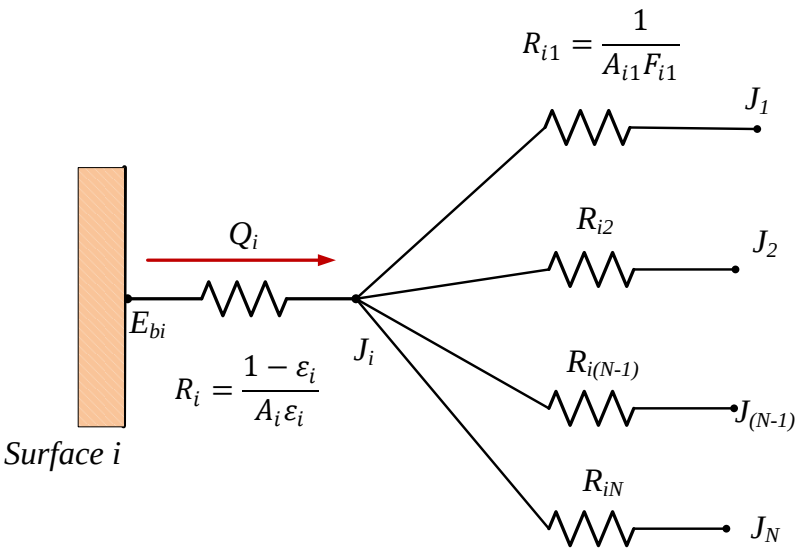

Figure 4-22 Electrical analogy of net radiation from surface I in an N surface enclosure

The net radiation between surface i and N surfaces can be calculated from the following:

$$Q_i = \sum_{j=1}^{N} Q_{ij} = \sum_{j=1}^{N} A_i F_{ij}(J_i - J_j) = \sum_{j=1}^{N} \frac{(J_i - J_j)}{R_{ij}} \text{ (W)} \tag{4-76}$$

or:

$$\frac{E_{bi} - J_i}{R_i} = \sum_{j=1}^{N} \frac{(J_i - J_j)}{R_{ij}} \text{ (W)} \tag{4-77}$$

For radiation heat transfer in a two surface enclosure, the radiation network model is presented in Figure 4-23.

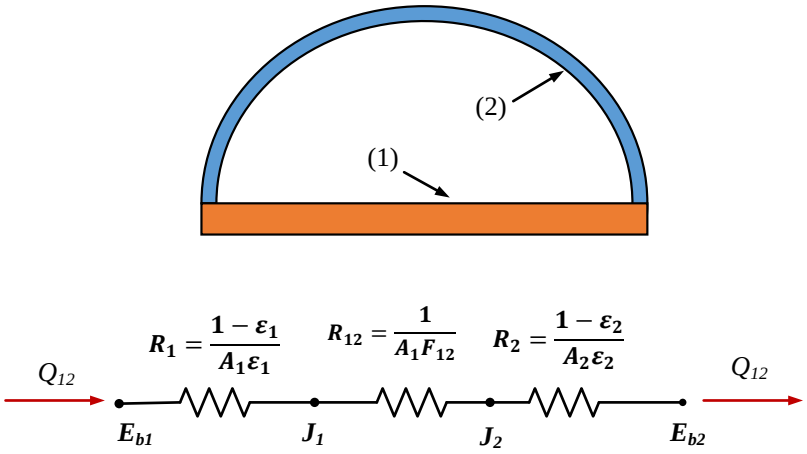

Figure 4-23 Schematic of radiation network modelling in two surface enclosure

The net heat transfer by radiation between two diffuse grey opaque surfaces can be obtained as follows:

$$Q_{12} = \frac{E_{b1} - E_{b2}}{R_1 + R_{12} + R_2} \text{ (W)} \tag{4-78}$$

or

$$Q_{12} = \frac{\sigma(T_1^4 - T_2^4)}{\frac{1-\varepsilon_1}{A_1\varepsilon_1} + \frac{1}{A_1F_{12}} + \frac{1-\varepsilon_2}{A_2\varepsilon_2}} \text{ (W)} \tag{4-79}$$

4.3 Boiling heat transfer

4.3.1 Overview of boiling

Boiling heat transfer occurs in liquids when the temperature of the liquid is higher than the saturation temperature. Boiling is two-phase heat transfer which depends on the latent heat of vaporisation of the liquid and the surface tension of the liquid-vapour interface. Boiling occurs at the solid-liquid interface when the liquid is in contact with a surface with a temperature higher than the saturation temperature of the liquid. The boiling curve of water at a pressure of 1 atm is shown in Figure 4-24. The boiling regimes shown are natural convection boiling, nucleate boiling, transition boiling, and film boiling.

Free convection boiling (natural convection boiling) takes a place when $\Delta T_{excess} = (T_{surface} - T_{saturation}) \leq 5\ ^{\circ}C$ where the surface temperature is slightly higher than the saturation temperature of the liquid.

The nucleate boiling regime occurs when the temperature difference between the heating surface and the liquid is in the range of $5\ °C\ \leq \Delta T_{excess} \leq 30°C$. It should be mentioned that nucleate pool boiling is the boiling regime occurring in heat pipes.

Transition boiling occurs when $\Delta T_{e,C}\ \leq \Delta T_e\ \leq \Delta T_{e,D}$ on Figure 4-24 where for water at 1 atm $\Delta T_{e,D} = 120\ °C$. It is also known as non-stable film boiling where the bubble formation is very quick where a film of vapour starts to exist between the liquid and the heating solid surface.

Film boiling exists when $\Delta T_{e,D}\ \leq \Delta T_e$ where the point D is referred to *Leidenfrost* point where the surface is covered with a vapour film at this point where the heat transfer in this regime is by conduction and radiation through the vapor.

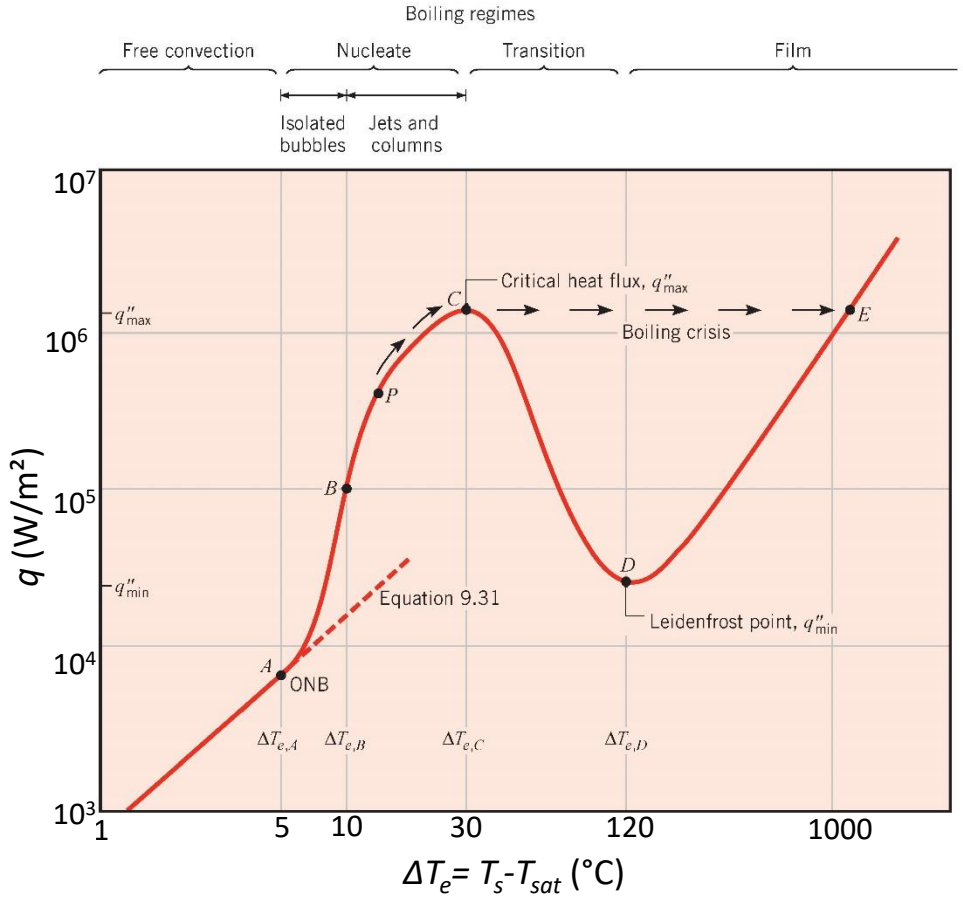

Figure 4-24 Boiling curve of water at saturation pressure of 1 atm: surface heat flux q as a function of excess temperature ΔT_e [75]

The rate of nucleate boiling heat transfer can be calculated through the following equation:

$$Q_{boiling} = h_b A_s (T_s - T_v) \tag{4-80}$$

where $Q_{boiling}$ is the heat transfer rate (W), h_b is the boiling heat transfer coefficient $(\mathrm{W/m^2.K})$, A_s is the surface area (m²), T_s and T_v are the surface and vapour temperature, respectively (K).

The electrical analogy can be applied to boiling heat transfer Eq.(4-80) as illustrated in Figure 4-25 and it yields [91]:

$$Q_{boiling} = \frac{T_s - T_v}{R_{boiling}} \tag{4-81}$$

where the heat transfer rate represents the current in Ohm's law, the temperature difference represents the potential, and the thermal resistance of boiling represents the electrical resistance where:

$$R_{boiling} = \frac{1}{h_b A_s} \tag{4-82}$$

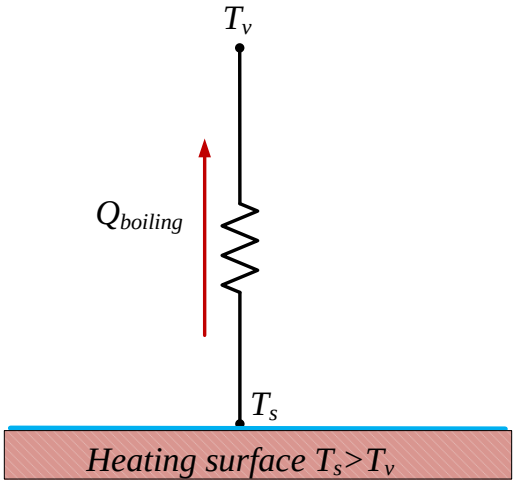

Figure 4-25 Illustration of the electrical analogy of nucleate boiling heat transfer

4.3.2 Common correlations of boiling in heat pipes

The boiling regime in thermosyphon heat pipes can be divided into two kinds: nucleate pool boiling where the liquid fills the evaporator section, and the falling film boiling where the heat is transferred from the wall at the evaporator section to the film falling back to the evaporator as illustrated in Figure 4-26.

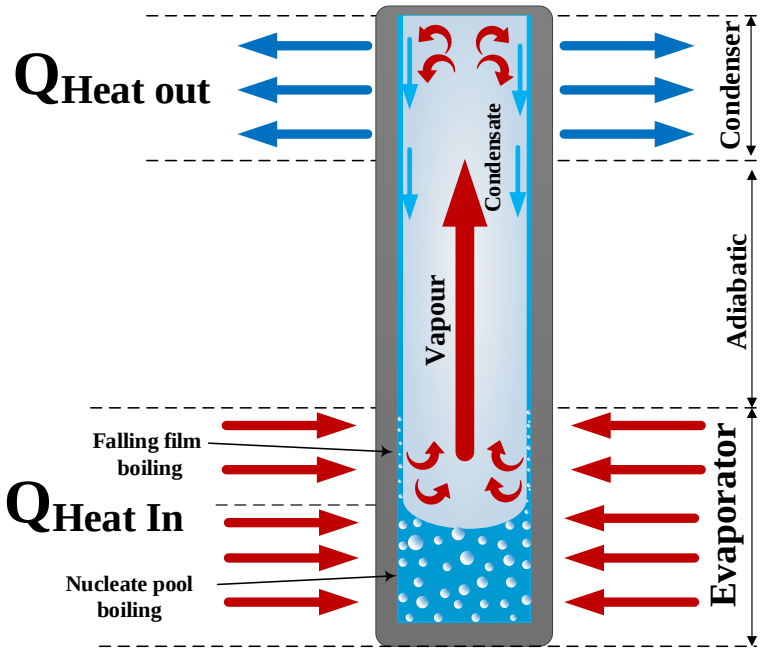

Figure 4-26 Illustration of boiling regimes in a heat pipe

The common correlations for boiling heat transfer in heat pipes are listed in Table 4-1.

Table 4-1 Common Nucleate pool boiling correlations used in heat pipes

Author	Equation	Eq.	Conditions
Rohsenow [92]	$q_{ei} = \mu_l . h_{fg} \left[\frac{g.(\rho_l - \rho_v)}{\sigma}\right]^{1/2} . \left[\frac{C_p.(T_{ei} - T_v)}{(C_{sf}.h_{fg}.Pr_l^n)}\right]^3$ where: $q_{ei} = h_{ei}.(T_{ei} - T_v)$	(4-83)	n=1 for water and n=1.7 for other liquids C_{sf} is a factor depends on the surface roughness and the working fluid
Cooper [93]	$h_{ei} = 55 p_r^{0.12-0.4343 \ln R_p} (-\log_{10} p_r)^{-0.55} M^{-0.5} q_{ei}^{0.67}$	(4-84)	$p_r = \frac{P}{P_{crit}}$
Gorenflo [94]	$h_{ei} = h_0 F_{PF} (q_{ei}/q_0)^n (R_p/R_{p0})^{0.133}$	(4-85)	$0.005 \leq p_r \leq 0.95$ $R_{p0} = 0.4\ \mu m$ R_p the mean surface roughness

			and $q_0 = 20000\ \mathrm{W/m^2}$
	$F_{PF} = 1.2p_r^{0.27} + 2.5p_r + \frac{p_r}{1-p_r}$	(4-86)	All fluids except water and helium
	$n = 0.9 - 0.3p_r^{0.3}$		
Gorenflo[94]	$F_{PF} = 1.73p_r^{0.27} + \left(6.1 + \frac{0.68}{1-p_r}\right)p_r^2$	(4-87)	For water and helium only where these are for water $P_{critical}$=220.6 (bar) M=18.02 h_0=5600 W/m².°C
	$n = 0.9 - 0.3p_r^{0.15}$		
McNelly[95]	$h_{ei} = 0.225\left(\frac{qC_p}{h_{fg}}\right)^{0.69}\left(\frac{Pk_l}{\sigma}\right)^{0.31}\left(\frac{\rho_l}{\rho_v} - 1\right)^{0.31}$	(4-88)	
Forster *And* *Zuber* [96]	$q_{ei} = 0.00122\left(\frac{k_l^{0.79}\,C_p^{0.45}\rho_l^{0.49}}{\sigma^{0.5}\mu_l^{0.29}h_{fg}^{0.24}\rho_v^{0.24}}\right)\Delta T_v^{1.24}\Delta p_v^{0.75}$	(4-89)	Δp_v is the difference between the vapor pressures at the heating surface and liquid temperatures
	Where:$\Delta T_v = (T_{ei} - T_v), \Delta p_v = P_{ei} - P_v$ and $q_{ei} = h_{ei}.\Delta T_v$		
Mostinski [97]	$h_{ei} = 3.7 \times 10^{-5}P_{crit}^{0.69}q_{ei}^{0.7}\left[1.8\left(\frac{P}{P_{crit}}\right)^{0.17} + 4\left(\frac{P}{P_{crit}}\right)^{1.2} + 10\left(\frac{P}{P_{crit}}\right)^{10}\right]$	(4-90)	
Stephan	$Nu = \frac{h_{ei}D_d}{k_l} = 0.24 \times 10^7 X_1^{0.67}X_4^{-1.58}X_3^{1.62}X_8^{5.22}$	(4-91)	$10^{-4} < \frac{P}{P_{crit}} < 0.88$ $\theta = 45°$

and Abdelsalam [98]	$X_1 = \left(\frac{q_{ei}D_d}{k_l T_v}\right),\ X_3 = \left(\frac{C_p T_v D_d^2}{\alpha^2}\right), X_4 = \left(\frac{h_{fg}D_d^2}{\alpha^2}\right), X_8 = \left(\frac{\rho_l - \rho_v}{\rho_l}\right)$ $D_d = 0.0208 \times \theta \left[\frac{\sigma}{g(\rho_l - \rho_v)}\right]^{\frac{1}{2}},\ \alpha = \frac{k_l}{\rho_l C_p}$		
Labuntsov [99]	$h_{ei} = 0.075\left[1 + 10\left(\frac{\rho_v}{\rho_l - \rho_v}\right)^{0.67}\right]\left(\frac{\rho_l {k_l}^2}{\mu_l \sigma T_{sat}}\right)^{0.33} {q"_{nb}}^{0.67}$	(4-92)	
Imura et al [100]	$h_{ei} = 0.32\left(\frac{{\rho_l}^{0.65}{k_l}^{0.3}{C_{p,l}}^{0.7}g^{0.2}}{{\rho_l}^{0.25}h_{fg}^{0.4}{\mu_l}^{0.1}}\right)\left(\frac{P_v}{P_{atm}}\right)^{0.3} {q"_{nb}}^{0.4}$	(4-93)	
Shiraishi et al. [101]	$h_{ei} = 0.32\left(\frac{{\rho_l}^{0.65}{k_l}^{0.3}{C_{p,l}}^{0.7}g^{0.2}}{{\rho_l}^{0.25}h_{fg}^{0.4}{\mu_l}^{0.1}}\right)\left(\frac{P_v}{P_{atm}}\right)^{0.23} {q"_{nb}}^{0.4}$	(4-94)	
Kiatsiriroat et al. [102]	$h_{ei} = C\left(\frac{\mu i_{lv}}{L_b \Delta T_{sat}}\right)\left(\frac{c_p \Delta T_{sat}}{i_{lv} Pr}\right)^n$ Where, $L_b = \left[\frac{\sigma}{g(\rho_l - \rho_v)}\right]^{1/2}$ $\begin{cases} C = 18.688\ for\ water \\ C = 17.625\ for\ ethanol \\ C = 20.565\ for\ triethylene\ glycol\ (TEG) \end{cases}$ $\begin{cases} n = 0.3572\ for\ water \\ n = 0.3300\ for\ ethanol \\ n = 0.3662\ for\ triethylene\ glycol\ (TEG) \end{cases}$	(4-95)	
Jakob and Hawkins [103]	$h_{ei} = 1042(\Delta T_x)^{\frac{1}{3}}$ $\rightarrow h_{ei,(range)} = [0 - 2060]\ (\mathrm{W/m^2.°C})$	(4-96)	$0 < \Delta T_{(range)} < 7.76$ $\frac{Q_{ei}}{A} < 16\ \left(\frac{\mathrm{kW}}{\mathrm{m^2}}\right)$ Horizontal Surface

	$h_{ei} = 5.56(\Delta T_x)^3$ $h_{ei,(range)} = [2180 - 16600]\ (\mathrm{W/m^2.°C})$	(4-97)	$16 < \frac{Q_{ei}}{A} < 240\ \left(\frac{\mathrm{kW}}{\mathrm{m^2}}\right)$ $7.32 < \Delta T_{(range)} < 14.4$ Horizontal Surface
	$h_{ei} = 537(\Delta T_x)^{\frac{1}{7}}$ $h_{ei(range)} = [0 - 670](\mathrm{W/m^2.°C})$	(4-98)	$0 < \Delta T_{(range)} < 4.51$ $\frac{Q_{ei}}{A} < 3\ \left(\frac{\mathrm{kW}}{\mathrm{m^2}}\right)$ Vertical Surface
	$h_{ei} = 7.96(\Delta T_x)^3$ $h_{ei,(range)} = [680 - 6680](\mathrm{W/m^2.°C})$ Where: $\Delta T_x = (T_{ei} - T_v)$	(4-99)	$4.41 < \Delta T_{(range)} < 9.43$ $3 < \frac{Q_{ei}}{A} < 63\ \left(\frac{\mathrm{kW}}{\mathrm{m^2}}\right)$ Vertical Surface

The subscript ei refers to the inner wall surface of the evaporator, and the subscript v refers to the vapor of the working fluid in the heat pipe.

The correlations used to calculate the heat transfer coefficient in falling film boiling regime are listed in Table 4-2.

Table 4-2 Correlations of falling film boiling in heat pipes

Author	Correlation	Eq.
Kopchikov [104]	$h^* = 0.1\left(\frac{k_l i_{lv}\rho_v}{\sigma T_{sat}} q_{fb}^{"}\right)\frac{1}{k_l}\left(\frac{{\mu_l}^2}{{\rho_l}^2 g}\right)^{1/3}$	(4-100)
El-Genk and Saber [105]	$h^* = \left(\frac{4}{3}\right)^{1/3} {Re_f}^{-1/3}\left({h_x}^3 + {h_{f,boiling}}^3\right)^{1/3}$	(4-101)
	$h_x = \left(\frac{4}{3}\right)^{1/3} {Re_f}^{-1/3}\left(\frac{k_l}{L_f}\right)$ $h_{f,boiling} = 1.155\times10^{-3}\left(\frac{k_l}{L_b}\right) {N_\mu}^{0.33} {Pr_l}^{0.35}\left(\frac{q^{"}_{fnb} L_b \rho_l}{\rho_v i_{lv}\mu_l}\right)^{0.7}\left(\frac{PL_b}{\sigma}\right)^{0.7}$ where, $Re_{fb} = \frac{4Q}{h_{fg}\mu_l \pi d_{ei}}$ $L_f = \left(\frac{{\mu_l}^2}{g\rho_l(\rho_l-\rho_v)}\right)^{\frac{1}{3}}$: Liquid film thickness scale $L_b = [\sigma/g(\rho_l-\rho_v)]^{1/2}$: Bubble length scale $N_\mu = \frac{\mu_l}{(\sigma\rho_l L_b)^{0.5}}$: Viscosity number	
Gogonin [106]	$h^* = 0.01\left(\frac{{\mu_l}^2}{{\rho_l}^2 g}\right)^{1/3} {L_b}^{-1} {Re_{fb}}^{0.8} {Pr_l}^{1/3} b {K_t}^{0.4} \overline{R_z}^{0.2}\left(\frac{k_l c_{p,l}\rho_l}{k_w c_{p,w}\rho_w}\right)^{-0.2}$	(4-102)
	$b = \left[1 + 10\left(\frac{\rho_v}{\rho_l-\rho_v}\right)^{2/3}\right]$ $K_t = \frac{(i_{lv}\rho_v)^2 L_b}{c_{p,l} T_{sat}\rho_l \sigma}$ $\overline{R_z} = R_z/L_f$	
Chun and Seban [107]	$h^* = 0.606\left(Re_f/4\right)^{-1/3}$	(4-103)
	$Re_f \le 2.44 Ka^{-1/11}$ $0.3\times10^5 \le q_{fb}^{"} \le 0.7\times10^5\ W.m^{-2}$	

4.4 Condensation heat transfer

4.4.1 Overview of condensation

Condensation heat transfer occurs when the vapour is in contact with a solid or a liquid surface with a temperature lower than the saturation temperature of the vapour.

Nusselt in 1916 [108] studied the heat transfer by condensation of vapour on a vertical plate where he developed his condensation theory based on the condensate film thickness. The condensation film thickness increases in the direction of the flow as a result of the continued condensation at the liquid-vapour interface. The latent heat released from the vapour is transferred through the liquid film to the vertical plate.

Heat transfer by condensation is expressed as follows:

$$Q_{condensation} = h_{condensation}.A_s(T_{sat} - T_s) \tag{4-104}$$

where the subscript s stands for the surface, and sat is for the saturated vapour.

Applying the electrical analogy on (4-104) yields [91]:

$$R_{condensation} = \frac{1}{h_{condensation}A_s} \tag{4-105}$$

The electrical analogy of the heat transfer by condensation is illustrated in Figure 4-27 where the heat transfer coefficient of condensation can be obtained from Table 4-4 depending on the geometry.

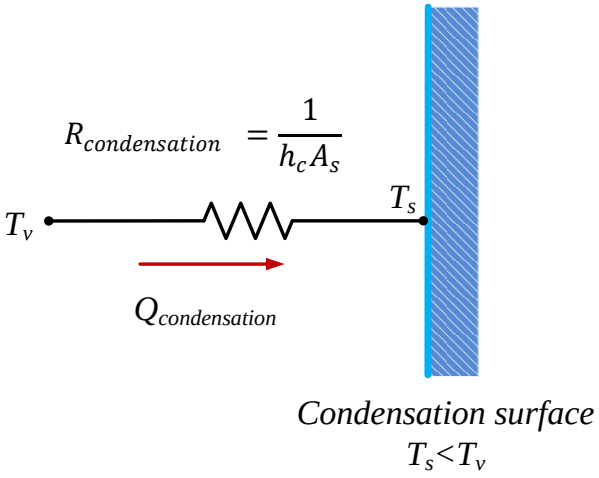

Figure 4-27 Schematic of condensation heat transfer electrical analogy

4.4.2 Common correlations of condensation in heat pipes

The common correlations of heat transfer coefficient by condensation are listed in Table 4-3.

Table 4-3 List of common correlations of the heat transfer coefficient in heat transfer by condensation

Author	Equation	Eq.	Conditions	State
Nusselt [108,109]	$h_{ci} = 0.943\left[\frac{\rho_l(\rho_l-\rho_v)gh_{fg}^{*}k_f^3}{l_c\mu_l(T_v-T_{ci})}\right]^{\frac{1}{4}}$	(4-106)	Properties in should be evaluated at the film temperature $T_f = \frac{(T_v+T_{ci})}{2}$ $0 < Re < 30$	**Laminar vertical**
	Rohsenow modifications $h_{fg}^{*} = h_{fg} + 0.68C_p(T_v - T_{ci})$	(4-107)	Equations may be used for vertical plates and cylinders and fluids with $Pr > 0.5$ & $\frac{C_pT}{h_{fg}} \leq 1$	
Nusselt [108]	$Re = \frac{4\dot{Q_{ci}}}{P\mu_l h_{fg}^{*}} = \frac{4A_s h_{ci}(T_v-T_{ci})}{P\mu_l h_{fg}^{*}}$	(4-108)	P: wetted perimeter $0 < Re < 30$	**Laminar-vertical**
	$h_{ci} \cong 1.47k_l Re^{-\left(\frac{1}{3}\right)}\left(\frac{g\rho_l^2}{\mu_l^2}\right)^{\frac{1}{3}}$	(4-109)	$0 < Re < 30$ $\rho_v \ll \rho_l$	
Kutateladze [110]	$h_{ci,wavy} = \frac{Re\ k_l}{1.08\ Re^{1.22} - 5.2}\left(\frac{g\rho_l^2}{\mu_l^2}\right)^{\frac{1}{3}}$	(4-110)	$30 < Re < 1800$ $\rho_v \ll \rho_l$	
	$Re_{ver,wavy} = [4.81 + \frac{3.7\ l_c\ k_l\ (T_v - T_{ci})}{\mu_l h_{fg}^{*}}\left(\frac{g\rho_l^2}{\mu_l^2}\right)^{\frac{1}{3}}]^{0.82}$	(4-111)	$T_f = \frac{(T_v+T_{ei})}{2}$ $h_{fg}^{*} = h_{fg} + 0.68C_p(T_v - T_{ei})$	
Nusselt [108]	$h_{ci} = 0.943\left[\frac{\rho_l(\rho_l-\rho_v)gh_{fg}^{*}k_l^3\ \cos\theta}{l_c\mu_l(T_v-T_{ci})}\right]^{\frac{1}{4}}$	(4-112)	for surface inclined by an angle Θ from the vertical	**Inclined**

Nusselt [108]	$h_{ci} = 0.725\left[\frac{\rho_l(\rho_l-\rho_v)gh_{fg}^{*}k_l^3}{D\mu_l(T_v-T_{ei})}\right]^{\frac{1}{4}}$	(4-113)		**Horizontal**
Chen [108,111]	$h_{ci} = 0.728[1+0.2(N-1)Ja]\left[\frac{\rho_l(\rho_l-\rho_v)gh_{fg}^{*}k_l^3}{ND\mu_l(T_v-T_{ei})}\right]^{\frac{1}{4}}$	(4-114)	The physical properties of the liquid film should be evaluated at an effective film temperature T_f $T_f = T_v + 0.25(T_v - T_{ci})$	**Horizontal - N rows**
	Provided that: $[(N-1)Ja] < 2$			
	Where $Ja = C_p(T_v - T_{ei})/h_{fg}$	(4-115)		
Nusselt [108]	$h_{ci} = 0.725\left[\frac{\rho_l(\rho_l-\rho_v)gh_{fg}^{*}k_l^3}{ND\mu_l(T_v-T_{ci})}\right]^{\frac{1}{4}}$	(4-116)		**Horizontal tube bank with N rows**
Jouhara and Robinson [112]	$h_{ci} = 0.85Re_f^{0.1}\exp\left(0.000067\frac{\rho_l}{\rho_v} - 0.14\right) \times 0.943\left[\frac{\rho_l(\rho_l-\rho_v)gh_{fg}^{*}k_l^3}{l_c\mu_l(T_v-T_{ci})}\right]^{\frac{1}{4}}$	(4-117)		**Wavy laminar and turbulent**
	where $Re_f = \frac{4\dot{Q}_{ci}}{\pi D\mu_l h_{fg}^{*}}$	(4-118)		
Hashimoto and Kaminaga [113]	$h_{ci} = 0.85{Re_f}^{0.1}exp\left(-6.7\times10^{-5}\frac{\rho_l}{\rho_v} - 0.6\right)h_{Nusselt}$			(4-119)
Rohsenow [114]	$h_{ci} = 1.51\left(\frac{P_v}{P_{crit}}\right)^{0.14} \times 0.943\left\{\frac{\rho_l(\rho_l-\rho_v)g{k_l}^3}{\mu_l L_c(T_v-T_{ci})}\left[h_{fg} + {}^3/_8\, c_{pl}(T_v-T_{ci})\right]\right\}^{1/4}$ where the fluid properties should be evaluated at a temperature: $T_f = T_{ci} + 0.31(T_{sat} - T_{ci})$			(4-120)

4.5 Natural convection heat transfer

The heat transfer by natural convection is determined through the derivation of the equation of motion of the natural convection flow in a laminar boundary layer.

$$u\frac{\partial u}{\partial x}+v\frac{\partial u}{\partial y}=\nu\frac{\partial^2 u}{\partial y^2}+g\beta(T-T_\infty) \tag{4-121}$$

where the left hand side of the equation represents the change of momentum of the fluid element. ν is the kinematic viscosity, g is the gravitational acceleration, and β is the coefficient of thermal expansion.

A non-dimensional number called Grashof number Gr_L results from non-dimensionalising the momentum equation, which is equal to:

$$\mathrm{Gr}_L=\frac{g\beta(T_s-T_\infty)L_c^3}{\nu^2} \tag{4-122}$$

where g is the gravitational acceleration (m/s²), and β is the coefficient of thermal expansion (1/K), T_S is the surface temperature (°C), T_∞ is the fluid temperature far from the surface (°C), L_c characteristic length of the geometry (m), ν is the kinematic viscosity m²/s.

Grashof number represents the ratio of the buoyancy force to the viscous force acting on the fluid.

Nusselt number Nu of the natural convection heat transfer can be presented in the following empirical correlation:

$$Nu=\frac{hL_c}{k}=C(\mathrm{Gr}_L\mathrm{Pr})^n=C\mathrm{Ra}_L^n \tag{4-123}$$

where Ra is Rayleigh number which represents the ratio of the buoyancy forces and the thermal and momentum diffusivities.

The heat transfer rate by natural convection can be obtained from:

$$Q_{convection}=hA_s(T_s-T_\infty)=\frac{(T_s-T_\infty)}{R_{convection}}\ (\mathrm{W}) \tag{4-124}$$

where $R_{convection}=hA_S\ (\frac{^\circ\mathrm{C}}{\mathrm{W}})$ is the thermal resistance of the heat transfer by natural convection in the electrical analogy.

Heat transfer by natural convection depends on the geometry of the surface which varies if it is flat or circular. It also depends on the inclination of the surface where the shape and the thickness of the thermal layer varies significantly.

Al-Arabi and Salman [115] presented a correlation for natural convection from inclined cylinders at constant heat flux:

Al-Arabi and Salman: [115]
$$\mathrm{Nu}_D = 0.6 - 0.488(\sin\theta)^{1.03}(\mathrm{GR}_D\mathrm{Pr})^{\frac{1}{4}+\frac{1}{12}(\sin\theta)^{1.75}} \quad (4\text{-}125)$$

The correlation is valid for the following: $\mathrm{Ra}_D = 10^{5.5} - 10^9$, $0° < \theta < 90°$ from vertical.

Oosthuizen [116] presented a correlation for inclined cylinders

Oosthuizen: [116]
$$\mathrm{Nu}_D = 0.42(\mathrm{Gr}_D\cos\varphi)^{1/4}\left[1+\left(\frac{1.31}{\bar{\bar{L}}^{\frac{1}{4}}}\right)^3\right]^{\frac{1}{2}} \quad (4\text{-}126)$$

Where $\bar{\bar{L}}$ is:

Oosthuizen: [116]
$$\bar{\bar{L}} = L/(D\ \tan\varphi), \quad 0 \le \varphi \le 90° \text{ from horizontal} \quad (4\text{-}127)$$

Rani et al. [117] developed an empirical correlation using a regression analysis method from the experimental data from the literature [118] and the results obtained from the correlation were compared with the experimental available in the literature in [116,118,119] and others.

Rani et al. [117]
$$\mathrm{Nu}_D = \left(0.54 + 0.39\left[\frac{\mathrm{PrGr}}{\left\{1+\left(\frac{0.559}{\mathrm{Pr}}\right)^{\frac{9}{16}}\right\}^{\frac{16}{9}}}\right]^{0.1685}\right)^2 \quad (4\text{-}128)$$

where the characteristic length is calculated from Eq.(4-129):

Characteristic length
$$L_c = \left[\frac{LD}{\left(\frac{L}{D}\right)\cos\varphi + \left(\frac{D}{L}\right)\sin\varphi}\right]^{1/2} \quad (4\text{-}129)$$

with φ the inclination angle from horizontal. The equation is applicable for the range of $0.68 \le \mathrm{Pr} \le 0.72$, and $1.4\times10^4 \le Gr \le 1.2\times10^{10}$.

Li and Tarasuk [120] developed a correlation for free convection around an inclined cylinder and compared his experimental data with the results from the correlations developed by Al-Arabi and Salman [115] , Morgan [121], and Oosthuizen [116] . The developed correlation exhibited good agreement with his experimental data and the other correlations in the literature.

$$\mathrm{Nu}_D = m(\varphi)\mathrm{Ra}_D^{n(\varphi)} \tag{4-130}$$

where

$$m(\varphi) = 0.5925 + 0.2278 \times 10^{-2} \times (\varphi) - 0.1436 \times 10^{-3} \times (\varphi)^2 + 0.1877 \times 10^{-5} \times (\varphi)^3 + 0.986 \times 10^{-8} \times (\varphi)^4 \tag{4-131}$$

$$n(\varphi) = 0.2295 + 0.1553 \times 10^{-2} \times (\varphi) - 0.7396 \times 10^{-4} \times (\varphi)^2 + 0.1157 \times 10^{-5} \times (\varphi)^3 - 0.5783 \times 10^{-8} \times (\varphi)^4 \tag{4-132}$$

The correlation was validated experimentally for the following conditions

Table 4-4 Conditions of the Eq.(4-130) of the average Nusselt number

Angle	m	n	Range of Ra_D	Error
0°	0.5925	0.2294	1.2×10^4 to 2.9×10^9	-6.4 to 6.3%
45°	0.5349	0.2313	1.1×10^4 to 3.3×10^9	-1.3 to 0.79%
60°	0.49	0.2313	1.2×10^4 to 2.5×10^9	-0.24 to 1.7%
75°	0.4375	0.2349	1.2×10^4 to 3.1×10^9	-4.6 to 2.9%
90°	0.3561	0.2339	1.4×10^4 to 3.1×10^9	-14.6 to 5.5%

Heo and Chung [122] derived correlations for natural convection heat transfer of inclined cylinders as presented in Eq. (4-133) and Eq.(4-134)

Laminar flow

$$\mathrm{Nu_D} = 0.3\mathrm{Ra}_D^{0.25}(1 + 0.7\cos\varphi) \quad Ra_D < 10^9 \tag{4-133}$$

Turbulent flow

$$\mathrm{Nu_D} = 0.13\mathrm{Ra}_D^{0.3}(1 + 0.6\cos\varphi) \quad Ra_D > 10^9 \tag{4-134}$$

Eq.(4-133) and Eq.(4-134) are applicable for: $3.7 \leq L/D \leq 25$, $1.69 \times 10^8 \leq \mathrm{Ra}_D \leq 5.07 \times 10^{10}$, and $Pr = 2094$.

4.6 Forced Convection heat transfer

Heat transfer by forced convection in pipes depends mainly on Reynolds number:

$$Re = \frac{\rho v D}{\mu} \tag{4-135}$$

where D is the hydraulic diameter (m) which is equal to the inner diameter for case of flow in a straight pipe, v is the flow velocity (m/s), ρ, μ are the density (kg/m³) and viscosity of the fluid (N.s/m²),

respectively. Reynolds number determines the regime of the flow where the flow is laminar when $Re < 2300$ and turbulent when $Re > 10000$. The flow when $2300 < Re < 10^5$ can be considered as a transitional flow. Reynolds number is a dimensional number representing the ratio of inertia to the viscous forces.

Heat transfer rate in forced convection can be calculated from:

$$Q_{F.convection} = h_{F.convection} A_s LMTD \tag{4-136}$$

where $h_{F.convection}$is the heat transfer coefficient of forced convection And A_s is the surface area (m²). LMTD is the logarithmic mean temperature ΔT_{LM}

$$LMTD = \frac{(T_s - T_{in}) - (T_s - T_{out})}{\ln\left(\frac{(T_s - T_{in})}{(T_s - T_{out})}\right)}$$

where T_s is the surface temperature, T_{in} is the inlet fluid temperature, T_{out} is the surface outlet temperature.

The heat transfer coefficient is expressed as a function of Nu as:

$$h = \frac{Nu.k}{D} \tag{4-137}$$

where Nu is Nusselt number of heat transfer by forced convection, which can be calculated from the correlations listed in Table 4-5. k is the thermal conductivity of the fluid (W/m.K), D is the hydraulic diameter (m).

Table 4-5 List of correlations of forced convection heat transfer coefficient

Reference	Equation	Eq.	conditions
Hausen [123]	$Nu = 3.66 + \frac{0.0668\, RePr\, D_{ci}/L_c}{1 + 0.04(Re\, Pr\, D_{ci}/L_c)^{2/3}}\left(\frac{\mu_b}{\mu_{ci}}\right)^{0.14}$	(4-138)	$Re < 2300$
Hausen [123]	$Nu = 0.116(Re^{0.66} - 125)Pr^{0.3}\left(\frac{\mu}{\mu_{ci}}\right)^{0.14}\left[1 + \left(\frac{D_{ci}}{L_c}\right)^{0.66}\right]$	(4-139)	$2300 < Re < 10000$
Petukhov [124]	$Nu = \frac{(f/8)RePr}{1.07 + 12.7(f/8)^{1/2}(Pr^{2/3} - 1)}\left(\frac{\mu_b}{\mu_{ci}}\right)^n$ where $f = (1.82\log_{10} Re - 1.64)^{-2}$	(4-140)	$0.5 < Pr < 2000$ $10^4 < Re < 5 \times 10^6$ $0.8 < \mu_b/\mu_{ci} < 40$ $n = 0.11$ for $T_{ci} > T_b$ and $n = 0.25\ T_{ci} < T_b$, $n = 0$ for gases Properties evaluated at

			$T_f = (T_{ci} + T_b)/2$ $T_b = \frac{T_{cold,in} + T_{cold,out}}{2}$
Sieder–Tate [125,126]	$Nu = \frac{hD_{ci}}{k} = 1.86(Re \cdot Pr \cdot D_{ci}/L_c)^{1/3} . \left(\frac{\mu}{\mu_{ci}}\right)^{0.14}$	(4-141)	$Re < 2300$ $RePrD_{ci}/L_c > 10$ fluid properties are evaluated at the mean bulk temperature of the fluid $T_b = \frac{T_{cold,in} + T_{cold,out}}{2}$
Petukhov-Gienlinski modification [127]	$Nu = \frac{(f/8)(Re - 1000)Pr}{1 + 12.7(f/8)^{1/2}(Pr^{2/3} - 1)}$	(4-142)	$2300 < Re < 5 \times 10^6$ $0.5 \leq Pr \leq 10^6$
Gnielinski [127]	$Nu = 0.0214(Re^{0.8} - 100)Pr^{0.4}$	(4-143)	$10^4 < Re < 5 \times 10^6$ $0.5 < Pr < 1.5$
Gnielinski [127]	$Nu = 0.012(Re^{0.87} - 280)Pr^{0.4}$	(4-144)	$3000 < Re < 10^6$ $1.5 < Pr < 500$
Sleicher and Rouse [128]	$Nu = 5 + 0.015Re^m \cdot Pr_{ci}^n$ $m = 0.88 - \frac{0.24}{Pr_{ci}+4}, n = \frac{1}{3} + 0.5e^{-0.6 \cdot Pr_{ci}}$	(4-145)	$10^4 \leq Re \leq 10^6$ $0.1 < Pr < 10^5$
Petukhov-Popov [124]	$Nu = \frac{(f/8)RePr}{k_1 + k_2(f/8)^{\frac{1}{2}}(Pr^{\frac{2}{3}} - 1)}$ where f is the friction factor: $f = (1.82 \log_{10} Re_D - 1.64)^{-2}$ $k_1 = 1 + 3.4f$ and $k_2 = 11.7 + \frac{1.8}{Pr^{\frac{1}{3}}}$	(4-146)	$10^4 < Re < 5 \times 10^6$ $0.5 < Pr < 2000$
Gnielinski [127]	$Nu = \frac{(f/8)(Re - 1000)Pr}{1 + 12.7(f/8)^{1/2}(Pr^{2/3} - 1)}\left[1 + (D_{ci}/L_c)^{2/3}\right]\Phi$ $\Phi = \left(\frac{Pr}{Pr_{ci}}\right)^{0.11}$ for liquids $\Phi = \left(\frac{T_b}{T_{ci}}\right)^{0.45}$ for gases	(4-147)	$2300 < Re < 5 \times 10^6$ $0.5 < Pr < 200$

4.7 Theoretical modelling of the single heat pipe

In the single heat pipe tests in the laboratory kiln, the heat transfer illustrated in Figure 4-28 is as follows:

The heater emits the heat directly to the evaporator section of the heat pipe and to the insulated walls. In addition, the heater heats the air in the kiln by natural convection. The kiln walls reradiate the heat in all directions since they are insulated, and the heat dissipated to outside is neglected.

The external evaporator surface of the heat pipe absorbs incident radiation and heat by natural convection from the hot air in the kiln. Then the heat is transferred from the external evaporator wall to the inner wall by conduction. Thus, the working fluid inside the heat pipe boils and evaporates. The vapour flows to the condenser where it releases the heat and condenses. The heat is transferred through the condenser wall to the outer surface of the condenser wall by conduction. Then the heat is transferred to the water stream by forced convection. The condensate returns to the evaporator section by gravity.

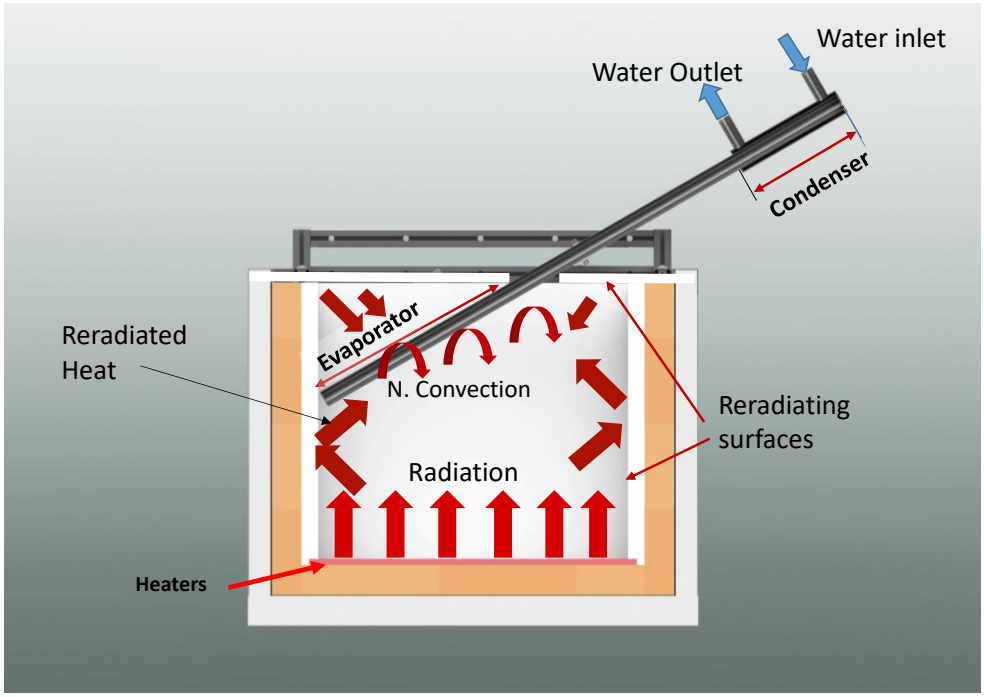

Figure 4-28 A schematic of the heat transfer in laboratory kiln

4.7.1 Thermal network model

The thermal modelling of the system was developed by applying the electrical resistance analogy approach to the heat transfer, where the thermal resistances are considered as electrical resistances [129]. Theoretical modelling of heat pipe through electrical analogy is a common practice followed in the literature in order to predict the thermal performance of a heat pipe [130].

The thermal network model and a schematic of the experimental system are illustrated in Figure 4-29.

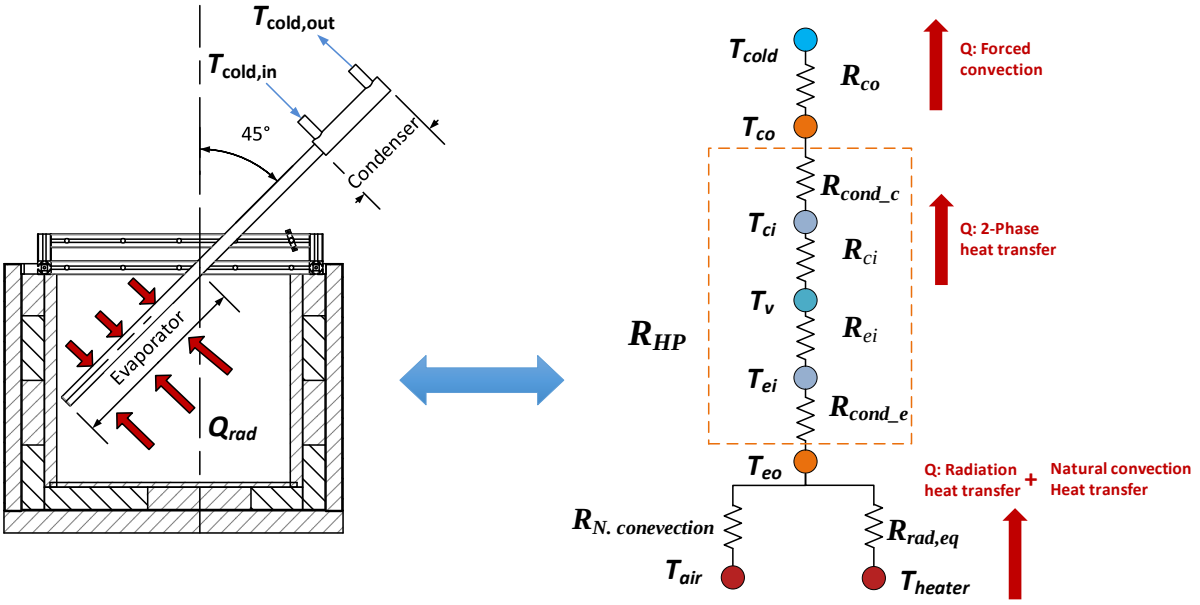

Figure 4-29 A schematic of the thermal network model by applying electrical analogy approach

The thermal resistances of heat transfer are calculated considering the heat transfer regime and based on the heat transfer background provided. The thermal resistances will be discussed separately in the following sections. It can be seen from Figure 4-29 that the heat pipe transfers the heat from the heater represented by T_{heater} and the hot air represented by T_{air} to the water flow represented by T_{cold}.

The symbols of thermal resistances shown in Figure 4-29 are:

$R_{rad,eq}$: Radiation heat transfer resistance (K/W)

$R_{N.convection}$: Natural convection heat transfer thermal resistance (K/W)

R_{cond_e}: Conduction thermal resistance of the evaporator wall (K/W)

R_{ei}: Boiling thermal resistance (K/W)

R_{ci}: Condensation thermal resistance (K/W)

R_{cond_c}: Conduction thermal resistance of the condenser wall (K/W)

R_{co}: Convection thermal resistance of condenser section (K/W)

The temperatures shown in Figure 4-29 are:

T_{Heater}: Heater temperature where it is the average heater plate temperature (K).

T_{eo}: HP outer wall evaporator temperature (K).

T_{ei}: HP inner wall evaporator temperature (K).

T_v: HP working fluid vapour temperature (K).

T_{ci}: HP inner wall condenser temperature (K).

T_{co}: HP outer wall condenser temperature (K).

T_{cold}: water coolant temperature (K).

The thermal resistance due to the vapour flow from the evaporator to the condenser is negligible in comparison to the other thermal resistances. Therefore, it was not considered in the theoretical modelling.

R_{HP}: Heat pipe equivalent thermal resistance where

$$R_{HP} = R_{eo} + R_{ei} + R_{ci} + R_{co} \text{ (K/W)} \tag{4-148}$$

The heat transfer rate by a heat pipe can be expressed as [131]:

$$Q_{HP} = \frac{T_{eo} - T_{co}}{R_{HP}} \text{ (W)} \tag{4-149}$$

4.7.2 Natural convection modelling

The thermal resistance of heat transfer by natural convection is calculated from $h_{N.convection}$ as provided in Eqs (4-125)-(4-134).

where

$$R_{N.convection} = \frac{1}{h_{N.convection} A_{eo}} \tag{4-150}$$

and A_{eo} is external evaporator surface area (m²).

4.7.3 Radiation modelling

Heat transfer by radiation to the heat pipe consists of two main components: Direct radiation from the heater to the heat pipe, and reradiated heat from the walls to the heat pipe.

To determine the heat transfer rate by radiation, several assumptions are made:

1. All surfaces are considered as opaque, diffuse, and grey
2. The effect of the natural convection on the walls is not considered. Thus, the wall can be considered as reradiating surfaces since they were insulated.
3. Steady state operating conditions exist
4. The radiosity and emitted heat are uniform per surface area

Assumption 2 is very common in heat transfer practice for insulated walls to simplify the problems.

The heat pipe received radiation directly from the heater and the walls which receives radiation from the heater. The experimental system consists of the following elements: heater (*H*), four side walls (W_1, W_2, W_3, W_4), a top wall (W_{top}), and the heat pipe (*HP*). The total number of parts is seven which can be presented in 7 nodes by the electrical analogy as shown in Figure 4-30. The resistances labels are shown in Figure 4-31. $R_{JH,EH}$, $R_{JHP,EHP}$ is the surface resistance of the heaters and the heat pipe, respectively. The other resistances illustrated in the 3D diagram are the space the resistance to radiation heat transfer between the nodes i.e. the experimental system components. However, it can be seen that solving this problem is very complex because it needs to determine many view factors which cannot be obtained theoretically using general equations of view factors.

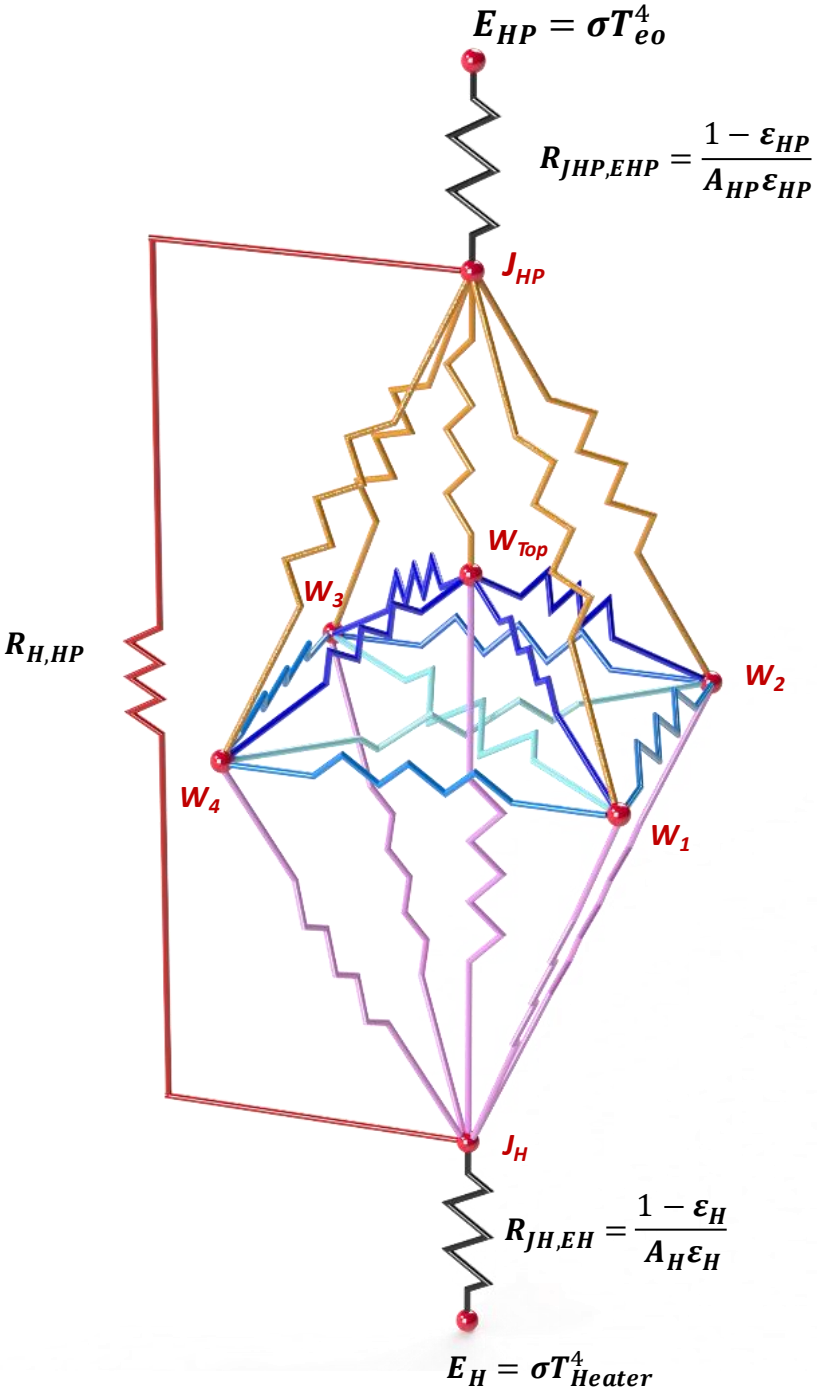

Figure 4-30 Electrical analogy diagram of the radiation thermal resistance of the single heat pipe tests

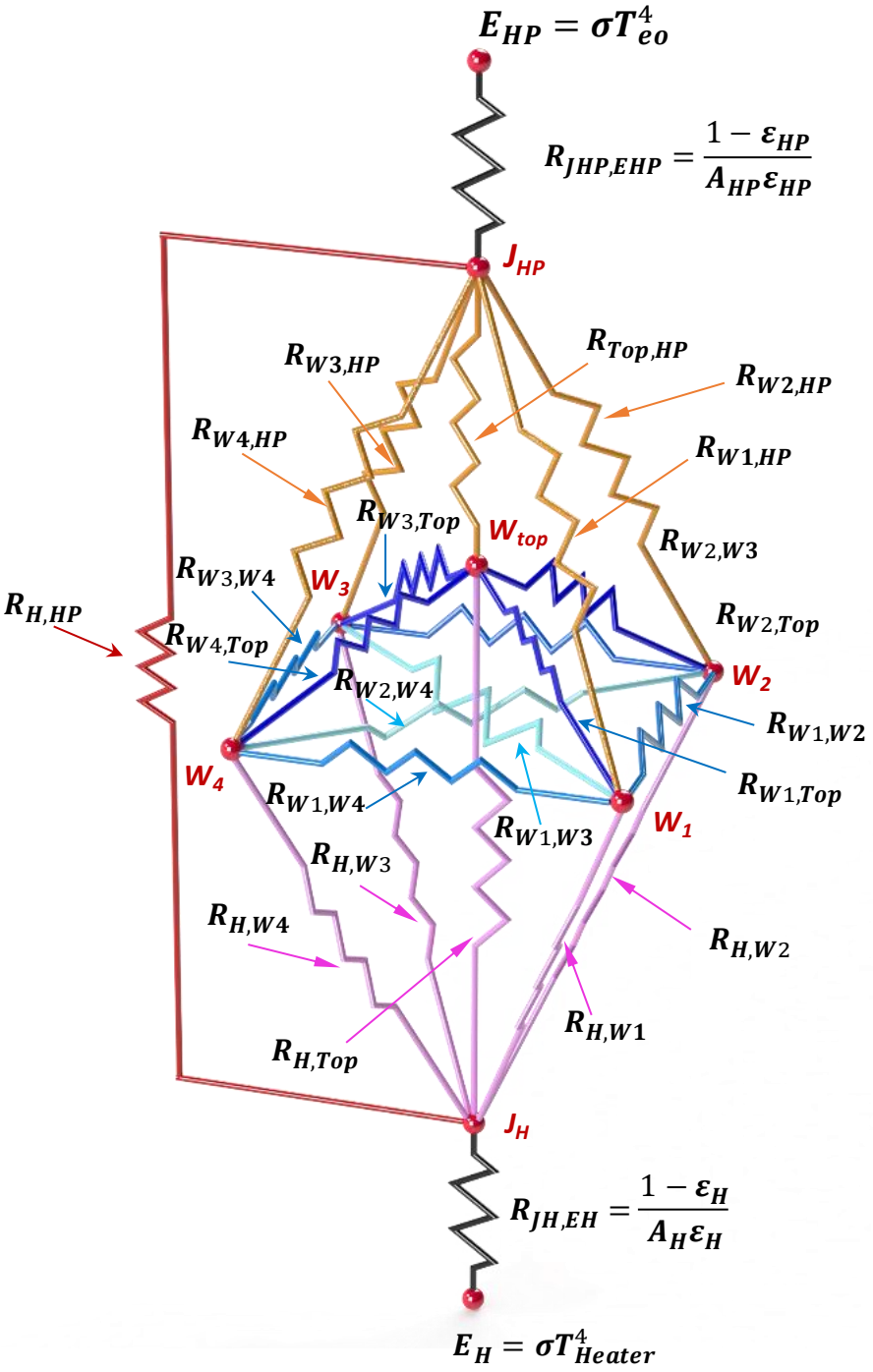

Figure 4-31 Electrical analogy diagram of the radiation thermal resistance of the single heat pipe tests with labelled resistances

Figure 4-32 illustrates an isolated view of the single heat pipe node obtained from thermal resistance model presented in Figure 4-31. The heat is transferred directly from the heaters to the single heat pipe and it is dependent on the resistance $R_{H,HP}$ which is the space resistance between the heater and the heat pipe. The heat is transferred from the walls to the single heat pipe and subjected to the space resistance between the single heat pipe and the walls. However, this model requires the

temperature of the heater, the four side walls, and the top wall in order to be solved and determining the overall heat recovery. In addition, it is very difficult to calculate the space resistances as there is no generalised equation for a view factor and an inclined cylinder.

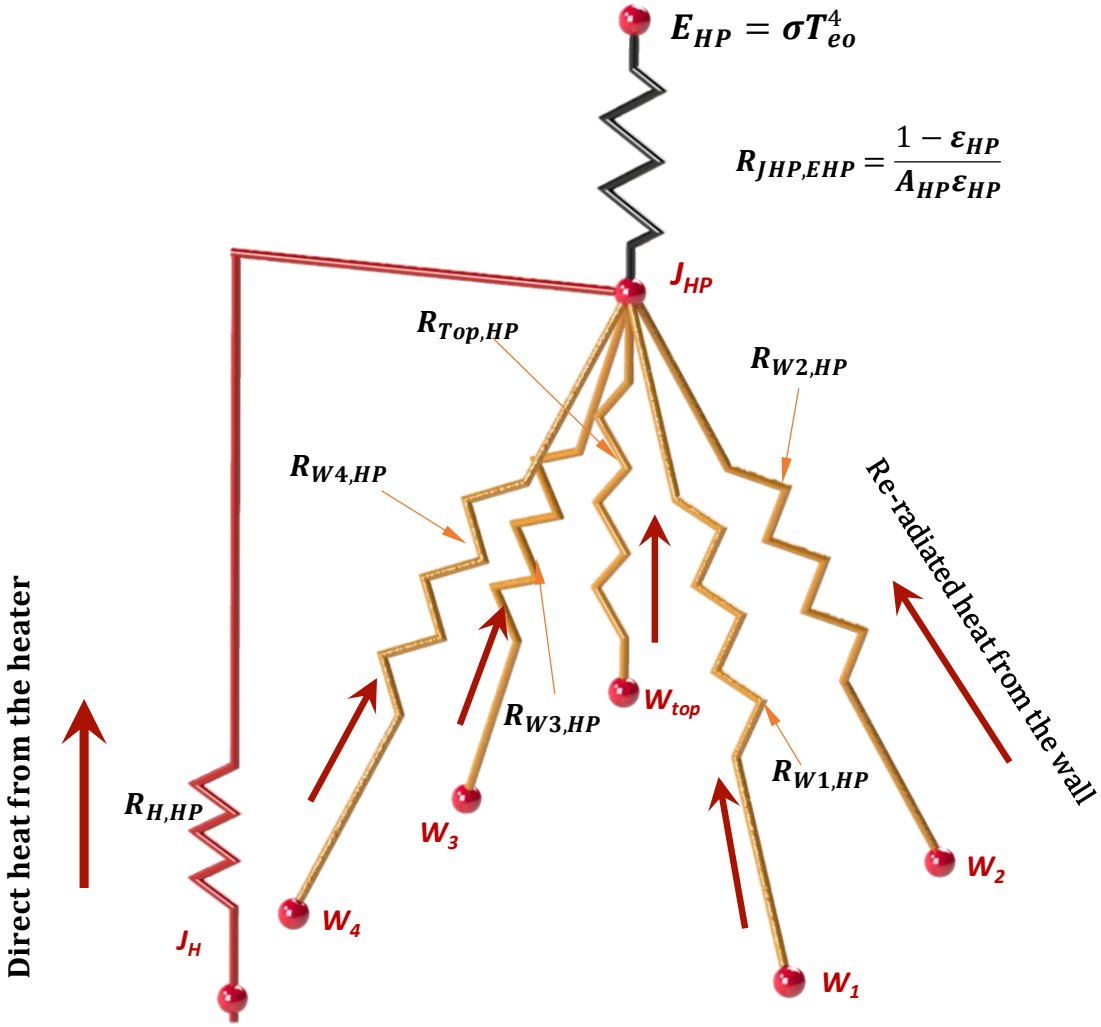

Figure 4-32 A three dimensional diagram focuses on the radiation thermal resistances of the single heat pipe applying the electrical analogy

Therefore, the four walls in addition to the top wall can be considered as a one part in a cavity shape as shown in Figure 4-33. Thus, the model is simplified into three parts: the heater, the wall, and the heat pipe.

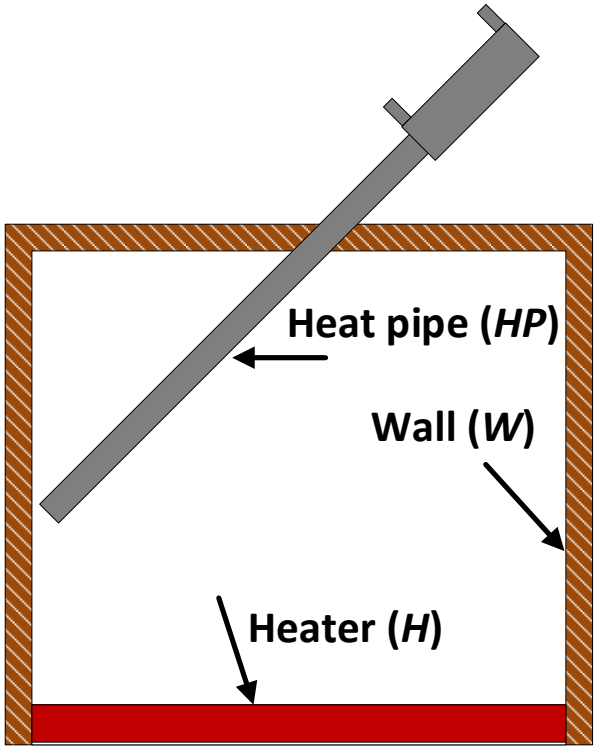

Figure 4-33 illustration schematic of the simplified radiation elements of the single heat pipe experiments

A simplified thermal resistance model and the equivalent thermal radiation resistance model are presented in Figure 4-34.

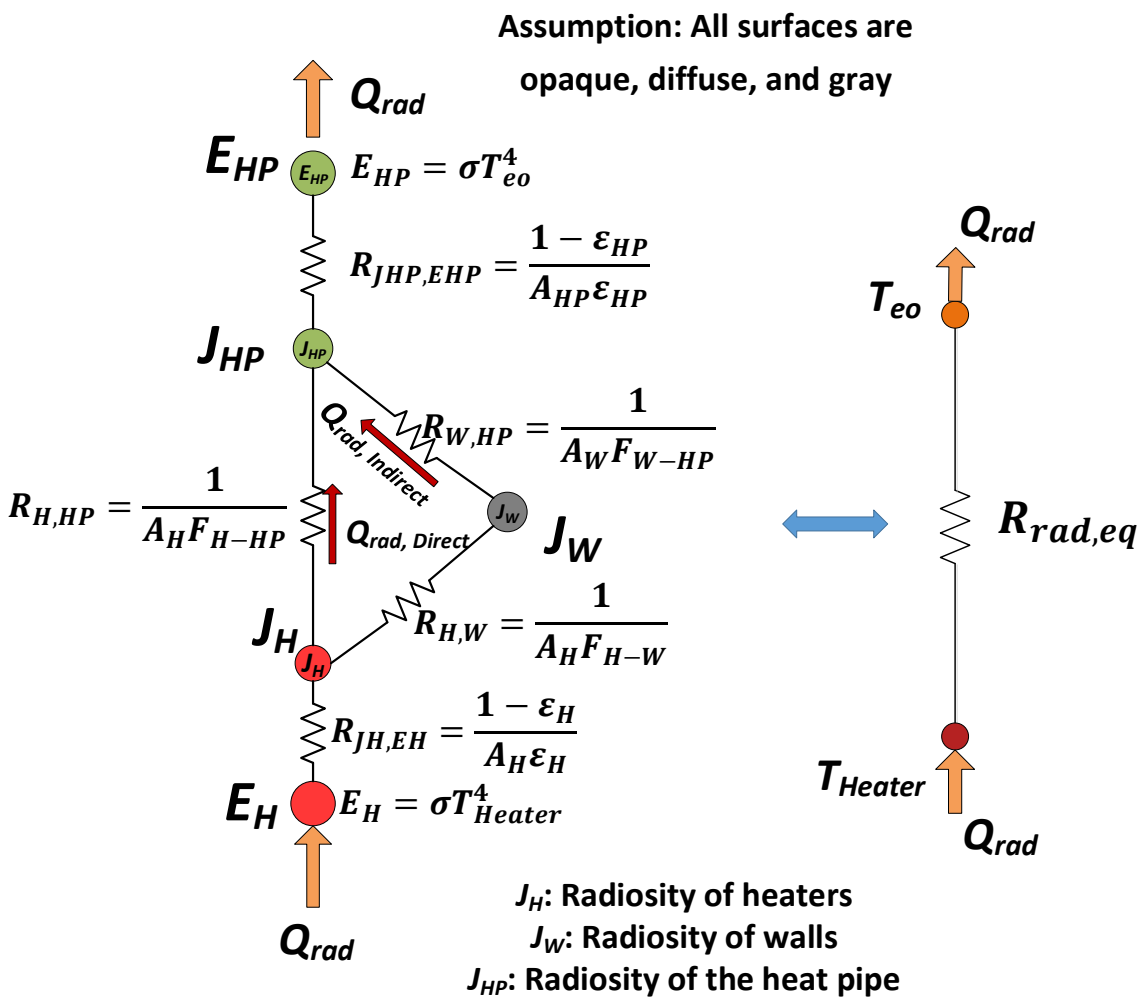

Figure 4-34 Illustration of the radiation heat transfer modelling

The symbols shown in Figure 4-34 are as follows:

T_{eo}: External evaporator surface temperature (K)

T_{wall}: Inner wall temperature (K)

T_{Heater}: Heater temperature (K)

E_H: Heat emitted from the heater surface (W/m²)

E_{HP}: Heat emitted from the evaporator of the FHP surface (W/m²)

J_H: Radiosity of the heater surface which is the overall radiation leaving the heater surface (W/m²)

J_{HP}: Radiosity of the evaporator surface which is the overall radiation leaving the evaporator surface (W/m²)

J_W: Radiosity of the surroundings (W/m²)

R_{E_H,J_H}: Heater surface resistance to radiation (m^{-2})

$R_{H,HP}$: Space resistance to radiation between the heaters and the FHP (m^{-2})

$R_{H,W}$: Space resistance to radiation between the heaters and the walls (m^{-2})

$R_{W,HP}$: Space resistance to radiation between the heaters and the walls (m^{-2})

$R_{E_{HP},J_{HP}}$: Evaporator surface resistance to radiation (m^{-2})

$R_{rad,eq}$: Equivalent Radiation heat transfer resistance (K/W)

It can be seen from Figure 4-34 that $R_{H,W}$ and $R_{w,HP}$ are linked in series since the wall is reradiating the heat. i.e $J_W = E_W$. It should be mentioned that when the walls are insulated and considered as reradiating surface, then the wall surface temperature and emissivity do not have an effect on the radiation heat transfer.

The equivalent resistance of these two resistances is linked in parallel with the space resistance $R_{H,HP}$.

The equivalent resistance is:

$$R_{space,eq} = \frac{1}{\frac{1}{R_{H,HP}} + \frac{1}{(R_{H,W} + R_{W,HP})}} \tag{4-151}$$

Hence, the net heat transfer by radiation can be obtained from the following:

$$Q_{rad} = Q_{H,HP} = \frac{E_H - E_{HP}}{\frac{1-\varepsilon_H}{\varepsilon_H A_H} + \frac{1}{A_H F_{H-HP} + \left[\frac{1}{A_H F_{H,W}} + \frac{1}{A_W F_{W,HP}}\right]^{-1}} + \frac{1-\varepsilon_{HP}}{\varepsilon_{HP} A_{HP}}} \tag{4-152}$$

Eq.(4-152) can be rearranged to be:

$$Q_{rad} = Q_{H,HP} = \frac{T_H - T_{eo}}{R_{rad,eq}} \tag{4-153}$$

where $R_{rad,eq}$ is expressed as:

$$R_{rad,eq} = \frac{\frac{1-\varepsilon_H}{\varepsilon_H A_H} + \frac{1}{A_H F_{H-HP} + \left[\frac{1}{A_H F_{H,W}} + \frac{1}{A_W F_{W,HP}}\right]^{-1}} + \frac{1-\varepsilon_{HP}}{\varepsilon_{HP} A_{HP}}}{\sigma(T_H^2 + T_{eo}^2)(T_H + T_{eo})} \tag{4-154}$$

The net heat radiation between the heater and the heat pipe can be calculated using the direct approach in Eq. (4-76) as follows:

The net radiation heat transfer rate to the heat pipe can be obtained be solving equations (4-155), (4-156), (4-157).

$$\frac{E_H - J_H}{\frac{1-\varepsilon_H}{\varepsilon_H A_H}} = \frac{J_H - J_{HP}}{\frac{1}{A_H F_{\mathrm{H-HP}}}} + \frac{J_H - J_W}{\frac{1}{A_H F_{\mathrm{H-W}}}} \tag{4-155}$$

$$\frac{E_{HP} - J_{HP}}{\frac{1-\varepsilon_{HP}}{\varepsilon_{HP} A_{HP}}} = \frac{J_H - J_{HP}}{\frac{1}{A_H F_{\mathrm{H-HP}}}} + \frac{J_W - J_{HP}}{\frac{1}{A_{HP} F_{\mathrm{HP-W}}}} \tag{4-156}$$

$$0 = \frac{J_H - J_W}{\frac{1}{A_H F_{\mathrm{H-W}}}} + \frac{J_{HP} - J_W}{\frac{1}{A_{HP} F_{\mathrm{HP-W}}}} \tag{4-157}$$

where the net heat radiation to the heat pipe is:

$$Q_{rad} = Q_{FHP} = \frac{E_{HP} - J_{HP}}{\frac{1-\varepsilon_{HP}}{\varepsilon_{HP} A_{HP}}} \tag{4-158}$$

Obtaining the values of J_H,J_W, J_{HP} is important to evaluate the magnitude of the direct radiation leaving the heater and incident on the heat pipe in comparison to the radiation incident on the heat pipe from the walls. The magnitudesE_{HP}, J_{HP} demonstrate the efficiency of the heat pipe surface in absorbing the incident radiation.

The view factors in the simplified approach were calculated as follows:

From the summation rule:

$$F_{H,H} + F_{H,HP} + F_{H,W} = 1 \tag{4-159}$$

where $F_{H,H}$= 0 as the heater surface is a plane surface.

The view factor $F_{H,HP}$ is calculated using equations (4-59) and (4-60), where the heat pipe was considered as a flat surface since there is no data provided in the literature to calculate the view factor of radiation between a plain surface and an inclined cylinder. Moreover, the pipe diameter is very small in comparison to the dimensions of the heater surface.

4.7.4 Boiling modelling

The boiling heat transfer consists of two regimes: nucleate pool boiling in the surface area starting from the bottom of the evaporator up to the liquid level, while falling film boiling occurs in the remaining surface area of the evaporator starting from the liquid level up to the end of the evaporator section.

The sum of the heat transfer by boiling in these two surfaces area is equal to the heat gained by the evaporator by natural convection and radiation as shown in (4-160):

$$Q_{rad} + Q_{N.Convection} = Q_{boi,Nucleate} + Q_{boil,film} \quad (4\text{-}160)$$

$$Q_{boi,Nucleate} = \frac{T_{ei} - T_v}{R_{ei,nucleate}} \quad (4\text{-}161)$$

where the thermal resistance of nucleate boiling is calculated from:

$$R_{ei,nucleate} = \frac{1}{h_{ei,nucleate} A_{ei,nucleate}} \quad (4\text{-}162)$$

The heat transfer coefficient of nucleate boiling is calculated using the equations provided in Table 4-1.

The heat transfer rate by nucleate falling film boiling is expressed as:

$$Q_{boi,film} = \frac{T_{ei} - T_v}{R_{ei,film}} \quad (4\text{-}163)$$

where the thermal resistance of nucleate falling film boiling is calculated from:

$$R_{ei,film} = \frac{1}{h_{ei,film} A_{ei,film}} \quad (4\text{-}164)$$

The heat transfer coefficient of falling film boiling is calculated using the equations provided in Table 4-2.

It should be mentioned that the temperature of the evaporator outer and inner walls T_{eo} and T_{ei} is not equal for the two boiling regimes while the working fluid vapor temperature is the same. The thermal resistances network model of the heat pipe becomes as shown in Figure 4-35.

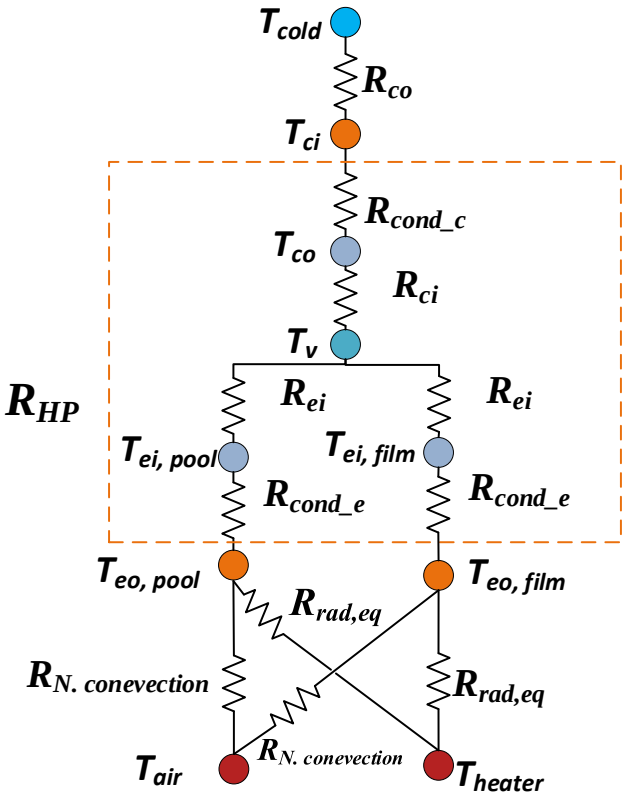

Figure 4-35 Thermal resistance network model of the single heat pipe considering two boiling regimes in the evaporator

4.7.5 Condensation modelling

The condensation heat transfer rate on the condenser surface is obtained from:

$$Q_{cond} = \frac{(T_v - T_{ci})}{R_{ci}} \tag{4-165}$$

The thermal resistance of condensation R_{ci} is obtained from:

$$R_{ci} = \frac{1}{h_{ci} A_{ci}} \tag{4-166}$$

The condensation heat transfer coefficient on the inner surface of the condenser h_{ci} is obtained from the correlations presented in Table 4-3, where the inclination angle from vertical was considered for calculating the heat transfer coefficient of condensation.

4.7.6 Conduction of the heat pipe walls

The heat transfer by conduction occurs on the evaporator wall in addition to the condenser wall.

The rate of heat transfer by conduction can be obtained from [132]:

$$Q_{cond,e} = \frac{T_{eo} - T_{ei}}{R_{cond,e}} \tag{4-167}$$

$$Q_{cond,c} = \frac{T_{ci} - T_{co}}{R_{cond,c}} \tag{4-168}$$

where the subscripts $cond, e$ and $cond, c$ stand for the conduction through the evaporator and the condenser, respectively.

The thermal resistance of conduction can be obtained from:

$$R_{cond,e} = \frac{\ln(\frac{D_{eo}}{D_{ei}})}{2\pi l_e k_s} \tag{4-169}$$

$$R_{cond,c} = \frac{\ln(\frac{D_{co}}{D_{ci}})}{2\pi l_c k_s} \tag{4-170}$$

where k_s is the thermal conductivity of the heat pipe shell case material which was stainless steel 304.

4.7.7 Forced convection modelling

The heat transfer rate can be calculated from the following:

$$Q_{F.convection} = \frac{\frac{[(T_v - T_i) - (T_v - T_o)]}{\ln\left(\frac{(T_v - T_i)}{T_v - T_o}\right)}}{h_{F,convection} A_{co,total}} \tag{4-171}$$

The equation can be rearranged to be:

$$Q_{F.convection} = \frac{\frac{(T_o - T_i)}{\ln\left(\frac{(T_v - T_i)}{T_v - T_o}\right)}}{h_{F,convection} A_{co,total}} \tag{4-172}$$

where $h_{F,convection}$ is the forced convection heat transfer coefficient (W/m².K). The heat transfer coefficient can be calculated from the correlations listed in Table 4-5.

The heat transfer area $A_{co,total}$ consists of the eternal condenser surface and the helical fins surface considering the thermal conductivity of the fins. The heat transfer area $A_{co,total}$ can be expressed as follows:

$$A_{co,total} = A_{co} + \eta A_{co,fins} \tag{4-173}$$

A detailed sectional view of the double pipe jacket of the condenser is presented in Figure 4-36. D_{co} is the external diameter of the condenser, D_{ji} is the internal diameter of the jacket cylinder, P is the helical fin pitch, t fin thickness, H_{fin} is the fin height where:

$$H_{fin} = \frac{(D_{ji} - D_{co})}{2} \tag{4-174}$$

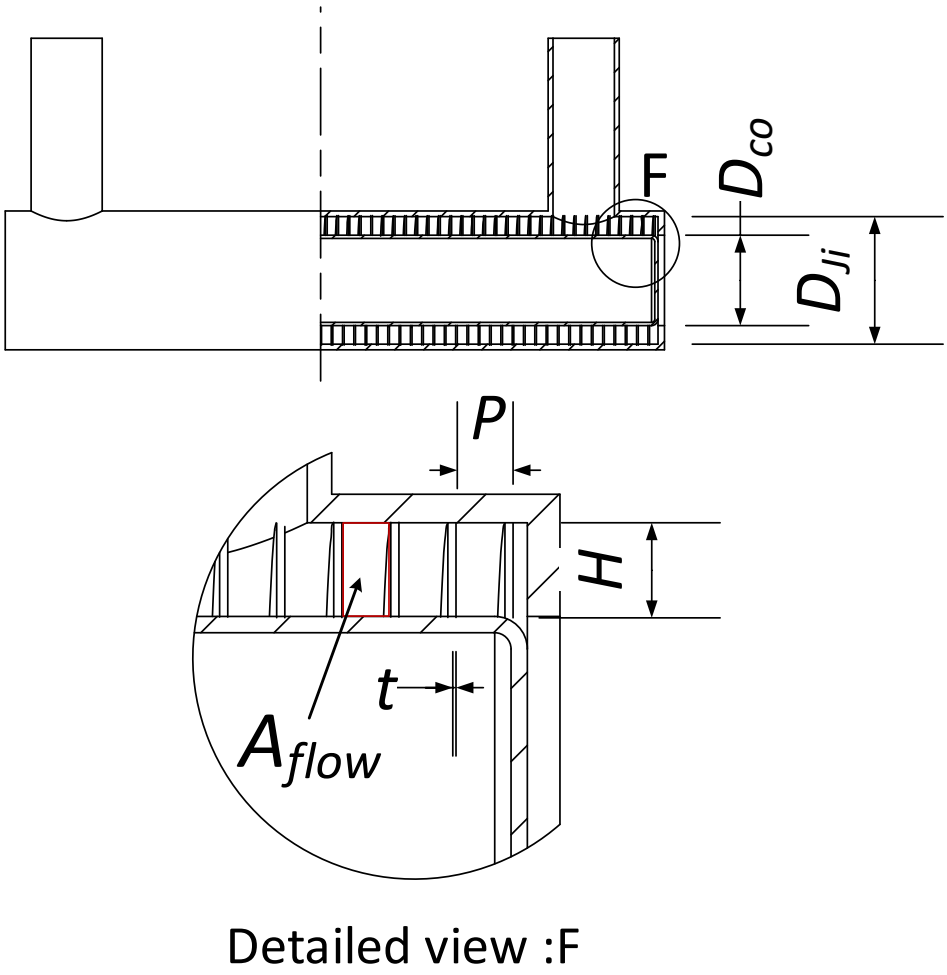

Figure 4-36 A detailed section view of the condenser

In order to obtain the heat transfer area, the efficiency of the fins is calculated from:

$$\eta_{fins} = \frac{\tanh(m.H_{fin})}{m.H_{fin}} \tag{4-175}$$

where m is:

$$m = \sqrt{\frac{2h_{F.convection}}{k_{fin}t_{fin}}} \tag{4-176}$$

The heat transfer area corresponding to the fins surface A_{fin} is calculated from:

$$A_{fins} = 2\pi H_{fin}L_{helical} \tag{4-177}$$

$L_{helical}$ is the average length of the helical path which is obtained from:

$$L_{helical} = \left[\pi\left(\frac{D_{ji} + D_{co}}{2}\right)^2 + P_{fin}^2\right]^{0.5}\frac{L_c}{P_{fin}} \tag{4-178}$$

where L_c/P_{fin} represents the number of turns of the helical path in the condenser cooling jacket.

The heat transfer area of the primary surface which is the external surface of the cylindrical condenser tube is:

$$A_{co} = \pi D_{co}(P_{fin} - t_{fin})L_c/P_{fin} \tag{4-179}$$

The Reynolds number used to evaluate the heat transfer coefficient is calculated by considering the hydraulic diameter of the helical path.

The hydraulic diameter D_h can be calculated from the general formula:

$$D_h = \frac{4A_{flow}}{P} \tag{4-180}$$

Hence, the hydraulic diameter can be calculated from Eq.(4-180):

$$D_h = \frac{2H_{fin}(P_{fin} - t_{fin})}{(H_{fin} + P_{fin} - t_{fin})} \tag{4-181}$$

where the flow area A_{flow} is:

$$A_{flow} = H_{fin}(P_{fin} - t_{fin}) \tag{4-182}$$

The rate of heat transfer to the water flow can be calculated from

$$Q_{recovery} = m_{water}Cp_{water}(T_{out,water} - T_{in,water}) \tag{4-183}$$

where from energy conservation the heat transferred to the water is equal to:

$$Q_{rad} + Q_{N.convection} = Q_{recovery} \tag{4-184}$$

By linking the equations presented, the heat pipe temperature and the heat recovery can be obtained.

4.8 Theoretical modelling of the flat heat pipe

This section presents the approach followed to calculate the heat transfer by the FHP system in the laboratory and the factory. The thermal network model of the FHP system is the same for laboratory

and factory except that the radiation conditions were different. The hot source temperature and surface area, heat pipe emissivity, the view factor, and the back-panel effect were the key factors influencing the FHP thermal performance. In addition to the radiative heat source, the FHP was absorbing heat from the air above the heaters by natural convection in the laboratory tests, while in the factory it was absorbing heat from the air by forced convection.

4.8.1 Thermal network model of the FHP at laboratory tests

Figure 4-37 illustrates the heat transfer to the FHP in the laboratory tests. In the laboratory tests, the heaters emit heat by radiation to the FHP and to ambient. In addition, heat is transferred from the heaters to the air by natural convection developing a thermal layer between the heaters and the FHP. The FHP consists of the parallel vertical pipes and a back panel. The back panel absorbs the heat by radiation from the heaters and by natural convection from the hot air. Then the heat is transferred by radiation from the back panel to the vertical tubes of the FHP. In addition, the back panel transfers some heat by conduction to the vertical pipes. Moreover, back panel partially reflects the incident radiation to the vertical pipes, the heaters, and ambient. Thus, the back panel acts as a radiation absorber and reflector which enhances the overall radiant heat recovery and increases the surface temperature of the FHP. The vertical pipes with the bottom collector represent the evaporator of the FHP.

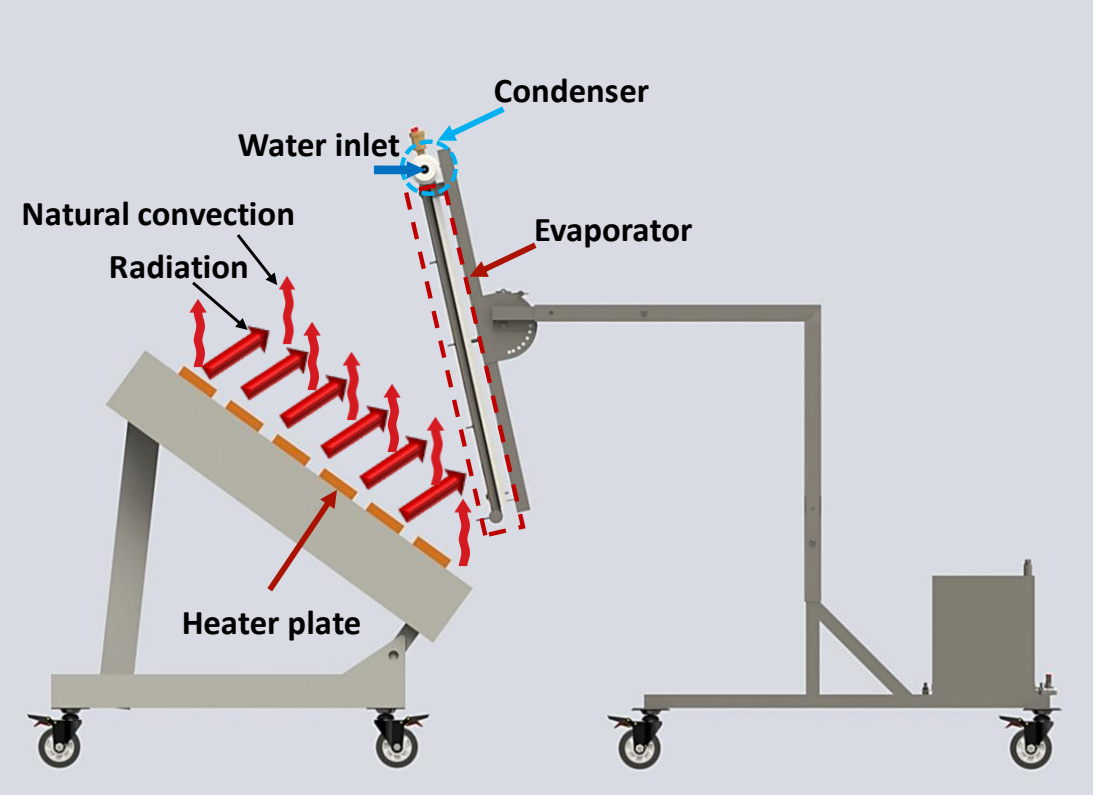

Figure 4-37 Illustration of the heat transfer to FHP at the laboratory

In summary, the parallel tubes with the bottom collector exchange radiation energy with the heaters, the back panel and ambient. The thermal resistances of radiation and natural convection circuit can be seen in Figure 4-38 following the electrical analogy approach. The heat is transferred through the walls of the evaporator of the FHP by conduction. Then the liquid working fluid inside absorbs the heat and boils. The vapour from the working fluid flows to the condenser of the FHP where it realises the latent heat by condensing on the outer wall of the horizontal condenser tubes. The heat is transferred to the inner wall of the horizontal tubes by conduction and then by forced convection to the water coolant flow. Finally, the condensate returns to the evaporator assisted by gravitational forces and the working cycle is repeated.

Therefore, the FHP is considered as a thermosyphon and the thermal resistances of the heat transfer in the FHP are also shown in Figure 4-38. Modelling the heat transfer to the FHP is very complex and requires simplification in order to be solved. Furthermore, the model presented in Figure 4-38 does not account for the heat losses from the back panel by natural convection when it was uninsulated. The conduction resistance $R_{conduction}$ between the back panel and the parallel pipes is neglected in

the theoretical modelling of the heat transfer because of the minimal contact area between the back panel and the parallel pipe.

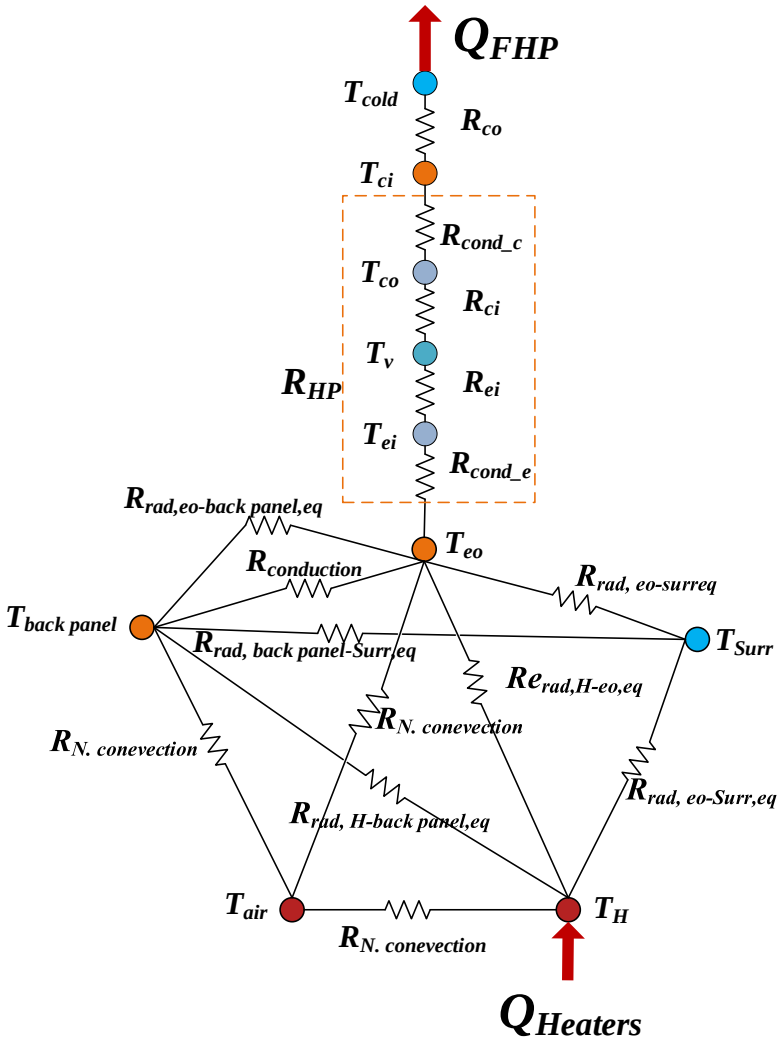

Figure 4-38 Complex thermal network modelling of the heat transfer of the FHP system with a back panel

The radiation thermal resistances circuit is illustrated in Figure 4-39. It can be seen the complexity of the circuit cannot be solved without using a numerical software solution.

The symbols used in the nodes of Figure 4-39 are:

T_H: Heater temperature where it is the average heater plate temperature (K).

T_{eo}: FHP outer wall evaporator temperature (K).

T'_{eo}: Back panel temperature (K).

T_{surr}: Surroundings temperature (K).

E_H: is the heat emitted from the heater surface (W/m²)

E_{eo}: Heat emitted from the evaporator of the FHP surface (W/m²)

E_{surr}: Heat emitted from the surroundings (W/m²)

J_H: Radiosity of the heater plate surface (W/m²)

J_{eo}: Radiosity of the evaporator surface (W/m²)

J_{surr}: Radiosity of the surrounding (W/m²)

R_{E_H,J_H}: Heater surface resistance to radiation (m^{-2})

$R_{E_{eo},J_{eo}}$: Evaporator surface resistance to radiation (m^{-2})

$R_{E_{eo'},J_{eo'}}$: Evaporator surface resistance to radiation (m^{-2})

$R_{J_H,J_{eo}}$: Space resistance to radiation between the heaters and the FHP (m^{-2})

$R_{J_H,J_{eo'}}$: Space resistance to radiation between the heaters and the back panel (m^{-2})

$R_{J_H,J_{surr}}$: Space resistance to radiation between the heaters and the back panel (m^{-2})

$R_{J_{eo},J_{eo'}}$: Space resistance to radiation between the back panel and the FHP (m^{-2})

$R_{J_{eo},J_{surr}}$: Space resistance to radiation between the FHP and the surroundings (m^{-2})

$R_{J_{eo'},J_{surr}}$: Space resistance to radiation between the back panel and the surroundings (m^{-2})

R_{rad}: Equivalent radiation heat transfer resistance (K/W)

The thermal resistances shown in Figure 4-42 are:

R_{cond_e}: Conduction thermal resistance of the evaporator wall (K/W)

R_{ei}: Boiling thermal resistance (K/W)

R_{ci}: Condensation thermal resistance (K/W)

R_{cond_c}: Conduction thermal resistance of the condenser wall (K/W)

R_{co}: Convection thermal resistance of condenser section (K/W)

The thermal resistance due to the vapour flow from the evaporator to the condenser is negligible in comparison to the other thermal resistance. Therefore, it was not considered in the theoretical modelling.

R_{HP}: Heat pipe equivalent thermal resistance where

$$R_{HP} = R_{eo} + R_{ei} + R_{ci} + R_{co} \text{ (K/W)} \tag{4-185}$$

$$Q_{FHP} = \frac{T_{eo} - T_{co}}{R_{HP}} \text{ (W)} \tag{4-186}$$

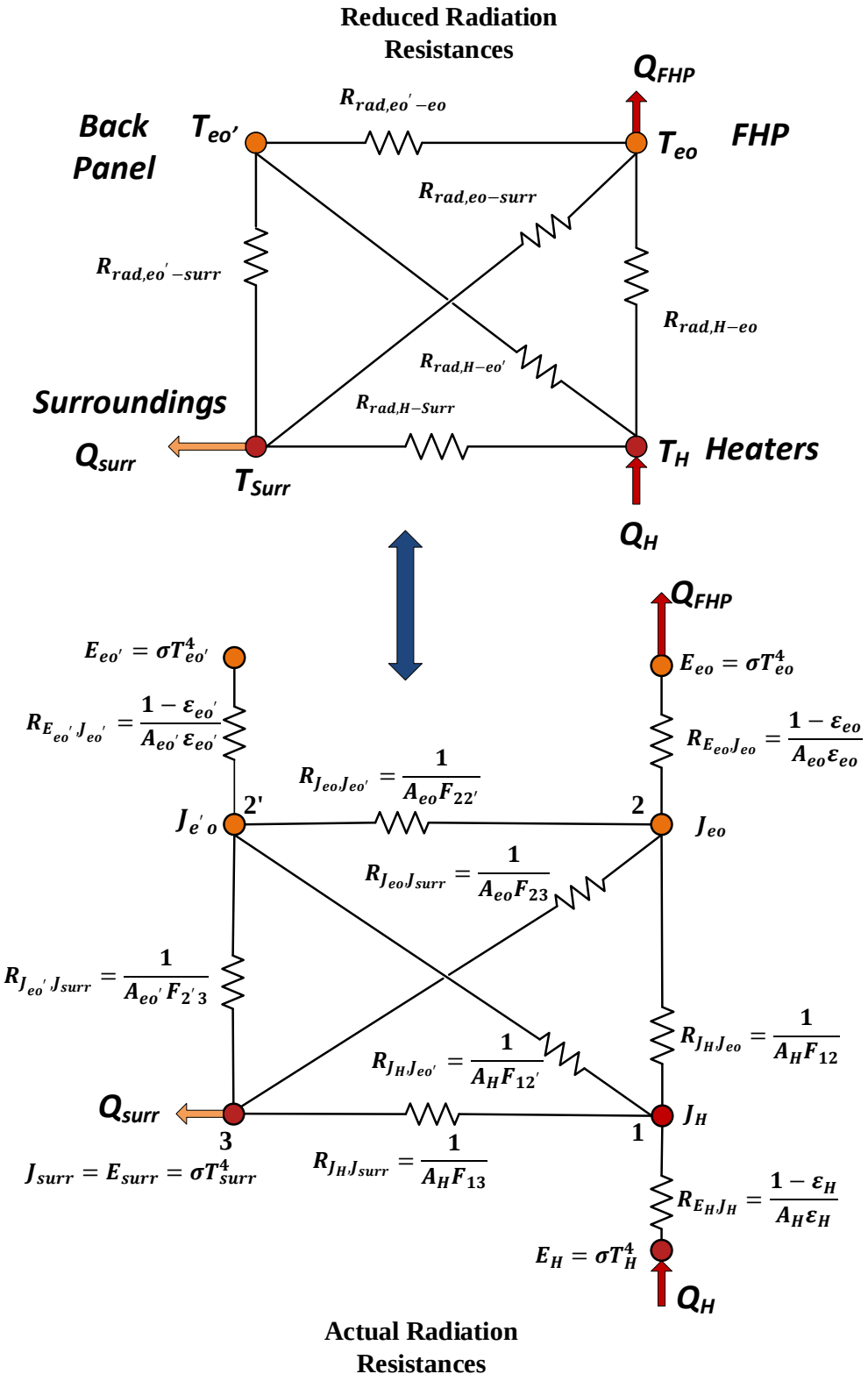

Figure 4-39 Schematic of the four node radiation thermal resistances circuit

The net heat by radiation to the FHP Q_{FHP} in Figure 4-39 can be determined by applying Eq.(4-76) which results in the following:

$$Q_H = \frac{\varepsilon_H}{1-\varepsilon_H}(E_H - J_H) = J_H - J_{eo}F_{12} - J_{surr}F_{13} - J_{eo'}F_{12'} \quad (4\text{-}187)$$

$$Q_{FHP} = \frac{\varepsilon_{eo}}{1-\varepsilon_{eo}}(E_H - J_H) = J_{eo} - J_{eo}F_{22} - J_H F_{21} - J_{surr}F_{23} - J_{eo'}F_{22'} \quad (4\text{-}188)$$

$$Q_{surr} = E_{surr} - J_{surr}F_{31} - J_{eo}F_{32} - J_{eo'}F_{32'} \quad (4\text{-}189)$$

$$Q_{eo'} = \frac{\varepsilon_{eo'}}{1-\varepsilon_{eo'}}(E_{eo'} - J_{eo'}) = J_{eo'} - J_H F_{2'1} - J_{eo}F_{2'2} - J_{surr}F_{2'3} \quad (4\text{-}190)$$

If the effect of natural convection on the back panel is neglected since it is insulated, then $Q_{eo'} = 0$ and the surface becomes as re-radiating surface since all the heat absorbed by the back panel is released by radiation again.

Eqs.(4-187), (4-188), (4-189), (4-190) can be solved by inverting them into a matrix and solving using programmed software such as MATLAB.

The radiation thermal resistance is reduced to three nodes in the thermal modelling and presented in Figure 4-40 and Figure 4-42. Figure 4-40 presents a schematic of the thermal modelling of the FHP considering the natural convection. Figure 4-42 presents a schematic of the thermal modelling of the FHP without considering the natural convection since the temperature of the air was not measured during the experiments. Q represents the heat emitted by the heaters, Q_{loss} represents the heat loss to surroundings, and Q_{FHP} represents the heat transferred by the FHP to the water coolant. The thermal modelling tool was built based on the thermal resistance circuit presented in Figure 4-42.

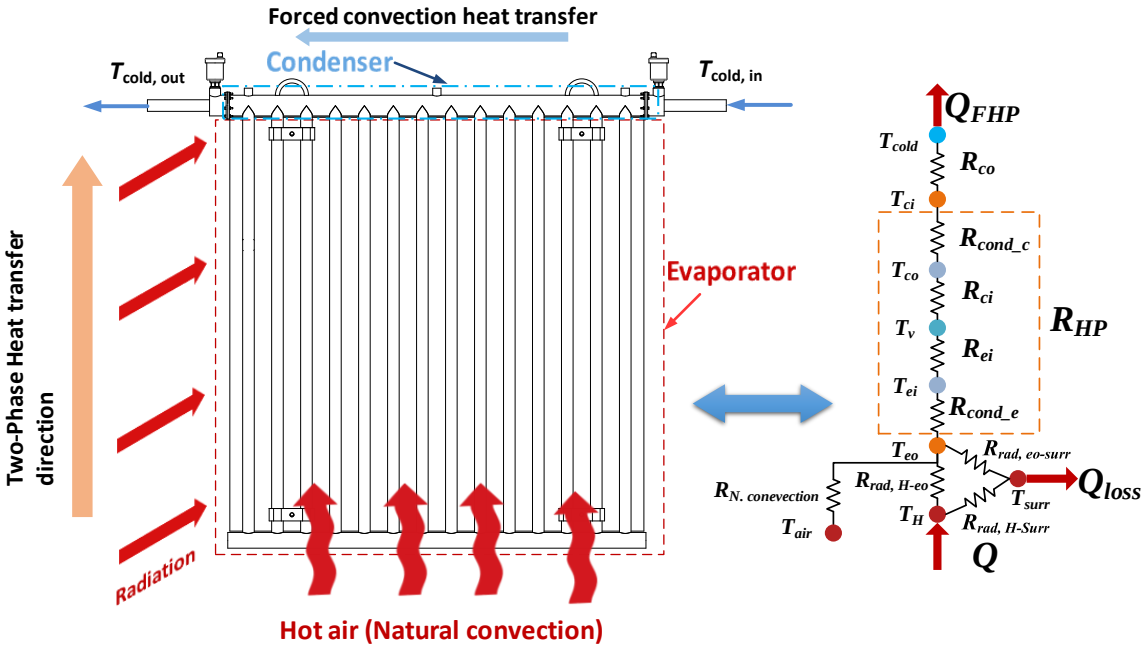

Figure 4-40 Schematic of the thermal resistances modelling of the FHP considering natural convection

Considering the FHP with the back panel as one structure, then the energy balance can be illustrated in Figure 4-41.

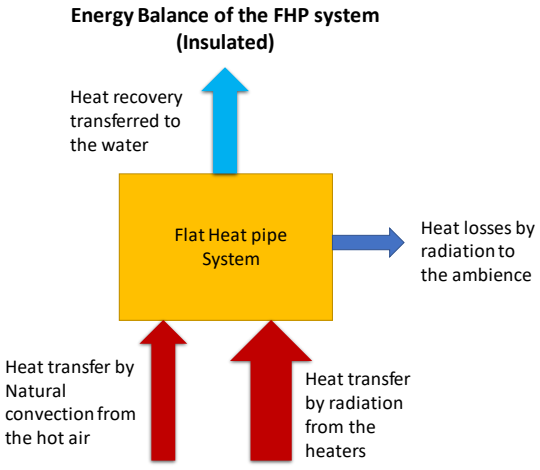

Figure 4-41 Energy balance of the FHP

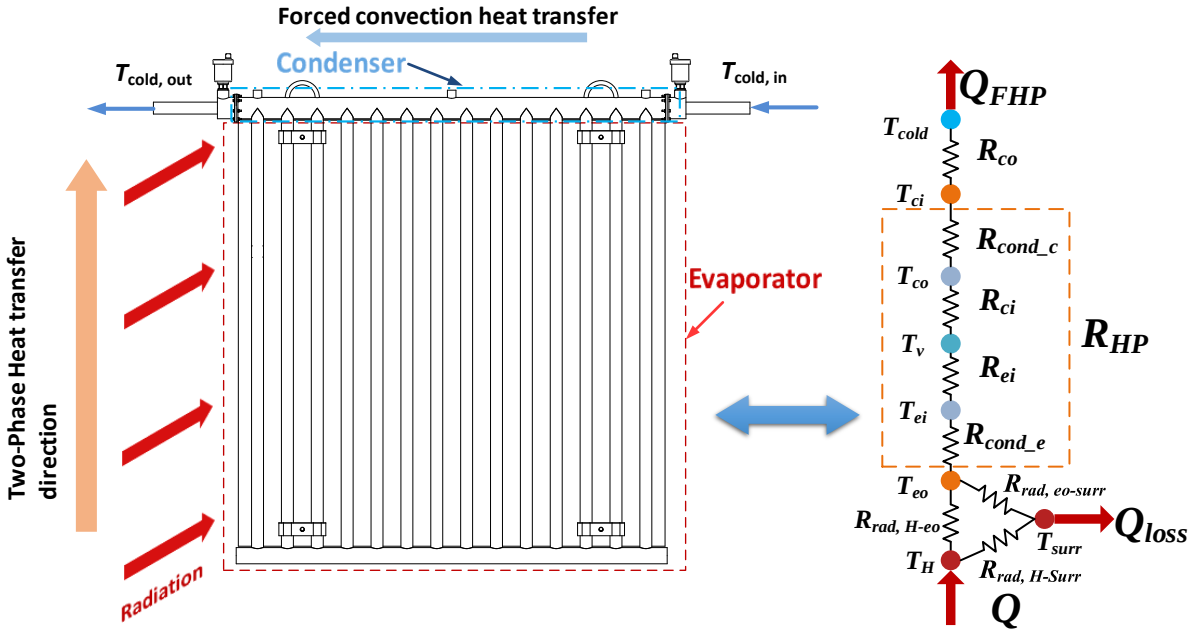

Figure 4-42 Schematic of the thermal network modelling of the FHP neglecting the natural convection

Based on the experiments conducted on the FHP in the laboratory, the radiation thermal resistances circuits are separated into the following cases:

1. FHP experiment with a back panel insulated from the back.
2. FHP without a back panel.
3. FHP with a back panel both black painted and not insulated from the back.

4.8.2 Radiation thermal resistances of the FHP experiment with a back panel insulated from the back

In the FHP test with a back panel insulated, the problem can be simplified by a further step to reduce the number of resistance nodes to three. The back panel was considered as a part of the FHP structure where the FHP forms a hypothetical flat surface to simplify the geometry. Radiation to the FHP surface is represented by the heat received by the highlighted plane in yellow and named (FHP) in Figure 4-43 (a), while the heater plate surface is represented by plane (H) as shown in Figure 4-43 (a).

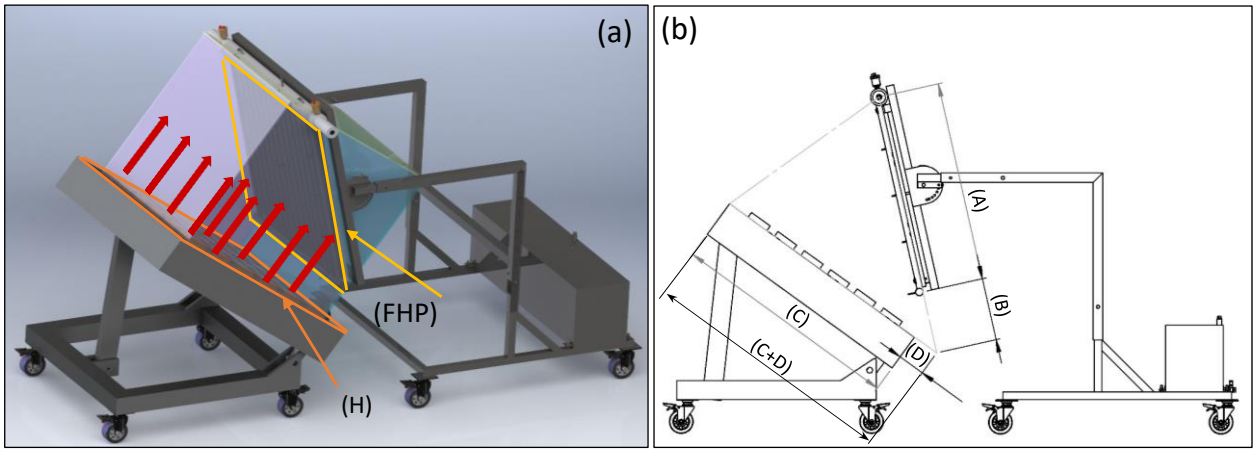

Figure 4-43 Planes nomenclature used in view factor determination

The thermal resistances network modelling is presented in Figure 4-44.

The symbols are again in Figure 4-44:

Node 1: It represents heater plate surface

Node 2: It represents the flat heat pipe

Node 3: It represents the surroundings

E_H: is the heat emitted from the heater surface (W/m²)

E_{eo}: Heat emitted from the evaporator of the FHP surface (W/m²)

E_{surr}: Heat emitted from the surroundings (W/m²)

J_H: Radiosity of the heater surface which is the overall radiation leaving the heater surface (W/m²)

J_{eo}: Radiosity of the evaporator surface which is the overall radiation leaving the evaporator surface (W/m²)

J_{surr}: Radiosity of the surrounding (W/m²)

R_{E_H,J_H}: Heater surface resistance to radiation (m^{-2})

$R_{J_H,J_{eo}}$: Space resistance to radiation between the heaters and the FHP (m^{-2})

$R_{E_{eo},J_{eo}}$: Evaporator surface resistance to radiation (m^{-2})

R_{rad}: Equivalent radiation heat transfer resistance (K/W)

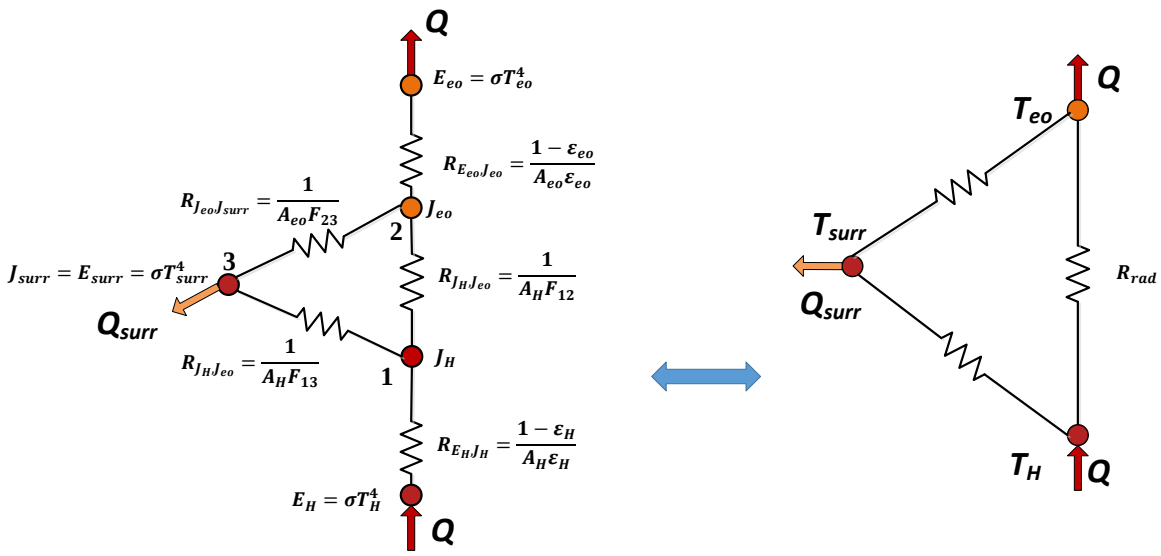

Figure 4-44 Schematic of thermal radiation resistance modelling

The surroundings are considered as a black body at the ambient temperature, the heaters and the FHP surfaces are assumed to be grey, diffuse and opaque. The radiosity and emittance of the surfaces are assumed to be uniform.

The net heat radiation between the heaters and the FHP surface is obtained from the radiation energy balance between the three bodies neglecting the effect of the natural convection through the following steps:

Applying Kirchhoff's law and summing the currents at node 1 in Figure 4-44 yields:

$$\frac{E_H - J_H}{\frac{1-\varepsilon_H}{\varepsilon_H A_H}} = \frac{J_H - J_{eo}}{\frac{1}{A_H F_{12}}} + \frac{J_H - J_{surr}}{\frac{1}{A_H F_{13}}} \tag{4-191}$$

Summing the currents at node 2 yields

$$\frac{E_{eo} - J_{eo}}{\frac{1-\varepsilon_{eo}}{\varepsilon_{eo} A_{eo}}} = \frac{J_{eo} - J_H}{\frac{1}{A_{eo} F_{21}}} + \frac{J_{eo} - J_{surr}}{\frac{1}{A_{eo} F_{23}}} \tag{4-192}$$

At node 3, the ambient temperature is given and since it is a black body then:

$$E_{surr} = J_{surr} = \sigma T_{surr}^4 \tag{4-193}$$

Equation (4-191) after substituting Eq. (4-193) can be rearranged to the following:

$$E_H = J_H + \frac{1-\varepsilon_H}{\varepsilon_H} F_{12} J_H - \frac{1-\varepsilon_H}{\varepsilon_H} F_{12} J_{eo} + \frac{1-\varepsilon_H}{\varepsilon_H} F_{13} (J_H - E_{surr}) \tag{4-194}$$

And from (4-192):

$$E_{eo} = J_{eo} + \frac{1-\varepsilon_{eo}}{\varepsilon_{eo}} F_{21}.J_{HP} - \frac{1-\varepsilon_{eo}}{\varepsilon_{eo}} F_{21}.J_H + \frac{1-\varepsilon_{eo}}{\varepsilon_{eo}} F_{23} (J_{eo} - E_{surr}) \tag{4-195}$$

Equation (4-194) yields:

$$J_H = \frac{E_H + \frac{1-\varepsilon_H}{\varepsilon_H}(F_{12} J_{eo} + F_{13} E_{sur})}{1 + \frac{1-\varepsilon_H}{\varepsilon_H}(F_{12} + F_{13})} \tag{4-196}$$

Equation (4-195) yields:

$$J_{eo} = \frac{E_{eo} + \frac{1-\varepsilon_{eo}}{\varepsilon_{eo}}(F_{21} J_H + F_{23} E_{sur})}{1 + \frac{1-\varepsilon_{eo}}{\varepsilon_{eo}}(F_{21} + F_{23})} \tag{4-197}$$

Hence from (4-196):

$$J_H = \frac{E_H + \frac{1-\varepsilon_H}{\varepsilon_H} F_{13} E_{sur}}{1 + \frac{1-\varepsilon_H}{\varepsilon_H}(F_{12} + F_{13})} + \frac{\frac{1-\varepsilon_H}{\varepsilon_H} F_{12}}{1 + \frac{1-\varepsilon_H}{\varepsilon_H}(F_{12} + F_{13})} J_{eo} \tag{4-198}$$

Hence from (4-198) and (4-195):

$$J_H = \left[\frac{E_H + \frac{1-\varepsilon_H}{\varepsilon_H} F_{13} E_{sur}}{1 + \frac{1-\varepsilon_H}{\varepsilon_H}(F_{12} + F_{13})}\right] + \left[\frac{\frac{1-\varepsilon_H}{\varepsilon_H} F_{12}}{1 + \frac{1-\varepsilon_H}{\varepsilon_H}(F_{12} + F_{13})}\right] \times \left[\frac{E_{eo} + \frac{1-\varepsilon_{eo}}{\varepsilon_{eo}}(F_{21} J_H + F_{23} E_{sur})}{1 + \frac{1-\varepsilon_{eo}}{\varepsilon_{eo}}(F_{21} + F_{23})}\right] \tag{4-199}$$

Eq.(4-199) can be rearranged as follows:

$$J_H = \frac{E_H + \frac{1-\varepsilon_H}{\varepsilon_H} F_{13} E_{sur}}{1 + \frac{1-\varepsilon_H}{\varepsilon_H}(F_{12}+F_{13})} + \frac{\frac{1-\varepsilon_H}{\varepsilon_H} F_{12}}{1 + \frac{1-\varepsilon_H}{\varepsilon_H}(F_{12}+F_{13})} \cdot \frac{E_{eo}}{1 + \frac{1-\varepsilon_{eo}}{\varepsilon_{eo}}(F_{21}+F_{23})} + \frac{\frac{1-\varepsilon_H}{\varepsilon_H} F_{12}}{1 + \frac{1-\varepsilon_H}{\varepsilon_H}(F_{12}+F_{13})} \cdot \frac{\frac{1-\varepsilon_{eo}}{\varepsilon_{eo}} F_{21} J_H}{1 + \frac{1-\varepsilon_{eo}}{\varepsilon_{eo}}(F_{21}+F_{23})} + \frac{\frac{1-\varepsilon_H}{\varepsilon_H} F_{12}}{1 + \frac{1-\varepsilon_H}{\varepsilon_H}(F_{12}+F_{13})} \cdot \frac{\frac{1-\varepsilon_{eo}}{\varepsilon_{eo}} F_{23} E_{sur}}{1 + \frac{1-\varepsilon_{eo}}{\varepsilon_{eo}}(F_{21}+F_{23})} \quad (4\text{-}200)$$

The second and the fourth terms can be added into one term, hence:

$$J_H = \frac{E_H + \frac{1-\varepsilon_H}{\varepsilon_H} F_{13} E_{sur}}{1 + \frac{1-\varepsilon_H}{\varepsilon_H}(F_{12}+F_{13})} + \frac{\frac{1-\varepsilon_H}{\varepsilon_H} F_{12}}{1 + \frac{1-\varepsilon_H}{\varepsilon_H}(F_{12}+F_{13})} \cdot \frac{\frac{1-\varepsilon_{eo}}{\varepsilon_{eo}} F_{21}}{1 + \frac{1-\varepsilon_{eo}}{\varepsilon_{eo}}(F_{21}+F_{23})} J_H + \frac{\frac{1-\varepsilon_H}{\varepsilon_H} F_{12}}{1 + \frac{1-\varepsilon_H}{\varepsilon_H}(F_{12}+F_{13})} \cdot \frac{E_{eo} + \frac{1-\varepsilon_{eo}}{\varepsilon_{eo}} F_{23} E_{sur}}{1 + \frac{1-\varepsilon_{eo}}{\varepsilon_{eo}}(F_{21}+F_{23})} \quad (4\text{-}201)$$

Rearranging Eq.(4-201) yields:

$$J_H = \frac{\frac{E_H + \frac{1-\varepsilon_H}{\varepsilon_H} F_{13} E_{sur}}{1 + \frac{1-\varepsilon_H}{\varepsilon_H}(F_{12}+F_{13})} + \frac{\frac{1-\varepsilon_H}{\varepsilon_H} F_{12}}{1 + \frac{1-\varepsilon_H}{\varepsilon_H}(F_{12}+F_{13})} \cdot \frac{E_{eo} + \frac{1-\varepsilon_{eo}}{\varepsilon_{eo}} F_{23} E_{sur}}{1 + \frac{1-\varepsilon_{eo}}{\varepsilon_{eo}}(F_{21}+F_{23})}}{1 - \left(\frac{\frac{1-\varepsilon_H}{\varepsilon_H} F_{12}}{1 + \frac{1-\varepsilon_H}{\varepsilon_H}(F_{12}+F_{13})} \cdot \frac{\frac{1-\varepsilon_{eo}}{\varepsilon_{eo}} F_{21}}{1 + \frac{1-\varepsilon_{eo}}{\varepsilon_{eo}}(F_{21}+F_{23})} \right)} \quad (4\text{-}202)$$

The radiosity of the heater surface can be determined from Eq.(4-202). The radiosity of the FHP J_{eo} can be determined from (4-197).

By determining J_H and J_{eo}, then, the net heat transfer rate by radiation to the FHP can be calculated from

$$Q_{FHP} = Q = \frac{E_{eo} - J_{eo}}{\frac{1-\varepsilon_{eo}}{\varepsilon_{eo} A_{eo}}} \quad (4\text{-}203)$$

The net radiation is going to be equal to the heat transfer to the water flow at the condenser section.

The losses from the front side of the FHP to the surroundings can be determined from the following equation

$$Q_{FHP-surr} = \frac{J_{eo} - E_{surr}}{\frac{1}{A_{eo} F_{23}}} \quad (4\text{-}204)$$

The view factor of the radiation from the heaters to the FHP F_{12} has to be determined, in order to calculate the radiosity of the heater plate J_H and the heat radiated towards the FHP. The view factor F_{12} can be calculated based on the assumption of considering the FHP with the back panel as one structure. Figure 4-43 (b) illustrates the heaters plate surface represented by dimension (C), while the FHP surface is represented by dimension (A). The view factor from surface (C) to surface (A) can be determined by following the view factor algebra approach, considering the superposition rule and reciprocity rule in radiation heat transfer:

$$F_{H\to FHP} = \frac{1}{A_{(C)}} (A_{(C,D)} F_{(C+D)\to(A+B)} - A_D F_{D\to(A+B)} - A_{(C+D)} F_{(C+D)\to B} + A_D F_{D\to B}) \quad (4\text{-}205)$$

where $A_{(C)}$ is the surface area of heater plate.

The view factors values are calculated using Eq.(4-52) from the catalogue of radiation heat transfer configuration factors [133] which yields:

$$F_{(C+D)\to(A+B)} = 0.5, F_{D\to(A+B)} = 0.782, F_{(C+D)\to B} = 0.188, F_{D\to B} = 0.689 \quad (4\text{-}206)$$

Hence the view factor from the heater plate to the FHP with the back panel attached is:

$$F_{H\to FHP} = \mathrm{F}_{12} = 0.361 \quad (4\text{-}207)$$

From the summation rule, the view factor $F_{H\to surr} = F_{13} = 1 - F_{12} = 0.639$.

The view factor of the FHP to the heater plate can be calculated from the reciprocity rule:

$$F_{FHP\to H} = F_{21} = \frac{A_H F_{12}}{A_{eo}} \quad (4\text{-}208)$$

The view factor of the FHP to the surroundings is calculated using the summation rule:

$$F_{FHP\to Surr} = F_{23} = 1 - F_{12} \quad (4\text{-}209)$$

4.8.3 FHP without a back panel

The thermal radiation resistance network of the FHP without a back panel is the same as in Figure 4-44. However, in this case the heat transfer area of the FHP evaporator A_{eo} is different:

$$A_{eo} = N_{parallel}\pi d_{parallel} l_e + \pi d_{bottom\ collector} l_{bottom\ collector}\ (\mathrm{m}^2) \tag{4-210}$$

where the area of the FHP receiving the incident radiation from the heaters is half of A_{eo} as it receives the radiation from the front face. However, this case does not affect the model as the space resistance between the heaters and the FHP can be calculated from:

$$R_{H,FHP} = \frac{1}{A_H F_{H-FHP}} \tag{4-211}$$

where the view factor F_{H-FHP} is not related to the condition of the back face of the FHP.

From the reciprocity rule:

$$A_H F_{H-FHP} = A_{eo,half} F_{FHP-H,half} = \frac{A_{eo}}{2} \times F_{FHP-H,half} = A_{eo} \times F_{FHP-H} \tag{4-212}$$

It can be seen from Eq.(4-212) that if $A_{eo,half}$ considers the front face only of the FHP, then the view factor of the FHP to the heaters will be twice as large as if we consider the whole FHP surface. This is due to the energy conservation presented in the left side of the Eq.(4-212). The heat transfer area with the surroundings is equal to A_{eo}.

The view factor from the heater plate to the FHP without a back panel was calculated analytically by making an approximation of considering that radiation from heaters incident on the FHP with the back panel consists of the radiation incident on the FHP parallel pipes and the bottom collector, in addition to the radiation from the heater plate to the spaces between the vertical pipes which represents the back panel surface not covered by the parallel pipes. As a result, the view factor for the case of the FHP without a back panel is:

$$F_{H\to FHP(no\ panel)} = F_{H\to FHP} - F_{H\to FHP(spaces)} \tag{4-213}$$

Hence:

$$F_{H\to FHP(no\ panel)} = 0.25 \tag{4-214}$$

The view factor of the heaters to the surroundings is obtained from the summation rule:

$$F_{H\to surr} = F_{13} = 1 - F_{12} = 0.75 \tag{4-215}$$

The view factor of the FHP to the heater plate can be calculated from the reciprocity rule:

$$F_{FHP\to H} = F_{21} = \frac{A_H F_{12}}{A_{eo}} \tag{4-216}$$

considering that A_{eo} is the whole external surface of the evaporator as explained before.

The view factor of the FHP to the surroundings is calculated using the summation rule:

$$F_{FHP\to Surr} = F_{23} = 1 - F_{12} \tag{4-217}$$

4.8.4 FHP with a back panel both black painted and not insulated from the back.

The radiation heat transfer is more complex when the flat heat pipe structure consists of the multi-channel heat pipe with an uninsulated back panel.

The parallel heat pipes with the bottom collector (FHP structure) absorb the heat directly from the heaters and absorb radiative heat emitted and reflected (radiosity) from the back panel. The back panel absorbs the heat and emits it to the FHP and surroundings from the front side and emits the heat to the surroundings from the back side. In addition, the back panel transfers the heat from the back side by natural convection.

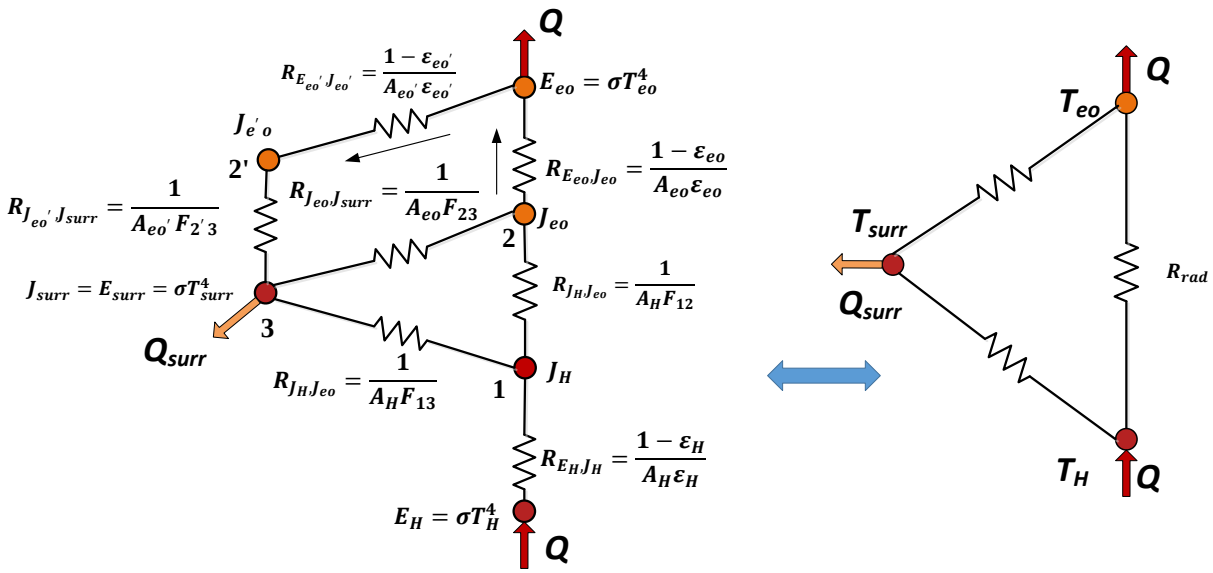

Figure 4-45 Radiation heat transfer modelling for uninsulated FHP

The net heat transfer by radiation considering the heat losses by radiation from the front and the back side is presented as follows:

$$Q = \frac{J_{HP} - E_{sur}}{\frac{1}{A_{HP}F_{23}}} - \frac{E_{eo} - E_{surr}}{\frac{1-\varepsilon_{eo'}}{\varepsilon_{eo'}} + \frac{1}{A_{eo'}F_{2'3}}} \tag{4-218}$$

It can be seen from Figure 4-45 that the surface resistance to radiation of the back panel back surface $R_{E_{eo'},J_{eo'}}$ and the space resistance to radiation between the back face of the back panel and the surroundings $R_{J_{eo'},J_{surr}}$ are in series where

$$R_{E_{eo'},J_{eo'}} = \frac{1-\varepsilon_{eo'}}{\varepsilon_{eo'}} \tag{4-219}$$

and:

$$R_{J_{eo'},J_{surr}} = \frac{1}{A_{eo'}F_{2'3}} \tag{4-220}$$

The view factors are the same for the case of the FHP with insulated back panel.

The view factor of the back panel back surface to the surroundings is $F_{2'3} = 1$.

4.8.5 Heater average temperature

The heaters were assembled on a plate and both were emitting radiation during the experiments. The plate was receiving the heat from the heaters by radiation and conduction. The temperature of the hot source in the thermal model was considered to be T_H which is illustrated in Figure 4-46.

The emitted energy corresponding to the average temperature T_H should be equal to the emitted energy from the heaters at temperature T_{Heater} and the heater plate $at\ temperature\ T_{plate}$.

Thus:

$$E_H = E_{heaters} + E_{plate} \tag{4-221}$$

or

$$\varepsilon_H A_H\ \sigma T_H^4 = \varepsilon_{Heater}\ A_{heaters}\sigma T_{Heater}^4 + \varepsilon_{plate}\ (A_H - A_{Heaters})\ \sigma T_{plate}^4 \tag{4-222}$$

Hence:

$$T_H^4 = \frac{A_{heaters}}{A_H}\frac{\varepsilon_{Heater}}{\varepsilon_H}\ T_{Heater}^4 + \frac{1-A_{heaters}}{A_H}\frac{\varepsilon_{plate}}{\varepsilon_H}\ T_{plate}^4 \tag{4-223}$$

The average temperature T_H was measured experimentally using the thermometer described in chapter 3. The equivalent emissivity was $\varepsilon_H = 0.9$.

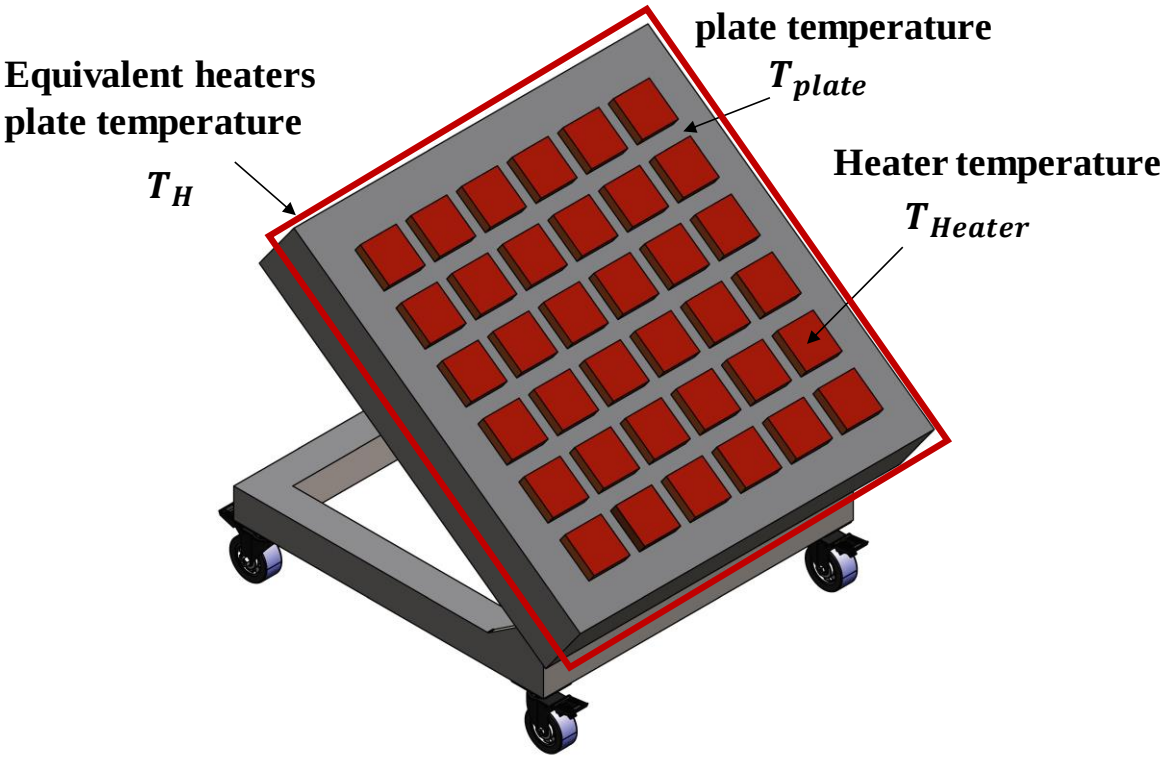

Figure 4-46 Illustration of the average heater plate temperature

4.8.6 Radiation modelling in the factory test

In the factory tests, the hot steel emits the radiative heat in all directions to the FHP, the walls, and the surroundings. The FHP absorbs the incident radiation on the evaporator surface from the hot steel and the hot side walls of the conveyor as shown in Figure 4-47. In addition to the incident radiation, the heat is transferred to the evaporator by forced convection from the hot air blown below the hot steel upwards. The FHP exchanges the heat with the surroundings also.

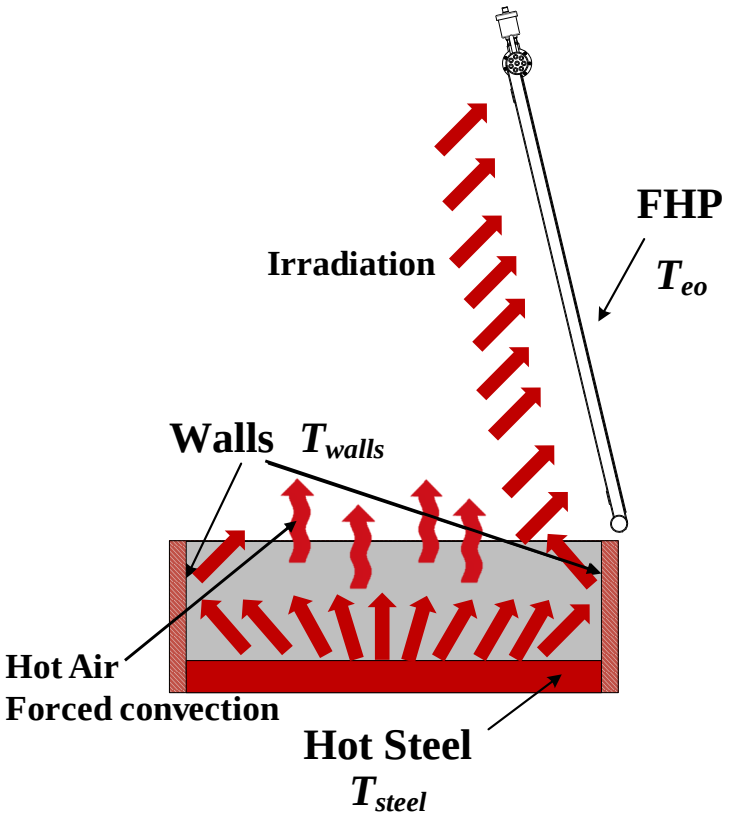

Figure 4-47 Schematic of the radiation incident on the FHP in the factory

4.8.6.1 Thermal radiation modelling of the FHP in the factory

The radiation thermal resistance circuit is shown in Figure 4-48. The FHP with the back panel was considered to form one structure with the same assumption as described for the FHP experiments in the laboratory in order to simplify the modelling. Figure 4-48 presents the simplified thermal radiation resistances corresponding to the temperatures and the actual surface and space radiation resistances.

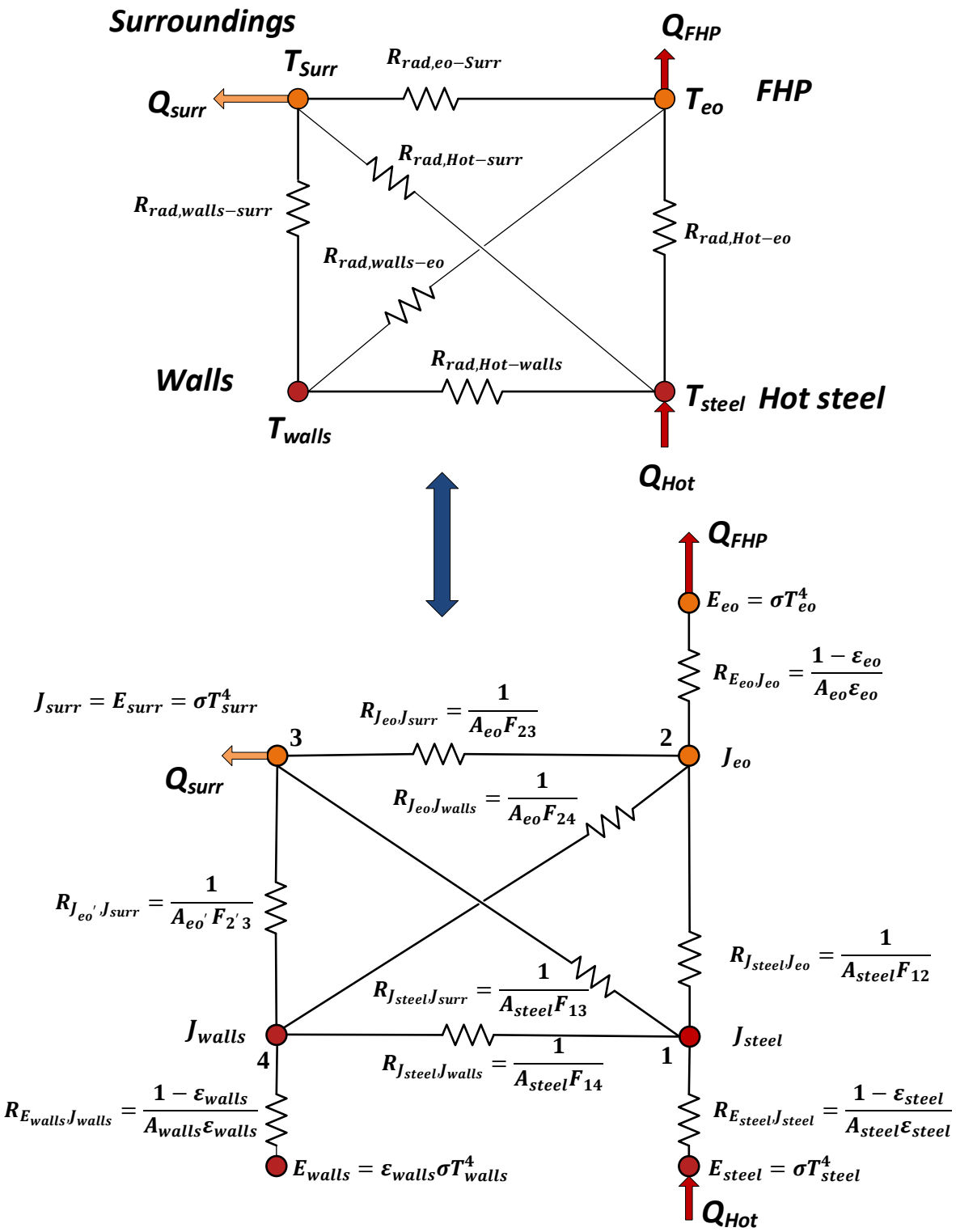

Figure 4-48 A schematic diagram of radiation thermal resistances of the FHP experiments in the factory

The model can be simplified by considering the hot steel and the walls as one structure as shown in Figure 4-49 where the hot source including the walls is represented by the temperature T_H.

The equivalent average temperature of the hot source associated with the hot steel and the walls is

$$T_H = \left(\frac{A_{steel} T_{steel}^4 + A_{walls} T_{walls}^4}{A_H} \right)^{1/4} \quad (4\text{-}224)$$

where A_{steel} is the surface area of the hot steel and the conveyor. A_{walls} is the wall surface area on both sides. Equation Eq.(4-224) was obtained from the energy conservation of radiation emitted by the surfaces. It was assumed that the emissivity values of walls and the steel are equal.

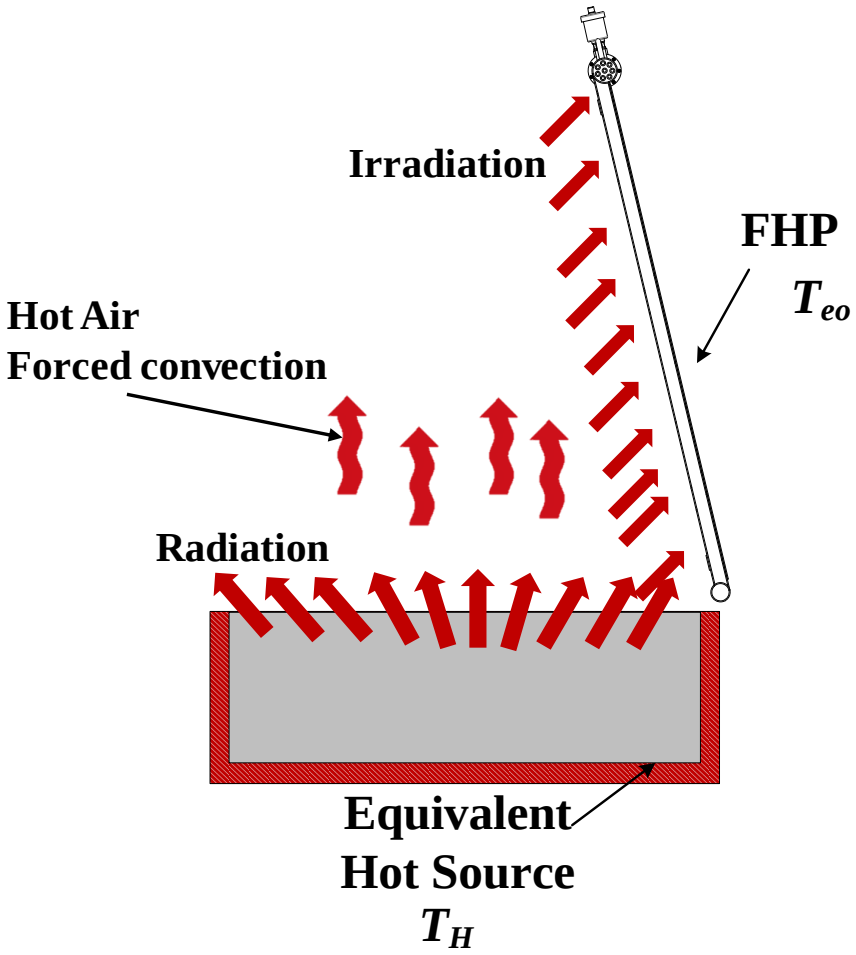

Figure 4-49 A schematic of the radiation heat transfer to the FHP from equivalent hot source

The radiation thermal resistance circuit based on the simplified assumptions is presented in Figure 4-50. It was implemented in the theoretical modelling tool to predict the FHP thermal performance.

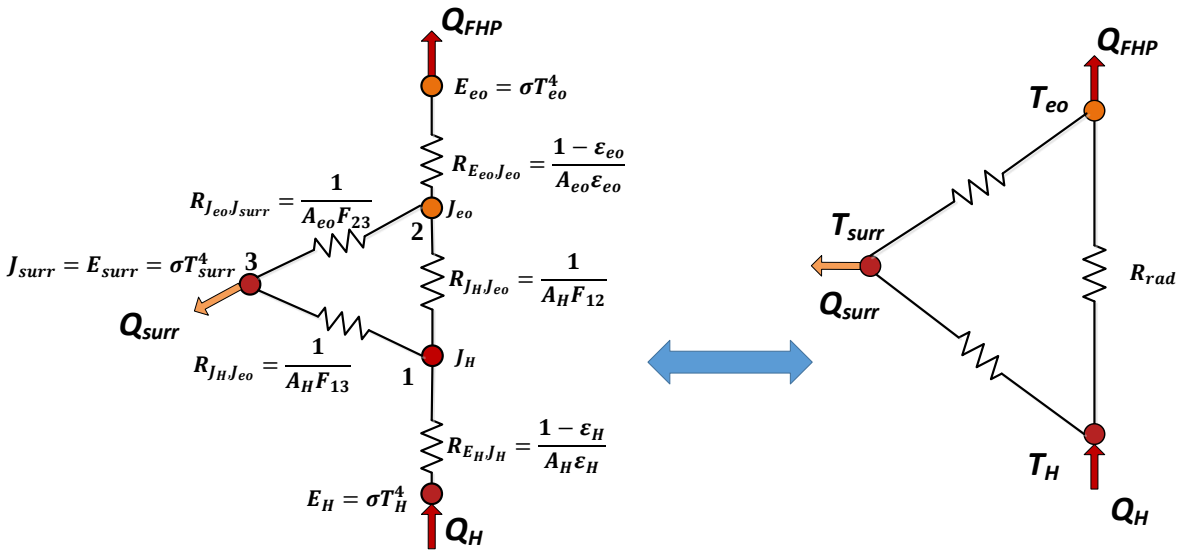

Figure 4-50 Radiation thermal resistances circuit of the equivalent hot source

The view factor of radiation from hot steel and walls to the FHP can be calculated from:

$$A_{walls}F_{42} + A_{steel}F_{12} = A_{eo}(F_{21} + F_{24}) \tag{4-225}$$

where the numbers 1,2,4 in the subscripts are steel, the FHP, and the walls, respectively as shown in Figure 4-48. From the reciprocity and summation rules it can be obtained:

$$A_{eo}(F_{21} + F_{24}) = A_{eo}F_{2\to(4+1)} = A_{eo}F_{2H} = A_HF_{H2} \tag{4-226}$$

Hence:

$$A_HF_H = A_{walls}F_{42} + A_{steel}F_{12} \tag{4-227}$$

Eq.(4-227) is used to determine the space resistance between the hot source and the FHP in Figure 4-50.

4.8.6.2 Steel temperature in the factory

The steel temperature in the factory and the average heat source temperature is discussed in a separate section later.

4.8.6.3 FHP positioning effect on the view factor

The FHP was not aligned perfectly to the conveyor barrier edge during the tests as shown in Figure 4-51. In the first tests of the FHP, the density of wires was very high which led to the FHP being far from the conveyor as shown in Figure 4-51 (a). This procedure was carried out to maintain an acceptable safety margin for the working fluid temperature in the heat pipe from the maximum allowed temperature and to avoid any unexpected increase in the temperature. Ideally, the FHP bottom collector should be aligned above the conveyor with a minimal margin as shown in Figure 4-51 (b). In other tests at the factory, the FHP was tested with the bottom collector above the conveyor.

This height and distance of the FHP from the edge significantly affects the view factor and in some cases the bottom collector was out of the conveyor and shaded from the radiation which also reduced the actual heat transfer area of the FHP receiving the radiation.

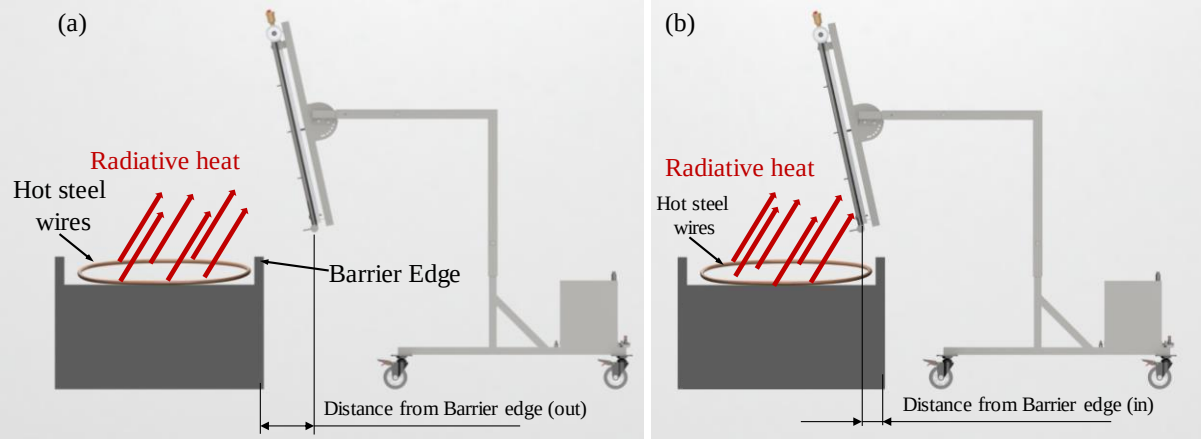

Figure 4-51 Demonstration of the FHP distance from the convertor. (a) FHP placed far from the barrier, (b) FHP placed above the barrier

Forced convection was not considered in the modelling tool to simplify the model. However, it is discussed separately in chapter 5.

4.8.7 Boiling

The working fluid boils at the evaporator, vaporises, and flows towards the condenser section. The heat transfer rate at the evaporator section is represented by:

$$Q = \frac{T_{ei} - T_v}{R_{ei}} \tag{4-228}$$

where:

Q: Heat transfer rate (W)

T_{ei}: Evaporator inner wall temperature (K)

T_v: Vapour temperature which is equal to the saturation temperature (K)

R_{ei}: Thermal resistance of heat transfer by boiling (K/W)

The thermal resistance of boiling can be calculated as follows:

$$R_{ei} = \frac{1}{h_{ei} A_{ei}} \tag{4-229}$$

A_{ei}: Evaporator inner surface area (m²)

$$A_{ei} = \frac{\pi}{2} \times D_{ei} \times L_e \times N_{evaporator\ pipes} + \frac{\pi}{2} \times D_{b.collector} \times L_{b.collector} \quad (4\text{-}230)$$

h_{ei}: Boiling heat transfer coefficient (W/m².K)

Two different regimes of boiling are recognised, the falling film boiling and nucleate pool boiling. Similarly, as presented for the single heat pipe, the energy balance at the evaporator section of the FHP is:

$$Q_{FHP} = Q_{rad} + Q_{N.Convection} = Q_{boi,Nucleate} + Q_{boil,film} \quad (4\text{-}231)$$

If the heat transfer by natural convection is neglected, then:

$$Q_{FHP} = Q_{rad} = Q_{boi,Nucleate} + Q_{boil,film} \quad (4\text{-}232)$$

where the heat transfer by nucleate boiling is calculated from:

$$Q_{boi,Nucleate} = \frac{T_{ei} - T_v}{R_{ei,nucleate}} \quad (4\text{-}233)$$

with the thermal resistance of nucleate boiling calculated from:

$$R_{ei,nucleate} = \frac{1}{h_{ei,nucleate} A_{ei,nucleate}} \quad (4\text{-}234)$$

The heat transfer coefficient of nucleate boiling is calculated using the equations provided in Table 4-1

$$Q_{boi,film} = \frac{T_{ei} - T_v}{R_{ei,film}} \quad (4\text{-}235)$$

where the thermal resistance of nucleate film boiling is expressed as follows:

$$R_{ei,film} = \frac{1}{h_{ei,film} A_{ei,film}} \quad (4\text{-}236)$$

The heat transfer coefficient of nucleate film boiling is calculated using the equations provided in Table 4-2.

The evaporator outer and inner wall temperatures at the liquid pool and the film sections are not equal due to the different individual view factors for the two sections and the energy balance between radiation heat transfer and the boiling heat transfer but the vapour temperature is the same in the equations (4-161) and (4-163).

The theoretical model of the FHP becomes as presented in Figure 4-52.

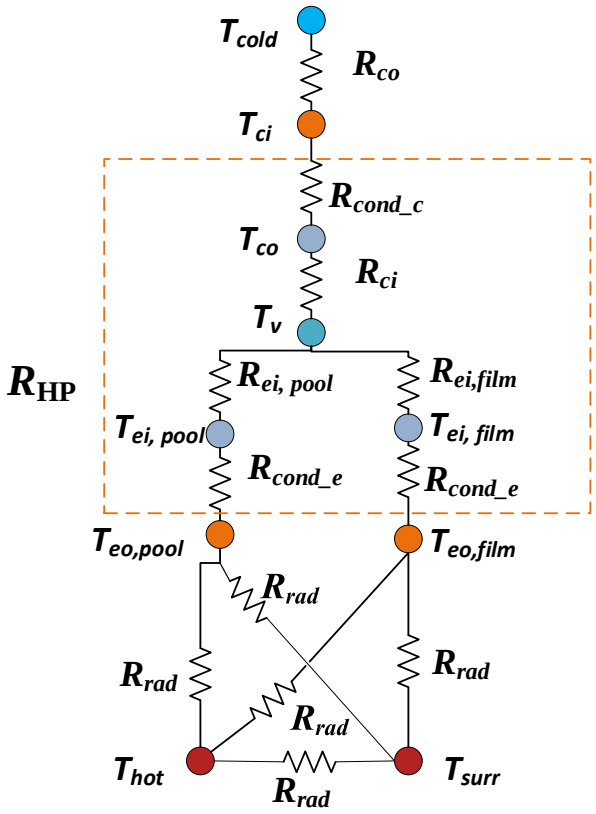

Figure 4-52 FHP resistances model including two regimes of boiling

4.8.8 Condensation

The heat transfer rate by condensation is represented as follows:

$$Q_{co} = \frac{(T_v - T_{co})}{R_{co}} \tag{4-237}$$

where

T_v: Vapour temperature (K)

T_{co}: Temperature of outer surface of the inner tubes

R_{co}: Thermal resistance of heat transfer by condensation

$$R_{co} = \frac{1}{h_{co}.A_{co}}$$

A_{co}: Heat pipe condenser area which represents the overall external surface area of the horizontal tubes in the condenser section (m²).

$$A_{co} = \pi \times D_{co} \times L_c \times N_{water\ tube} \quad (4\text{-}238)$$

D_{co}: Condenser outer diameter (m)

L_c: Condenser length (m)

$N_{water\ tube}$: Number of water tubes

h_{co}: Condensation heat transfer coefficient (W/m².K)

The condensation heat transfer coefficient can be calculated by using the Nusselt correlation Eq.(4-116) in Table 4-3:

$$h_{co} = 0.725 \left[\frac{\rho_l(\rho_l - \rho_v) g h_{fg}^* k_l^3}{D_{co} \mu_l (T_v - T_{co})} \right]^{\frac{1}{4}} \times \frac{1}{N_{tube\ rows}^{1/4}} \quad (4\text{-}239)$$

$N_{tube\ rows}$ is the number of rows of tubes where the condensate drops from the top tube to the tube below it.

Figure 4-53 (A) shows a three-dimensional view of the FHP. Figure 4-53 (B) shows a two-dimensional section of the FHP condenser section. The condensate drops from the top tube to the outer wall surface of the tube below because of the gravitational force and returns to the evaporator. The condensate droplets dropping from the upper tubes increase the condensate film on the lower tubes decreasing the overall heat transfer coefficient.

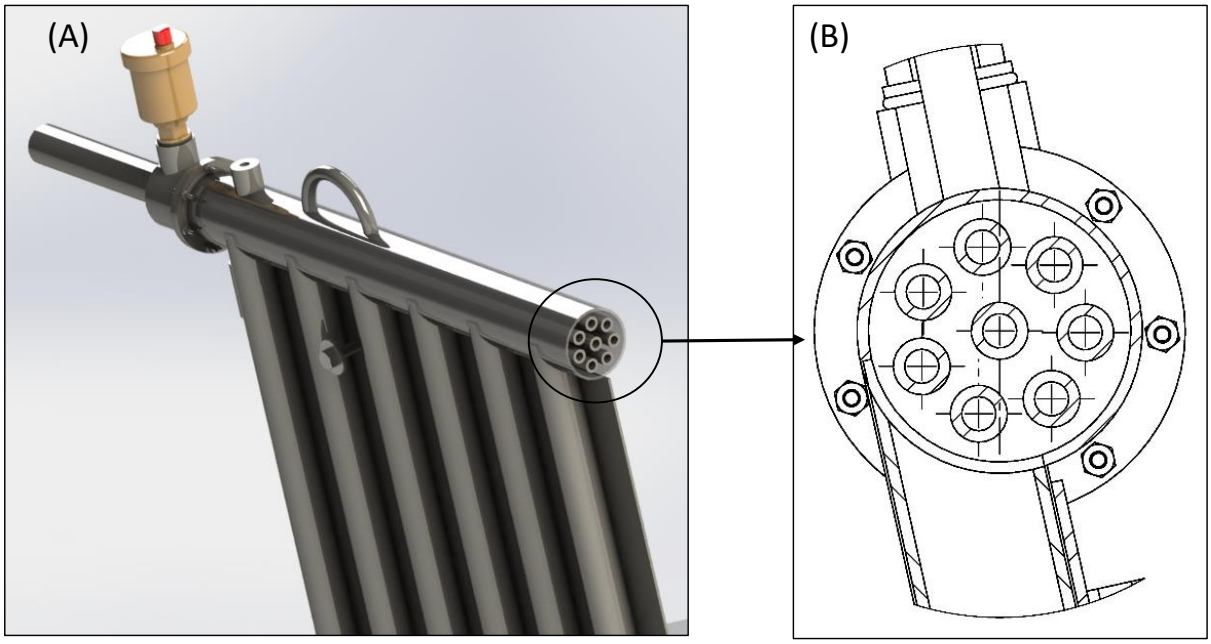

Figure 4-53 :(A) 3D section view of the FHP. (B) Section view of the FHP condenser

4.8.9 Conduction of the walls

The heat transfer by conduction at the evaporator is given as follows:

$$Q = \frac{T_{eo} - T_{ei}}{R_{cond,e}} \tag{4-240}$$

$R_{cond,e}$: The thermal resistance of evaporator wall conductivity is given as follows:

$$R_{cond,e} = \frac{\ln(D_{eo}/D_{ei})}{\pi l_e k_s N_{evaporator\ pipes}} \tag{4-241}$$

D_{eo}: Outer diameter of the evaporator pipes (m)

D_{ei}: Inner diameter of the evaporator pipes (m)

l_e: Length of the evaporator pipes

k_s: Thermal conductivity of evaporator wall (W/m.K)

where the heat transfer area is considered to be half of the cylindrical pipe.

In a similar way, the heat transfer by conduction at the condenser and the thermal resistance of the wall of the condenser are given as follows:

$$Q = \frac{T_{co} - T_{ci}}{R_{cond,c}} \tag{4-242}$$

$$R_{cond,c} = \frac{\ln(D_{co}/D_{ci})}{2\pi l_c k_s N_{water\ tube}} \quad (4\text{-}243)$$

D_{co}: Outer diameter of the condenser tubes (m)

D_{ci}: Inner diameter of the condenser tubes (m)

l_c: Length of the condenser tubes

k_s: Thermal conductivity of condense wall (W/m.K)

4.8.10 Forced convection

Heat is transferred by forced convection from the inner surface of the condenser tubes to the water. The heat transfer rate is expressed as follows:

$$Q_{co} = h_{ci}.A_{ci}.LMTD = \frac{LMTD}{R_{ci}} \quad (4\text{-}244)$$

where:

$LMTD$ is the logarithmic mean temperature of the cooling fluid (K):

$$LMTD = \left(\frac{(T_{ci} - T_{cold,in}) - (T_{ci} - T_{cold,out})}{\ln\left(\frac{T_{ci} - T_{cold,out}}{T_{ci} - T_{cold,in}}\right)} \right) \quad (4\text{-}245)$$

h_{ci}: Heat transfer coefficient of forced convection (W/m².K)

The forced convection heat transfer coefficient is calculated by using the forced convection heat transfer coefficient correlations in Table 4-5 based on the Reynolds number of the flow in the pipes.

The heat transfer rate in the condenser section can be calculated from the following equation also:

$$Q = \dot{m}.C_p.(T_{cold,out} - T_{cold,in}) \quad (4\text{-}246)$$

4.9 Theoretical Modelling tool

Two theoretical modelling tools were built in VBA application programming language where the correlations used to calculate the heat transfer coefficient were programmed in the tool. The first modelling tool was built to predict and analyse the thermal performance of the single heat pipe in the

kiln. A programming code was written to enable the calculation and applying iteration loops until the heat absorbed by the heat pipe is equal to the heat transferred to the water coolant. This required also the programming of the fluid properties in the modelling tool to be evaluated at the working temperature of the working fluid of the heat pipe and the average temperature of the coolant. The second modelling tool was built to predict the performance of the FHP which was based on the thermal model presented in Figure 4-42. The logical flow chart of the programming code of the FHP modelling tool was similar to the one of the single heat pipe. Figure 4-54 presents the flow chart of the modelling tool calculation steps. The user input the geometry of the FHP or the single heat pipe including the lengths of the evaporator and condenser. Then the next step is to input the heater temperature T_H, water inlet temperature and the water flow rate in addition to the temperature of the surroundings. The tool assumes a temperature T_{eo} and calculates the heat transfer coefficients and compare the energy balance between the heat input to the FHP and the heat recovery through the water flow. The tool changes T_{eo} until the energy balance is achieved and then it views the required results including the heat recovery and the temperature of the heat pipes.

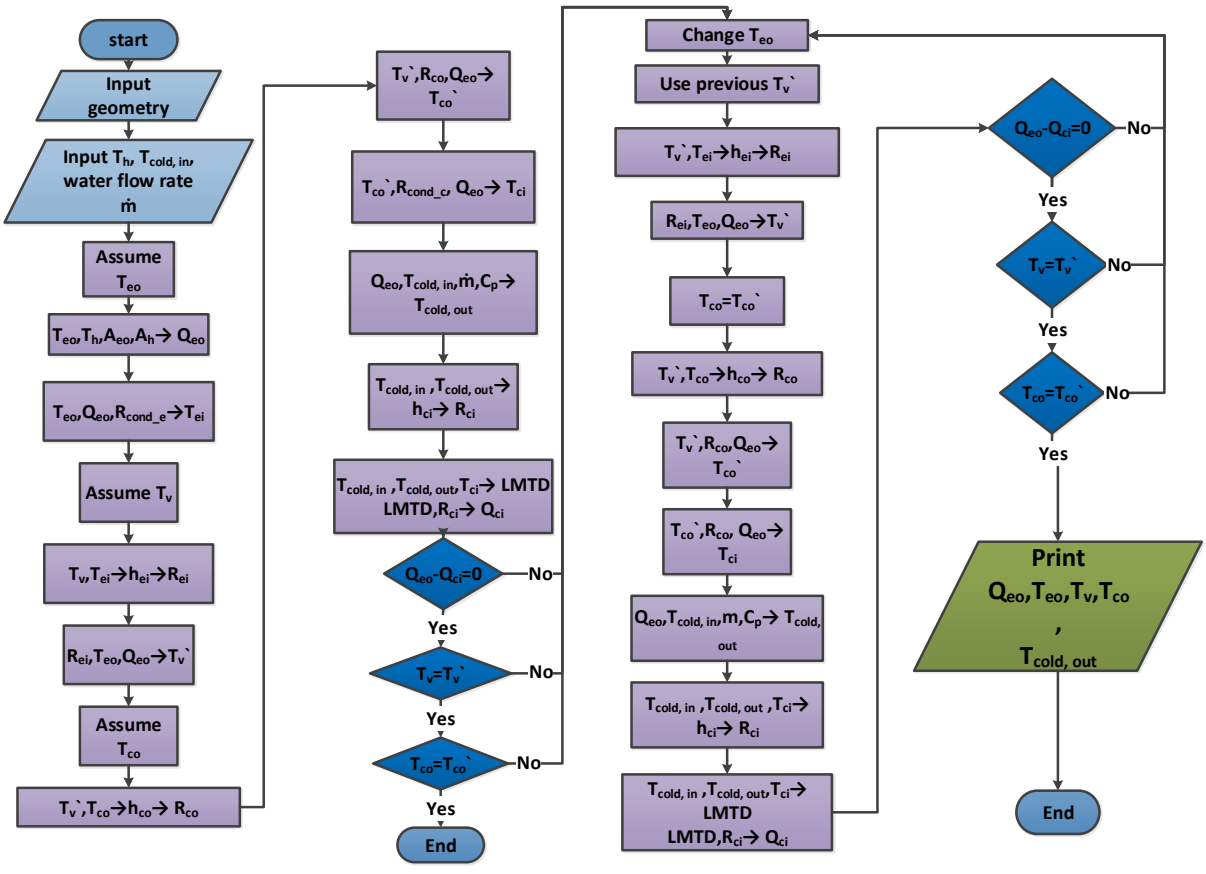

Figure 4-54 Flow chart schematic of the modelling tool algorithm

Chapter 5: Method of Data Analysis

This chapter describes the methodology of analysing the experimental data obtained from the thermocouples and the flow meter during steady state tests. The experimental measurements were then used to calculate the heat recovery and the thermal resistances to validate the theoretical model

5.1 Heat recovery

The heat recovery was measured using the readings of the flow rate and the water inlet and outlet temperatures as follows:

$$Q_{recovery} = m_{water} C_{p,water} (T_{out,water} - T_{in,water}) \quad (5\text{-}1)$$

5.2 Conduction Thermal resistance of the evaporator wall

The conduction thermal resistance was calculated based on the geometry of the evaporator and the thermal conductivity as expressed in the following equation:

$$R_{cond,e} = \frac{\ln(\frac{D_{eo}}{D_{ei}})}{2\pi l_e k_s} \quad (5\text{-}2)$$

5.3 Conduction thermal resistance of the condenser wall

The conduction thermal resistance at the condenser as calculated from the following equation:

$$R_{cond,c} = \frac{\ln(\frac{D_{co}}{D_{ci}})}{2\pi l_c k_s} \quad (5\text{-}3)$$

5.4 Overall conductance of the condenser double pipe heat exchanger

The conductance of the condenser heat exchanger UA was determined using the measured heat recovery, the temperature readings of the water inlet, water outlet, and the vapour temperature of the heat pipe as expressed in the following equation:

$$UA = \frac{\left(\frac{(T_v - T_{cold,in}) - (T_v - T_{cold,out})}{\ln\left(\frac{T_v - T_{cold,out}}{T_v - T_{cold,in}}\right)} \right)}{Q_{recovery}} \quad (5\text{-}4)$$

5.5 Equivalent radiation thermal resistance

The equivalent radiation thermal resistance is dependent on the heater temperature, heat pipe temperature, heater and heat pipe surface emissivity value. If the walls are well insulated and there is no heat loss through walls to the ambient and the walls does not exchange heat with the air then the equivalent radiation thermal resistance should be independent from the inclination angle of the heat pipe due to energy conservation. The equivalent radiation thermal resistance can be determined experimentally based on the heat recovery by radiation Q_{rad}, heater temperature, and the heat pipe temperature.

$$R_{rad,eq} = \frac{T_H - T_{eo}}{Q_{rad}} \tag{5-5}$$

Where Q_{rad} was calculated from the measured heat recovery $Q_{recovery}$ and determining the heat transfer by natural convection theoretically as follows:

$$Q_{rad} = Q_{recovery} - Q_{N.convection} \tag{5-6}$$

The heat transfer by natural convection was determined through the measured air temperature and the average temperature of the heat pipe evaporator as follows:

$$Q_{N.convection} = h_{N.convection} . A_{eo}(T_{air} - T_{eo}) \tag{5-7}$$

Where T_{eo} is the arithmetic average temperature of the heat pipe evaporator.

5.6 Equivalent radiation space resistance

Equivalent radiation space resistance is dependent on the view factor between the heater, the heat pipe, and the walls of the kiln. The radiation space resistance was calculated experimentally after determining the heat recovery by radiation and the emissivity of the heater and the heat pipe through the following equation:

$$R_{space,eq} = \frac{\sigma(T_H^4 - T_{eo}^4)}{Q_{rad}} - \frac{1 - \varepsilon_{HP}}{\varepsilon_{HP} A_{HP}} - \frac{1 - \varepsilon_H}{\varepsilon_H A_H} \tag{5-8}$$

5.7 Average evaporator temperature

The average evaporator temperature was determined from the arithmetic average of the temperature reading from the seven thermocouples place on the external wall of the evaporator.

$$T_{eo} = \frac{T_{E1b} + T_{E1m} + T_{E1t} + T_{E2b} + T_{E2lm} + T_{E2um} + T_{E2t}}{7} \tag{5-9}$$

And then the average temperature of the internal evaporator wall can be determined by substituting the average temperature of the external evaporator wall T_{eo} and using the measured heat transfer rate in $Q_{recovery}$ in the following equation:

$$Q_{recovery} = Q_{cond,e} = \frac{T_{eo} - T_{ei}}{R_{cond,e}} \quad (5\text{-}10)$$

5.8 Boiling heat transfer resistance

The boiling heat transfer resistance can be calculated using one of two methods. The first method is by using the average temperature of the seven thermocouples, or by dividing the evaporator into two regions as a nucleate pool boiling region and falling film region and then the boiling heat transfer is the equivalent resistant of these two regions.

5.8.1 The average boiling heat transfer resistance

The average boiling heat transfer resistance can be determined experimentally from the following equation

$$R_{ei,average} = \frac{T_{ei} - T_v}{Q_{recovery}} \quad (5\text{-}11)$$

Where T_{ei} is calculated based on the average of the readings of the seven thermocouples as follows:

$$T_{ei} = \frac{T_{E1b} + T_{E1m} + T_{E1t} + T_{E2b} + T_{E2lm} + T_{E2um} + T_{E2t}}{7} - R_{cond,e} \times Q_{cond,e} \quad (5\text{-}12)$$

5.8.2 Equivalent Boiling heat transfer resistance

Another method is to consider the effect of the pool nucleate boiling and the nucleate falling film boiling in the evaporator. The evaporator was considered to consist of two separate regions: the pool boiling region and the falling film region where:

$$Q_{ei} = Q_{boi,Nucleate} + Q_{boil,film} \quad (5\text{-}13)$$

The equation can be re-arranged by applying the electrical analogy approach to be

$$Q_{ei} = \frac{(T_{ei,nucleate} - T_v)}{R_{ei,nucleate}} + \frac{(T_{ei,film} - T_v)}{R_{ei,film}} \quad (5\text{-}14)$$

This method requires more thermocouples on the evaporator to increase its accuracy.

The model of Eq(5-14) is illustrated in Figure 5-1.

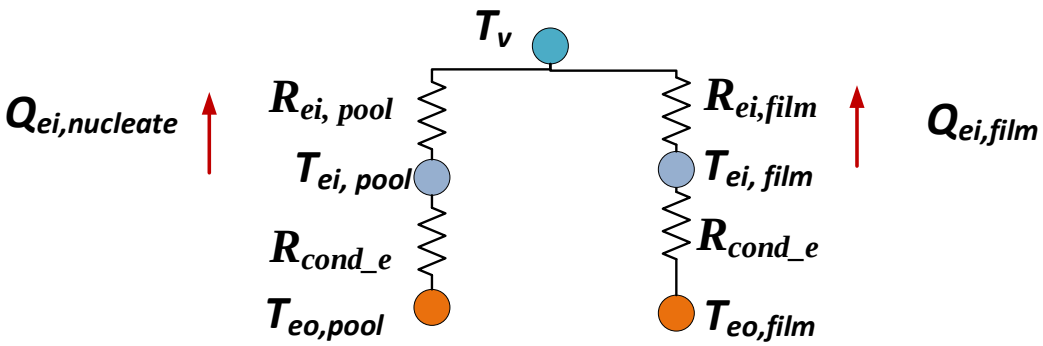

Figure 5-1 Theoretical model of the heat transfer through two regimes, namley nucleate boiling and falling film boiling at the evaporator

The experimental measurement are only the temperature readings of $T_{eo,nucleate}$, $T_{eo,film}$. Thus, in order to calculate the inner wall temperature $T_{ei,film}$, $T_{eo,nucleate}$, for the experimental equivalent thermal resistance, it was needed to assume that the heat flux was uniform along the evaporator surface. In this case, the internal wall temperature of the evaporator was calculated through the modelling of heat transfer by conduction through the evaporator wall as follows:

$$T_{ei,nucleate} = T_{eo,nucleate} - Q_{ei} \times R_{e,nucleate,conduction} \tag{5-15}$$

Where

$$R_{e,nucleate,conduction} = \frac{\ln(\frac{D_{eo}}{D_{ei}})}{2\pi l_{e,nucleate} k_s}$$

$l_{e,nucleate}$ is the length of the evaporator corresponding to the nucleate boiling region which was equal to 0.24 m.

$$T_{eo,nucleate} = \frac{T_{E1b} + T_{E1m} + T_{E2b} + T_{E2lm}}{4}$$

The nucleate boiling surface area was corresponding to the ratio of 0.24/0.413 of the overall evaporator surface area. While the falling film boiling area was corresponding to 0.173/0.413.

The experimental nucleate pool boiling thermal resistance was calculated from:

$$R_{ei,nucleate} = \frac{T_{ei} - T_v}{Q_{ei,nucleate}} \tag{5-16}$$

The experimental nucleate falling film boiling thermal resistance was calculated from:

$$R_{ei,film} = \frac{T_{ei} - T_v}{Q_{ei,film}} \tag{5-17}$$

Hence, the experimental equivalent boiling heat transfer resistance can be expressed as:

$$R_{ei,eq} = \frac{1}{\frac{1}{R_{ei,nucleate}} + \frac{1}{R_{ei,film}}} \tag{5-18}$$

This approximation consider as the two resistances are in connected in parallel to the same evaporator temperature node which can be only applicable when the evaporator temperature difference is less than 3 °C. Therefore, the experimental equivalent boiling thermal resistance was compared with the average boiling thermal resistance in order to validate the effect of the equal heat flux assumption and to verify this approximation.

5.8.3 Theoretical nucleate boiling heat transfer resistance

The thermal resistance of nucleate boiling can be expressed as:

$$R_{ei,nucleate} = \frac{T_{ei,nucleate} - T_v}{Q_{ei,nucleate}} \tag{5-19}$$

The nucleate boiling resistance was calculated by determining the theoretical heat transfer coefficient and solving the following correlations together to achieve the energy balance as follows:

$$Q_{conduction,nucleate} = Q_{ei,nucleate} \tag{5-20}$$

$$Q_{ei,nucleate} = \frac{T_{ei,nucleate} - T_v}{R_{ei,nucleate}} \tag{5-21}$$

$$R_{ei,nucleate} = \frac{1}{h_{ei,nucleate} A_{ei,nuleate}} \tag{5-22}$$

$$Q_{cond,e,nucleate} = \frac{T_{eo,nucleate} - T_{ei,nucleate}}{R_{cond,e,nucleated}} \tag{5-23}$$

$$R_{e,nucleate,conduction} = \frac{\ln(\frac{D_{eo}}{D_{ei}})}{2\pi l_{e,nucleate} k_s}$$

Where $h_{ei,nucleate}$ is the heat transfer coefficient calculated using the prediction correlation.

5.8.4 Theoretical film boiling heat transfer resistance

A similar approach to the nucleate boiling resistance calculation one was followed. The theoretical nucleate falling film heat transfer resistance was calculated by calculated the average evaporator temperature on the internal wall.

The theoretical thermal resistance of nucleate falling film boiling is calculated from solving the following correlations:

$$Q_{conduction,film} = Q_{ei,film} \tag{5-24}$$

$$Q_{ei,film} = \frac{T_{ei,film} - T_v}{R_{ei,film}} \tag{5-25}$$

$$R_{ei,film} = \frac{1}{h_{ei,film} A_{ei,film}} \tag{5-26}$$

$$Q_{cond,e,film} = \frac{T_{eo,film} - T_{ei,film}}{R_{cond,e,film}} \tag{5-27}$$

$$R_{conduction,e,film} = \frac{\ln(\frac{D_{eo}}{D_{ei}})}{2\pi l_{e,nucleate} k_s}$$

It is important to mention that $T_{ei,nucleate}$ and $T_{ei,film}$ are different for each theoretical correlation of the heat transfer coefficient were calculated at. For instance, when $T_{ei,nucleate}$ is calculated using *Rohsenow* [92] correlation will have a different value than the case when it is calculated using *Imura* [100] correlation.

After determining the theoretical nucleate pool boiling and thin film nucleate boiling thermal resistance, the theoretical equivalent boiling thermal resistance was obtained by Eq.(5-18) as a combination of the two resistances. By using Eq.(5-18), the model is based on assuming that the two resistances are in parallel which is not the case in real situation. Nevertheless, this assumption will be evaluated against the average method to show the best combination of correlations which can predict the same value of the thermal resistance as the average method. The value of this assumption that it is easier to be implemented in theoretical predictions for unknown cases than the real model.

The accurate model of the combination between the two boiling regimes cannot be combined in one thermal resistance. This model can predict the heat transfer rate in each boiling regime separately then the overall boiling heat transfer rate is the total of both which is expressed as:

$$Q_{ei} = Q_{ei,nucleate} + Q_{ei,film} \tag{5-28}$$

The equation can be re-written as follows:

$$Q_{ei} = \frac{T_{ei,nucleate} - T_v}{R_{ei,nucleate}} + \frac{T_{ei,film} - T_v}{R_{ei,film}} \tag{5-29}$$

Again $R_{ei,nucleate}$ is calculated theoretically through Rhosenow or Imura correlation of boiling heat transfer. $R_{ei,film}$ is calculated through correlations for nucleate film boiling developed by applying Nusselt theory approach such as Nusselt modified by Rohsenow [114], Jouhara [112], and Shirashi [101].

5.9 Condensation heat transfer resistance

The condensation heat transfer resistance was determined from the following equation:

$$R_{condensation} = \frac{T_v - T_{ci}}{Q_{recovery}} \tag{5-30}$$

Where condenser internal wall temperature T_{ci} was calculated from the following equation:

$$T_{ci} = T_{co} + Q_{recovery} . R_{cond,c} \tag{5-31}$$

Where T_{co} is obtained from following:

$$T_{co} = \frac{T_{out,water} - T_{in,water} . e^{\left(\frac{T_{out,water} - T_{in,water}}{Q_{recovery} R_{co}}\right)}}{1 - e^{\left(\frac{T_{out,water} - T_{in,water}}{Q_{recovery} R_{co}}\right)}} \tag{5-32}$$

Where R_{co} is the heat transfer by forced convection at the outer wall of the condenser.

Forced convection heat transfer resistance

The resistance of forced convection heat transfer is calculated from the following equation:

$$R_{co} = \frac{1}{h_{co} A_{co,total}} \tag{5-33}$$

h_{co} is the heat transfer coefficient by forced convection (W/m²), and A_{co} is the overall surface area of the condenser shell as follows:

$$A_{co,total} = A_{co} + \eta A_{co,fins} \tag{5-34}$$

The heat transfer coefficient was determined using the correlation of Hausen [123].

Chapter 6: Results and Discussion

6.1 Introduction

This chapter presents and discusses the experimental and theoretical results of the experiments conducted on the single heat pipe and the flat heat pipe.

The first section presents and discusses the results obtained from testing the single heat pipe unpainted and painted with black paint. The results comprise the thermocouple temperature readings of the heater, walls, heat pipe evaporator wall, heat pipe vapour working fluid, and the temperature of the water inlet and outlet at steady state. The temperature was presented as a function of the heater temperature and categorised based on the heat pipe inclination angle and surface condition (unpainted and painted). Then the experimental thermal resistances were presented and compared with the theoretical predictions using the correlations presented in chapter 4. Finally, the theoretical results obtained by the modelling tool were compared with the experimental results.

The second section presents the results of the experiments conducted on the FHP in the laboratory with the different conditions presented in the chapter on experimental apparatus. The results presented are the heater temperature, FHP thermocouple temperatures, and water inlet and outlet temperature at steady state. The results were plotted as a function of the heater temperatures and categorised according to the FHP surface condition. This section compares the heat recovery dependence on the experimental conditions with the theoretical values.

The third section presents the results obtained from testing the FHP at the factory with FHP thermocouple temperatures and waste heat recovery presented. The dependence of the results on the steel wire diameter, the distance from laying head and the FHP inclination angle is assessed.

The link between the single heat pipe and the full-scale heat pipe is that the single heat pipe was tested under controlled and fully instrumented environment to characterise the two-phase heat transfer and compare the effect inclination angle on the thermal performance of the heat pipe. The experimental results were used to validate the theoretical model of the heat pipe. The full scale heat pipe differed from the single heat pipe in the dimensions, the ratio of the evaporator area to the condenser area, and the condenser design. The difference in the mechanical design between the single heat pipe and the full-scale heat pipe was considered in the theoretical modelling since it considerably affects the thermal resistances. From a thermal point of view, equivalent radiation thermal resistance was also different. However, the validation of the theoretical model of the single heat pipe indicated the most appropriate correlations to be used in the model of the full scale heat pipe and validated the assumption and validity of the model. The difference between the tests of the

Full FHP at the laboratory and the factory was only the heat source effective temperature, heat source area, view factor, and the emissivity which were also considered the theoretical model.

6.2 Single heat pipe results and discussion

This section presents the results of temperature measurements at steady state, where heater, air and heat pipe vapour temperatures were nearly constant, for the heat pipe both unpainted and with a black paint coating. The results for temperature versus time are only plotted for the case of the vertical heat pipe due to the large number of experiments (a total of 28). The results for the other experiments are presented by the average temperature of each thermocouple during steady state operation. The last part of this section compares and discusses the results obtained by the theoretical correlations and the theoretical model.

It is important to clarify some definitions used in the description of results and discussion. The frequency of temperature change is the number of changes of the temperature reading of a thermocouple between the maximum and minimum value within a certain period. The intensity of temperature change is the same expression of frequency of the temperature variation. The frequency of temperature change corresponds to the frequency of boiling occurring in the evaporator.

The range of temperature variation is the range of the temperature between minimum value and maximum value during the steady state test.

The thermocouples placed on the evaporator were seven thermocouples where placed on the evaporator surface. Three thermocouples were welded on the lower side of the evaporator facing the heater directly. The thermopiles were named *E1b*, *E2m*, and *E2t*, where the number *1* represents the lower side of the evaporator. The letters *b*, *m*, and *u* represent the bottom, the middle, and the top of the evaporator, respectively. Four thermocouples were placed on the upper side of the evaporator and named as follows: *E2b*, *E2lm*, *E2um*, *E2t*. The number 2 represents the upper side of the evaporator. Again, the letters *b*, *lm*, *um*, and *t* represents the bottom, the lower middle, the upper middle, and the top of the evaporator, respectively.

The thermocouple position is illustrated in Figure 6-1 and Figure 6-2. The inclination angle is illustrated in Figure 6-3.

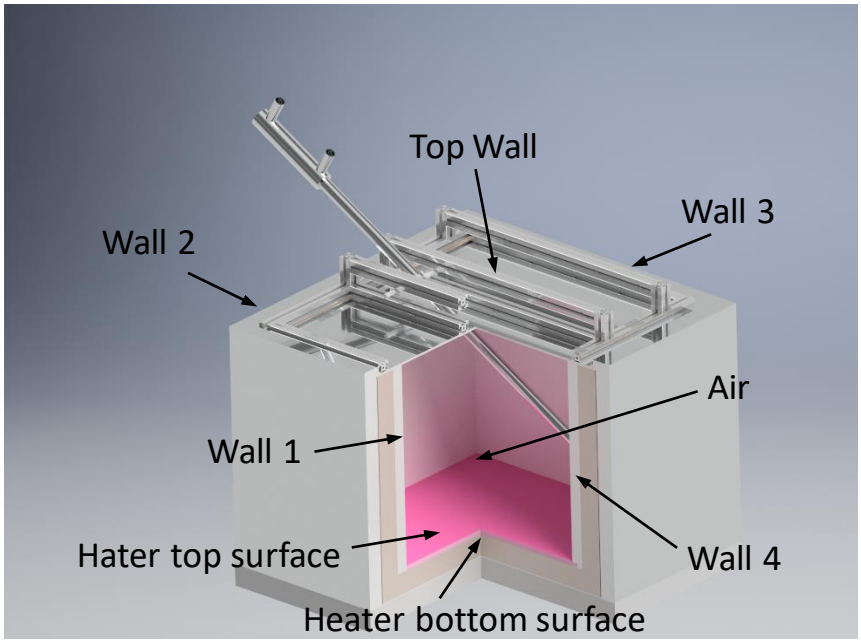

Figure 6-1 Thermocouple positioning in the laboratory kiln

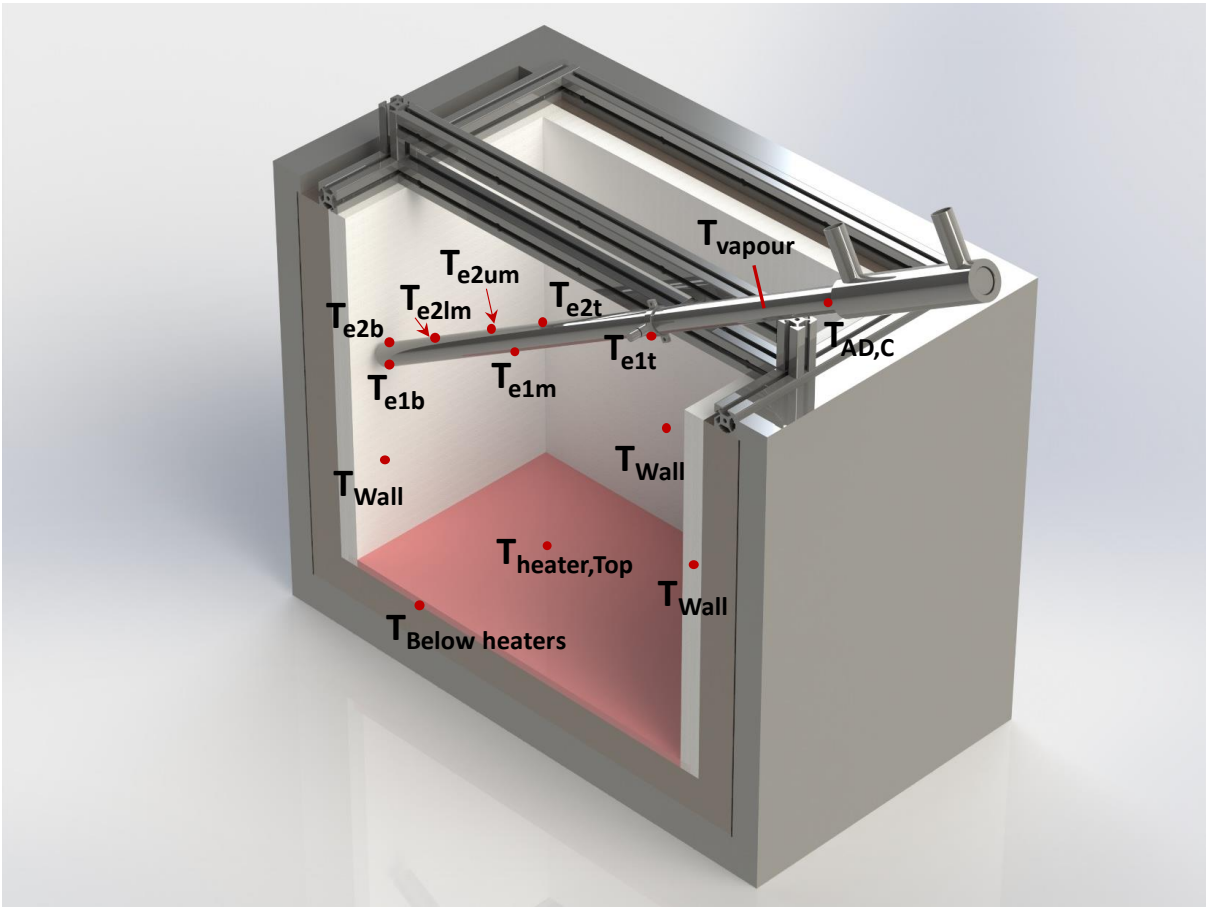

Figure 6-2 Thermocouple positioning on the single heat pipe in the laboratory kiln

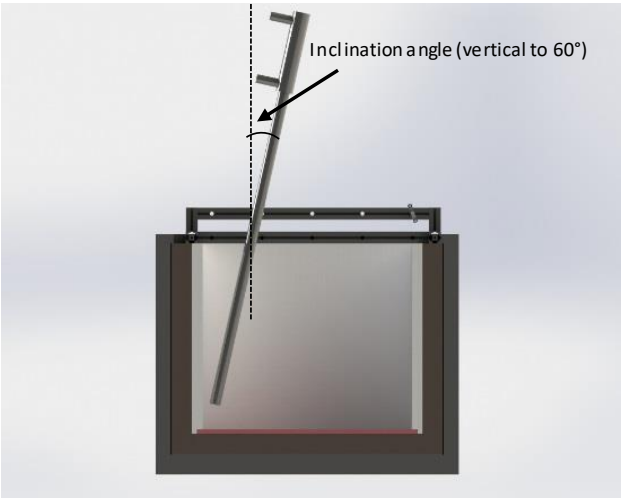

Figure 6-3 Illustration of the inclination angle measured from vertical

6.2.1 Results of experimental temperature measurements without paint

6.2.1.1 Vertical heat pipe

The temperature of the heater, the walls, and the air when testing the single heat pipe at the vertical position are presented versus the heater temperature in Figure 6-4. The heat pipe was tested at heater top surface temperatures of 192 °C, 295 °C, 396 °C, and 496 °C. The temperature of the bottom surface of the heater was higher than the top surface due to the high thermal resistance of conduction of the insulated bottom wall. The bottom surface temperature was higher than top surface by about 33 °C at a heater top surface temperature of 193 °C and this increased to 52 °C at a top surface temperature of 496 °C. The wall temperatures were not measured similarly since thermocouples were installed in the insulation of the walls measuring the temperature in the walls not on the wall surfaces. However, the wall temperature does not affect the radiation heat transfer in the kiln since they were insulated. Wall 1 had the lowest temperature with a maximum temperature of 149.8 °C at a heater surface temperature of 496 °C. The wall which had the highest temperature was the top wall which was a stainless-steel panel insulated from the back side. The temperature of the top wall was close to the air temperature with a temperature difference of 27 °C at a heater surface temperature of 496 °C. The air temperature increased with the increase in the heater surface temperature. The air temperature was 10-25 °C less than the heater surface temperature.

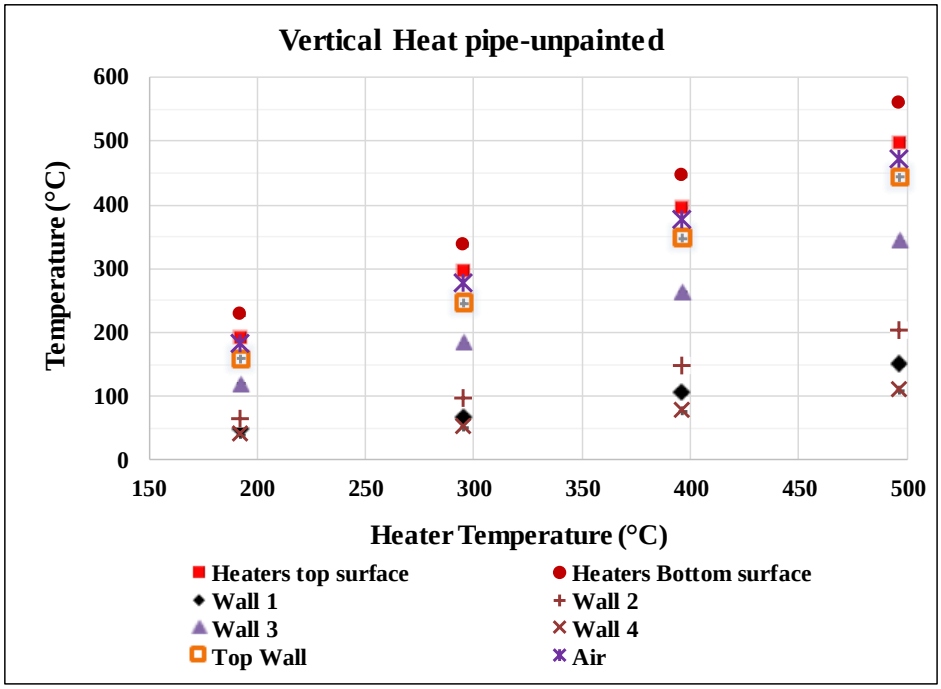

Figure 6-4 Heater and wall temperatures for the vertical heat pipe-unpainted test

The variations of the temperatures of the heat pipe and the water inlet and outlet at a heater temperature of 200 °C are plotted in Figure 6-5. The temperature was changing significantly along the evaporator with time due to the geyser boiling encountered in this experiment. The geyser boiling occurred due to the low heat flux and the high latent heat of vaporisation of the water working fluid in the heat pipe. Moreover, the temperature of the heat pipe was varying in frequent cycles during this time. The thermocouples E1b, E1m, E1t were placed on the evaporator side exposed directly to the radiant heat from the heater while the thermocouples E2b, E2lm, E2um, and E2t were facing the wall and a narrow strip area of the heater. The evaporator temperature increased while the vapour temperature was nearly constant until the geyser boiling took a place. This can be explained by understanding the geyser boiling phenomenon where the liquid filling the lower half of the evaporator was superheated as it can be seen from the thermocouples E1b, E2b, E1m, E2lm, and E2um. The highest temperature was exhibited by E1b at the bottom of the evaporator. A slug bubble starts to grow until the internal pressure is higher than sum of the pressure corresponding to the liquid column and the internal pressure in the heat pipe which corresponds to the saturation pressure of the vapour. Then the bubble which has a diameter equal to the heat pipe diameter suddenly blows up pushing the liquid above it to the condenser section causing the heat pipe to vibrate and making a distinctive sound. The hot expelled liquid raises the temperature of the top half of the evaporator while the temperature at the pool boiling level at the lower half decreases. Then the hot liquid and the condensed vapour at the condenser are mixed and flow back to the evaporator. Then the cycle is repeated resulting in a zigzag temperature curve. This can be clearly seen at thermocouple E2t which

was matching the falling film surface and was at a low temperature close to the vapour temperature. Then once the geyser boiling occurred, E2t and the vapour temperature increased while the temperature of the lower half of the evaporator decreased. However, the thermocouple E1t did not exhibit the same behaviour as E2t since it was oscillating between the vapour temperature and the superheated temperature. It might be that that thermocouple reflected a superheated wall temperature since it was on the evaporator wall at the level of the top wall. Furthermore, the heat flux was not uniform axially nor radially at the evaporator. The maximum was the heat flux was at the two ends of the evaporator and it was less at the middle.

The temperature of E1b varied between 36 °C and 50 °C, while the temperature of E1t varied between 15.6 °C and 42.5 °C. E2t varied between 15.4 °C and 34 °C The vapour temperature varied between 14.5 °C and 34 °C.

It can be noted that the water outlet temperature was higher than the water inlet temperature during the geyser boiling cycle and it suddenly increased when the geyser boiling occurred. The heat flux was determined from calculating an average for the heat recovery obtained from the average temperature difference between the water inlet and water outlet. The average heat recovery was 57 W and the corresponding heat flux was 1.6 kW/m². It can be seen that the geyser boiling cycle was every 180 seconds approximately at the maximum duration .The geyser boiling cycle is shorter than in the results reported by *Jouhara et al.*[134] for a heat flux of 2.17 kW/m², which was every 400 seconds.

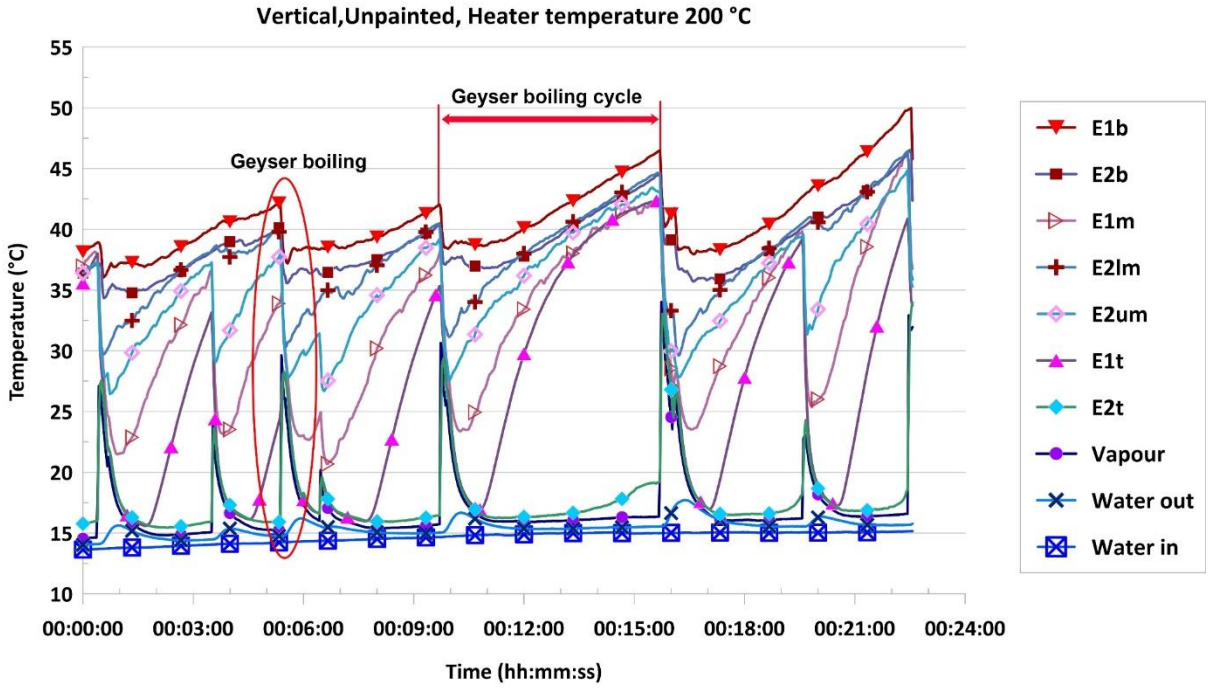

Figure 6-5 Variation of the temperature with time for the vertical unpainted heat pipe at heater temperture 200 °C

The heat pipe temperature measurements at a heater temperature of 300 °C are presented in Figure 6-6. It can be noted that the increase in the heater temperature increased the frequency of the geyser boiling. The oscillation of the temperature reading was less with some sudden higher zigzag-shape reading where E1b varied between 36.3 °C and 55 °C, E1t varied between 18.3 °C and 58.8 °C. The vapour temperature varied between 16.6 °C and 41.4 °C. It can be noted that E1t and E2t did not follow the behaviour of the steam temperature curve at some point of the test where the temperature of the falling film part of the evaporator was increasing until the geyser boiling occurred, unlike the vapour temperature. It might be that top half of the evaporator was dried out because of the high heat flux with respect to the film thickness. However, the geyser boiling continued taking place and thus the falling film boiling occurred again. The average heat flux obtained from the average heat recovery was 3.6 kW/m².

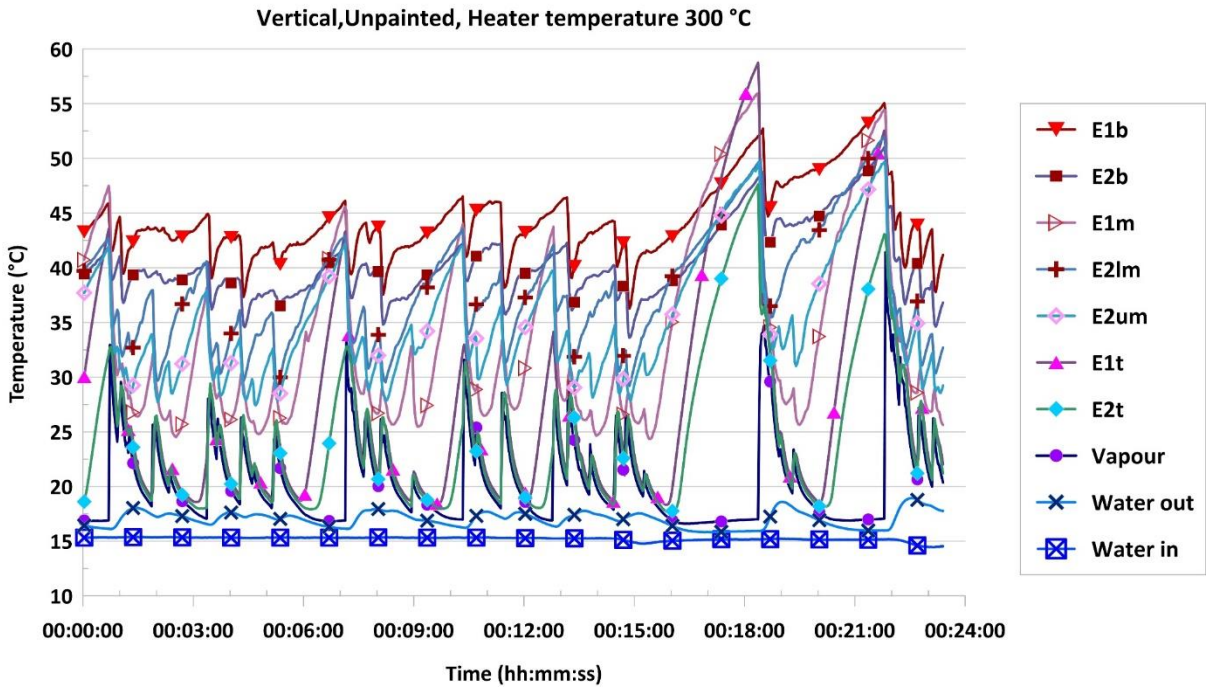

Figure 6-6 Variation of the temperature with time for the vertical unpainted heat pipe at heater temperture 300 °C

Figure 6-7 presents the heat pipe temperature at a 400 °C heater temperature. The increase of the heater temperature improved the performance of the heat pipe remarkably, where the frequency of the temperature oscillation was much higher whereas the temperature change of each thermocouple versus time was less. The reason can be attributed to the nucleation site activated because of the heat flux in this test. E1b was varying between 36.4 and 48 °C and achieved an average reading of 39 °C. E1t varied between 20.4 and 29.5 °C, an average of 25.8 °C. The vapour temperature was oscillating around 23.6 °C as an average value. Moreover, the geyser boiling was rarely encountered during the test and with much less effect than in the previous tests. The average heat flux was 6 kW/m².

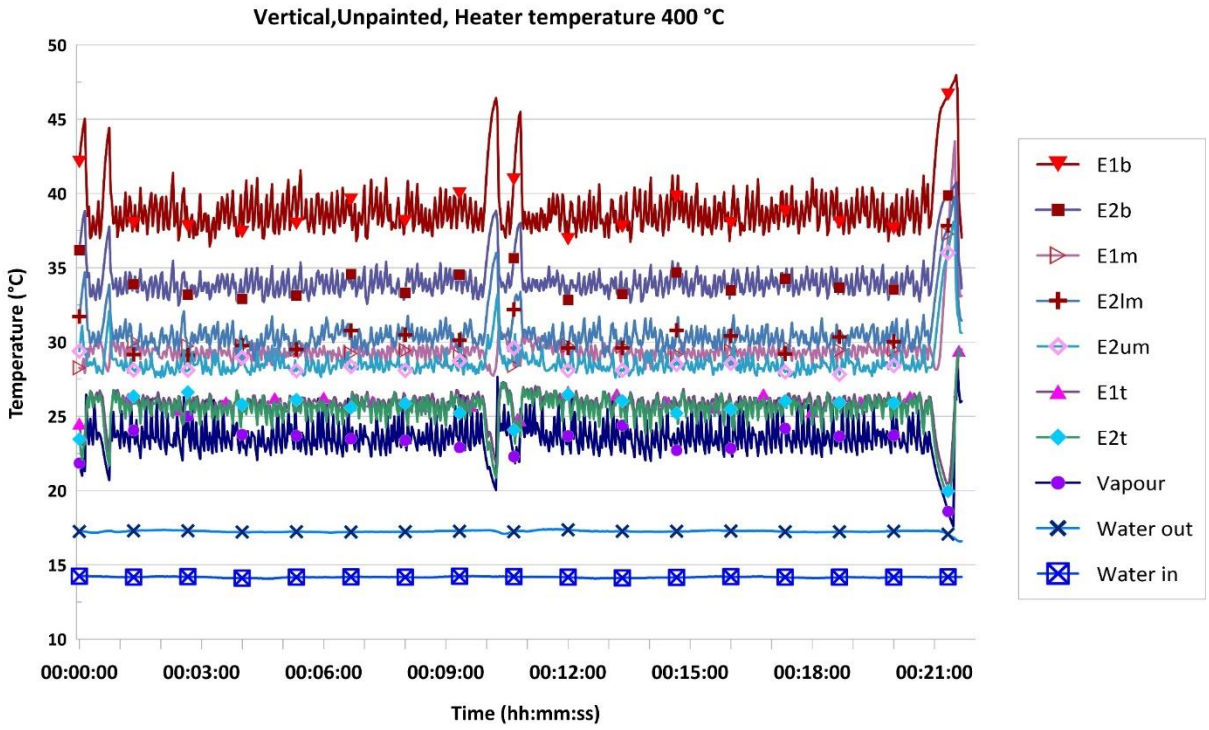

Figure 6-7 Variation of the temperature with time for the vertical unpainted heat pipe at heater temperture 400 °C

The results of the heat pipe and water temperature at a heater temperature of 500 °C are shown in Figure 6-8. The results show a steady condition of the heat pipe performance and the temperature variance is less than in the previous experiments. The experimental heat flux was 9.4 kW/m². The evaporator bottom average temperature E1b was 40.9 °C showing some sudden peaks of 46.4 °C. The average temperature of the evaporator top was 33.8 °C. The average vapour temperature was 29.7 °C.

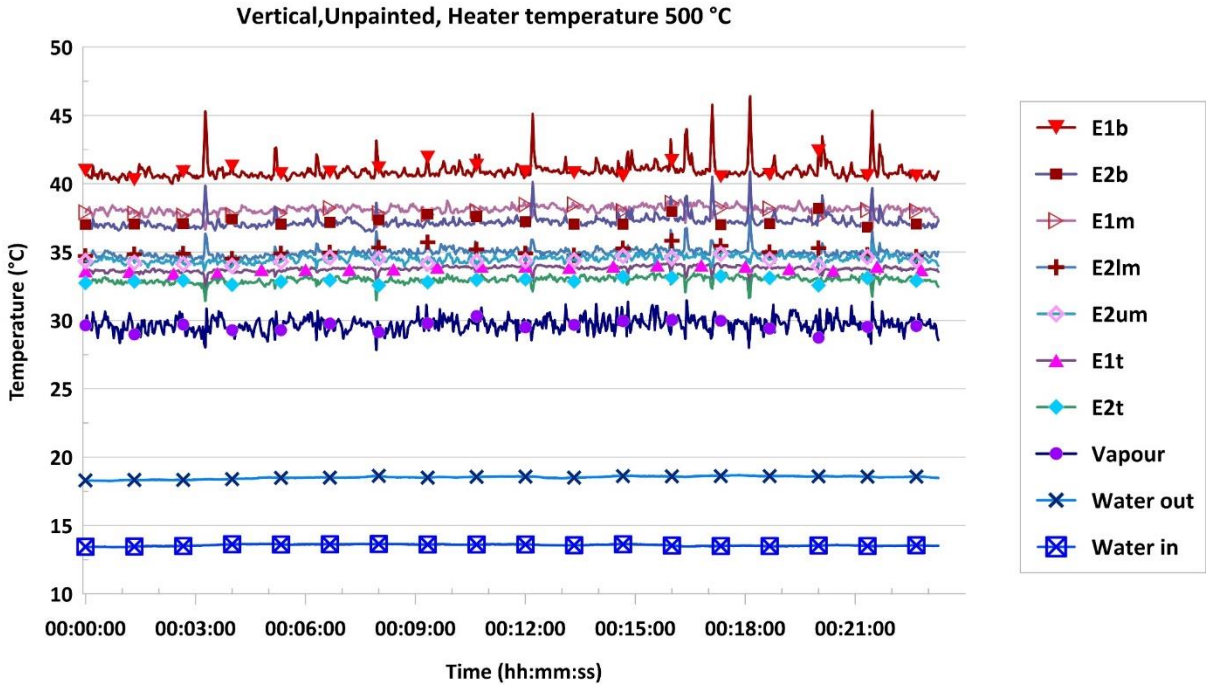

Figure 6-8 Variation of the temperature with time for the vertical unpainted heat pipe at heater temperture 500 °C

The average temperatures measured by the thermocouples placed on the heat pipe in addition to the water inlet and outlet temperatures are presented in Figure 6-9.

When the heater surface temperature was 192°C, the temperature of the evaporator at the bottom was 39.3 °C and decreased gradually along its length to be 16.9 °C at the top of the evaporator. The average vapour temperature was 16.2 °C. The water inlet and outlet temperatures were 14.2 °C and 15 °C, respectively. The axial average temperature variance along the evaporator decreased by increasing the heater temperature which agrees with conclusion drawn from results of the temperature reading as a function of time in the previous figures. The difference in temperature between the bottom and the top of the evaporator decreased to be 7.9 °C at a heater temperature of 496 °C because of the absence of geyser boiling. The difference between the average evaporator temperature and the vapour temperature was also less. The difference between the water inlet and outlet temperature increased from 0.8 °C at a 192°C heater temperature to 4.8 °C at a heater top surface temperature of 496 °C.

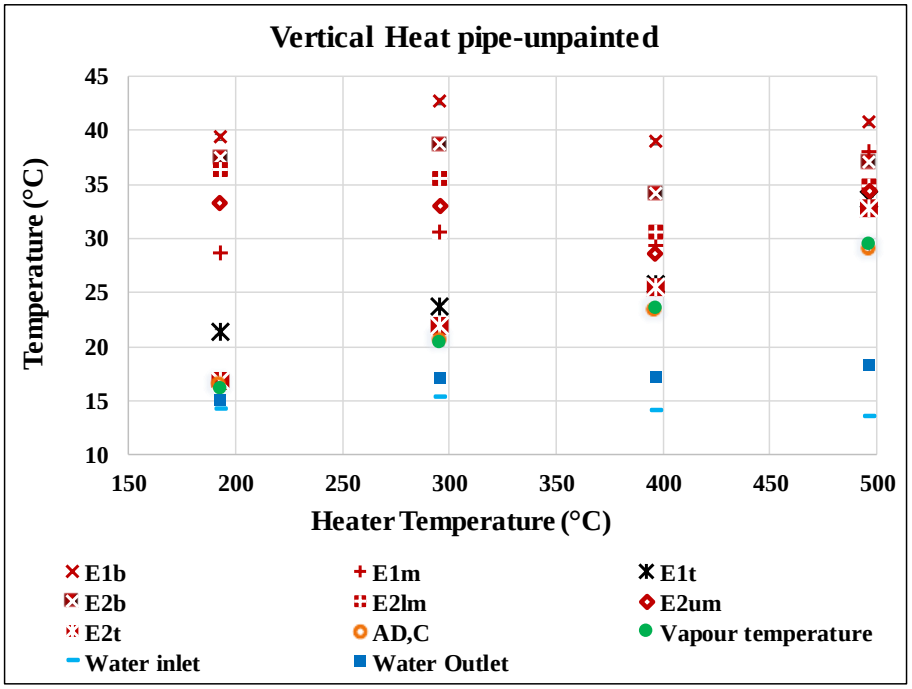

Figure 6-9 Heat pipe and water temperature of vertical heat pipe – unpainted test

6.2.1.2 45° degrees

In the experiment for the 45° inclined unpainted heat pipe without paint, the results of heater and wall temperatures are shown in Figure 6-10. The results obtained are similar to those for the vertical heat pipe with the air temperature less than the heater temperature by approximately 20 °C, and the top wall temperature less than air temperature by about 31°C. The air temperature in this test was less than the air temperature for the vertical position by about 5.8 °C.

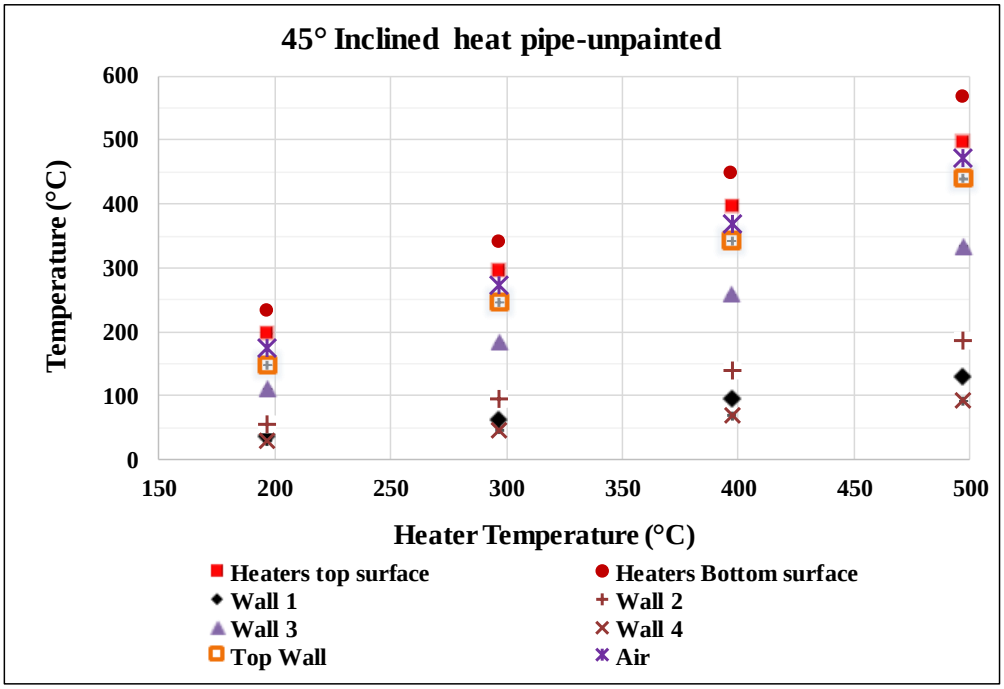

Figure 6-10 Heater and wall temperatures for the 45° inclined heat pipe- unpainted test

The average heat pipe and water flow temperatures are illustrated in Figure 6-11. The heat pipe temperature as function of time is not presented to reduce the total number of figures and because the average temperature can represent a similar conclusion as was shown for the vertical case. Geyser boiling took place in this test until the heater surface temperature exceeded 410 °C which accounts for 6 kW/m² of heat flux. It was noted that the intensity of temperature fluctuations increased with the increase in the heater temperature due to the active nucleation sites. However, the temperature variance of each thermocouple per unit time was decreasing with the increase in the heater temperature. This explains the high temperature of the thermocouple of the top evaporator facing the top wall (E2t) where it measures a superheated wall temperature matching a vapour volume in the evaporator in comparison to the temperature at the bottom of the evaporator due to the geyser boiling, whereas E1t was always close to the vapour temperature due to the falling film boiling. In summary, the temperature distribution was less scattered with the increase in the heater temperature. The maximum temperature difference on the evaporator surface at a heater temperature of 497 °C was 10.6 °C.

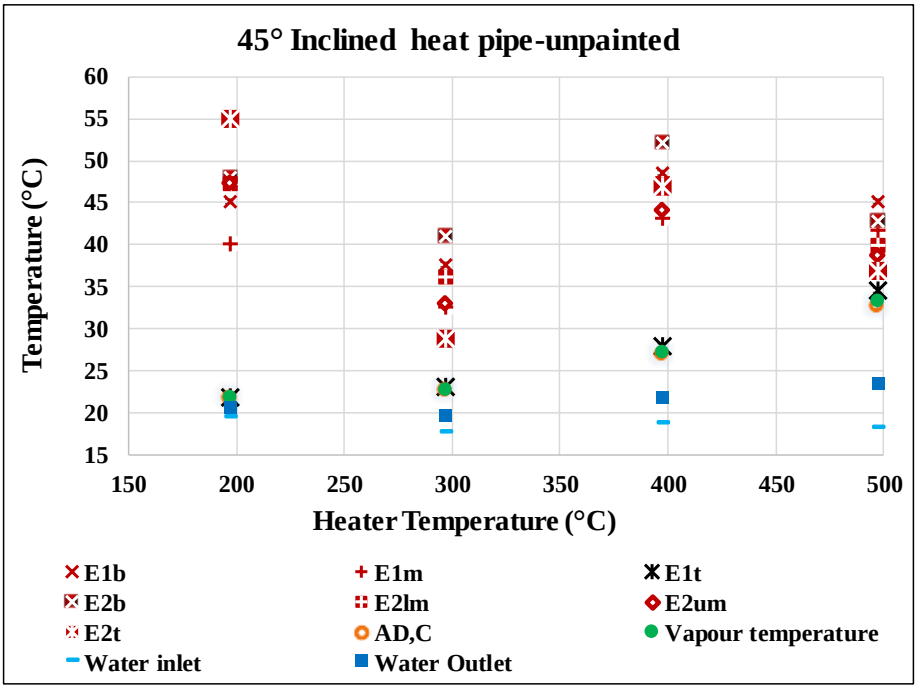

Figure 6-11 Heat pipe and water temperature for 45° inclined heat pipe –unpainted test

6.2.1.3 60° degrees

The temperatures of the heater, the walls and the air in the case of the 60° inclination angle are illustrated in Figure 6-12. The air temperature in this experiment was 5 °C to 14 °C less than the one in the vertical test with similar behaviour of the results. The air temperature depends on the heat throughput to the kiln and the heat transfer to the heat pipe by natural convection and the heat losses to the ambient through heating up the walls. The air temperature was 20 to 34.5 °C less than the heater temperature. The top wall was 43.9 °C and 23.8 °C less than the air temperature at heater temperatures of 200 °C and 500 °C, respectively. The large temperature difference between the air and the wall at a low heater temperature was because the wall absorbed the heat slowly and its temperature increased slowly with the time.

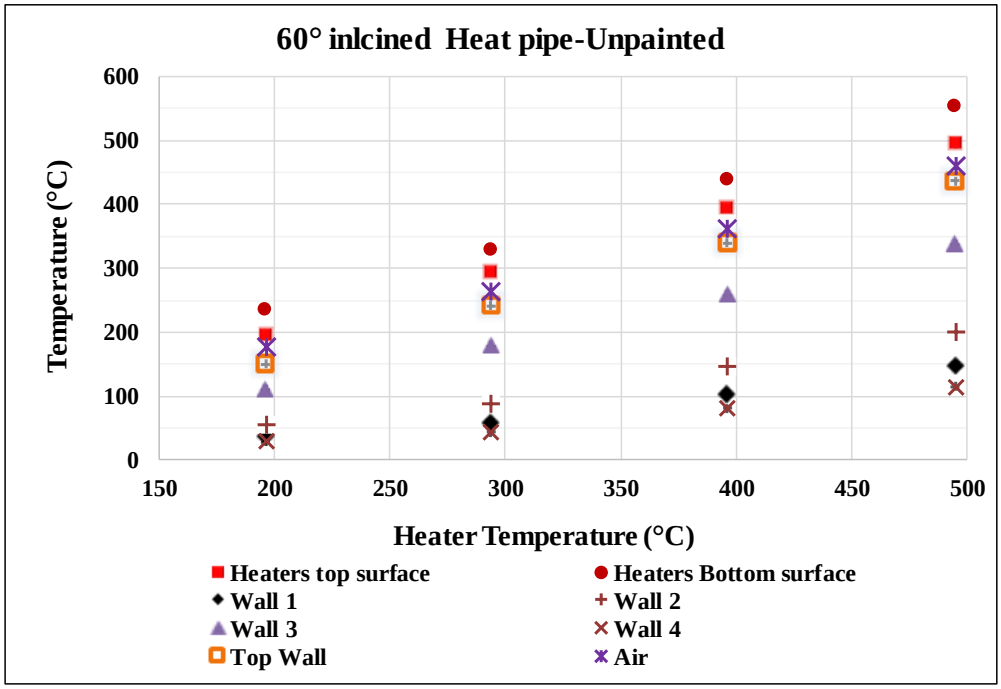

Figure 6-12 Heater and wall temperatures for the 60° inclined heat pipe- unpainted test

The average heat pipe and water inlet and outlet temperatures are presented in Figure 6-13. The water inlet temperature was higher in this experiment depending on the weather for the day of the test. As a result, the vapour temperature of the heat pipe was higher. The temperature distribution along the evaporator length was decreasing from the bottom towards the top. At a heater temperature of 196.1 °C, the thermocouple E2b was 41.8 °C whereas the thermocouple E1b was 39.5 °C. The top of the evaporator E1t was 24.2 °C while the vapour was 22.4 °C. Similar to the test at 45°, E1t was very close to the vapour temperature while E2t exhibited much higher temperatures. The temperature distribution on the evaporator surface at a heater temperature of 495 °C was more uniform with a maximum difference of 5.1°C. This was due to the absence of the geyser boiling unlike what was encountered at lower heater temperatures. The water inlet to outlet temperature difference was 6.2 °C at the same flow rate of other tests of 1 l/min.

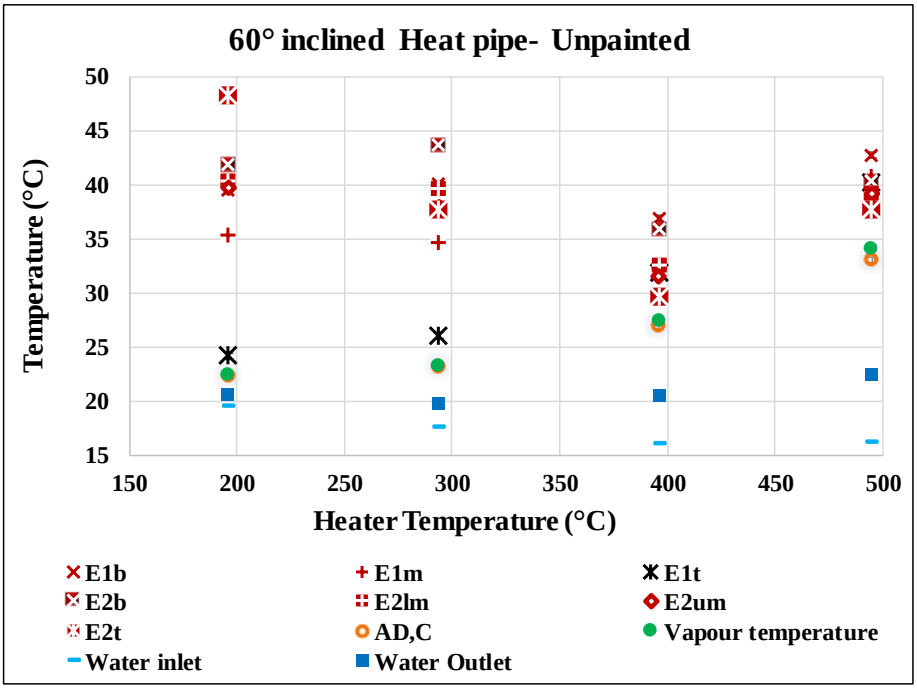

Figure 6-13 Heat pipe and water temperature for 60° heat pipe –unpainted test

6.2.2 Results of experimental temperature measurements with black paint

6.2.2.1 Vertical heat pipe

In the experiment of vertical black-painted heat pipe, the results of heater and wall temperatures are shown in Figure 6-14. The heater temperatures were 197.2 °C, 298.1 °C, 399.3 °C, 496.7 °C. At the heater temperature of 496 °C, the air temperature was 13.6 °C less than the heater temperature and 28°C higher than the top wall temperature.

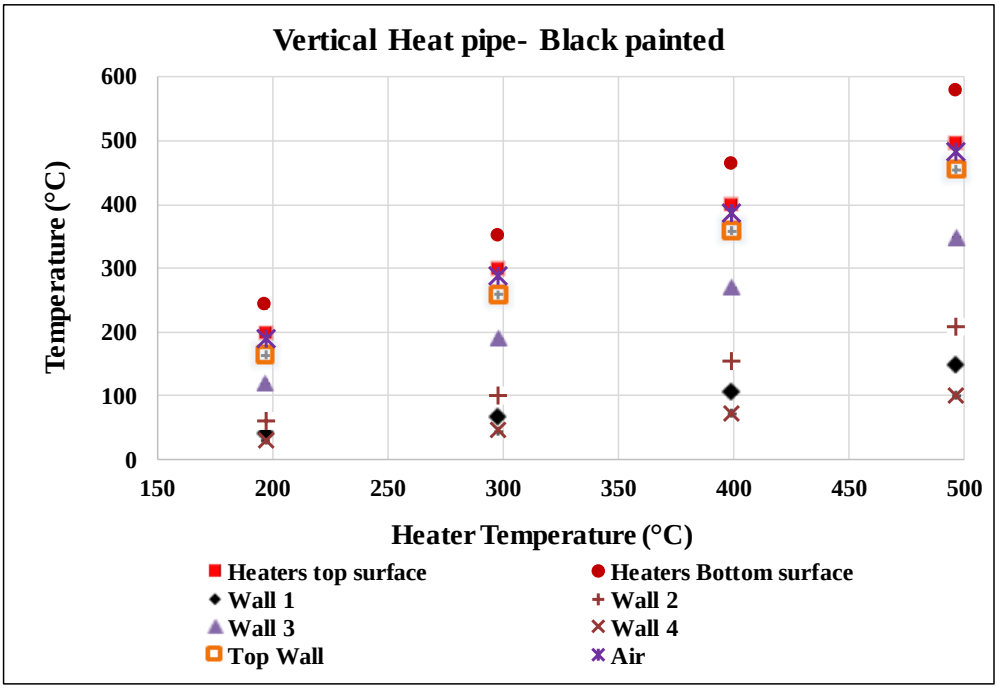

Figure 6-14 Heater and wall temperatures of the vertical heat pipe-black painted test

Figure 6-15 presents the temperature variation as a function of time for of the black-painted heat pipe at vertical orientation at a heater temperature of 200 °C.

The geyser boiling took a place also in this test but with higher intensity and with a shorter geyser boiling cycle because of the higher radial heat flux, and thus the temperature fluctuation was less and the liquid pool was less superheated. The E1b temperature variation was 3 - 5 °C, reaching a maximum reading of 45 °C. The vapour temperature variation was 8 - 12 °C, reaching a peak of 34.1 °C. The average heat flux was 2.7 kw/m².

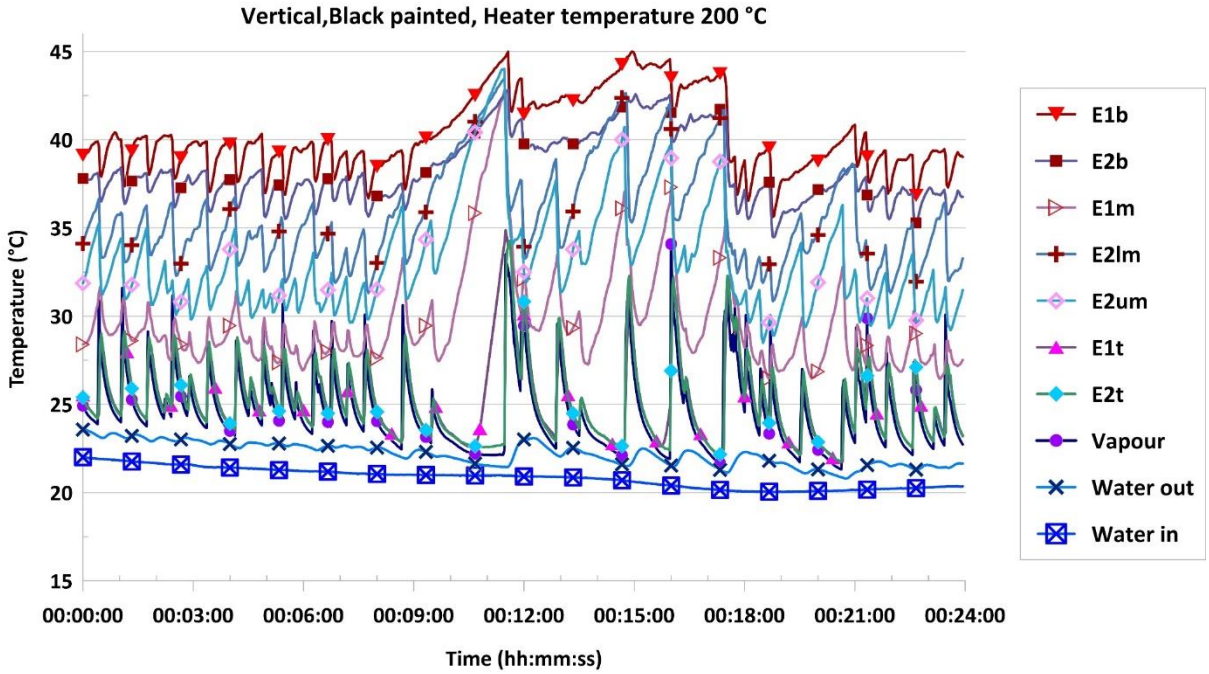

Figure 6-15 Variation of the temperatures with time for the vertical black-painted heat pipe at heater temperture 200 °C

Figure 6-16 shows the variation of the heat pipe evaporator temperature with time at a heater temperature of 300 °C. A steady state can be observed due to the vigorous bubble activity in this test with some sudden geyser boiling occurrences. The temperature variance of E1b was 3 °C while the vapour temperature change was 2 °C. The average heat flux was 5.3 kw/m².

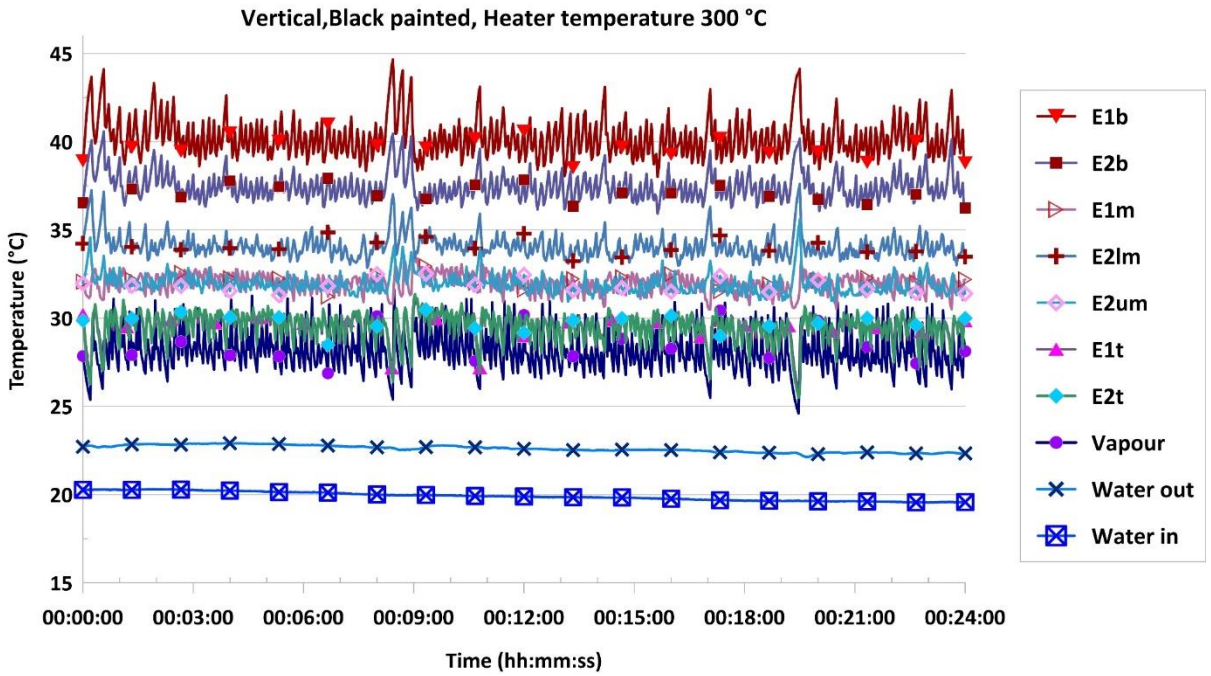

Figure 6-16 Variation of the temperatures with time for the vertical black painted heat pipe at heater temperture 300 °C

Figure 6-17 presents the variation of the heat pipe evaporator temperature as a function of time at a heater temperature of 400 °C. A steady state can be also observed for this test with some rare geyser boiling indicators. The temperature of the heat pipe was changing smoothly following the change in the water inlet temperature. E1b varied between 42 and 51 °C in the test, while the vapour temperature varied between 31.2 °C and 37.4 °C. The calculated heat flux was 9.2 kw/m²

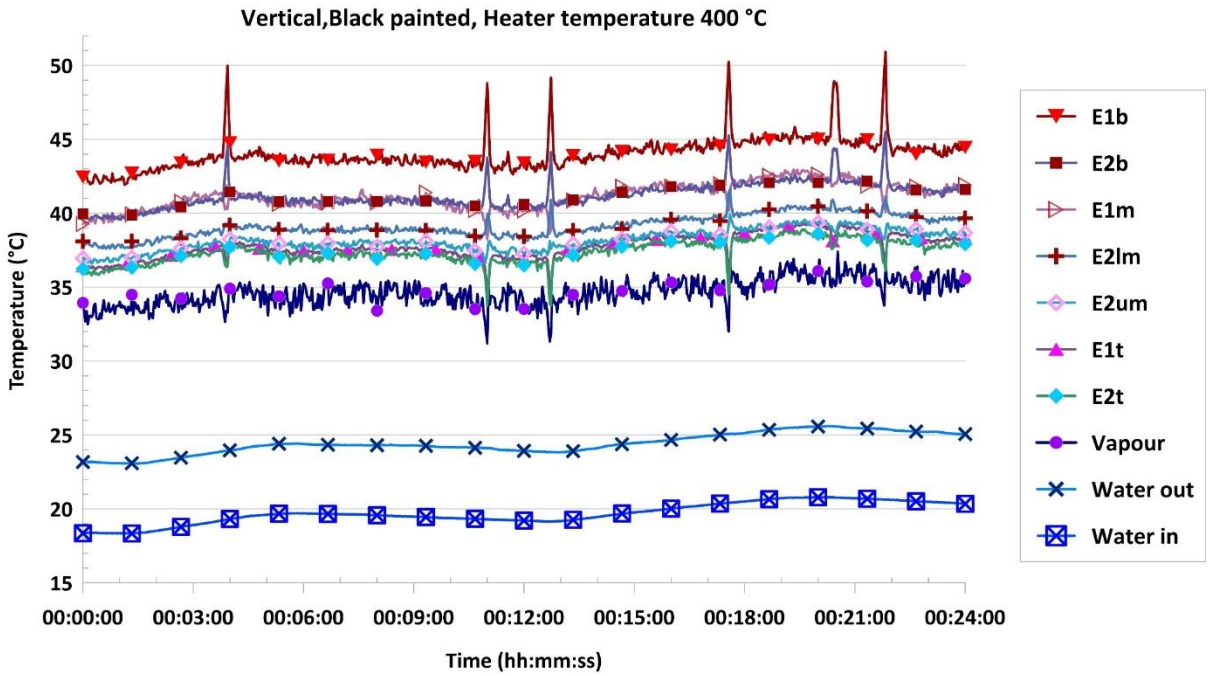

Figure 6-17 Variation of the temperatures with time for the vertical black painted heat pipe at heater temperture 400 °C

Figure 6-18 illustrates the variation of the heat pipe evaporator temperature with time at a heater temperature of 500 °C. The heat pipe exhibited a steady state operation without encountering geyser boiling where the calculated heat flux was 14.2 kW/m². E1b was around an average value of 50 °C, while the vapour temperature was 40.3 °C.

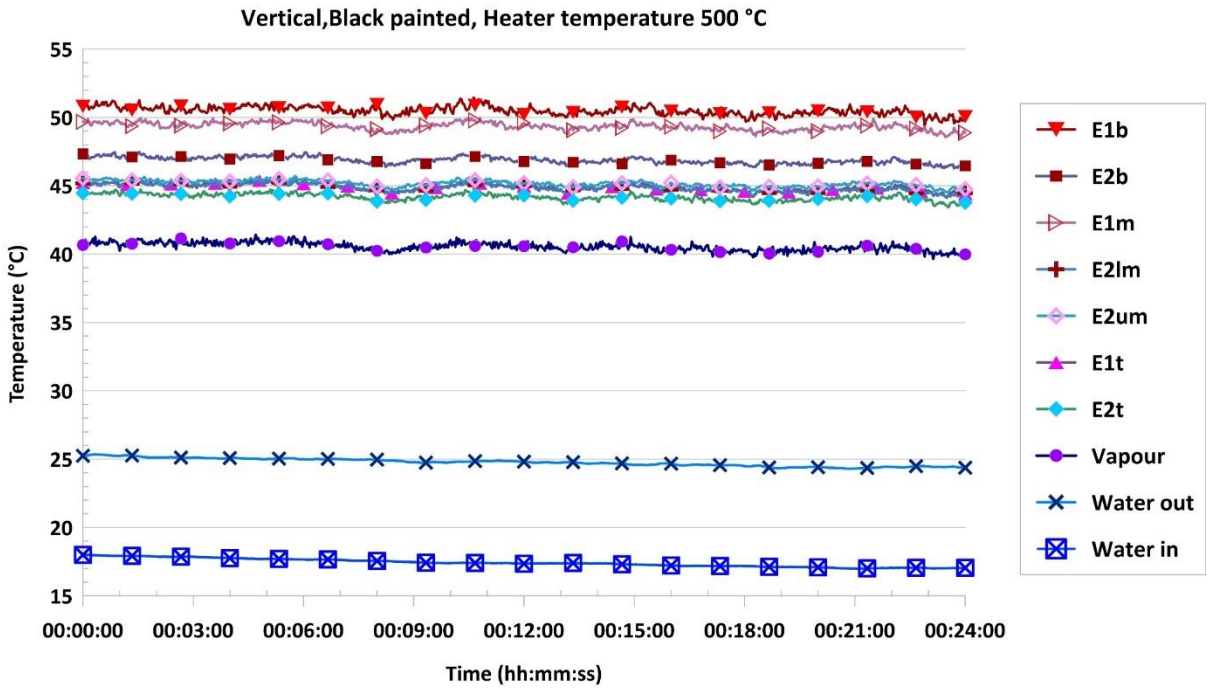

Figure 6-18 Variation of the temperatures with time for the vertical black painted heat pipe at heater temperture 500 °C

The average temperature measurements of the heat pipe and the water inlet and outlet temperatures are illustrated in Figure 6-19. The evaporator thermocouple temperatures were scattered but much less than the case for the unpainted heat pipe. Furthermore, the thermocouples did not exhibit any oscillation or indication of geyser boiling at a heater temperature of 496.9 °C.

Thermocouples E1t and E2t, which indicate the temperature of the falling film of liquid, exhibited a temperature of 25.7 °C at a heater temperature of 200 °C, whereas the vapour temperature was 25.3 °C. It can be seen that E1t and E2t have the same temperature. The temperature variation along the heat pipe evaporator varied between 13.51 °C and 6.27 °C at heater temperatures of 200 °C and 500 °C, respectively. The temperature difference between the evaporator and the vapour was 6 °C at a heater temperature of 496.9 °C because of the absence of geyser boiling. At a heater temperature 500 °C, the temperature difference between E1t and the vapour temperature increased which can be attributed to the increased heat flux and the boiling heat transfer resistance.

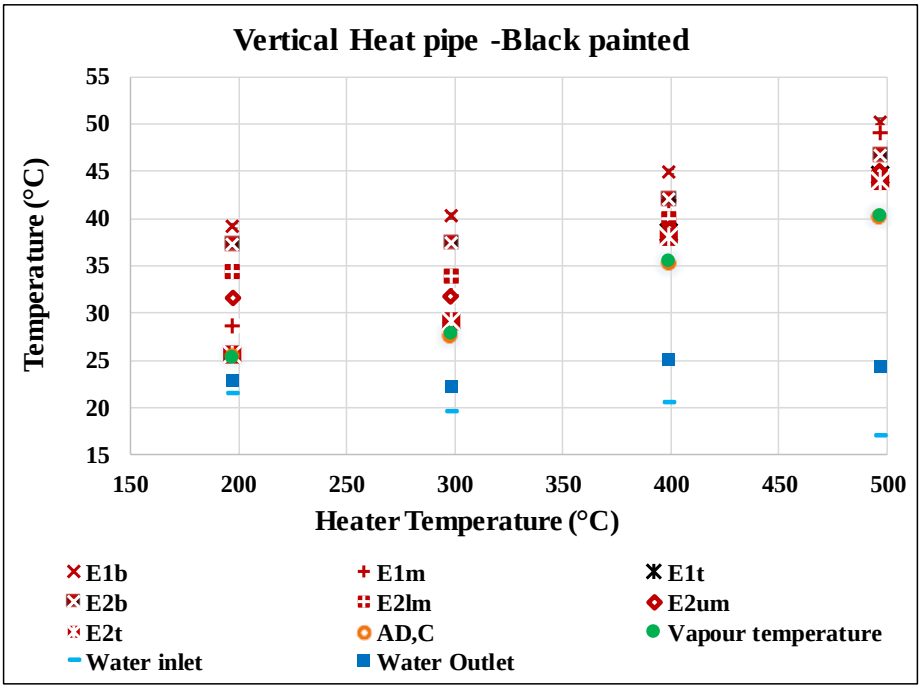

Figure 6-19 Heat pipe and water temperatures of the vertical heat pipe-black painted test

The maximum temperature difference of the outer evaporator wall at vertical orientation for the black painted and unpainted cases is presented in Figure 6-20. The maximum temperature difference is plotted as function of the radial heat flux on the outer wall of the evaporator which was dependent on the heater temperature. The maximum temperature difference was decreasing with the increase of the heat flux due to the increase in the nucleation boiling sites and the minimisation of the occurrence of geyser boiling until it was eliminated when the heat flux was higher than 6 kW/m². Moreover, the heat flux for the painted heat pipe was much higher than for the case of the unpainted one at the same heater temperature. It can be noted that the maximum temperature difference for the black painted heat pipe is less than for the unpainted one's lower heat flux. For example, at a heat flux of 3.4 kW/m² for the unpainted case, the maximum temperature difference was 20.7 °C, while for a heat flux of 2.7 kW/m² for the black-painted heat pipe, the maximum temperature difference was 13.5 °C. In both cases, the temperature difference was due to the superheated liquid resulting from the geyser boiling phenomenon. Furthermore, the maximum temperature difference of the evaporator surface was 6.3 °C at a heat flux of 14.2 kW/m², which was achieved for a black painted heat pipe, although the heat pipe did not exhibit any geyser boiling indication. This value of temperature difference can be attributed to the fact that the heat pipe was exposed to neither a radial uniform heat flux nor an axial one where the back half of the evaporator was receiving a minimum heat flux of radiation.

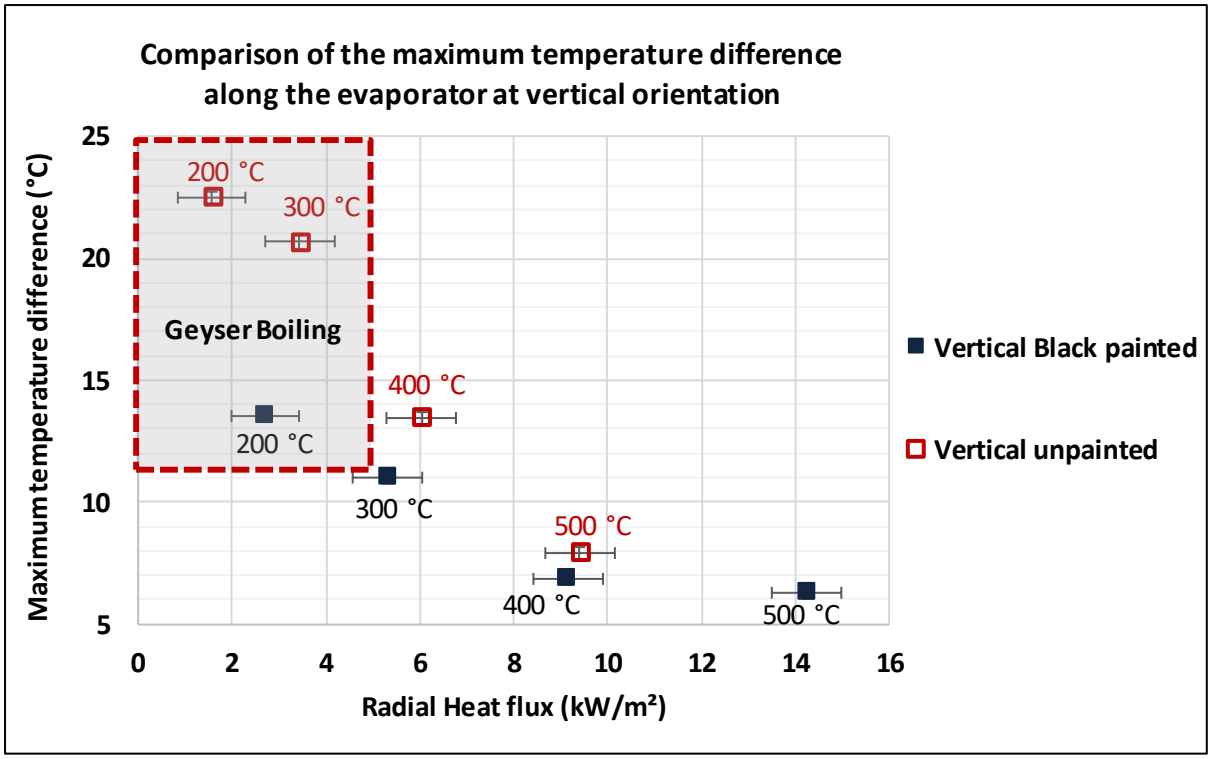

Figure 6-20 A comparison of the maximum temperature difference along the evaporator at vertical orientation of unpainted and black painted heat pipe

It can be concluded from the experimental results presented that the black paint enhanced significantly the functionality of the heat pipe in terms of boiling heat transfer where the geyser boiling disappeared at lower heat flux and lower heater temperature than the case for an unpainted heat pipe. In addition, the black painted heat pipe showed less temperature difference than the unpainted case along the evaporator of the heat pipe.

In the experiment of 12.5° inclination angle and black painted heat pipe, the results of heater and walls temperatures are shown in Figure 6-21. The heat pipe was tested at the following heater temperatures: 199.8 °C, 301 °C, 402 °C, and 497.9 °C. The air temperature was 5 °C to 10 °C more than the air temperature for vertical unpainted case. The air temperature was 11.7 °C to 18.6 °C less than the heater temperature. The top wall temperature was 27 °C to 34 °C less than the air temperature.

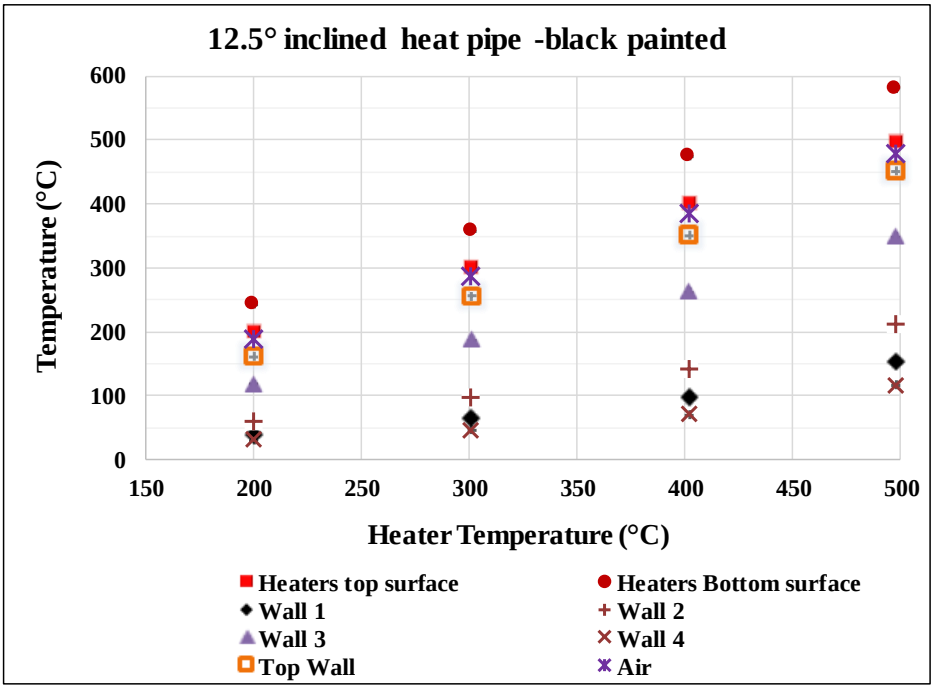

Figure 6-21 Heater and walls temperatures for the 12.5° inclined heat pipe- black painted test

The temperature of the heat pipe and the water inlet and outlet temperatures are plotted in Figure 6-22. At a heater temperature of 200 °C, the temperature of the thermocouple E1t was 27 °C which was very close to the vapour temperature which was 26 °C, while the other thermocouples were scattered between 34.8 °C and 44.1 °C. The heat pipe evaporator and vapour temperature increased with increasing heater temperature. The evaporator temperature variance decreased to be 4.4 °C at a heater temperature of 497.9 °C.

The difference in the water temperature increased to reach 8.1 °C at the heater temperature of 498 °C.

Geyser boiling was observed at the heater temperature of 200° where the heat flux was 5.7 kW/m². Some signs of sudden and short geyser boiling were observed at heater temperatures of 300 °C and 400 °C similar to the vertical case. However, the temperature difference along the evaporator for 12.5° is less than for the vertical case.

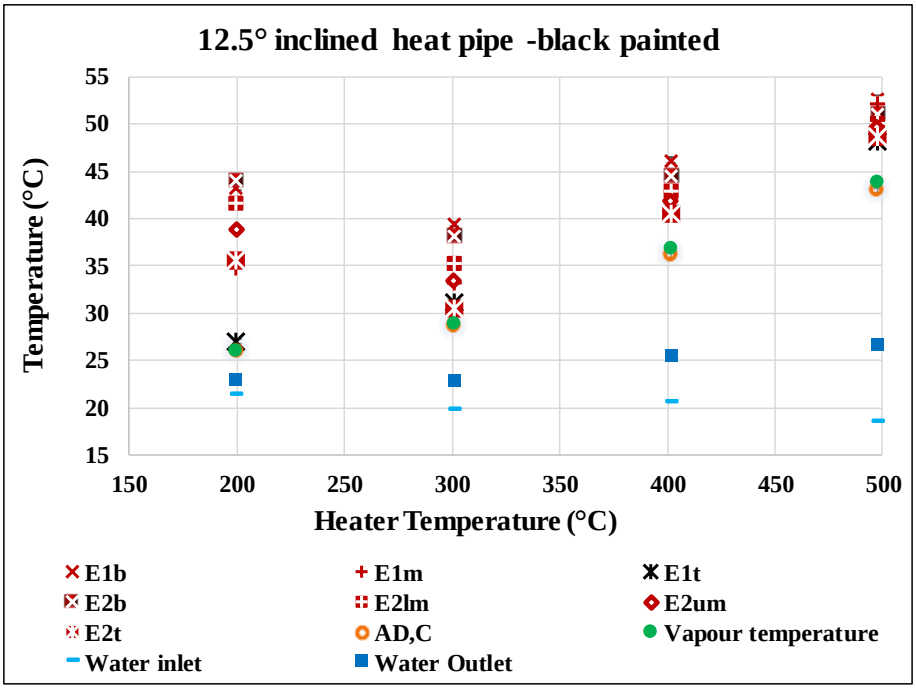

Figure 6-22 Heat pipe and water temperatures for 12.5° inclined heat pipe – black painted test

6.2.2.2 45° degrees

The heater and wall temperatures of the black painted heat pipe at 45° inclination angle are illustrated in Figure 6-23. The heater temperatures were as follows: 201°C, 300.1 °C, 397.2 °C, 497.2 °C. The air temperature was 31 °C to 48.6 °C less than the heater temperature. The top wall was 19 to 13.4 °C cooler than the air.

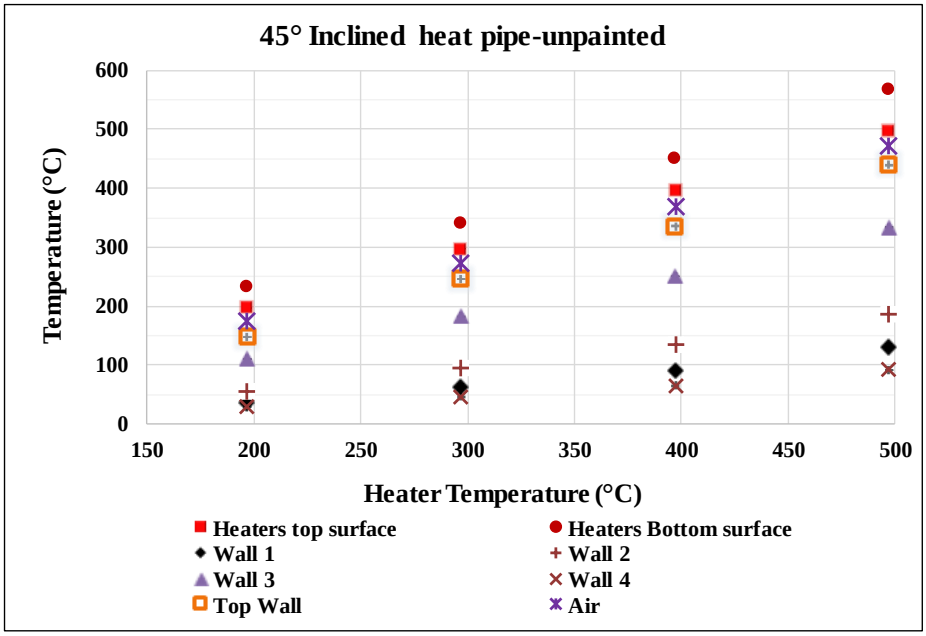

Figure 6-23 Heater and wall temperatures for the 45° inclined heat pipe- black painted test

Figure 6-24 presents the temperatures of the heat pipe and the water inlet and outlet temperatures. The evaporator temperature varied between 43.4 and 59.7 °C except E1t which was 25.5 °C, while the

vapour temperature was 23.5 °C at a heater temperature of 200 °C. The temperature distribution of the heat pipe evaporator was more uniform at higher heater temperatures due to enhancement in the boiling regime and specifically at heater temperature of 500°C where geyser boiling was not encountered. The temperature variance of the evaporator surface was 34.5 °C at a heater temperature of 200 °C. In contrast, the temperature variance along the evaporator was 4.9 °C at a heater temperature of 500 °C.

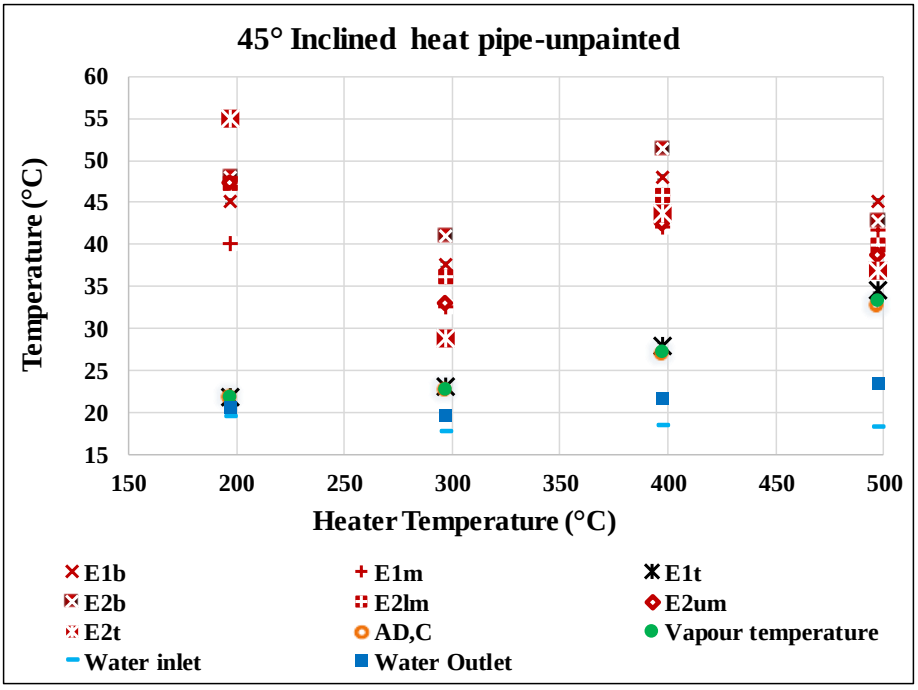

Figure 6-24 Heat pipe and water temperatures for the 45° inclined heat pipe- black painted test

By comparing the black painted heat pipe case with the unpainted one at the same inclination angle of 45° and for the same heater temperature, the radial heat flux in the black painted case was higher due to the higher emissivity of the surface. For both cases, the temperature difference along the evaporator was decreasing with the increase of the heat flux as shown in Figure 6-25. However, the temperature difference for the unpainted case was 10.6 °C at a heater temperature of 500 °C and heat flux of 10.2 kW/m². In contrast, the black painted case exhibited better temperature differences along the evaporator at a heat flux of 9.3 kW/m² at a heater temperature of 400 °C, and furthermore the temperature difference decreased to 4.9 °C at a heat flux of 15 kW/m² at a heater temperature of 500 °C.

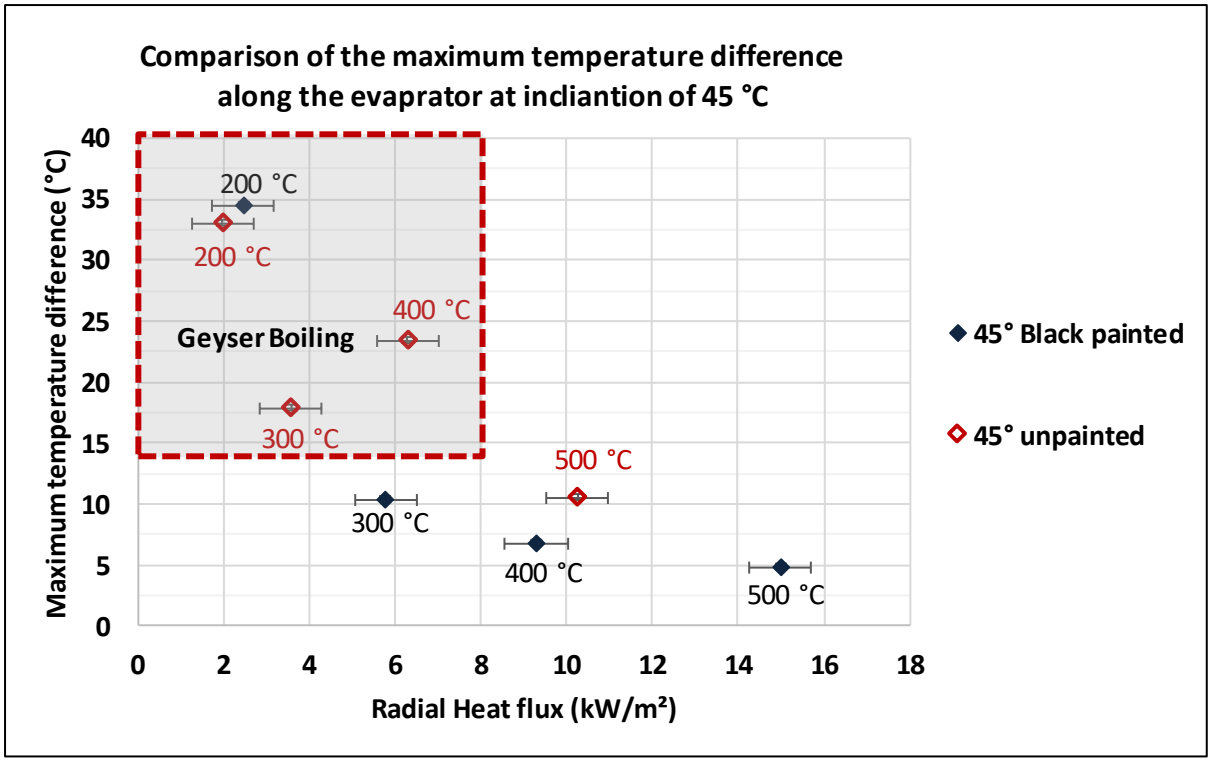

Figure 6-25 A comparison of the maximum temperature difference along the evaporator at 45° inclination angle for unpainted and black painted heat pipe cases

Geyser boiling was eliminated and bubble activity was vigorous at a heat flux of 5.8 kW/m² for the black painted case while geyser boiling was still encountered until the heat flux reached 10.2 kW/m² for the unpainted case. The significant effect of the black paint on reducing the limit of heat flux to eliminate geyser boiling is similar to the findings for the case of the vertical heat pipe.

6.2.2.3 60° degrees

Figure 6-26 illustrates the heater and wall temperatures for the black painted heat pipe at 60° inclination angle. The heater temperatures were 195.6 °C, 295.8 °C, 397.8 °C, and 494.8 °C. The air temperature was less than the heater temperature by 24.4 °C to 48.7 °C at heater temperatures of 200 °C to 500 °C, respectively. The top wall temperature was 11.2 °C to 18.7 °C less than the air temperature.

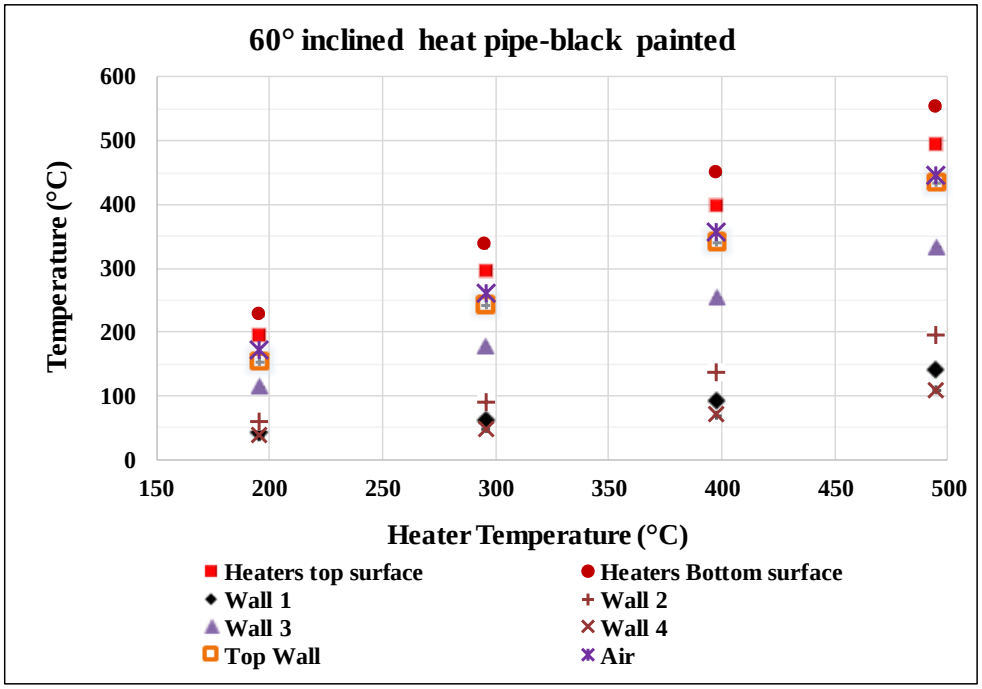

Figure 6-26 Heater and wall temperatures for the 60° inclined heat pipe- black painted test

Figure 6-27 presents the heat pipe and water temperatures. The heat pipe evaporator temperature varied between 23.6 and 34.2 °C while the vapour temperature was 23 °C at a heater temperature of 200 °C. At a heater temperature of 500 °C, the evaporator temperature varied between 44 °C and 47 °C showing a 3 °C temperature difference, where the vapour temperature was 39.3 °C. The water temperature increased 8 °C between the inlet and the outlet.

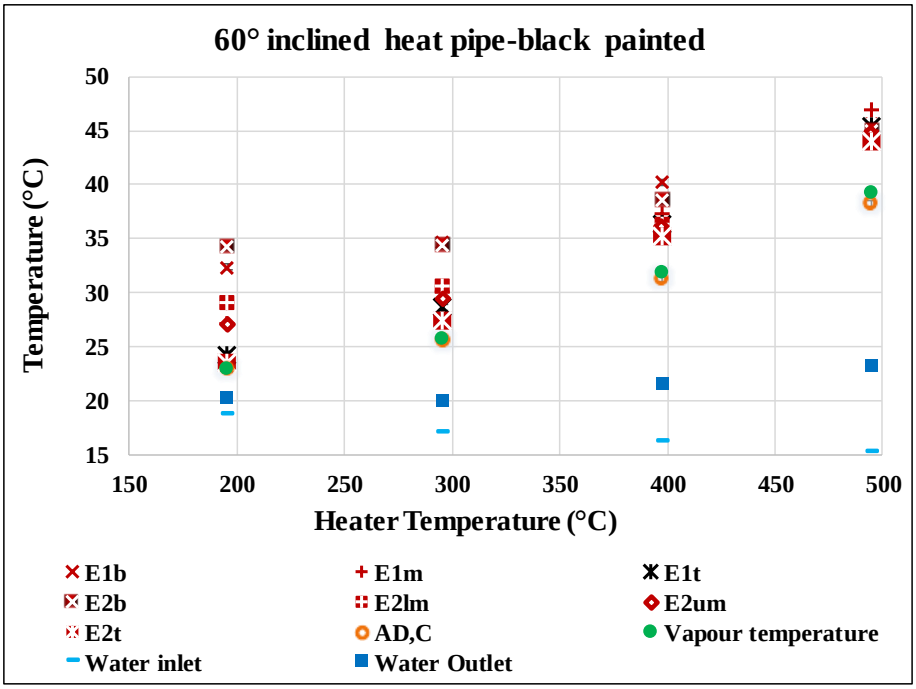

Figure 6-27 Heat pipe and water temperatures for 60° inclined heat pipe – black painted test

A comparison of the experimental measurements of the maximum temperature difference at inclination angle 60° between the unpainted heat pipe and the black painted one is presented in Figure 6-28. The black painted case showed smaller temperature differences along the evaporator wall at less heat flux when compared with the unpainted case. Furthermore, the maximum temperature difference for the case of an inclination of 60 °C was the least among all the inclination angles tested. The reason can be attributed to the fact that the inclination angle decreases the minimum heat flux limit to overcome geyser boiling. It can be also attributed to the change of the axial and radial heat fluxes at the outer wall of the evaporator that vary with the inclination angle.

For the unpainted heat pipe, the maximum temperature difference was 5.1 °C at a heat flux of 11.9 kW/m², while the maximum temperature difference at a heat flux of 10.2 kW/m² and 15.5 kW/m² was 4.9 °C and 3 °C, respectively for the painted heat pipe, which is an acceptable temperature variance in heat pipes.

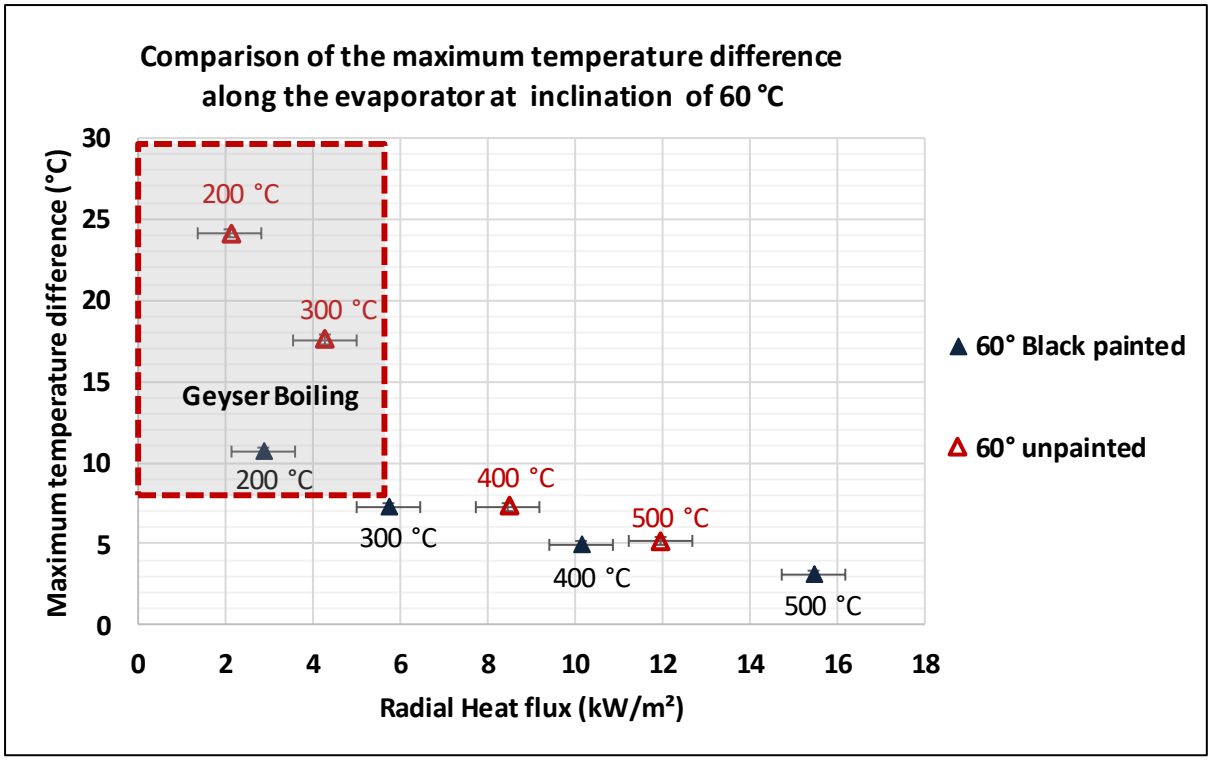

Figure 6-28 A comparison of the maximum temperature difference along the evaporator at 45° inclination angle for unpainted and black painted heat pipe cases

Geyser boiling was eliminated when the heat flux reached 8.5 kW/m² for the unpainted heat pipe case with some sudden temperature fluctuation. The black paint decreased the geyser boiling cycle period remarkably due to the vigorous and intense nucleation activity. The experimental results for the black painted case showed considerably less temperature variance versus time at a heat flux of 2.9 kW/m² with minor sudden occurrence of large fluctuations (sudden geysering). The temperature fluctuation was further decreased as the heat flux increased and the temperature difference along the evaporator decreased as well. The results indicated that the liquid pool was not superheated as much as the case of unpainted heat pipe. Moreover, the black paint decreased the temperature difference along the evaporator at a lower heat flux in comparison to the unpainted heat pipe case.

6.2.3 Discussion on the experimental results

The air temperature was different for each test due to the energy balance between the heat input from the heater and the heat output through the heat pipe at a steady state condition, since the kiln represents a closed insulated enclosure.

A general conclusion can be drawn from the results that the heat pipe evaporator temperature difference decreased from about 34.5 °C at a heater temperature of 200 °C to 3 °C at a heater temperature of 500 °C. The heat pipe thermal performance showed a strong dependency on the heat flux. The increase in the heater temperature increased the heat transfer by radiation and natural

convection which increased the heat flux through the heat pipe. Thus, the intensity of bubble nucleation activity increased and this enhanced the uniformity of the evaporator temperature.

The geyser boiling encountered in the heat pipe was considerably influenced by the heat flux, the inclination, and the black paint. In summary, geyser boiling took a place at a vertical orientation of the unpainted heat pipe until the heater temperature exceeded 300 °C, where the heat flux was 3.4 kW/m². For a 45° inclination angle, geyser boiling was encountered until the heat flux exceeded 6.3 kw/m². For 60 degrees, geyser boiling was encountered when the heat flux was 4.3 kW/m² at a heater temperature 300 °C, and the active nucleation boiling sites significantly increased at 8.5 kW/m².

The black paint reduced the limit of heat flux to eliminate geyser boiling at all inclination angles. Moreover, the black painted heat pipe exhibited a better temperature distribution along the evaporator. The inclination of the heat pipe enhanced the boiling nucleation intensity and the temperature distribution along the evaporator. The minimum temperature difference was observed at an inclination of 60° at all heater temperatures. The effect of the black paint and the inclination on the temperature distribution along the evaporator will be discussed in detail in the following section.

It can be noted that the thermocouple AD, which is welded on the external surface of the heat pipe, exhibited a very close reading of the temperature to the vapour thermocouple welded inside the heat pipe. This validates the method that a well-insulated thermocouple placed on the external surface of the adiabatic section of a heat pipe measures the saturation temperature at steady state with less than 1 °C difference. The vapour temperature was increasing with the increase of the heater temperature as a result of the increase of the heat flux.

6.2.3.1 Comparison between the excess temperatures and the heat flux for different inclination angles

Heat flux is considered as a function of the excess temperature, which is the temperature difference between the internal surface of the evaporator and the vapour ($T_{ei} - T_v$), in heat transfer theory on nucleate boiling under constant pressure. However, in experimental practice with heat pipes, the excess temperature was a function of the heat flux at the internal surface of the evaporator q_{ei} and in addition the pressure was varying as function of the vapour temperature. Therefore, the experimental results of the excess temperature are plotted on the Y-axis as a function of the heat flux (X-axis). It should be mentioned that the heat flux in this section is based on the internal surface area of the evaporator instead of the external surface area to be consistent with the temperature difference between the internal evaporator wall and the vapour.

Figure 6-29 presents a comparison of the excess temperature versus the heat flux for the cases of both black painted heat pipe and unpainted heat pipe at the vertical orientation. It can be seen that excess temperature decreases with the increase of the heat flux for both cases. Furthermore, the excess temperature was considerably higher for the unpainted heat pipe in comparison with the black painted one at a similar heat flux. The excess temperature was more than 6 °C at heat fluxes less than 6 kW/m² due to the geyser boiling taking place during the tests for both cases: black painted and unpainted heat pipe, as highlighted in the box. The excess temperature was not influenced significantly with the heat flux when the latter was higher than 10 kW/m².

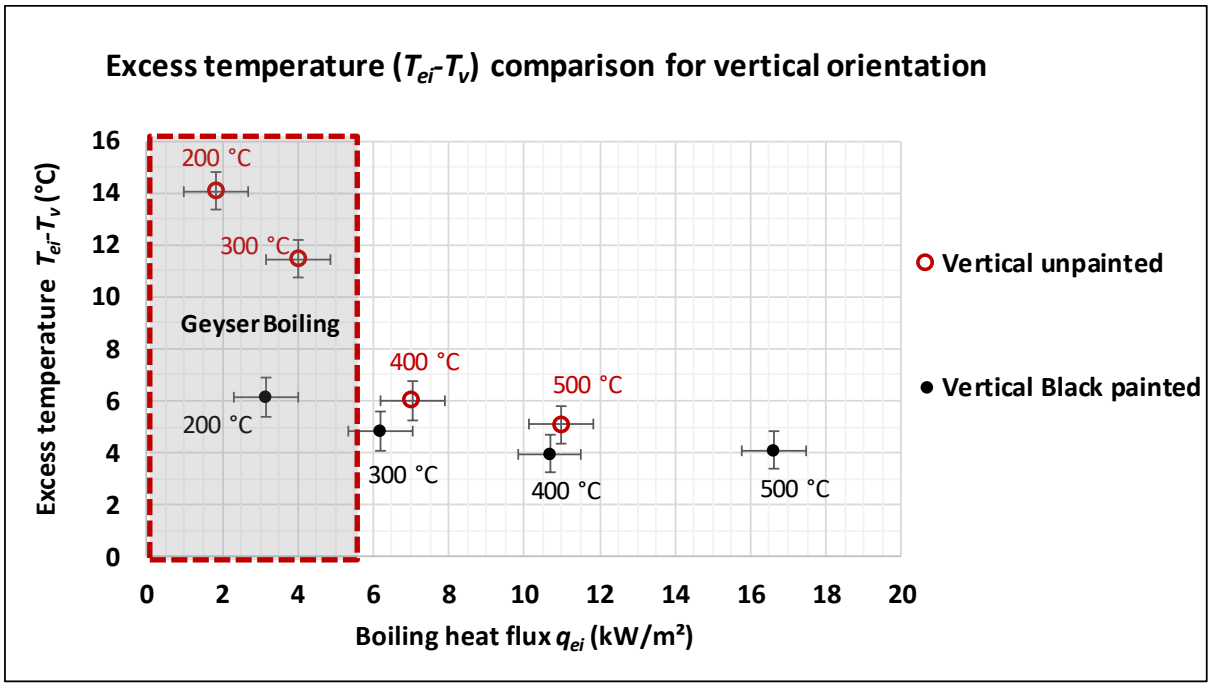

Figure 6-29 Boiling heat flux versus the excess temperature at vertical orientation

Figure 6-30 shows a comparison of the excess temperature as function of heat flux for the cases of the black painted heat pipe and the unpainted heat pipe at an inclination angle of 45°. The excess temperature was largely high when geyser boiling occurred at boiling heat fluxes lower than 7.5 kW/m². The excess temperature dropped below 6 °C when the heat flux exceeded 6 kW/m² for the black painted heat pipe and 12 kW/m² for the unpainted case. Moreover, the excess temperature was slightly affected by the increase of the heat flux when it exceeded 10 kW/m².

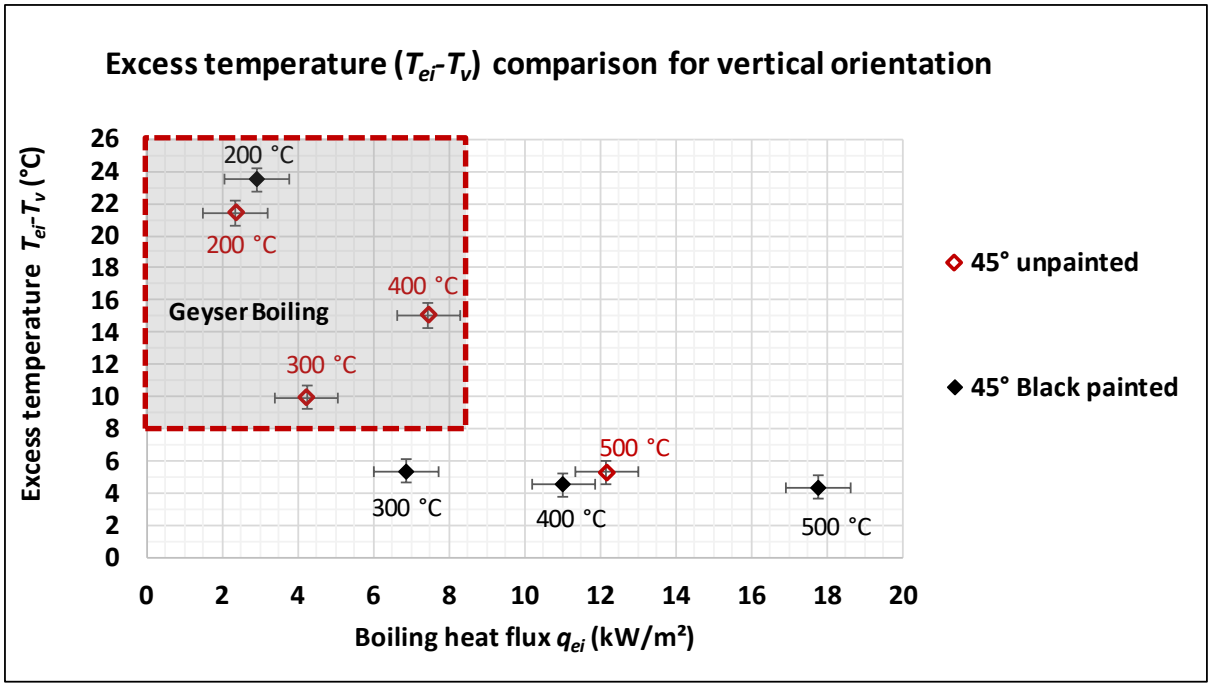

Figure 6-30 Boiling heat flux versus the excess temperature at 45° inclination

Figure 6-31 illustrates a comparison of the excess temperature as function of heat flux for the cases of the black painted heat pipe and the unpainted heat pipe at an inclination angle of 60°. Similar to the vertical and 45° cases, the excess temperature of the unpainted heat pipe is significantly higher than the black painted heat pipe at similar heat fluxes. In addition, for the unpainted heat pipe, the excess temperature suddenly dropped down when the heat flux reached 10 kW/m² due to the elimination of geyser boiling and thus the elimination of the superheated pool liquid. However, the black painted heat pipe did not exhibit a remarkable change in the excess temperature although the heat flux increased from 3.4 kW/m² to 18.4 kW/m² due to the high intensity of active nucleation sites during the test.

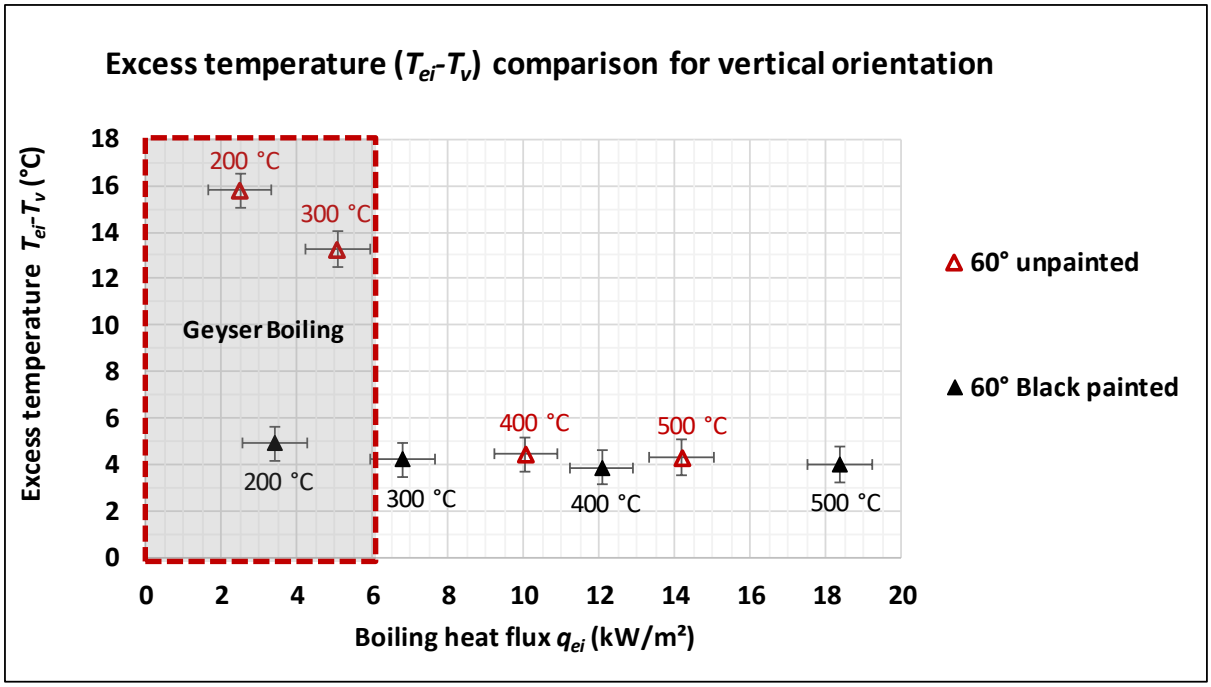

Figure 6-31 Boiling heat flux versus the excess temperature at 60° inclination

It can be concluded that when the heat pipe was functioning with no presence of geyser boiling or large temperature variation, the excess temperature was between 4° and 6 °C and approximately independent of the heat flux. The plotted experimental results give more understanding for analysing the heat transfer coefficient of boiling in the following sections

6.2.3.2 Effect of the black paint and inclination on the overall heat recovery

The overall average heat recovery of the heat pipe during all the experiments is presented in Figure 6-32 . It can be seen the heat recovery increased with the increase of the heater temperature and varied between 53 W and 568 W. The amount of heat recovery of the unpainted heat pipe at different inclinations at a heater temperature of 200 °C was nearly the same due to the geyser boiling. However, the amount of heat recovery varied between 342 W and 434 W at a heater temperature of 500 °C.

The amount of heat recovery of the black painted heat pipe was superior to the unpainted one at the same conditions. Furthermore, the heat recovery of the vertical black painted heat pipe at a heater temperature of 500 °C was 517 W, which was higher than for the 60° inclined unpainted heat pipe. This indicates that the black paint has a stronger effect than the inclination angle on the overall heat recovery.

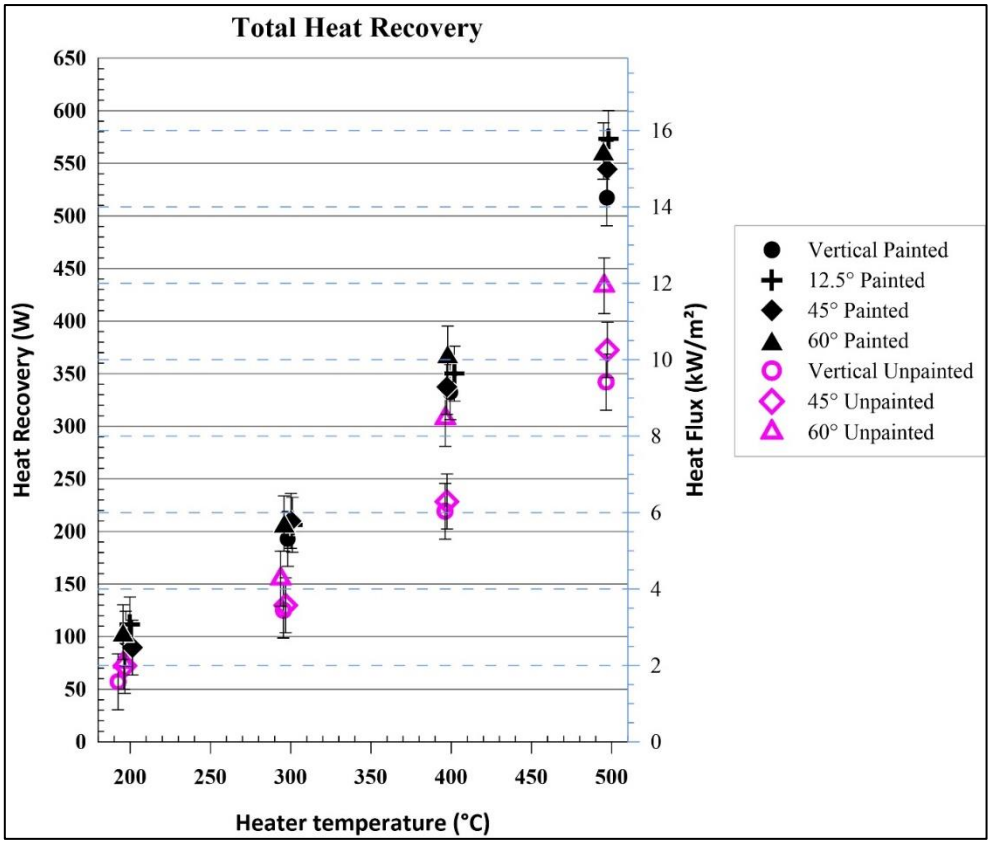

Figure 6-32 Total heat recovery of the single heat pipe

The effect of the black paint on the overall heat recovery is presented in Figure 6-33, which compares the heat recovery from a black painted heat pipe to the unpainted one at the same inclination angle. It can be seen that the black paint increased the heat recovery significantly at a low heater temperature (200 °C) more than the case at high heater temperature (500 °C). The heat recovery increased 72% for the vertical heat pipe at a heater temperature of 200 °C, while it increased 50% at a heater temperature of 500 °C. A similar result can be seen for the case of a 45° inclination angle where the percentage of the heat recovery increase decayed versus the heater temperature except the case of a heater temperature of 200 °C. The heat recovery at 200 °C was considerably lower hence the heat flux was low and geyser boiling was observed for both cases with minimal active nucleate boiling sites.

The heat recovery increased about 37% at a heater temperature of 200 °C at 60° inclination angle while it reduced to approximately 30% at heater temperature of 500 °C. The heat recovery at an inclination of 12.5° was surprisingly higher than the one at 60°

By comparing the three inclination angles (vertical, 45°, and 60°), it can be noted that the effect of the black paint decreases with the increase of the inclination angle. The black paint increased the heat flux to a level eliminating the geyser boiling and activates more nucleation sites at the vertical

orientation, while the boiling regime and the heat pipe performance was steady at an inclination angle of 60°.

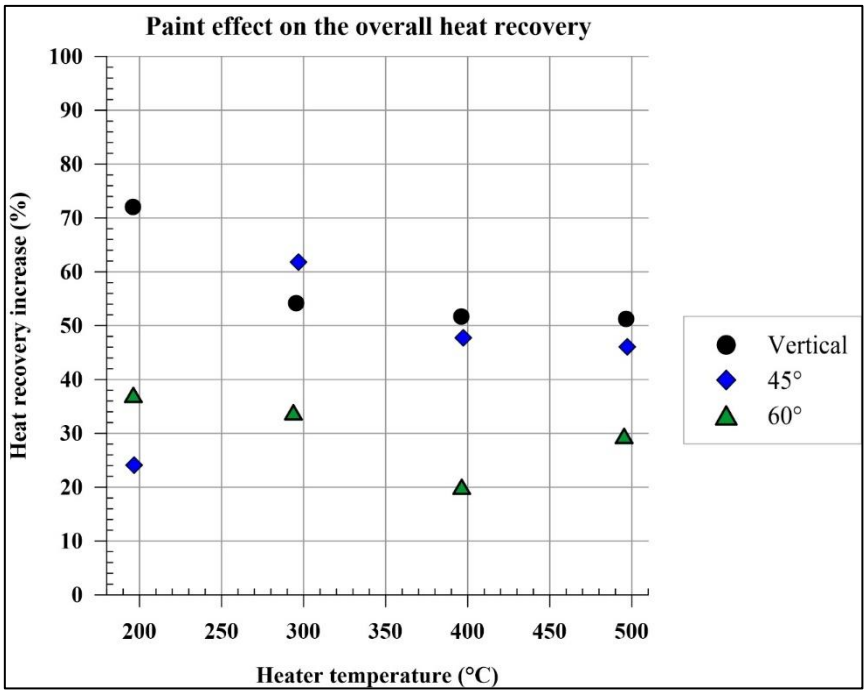

Figure 6-33 Effect of Black paint on the overall heat recovery at different inclination angle: vertical, 45°, and 60°

The effect of the inclination angle on the overall heat recovery is presented in Figure 6-34. The results obtained from the inclined unpainted heat pipe are compared with the vertical unpainted heat pipe, while the results of the inclined black painted heat pipe are compared with the vertical black painted one. Unlike the black paint, the inclination angle influences the heat transfer by natural convection where it increases with the increase of the inclination angle from vertical reaching a maximum value at a horizontal orientation.

For the unpainted heat pipe cases, the inclination angle of 45° enhanced the heat recovery about 27% at a heater temperature of 200 °C, whereas it was enhanced 33% at an angle of 60°. As the thermal performance of the vertical unpainted heat pipe enhanced with the increase of the heater temperature, the inclination angle effect decreased accordingly. At a heater temperature of 500°, the effect of 45° inclination angle was a 9% improvement while it was 27% for an angle of 60°.

Moreover, the inclination of the heat pipe increased the active nucleation boiling sites and decreased the temperature variance along the heat pipe and reduced the geyser boiling cycles, therefore the effect of the inclination angle for the case of the unpainted heat pipe is higher than the painted one at the same inclination angle.

The effect of the inclination angle of 45° varied between 2% and 9%. The overall heat recovery at a heater temperature of 200 °C at an inclination angle of 45° was less than the vertical orientation owing to the fact that geyser boiling occurred at 45° which was not the case at a vertical orientation. The effect of the inclination at 12.5° declined then recovered with the increase of the heater temperature. It reached 11% at heater temperature of 500 °C which was slightly higher than the effect of the inclination of 60°.

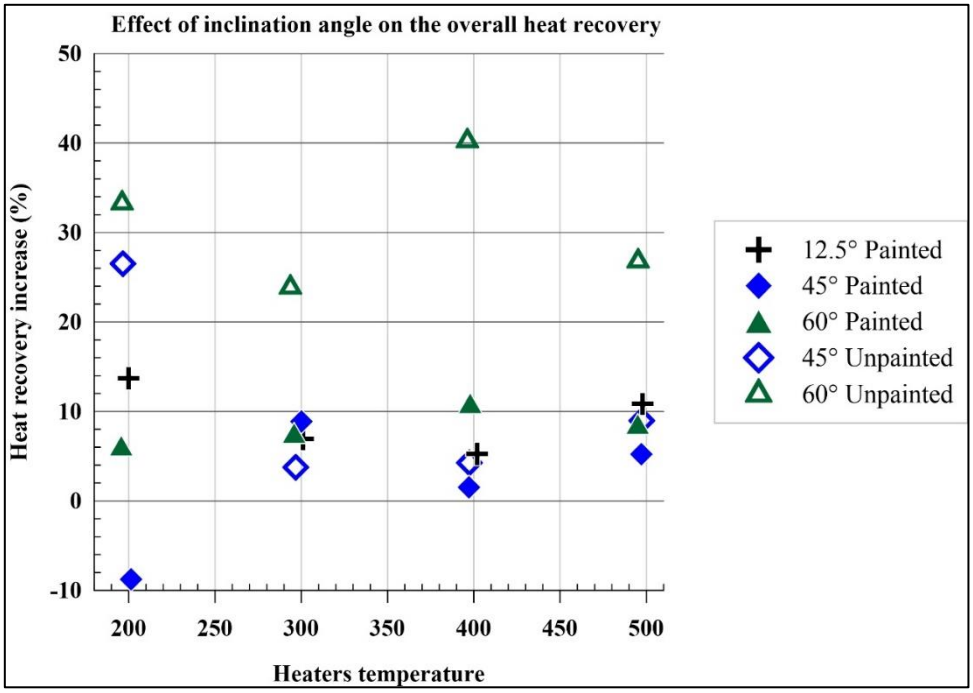

Figure 6-34 Effect of the inclination on the overall heat recovery for two different cases: unpainted heat pipe and black painted heat pipe

6.2.3.3 Experimental natural convection gain and its influence on the overall heat transfer

The heat transfer by natural convection was calculated using the equation Eq.(4-128) recommended in chapter 4 and developed by *Rani* et al. [117] using the temperatures of the air and the heat pipe surface measured experimentally. Figure 6-35 illustrates the natural convection heat transfer rate for the tests conducted on the single heat pipe. The heat transfer rate by natural convection was increasing linearly with the increase of the heater temperature. The heat transfer rate for the vertical heat pipe for both unpainted and black painted cases were nearly equal. Moreover, the natural convection heat transfer rate for the inclined heat pipe tests was higher than for the vertical case. At a heater temperature of 500 °C, the heat transfer rate varied between 122 W and 158.8 W. It would be expected that the highest heat transfer rate is at an inclination angle of 60°. However, the heat transfer rate at an inclination angle of 45° was the highest due to the high air temperature of 471 °C, whereas it was 461 °C at a 60° inclination angle. The natural convection for the black painted heat pipe condition was less than the unpainted one due to the lower air temperature. Furthermore, the heat

transfer rate for the black painted heat pipe was slightly affected by the inclination angle at the same heater temperature due to the difference in the air temperature during the tests. In summary, the rate of heat transfer by natural convection varied depending on the inclination angle and was strongly affected by the air temperature in the kiln.

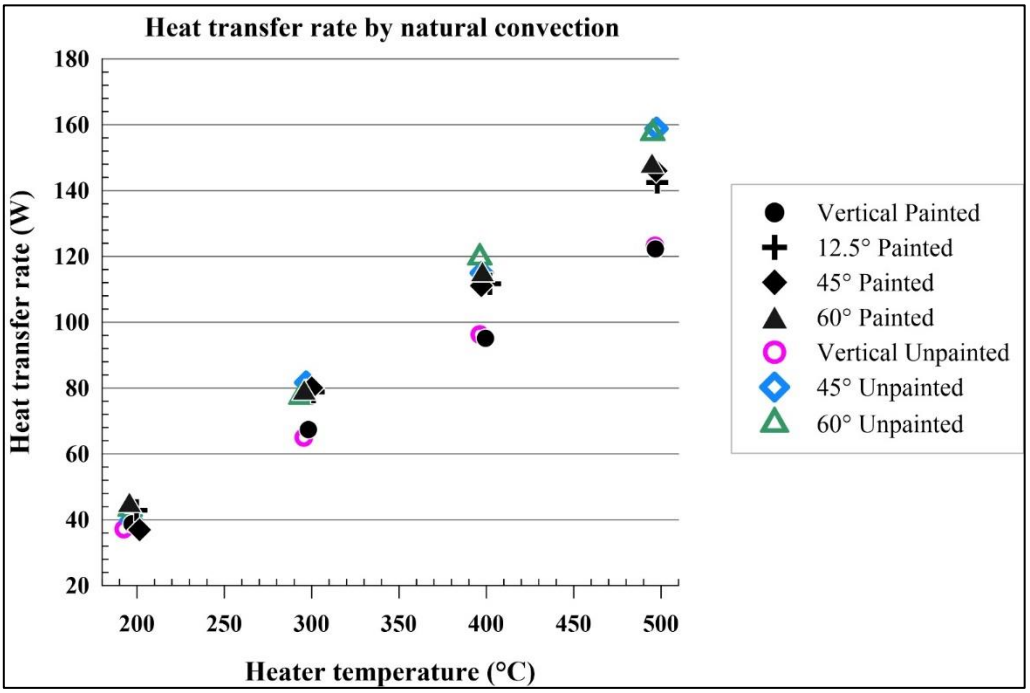

Figure 6-35 A comparison of the heat transfer rate by natural convection for the single heat pipe tests

Figure 6-36 presents the influence of the natural convection on the overall heat recovery through the heat pipe as a percentage. It can be noted that the proportion of the natural convection decreased with the increase of the heater temperature. For the vertical unpainted heat pipe case, the natural convection effect fell from 65% at a heater temperature of 200 °C to 36% at a heater temperature of 500 °C. Furthermore, the percentage for the vertical black painted varied between 43% and 36 % at heater temperatures of 200 °C and 500 °C, respectively. Similarly, the percentage of the natural convection for inclined black painted heat pipe cases was less than for the unpainted ones. In fact, the increase in the emissivity of the heat pipe by using the black paint increased the radiation heat transfer rate, which consequently increased the overall heat transfer, whereas the heat transfer rate by natural convection remained nearly of the same magnitude. Therefore, the effect of the natural convection for the vertical painted case is less than the unpainted one.

By comparing the effect of the natural convection with respect to the inclination angle, it can be noted that it varied widely depending on inclination angle with the unpainted heat pipe, while the variance of the percentage decreased for the black painted case at the same heater temperature. For instance,

the percentage of the natural convection for the 45° unpainted heat pipe test is 42.62% while it is 36% for the unpainted vertical one, while it was 25% and 24% for the black painted heat pipe at 45° and the vertical, respectively. Hence, three-quarters of the overall heat transfer was accounted for by radiation heat transfer, which shows the superiority of radiation heat transfer at high heater temperatures. This can be explained by the fact that radiation heat transfer is proportional to the difference in fourth power of temperature between heat pipe and the heater, while natural convection is approximately proportional to the temperature difference between air and the evaporator surface to the power of 1.25 to 1.33.

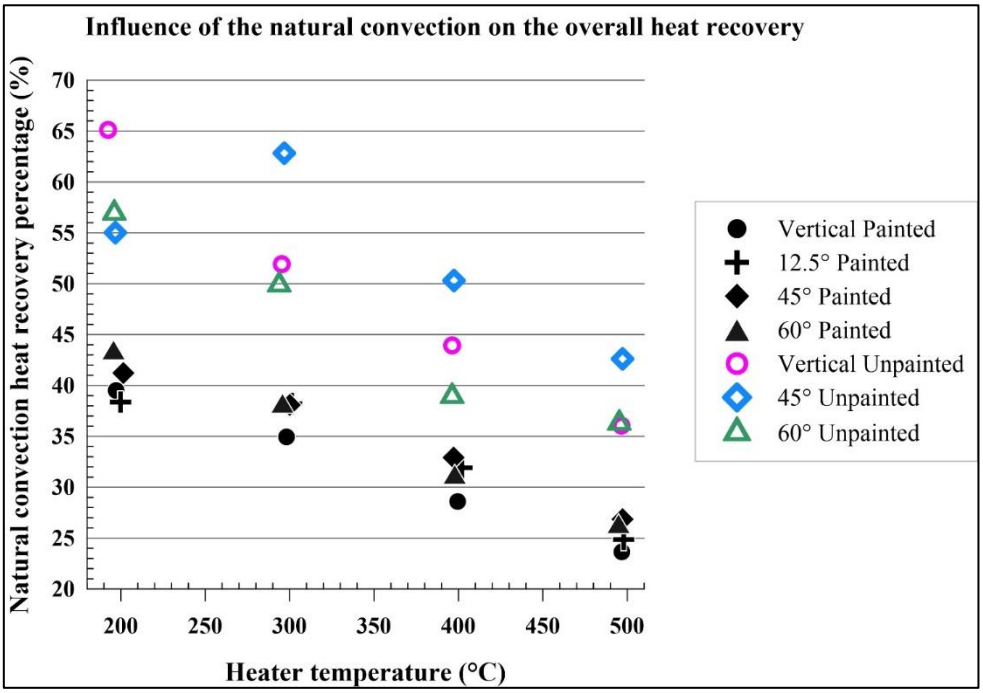

Figure 6-36 Influence of heat transfer by natural convection on the overall heat recovery

6.2.3.4 Experimental Radiation heat recovery comparison

Figure 6-37 presents the experimental radiant heat gain versus the heater temperature at different conditions. The experimental radiation heat transfer was obtained from subtracting the natural convection component from the overall heat transfer rate. The radiation heat transfer rate increased with the increase of the heater temperature. The heat transfer rate for the black painted heat pipe was higher than for the unpainted one. The heat transfer rate for the unpainted heat pipe at a heater temperature of 200 °C was in the range of 20 W to 32 W depending on the orientation of the heat pipe. The radiation heat transfer increased to 219 W for the vertical heat pipe while it reached 276 W for the 60° inclined heat pipe at heater temperature of 500 °C. The results of the unpainted case show that the radiation heat transfer rate at an inclination angle of 45° was almost the same as for the vertical case, while it was significantly increased for an inclination angle of 60°. However, the results

of the black painted case show that the radiation heat recovery was slightly varying with respect to the inclination angle. At a heater temperature of 200 °C, the heat transfer rate of both the vertical orientation and inclination of 60° were the same at 59 W. The radiation heat recovery of the vertical orientation was 395 while it was 413 W for the inclination angle of 60° at a heater temperature of 500 °C. The maximum radiation heat transfer rate was 431 W for an inclination of 12.5 ° at the same heater temperature. Moreover, it can be noted that the heat transfer rate increased considerably with the increase of the heater temperature regardless of the inclination angle.

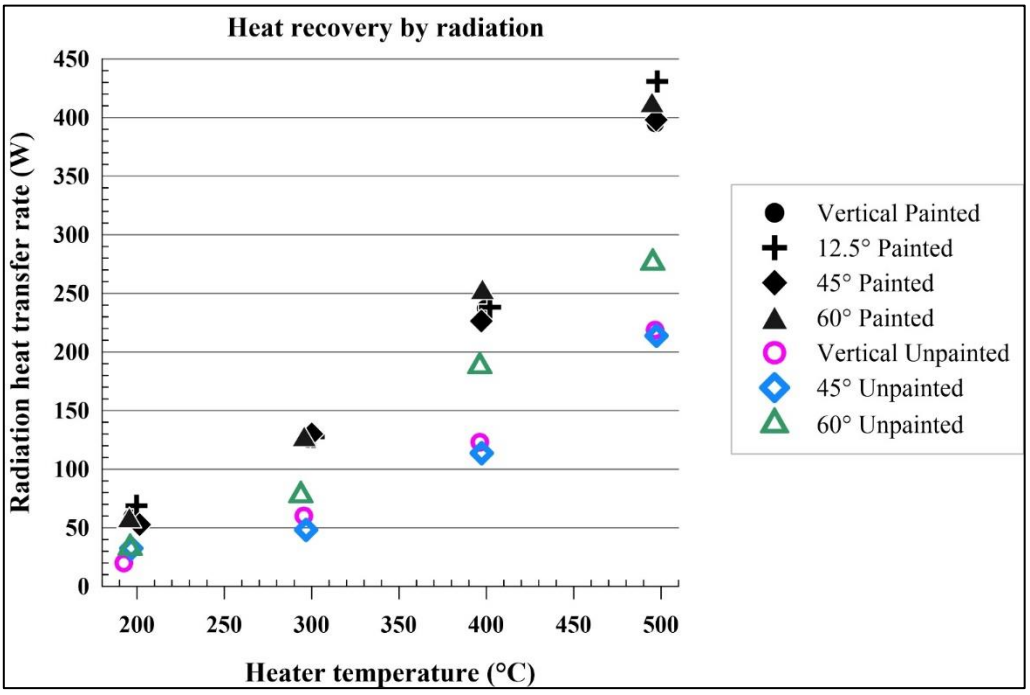

Figure 6-37 Experimental heat recovery by radiation

Figure 6-38 presents the effect of the black paint on the radiation heat transfer, where the black paint increased the emissivity. It would be expected to have the same percentage of increase regardless of the heater temperature of the experiment. However, it can be seen that the effect reached 200% of increase at a heater temperature of 200°C for the vertical case and 170% for the case of 45° at a heater temperature of 300 °C. In contrast, the effect fell at a heater temperature of 500 °C to 80% and 86% for vertical and inclination angle of 45°, respectively. As it was observed that the nucleation boiling was eliminated at a heater temperature of 500 °C, it can be noted that the effect exceeded 100% of heat transfer increase for the cases when geyser boiling was encountered for the cases of the unpainted surface when it was eliminated, or more nucleate boiling sites were active. These results reveal that the measured heat transfer rate for the cases when the geyser boiling was encountered was less than the actual heat transfer rate assuming that the emissivity is independent from the

temperature. Furthermore, the effect of the emissivity on the on the heat transfer rate and the radiation thermal resistance will be analysed theoretically in the following sections.

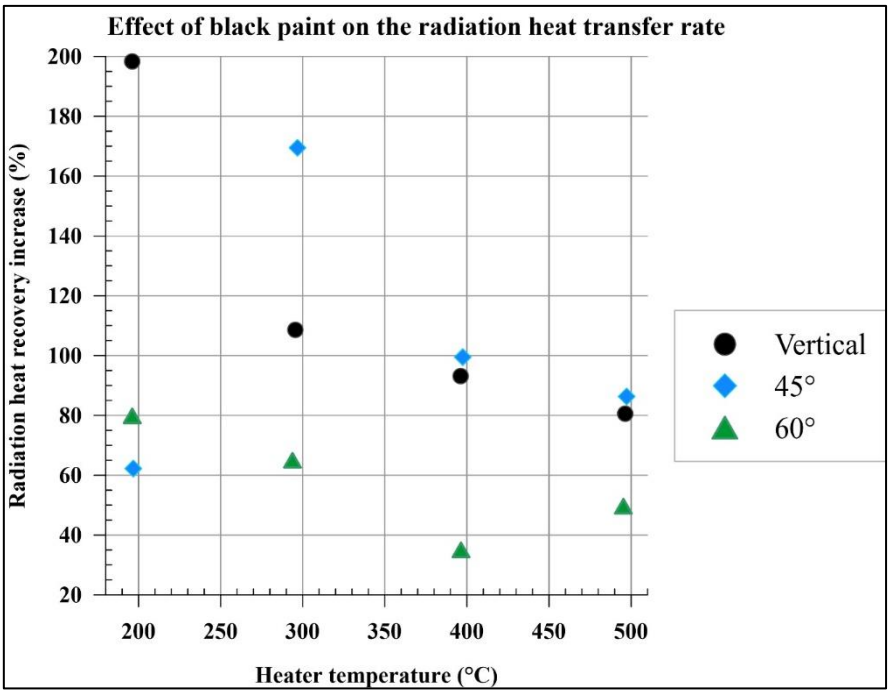

Figure 6-38 Effect of black paint on the heat transfer by radiation at different inclination angles

6.2.4 Validation of the theoretical modelling and discussion

6.2.5 Experimental versus theoretical boiling thermal resistance

The heat flux and the liquid falling film due to the inclination mainly affected boiling heat transfer. The heat flux on the heat pipe in turn was also a function of the inclination and the heater temperature due to the influence of radiation and natural convection heat transfer. The external surface paint also affected the heat flux as it increased the absorbed radiative heat. Neither the heat flux along the evaporator nor the radial heat flux was uniform, which represents a complex study. Furthermore, the heat flux was determined by measuring the heat transfer rate to the water coolant which is only accurate when the heat pipe does not encounter geyser boiling with uncertainty of less than ±20%. Therefore, the thermal resistance of boiling heat transfer will be discussed for the high heat flux cases when the radial heat flux is higher than 5 kW/m² or 6 kW/m² depending on the test conditions i.e orientation and paint conditions. Figure 6-39 presents the overall experimental thermal resistance of boiling heat transfer as a function of the heat flux for different experimental conditions. The overall thermal resistance significantly decays with the increase of the heat flux within the geyser-boiling region until it approximately exceeds 6 kW/m². The high thermal resistance was due to the geyser boiling encountered in the heat pipe which strongly influenced the thermal performance. Furthermore, it can be noticed that the boiling thermal resistance is not affected by the heat flux or

the inclination of the heat pipe when the heat flux is higher than 9 kW/m². The boiling thermal resistance decreased to 0.001 °C/W when the heat flux was higher than 14 kW/m².

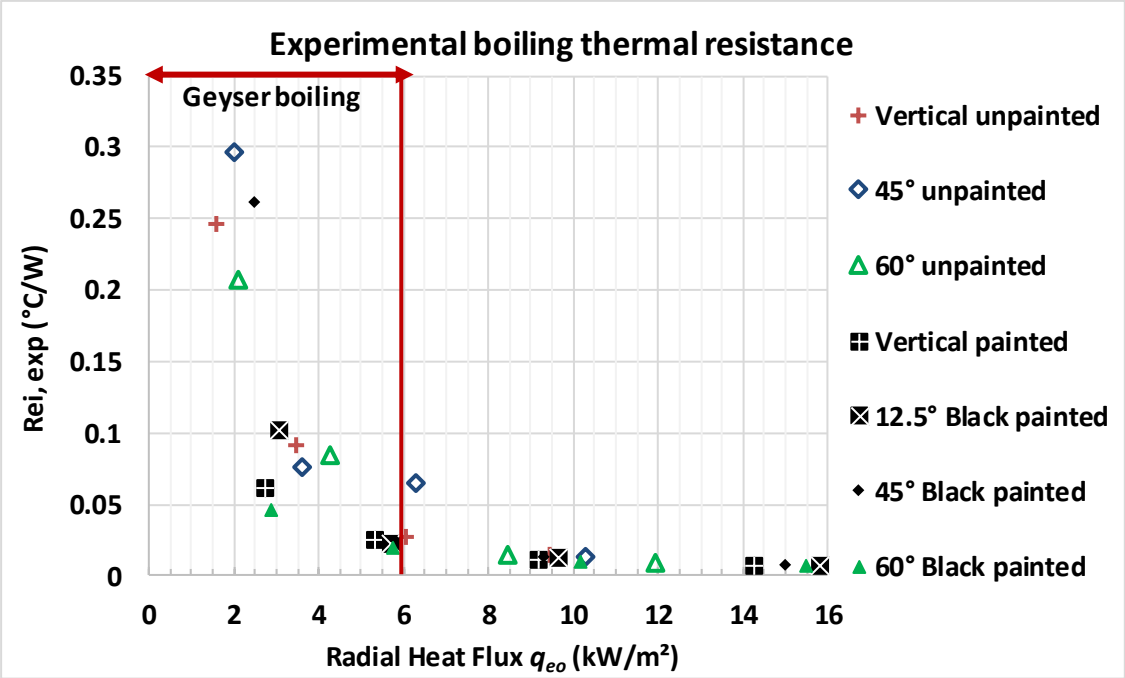

Figure 6-39 Experimental overall thermal resistance of boiling heat transfer

The average boiling heat transfer is presented in Figure 6-40. It can be seen that the overall heat transfer coefficient is low at a heat flux of 2 kW/m² due to the geyser boiling. Moreover, the experimental overall heat transfer coefficient was not significantly affected by the orientation of the heat pipe. It can be seen the data of overall boiling heat transfer coefficient has a linear fitting with the heat flux.

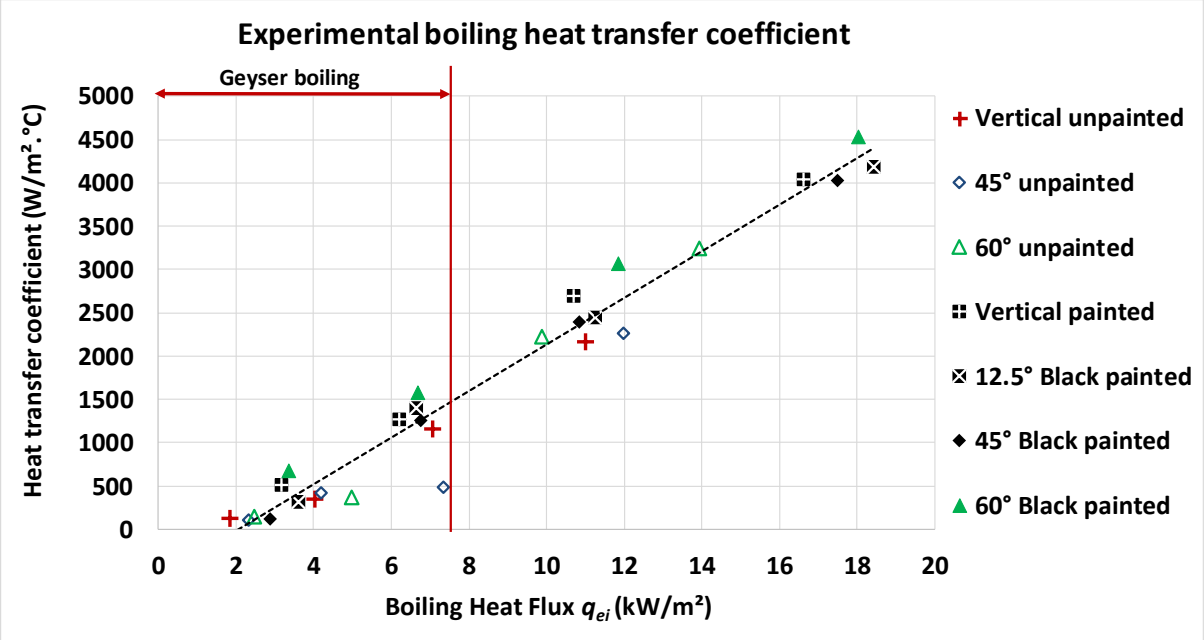

Figure 6-40 Experimental average boiling heat transfer coefficient

6.2.5.1 Predictions of the overall boiling thermal resistance

The general correlations of nucleate pool boiling are used to predict the boiling thermal resistance and plotted versus the heat flux for different experimental conditions in Figure 6-41. The theoretical thermal resistance using these correlations is much higher than the experimental value regardless of the heat flux. This can be attributed to the conditions for which the correlation was obtained and the range of the heat flux of their experimental values. Therefore, it is necessary to investigate other correlations of boiling heat transfer.

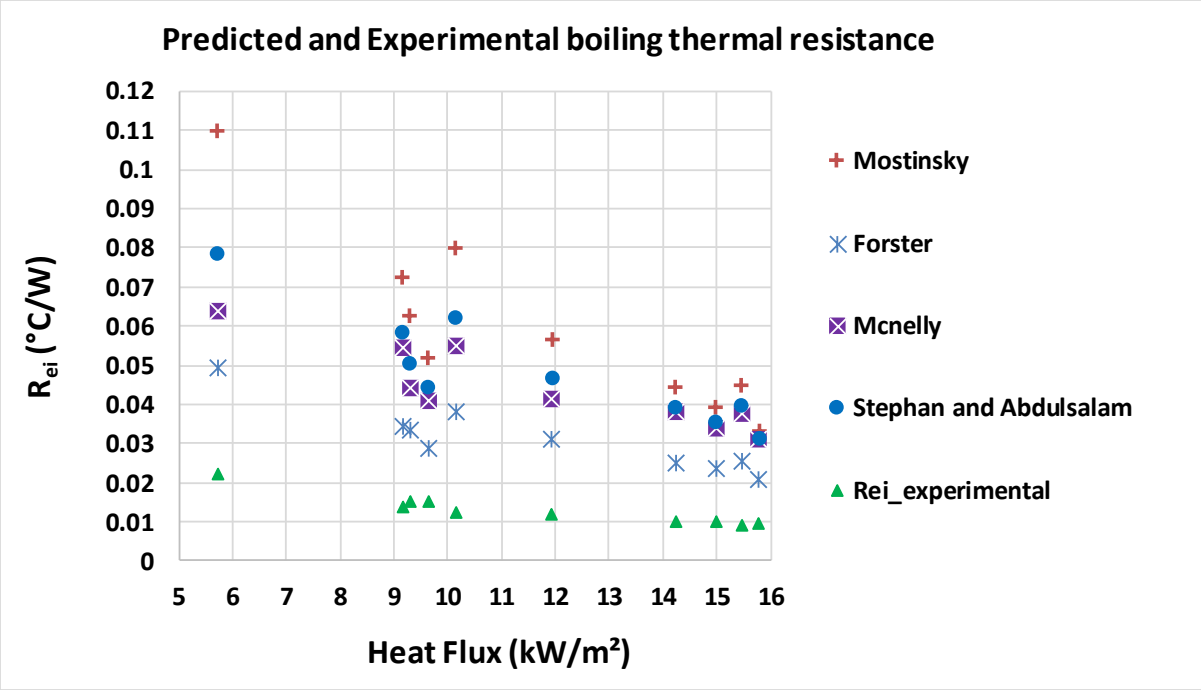

Figure 6-41 A comparison between experimental thermal resistance of boiling heat transfer and theoretical predictions using general nucleate boiling heat transfer correlations

The experimental versus theoretical thermal resistance of boiling heat transfer is presented in Figure 6-42. The experimental results are compared with the predictions for the cases when the geyser boiling was not encountered i.e. the heat flux was approximately higher than 5 kW/m². The selected cases are based on the uncertainty of the experimental data with error being less than 20% since the theoretical predictions are applicable for steady and homogenous boiling regimes. Furthermore, the plotted cases are for when the temperature difference at the evaporator was less than 7 °C in order to be a uniform phase-change mechanism along the evaporator. The predicted thermal resistances were lower than the experimental values at low heat flux. Furthermore, the theoretical predictions did not show a trend versus the heat flux except for the thermal resistance obtained using the Rohsenow correlation. The theoretical thermal resistance using Kiatsiriroat showed approximately a constant value of the thermal resistance versus the heat flux. However, the thermal resistance had very good agreement with the experimental values within the boiling heat flux range of 10 kW/m² to 14 kW/m². Furthermore, the correlation of Imura was much lower than the experimental value for low boiling heat flux (7 kW/m²) while it showed good agreement at boiling heat fluxes higher than 10 kW/m². The correlation of Labunstov was higher than the experimental thermal resistance within the heat flux range of 9 kW/m² to 15.5 kW/m². Similar findings of Labunstov predictions were obtained by *Jafari et al* [135] within the same heat flux range for a copper heat pipe. The results by Jafari et al. [135] also showed very good agreement between Rohsenow, Imura, and the experimental results.

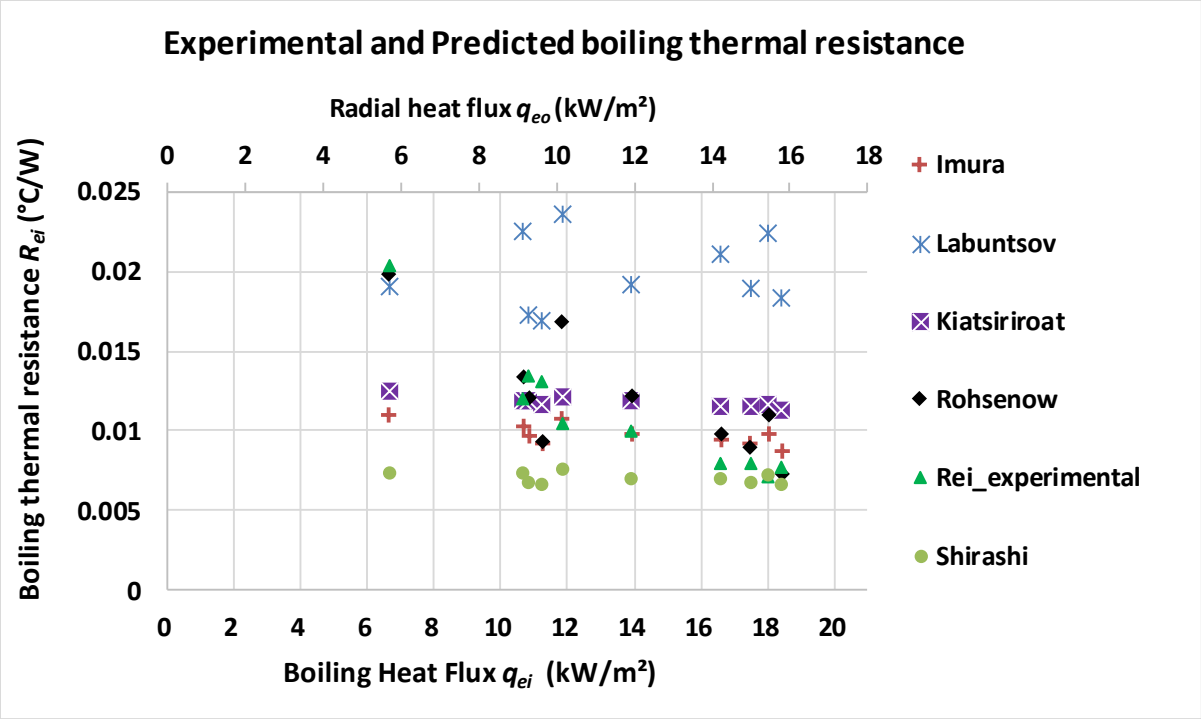

Figure 6-42 Thermal resistance of boiling heat transfer of different correlations

The theoretical thermal resistance of boiling using difference correlations versus the experimental resistance are presented in Figure 6-43. Labuntsov [99] over-predicts the measurements for low thermal resistance. The theoretical predictions using Imura [100], and Kiatsiriroat [102] were over predicting the thermal resistance when it is lower than 0.012 °C/W and under-predicting for high thermal resistance when the thermal resistance is higher than 0.012 °C/. However, the accuracy of the prediction was very good within a range of ±25% for experimental thermal resistance within the range of 0.0079 °C/W and 0.013 °C/W. The prediction using Shirashi [101] correlation had similar trend to Imura with a lower prediction of the thermal resistance. It showed good agreement when the experimental resistance is lower than 0.01 °C/W. *Jouhara et al.* [112] conducted modelling studies of a small diameter heat pipe and compared the evaporator thermal resistance with a predicted thermal resistance using various correlations including Imura and Labuntsov. Labuntouv showed good agreement at heat fluxes within the range of 6 kW/m² to 16 kW/m² while Imura under-predicted the experimental results. The ratio of the diameter to the length of the evaporator in addition to the inner diameter affects the applicability and the accuracy of the boiling heat transfer correlations.

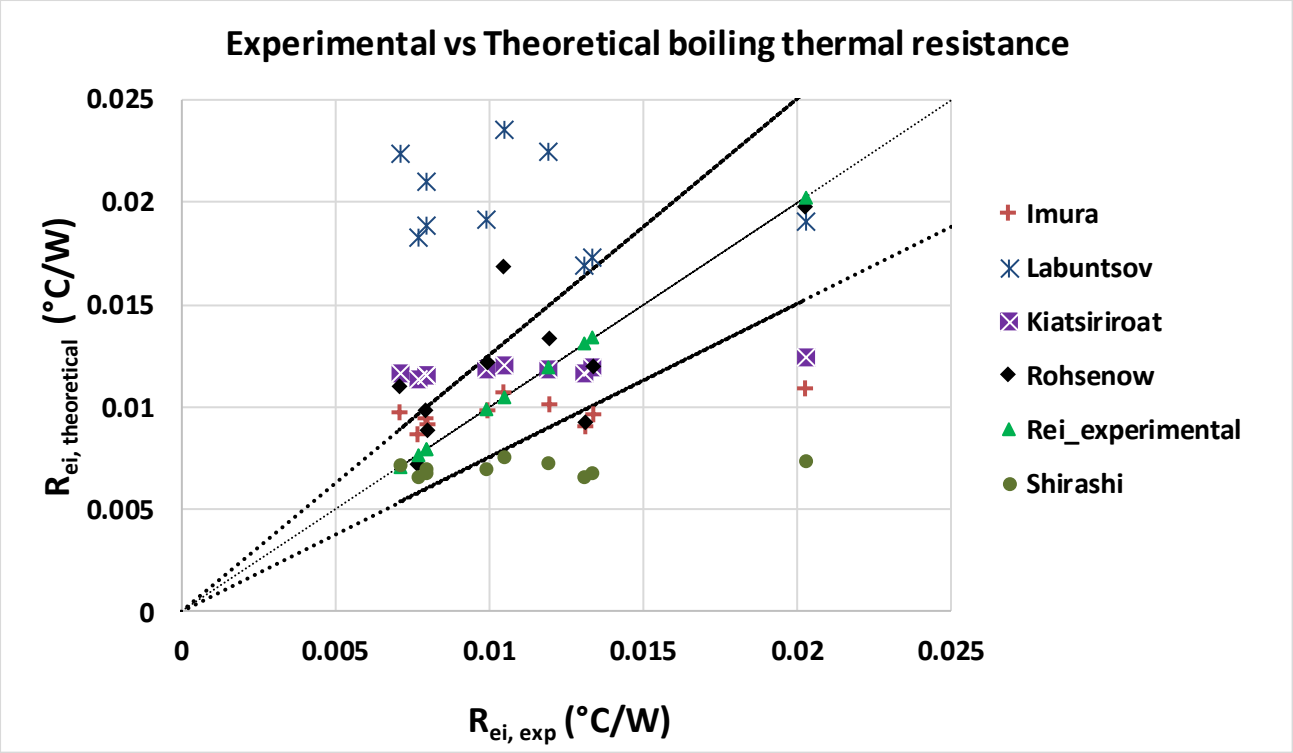

Figure 6-43 Experimental versus theoretical boiling thermal resistance

6.2.5.2 Predictions of the nucleate pool boiling thermal resistance and the falling film thermal resistance

This section presents the results of a different model applied to predict the heat transfer by boiling in the evaporator. The overall heat transfer by boiling can be predicted by considering it consists of two regimes: nucleate pool boiling at the liquid level at the evaporator and nucleate falling film boiling at the surface between the liquid level and the end of the evaporator section. The results of the prediction of boiling heat transfer using different combination of boiling heat transfer correlations is presented in Figure 6-44. Two correlations were used to predict the heat transfer at the pool region (Imura [100], and Rhosenow [92]). At the falling film region, Nusselt theory can be applied to predict the boiling heat transfer rate. Therefore, three correlations were used to predict the boiling heat which they were: Nusselt modified by Rohsenow [114], Jouhara [112], and Shirashi [101]. As a result, different six combinations were compared with the experimental heat transfer rate measured through the water flow rate. As it can be seen, that most of these combinations had prediction accuracy within 30% error when the heat transfer rate exceeded 300 W. The comparison cases where selected based on the absence of the geyser boiling and the evaporator temperature difference is less than 7 °C. It can be seen also that Imura& Jouhara, and Rohsenow& Jouhara represents are the best combination to predict the experimental results for the most cases. Rohsenow& Shirashi exhibited very good predictions but it was over predicting for some cases at experimental heat transfer rate lower than

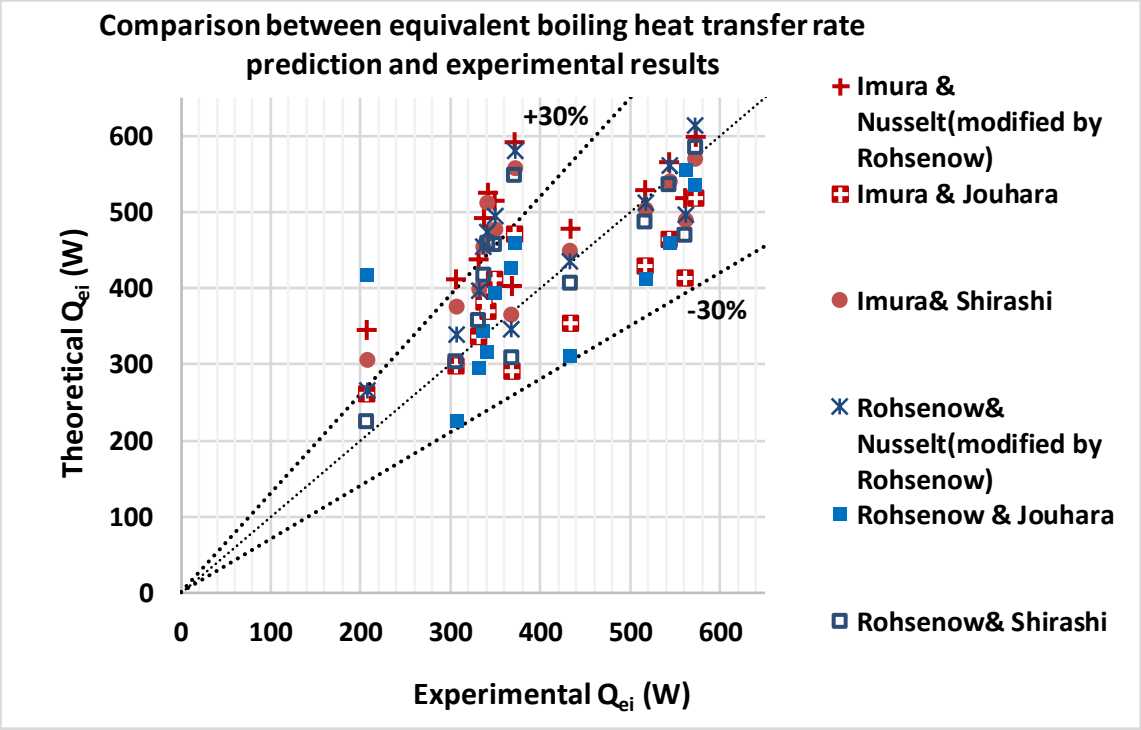

Figure 6-44 A comparison between the theoretical prediction and experimental boiling heat transfer rate considering two boiling regimes: nucleate falling film boiling and nucleate pol boiling

400 W. It is difficult to evaluate each correlation individually for each boiling region as the heat flux was not measured experimentally. Furthermore, this approach is very complicated to be employed in theoretical modelling because it needs two separate evaporator temperatures which complicates the radiation heat transfer the boiling heat transfer models due to increasing the variables and correlations to be solved.

A simplified approach can be followed where the overall boiling thermal resistance can be predicted by determining the equivalent thermal resistance of both the nucleate pool boiling and the nucleate falling film boiling. It was assumed that the heat flux is axially and radially uniform along the evaporator in order to determine the Reynolds number of the falling film and to calculate the temperature of the internal surface of the evaporator. The heat flux should be uniform and the boiling in the heat pipe steady, in order to obtain predictions close to the experimental results. Therefor this modelling approach will be applied when the heat flux was higher than 10 kW/m² where the uncertainty of the experimental results is at the minimum (<20%). Figure 6-45 shows a comparison between the overall thermal resistance of the boiling of the evaporator and the equivalent resistance of nucleate pool boiling and falling film boiling. It can be seen that the equivalent thermal resistance is 25% less than the overall resistance value. This variation is based on the assumption that the heat flux is uniform.

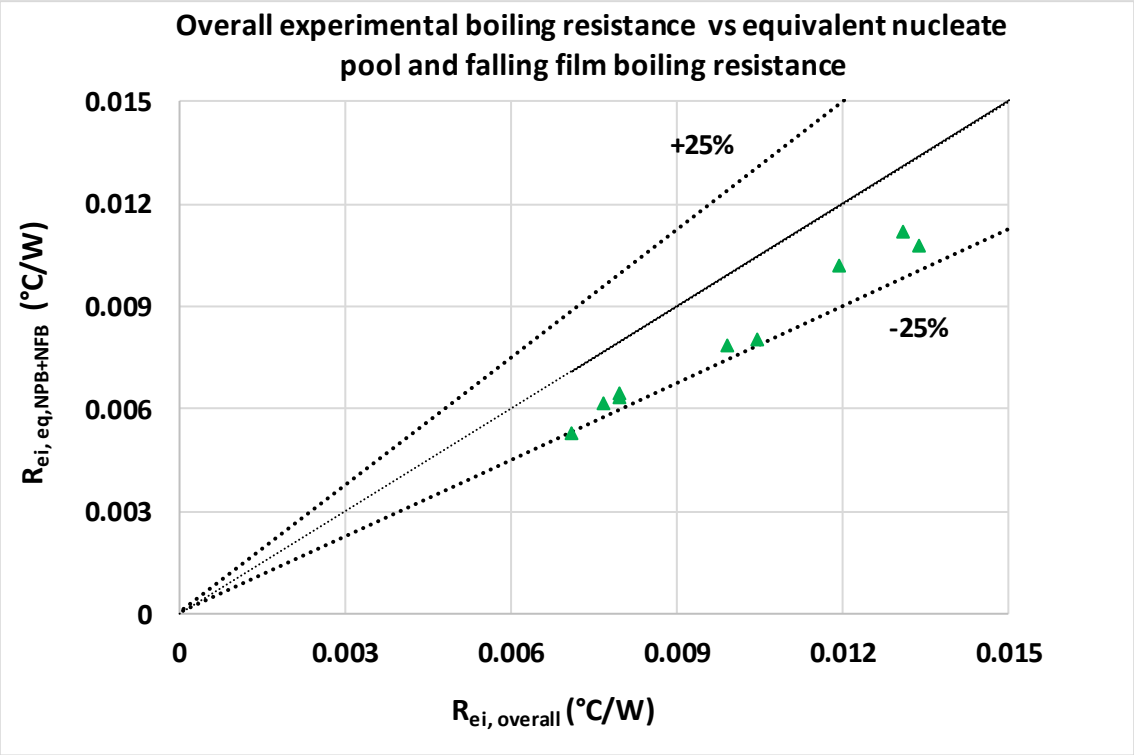

Figure 6-45 Comparison between the overall boiling thermal resistance and the equivalent thermal resistance of nucleate pool boiling and falling film boiling

The nucleate pool boiling thermal resistance was determined using *Imura* and *Rohsenow* correlations while the nucleate falling film boiling was determined using *Jouhara*, *Shirashi*, and *Nusselt modified by the Rohsenow* correlation.

The equivalent boiling thermal resistance obtained from the combination of those correlations in addition to the experimental equivalent and overall boiling thermal resistances are plotted versus heat flux (q_{ei}) in Figure 6-46.

As it can be seen that the combination of Rohsenow & Jouhara is much higher than the experimental value. Imura & Nusselt modified by Rohsenow is very close to the experimental value for boiling heat fluxes higher than 14 kW/m². For a heat flux lower than 12 kW/m², the best results were obtained by Imura & Jouhara and Rohsenow& Shirashi which agrees with the observations from Figure 6-44.

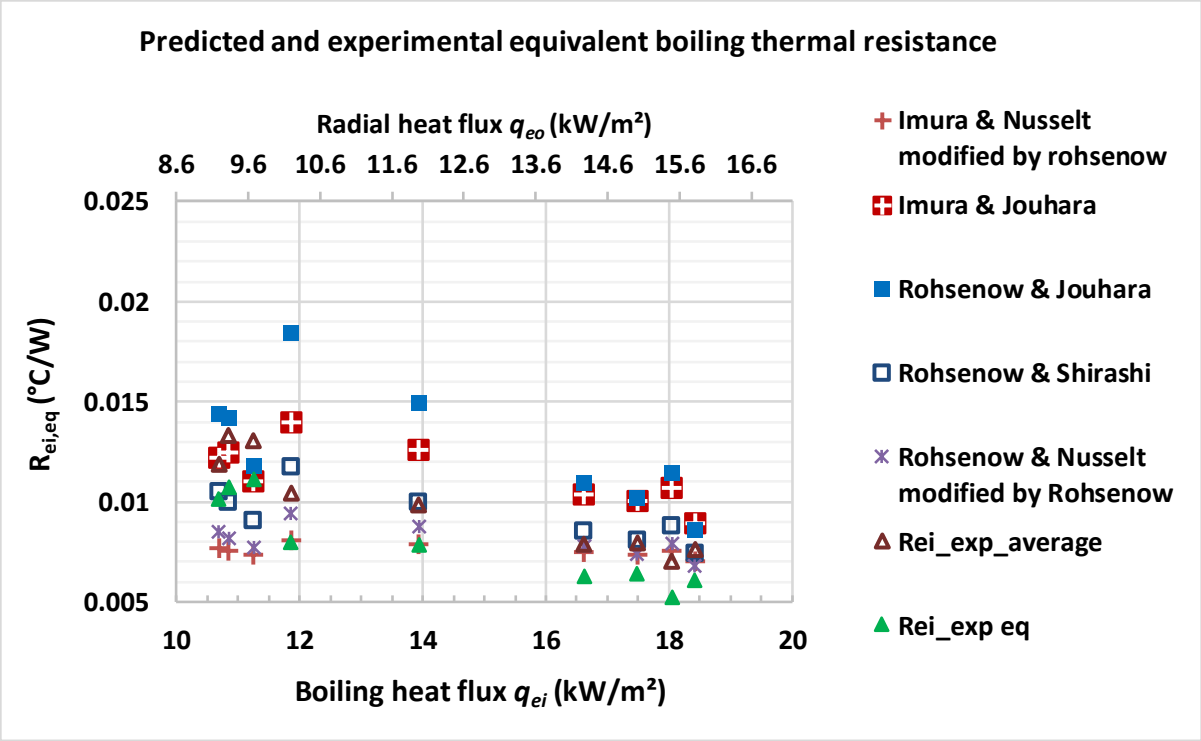

Figure 6-46 A comparison between the experimental and theoretical equivalent thermal resistance of boiling heat transfer using different combination of correlations as a function of the heat flux

The thermal resistances obtained from the theoretical correlations are compared versus the experimental average boiling thermal resistant and plotted in Figure 6-47 since there is error of 25 % due to the approximation. It can be noticed that the no set of combinations can predict the whole range of the thermal resistance. The combination of Rohsenow with Shirashi had the best accuracy for the range of 0.005 °C/W to 0.007 °C of the thermal resistance. Furthermore, Imura & Nusselt modified by Rohsenow exhibited the best accuracy for the range of 0.008 °C/W to 0.001 °C/W, while for thermal resistances higher than 0.001 °C/W, Rohsenow & Nusselt modified by Rohsenow showed good agreement with under prediction of 30%. Moreover, Imura & Jouhara tends to over-predict the thermal resistance within +30% for the same range.

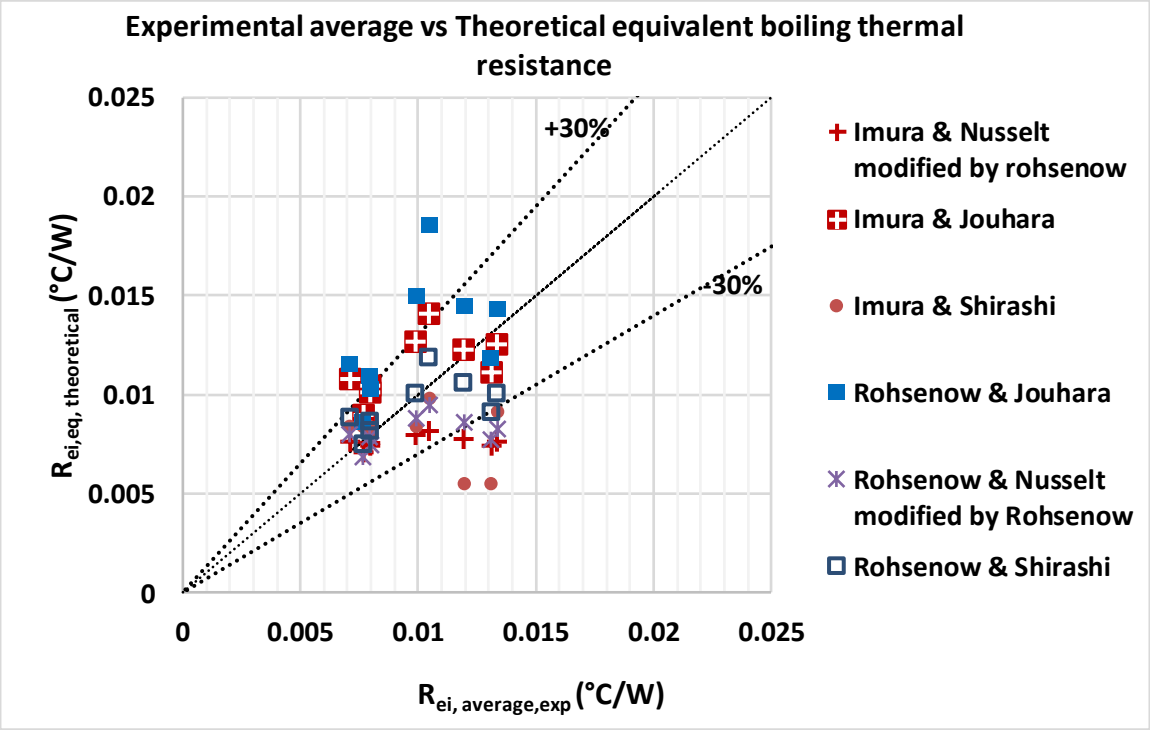

Figure 6-47 Predicted versus experimental thermal resistance of boiling heat transfer using two different correlations of nucleate boiling

These findings are very important for future work where more thermocouples can be installed and the tests can be re-conducted under uniform heat flux conditions and compared with the results from the radiative heat pipe to re-assist the accuracy of these correlations.

6.2.6 Experimental versus theoretical condenser thermal resistance

The condensation thermal resistance could not be determined experimentally through a direct approach by measuring the condenser wall temperature due to technical restrictions to weld thermocouples on the condenser wall. Moreover, the mass flow rate of the coolant was constant for all the experiments and, considering that, the convection thermal resistance is not influenced by the inclination of the condenser or the heat flux directly. Therefore, the overall thermal resistance of the condenser will be presented and compared versus the heat flux. The overall thermal resistance of the condenser is presented in Figure 6-48 as a function of the heat flux and for difference experimental conditions. The experimental results demonstrate that the overall condenser thermal resistance increases with the increase of the heat flux due to the increase in the film thickness which decreases the heat transfer coefficient. It can be seen that the thermal resistance for the unpainted heat pipe was less than for the painted heat pipe although that the heat flux was similar such as in the case of 45° at a heat flux of 10 kW/m². The thermal resistance of the vertical and 60° inclined painted heat pipe was not influenced by the heat flux when it exceeded 9 kW/m². The thermal resistance of condensation theoretically increases with the increase of the inclination angle θ from vertical due to

the decrease in the gravity force. However, it can be seen that the overall thermal resistance of the condenser decreased by increasing the tilting angle. The thermal resistance was 0.037 °C/W for the case of vertical heat pipe while it was 0.035 for 60° inclined one.

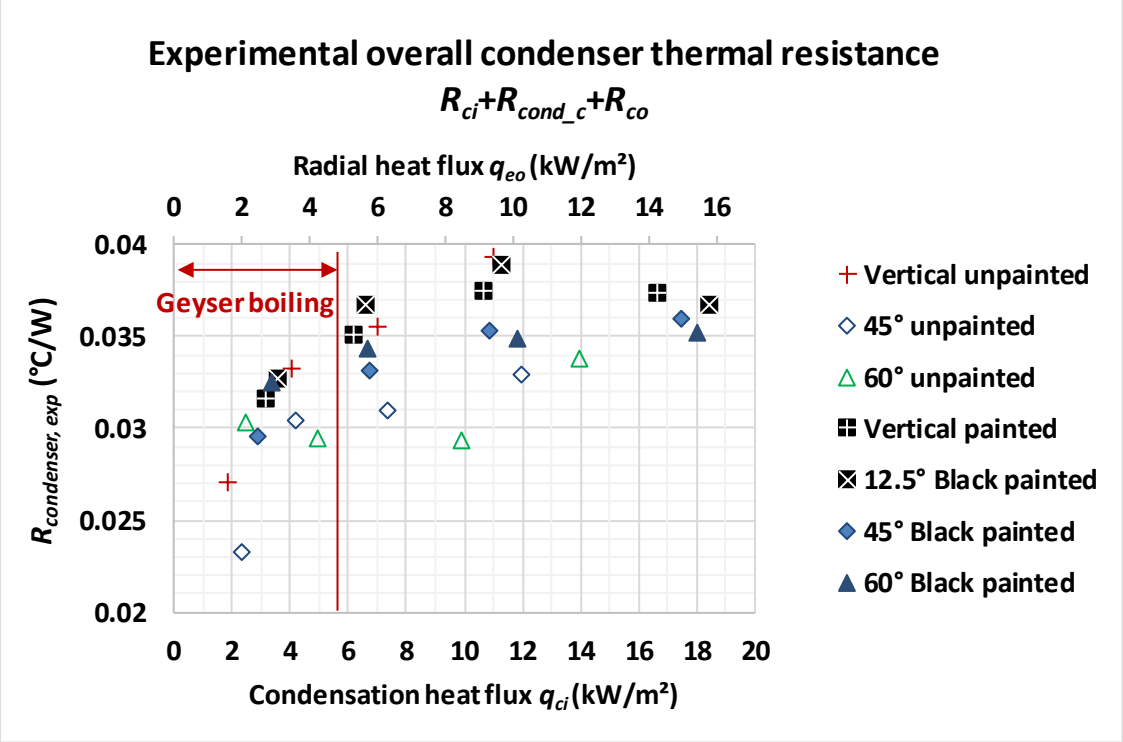

Figure 6-48 Experimental overall thermal resistance of the condenser

A modelling validation of the thermal resistance of condensation can be approached through calculating the conduction thermal resistance and determining the condenser inner wall temperature.

Figure 6-49 presents the calculated experimental condensation thermal resistance versus the condensation heat flux for various conditions. The trend of the condensation thermal resistance is the same of the condenser overall thermal resistance. The condenser thermal resistance was nearly constant when the condensation heat flux exceeded 10 kW/m².

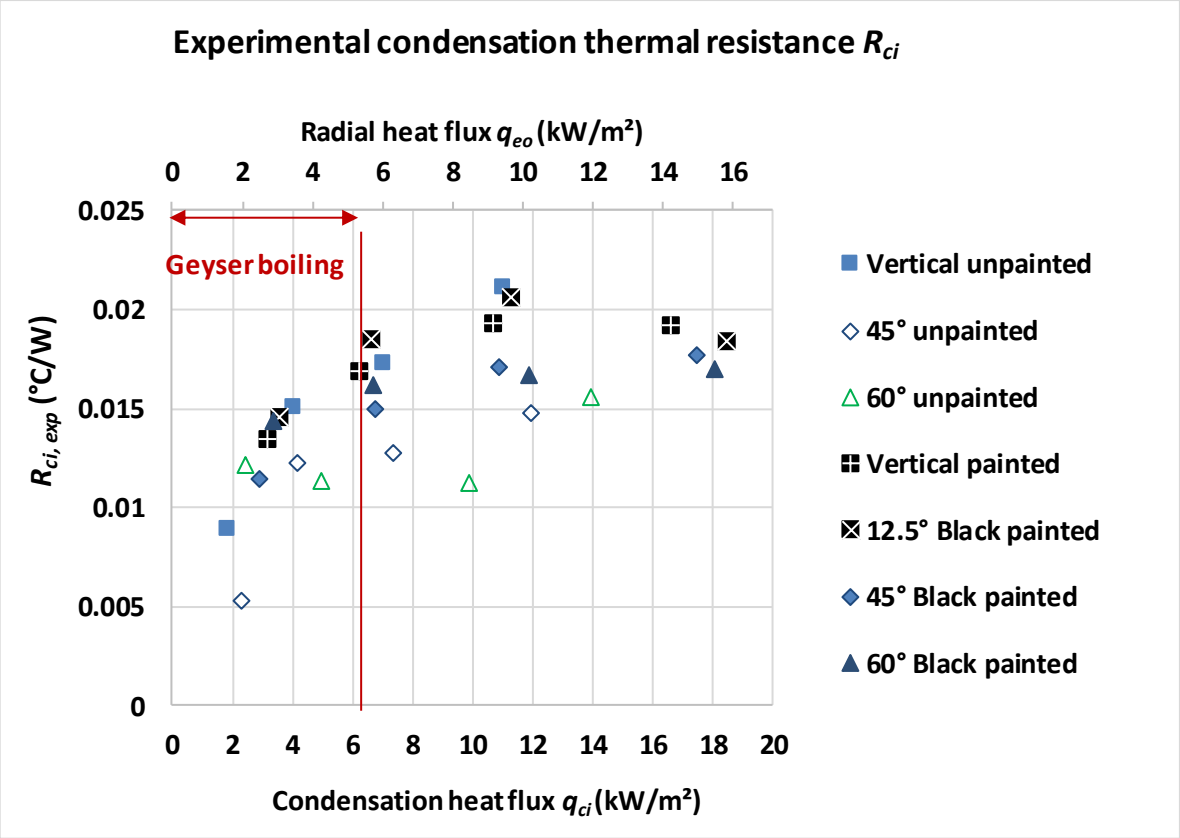

Figure 6-49 Experimental comparison of condensation thermal resistance with heat flux

Then experimental condensation thermal resistance is compared with theoretical prediction in Figure 6-50. The theoretical condensation resistance was calculated using Rohsenow's modification of Nusselt heat transfer. The correlations of Nusselt and Jouhara are not plotted as the error in the prediction exceeded 50 %. It can be seen the predicted results have excellent agreement with the experimental results within ±15% error except for two cases where they are within +21% error.

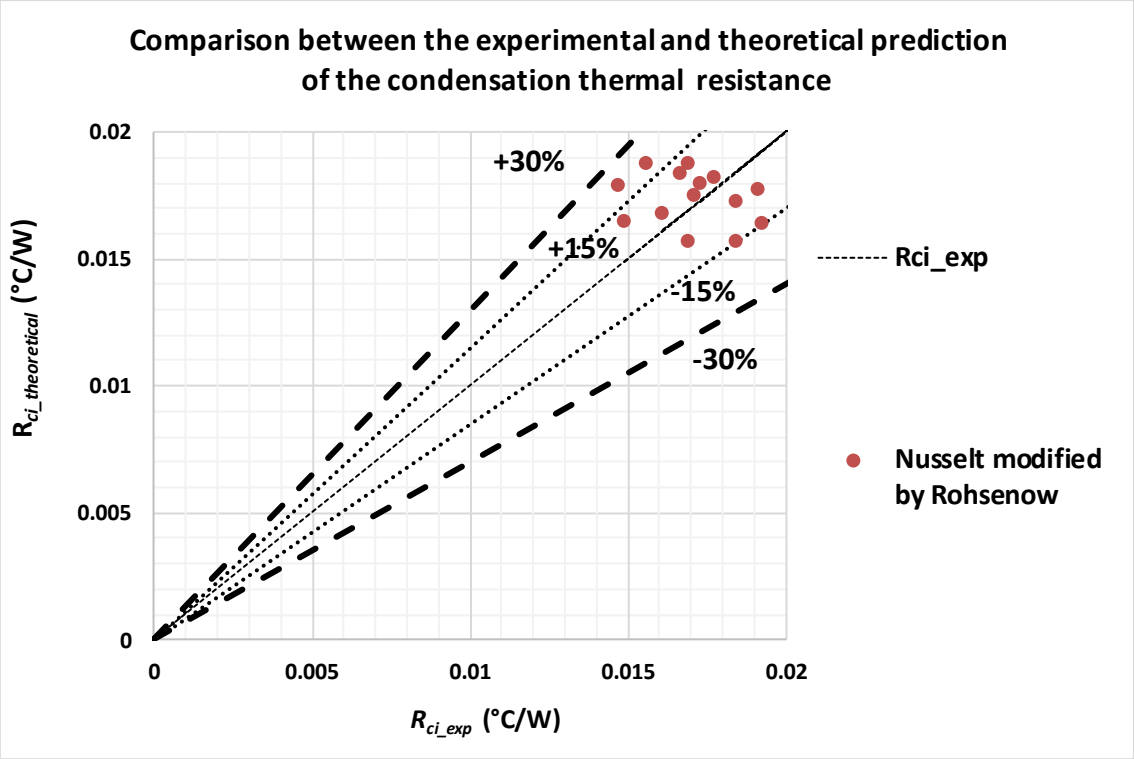

Figure 6-50 A comparison between the experimental and theoretical condensation thermal resistance

6.2.7 Theoretical forced convection heat transfer at the condenser

The resistance of the forced convention heat transfer cannot be experimentally determined by means of temperature, as there were no thermocouples placed on the condenser tube surface. The forced convection thermal resistance was calculated using the correlation of Hausen which was 0.0936 °C/W.

6.2.8 Radiation thermal resistances analysis

The overall radiation thermal resistance is associated with multiple factors as follows: the emissivity of the heaters which was a function of the heater temperature and surface condition, i.e. black painted and unpainted, and the view factor of the heat pipe.

It was observed from theory that the space thermal resistances $R_{H,HP}$, $R_{H,W}$, and $R_{W,HP}$ are independent of the temperature since the walls are considered to be re-radiating the heat, therefore the space resistance equivalent of those resistances should be compared with the experimental one at different inclinations and emissivity. Furthermore, based on energy conservation and the assumptions made for the model, the overall thermal resistance was also independent of the inclination of the heat pipe. The inclination angle theoretically affects the direct and re-radiated radiative heat from the heater to the heat pipe. Figure 6-51 presents a comparison between the theoretical equivalent space resistance and the experimental one calculated by measuring the evaporator temperature, heater temperature, and radiation heat transfer rate. It can be seen that the theoretical resistance had constant value of 30 m^{-2} while the experimental value varied depending on

the test condition. Therefore, the theoretical equivalent space resistance was corrected based on experimental findings with a correction factor varied between 1.11 and 1.83.

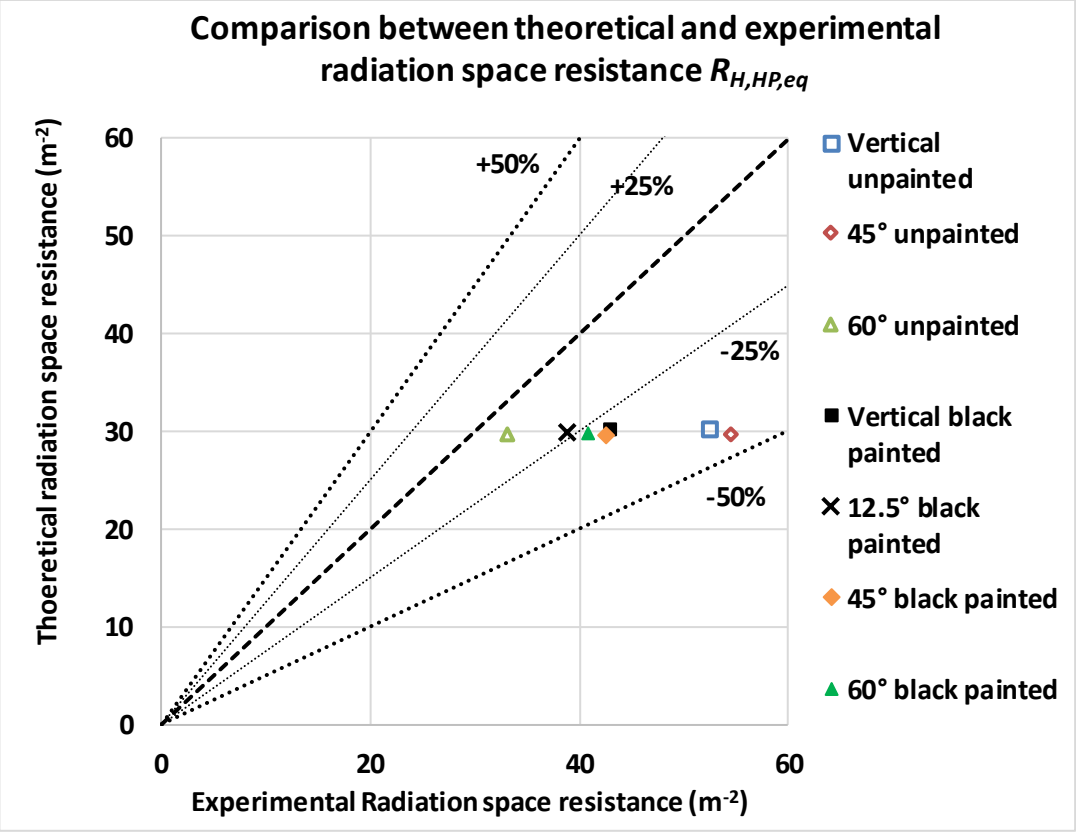

Figure 6-51 Theoretical vs experimental radiation space resistance

6.2.9 Total thermal resistance of the heat pipe (experimental and theoretical)

The total thermal resistance of the heat pipe is presented in Figure 6-52. Similar to the boiling thermal resistance trend, the thermal resistance of the heat pipe decays with the increase of the heat flux until it reaches a value of 0.046 °C/W. The thermal resistance of the heat pipe was approximately steady for radial heat fluxes higher than 8 kW/m² regardless of the inclination. For heat fluxes less than 8 kW/m², the thermal resistance of the heat pipe when geyser boiling was encountered is higher than the cases where the geyser boiling was eliminated.

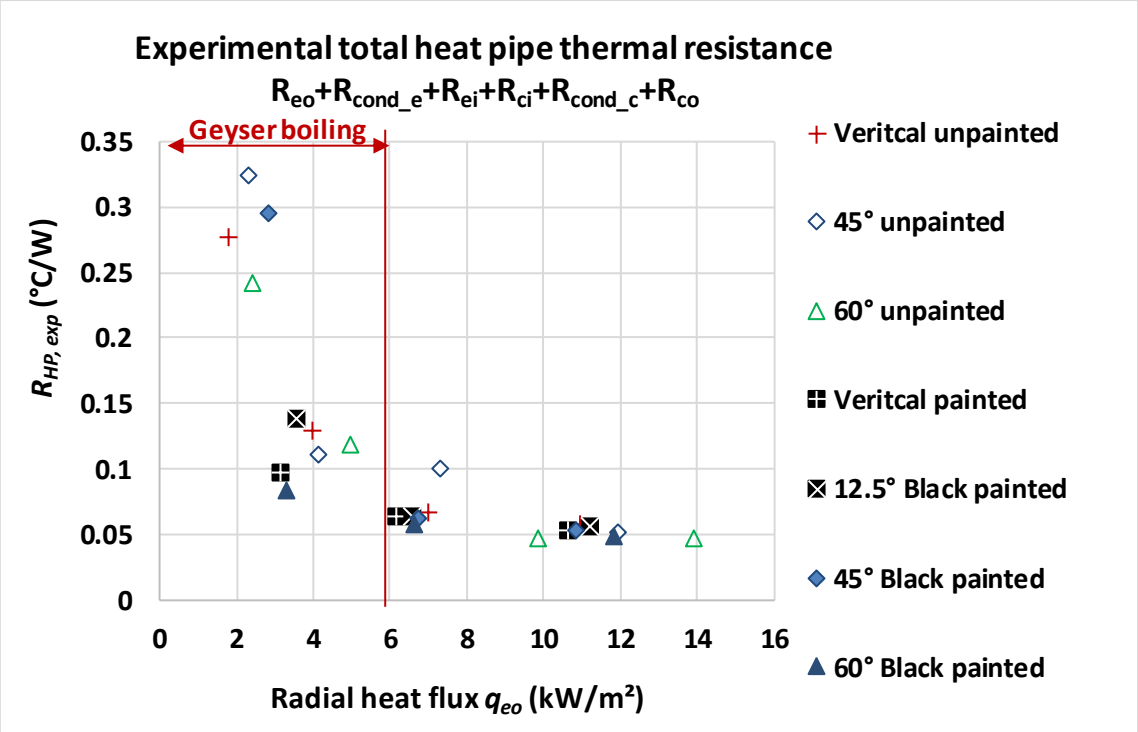

Figure 6-52 Experimental total thermal resistance of the heat pipe

6.2.10 Theoretical modelling tool predictions for the heat recovery

The theoretical overall heat recovery using the modelling tool are presented versus the experimental heat recovery in Figure 6-53. The modelling tool predictions show an excellent agreement with the experimental results within an error of 10% and less than 10 % for the cases when the heat recovery is over 200 W. The high accuracy of the modelling tool is achieved by selecting the single phase and two-phase heat transfer correlations properly in addition to the correction of the radiation space resistance.

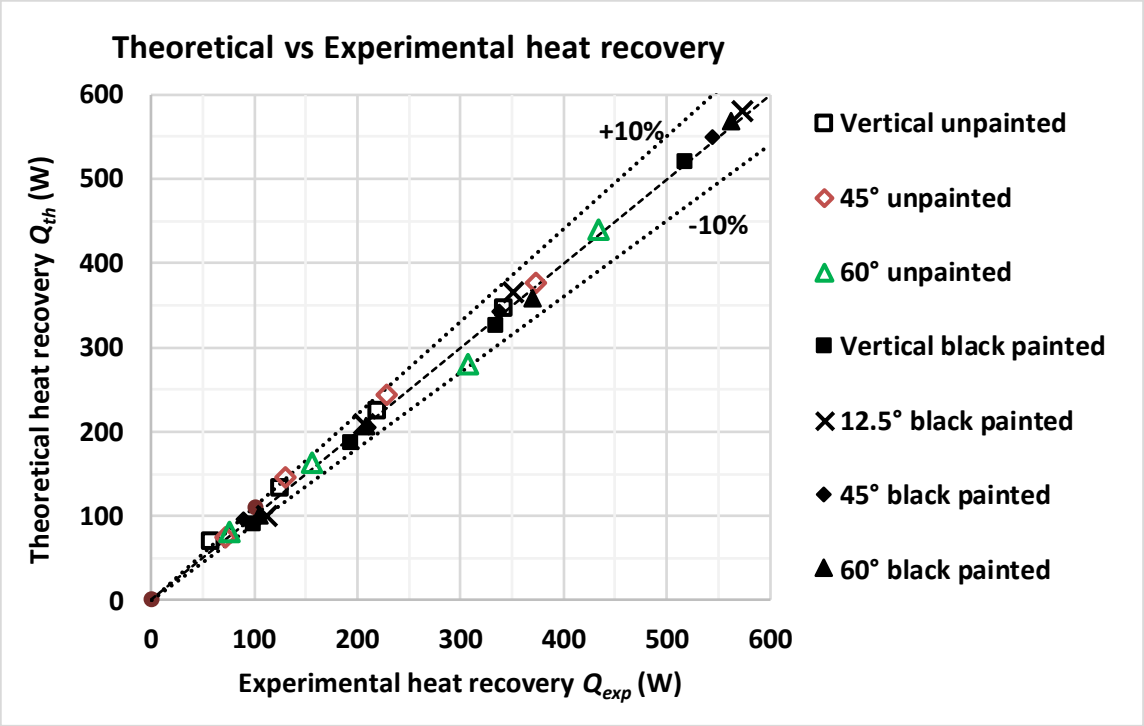

Figure 6-53 A comparison between the theoretical and experimental heat recovery

6.2.11 Theoretical prediction of the heat pipe temperature

Due to the large number of experiments and since the theoretical resistance modelling is well detailed before, in addition to the excellent prediction accuracy of the heat recovery, this section will present a comparison of the heat pipe temperature at steady state for one case when the heat pipe was black painted and tilted at 60° from vertical at heater temperature of 500 °C as shown in Figure 6-54. It can be seen that the outer wall evaporator temperature is 2.6 °C higher than the experimental measurement and the difference in vapour temperature is less than 1 °C. Furthermore, the difference of the water outlet temperature between the prediction and the experimental measurements is 0.06 °C.

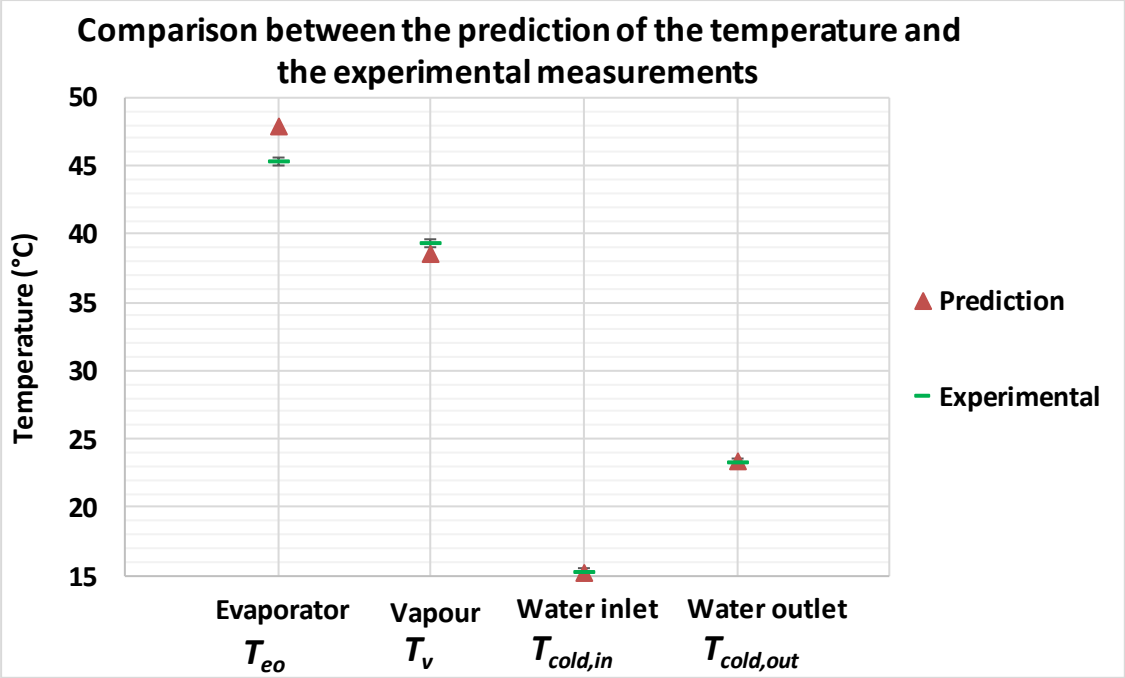

Figure 6-54 Theoretical prediction versus experimental measurement of the heat pipe temperatures

6.3 Flat Heat pipe in the laboratory

This section presents and discusses the experimental and theoretical results for the examination of the FHP in the laboratory. The FHP was tested at different heater temperatures (400 °C, 470 °C, 500 °C, 580 °C) which correspond to an average heat source of (397 °C, 427 °C, 488.8 °C, 544.2°C), respectively.

The experimental results of the heat recovery in the laboratory and discussion were published by the author in *Almahmoud and Jouhara* [136].

The FHP was tested in the laboratory with different configurations as shown in Chapter 3 in Figure 3-44, Figure 3-45, Figure 3-46, Figure 3-47, and Figure 3-48.

It was noted that the best case of FHP thermal performance was when the FHP was assembled with the back panel and painted with black paint at an average heat source temperature of 544 °C. Therefore, the experimental results of this case are discussed.

The temperatures of the FHP during the test with black paint and back panel at a heater temperature of 580 °C corresponding to an average heat source of 544 °C is presented in Figure 6-55. The temperature of the bottom collector was 73 °C and the average of the temperature readings of the 9 thermocouples on the vertical pipes was 68.4 °C. The average temperature of the adiabatic section was 52.6 °C. The temperature of the water inlet was 21 °C, and the temperature of the water outlet

was 27.9 °C. The large temperature difference between the evaporator and the adiabatic section is due to the high thermal resistance of boiling compared with the low heat flux of 12.6 kW/m².

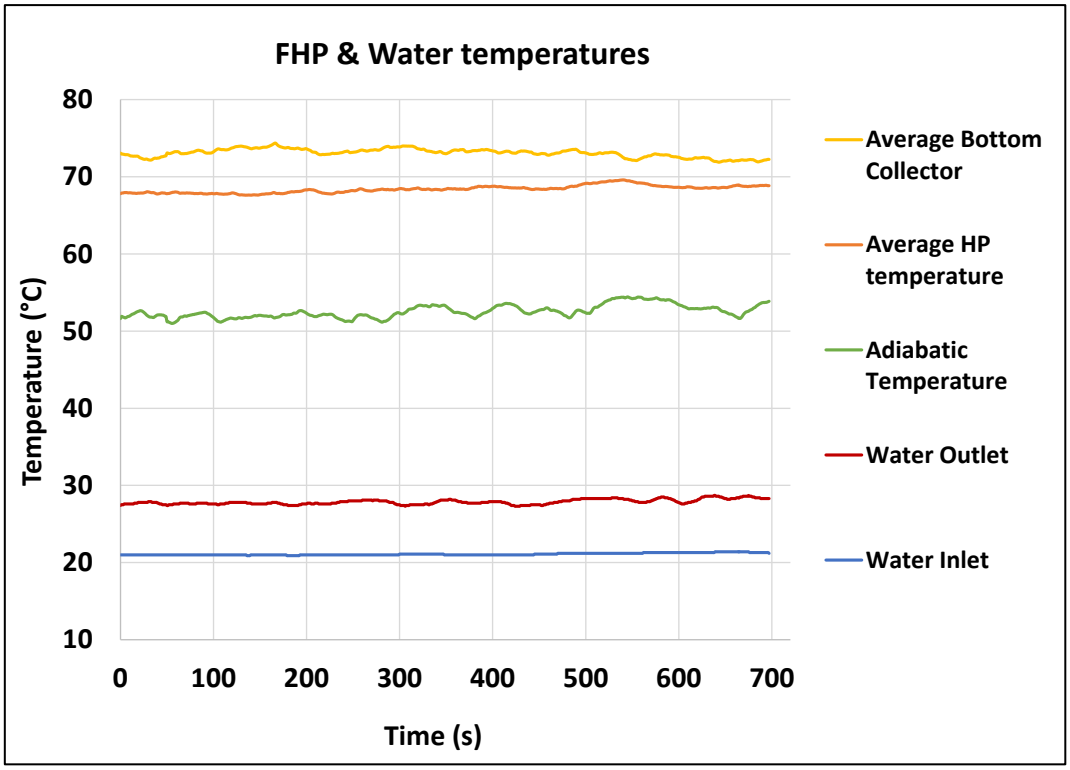

Figure 6-55. FHP and water temperatures for FHP tests with a back panel and black paint at heater temperature 580°C

The amount of heat recovery is presented in Figure 6-56. The heat transfer rate ranged between 7.9 kW and 9.4 kW with an average value of 8.4 kW. The fluctuation in the results was caused by the high mass flow rate of the water in comparison to the temperature difference between the inlet and outlet of the water. It should be noted that a fluctuation of 0.5 °C in the water temperature difference between the inlet and the outlet results in a 700 W of heat recovery difference at a water flow rate of 18 l/min.

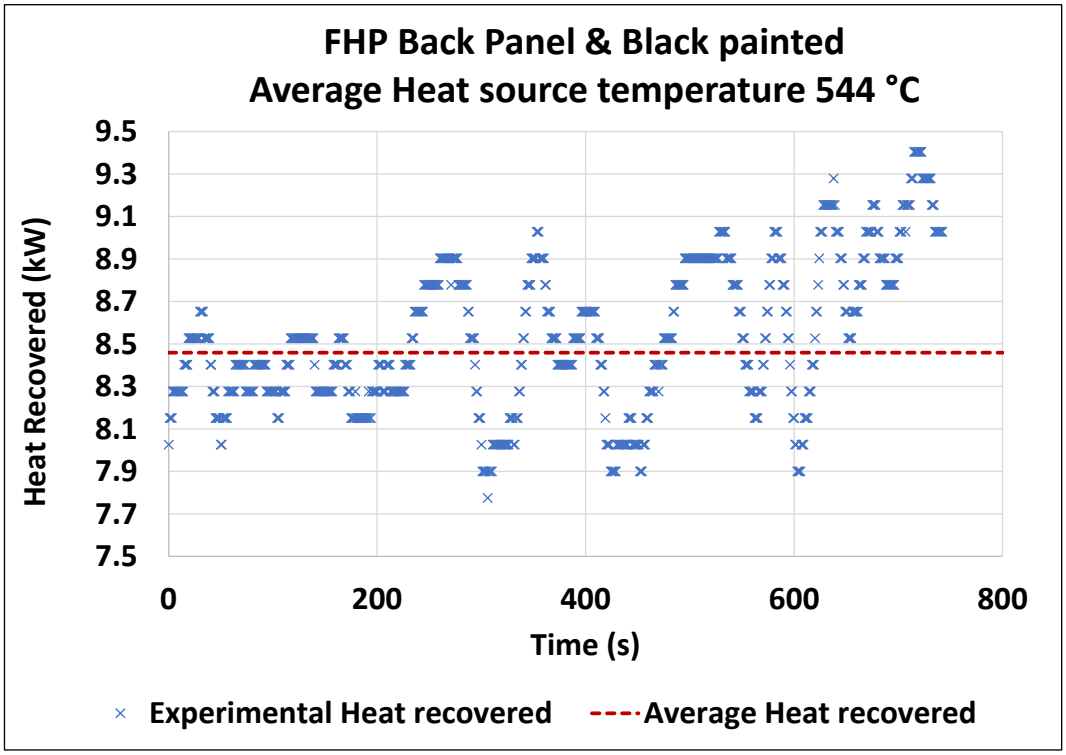

Figure 6-56. Heat recovery by black painted FHP with a back panel at heater temperature of 580°C

The temperature measurement of the evaporator, adiabatic section, water inlet, and water outlet of the FHP for the case black painted with a back panel at different heat recovery levels are plotted in Figure 6-57. The evaporator temperature increased about 10 °C when the heat recovery increased from 2.8 kW to 8.4 kW. Moreover, the adiabatic temperature increased about 12 °C for the same heat recovery increase. The water temperature difference increased from 2.9 °C to 6.8 °C.

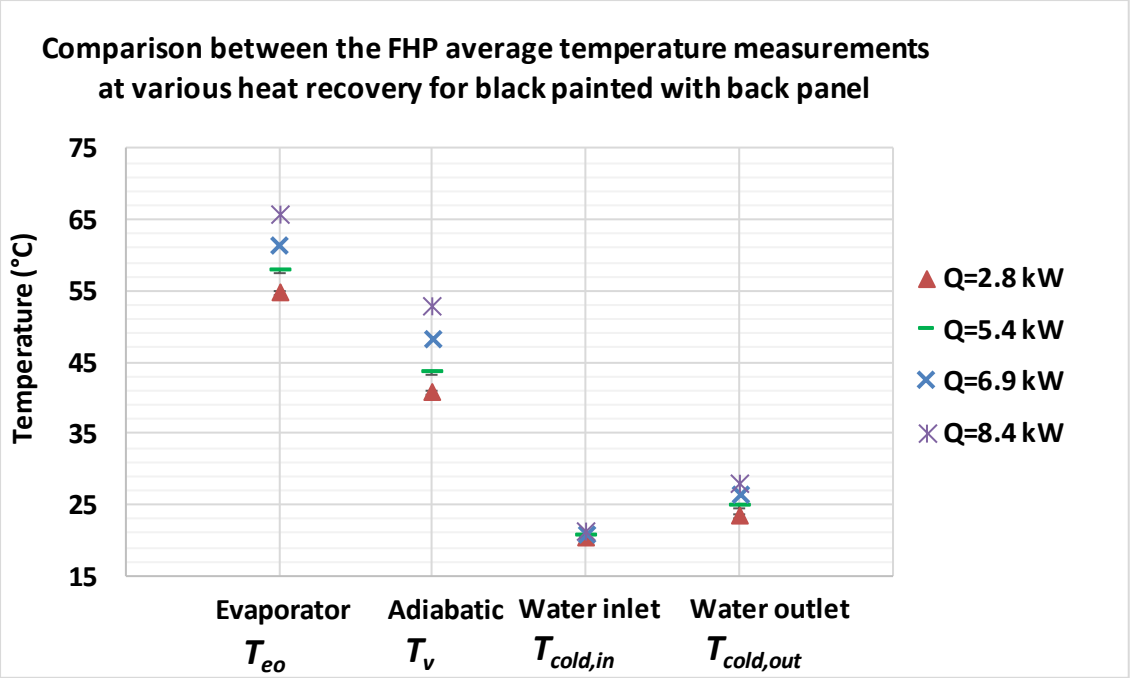

Figure 6-57 A comparison between the FHP (back panel and black painted) temperature measurements at different heat recovery

6.3.1 FHP with back-panel and black panel at water temperature 70 °C

The FHP was tested at a water inlet of 70 °C to validate the possibility of using it as waste heat recovery technology where the coolant water will be used for heating process at the factory.

The experimental temperature measurements of the FHP with a heat source of 544 °C corresponding to a heater temperature of 580 °C are presented in Figure 6-58.

The temperature of the bottom collector and the vertical pipes was 97.9 °C and 99.6 °C, respectively. The temperature of adiabatic section of the FHP was 93.6 °C. The water inlet temperature was 69.1 °C and the water outlet temperature was 73.1 °C. The back panel temperature was measured in this test and its temperature reached 261 °C. It should be highlighted that the back panel was insulated from the rear while testing the FHP at a water inlet temperature of 70 °C. Furthermore, The FHP did not show any signs of geyser boiling for a heat source temperature greater than 427 °C.

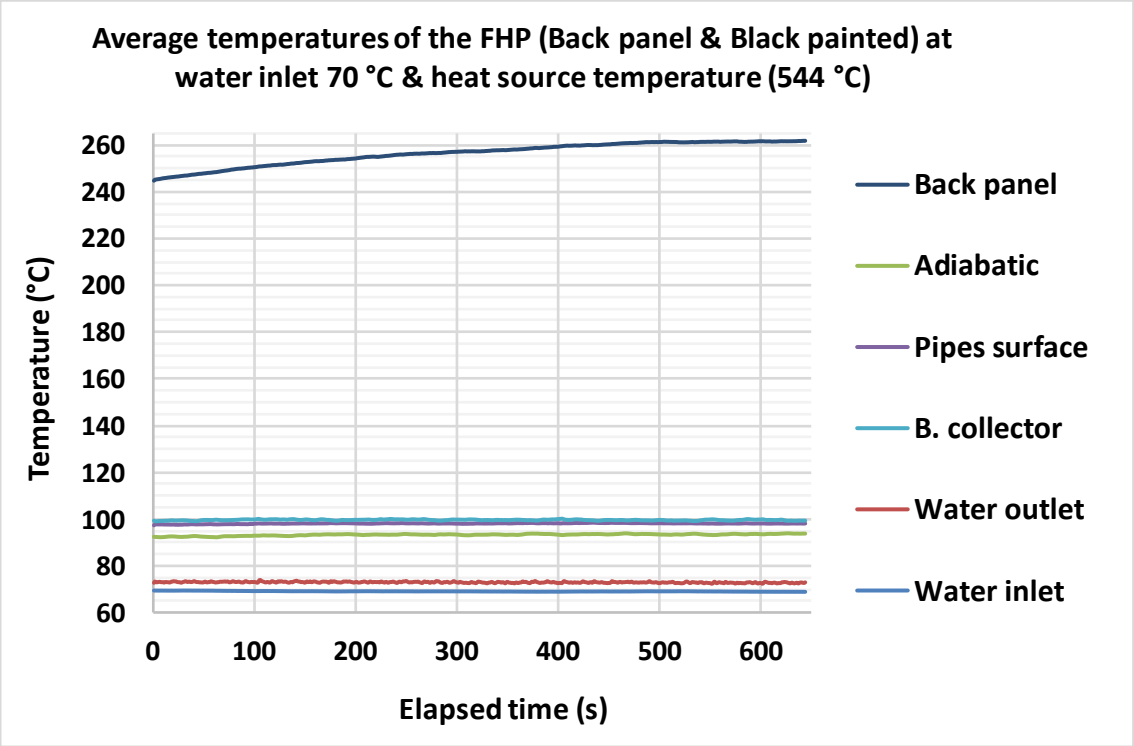

Figure 6-58 FHP and water temperatures for FHP tests with a back panel and black paint at heat source temperature 544 °C

The experimental heat recovery of the FHP is presented in Figure 6-59. The heat recovery was fluctuating with time as result of the high water mass flow rate (25 l/min) in comparison to the water inlet and outlet temperature difference. The heat recovery reached a peak of 8.2 kW while the average heat recovery was 6.7 kW. It can be noticed that the heat recovery when the water inlet temperature was 70 °C was less than for the case of water inlet temperature at 20 °C. The experimental heat recovery at various conditions is compared in the following section.

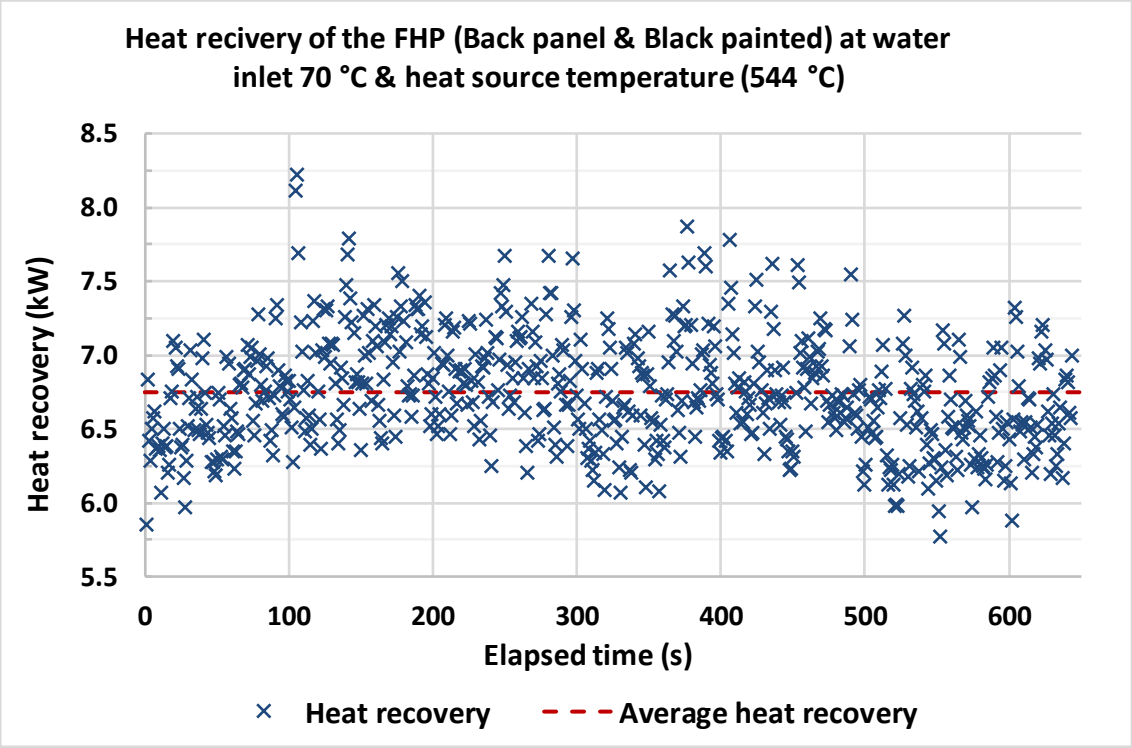

Figure 6-59 Heat recovery by black painted FHP with a back panel at heat source temperature of 544 °C

6.3.2 Comparison between the experimental heat recovery versus different heat source temperatures

The results from tests on the FHP are shown in Figure 6-60. It can be seen that the heat recovery increased with increasing the average heat source temperature. The trend of the curves for heat recovery are, in general, consistent with the increase in electrical heater input. The magnitude of the rate of heat recovery varied between 0.4 kW and 8.5 kW (2 to 12.6 kW/m² of heat flux per evaporator surface area) during the tests. Furthermore, the amount of heat recovery for the FHP unpainted and without a back panel was very low and the effect of the heater temperature had an insignificant influence on the performance of the FHP as shown in Figure 6-60. The radiation heat flux incident on the FHP at this case was insufficient where a major part of it reflected away from the FHP. In addition, the FHP parallel pipes exchange heat with the surroundings by radiation and natural convection which was not the case when the back panel was is attached.

It can also be seen that the best thermal performance and highest heat recovery was obtained for the case of the FHP attached to the back panel and painted with black paint.

It can be noticed that water inlet temperature has a significant effect on the FHP heat recovery by comparing the cases of back panel and black painted at the two different water temperatures. The highest heat recovery was obtained when the water inlet temperature was 21 °C while it was less for

water inlet temperature of 70 °C. In fact, the heat pipe working temperature is a function of the heat flux, the heat source temperature, and the coolant inlet and outlet temperatures. The increase in the coolant inlet temperature increases the operating temperature of the FHP at the same heat source temperature in order to achieve the energy balance between energy input and energy output. As a result, the evaporator temperature increases which increases the heat loss to the surroundings by radiation and natural convection, and also decreases the net heat transfer by radiation between the FHP and the heater which is dependent on the temperature difference between the heater and the FHP to the fourth power.

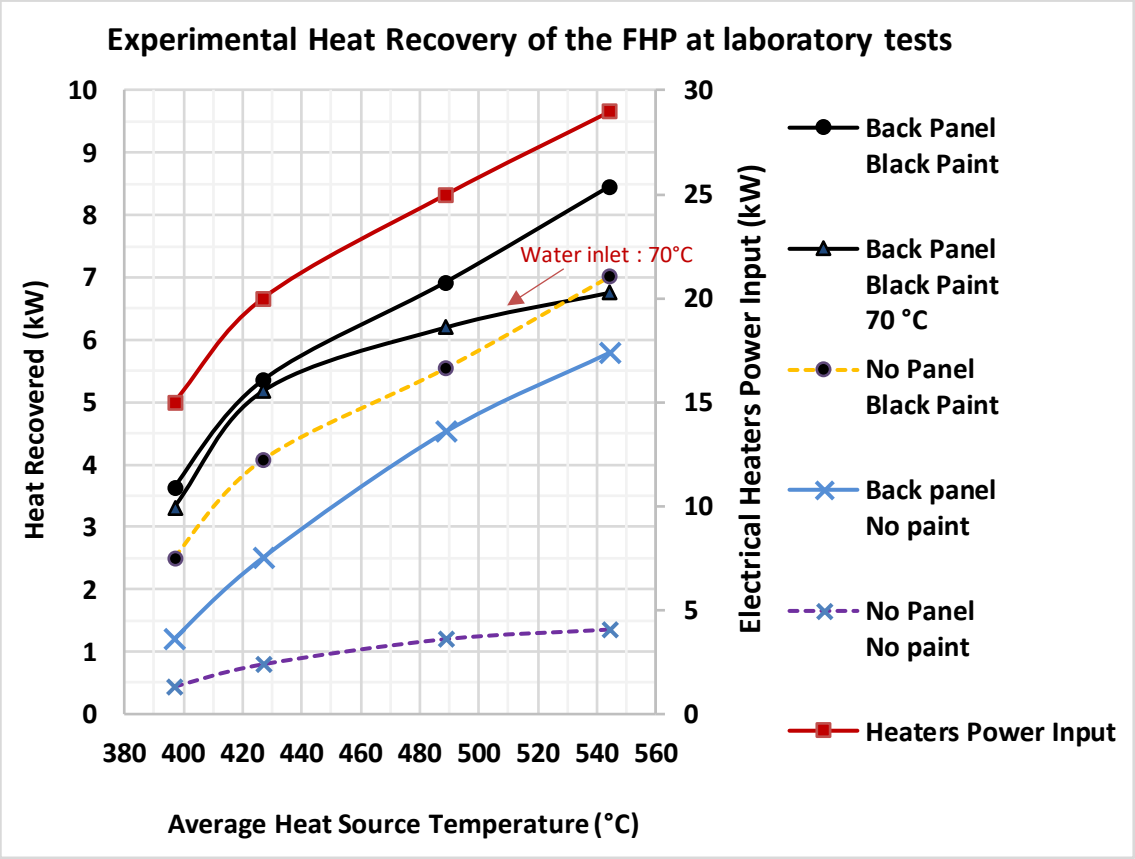

Figure 6-60 A comparison of the heat recovery versus source temperature at different conditions

The FHP effectiveness, which is defined as the ratio of the heat recovered to the incident radiation on the overall FHP surface, was 88% for the case of black paint with back panel and 57% for the case of the FHP black painted with no back panel.

The effect of the black paint and the back panel on the heat recovery is discussed in the following sections.

6.3.3 Effect of the back panel on the heat recovery

The effect of the back panel on the FHP thermal performance is presented in Figure 6-61 for two cases: when the FHP was not painted and when was painted black. In the case when the FHP was unpainted, the amount of heat recovery considerably increased when compared to the test without a panel. This was due to the fact that the back panel acted as a re-radiating surface, which increased the heat transfer area of the FHP. The back panel absorbed thermal radiation, then re-emitted it and reflected radiative heat, and the pipes absorbed a part of this heat. In the case of an unpainted FHP the increase in heat recovery increased from 175% at a heat source temperature of 397 °C to 330% at a heat source temperature of 544 °C. Moreover, in this case, the improvement due to the back panel increased with the increment of the heater temperature due to the increase in its own temperature. In contrast, the effect of the back panel on the painted FHP varied only between 11% and 31%. The impact of the back panel in the case of the unpainted FHP was greater than for the black painted FHP case. This was because of the low thermal performance and heat recovery for the case of the FHP without a back panel and unpainted. Moreover, the unpainted back panel was insulated, which reduced heat losses by natural convection and radiation to the surroundings and which also enhanced the boiling mechanism in the evaporator. The insulated unpainted back panel lost the heat from one side, while the black panel lost heat from both sides, the front and the back. The efficiency of the black back panel would be enhanced by adding insulation on the back side of it.

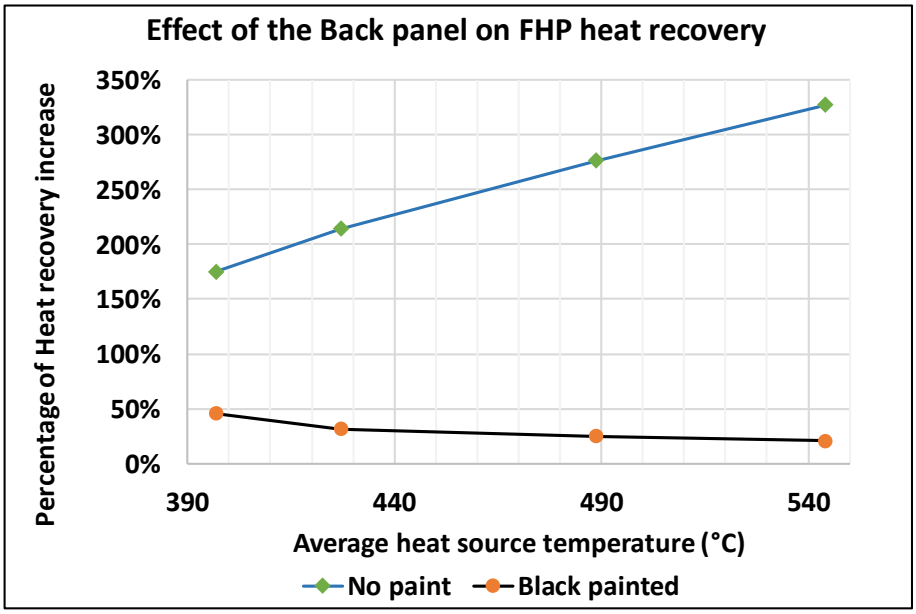

Figure 6-61 Effect of the back panel on FHP heat recovery

6.3.4 Effect of the black paint

The effect of the black paint on the thermal performance of the FHP is discussed for two cases as well: when the back panel was detached from the FHP and when it was assembled, as shown in Figure 6-62.

The influence of the black paint on the heat transfer rate varied between 360% and 470% in the case of the FHP without a back panel. It can be noted that the heat recovery improvement appeared to decrease with increasing heater temperature. The unpainted FHP was unable to operate without a back panel at low heater temperatures, which shows the significant impact of the black paint on the heat recovery. It can be understood that the incident radiation was reflected from on the unpainted FHP pipes surface and the FHP was uninsulated from the back, which increased the heat loss by natural convection and radiation. By increasing the heater temperatures, the unpainted FHP was operating under geyser boiling condition. However, the increase in the thermal performance with the increase of the heat source temperature of the unpainted FHP was less than for the case of the black painted FHP, indicating an increase of the impact of the paint.

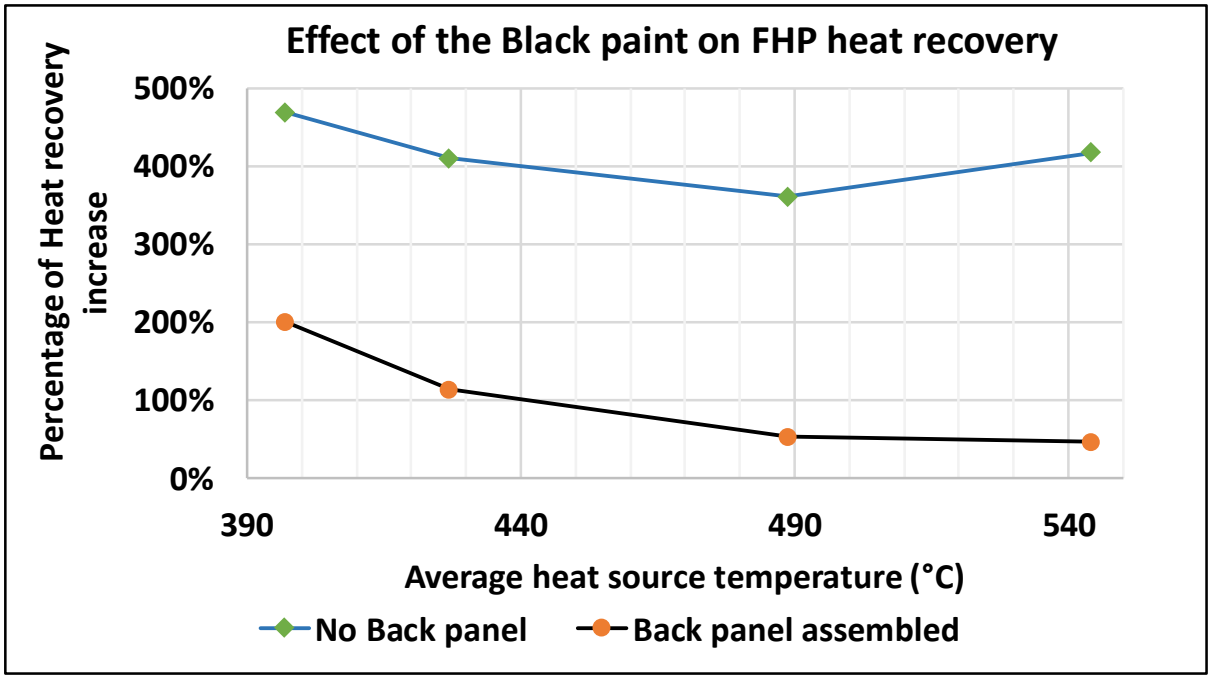

Figure 6-62 Effect of the black paint on FHP heat recovery

In the case of the FHP assembled with the back panel the enhancement due to the black paint decreased from 200% to 46%. The impact of the black paint decreased with the increased hot source temperature due to the following reasons. At heater plate temperatures of 400 °C and 488 °C, the FHP with a back panel was also working with presence of geyser boiling. The increase in the heater temperature increased the amount of heat recovery but also increased the surface temperature of the FHP and the back panel. As a result, heat losses to the surroundings increased and heat losses by

radiation started to play a significant role. Since the black painted back panel was uninsulated, increasing heat losses decreased the overall gain due to the black paint.

By comparing the impact of the back panel with the impact of the black paint at heat source temperatures higher than 490 °C (at heater temperatures higher than 500 °C) when the FHP was operating properly, it can be observed that the black paint has a more significant impact than the back panel.

6.3.5 Theoretical modelling

The theoretical predictions based on the model presented in the theoretical heat transfer modelling chapter are compared against the experimental results for the four cases of the experiments.

The theoretical results versus experimental results for heat recovery in the case of the FHP with no panel and unpainted are shown in Figure 6-63. It can be noted that the theoretical heat recovery increases with increasing heat source temperature and the difference between the experimental results and the predictions was higher at higher heat source temperatures. The FHP was not operating properly due to the inadequately low heat fluxes for this arrangement, which could not be represented in the theoretical model.

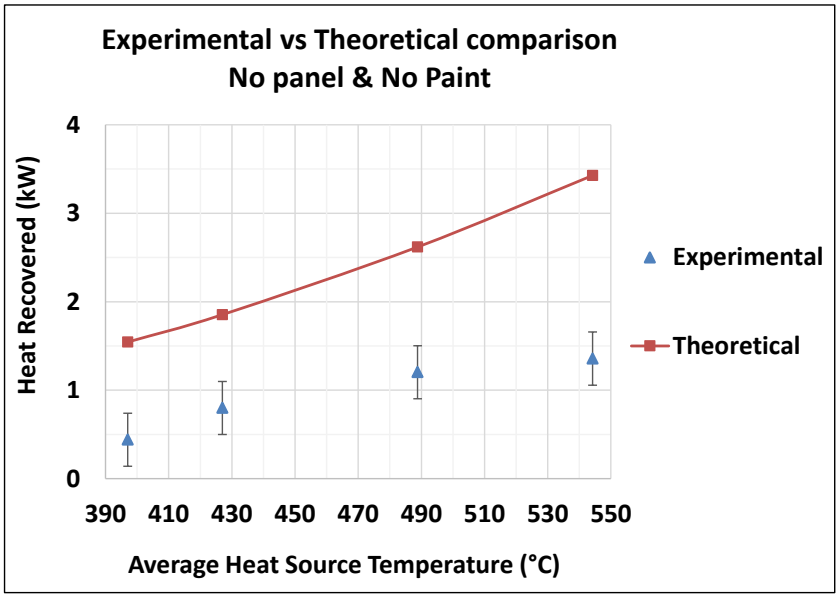

Figure 6-63 Comparison between experimental and theoretical prediction of the heat recovery in the case no panel and no paint

The theoretical and experimental results in the case of the FHP when with no panel and with black paint are illustrated in Figure 6-64. It can be observed that the prediction of heat recovery was less than the experimental results when the overall heat recovery was more than 3 kW. The theoretical model does not consider heat recovery by natural convection which explains the variance between

the experimental and theoretical results. Furthermore, the calculation of the view factor and the space resistance significantly affects the predicted amount of heat recovery. At a heat source temperature of 390 °C, the heat flux corresponding to the heat source temperature and the hot air temperature was under the required value which enables the FHP to operate ideally without geyser boiling. Therefore, the prediction of the heat recovery is slightly higher than the experimental result.

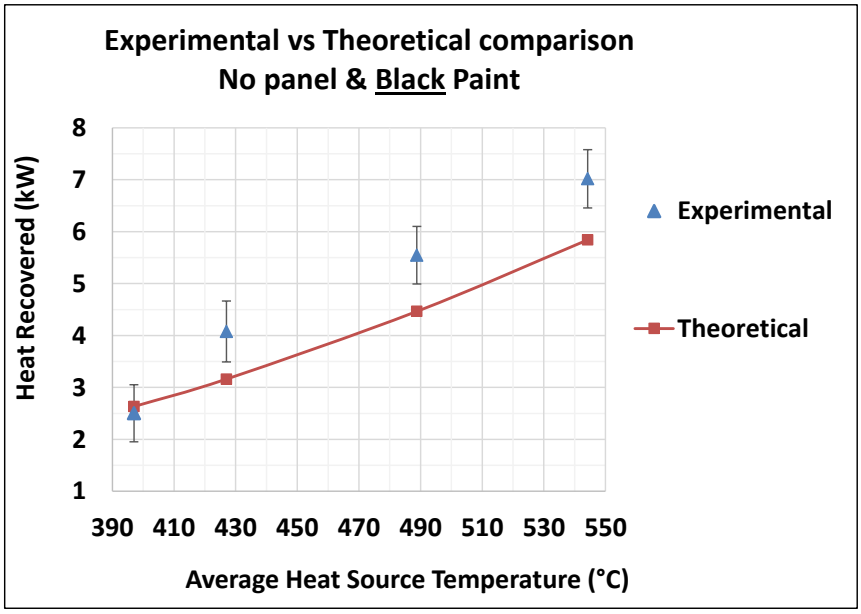

Figure 6-64 Comparison between experimental and theoretical prediction of the heat recovery in the case with no panel and black paint

Figure 6-65 shows a comparison between predictions and experiment obtained from testing the unpainted FHP attached to the back panel (Back panel & No paint). It can be observed that the predicted heat recovery at a heat source temperature of 390 °C was higher than the experimental results while it was less than the experimental results for higher heat source temperatures. The FHP was operating under geyser boiling condition when the heat source temperature was lower than 490 °C. Furthermore, it can be seen that the error of the prediction is within the uncertainty of the experimental results.

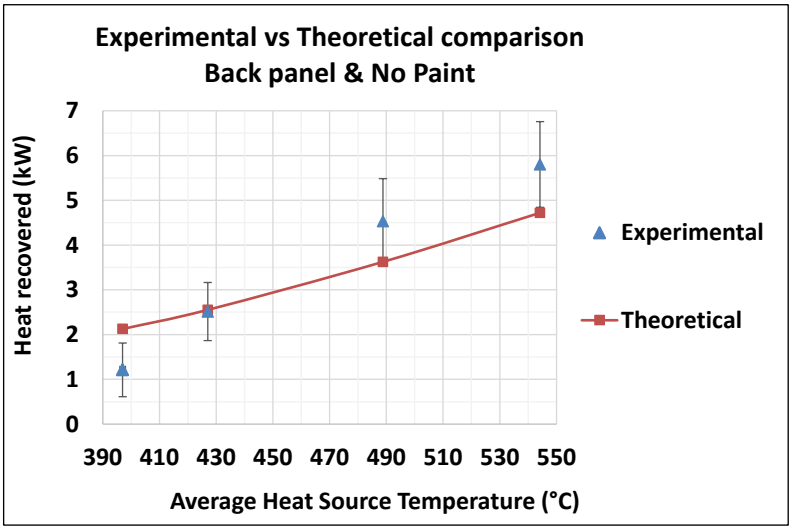

Figure 6-65 Comparison between experimental and theoretical prediction of the heat recovery in the case back panel and no paint

Figure 6-66 presents a comparison between the theoretical prediction against the experimental results for the case of the FHP with back panel and painted black. It can be noticed that the prediction was very close to the experimental result at heat source temperature of 390 °c, while the theoretical model under-predicts the experimental results when the heat source temperature increased due to the ideal performance of the FHP with the absence of geyser boiling. It can be also observed that the difference between the experimental results and the prediction decreases by increasing the heat source temperature since the radiation starts to play a significant role in comparison to natural convection.

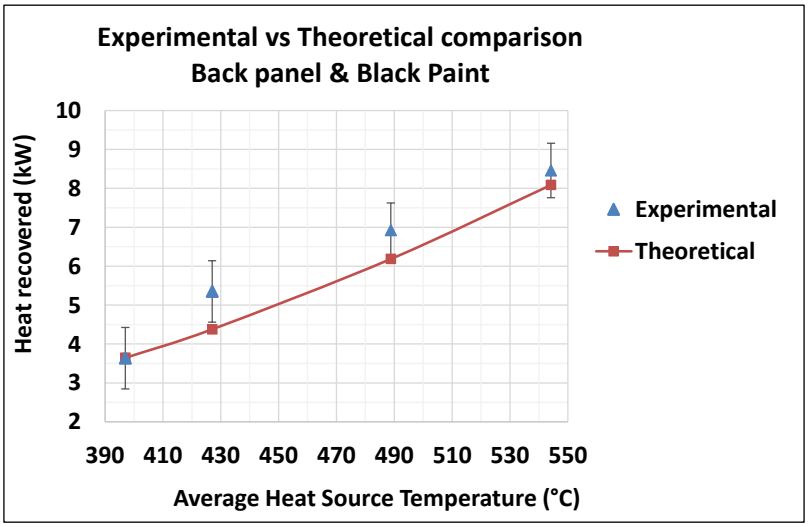

Figure 6-66 Comparison between experimental and theoretical prediction of the heat recovery in the case back panel and black paint

The theoretical predictions are compared against the experimental results obtained from all the tests in Figure 6-67. It can be seen that most of the predictions lie within a +/- 25% error. Furthermore, the

error in the predictions exceeds 25% when the FHP heat recovery is less than 3 kW. This can be explained by the fact that the FHP functionality was not ideal due to geyser boiling occurring in the heat pipe. When the temperature of the heater was increased, the heat flux increased which enhanced the performance of the heat pipe. It can be seen that the theoretical results are under-predicted to within 25% for the other tests. The modelling tool does not account for natural convection, while the FHP absorbs heat by radiation and natural convection in the real environment.

Furthermore, an error of 25% is accepted due to the unique geometry of the FHP where an additional error results from calculating the view factor and the space resistance of the FHP.

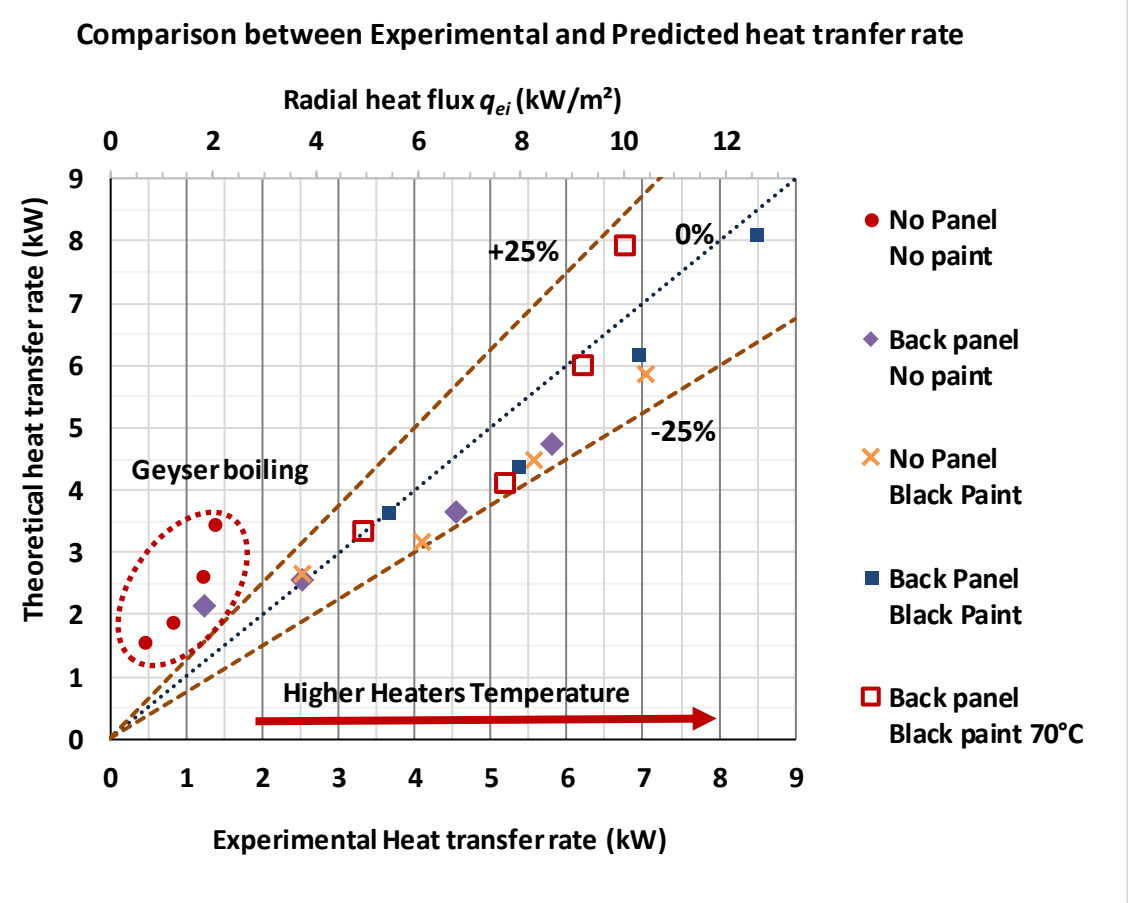

Figure 6-67 Comparison between the experimental heat recovery of the FHP and the theoretical predictions

Similar to what has been conducted on the single heat pipe, the space resistance of the FHP can be corrected to achieve higher accuracy of the model prediction and this can be carried out in future work.

The experimental temperature measurements versus the predicted temperature of the FHP evaporator, adiabatic section, water inlet, and water outlet for the case of FHP with back panel and painted with black at water inlet of 70 °C and heat recovery of 3.3 kW are presented in Figure 6-68.

The difference between the experimental measurements of the evaporator and the adiabatic section and the prediction is less than 3 °C which validates the accuracy of the correlations used in the model.

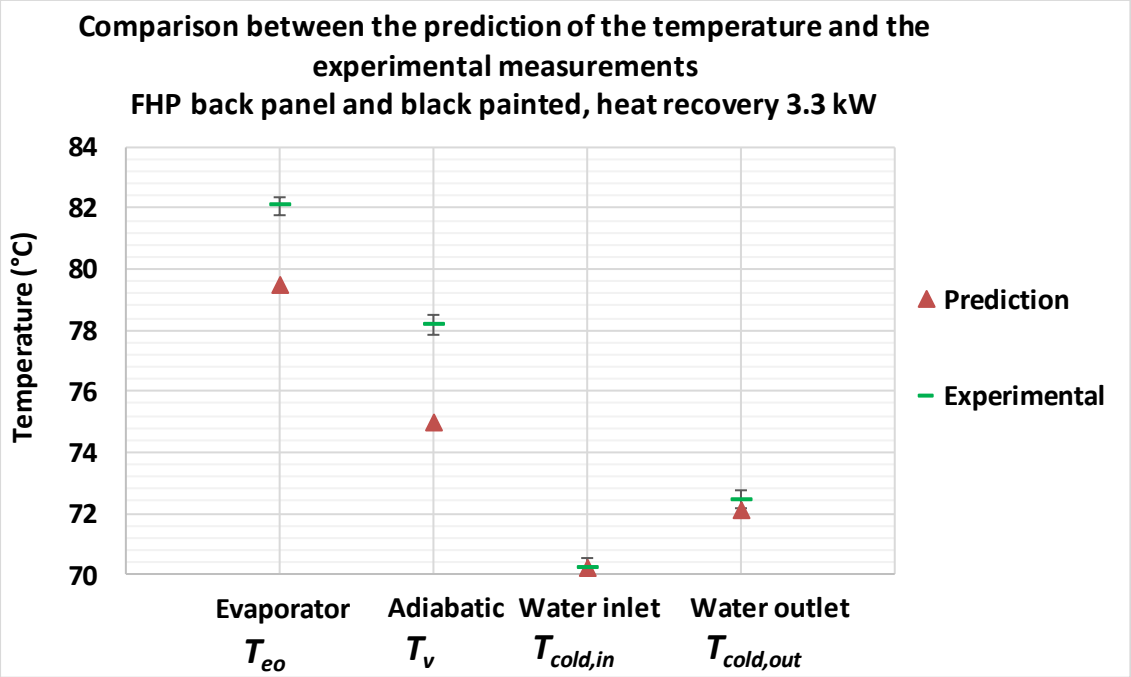

Figure 6-68 Comparison between the experimental measurements of the temperature and the theoretical predictions for FHP black painted and back panel

6.3.6 FHP overall thermal resistance comparison

The overall thermal resistance of the FHP including the thermal resistance of the forced convection at various conditions is presented in Figure 6-69. It can be seen that the thermal resistance of the FHP for the cases black painted with and without a back panel decreases with the increase in the heat recovery (heat flux), while the thermal resistance of the FHP for the case with a back panel and black painted at a water inlet temperature of 70 °C slightly increases. However, the overall thermal resistance of the FHP for the case with a back panel and black painted at a water inlet of 70 °C was less than the case for water inlet temperature of 21°C. This comparison clearly indicates that the decrease in the heat recovery with the increase of the water inlet temperature was due to the decrease in the equivalent radiation thermal resistance.

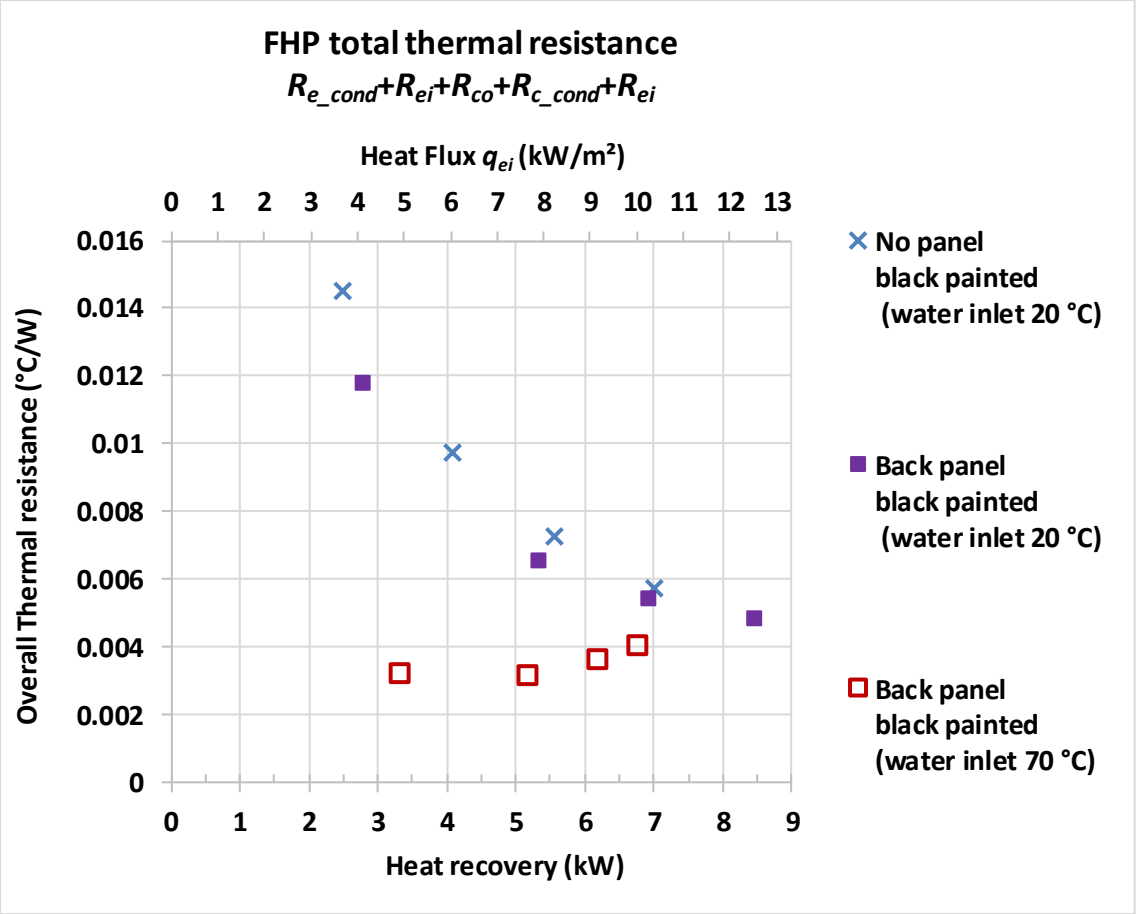

Figure 6-69 A comparison of the overall thermal resistance of the FHP at laboratory tests at difference conditions

6.3.7 Assessment of the effect of the natural convection on the prediction of the theoretical heat recovery

The air temperature around the FHP was unmeasured, therefore the gain of heat by natural convection will be assessed theoretically. The air temperature is between the heat source temperature and the ambient. If the air temperature is less than the FHP surface temperature, then the FHP loses heat by natural convection to the ambient. In contrast, if the air temperature is higher than the FHP, then the FHP gains heat by natural convection. As was observed from the results the heat recovery varied significantly when the water inlet temperature increased. In addition, the modelling tool under-predicted the heat recovery for most of the cases. Therefore, it is vital to analyse the effect of the natural convection on the heat recovery in comparison with the radiative heat.

Based on the heat pipe evaporator surface temperature, the heat transfer by natural convection is estimated for different air temperature varying from ambient temperature of 30.0°C to 540 °C which is the temperature of the heat source. The estimation of heat transfer rate at different assumed air temperatures is presented in Figure 6-70 for two cases: the first case for an evaporator surface

temperature of 68 °C (FHP with back panel and black painted at water inlet temperature of 21 °C) and the other case is the same FHP set-up but surface temperature of 98 °C where the water inlet temperature was 70 °C. The negative heat transfer rate means that the FHP loses heat to the air that is achieved when the air temperature is lower than the surface temperature. At an assumed air temperature of 200 °C, the FHP at surface temperature of 68 °C gains 1.3 kW while the FHP at a surface temperature of 98 °C absorbs 1 kW. Thus, the ratio of the gain of heat between the two cases is 29.4%. Furthermore, the difference in heat transfer rate between the two cases is between 236 W to 373 W, which is still less than the difference in the overall rate of heat recovery transferred through the FHP to the coolant.

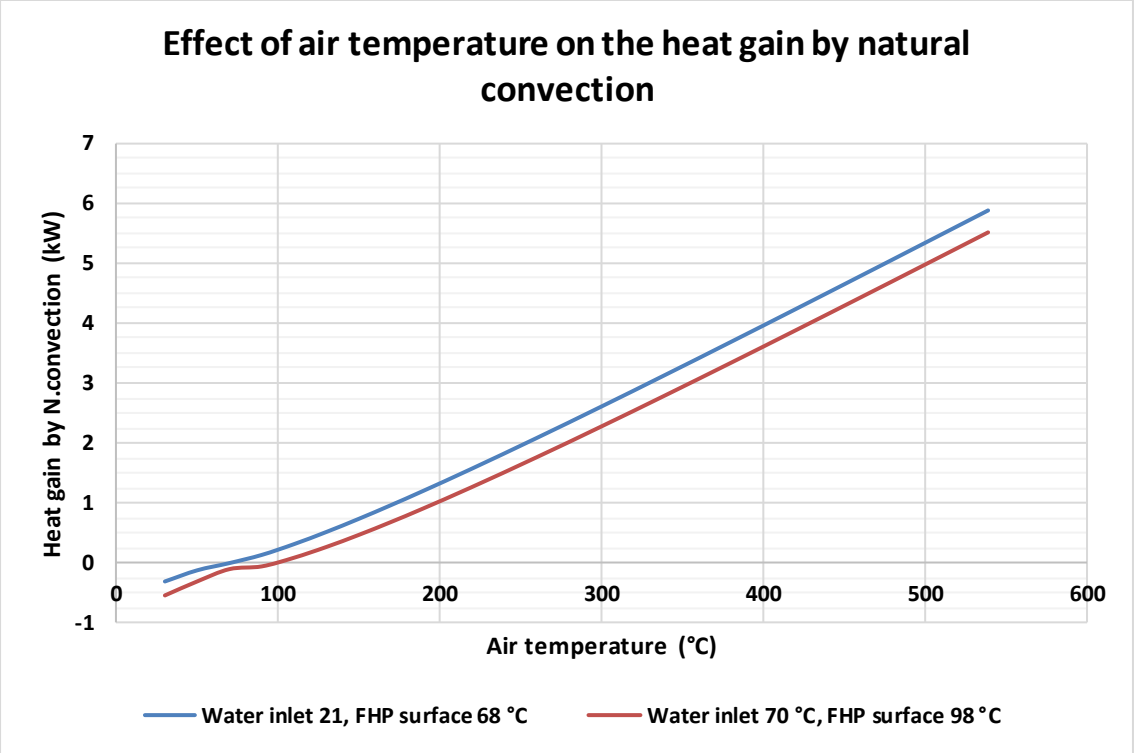

Figure 6-70 Estimation of heat transfer rate by natural convection at various assumed air temperature

Another factor that explains the difference in the heat recovery as a function of the water inlet temperature, is the UA value of the FHP as a heat exchanger or in other terms the overall thermal resistance of the FHP. The FHP transfers the heat from a heat source at a certain temperature to the coolant. The increase in the coolant temperature decreases the Logarithmic mean temperature difference and affects the thermal performance of the FHP. In addition, the increase in the surface temperature of the FHP increases the heat losses to the surroundings by radiation and decreases the heat gain from the FHP. The theoretical predictions of the FHP tests had an under-prediction of 25% due to the accuracy of determining the space resistance and the natural convection. The difference in

the heat recovery between the case of coolant inlet temperatures at 21°C and 70°C is 25% as a maximum variation. Since the gain from natural convection was not significantly changed by changing the air temperature, then it can be concluded that the reason is related to the radiation gain from the heaters and radiation losses to the ambient. This can be confirmed by the fact that the positioning of the FHP affects the space resistance significantly if it was not identical between the two tests.

6.4 Flat heat pipe at the factory

This section presents the experimental and theoretical results obtained from testing the FHP at the factory. The first section presents the results that were published in a journal article by *Jouhara et al.* [137].

6.4.1 Results for FHP Initial test at the factory

The initial test was conducted on the FHP with a back panel and unpainted where the FHP was positioned far from the barrier as an initial test for safety considerations.

Figure 6-71 illustrates the average temperature measurements versus time of the FHP parallel pipe surfaces, bottom collector, back panel, the average temperature of the evaporator section, and the adiabatic section. The variation in the temperature versus time in the experiments is due to the characteristic of the steel production process; the steel wires are produced for about 120 seconds and then the production is paused for 40 seconds. The temperature distribution of the FHP parallel pipes' surfaces during the hot wire production varied between 78.4 °C and 104.5 °C. The back-panel temperature ranged between 162°C and 191.3°C, as expected, higher than the temperature of the FHP surface because it was acting as re-radiator since it was insulated from the back and heat was re-emitted to the FHP parallel pipes and the surroundings.

The average temperature of the bottom collector reached a maximum of 65.4 °C and a minimum of 61.4 °C when the production was stopped. The bottom collected exhibited lower temperatures than the adiabatic section due to the fact the bottom collector was not exposed sufficiently to the steel, which caused sub-cooling of the working fluid in the FHP. The average temperature of the evaporator including the bottom collector varied between 78.6 °C and 91.7 °C. The average temperature from the thermocouples placed on the top header, which represents the adiabatic section, varied between 66.7 °C and 73.1 °C.

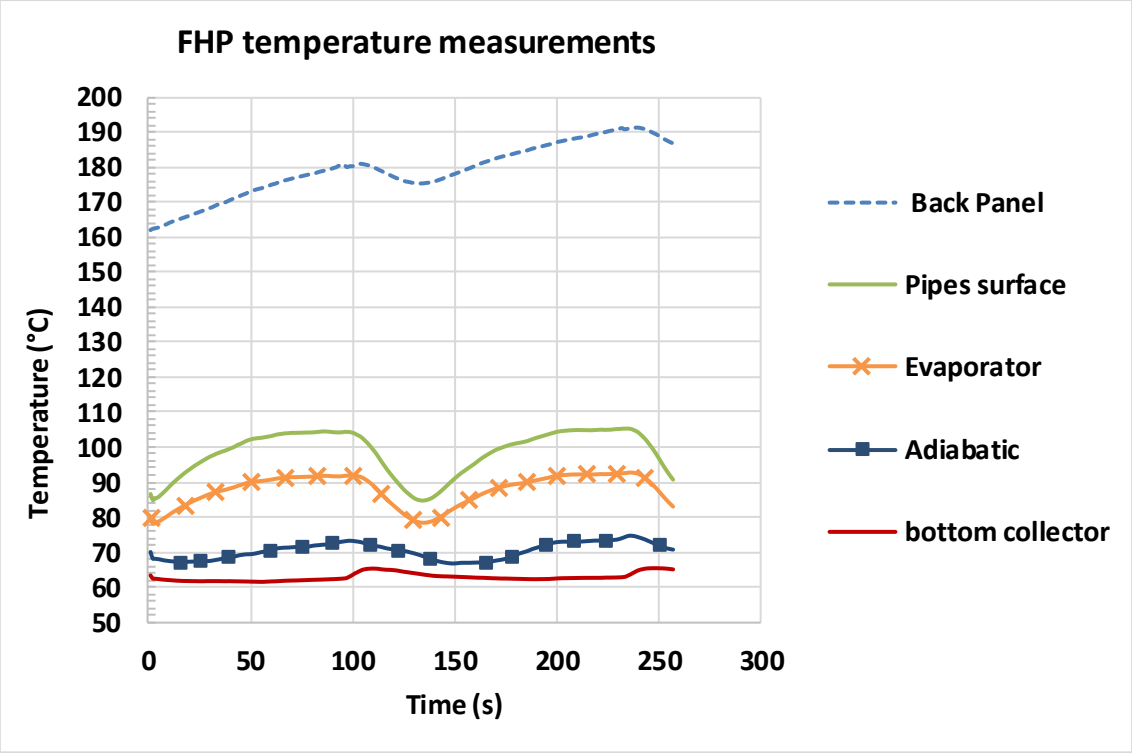

Figure 6-71 FHP temperature measurements in the initial test

Water inlet and outlet temperatures are presented in Figure 6-72. The outlet temperature varied with time as a result of the variable thermal performance of the FHP and the variation in the average heat source temperature. The water inlet temperature was nearly constant at 26 °C while the average temperature of the water outlet was 33.4°C.

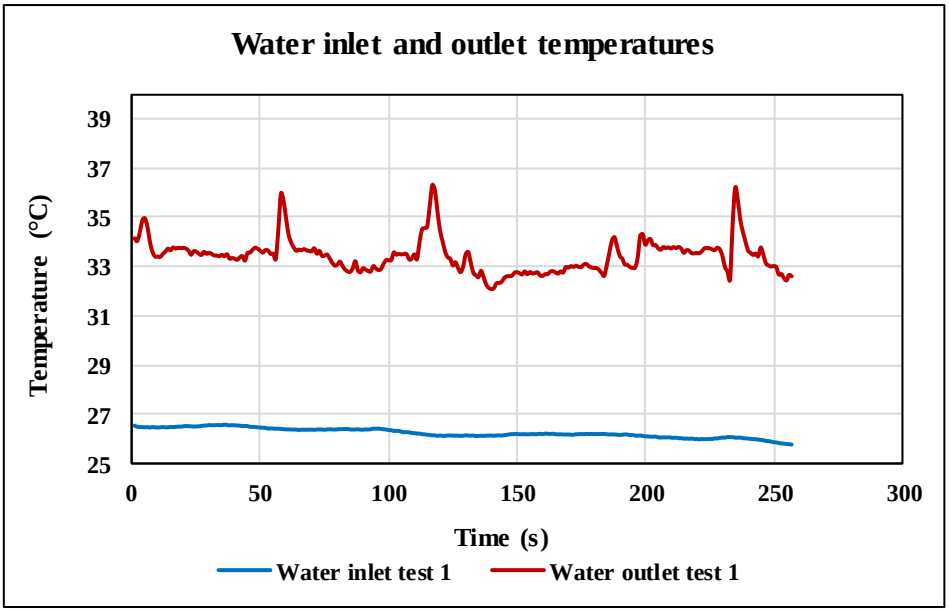

Figure 6-72 Water inlet and outlet temperatures

The experimental and theoretical heat transfer rates are illustrated in Figure 6-73. The heat transfer rate varied between a maximum value of 16.9 kW and a minimum value of 9.9 kW with an average value of 12 kW due to intermittency in the steel production process. The rate of heat transfer calculated by the theoretical method was 11 kW. It can be observed that the theoretical results are less than the experimental values because the theoretical model does not include the heat transfer by forced convection from the hot air above the steel wires. Prediction of heat recovery within an error of 30% of the experimental values is acceptable under the conditions of conducting the tests in an industrial environment. Moreover, determining the overall radiation resistance is complex for the experiments at the factory, particularly when the bottom collector was not exposed to the radiation from the hot wires.

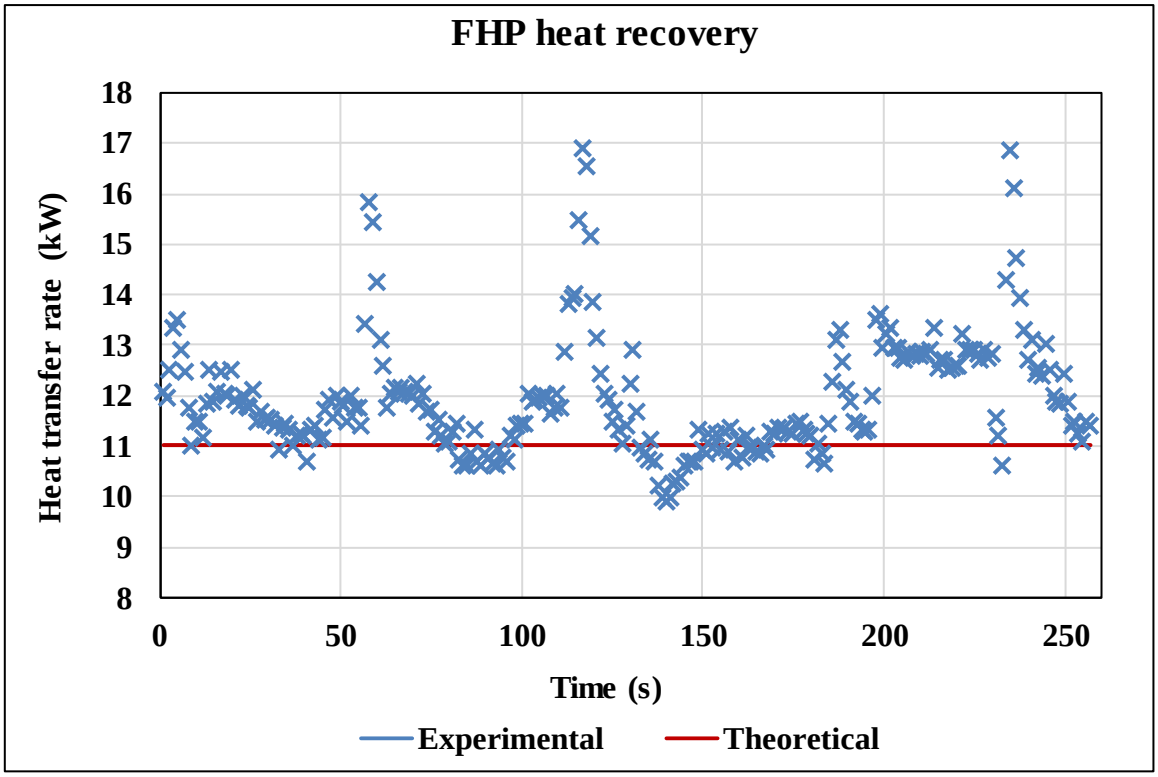

Figure 6-73 Experimental and theoretical heat recovery of the FHP at test 1

The heat transfer rates of the FHP above a production line are significantly greater than during laboratory tests. This is due to the higher steel temperature and the average heat source, which was measured to be 580 °C. Furthermore, the air temperature surrounding the FHP in the industrial tests is much higher than the tests in the laboratory and there was a higher air velocity and temperature. The uneven surface created by the steel wires could also result in a higher effective emissivity of the heat source.

6.4.2 Effect of steel wires temperature and diameter on the heat recovery

The FHP was also tested for different diameters of steel with a back panel and unpainted.

The experimental results obtained from the tests at three distances from the laying head for four different wire diameters are presented in Figure 6-74. By comparing the results for three different diameters for the case of the FHP with a back panel, unpainted, and insulated, it can be seen that the variation of the heat recovery with the distance from the laying head has a similar trend. Moreover, the increase of the steel diameter from 5.5 mm to 13 mm has significantly increased the heat recovery from 5.2 kW to 7.1 kW, corresponding to a 37% increase in the heat recovery. Furthermore, the heat recovery for the black painted heat pipe was significantly higher than the unpainted black heat pipe at the shortest distance from the laying head. Although the wires' cooling fan was running at the same speed as in other tests, the heat recovery was slightly higher than heat recovery for the case of the

8mm steel diameter in comparison with the case for a diameter of 5.5 mm. This can be attributed to the positioning of the bottom collector distance from the barrier as was observed previously in the FHP in the laboratory and the factory during the initial tests. The maximum steel temperature is shown in the chart, while the average conveyor temperature is different depending on the steel diameter, therefore it is not reported. The combined effect of the black painted heat pipe with increase in the steel diameter has significantly increased the heat recovery at the distance of 2 m from the laying head (the beginning of the cooling zone). The increase in comparison with the heat recovery at a diameter of 13 mm is 47%.

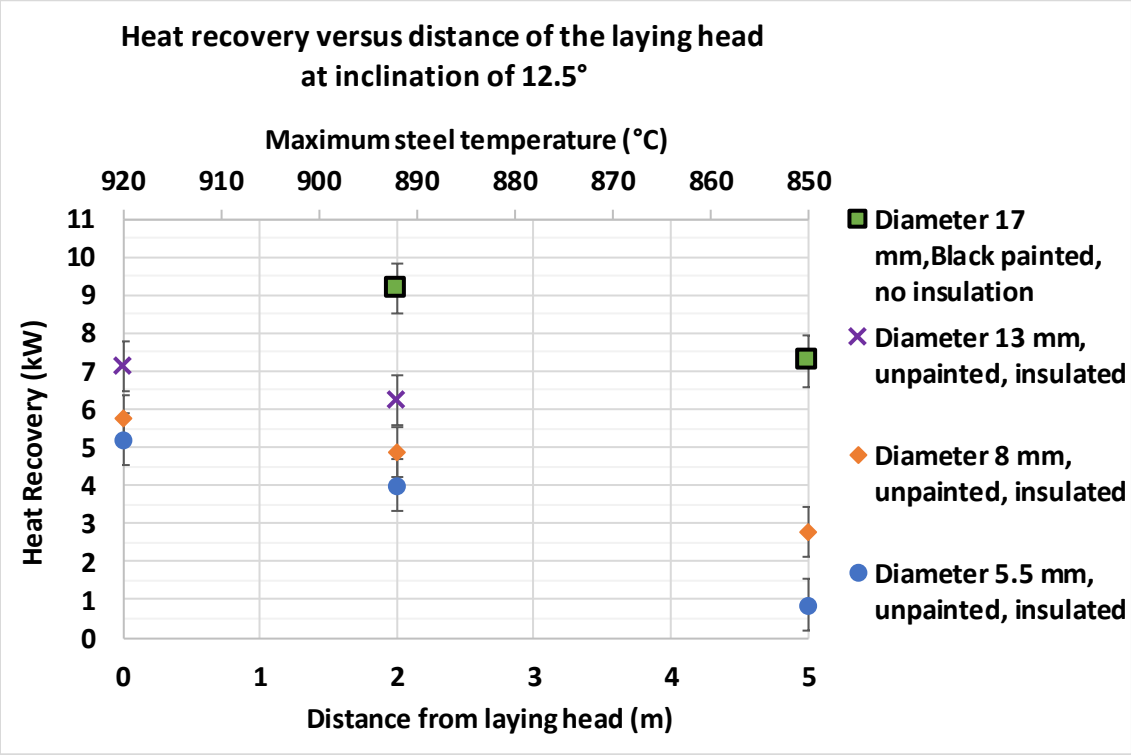

Figure 6-74 Comparison of heat recovery of the FHP in factory tests with back panel at different steel diameters as a function to the distance from the laying head

6.4.3 FHP with back-panel and black panel

The experimental temperature measurements of testing the FHP at the factory with a back panel and black painted are presented in Figure 6-75. The temperature measurement of the FHP varied versus the time because of the intermittent steel production process. The parallel pipe temperatures were higher than those of the bottom collector as they were exposed to higher heat fluxes than the bottom collector. The average evaporator temperature was very close to the pipe surface temperature which varied between 70 °C and 93 °C. The adiabatic section temperature of the FHP varied between 58 °C and 85 °C. It can be seen that, at the time of 50 seconds on the chart, the adiabatic temperature was higher than the evaporator which can be attributed to a latency due to the insufficiency of the heat

flux incident on the bottom collector at the beginning of the test. Moreover, the maximum temperature of all the measurements was higher at the time of 50 seconds than for the rest of the experiments, which indicates a change in the production of the steel or the average temperature.

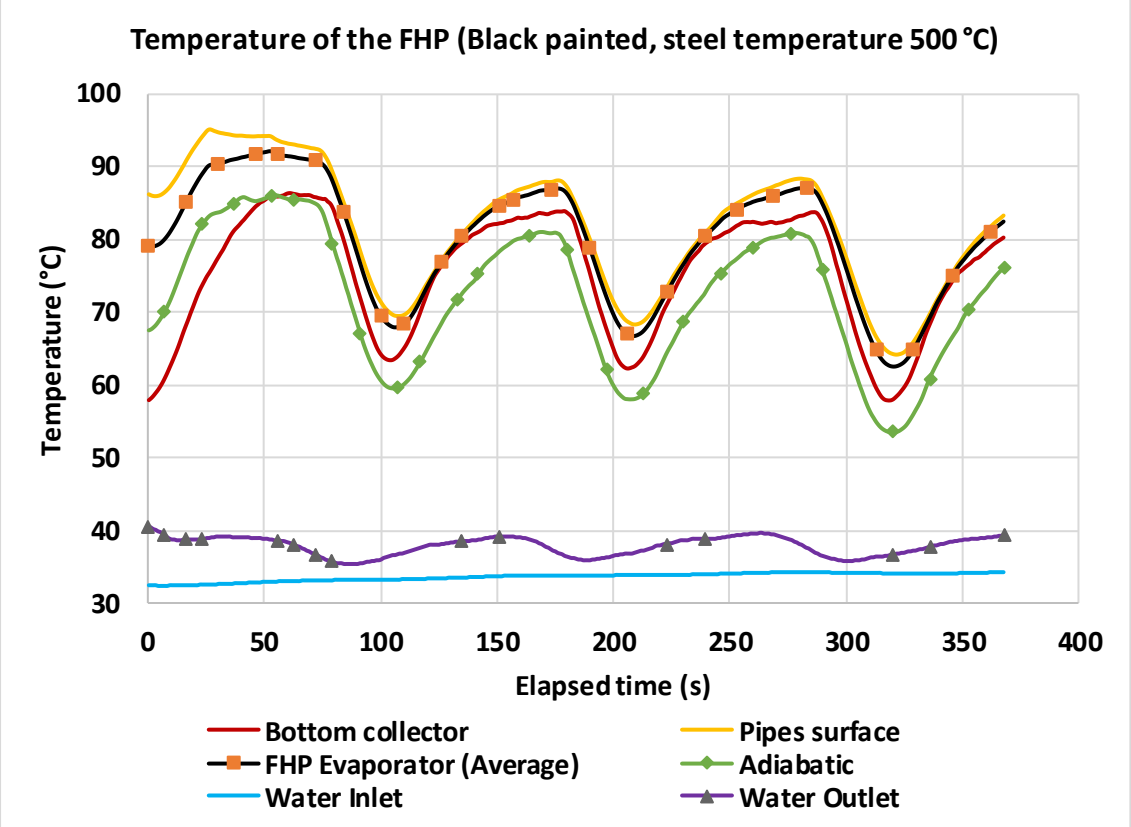

Figure 6-75 FHP (Black painted & back panel) temperature distribution as a function of time during the factory test

A comparison between the predicted and experimental heat recovery is presented in Figure 6-76. It can be seen that the heat recovery varied with time due to the characteristic of the steel production intermittency. The heat recovery was 14 kW at the beginning of the measurements and fell below 4 kW when the production stopped, then it varied between 4 kW and 9 kW. Figure 6-76 is an example of the variation of measurements of the experimental heat recovery within the steel production for the same conditions during a short period. The theoretical predicted heat recovery is 8.4 kW and it is presented as a steady state, assuming that the conveyor is at a constant temperature. The predicted heat recovery has a good agreement with the experimental heat recovery with less than 10% error. The theoretical modelling tool can predict the heat recovery with low error when the predicted equivalent thermal resistance is very close to the experimental one, since the radiation resistance is the highest thermal resistance in the thermal model.

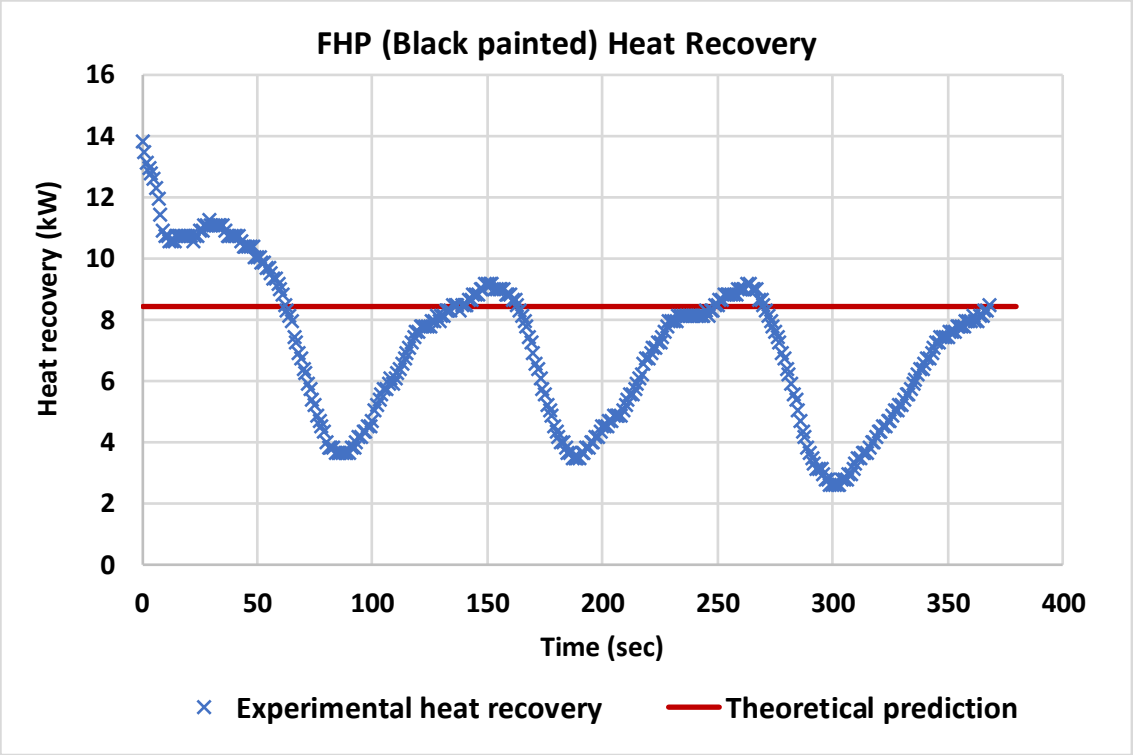

Figure 6-76 Theoretical and experimental prediction of the heat recovery of the FHP (black painted and back panel at steel temperature of 500 °C

6.4.4 Effect of inclination

The effect of the inclination on the heat recovery was investigated experimentally at a steel wire diameter of 13 mm when the FHP was assembled with a back panel and unpainted. A comparison between the heat recovery at an inclination angle of 12.5° and 25° is presented in Figure 6-77. It can be seen that the heat recovery for the case of a 13mm steel diameter at 12.5° was 7.1 kW while it was 8 kW for 25°. The increase in the heat transfer rate was about 12%, which could be further increased if the bottom collector was exposed properly to the radiation from the steel wires. This was not achievable during the experiment due to some technical difficulties with the stand arms.

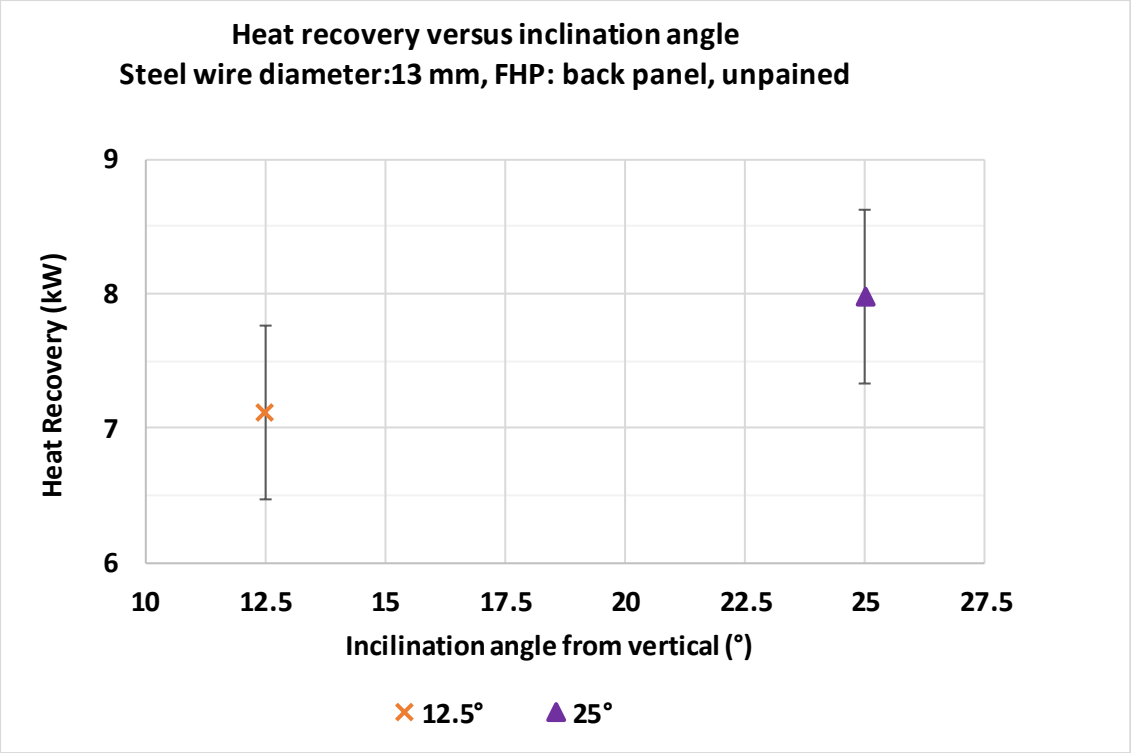

Figure 6-77 Comparison of the heat recovery at two different inclination angles

6.4.5 Evaluation of the back panel of the black painted heat pipe

The FHP was examined without a back panel when it was black painted at two different distances from the laying head. A comparison between the heat recovery for the case of the FHP with back panel and painted with black paints versus the case without a back panel is presented in Figure 6-78. The heat recovery for the case without a back panel at the laying head was 11.6 kW, while it increased to 12.6 kW at distance of 2 m. However, the heat recovery obtained when the FHP was assembled with the back panel reached 9.1 kW which is less than the case without a back panel. As seen before, the heat recovery can change during the experiment without a clear reason. The reason cannot be identified without a continuous measurement of the steel temperature during each test which was not possible technically.

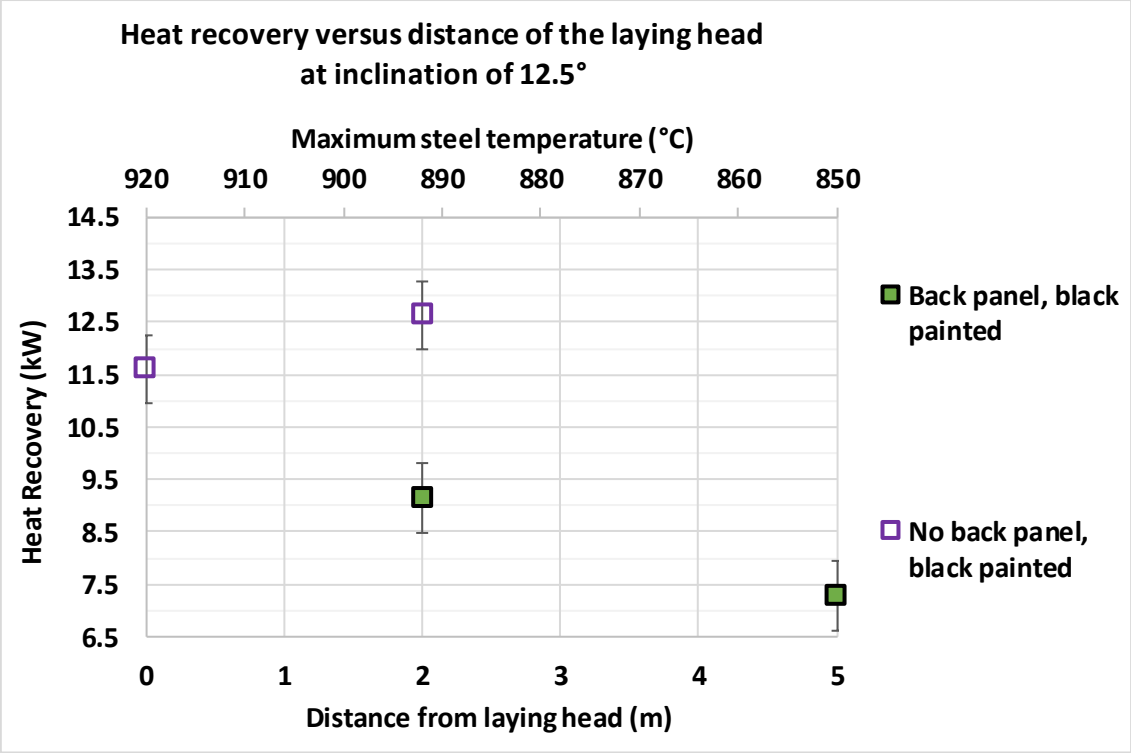

Figure 6-78 Experimental heat recovery of the FHP at different distances from the laying head and different configurations

The heat transfer by the forced convection was not considered in the modelling tool in order to simplify it due to the complex geometry and conditions of the test. However, the effect of the forced convection can be evaluated separately.

The air temperature was measured to be around 60 °C, and the air velocity was within the range of 5-6 m/s.

By considering these values to calculate the heat transfer coefficient by forced convection over the FHP with a back panel, the heat transfer coefficient was calculated through the correlation reported in [75] by considering the pipes with a back panel as a flat surface. Hence the heat transfer coefficient is 23.8 W/m².°C, and the heat transfer over the parallel pipes is 820 W as a heat loss to the air ,for the case of black painted with a back panel, since the air temperature is less than that of the parallel pipes.

Moreover, the heat transfer by forced convection over the FHP without a back panel can be calculated through a general correlation of forced convection heat transfer around a single cylinder or by using the *Žukauskas* [138] correlation considering the correction factor for one row of cylinders. The heat transfer coefficient is 54 W/m².°C and the heat transfer rate is 1.8 kW as a heat loss to the air. If the air temperature is 28 °C higher than the parallel pipe, then this quantity becomes as a heat gain.

6.5 General discussion on the results of the lab-scale and full scale heat pipe heat exchangers

The single heat pipe heat exchanger operated within a closed kiln where the natural convection played a significant role on the heat recovery for heater temperature below 400 °C. The single heat recovered between 73 W and 573 W of heat recovery at heater temperature between 200 °C and 500 °C, respectively. The corresponding heat flux range was between 2.1 kW/m² and 15.8 kW/m².

The full-scale FHP had larger evaporator surface area in addition to the back panel that reflected and re-radiated part of the radiative heat that was not incident directly on the parallel pipes of the evaporator. Depending on the experimental conditions, the FHP recovered between 0.4 kW and 8.5 kW at the laboratory which corresponds to heat flux range between 0.6 kW/m² and 12.6 kW/m². The FHP exhibited amount of heat recovery up to 12 kW corresponding to range of heat flux of 17.8 kW/m².

The lab-scale single heat pipe heat exchanger had a different design and size of the condenser in comparison to the full-scale. The condenser design of the FHP could not be the same of the lab-scale to avoid the increase in the pressure drop due to up-scaling the system and regarding thermal design considerations such as the ratio of the evaporator area to the condenser area.

The heat pipe heat exchanger presented by *Delpech and Jouhara* [71] exhibited a heat recovery up to 3 kW with unpainted surface corresponding to 7.1 kW/m² of heat flux per evaporator surface area at heater temperature of 500 °C. The heat flux of the unpainted single heat pipe in this research reached 12.1 kW/m² which is higher than the achieved by *Delpech and Jouhara* [71]. The mechanical design of the evaporator and the condenser has a significant role on the performance of the heat pipe, in addition to the ration of the evaporator area to the condenser area.

The heat pipe presented by *Tsai* et al.[37] reached about 6.2 kW/m² which is less than the heat pipe heat exchanger in this research. However, vapour chamber and flat heat pipe for electronic cooling can be designed for higher heat flux due to the advantage of implementing wick structure in the evaporator surface which is not needed for the heat pipe in this application.

It can be concluded that the experimental results of testing the FHP proven the concept as a viable waste heat recovery by radiation in the steel industry. Moreover, the heat recovery during the laboratory tests exhibited that FHP recovers the heat effectively when the heat source temperature is higher than 400 °C. As a result, the FHP can be utilised to recover the heat from any other radiative sources such as hot glass or ceramics provided that the heat source temperature is higher than 400 °C and the FHP close as possible to the heat source to minimise the radiation space resistance.

The theoretical modelling tool was validated through experimental results with very agreement with the experimental results. This was achieved through careful selection of the heat transfer correlations of the two-phase and single phase heat transfer. The theoretical modelling tool can be used to scale the FHP and to predict the thermal performance of the FHP with respect to the heat recovery and the operating temperature at different heat source temperature. The theoretical modelling tool can be employed to theoretically predict the feasibility of utilising the FHP to recover the heat from other hot sources in other industries. However, the radiation space resistance significantly affects the heat recovery. Therefore, it should be calculated as accurate as possible to match the expected installation.

Chapter 7: Conclusion and suggestions for future work

This chapter presents a summary of the objectives and results of this research in addition to the contribution to the knowledge and the future work.

The main objective of this research was to examine and characterise a radiative heat pipe based heat exchanger for waste heat recovery in the steel industry. The research was conducted by studying experimentally and theoretically a laboratory scale single heat pipe and a full scale heat pipe heat exchanger at laboratory and in a steel factory.

7.1 Conclusion from the study

A literature review on the state of the art on heat pipe technology and radiative waste heat recovery technologies was conducted. The literature review showed the gap on investigating heat pipe technology for radiation heat recovery.

The first part of the research was an investigation on a single radiative lab-scale heat pipe experimentally and theoretically. The single heat pipe was examined at different heater temperatures in a laboratory scale kiln. The study also examined the effect of the inclination and the heat pipe surface emissivity by painting the heat pipe with high temperature black paint. A theoretical modelling tool was programmed on VBA to predict the thermal performance of the heat pipe. The theoretical predictions were compared with the experimental results for various conditions. The modelling of the two-phase heat transfer in the heat pipe was conducted by using state of the art of correlations available in the literature, which are widely used, and the theoretical results showed high agreement with the experimental data.

It was found that natural convection had a significant impact on the insulated walls which were assumed as re-radiators. A correction factor was obtained from the experimental results to feed into the model, and thus an excellent agreement with less than 10% error was achieved.

It was observed that the heater temperature had a significant effect on the heat recovery through the heat pipe. In addition, the boiling regime with respect to geyser boiling in the evaporator of the heat pipe was considerably dependent on the heat flux. The findings revealed that the geyser boiling was eliminated for heat fluxes higher than 5 kW/m^2. An increase in the inclination angle from vertical enhanced the thermal performance of the FHP with respect to the uniformity of temperature distribution and the heat recovery. The best thermal performance was obtained at an inclination angle of 60° among the tested inclination angles. Moreover, the black paint increased the heat recovery of the heat pipe remarkably. Thus, a higher heat flux was achieved at lower heater temperatures and the geyser boiling was eliminated at a lower heat flux limit. At higher heater temperatures, the heat pipe

exhibited less temperature difference along the evaporator. The best case was obtained at an inclination angle of 60° at a heater temperature of 500 °C with 3 °C maximum temperature difference along the evaporator surface. The heat recovery by radiation was compared with the natural convection gain which was determined theoretically. It was observed that the percentage of the natural convection in the overall heat recovery decreases significantly with the increase of the heater temperature to below 25% at a heater temperature of 500 °C.

The single heat pipe with a black painted evaporator with length of 0.41 m recovered around 580 W from a 0.27 m² heater area and its temperature was 500 °C in an insulated kiln.

The validation of the boiling heat transfer prediction revealed that the correlation developed by *Imura* showed the best agreement with the experimental results regarding the overall boiling thermal resistance. In addition, the correlation developed by *Rohsenow* has good agreement with the experimental results provided the appropriate surface factor (C_{SF}) is used. The modelling of nucleate pool boiling and nucleate film boiling could not be applied to all the tests due to the presence of geyser boiling and the uncertainty with the measured heat recovery. However, the combination of the *Imura* correlation with the correlation of *Nusselt*, as modified by *Rohsenow*, showed a good agreement within most of the study range. The combination of *Rohsenow* with *Jouhara* showed better agreement for higher fluxes.

Nusselt's theory was applied to predict the condensation heat transfer by using the correlation of *Nusselt* as modified by *Rohsenow* and this showed excellent agreement with the experimental results.

The overall thermal resistance of the single heat pipe was not significantly affected by the thermal performance when it overcame the geyser boiling. The single heat pipe exhibited a nearly constant thermal resistance regardless of the inclination angle or the heat flux when the heat flux was within the range of 10 kW/m² to 14 kW/m².

A full scale radiative Flat Heat Pipe based heat exchanger was investigated experimentally and theoretically in the other part of the study. The FHP consisted of parallel stainless steel tubes assembled by a bottom collector and a top header. The FHP was cooled by water through a shell and tube heat exchanger fitted within the top header. The FHP was examined at laboratory conditions where it recovered the heat by radiation from heaters installed on a flat plate to simulate the heat emitted from hot steel.

The FHP thermal performance was investigated at difference heater temperatures and different arrangements. The heater temperature had a notable effect on the heat recovery of the FHP. The effect of the back panel attached to the back of the FHP was also investigated by testing the FHP with

and without it. The effect of the emissivity of the FHP was also investigated by painting the FHP with a black paint. The FHP heat recovery was compared for different arrangements, with and without the presence of the back panel and black paint. The highest heat recovery of 8.5 kW was obtained for the case of the FHP with a back panel and black painted at an average heat source temperature of 544°C.

Moreover, the black paint enhanced the thermal performance of the FHP regarding the elimination of geyser boiling, similar to the findings for the single heat pipe tests.

The FHP was investigated in the factory to validate its viability as a waste heat recovery technology under industrial conditions. The FHP was investigated at different steel temperatures, different steel wires, and different FHP emissivity.

The heat recovery of the FHP was significantly higher than what was obtained in the laboratory due to the higher temperature of the steel and the higher temperature of the air surrounding the FHP.

The FHP achieved 17 kW as a maximum heat recovery and 12.5 kW on average.

The steel wires' diameter had significant effect of the heat recovery, which varied between 5.2 and 7.1 kW for steel diameters of 5.5 mm and 13 mm, respectively, corresponding to a 37% increase in the heat recovery.

The positioning of the FHP from the barrier had a significant role on the heat recovery where the ideal positioning was found to expose both the bottom collector and the parallel pipes of the FHP. The positioning of the FHP affects the overall surface area of the FHP exposed to radiation and significantly changes the view factor and the space resistance of the FHP to radiation.

It was observed during the tests that the FHP had a quick response to heat source temperature change, where the thermal performance of the FHP was varying with time as a function of the intermittency of the production process, which in turn changed the average conveyor temperature.

The developed modelling tool predicted the heat recovery of the tests at the factory with less than 30% error. The accuracy of the FHP modelling tool can be enhanced further by determining accurately the FHP overall space resistance to radiation.

7.2 Impact on the research field

Published literature two-phase heat transfer in heat pipes focuses on uniform constant heat flux. However, the investigation on the single heat pipe in the laboratory scale kiln provided deep study on the two-phase heat transfer under non-uniform heat flux condition. The experimental results were compared with correlations of boiling heat transfer to determine the appropriate correlations and applicable range through two different models of boiling. The first model reported the average

thermal resistance of the evaporator through average temperature assumption. The second model validated different combination of boiling heat transfer correlations showing the most agreed with the experimental results within a certain range of heat flux.

Moreover, the experimental work identified the lowest value of heat flux to avoid geyser boiling in the heat pipe which dramatically decreases its effective thermal conductivity. In addition, the research studied experimental the effect on inclination angle on the geyser boiling under non-uniform heat flux condition.

The second part of the research characterised a novel FHP for waste heat recovery by thermal radiation. The experimental results studied the effect of black paint on increasing the heat recovery by the system. Moreover, the tests carried out in the laboratory and the factory proved the concept of the FHP as a waste heat recovery technology from radiative sources.

Furthermore, a theoretical modelling tool was developed to predict of the thermal performance of the single heat pipe and the FHP with respect to the heat recovery, operating temperature, and thermal resistance of the heat pipe. The theoretical modelling tool validated through the experimental results is advantageous to assess the potential of the FHP for waster recovery in other industries such as glass or cement.

7.3 Suggestions for future work

One of the limitations in the study was measuring the heat flux along the evaporator of the single heat pipe directly, therefore it was measured through the heat recovery by the water stream. This approach was not accurately representing the radial heat flux on the evaporator during the geyser boiling as the heat pipe performance fluctuated under this condition. In addition it was not possible to determine the distribution of heat flux along the evaporator. Therefore, single heat pipe can be examined under a uniform heat flux using condition to compare its thermal performance and findings with the current study.

The outcome of the future work can give more understanding on the geyser boiling in heat pipes for the same inner diameter and the heat flux to evaluate the effect of the uniformity of heat flux. The outcome can also help to predict the limit of the heat flux which initiates geyser boiling and the limit where it is eliminated. A future study can focus on the prediction of the average heat transfer rate under the geyser boiling regime.

Most of the boiling correlations are validated for heat flux range higher than 20 kW/m² in the literature. Therefore, future work can investigate developing a better correlation of boiling heat transfer in thermosyphons for heat flux less than 20 kW/m² similar to the heat flux in this current

study. This research gap was observed because heat pipes are generally applied to high heat flux applications, unlike the situation with radiative heat recovery applications.

It was assumed in the modelling of laboratory-kiln that the insulated walls acted as re-radiators while neglecting the effect of natural convection. A future work on numerical modelling is needed to investigate the view factor of the single heat pipe at different inclinations and to include the effect of natural convention on the walls of the kiln which were considered as re-radiators.

The FHP had a unique design where its space resistance was determined through an analytical approach using the basic radiation heat transfer rules. In order to enhance the prediction accuracy of the theoretical modelling tool, a CFD and numerical modelling study can be conducted to determine the view factor of the FHP with and without a back panel. In addition, the numerical software such as ANSYS can determine the distribution of the radiative heat flux incident on the FHP surface which is quite difficult to be implemented using the current modelling tool. The investigation on the FHP can be continued to test it at inclination angles bigger than 25° and by investigating development of different design of the back panel to increase the heat recovery by the system.

References

[1] Hasanbeigi A, Arens M, Cardenas JCR, Price L, Triolo R. Comparison of carbon dioxide emissions intensity of steel production in China, Germany, Mexico, and the United States. Resour Conserv Recycl 2016;113:127–39. https://doi.org/10.1016/j.resconrec.2016.06.008.

[2] SETIS. Energy Efficiency and CO2 Reduction in the Iron and Steel Industry 2014:1–4. www.worldsteel.org/publications/position-papers/Steel-s-contribution-to-a-low-carbon-future.html (accessed January 5, 2020).

[3] Carbon trust. International Carbon Flows- Steel. 2011.

[4] Energy Element, Ecofys, College I, Stevenson P. The potential for recovering and using surplus heat from industry. 2014.

[5] Zhang H, Wang H, Zhu X, Qiu YJ, Li K, Chen R, et al. A review of waste heat recovery technologies towards molten slag in steel industry. Appl Energy 2013;112:956–66. https://doi.org/10.1016/j.apenergy.2013.02.019.

[6] Dal Magro F, Meneghetti A, Nardin G, Savino S. Enhancing energy recovery in the steel industry: Matching continuous charge with off-gas variability smoothing. Energy Convers Manag 2015;104:78–89. https://doi.org/10.1016/j.enconman.2015.05.012.

[7] Zhang Q, Zhao X, Lu H, Ni T, Li Y. Waste energy recovery and energy efficiency improvement in China's iron and steel industry. Appl Energy 2017;191:502–20. https://doi.org/10.1016/j.apenergy.2017.01.072.

[8] Liu J, Yu Q, Peng J, Hu X, Duan W. Thermal energy recovery from high-temperature blast furnace slag particles. Int Commun Heat Mass Transf 2015;69:23–8. https://doi.org/10.1016/j.icheatmasstransfer.2015.10.013.

[9] Gutiérrez Trashorras AJ, Álvarez EÁ, Río González JL, Suarez Cuesta JM, Bernat JX. Design and evaluation of a heat recuperator for steel slags. Appl Therm Eng 2013;56:11–7. https://doi.org/10.1016/j.applthermaleng.2013.03.019.

[10] Kaşka Ö. Energy and exergy analysis of an organic Rankine for power generation from waste heat recovery in steel industry. Energy Convers Manag 2014;77:108–17. https://doi.org/10.1016/j.enconman.2013.09.026.

[11] Ghosh S, Margatan K, Ahn CH, Bahk JH. Radiant heat recovery by thermoelectric generators: A theoretical case-study on hot steel casting. Energy Convers Manag 2018;175:327–36.

https://doi.org/10.1016/j.enconman.2018.08.106.

[12] Yin Q, Chen Q, Du W-J, Ji X-L, Cheng L. Design requirements and performance optimization of waste heat recovery systems for rotary kilns. Int J Heat Mass Transf 2016;93:1–8. https://doi.org/10.1016/j.ijheatmasstransfer.2015.08.078.

[13] Du WJ, Yin Q, Cheng L. Experiments on novel heat recovery systems on rotary kilns. Appl Therm Eng 2018;139:535–41. https://doi.org/10.1016/j.applthermaleng.2018.04.125.

[14] Reay D, Kew P. Heat Pipes 2006.

[15] Vasiliev LL. Heat pipes in modern heat exchangers. Appl Therm Eng 2005;25:1–19. https://doi.org/10.1016/j.applthermaleng.2003.12.004.

[16] Faghri A. Heat Pipes: Review, Opportunities and Challenges. Front Heat Pipes 2014;5. https://doi.org/10.5098/fhp.5.1.

[17] Shabgard H, Allen MJ, Sharifi N, Benn SP, Faghri A, Bergman TL. Heat pipe heat exchangers and heat sinks: Opportunities, challenges, applications, analysis, and state of the art. Int J Heat Mass Transf 2015;89:138–58. https://doi.org/10.1016/j.ijheatmasstransfer.2015.05.020.

[18] Dow Chemical Company. Dowtherm A - Heat Transfer Fluid, Product Technical Data. 1997.

[19] National Refrigerants Inc. Technical Guidelines Performance : Technical Guidelines THERMODYNAMIC PROPERTIES OF R-404A. Renew Sustain Energy Rev 2010;80:64–5.

[20] Honeywell. R-410A datasheet n.d. https://web.archive.org/web/20140327112424/http://www.honeywell.com/sites/docs/DF382521E-C109-2ABD-7323-C1505584FD62.pdf (accessed August 27, 2018).

[21] US Department of Commerce. NIST Chemistry WebBook, SRD 69 n.d. https://www.nist.gov/ (accessed August 27, 2018).

[22] Wallin P. Heat Pipe, selection of working fluid. 2012.

[23] Anderson WG, Rosenfeld JH, Angirasa D, Mi Y. Evaluation of Heat Pipe Working Fluids In The Temperature Range 450 to 700 K. 2004.

[24] Dhingra D. TigerPrints Thermo-physical Property Models and Effect on Heat Pipe Modelling. 2014.

[25] Jain PK. Influence of Different Parameters on Heat Pipe Performance Sharmishtha Singh Hada under the guidance of Prof. vol. 5. 2015.

[26] Faghri A. Heat Pipe Science and Technology. 2nd editio. Global Digital Press; 2016.

[27] ESDU 80017. Thermophysical properties of heat pipe working fluids: operating range between –60 °C and 300 °C, London: ESDU International plc; 1980.

[28] Jouhara H, Chauhan A, Nannou T, Almahmoud S, Delpech B, Wrobel LC. Heat pipe based systems - Advances and applications. Energy 2017;128:729–54. https://doi.org/10.1016/j.energy.2017.04.028.

[29] Ma H, Yin L, Shen X, Lu W, Sun Y, Zhang Y, et al. Experimental study on heat pipe assisted heat exchanger used for industrial waste heat recovery. Appl Energy 2016;169:177–86. https://doi.org/10.1016/j.apenergy.2016.02.012.

[30] Tian E, He Y-L, Tao W-Q. Research on a new type waste heat recovery gravity heat pipe exchanger. Appl Energy 2017;188:586–94. https://doi.org/10.1016/j.apenergy.2016.12.029.

[31] Delpech B, Milani M, Montorsi L, Boscardin D, Chauhan A, Almahmoud S, et al. Energy efficiency enhancement and waste heat recovery in industrial processes by means of the heat pipe technology: Case of the ceramic industry. Energy 2018;158:656–65. https://doi.org/10.1016/j.energy.2018.06.041.

[32] Meisel P, Jobst M, Lippmann W, Hurtado A. Design and manufacture of ceramic heat pipes for high temperature applications. Appl Therm Eng 2015;75:692–9. https://doi.org/10.1016/j.applthermaleng.2014.10.051.

[33] Jung EG, Boo JH. Thermal numerical model of a high temperature heat pipe heat exchanger under radiation. Appl Energy 2014;135:586–96. https://doi.org/10.1016/j.apenergy.2014.08.092.

[34] Yoo JH, Kang HK, Lee YI, Park SW, Lee DC YJ. An experimental study on the operational characteristics and performance of the sodium heat pipe heat exchanger. Proc. Soc. air-conditioning Refrig. Eng. Korea summer Annu. Conf., 2004, p. 725–30.

[35] Wang S, Chen J, Hu Y, Zhang W. Effect of evaporation section and condensation section length on thermal performance of flat plate heat pipe. Appl Therm Eng 2011;31:2367–73. https://doi.org/10.1016/j.applthermaleng.2011.03.037.

[36] Wang Y, Vafai K. An experimental investigation of the thermal performance of an asymmetrical flat plate heat pipe. Int J Heat Mass Transf 2000;43:2657–68. https://doi.org/10.1016/S0017-9310(99)00300-2.

[37] Tsai M, Kang S, Vieira K, Paiva D. Experimental studies of thermal resistance in a vapor chamber heat spreader. Appl Therm Eng 2013;56:38–44. https://doi.org/10.1016/j.applthermaleng.2013.02.034.

[38] Ji X, Xu J, Abanda AM, Xue Q. A vapor chamber using extended condenser concept for ultra-high heat flux and large heater area. Int J Heat Mass Transf 2012;55:4908–13. https://doi.org/10.1016/j.ijheatmasstransfer.2012.04.018.

[39] Tang Y, Yuan D, Lu L, Wang Z. A multi-artery vapor chamber and its performance. Appl Therm Eng 2013;60:15–23. https://doi.org/10.1016/j.applthermaleng.2013.06.014.

[40] Peng H, Li J, Ling X. Study on heat transfer performance of an aluminum flat plate heat pipe with fins in vapor chamber. ENERGY Convers Manag 2013;74:44–50. https://doi.org/10.1016/j.enconman.2013.05.004.

[41] Chen JS, Chou JH. Cooling performance of flat plate heat pipes with different liquid filling ratios. Int J Heat Mass Transf 2014;77:874–82. https://doi.org/10.1016/j.ijheatmasstransfer.2014.06.029.

[42] Aghvami M, Faghri A. Analysis of flat heat pipes with various heating and cooling configurations. Appl Therm Eng 2011;31:2645–55. https://doi.org/10.1016/j.applthermaleng.2011.04.034.

[43] Liu Z, Gai D, Li H, Liu W, Yang J, Liu M. Investigation of impact of different working fl uids on the operational characteristics of miniature LHP with fl at evaporator. Appl Therm Eng 2011;31:3387–92. https://doi.org/10.1016/j.applthermaleng.2011.06.023.

[44] Oro MV, Bazzo E. Flat heat pipes for potential application in fuel cell cooling. Appl Therm Eng 2015;90:848–57. https://doi.org/10.1016/j.applthermaleng.2015.07.055.

[45] Ye X, Zhao Y, Quan Z. Experimental study on heat dissipation for lithium-ion battery based on micro heat pipe array (MHPA). Appl Therm Eng 2018;130:74–82. https://doi.org/10.1016/j.applthermaleng.2017.10.141.

[46] Azad E. Interconnected heat pipe solar collector. Int J Eng Trans A Basics 2009;22:233–42.

[47] Azad E. Performance analysis of wick-assisted heat pipe solar collector and comparison with experimental results. Heat Mass Transf 2009;45:645–9. https://doi.org/10.1007/s00231-008-0455-8.

[48] Zhu T, Diao Y, Zhao Y, Li F. Thermal performance of a new CPC solar air collector with flat micro-

heat pipe arrays. Appl Therm Eng 2016;98:1201–13. https://doi.org/10.1016/j.applthermaleng.2016.01.033.

[49] Wolf M. Performance analyses of combined heating and photovoltaic power systems for residences. Energy Convers 1976;16:79–90. https://doi.org/10.1016/0013-7480(76)90018-8.

[50] Chow TT, Pei G, Fong KF, Lin Z, Chan ALS, Ji J. Energy and exergy analysis of photovoltaic–thermal collector with and without glass cover. Appl Energy 2009;86:310–6. https://doi.org/10.1016/j.apenergy.2008.04.016.

[51] Moradgholi M, Nowee SM, Abrishamchi I. Application of heat pipe in an experimental investigation on a novel photovoltaic/thermal (PV/T) system. Sol Energy 2014;107:82–8. https://doi.org/10.1016/j.solener.2014.05.018.

[52] Hu M, Zheng R, Pei G, Wang Y, Li J, Ji J. Experimental study of the effect of inclination angle on the thermal performance of heat pipe photovoltaic/thermal (PV/T) systems with wickless heat pipe and wire-meshed heat pipe. Appl Therm Eng 2016;106:651–60. https://doi.org/10.1016/j.applthermaleng.2016.06.003.

[53] Wu SY, Zhang QL, Xiao L, Guo FH. A heat pipe photovoltaic/thermal (PV/T) hybrid system and its performance evaluation. Energy Build 2011;43:3558–67. https://doi.org/10.1016/j.enbuild.2011.09.017.

[54] Wang Z, Qiu F, Yang W, Zhao X, Mei S. Experimental investigation of the thermal and electrical performance of the heat pipe BIPV/T system with metal wires. Appl Energy 2016;170:314–23. https://doi.org/10.1016/j.apenergy.2016.02.140.

[55] Yanhua D, Kairong Z, Yaohua Z. Novel flat plate heat pipe. CN200920246791, 2009.

[56] Hou L, Quan Z, Zhao Y, Wang L, Wang G. An experimental and simulative study on a novel photovoltaic-thermal collector with micro heat pipe array (MHPA-PV/T). Energy Build 2016;124:60–9. https://doi.org/10.1016/j.enbuild.2016.03.056.

[57] Jouhara H, Lester SP. Heat pipe apparatus. GB11410924.3, 2014.

[58] Jouhara H, Milko J, Danielewicz J, Sayegh MA, Szulgowska-Zgrzywa M, Ramos JB, et al. The performance of a novel flat heat pipe based thermal and PV/T (photovoltaic and thermal systems) solar collector that can be used as an energy-active building envelope material. Energy 2016;108:148–54. https://doi.org/10.1016/j.energy.2015.07.063.

[59] Jouhara H, Szulgowska-Zgrzywa M, Sayegh MA, Milko J, Danielewicz J, Nannou TK, et al. The

performance of a heat pipe based solar PV/T roof collector and its potential contribution in district heating applications. Energy 2017;136:117–25. https://doi.org/10.1016/j.energy.2016.04.070.

[60] Mahdavi M, Qiu S, Tiari S. Numerical investigation of hydrodynamics and thermal performance of a specially configured heat pipe for higherature thermal energy storage systems. Appl Therm Eng 2015;81:325–37. https://doi.org/10.1016/j.applthermaleng.2015.02.031.

[61] Liao Z, Faghri A. Thermal analysis of a heat pipe solar central receiver for concentrated solar power tower. Appl Therm Eng 2016;102:952–60. https://doi.org/10.1016/j.applthermaleng.2016.04.043.

[62] Yang L, Zhou RW, Ling X, Peng H. Experimental investigate on heat transfer performance of Flat Heat Pipe Receiver in Solar Power Tower Plant. Appl Therm Eng 2016;109:662–6. https://doi.org/10.1016/j.applthermaleng.2016.07.075.

[63] Boo JH, Kim SM, Kang YH. An Experimental Study on a Sodium Loop-type Heat Pipe for Thermal Transport from a High-temperature Solar Receiver. Energy Procedia 2015;69:608–17. https://doi.org/10.1016/j.egypro.2015.03.070.

[64] Koepf EE, Advani SG, Prasad AK. Experimental investigation of ZnO powder flow and feeding characterization for a solar thermochemical reactor. Powder Technol 2014;261:219–31. https://doi.org/10.1016/j.powtec.2014.04.036.

[65] Wang X, Ma T, Zhu Y, Chen H, Zeng J. Experimental investigation on startup and thermal performance of a high temperature special-shaped heat pipe coupling the flat plate heat pipe and cylindrical heat pipes. Exp Therm Fluid Sci 2016;77:1–9. https://doi.org/10.1016/j.expthermflusci.2016.03.013.

[66] Ma T, Zhu Y, Chen H, Wang X, Zeng J, Lu B. Frozen start-up performance of a high temperature special shaped heat pipe suitable for solar thermochemical reactors. Appl Therm Eng 2016;109:591–9. https://doi.org/10.1016/j.applthermaleng.2016.08.091.

[67] El-Genk MS. Space nuclear reactor power system concepts with static and dynamic energy conversion. Energy Convers Manag 2008;49:402–11. https://doi.org/10.1016/j.enconman.2007.10.014.

[68] Zhang W, Wang C, Chen R, Tian W, Qiu S, Su GH. Preliminary design and thermal analysis of a liquid metal heat pipe radiator for TOPAZ-II power system. Ann Nucl Energy 2016;97:208–20. https://doi.org/10.1016/j.anucene.2016.07.007.

[69] Wang C, Chen J, Qiu S, Tian W, Zhang D, Su GH. Performance analysis of heat pipe radiator unit for space nuclear power reactor. Ann Nucl Energy 2017;103:74–84. https://doi.org/10.1016/j.anucene.2017.01.015.

[70] Guangren W, Baihua C, Guofeng W, Keming B, Bo F, Ye H, et al. Experiment research on heat transfer performance of high temperature heat pipe with arteries. At Energy Sci Technol 2014;48:447–52.

[71] Delpech B, Axcell B, Jouhara H. Experimental investigation of a radiative heat pipe for waste heat recovery in a ceramics kiln. Energy 2018. https://doi.org/10.1016/j.energy.2018.12.133.

[72] Llera R, Lago F, Jouhara H. Industrial Thermal Energy Recovery conversion and Management Project Acronym : I-ThERM Grant Agreement No : 680599 D6 . 1 Environment characterization and site selection From ArcelorMittal March 2016. 2016.

[73] Llera R, Lago F, Jouhara H. Project Title : Industrial Thermal Energy Recovery conversion and Management Project Acronym : I-ThERM Grant Agreement No : 680599 D6 . 2 Thermal characterisation of the hot streams From ArcelorMittal September 2016. 2016.

[74] Kothandaraman CP. Heat and mass transfer data book. New Delhi: New Age International; 2004.

[75] Bergman TL, Incropera FP, DeWitt DP, Lavine AS. Fundamentals of heat and mass transfer. John Wiley & Sons; 2011.

[76] Kreith F, Manglik RM, Bohn MS. Principles of heat transfer. Cengage learning; 2011.

[77] A. Cengel Y, J. Ghajar A. Heat and Mass Transfer: Fundamentals and applications. Fifth. 2014.

[78] Howell JR. A catalog of radiation heat transfer configuration factors. Http//Www Me Utexas Edu/~ Howell/Sectionc/C11 Html 2001.

[79] Hamilton DC, Morgan WR. Radiant-interchange configuration factors 1952.

[80] Hottel HC. Radiant heat transmission between surfaces separated by non-absorbing media. Trans ASME 1931;53.

[81] Ehlert JR, Smith TF. View factors for perpendicular and parallel rectangular plates. J Thermophys Heat Transf 1993;7:173–5.

[82] Gross U, Spindler K, Hahne E. Shapefactor-equations for radiation heat transfer between plane rectangular surfaces of arbitrary position and size with parallel boundaries. Lett Heat Mass

Transf 1981;8:219–27.

[83] Boeke W, Wall L. Radiative exchange factors in rectangular spaces for the determination of mean radiant temperature. Build Serv Eng 1976;43:244–53.

[84] Chekhovskii IR, Sirotkin V V, Chu-Dun-Chu I V, Chebanov VA. Determination of radiative view factors for rectangles of different sizes. High Temp Sci 1979;17:116–9.

[85] Byrd LW. Discussion:“View Factor Algebra for Two Arbitrarily Sized Non-opposing Parallel Rectangles.” J Heat Transfer 1993;115:517–8.

[86] Krishnaprakas CK. View factor between inclined rectangles. J Thermophys Heat Transf 1997;11:480–1.

[87] Yuen WW. A Simplified Approach to Shape-Factor Calculation Between Three-Dimensional Planar Objects. J Heat Transfer 1980;102:386–8.

[88] Howell JR, Siegel R. Thermal Radiation Heat Transfer. 6th editio. Washington DC: CRC Press; 2015. https://doi.org/https://doi.org/10.1201/b18835.

[89] Sparrow EM, Cess DR. Radiation Heat Transfer Augmented Edition, Hemisphere 1978.

[90] Feingold A, Gupta KG. New Analytical Approach to the Evaluation of Configuration Factors in Radiation from Spheres in Infinitely Long Cylinders, ASME; 1969.

[91] Chang SW, Lo DC, Chiang KF, Lin CY. Sub-atmospheric boiling heat transfer and thermal performance of two-phase loop thermosyphon. Exp Therm Fluid Sci 2012;39:134–47. https://doi.org/10.1016/j.expthermflusci.2012.01.017.

[92] Rohsenow WM. A method of correlating heat transfer data for surface boiling of liquids. Cambridge, Mass.: MIT Division of Industrial Cooporation,[1951]; 1951.

[93] Cooper MG. Heat Flow Rates in Saturated Nucleate Pool Boiling-A Wide-Ranging Examination Using Reduced Properties. In: Transfer JPH and TFIBT-A in H, editor. vol. Volume 16, Elsevier; 1984, p. 157–239. https://doi.org/http://dx.doi.org/10.1016/S0065-2717(08)70205-3.

[94] Gorenflo D. Pool Boiling in VDI-Heat Atlas (English Version). VDI-Verlag, Dusseldorf, Ger 1993.

[95] McNelly MJ. A correlation of the rates of heat transfer to nucleate boiling liquids. J Imp Coll Chem Eng Soc 1953;7:18–34.

[96] Forster HK, Zuber N. Bubble dynamics and boiling heat transfer. AIChE J 1955;1:531–5.

[97] Mostinski IL. Application of rule of corresponding states for the calculation of heat transfer and

critical heat flux to boiling liquids. Br Chem Eng Abstr FOLIO 1963:580.

[98] Stephan K, Abdelsalam M. Heat-transfer correlations for natural convection boiling. Int J Heat Mass Transf 1980;23:73–87. https://doi.org/http://dx.doi.org/10.1016/0017-9310(80)90140-4.

[99] Labuntsov DA. Heat transfer problems with nucleate boiling of liquids. Therm Eng(USSR)(Engl Transl), v 19, No 9, Pp 21-28 1973.

[100] Imura H, Kusuda H, Ogata J-I, Miyazaki T, Sakamoto N. Heat transfer in two-phase closed-type thermosyphons. JSME Trans 1979;45:712–22.

[101] Shiraishi M, Kikuchi K, Yamanishi T. Investigation of heat transfer characteristics of a two-phase closed thermosyphon. J Heat Recover Syst 1981;1:287–97. https://doi.org/10.1016/0198-7593(81)90039-4.

[102] Kiatsiriroat T, Nuntaphan A, Tiansuwan J. Thermal performance enhancement of thermosyphon heat pipe with binary working fluids. Exp Heat Transf 2000;13:137–52. https://doi.org/10.1080/089161500269517.

[103] Jakob M, Hawkins GA. Elements of heat transfer. Wiley; 1957.

[104] Kopchikov IA, Voronin GI, Kolach TA, Labuntsov DA, Lebedev PD. Liquid boiling in a thin film. Int J Heat Mass Transf 1969;12:791–6. https://doi.org/10.1016/0017-9310(69)90182-3.

[105] El-Genk MS, Saber HH. Determination of operation envelopes for closed, two-phase thermosyphons. Int J Heat Mass Transf 1999;42:889–903. https://doi.org/10.1016/S0017-9310(98)00212-9.

[106] Gogonin II. The dependence of boiling heat transfer on the properties and geometric parameters of heat-transfer wall. High Temp 2006;44:913–21.

[107] Chun KR, Seban RA. Heat transfer to evaporating liquid films. J Heat Transf 1971;93:391–6. https://doi.org/10.1115/1.3449836.

[108] Nusselt W. Die Oberflachenkondesation des Wasserdamffes the surface condensation of water. Zetrschr Ver Deutch Ing 1916;60:541–6.

[109] Rohsenow WM. Heat transfer and temperature distribution in laminar film condensation. Trans Asme 1956;78:1645–8.

[110] Kutateladze SS. Fundamentals of Heat Transfer (2nd Edn.) Edward Arnold. New York 1963:247.

[111] Chen MM. An analytical study of laminar film condensation: part 2—single and multiple horizontal tubes. J Heat Transfer 1961;83:55.

[112] Jouhara H, Robinson AJ. Experimental investigation of small diameter two-phase closed thermosyphons charged with water, FC-84, FC-77 and FC-3283. Appl Therm Eng 2010;30:201–11. https://doi.org/10.1016/j.applthermaleng.2009.08.007.

[113] Hashimoto H, Kaminaga F. Heat transfer characteristics in a condenser of closed two-phase thermosyphon: Effect of entrainment on heat transfer deterioration. Heat Transf Res 2002;31:212–25. https://doi.org/10.1002/htj.10030.

[114] Rohsenow WM. Heat transfer and temperature distribution in laminar film condensation. Trans Asme 1956;78:1645–8.

[115] Al-Arabi M, Salman YK. Laminar natural convection heat transfer from inclined surfaces. Int J Heat Mass Transf 1980;23:45–51.

[116] Oosthuizen PH. Experimental study of free convective heat transfer from inclined cylinders. J Heat Transfer 1976;98:672–4.

[117] Rani N, Setia H, Dutt M, Wanchoo R. K. Natural Convection Heat Transfer from Inclined Cylinders : A Unified Correlation. Int J Math Comput Phys Electr Comput Eng 2014;8:100–5.

[118] Bansal JC. Natural convection heat transfer from inclined cylinders. Panjab university, 1976.

[119] AL-Arabi M, Khamis M. Natural Convection Heat Transfer from inclined cylinders. Int J Heat Mass Transf 1982;25:3–15. https://doi.org/10.1002/9781119476962.ch5.

[120] Li J, Tarasuk JD. Local free convection around inclined cylinders in air: An interferometric study. Exp Therm Fluid Sci 1992;5:235–42. https://doi.org/10.1016/0894-1777(92)90010-3.

[121] Morgan VT. The overall convective heat transfer from smooth circular cylinders. Adv. heat Transf., vol. 11, Elsevier; 1975, p. 199–264.

[122] Heo JH, Chung BJ. Natural convection heat transfer on the outer surface of inclined cylinders. Chem Eng Sci 2012;73:366–72. https://doi.org/10.1016/j.ces.2012.02.012.

[123] Hausen H. Darstellung des Warmeuberganges in Rohren durch verallgemeinerte Potenzbeziehungen. Z VDI Beihefte Verfahrenstech 1943:91–8.

[124] Petukhov BS. Heat Transfer and Friction in Turbulent Pipe Flow with Variable Physical Properties. Adv Heat Transf 1970;6:503–64. https://doi.org/10.1016/S0065-2717(08)70153-9.

[125] Sieder EN, Tate GE. Heat transfer and pressure drop of liquids in tubes. Ind Eng Chem 1936;28:1429–35.

[126] Knudsen JG. DL Katz Fluid dynamics and heat transfer. Chem Eng Ser McGraw-Hill, New York, NY 1958.

[127] Gnielinski V. New equations for heat and mass-transfer in turbulent pipe and channel flow. Int Chem Eng 1976;16:359–68.

[128] Sleicher CA, Rouse MW. A convenient correlation for heat transfer to constant and variable property fluids in turbulent pipe flow. Int J Heat Mass Transf 1975;18:677–83.

[129] Faghri A. Review and Advances in Heat Pipe Science and Technology. J Heat Transfer 2012;134:123001. https://doi.org/10.1115/1.4007407.

[130] Remella KS, Gerner FM. Simplified Mathematical Model of a novel 'Closed Loop Two-Phase Wicked Thermosyphon (CLTPWT).' Int J Therm Sci 2017;114:281–95. https://doi.org/10.1016/j.ijthermalsci.2017.01.002.

[131] Gedik E. Experimental investigation of the thermal performance of a two-phase closed thermosyphon at different operating conditions. Energy Build 2016;127:1096–107. https://doi.org/10.1016/j.enbuild.2016.06.066.

[132] Mroue H, Ramos JB, Wrobel LC, Jouhara H. Performance evaluation of a multi-pass air-to-water thermosyphon-based heat exchanger. Energy 2017. https://doi.org/10.1016/j.energy.2017.04.111.

[133] R. Howell J, Pinar Menguc M, Siegel R. A catalog of radiation heat transfer configuration factors. Therm. Radiat. heat Transf. 6th ed., CRC Press; 2015.

[134] Jouhara H, Ajji Z, Koudsi Y, Ezzuddin H, Mousa N. Experimental investigation of an inclined-condenser wickless heat pipe charged with water and an ethanol-water azeotropic mixture. Energy 2013;61:139–47. https://doi.org/10.1016/j.energy.2012.09.033.

[135] Jafari D, Di Marco P, Filippeschi S, Franco A. An experimental investigation on the evaporation and condensation heat transfer of two-phase closed thermosyphons. Exp Therm Fluid Sci 2017;88:111–23. https://doi.org/10.1016/j.expthermflusci.2017.05.019.

[136] Almahmoud S, Jouhara H. Experimental and theoretical investigation on a radiative flat heat pipe heat exchanger. Energy 2019;174:972–84. https://doi.org/10.1016/j.energy.2019.03.027.

[137] Jouhara H, Almahmoud S, Chauhan A, Delpech B, Bianchi G, Tassou SA, et al. Experimental and

theoretical investigation of a flat heat pipe heat exchanger for waste heat recovery in the steel industry. Energy 2017;141:1928–39. https://doi.org/10.1016/j.energy.2017.10.142.

[138] Cornwell K, Houston SD. Nucleate pool boiling on horizontal tubes: A convection-based correlation. Int J Heat Mass Transf 1994;37:303–9. https://doi.org/10.1016/0017-9310(94)90031-0.

[139] Taylor J. Introduction to error analysis, the study of uncertainties in physical measurements. 1997.

[140] Sadiq H, Wong M., Tashan J, Al-Mahaidi R, Zhao X-L. Determination of Steel Emissivity for the Temperature Prediction of Structural Steel Members in Fire. J Mater Civ Eng 2013;25:167–73. https://doi.org/10.1061/(ASCE)MT.1943-5533.

[141] Zhang K, Yu K, Liu Y, Zhao Y. An improved algorithm for spectral emissivity measurements at low temperatures based on the multi-temperature calibration method. Int J Heat Mass Transf 2017;114:1037–44. https://doi.org/10.1016/j.ijheatmasstransfer.2017.06.133.

[142] Morrell R. Handbook of properties of technical and engineering ceramics. Hmso; 1987.

[143] Clarke T. Comment on the report " Observation of abundant heat production from a reactor device and of isotopic changes in the fuel " by Levi et al. Report 2015:1–13.

[144] Fichera C, Carra F, Küchler D, Toivanen V. Numerical study of the thermal performance of the CERN Linac3 ion source miniature oven. Nucl Instruments Methods Phys Res Sect A Accel Spectrometers, Detect Assoc Equip 2018;901:21–31. https://doi.org/10.1016/j.nima.2018.05.036.

[145] Wood WD, Deem HW, Lucks CF. Thermal radiative properties. Plenum Press; 1964.

[146] BÜYÜKALACA O. Gözenekli Seramiklerde Işınım Yayma Sayısının Ölçümü/Measurement of Radiation Emissions in Porous Ceramics. Tr J Eng Environ Sci 1998;22:131–44.

[147] Mironov RA, Zabezhailov MO, Borodai SP. Theoretical-Experimental Determination of the Temperature Dependence of the Integral Emissivity of an Alumina Ceramic. Refract Ind Ceram 2015;55:424–7. https://doi.org/10.1007/s11148-015-9738-z.

[148] Sully AH, Brandes EA, Waterhouse RB. Some measurements of the total emissivity of metals and pure refractory oxides and the variation of emissivity with temperature. Br J Appl Phys 1952;3:97–101. https://doi.org/10.1088/0508-3443/3/3/307.

[149] Touloukian YS, DeWitt DP. Thermal radiative properties-metallic elements and alloys.

Thermophys Prop Matter-The TPRC Data Ser 1970;7.

Appendices

Appendix 1: Error analysis and Uncertainties of experimental results

The level of uncertainty for the experimental heat recovery values came from the temperature measurements, and the flow rate meter. The uncertainty associated the readings of the temperature is (0.05% ±0.38), while the one associated with the flow meter is ±1% of the full scale.

According to [139], the propagation of uncertainties associated with the calculated heat transfer rate values (S_Q), can be calculated from:

$$S_Q = Q_{out} \times \sqrt{\left(\frac{S_{\dot{V}}}{\dot{V}}\right)^2 + \left(\frac{S_{(T_{water,out}-T_{water,in})}}{(T_{water,out} - T_{water,in})}\right)^2} \tag{7-1}$$

Where the error associated with temperature difference between the water inlet and outlet is:

$$S_{(T_{water,out}-T_{water,in})} = \sqrt{S_{T_{water,out}}^2 + S_{T_{water,in}}^2} \tag{7-2}$$

The thermal resistance of boiling is calculated from:

$$R_{ei} = \frac{T_{ei} - T_v}{Q} = \frac{T_{eo} - T_v}{Q} - \frac{\ln(\frac{D_o}{D_i})}{2\pi l_e k_s} \tag{7-3}$$

The propagation of uncertainties associated with the calculated boiling thermal resistance is:

$$S_{R_{ei}} = R_{ei}\sqrt{\left(\frac{S_{(T_{ei,av}-T_v)}}{(T_{\mathrm{ei}} - T_v)}\right)^2 + \left(\frac{S_Q}{Q}\right)^2} \tag{7-4}$$

Where:

$$S_{(T_{eo,av}-T_v)} = \sqrt{S_{T_{eo,av}}^2 + S_{T_v}^2} \tag{7-5}$$

Hence:

$$S_{R_{ei}} = R_{ei}\sqrt{\frac{S_{T_{eo,av}}^2 + S_{T_v}^2}{(T_{eo} - T_v)^2} + \left(\frac{S_Q}{Q}\right)^2} \tag{7-6}$$

The propagation of uncertainties associated with the calculated overall thermal resistance is calculated as follows:

$$R_{HP,total} = \frac{LMTD}{Q} = \frac{T_o - T_i}{\ln\left(\frac{T_{eo,av} - T_i}{T_{eo,av} - T_i}\right) Q} = \frac{T_o - T_i}{\left[\ln\left(T_{eo,av} - T_i\right) - \ln\left(T_{eo,av} - T_o\right)\right] Q} \quad (7\text{-}7)$$

$$S_{R_{HP,total}} = R_{HP,total} \sqrt{\left(\frac{S_{T_o - T_i}}{T_o - T_i}\right)^2 + \left(\frac{S_Q}{Q}\right)^2 + \left(\frac{S_{\ln(T_{eo,av} - T_i) - \ln(T_{eo,av} - T_o)}}{\ln\left(T_{eo,av} - T_i\right) - \ln\left(T_{eo,av} - T_o\right)}\right)^2} \quad (7\text{-}8)$$

By rearranging the equation:

$$S_{R_{HP,total}} = R_{HP,total} \sqrt{\left(\frac{S_{T_o - T_i}}{T_o - T_i}\right)^2 + \left(\frac{S_Q}{Q}\right)^2 + \frac{S^2_{\ln(T_{eo,av} - T_i)} + S^2_{\ln(T_{eo,av} - T_o)}}{\left[\ln\left(T_{eo,av} - T_i\right) - \ln(T_v - T_o)\right]^2}} \quad (7\text{-}9)$$

$$S_{R_{HP,total}} = R_{HP,total} \sqrt{\left(\frac{S_{T_o - T_i}}{T_o - T_i}\right)^2 + \left(\frac{S_Q}{Q}\right)^2 + \frac{\frac{S^2_{T_{eo,av} - T_i}}{\left(T_{eo,av} - T_i\right)^2} + \frac{S^2_{T_{eo,av} - T_o}}{\left(T_{eo,av} - T_o\right)^2}}{\left[\ln\left(T_{eo,av} - T_i\right) - \ln\left(T_{eo,av} - T_o\right)\right]^2}} \quad (7\text{-}10)$$

$$S_{R_{HP,total}} = R_{HP,total} \sqrt{\left(\frac{S_{T_o - T_i}}{T_o - T_i}\right)^2 + \left(\frac{S_Q}{Q}\right)^2 + \frac{\frac{S^2_{T_{eo,av}} + S^2_{T_i}}{\left(T_{eo,av} - T_i\right)^2} + \frac{S^2_{T_{eo,av}} + S^2_{T_o}}{\left(T_{eo,av} - T_o\right)^2}}{\left[\ln\left(T_{eo,av} - T_i\right) - \ln\left(T_{eo,av} - T_o\right)\right]^2}} \quad (7\text{-}11)$$

Hence:

$$S_{R_{HP,total}} = R_{HP,total} \sqrt{\left(\frac{S_{T_o - T_i}}{T_o - T_i}\right)^2 + \left(\frac{S_Q}{Q}\right)^2 + \frac{\frac{\sum_{i=1}^{i=7} S^2_{T_{eo,i}} + S^2_{T_i}}{\left(T_{eo,av} - T_i\right)^2} + \frac{\sum_{i=1}^{i=7} S^2_{T_{eo,i}} + S^2_{T_o}}{\left(T_{eo,av} - T_o\right)^2}}{\left[\ln\left(T_{eo,av} - T_i\right) - \ln\left(T_{eo,av} - T_o\right)\right]^2}} \quad (7\text{-}12)$$

The propagation of uncertainties associated with the calculated thermal resistance of the condenser is as follows:

$$S_{R_{condenser}} = R_{condenser}\sqrt{\left(\frac{S_{T_o-T_i}}{T_o-T_i}\right)^2+\left(\frac{S_Q}{Q}\right)^2+\frac{\frac{S_{T_v}^2+S_{T_i}^2}{(T_v-T_i)^2}+\frac{S_{T_v}^2+S_{T_o}^2}{(T_v-T_o)^2}}{[\ln(T_v-T_i)-\ln(T_v-T_o)]^2}} \quad (7\text{-}13)$$

Table A1-1 Uncertainty associated with the heat recovery

T_water inlet (°C)	T water outlet (°C)	Flow (V) (kg/s)	Sv (± kg/s)	Q (W)	S_Q (±W)	S_Q (%)
21.48282	22.87732	0.016833	0.000168	98.2	26.01414	0.264981
19.59673	22.33739	0.016833	0.000168	193.0	26.09454	0.13524
20.50262	25.22608	0.016833	0.000168	332.5	26.23489	0.078892
17.09009	24.43659	0.016833	0.000168	517.2	26.63371	0.051491
18.82276	20.30333	0.016833	0.000168	104.2	26.07958	0.250192
17.10272	20.05135	0.016833	0.000168	207.6	26.22371	0.126315
16.31985	21.55961	0.016833	0.000168	368.9	26.43522	0.071654
15.29585	23.27297	0.016833	0.000168	561.7	26.8422	0.047789

Table A1-2 Uncertainty associated with the average evaporator temperature T_{eo}

E1b	E1m	E1t	E2b	E2lm	E2um	E2t	T_{eo}	T_{eo} error
(°C)	(°C)	(°C)	(°C)	(°C)	(°C)	(°C)	(°C)	± (°C)
32.4	27.2	24.3	34.2	29.1	27.2	23.6	28.3	0.7
34.6	30.1	28.7	34.5	30.6	29.5	27.4	30.8	0.7
40.2	37.4	36.4	38.6	36.4	36.1	35.3	37.2	0.7
46.8	47.0	45.5	44.9	44.5	44.8	44.0	45.3	0.8

Table A1-3 Uncertainty associated with the boiling thermal resistance

T_{eo}	T_{eo} error	T_v	T_v error	R_{ei} error (absolute)	R_{ei} error %
(°C)	(°C)	(°C)	(°C)	± (°C/W)	%
28.3	0.7	23.0	0.3	0.01350	28.7
30.8	0.7	25.8	0.3	0.00398	19.6
37.2	0.7	32.0	0.3	0.00171	16.3
45.3	0.8	39.3	0.3	0.00100	14.1

Table A1-4 Uncertainty associated with the boiling thermal resistance

T water in	T water out	Teo	Q	RHP	RHP error	RHP error (%)
(°C)	(°C)	(°C)	(W)	(°C/W)	± (°C/W)	%
21.48282	22.87732	31.82	98.2	0.097993	0.007288	7.437246
19.59673	22.33739	33.40	193.0	0.064149	0.001609	2.508024
20.50262	25.22608	40.68	332.5	0.053251	0.000663	1.244597
17.09009	24.43659	46.35	517.2	0.049122	0.00038	0.77417
18.82276	20.30333	28.29	104.2	0.083545	0.001746	2.090215
17.10272	20.05135	30.78	207.6	0.058472	0.000432	0.738585
16.31985	21.55961	37.21	368.9	0.049176	0.000173	0.352371
15.29585	23.27297	45.35	561.7	0.046034	0.000101	0.219995

Appendix 2: Laboratory Emissivity measurement

The emissivity values for common materials published in the literature are vague and general and the surface preparation and any coating on the real material makes the emissivity of the surface differ from those in tables in the literature. Therefore, it is very necessary to determine the emissivity of the materials used in this research.

The experimental measurement of the hemispherical emissivity of a surface requires special instrumentation and it is a complicated method. Another method to measure the approximate emissivity of a material in the laboratory is through the thermography approach by using a thermal imaging camera. This method was used [140] as a non-destructive emissivity measurement. The Infra-Red camera emissivity measurement is based on Planck's law where higher temperature objects emit heat at shorter wavelength. Therefore, using a detector at long wavelength minimises the atmospheric effects on the radiation received. The experimental method is based on the following approach: that the emissivity of a black body is 1 while for real bodies it varies between 0 and 1. Thus the emitted energy from a black surface at any temperature will be the maximum in comparison to any other surfaces at the same temperature. For an isothermal surface which has unknown emissivity, the emissivity can be determined by attaching a tape of known emissivity. Then by using the thermal imaging camera and thermal imaging software, the temperature reading from the tape and from the studied surface can be compared. The software allows the insertion of local measuring points and defining the emissivity values separately from the whole image. For example, $\varepsilon = 0.95$ for TESTO IR thermal imaging masking tape. Since the surface is isothermal, the emissivity of the image or the other points of the studied surface should have the same temperature as the tape. Therefore, the emissivity of the image (or the studied point of the surface) is changed until the temperature of the tape is equal to the temperature of the surface. Hence, the emissivity is determined. It should be noted that thermal imaging cameras normally measure in the spectral range of 7.5 to 13 μm. Therefore, the measured emissivity is applicable for the range of the thermal camera only. Another method to determine the emissivity of the surface is by measuring its temperature directly through a thermocouple and modifying the emissivity of the surface in the thermal image in the software until its temperature is equal to the temperature reading using the thermocouple.

Finally, the determined emissivity value can be compared with the spectral emissivity values from the literature for the IR measuring range to determine the associated hemispherical emissivity value.

Ceramic heater temperature uniformity and emissivity

In order to determine the emissivity of the ceramic heaters made of alumina, two types of masking tape of known emissivity value were attached to the surface and the temperature was measured using a thermocouple as shown in Figure A2-1. The Testo IR masking tape is a rated tape for thermography and its emissivity is $\varepsilon = 0.95$. Similarly, the black masking tape has an emissivity value of $\varepsilon = 0.95$. A thermal image was taken using FLIR T430sc thermal imaging camera which measures the temperature in the thermal radiation spectral range 7.5 to 13 μm. The surface of the heaters was also measured using a thermocouple.

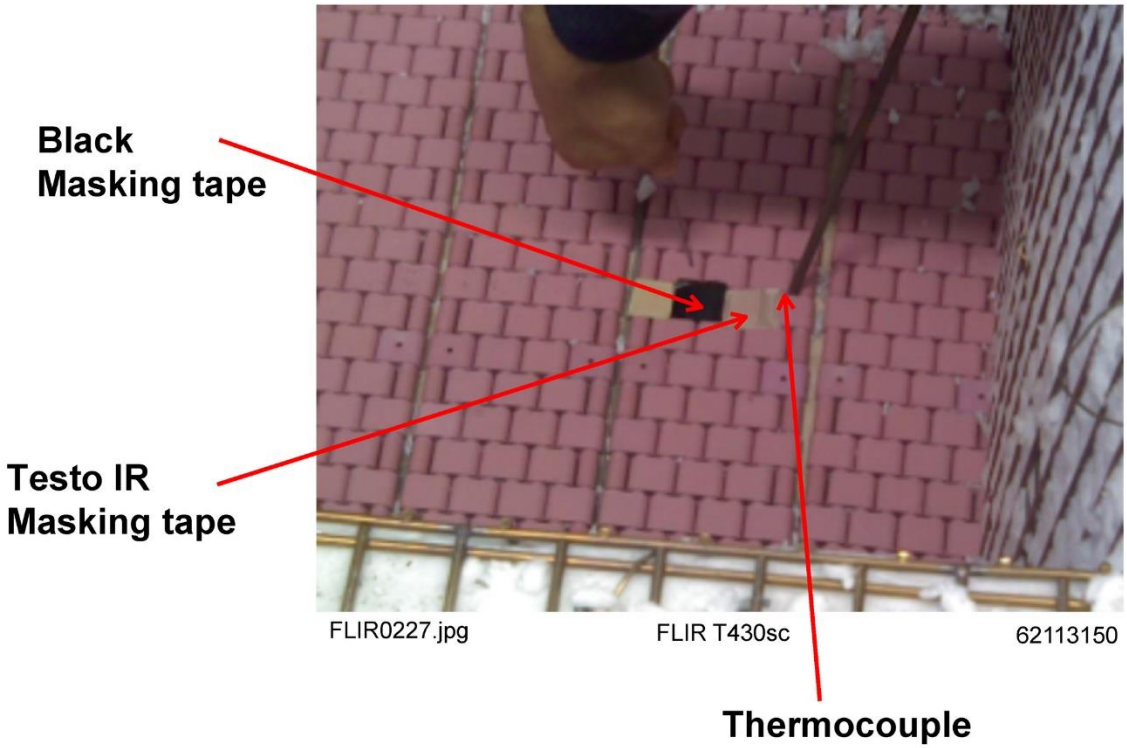

Figure A2-1 A photo of the experimental setup during the measuements of the heaters temperatrure

By using FLIR tool thermal imaging software, the temperature on the masking tapes' surfaces at emissivity of $\varepsilon = 0.95$ was compared with the heater surface. The obtained emissivity of the heater surface was $\varepsilon = 0.88$ which results in associated temperature of 107.5 °C as presented in Figure A2-2. The point Sp1 represents the black tape, Sp2 represents the TESTO masking tape, and Sp3 and Li represent the ceramic heaters surface where Li is the line measuring the heaters temperature diagonally.

It can be seen from the line Li that the maximum temperature difference on the heating surface is 30 °C where the temperature 90 °C corresponds to the tiles in the gap between the heaters.

The obtained emissivity value $\varepsilon = 0.88$ has a good agreement with the value published in [141] for the spectral emissivity of alumina at a temperature of 100 °C within the spectral range of 7.5 to 13 μm. The variance in the values is due to the disturbance from the surroundings and the different experimental setup.

The spectral emissivity of alumina reported by [141] is presented in Figure A2-3.

The total emissivity of alumina within the temperature range 300°C and 500 °C varies in the literature. The total emissivity of alumina ceramics decreases with the temperature. The total emissivity of alumina ceramic is listed below.

Table A2-1 Total emissivity of alumina at different temperatures

Temperature (°C)	Reference	200	300	400	500
Total Emissivity	Morell [142,143]	0.7	0.795	0.75	0.65
	Reported by Fichera et al [144] but originally from [145]	0.72	0.68	0.645	0.61
	Pure Alumina by BÜYÜKALACA [146]	0.7	0.688	0.635	0.56
	Mironov [147]	0.73	0.75	0.745	0.75

The emissivity values reported by [144] and [146] are the most reliable data and they will be used in the theoretical modelling and analysis.

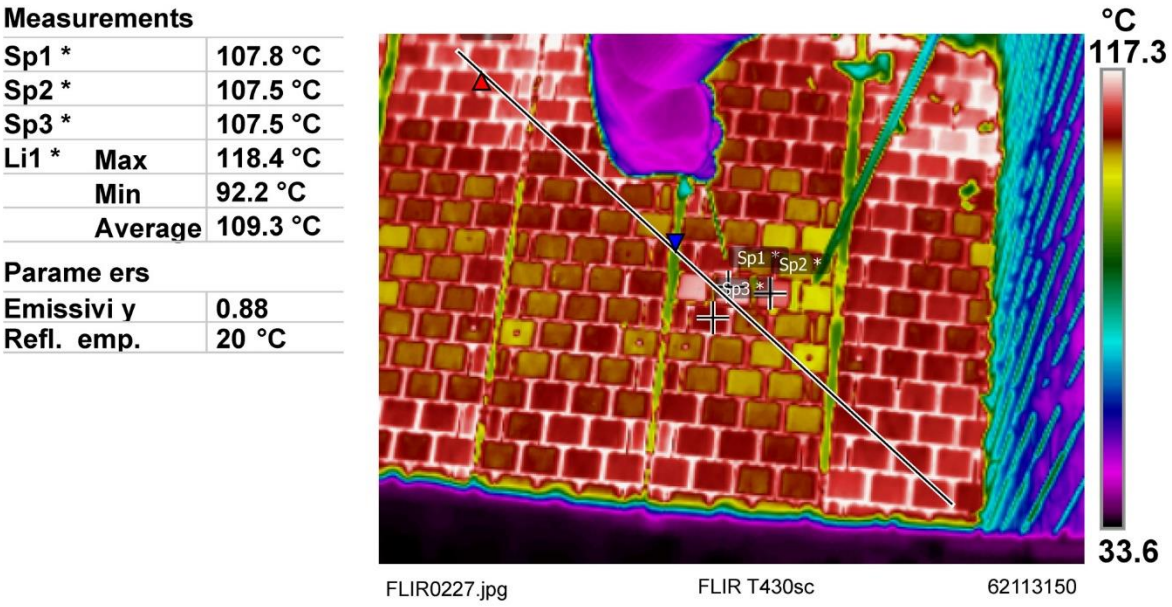

Figure A2-2 Thermal image of the ceramic heaters

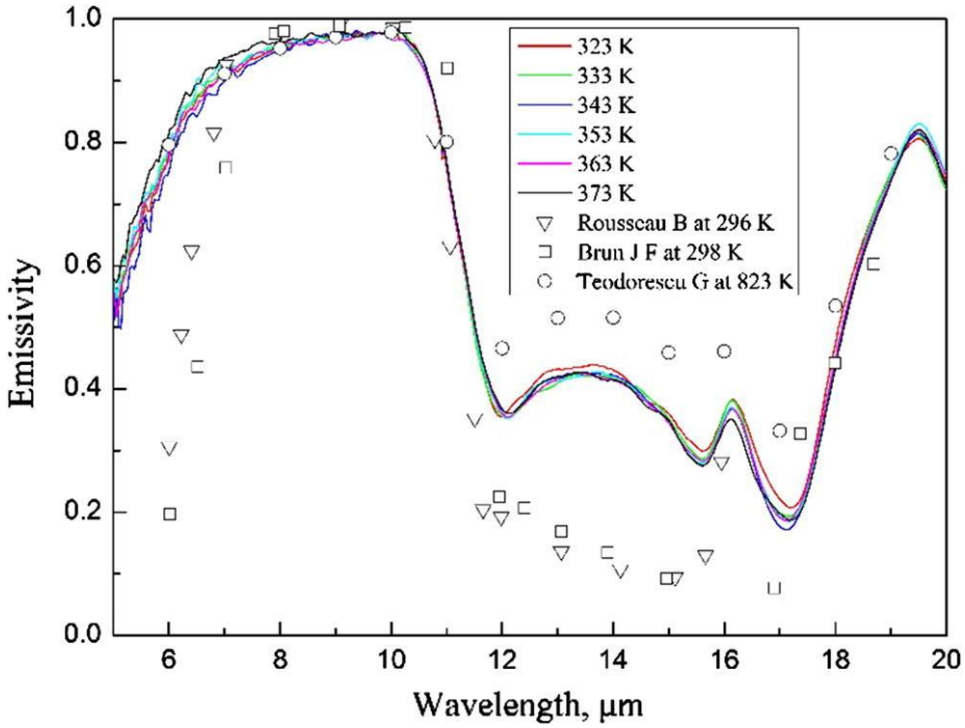

Figure A2-3 Normal spectral emissivity of high purity alumina [141]

Stainless steel 304 emissivity

The emissivity of the single heat pipe and the FHP which were constructed from stainless steel 304 was measured using the approach used in measuring the emissivity of the ceramic heaters.

A piece of TESTO IR masking tape was attached to the surface of the pipe and a thermal image was taken at different temperature of the surface and the temperature was also compared with temperature measured using the welded thermocouples. A photo of the pipe is presented in Figure A2-4.

Figure A2-4 A photo of the stainless steel pipe and the TESTO IR masking tape

The thermal image measurements of the stainless-steel pipe at temperature 57 °C are shown in Figure A2-5. It can be seen that the measured emissivity varied between 0.41 and 0.46 in box1 and box2.

The high temperature spots around the thermocouples are due to the high emissivity of the oxidised surface because of the thermocouples' brazing. The thermocouple's end does not show high temperature which implies that the thermocouple's surface and the filling rod used for brazing has a low emissivity value, leading to good temperature measurements under radiation heat transfer.

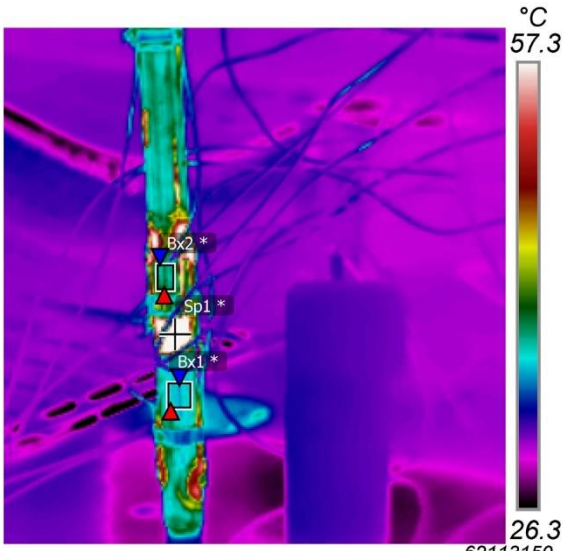

Measurements		
Bx1 *	Max	56.8 °C
	Min	52.9 °C
	Average	55.1 °C
Bx2 *	Max	57.5 °C
	Min	52.1 °C
	Average	54.1 °C
Sp1 *		56.9 °C

Parameters	
Emissivity:	
General	ε=0.9
Bx1	ε=0.46
Bx2	ε=0.41
Sp1	ε=0.95
Refl. temp.	20 °C

Figure A2-5 Thermal imaging measuements of the stainless steel pipe at temperture 57 °C

The experiment was repeated at a temperature of 58 °C and the emissivity obtained for stainless steel was 0.42 as shown in Figure A2-6. The temperature within the box varied about by 8 °C which can be caused by the surface roughness and the reflectivity from the background as the surface is cylindrical.

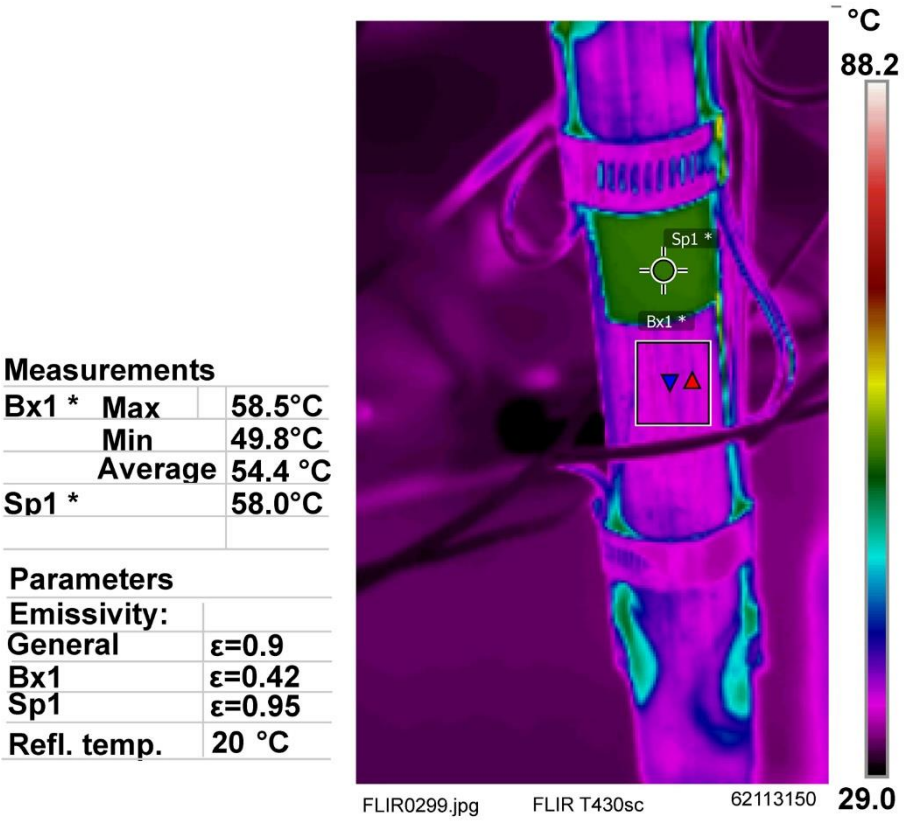

Figure A2-6 Thermal imaging measuements of the stainless steel pipe at temperture 58 °C

The emissivity at a temperature of 70 °C was 0.38 with a temperature variance in the box around 6 °C as presented in Figure A2-7. A thermal image of the stainless steel pipe at a temperature of 80 °C is shown in Figure A2-8. The emissivity of the surface in box 1 is 0.39 with a temperature variance of 12 °C. The emissivity used for the spot measurement Sp2 on the heat pipe surface was 0.3 which is significantly different from the one used in the box. It can be concluded that local surface temperature of the heat pipe is very sensitive to the emissivity when it is measured by thermography method. Furthermore, the box measurement gives approximate results better than the spot measurement as it covers wider area.

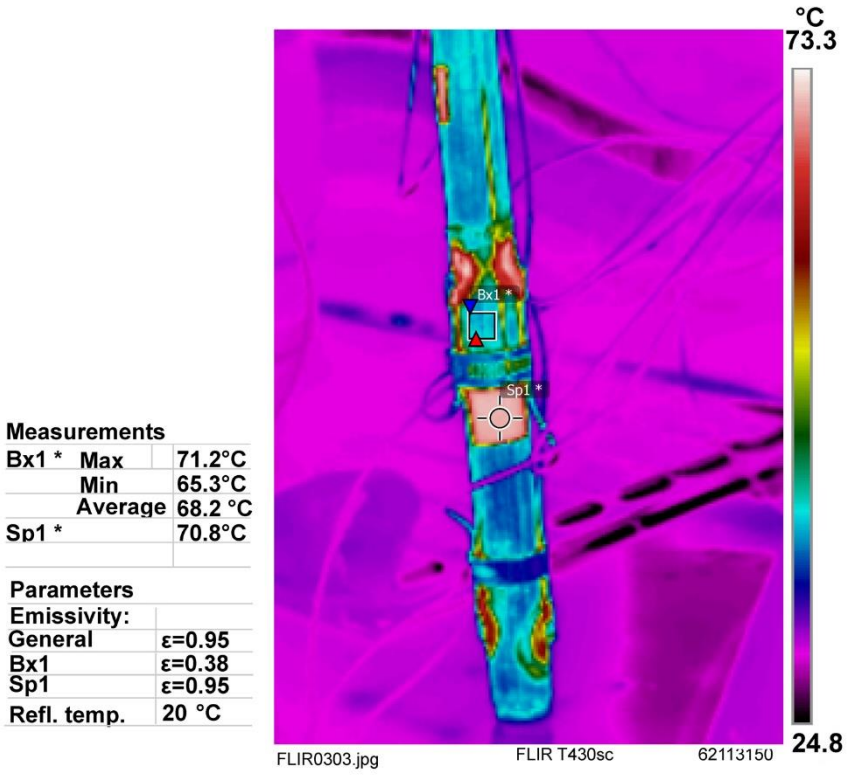

Figure A2-7 Thermal imaging measuements of the stainless steel pipe at temperture 70.8 °C

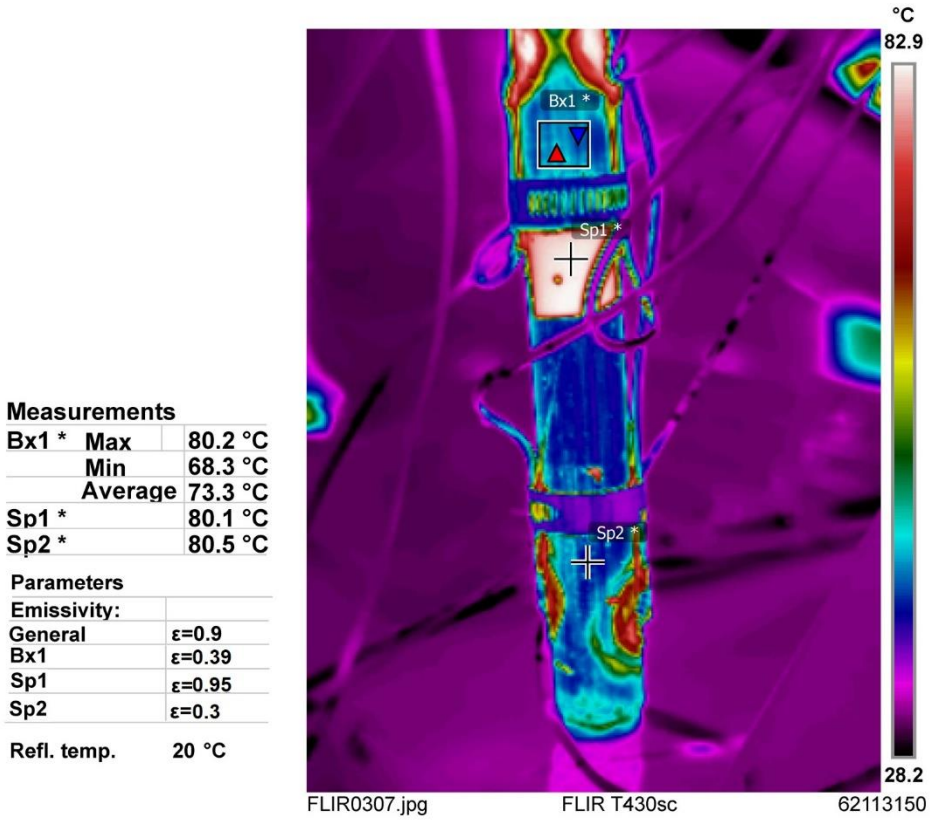

Figure A2-8 Thermal imaging measuements of the stainless steel pipe at temperture 80 °C

The emissivity of metals varies significantly with temperature, surface roughness, and surface oxidisation. The emissivity of stainless steel has been studied widely in the literature. However, the actual condition of the studied samples is often not shown, which makes it difficult to identify the correct emissivity to be used for the stainless steel 304 tubes and plate used in this research.

The total emissivity of polished SS 304 is 0.2 at 400 °C while it reaches 0.87 for an oxidised surface at the same temperature [145]. The stainless steel 304 tubes can be coated as well to provide additional protection against corrosion which also changes its emissivity. *Sully et al*. [148] reported an emissivity for rolled stainless steel to be ε = 0.45 at 400 °C. Emissivity values of stainless steel at different conditions are listed in Table A2-2.

Table A2-2 List of emissivity of Stainless steel 304 (18/8)

Temperature °C	Emissivity	condition	reference
39	0.248	polished	[149]
128	0.304		
209	0.354		
82	0.51	Sand-blasted	
104	0.5		
131	0.511		
183	0.484		

The spectral emissivity of selected materials versus wavelength is presented in Figure A2-9. The spectral emissivity of polished stainless steel decreases with the increase in the wavelength and the spectral emissivity in the spectral range 7.5 -13 μm is less than at shorter wavelengths. Figure A2-10 shows the total emissivity of selected materials including polished stainless steel. For polished stainless steel at a temperature of 800 K, the emissivity is 0.26 which is higher than the average spectral emissivity of the spectral range 7.5 -13 μm at the same temperature. Hence the emissivity of the stainless steel tubes used to construct the single heat pipe and the flat heat pipe system is higher than 0.4 based on the laboratory measurements. A value of 0.45 is considered to be the emissivity of the unpainted stainless steel.

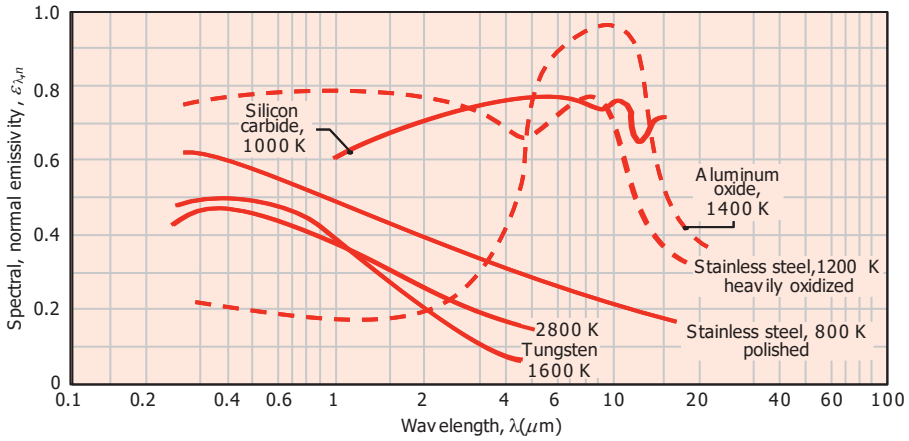

Figure A2-9 Spectral emissivity of different materials versus wavelength [75]

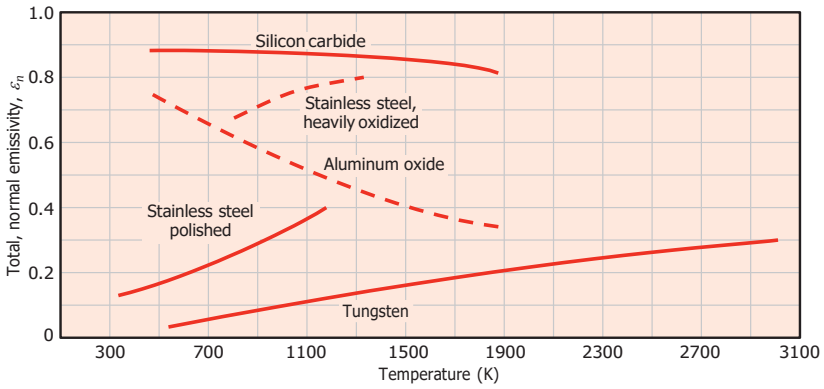

Figure A2-10 Dependence of total emissivity of selected materials on the temperature [75]

Steel temperature at the factory

The temperature of the steel rod wires of diameter 13mm was measured at different distances from the laying head as listed in Table A2-3.

Table A2-3 Position distance from the laying head at the steel factory

Position (#)	Distance (m)
Position 1	2.5
Position 2	5
Position 3	7.5
Position 4	10
Position 5	12.5

A thermal image of the steel wires at position 1 is presented in Figure A2-11. The emissivity settings in the image is 0.5, it can be seen that the maximum temperature of the steel is 1300°C which is very close to the melting point, therefore the emissivity of the steel is higher than 0.5.

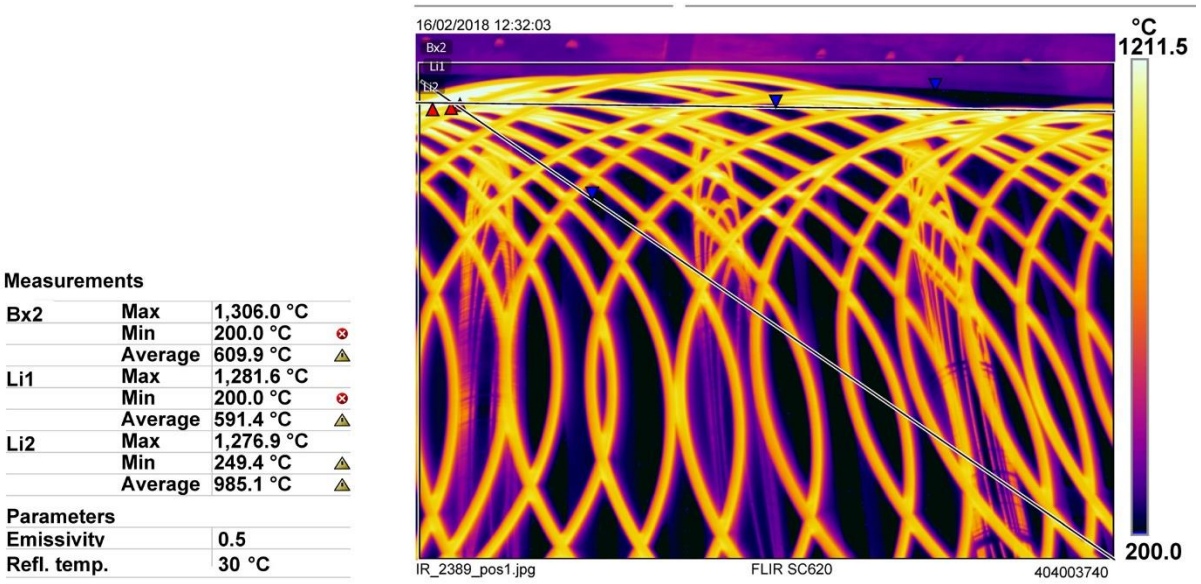

Figure A2-11 Thermal image measurement of the steel in the factory at position 1, 2.5 m from the laying head, emissivity 0.5

Steel emissivity can reach up-to 0.9 depending on the alloy. Sadiq et al [140] obtained an emissivity of carbon steel of 0.7 for high temperatures. The emissivity used in the following images is 0.85 which is an average value for different steel conditions and alloys. The steel temperature at position 1 is presented in Figure A2-12 for emissivity 0.85.

The measurement box Bx2 measures the temperature in the whole view-range of the photo, the measurement line Li1 measures the temperature diagonally, and the measurement line Li2 measures the temperature of the steel close to the edge. The maximum temperature of the steel is 908 °C while the minimum temperature in the photo is 200 °C because the thermal imaging camera does not detect any temperature below 200 °C. The average temperature obtained from Bx1 is 444 °C considering the minimum temperature is 200 °C. The real average temperature is higher than this value because the photo does not show the other edge of the conveyor where the steel temperature is very close to the far edge shown in the photo. The temperature measurement from Li1 and Li2 is presented in Figure A2-13. The diagonal line Li1 shows the temperature of the steel and the gaps where the steel temperature varied between 900 °C at the edge and 700 °C at the centre. The fluctuations of the temperature under 700 °C are due to the temperature of the rollers. The measurement line Li2 shows that the steel temperature at the edge was above 700 °C with some points exceeding 800 °C to 900 °C, again the sudden slopes represents the gaps between the steel wires.

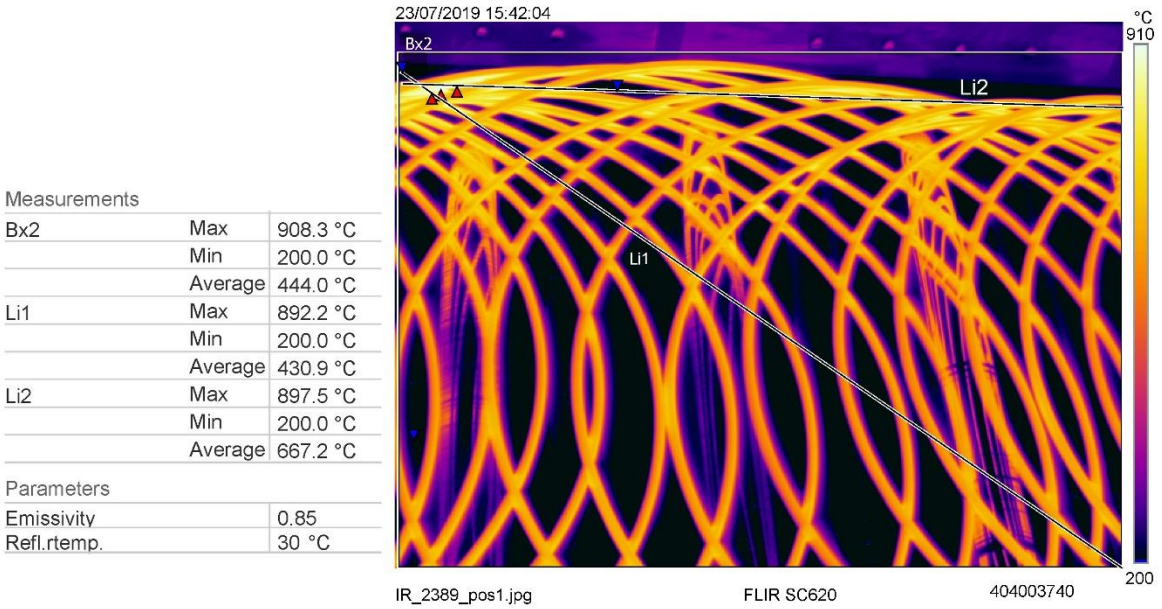

Figure A2-12 Thermal image measurement of the steel in the factory at position 1, 2.5 m from the laying head, emissivity 0.85

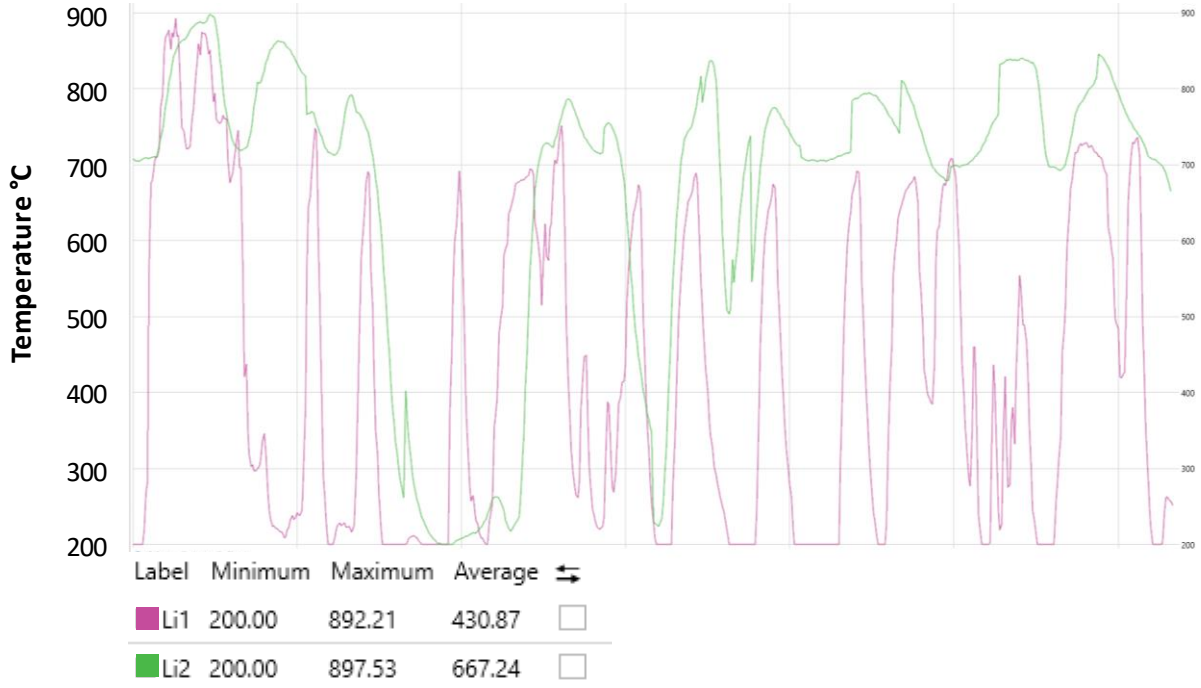

Figure A2-13 Temperature profile from line 1 and line 2 of the steel theraml image at position 1

Figure A2-14 shows a thermal image of the steel at position 2. The maximum temperature of the steel decreased to 866 °C due to the cooling process. As a result, the average temperature decreased to 421.5 °C. The temperature distribution of the steel by Li1 and Li2 is shown in Figure A2-15. Li1 shows that the temperature of the steel varied between 780 °C and 680 °C approximately. The steel

temperature at the edge is higher as exhibited by the line Li2. The maximum temperature was about 850 °C where the steel wires were stacked above each other due to the insufficient cooling.

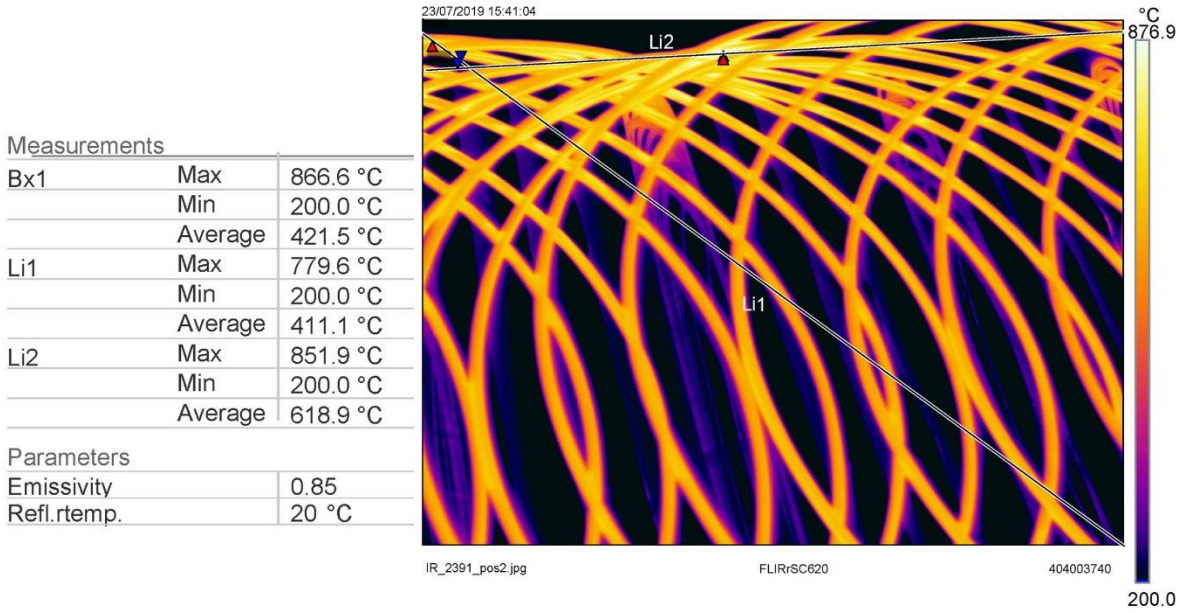

Figure A2-14 Thermal image measurement of the steel in the factory at postion 2, 5 m from the laying head

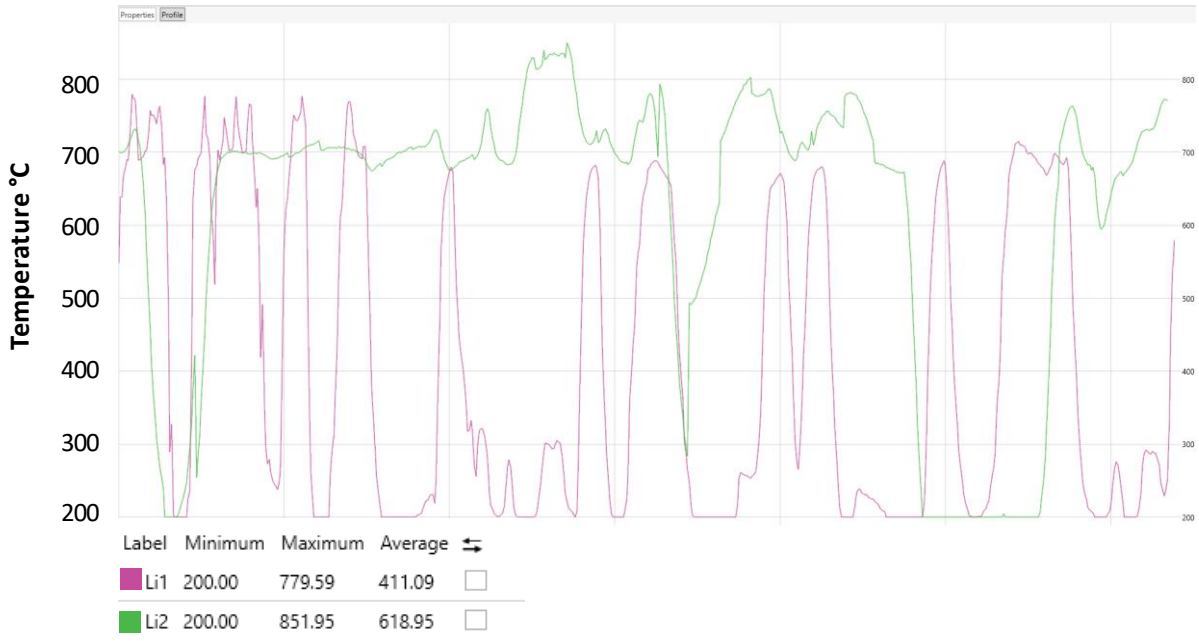

Figure A2-15 Temperature profile from line 1 and line 2 of the steel theraml image at position 2

The steel temperature at a distance of 7.5 from the laying head is presented in Figure A2-16. The maximum temperature of the steel decreased to 838 °C with an average temperature of 395 °C. The

steel and roller temperature profile is shown in Figure A2-17. The steel temperature at the conveyor edge was about 800 °C while it decreased to the range 660- 700 °C at the centre as seen from Li1. The steel temperature at the edge was in the range 700 to 800 °C.

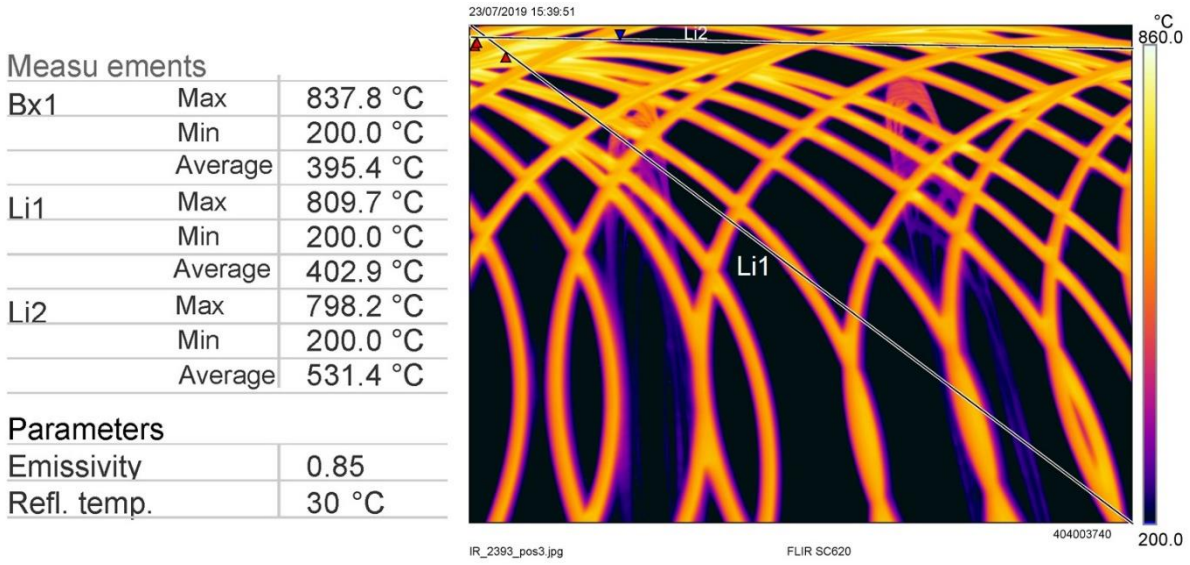

Figure A2-16 Thermal image measurement of the steel in the factory at position 3, 7.5 m from the laying head

Figure A2-17 Temperature profile from line 1 and line 2 of the steel thermal image at position 3

The steel temperature at position 4 which is 10 m from the laying head is presented in Figure A2-18. The maximum steel temperature was 820 °C where the steel wires are stacked and the average temperature of the image area is 400 °C. The average temperature is very close to the average

temperature at position 3. Furthermore, the steel temperature profile diagonally varied between 700 °C and 600 °C from the edge to the centre as measured by the line Li1. The steel temperature at the edge was varying around 700 °C, while the maximum temperature was 814 °C as measured by the line Li2. By comparing the temperature profile in Figure A2-19 with Figure A2-17, it can be noted that the steel temperature decrease was low, which could be caused by the low fan speed.

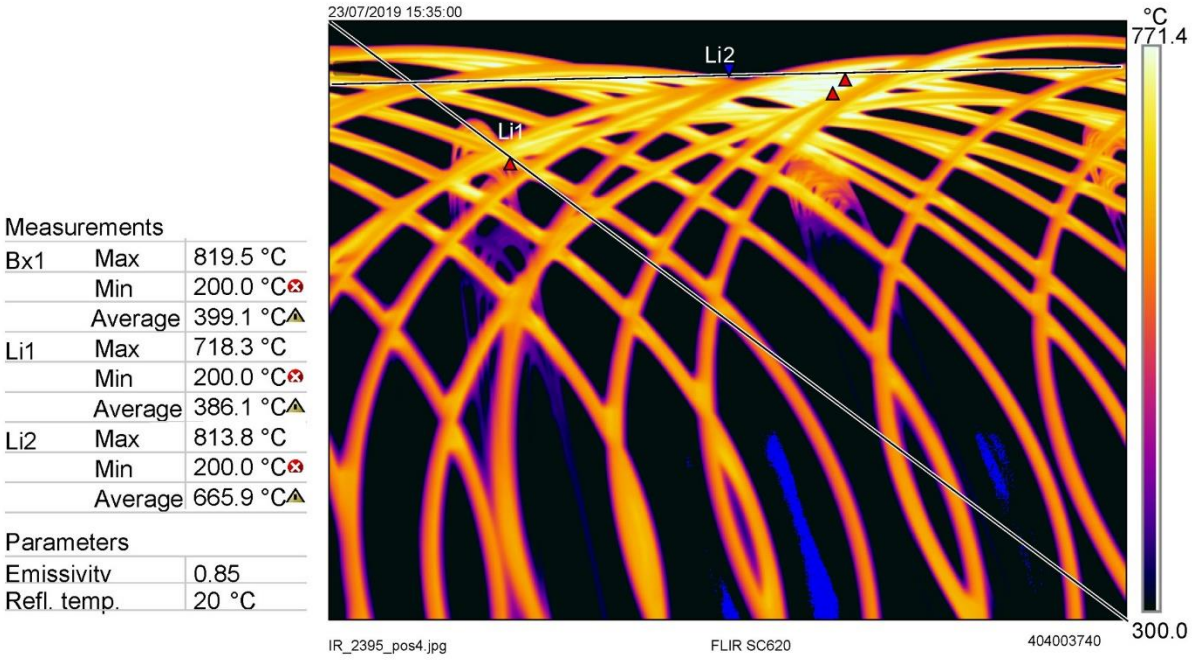

Figure A2-18 Thermal image measurement of the steel in the factory at position 4, 10 m from the laying head

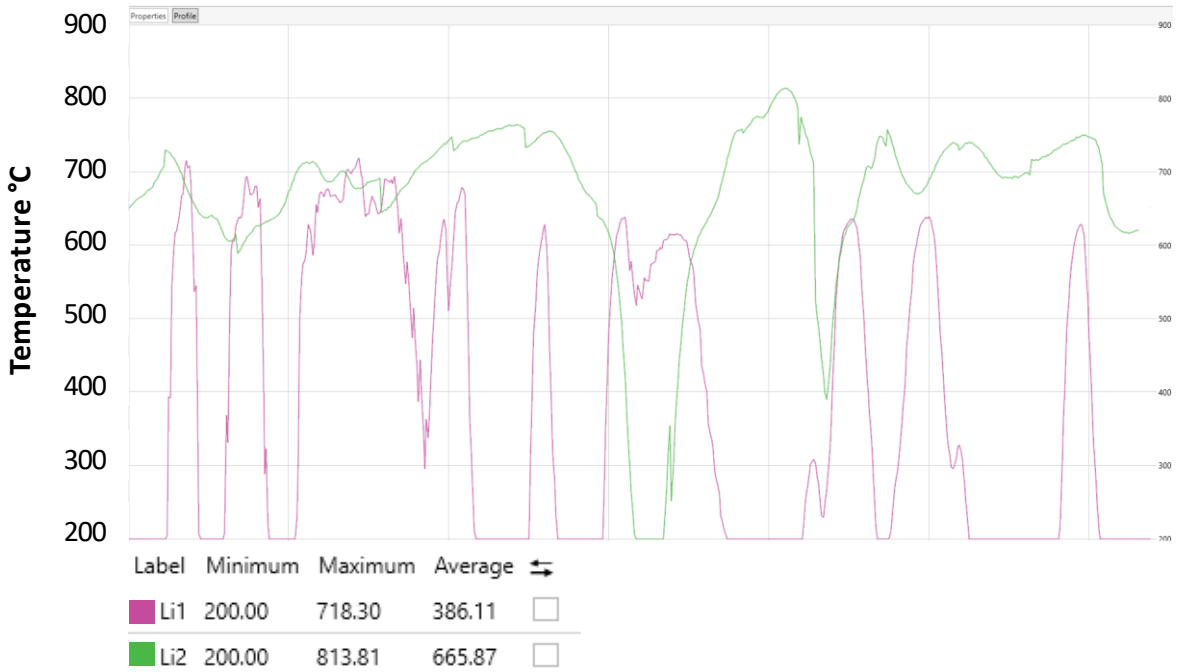

Figure A2-19 Temperature profile from line 1 and line 2 of the steel thermal image at position 4

The steel temperature 12.5 m away from the laying head is presented in Figure A2-20. The maximum steel temperature obtained from the measurements box Bx1 was 764 °C, while the average temperature was 380 °C. The steel temperature was varying around 600 °C while it varied between 600 °C and 760 °C at the edge as measured by the lines Li1 and Li2, respectively, in Figure A2-21.

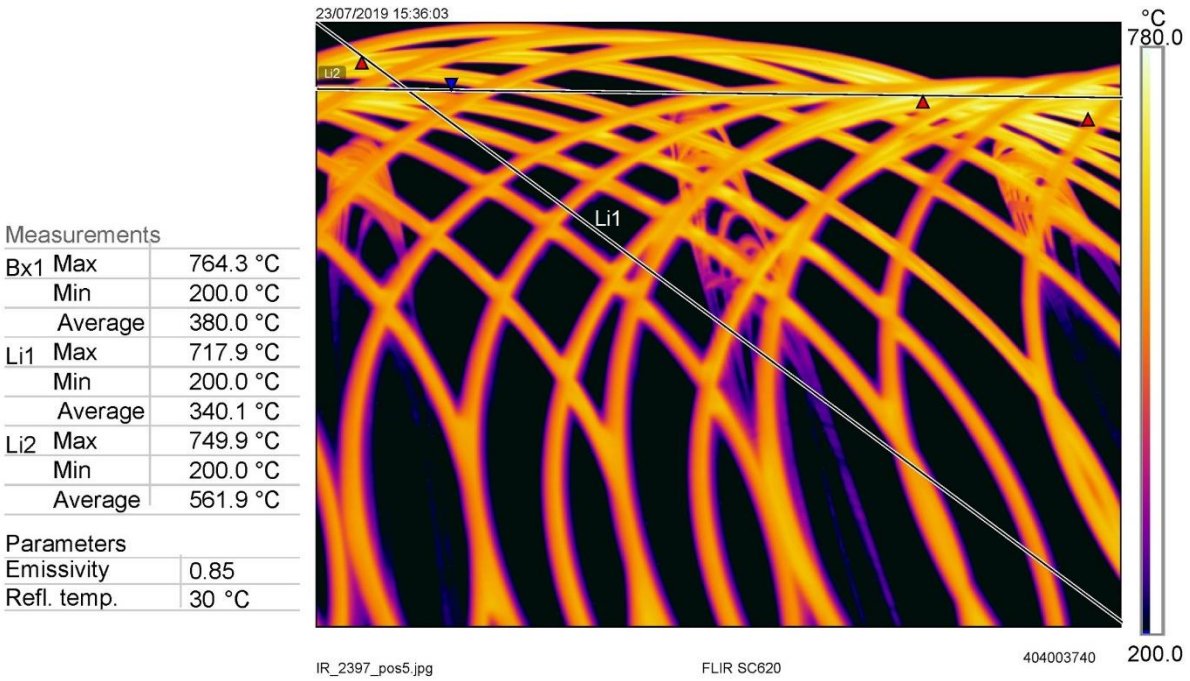

Figure A2-20 Thermal image measurement of the steel in the factory at position 5, 12.5 m from the laying head

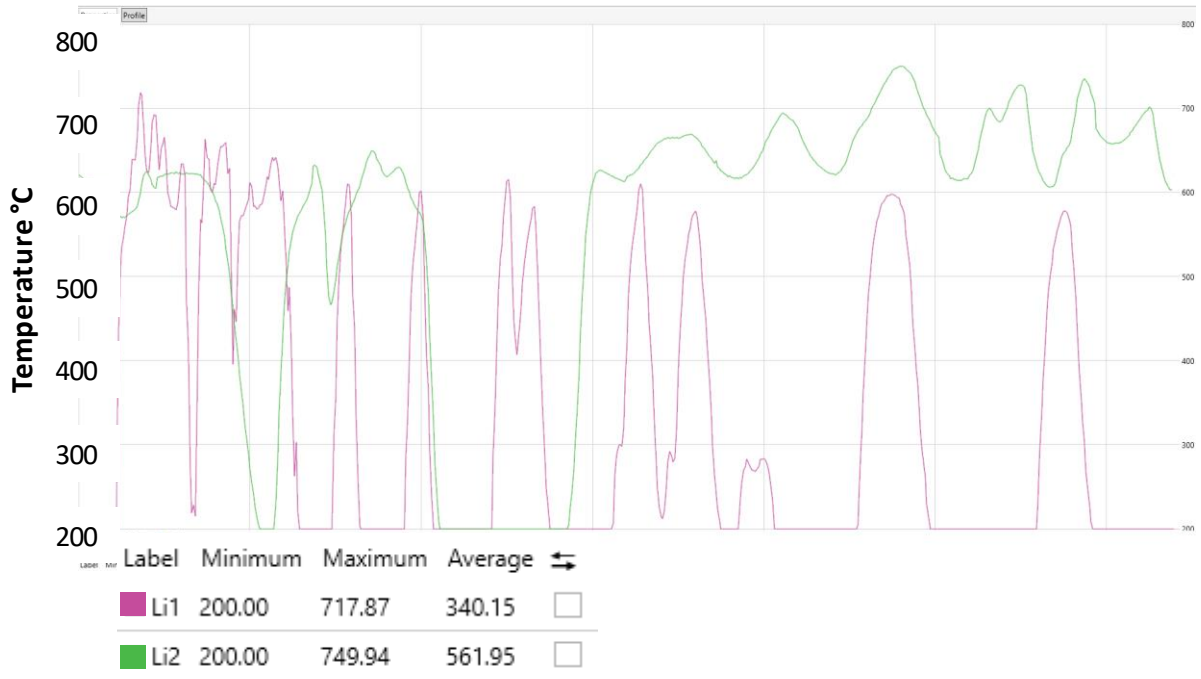

Figure A2-21 Temperature profile from line 1 and line 2 of the steel thermal image at position 5

It should be noted that the steel temperature change across the conveyor depends on the diameter of the steel and the quality required for the final product. The presented figures give an approximate description of the steel temperature and the average temperature of the conveyor.

The emitted heat from the steel is calculated accurately from the following:

$$Q_{rad,steel} = \int_{A} \int_{T_{1,steel}}^{T_{2,steel}} \int_{0}^{\infty} \varepsilon_{\lambda,T,steel} E_{\lambda,T}\, dA_{steel}\, dT_{steel}\, d\lambda \tag{7-14}$$

where T_1, T_2 are the temperature range of the steel on the conveyor.

The radiative heat emitted from the rollers can be calculated from:

$$Q_{rad,rollers} = \int_{A} \int_{T_{1,rollers}}^{T_{2,rollers}} \int_{0}^{\infty} \varepsilon_{\lambda,T,rollers}\, E_{\lambda,T}\, dA_{rollers}\, dT_{rollers}\, d\lambda \tag{7-15}$$

The radiative heat emitted from the gaps between the steel and the rollers can be calculated from:

$$Q_{rad,rollers} = \int_{A} \int_{T_{1,gaps}}^{T_{2,gaps}} \int_{0}^{\infty} \varepsilon_{\lambda,T,gaps} E_{\lambda,T}\, dA_{gaps}\, dT_{gaps}\, d\lambda \tag{7-16}$$

The total emitted heat from the conveyor is:

$$Q_{rad,conveyor} = Q_{rad,steel} + Q_{rad,rollers} + Q_{rad,gaps} \tag{7-17}$$

However, the equation can be simplified based on the thermal image analysis. The steel temperature was nearly uniform far from the edge showing a contrast between the steel temperature at the edge and the centre. Moreover, the rollers and the gap temperature did not exhibit wide variance in the temperature.

The equivalent average temperature of the conveyor as one heat source with a rectangle surface area can be calculated theoretically from energy conservation as expressed by:

$$\begin{aligned} Q_{rad,eq} &= \varepsilon_{eq} A_{conveyor} \sigma T_{H,eq}^4 \\ &= \varepsilon_{steel} A_{steel} \sigma \left(T_{steel,edge}^4 + T_{steel,centre}^4\right) \\ &+ \varepsilon_{rollers} A_{rollers} \sigma T_{rollers}^4 + \varepsilon_{gaps} A_{gaps} \sigma T_{gaps}^4 \end{aligned} \tag{7-18}$$

Equation (7-18) can be further simplified by considering the gaps as a black body and the steel as one structure with uniform emittance. However, the equivalent average hot source temperature is obtained from the factory thermal camera to simplify the modelling circuit.

Appendix 3: Experimental investigation on the pressure drop of the FHP condenser

Introduction

In this investigation, the pressure drop between the inlet and the outlet was measured. The pressure drop was measured using water as a cooling fluid at various flow rates.

Experimental Setup

The temperature of the steam inside the shell and tube was measured by installing thermocouples on the outer shell of the condenser section. The inlet and outlet coolant temperatures were also measured using K-type thermocouples. The water flow rate was measured using a flow meter (Omega FTB-371), air flow rate was determined by measuring the air velocity at the inlet of the system using (Testo 425) anemometer. Pressure transducers were used to measure the pressure drop of water, whilst the pressure drops of the air was measured using an anemometer. The experimental setup is shown in Figure A3-

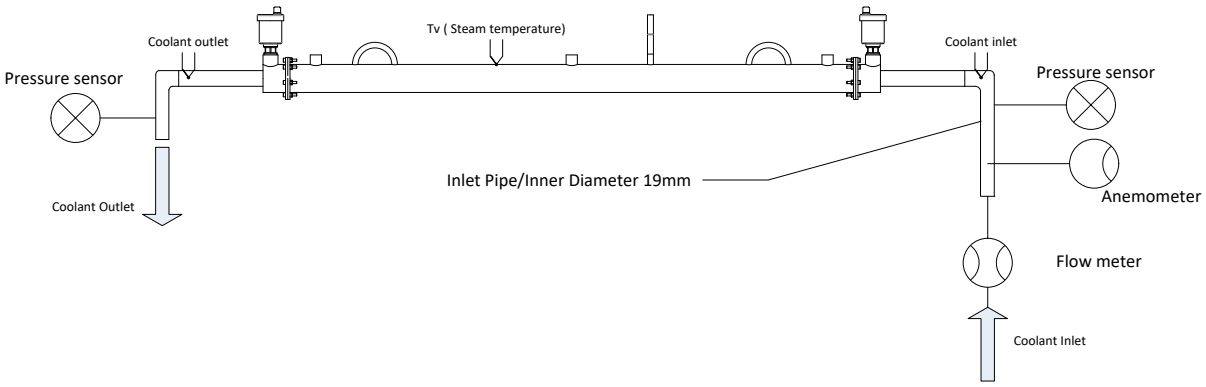

Figure A3-1 Experimental setup

The hydraulic resistance model is shown in Figure A3-2. The pressure drop results from the fittings of the pressure sensor at the inlet, elbow, sudden expansion piece and sudden change in the area from the expansion to the 8 pipes of the condenser, the sudden expansion in the area from the 8 pipes to the connection piece, the reducer, elbow, and the pressure sensor tee at the outlet.

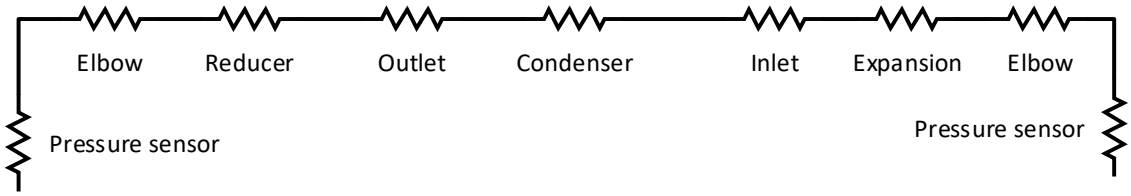

Figure A3-2 Model of the hydraulic resistances in the setup

Experimental procedure

The test using water as a coolant was divided to two basic conditions:

- The system was cooled at constant inlet temperature and constant steam temperatures at various flow rates.
- The HE performance was investigated by changing the coolant flow rate at constant electrical heat input. This results in changing the steam temperature depending on the overall heat transfer coefficient and the flow rate.

The heat transfer characteristics depend on the fluid physical properties and Reynolds number which depends on the mass flow rate.

Results

The pressure drop versus Reynolds number and the flow rate is presented in Figure A3-3 and Figure A3-4.

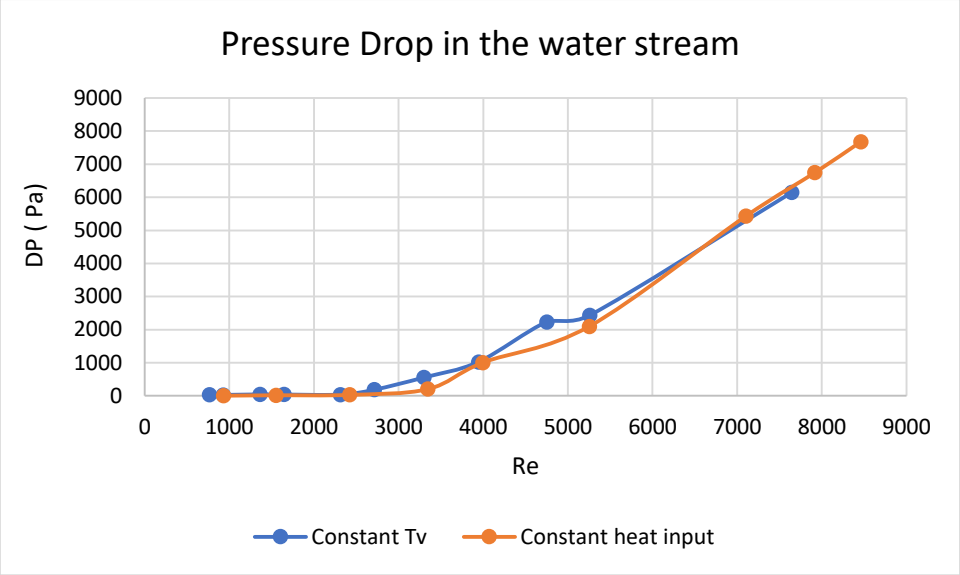

Figure A3-3 Pressure drop of the water stream through the FHP condenser

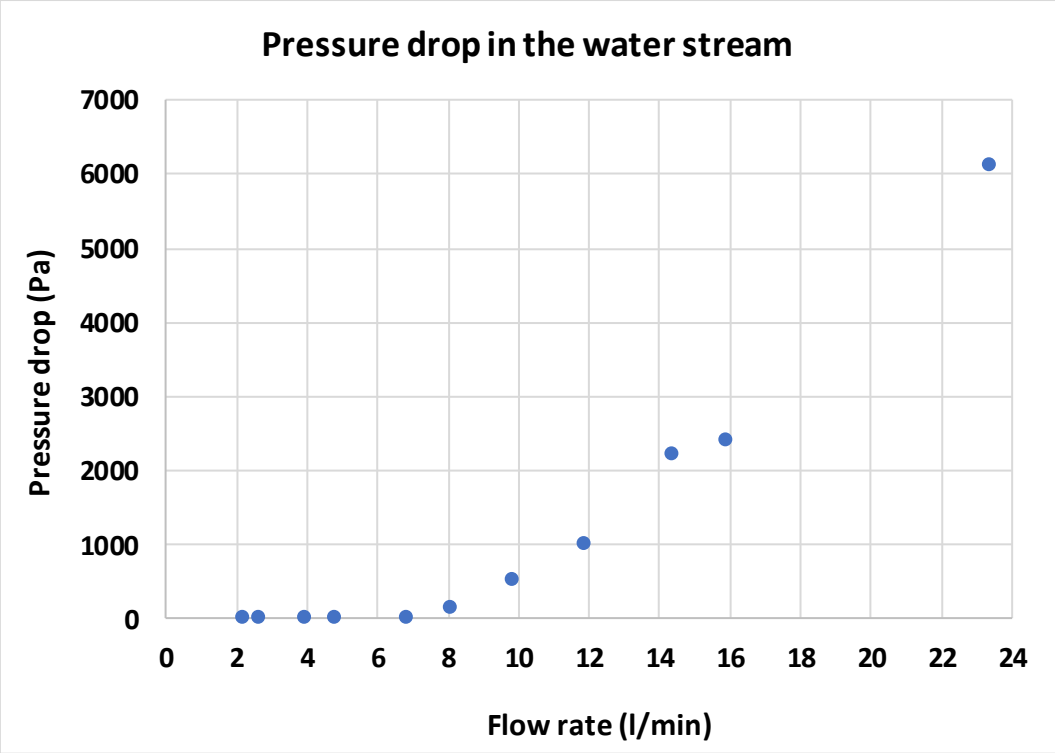

Figure A3-4 Pressure drop of water stream through the FHP condenser

Table A3-1 Water coolant, constant steam temperature

Flow Rate In 8 pipes	Flow Rate In one pipe	Steam (Water Vapour) Temperature	Water Inlet	Water Outlet	Heat transfer rate (based on DT)	Δ P Pressure Drop	Pipe Diameter	Velocity	Re	Test File
LPM	LPM	°C	°C	°C	(W)	(Pa)	m	(m/s)		
23.3	2.9125	57.22150479	19.3270956	20.98331497	2686.098791	6144.111776		0.965706	7643.98	DP2
14.3	1.7875	57.56661048	19.6008142	21.73063034	2119.523943	2231.986028		0.592686	4748.781	DP3
11.8	1.475	56.88231402	19.8864647	21.96978004	1710.613567	1023.652695		0.48907	3943.03	DP5
15.85	1.98125	56.83266248	19.7086533	21.54212854	2022.420441	2434.131737		0.656929	5258.468	DP6
9.8	1.225	56.76725903	20.1375267	22.27972415	1460.669696	552.3952096		0.406177	3296.498	DP7
6.8	0.85	56.47584107	20.7605477	22.5730988	857.4058738	36.42714571	0.008	0.281837	2312.151	DP8
8	1	56.57979376	20.5143846	22.5544988	1135.414991	183.8323353		0.331573	2711.738	DP24
4.75	0.59375	57.36010569	21.151497	23.70998443	845.1465561	38.82235529		0.196871	1644.163	DP9
3.9	0.4875	57.19313842	21.4515206	24.22721357	752.6973709	42.86427146		0.161642	1362.787	DP10
2.6	0.325	57.61807454	21.6855329	25.86639351	755.5461103	26.78868552		0.107761	928.2902	DP11
2.11	0.26375	56.82626188	22.5652222	26.43304371	567.0811664	35.77844311		0.087452	765.8361	DP12

Cooling by water at constant heat transfer rate (Constant electrical input)

Table A3-2 Water coolant, Constant heat input

Flow Rate In 8 pipes	Flow Rate In one pipe	Steam (Water Vapour) Temperature	Water Inlet	Water Outlet	Heat transfer rate (based on DT)	Δ P Pressure Drop	Pipe Diameter	Velocity	Re	Test File
LPM	LPM	°C	°C	°C	(W)	(Pa)	m	(m/s)		
2.2	0.275	71.00821262	22.8104794	40.13733373	2641.307098	3.542914172	0.008	0.091183	928.9676	DP13
4.05	0.50625	67.97071003	22.251295	31.50204631	2600.84363	16.46706587		0.167859	1550.054	DP14
6.8	0.85	64.88696168	20.9206569	26.35747784	2569.801888	28.39321357		0.281837	2420.248	DP23
9.7	1.2125	60.9185256	20.3128802	24.22027585	2635.983356	201.746507		0.402032	3344.761	DP16
11.8	1.475	59.57230599	19.8906657	23.08192814	2619.769111	1004.041916		0.48907	3995.29	DP18
15.7	1.9625	58.43336093	19.7547741	22.19923812	2670.482643	2097.904192		0.650712	5252.307	DP19
21.5	2.6875	57.39368797	19.5800585	21.30438762	2580.223634	5428.493014		0.891102	7101.925	DP20
25.7	3.2125	57.0532264	19.5747261	21.03031737	2603.726475	7679.491018		1.065178	8461.055	DP21
24	3	57.21012879	19.6053114	21.16603772	2607.032684	6742.51497		0.994718	7917.057	DP22

Conclusion

A shell and tube heat exchanger thermal performance was examined by cooling it by water. The effect of the heat input and the flow rate on the pressure drop was examined. It was observed that increasing the heat input results in increasing the pressure drop. In addition, the flow rate has a significant effect on the pressure drop.

Moreover, no pressure drop measurement was needed on the single heat pipe as the single heat pipe was laboratory scale only for investigation the heat transfer and the two phase heat transfer within the heat pipe.

Appendix 4: Best paper award certificate

chemengineering
an Open Access Journal by MDPI

CERTIFICATE
BEST PAPER AWARD

This certificate is given to

Mr. Sulaiman Almahmoud

Author of "Theoretical investigation on a single radiative laboratory-scale heat pipe heat exchanger"
International Conference on Advances in Energy Systems and Environmental Engineering (ASEE19)
Sponsored by *ChemEngineering*, MDPI

MDPI Academic Open Access Publishing since 1996
Basel, July 2019

Dr. Shu-Kun Lin
President & Publisher
MDPI